Asymmetric Mixed-Valent Systems: Synthesis and Analysis of their Spin and Charge Distribution

Dissertation

for the academic degree of doctor in the natural sciences

(Dr. rer. nat)

by

Christopher Hassenrück

at the

Universität Konstanz

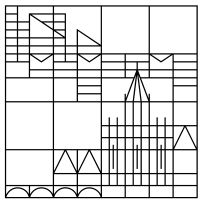

Section of Mathematics and Natural Sciences

Department of Chemistry

Konstanz, 2019

Konstanzer Online-Publikations-System (KOPS)
URL: http://nbn-resolving.de/urn:nbn:de:bsz:352-2-g19en5g9vwzv7

Tag der mündlichen Prüfung: 14.06.2019
1. Referent/Referentin: Prof. Rainer F. Winter
2. Referent/Referentin: Prof. Sebastian Polarz

This work was prepared from October 2015 to December 2018 in the research group of PROF. RAINER F. WINTER, Department of Inorganic Chemistry, University of Konstanz, Germany.

“The more original the discovery, the more obvious it seems afterward.”

ARTHUR KOESTLER

Danksagung

Als erstes möchte ich mich ganz herzlich bei Prof. RAINER WINTER bedanken. Durch ihn war es mir möglich einerseits meine Masterarbeit als dann auch die anschließende Doktorarbeit über dieses spannende Thema anzufertigen. Vielen Dank für die Aufnahme in die Arbeitsgruppe und besonders für die hervorragende Betreuung! Ich werde diese tolle Zeit nie vergessen. Weiterhin möchte ich mich bei Prof. WINTER für die Übernahme des Erstgutachtens bedanken. Des Weiteren möchte ich mich bei Prof. SEBASTIAN POLARZ für die Übernahme des Zweitgutachtens bedanken, sowie Prof. VALENTIN WITTMANN für die Übernahme des Prüfungsvorsitzes.

Natürlich ist die Arbeit ohne tolle Arbeitskollegen nicht vorstellbar. Zuallererst möchte ich mich bei Dr. STEFAN SCHEERER bedanken, der mich in sein damaliges Labor aufgenommen hat, welches ich dann quasi „vererbt“ bekomme habe. Weiterhin möchte ich mich besonders bei den weiteren „Bewohnern“ von L748 PATRICK ANDERS, STEFAN BITTER und RONJA SCHNECK für die gute Zeit bedanken. Ihr hattet stets ein offenes Ohr und ein gutes Auge für jedwede Probleme, sei es in der DFT, synthetisch, organisatorisch oder auch in Designfragen. Es freut mich auch, dass mein ehemaliger Bachelorstudent ANDRÉ MANG jetzt in dieses Labor eingezogen ist. Diesem möchte ich ganz herzlich danken, dass ich seine damalige Bachelorarbeit betreuen durfte und natürlich für seine tollen Ergebnisse.

Grundsätzlich jeder in der Arbeitsgruppe, ob „Ruthenium“- „Eisen“- oder „Platin-Mensch“, hatte immer ein offenes Ohr für synthetische, spektroskopische, elektrochemische oder auch persönliche Probleme. Das ist nicht selbstverständlich und daher möchte ich meinen Dank dafür besonders hervorheben.

Bedanken möchte ich mich auch bei den fleißigen Korrekturlesern dieser Arbeit CHRISTINA MUCK und JESSICA HASSENRÜCK.

Mit Rat und Tat stand auch immer Dr. MICHAEL LINSEIS zur Verfügung. Selbst wenn man ihn zum tausendsten Mal am Tag fragt, war er immer bereit zu helfen, sei es in der DFT, im Praktikum, in Sachen Kristallstrukturen, in Computerangelegenheiten und bei allgemeinen Verständnisfragen.

Für NMR Messungen bedanke ich mich bei ANKE FRIEMEL und ULRICH HAUNZ. BERNHARD WEIBERT, möchte ich danken für die röntgenographischen Messungen und Dr. SERIHY DEMESHO aus Göttingen für die Messungen der Mößbauerspektren auch wenn nicht alle hier in diese Dissertation aufgenommen werden konnten.

Für die interessanten Kooperationen bedanke ich mich bei Prof. BENNO BILDSTEIN von der Universität Innsbruck und Prof. NICOLAS LONG vom Imperial College, London und

gleichermaßen bei deren ehemaligen Doktoranden Dr. STEFAN VANICEK und Dr. LUCY WILSON aber auch Dr. NORA-ANN WESTRATE von der University Pretoria, Südafrika.

Meiner Frau JESSICA möchte ich von ganzem Herzen danken, dass sie immer für mich da ist und mir in allen Lebenslagen zur Seite steht. Erst durch sie wurden die letzten Jahre zu etwas ganz Besonderem.
Ein Dankeschön geht auch an meine Familie und Freunde für den Beistand in den letzten Jahren.
Zu guter Letzt danke ich der DFG für die Finanzierung dieser Arbeit und den Zugang zum Rechencluster des BWHPC.

Table of contents

Danksagung **8**

List of Abbreviations **13**

List of Synthesized Compounds **14**

1. Introduction **17**

1.1. The Origins of Organometallic Chemistry 17
1.2. Mixed-Valent Compounds 22
1.3. Classification System by ROBIN and DAY 23
1.4. Alkenylruthenium Complexes 29
1.5. Asymmetric Dinuclear Complexes with π-Conjugated Bridging Ligands 33
1.6. Heterobimetallic Complexes derived from Ethynyl-Metallocenes 39
1.7. Mixed-Valent Triarylamine-Compounds 43
1.8. Valence Tautomerism 47

2. Objectives **53**

3. Publications **55**

3.1. Record of Contributions 55
3.2. Paper 1: Oxidized Styrylruthenium-Ferrocene Conjugates: From Valence Localization to Valence Tautomerism 57
3.2.1. Abstract 58
3.2.2. Introduction 58
3.2.3. Results and Discussion 60
3.2.4. Synthesis and Characterization 60
3.2.5. Spectroscopic Studies on the Oxidized Forms 62
3.2.6. Conclusions 65
3.2.7. Experimental Section 65
3.2.9. Supporting Information 69
3.3. Paper 2: Manipulation and Asessment of Charge and Spin Delocalization in Mixed-Valent Triarylamine Vinylruthenium Conjugates 84

3.3.1. Abstract 85
3.3.2. Introduction 85
3.3.3. Results and Discussion 86
3.3.4. Conclusions 92
3.3.5. Experimental Section 93
3.3.6. Supporting Information 98
3.4. Paper 3: Mixed-Valent Ruthenocene-Vinylruthenium Conjugates: Valence Delocalization Despite Chemically Different Redox Sites 138
3.4.1. Abstract 139
3.4.2. Introduction 139
3.4.3. Synthesis and Characterization 140
3.4.4. Electrochemistry 141
3.4.5. IR-Spectroelectrochemistry 142
3.4.6. EPR Spectroscopy 143
3.4.7. UV/vis/NIR Spectroscopy 144
3.4.8. $\Delta E_{1/2}$ and the Electronic Coupling 146
3.4.9. Summary and Conclusion 146
3.4.10. Experimental Section 147
3.4.11. Supporting Information 152
4. Summary 203
5. Outlook 211
6. Zusammenfassung 213
7. List of References 221
7.1. Chapter 1 Introduction 221
Chapter 3.2 Publication 1 227
7.2. Chapter 3.3 Publication 2 230
7.3. Chapter 3.4 Publication 3 236
8. Appendix: Publications as co-author 240

List of Abbreviations

acac	acetylacetonate
CO	carbon monoxide
Cp	η^5-cyclopentadienyl
Cp*	1,2,3,4,5- η^5-pentamethylcyclopentadienyl
CR	charge resonance
DCE	1,2-dichloroethane
DCM	dichloromethane
DFT	density functional theory
EPR	electron paramagnetic resonance
^{i}Pr	isopropyl
HOMO	highest occupied molecular orbital
HOSO	highest occupied spin orbital
IR	infrared
IVCT	inter valence charge transfer
LMCT	ligand to metal charge transfer
LUMO	lowest unoccupied molecular orbital
LUSO	lowest unoccupied spin orbital
Me	methyl
MLCT	metal to ligand charge transfer
NIR	near infrared
NMR	nuclear magnetic resonance
MO	molecular orbital
TBA	tetra-*n*-butylammonium
^{t}Bu	*tert*. butyl
TD-DFT	time dependent density functional theory

List of Synthesized Compounds

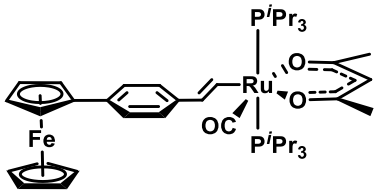

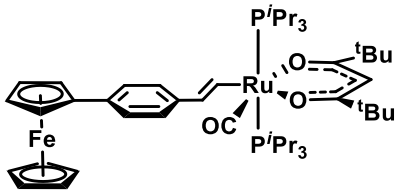

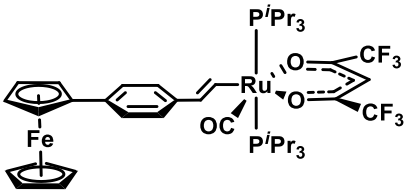

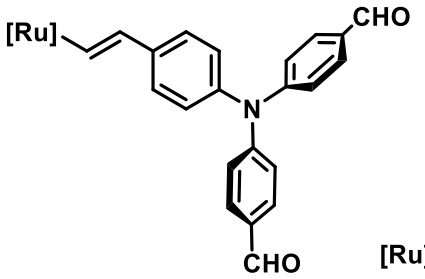

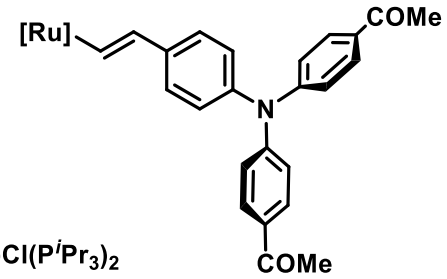

[Ru] = Ru(CO)Cl(P^{i}Pr$_3$)$_2$

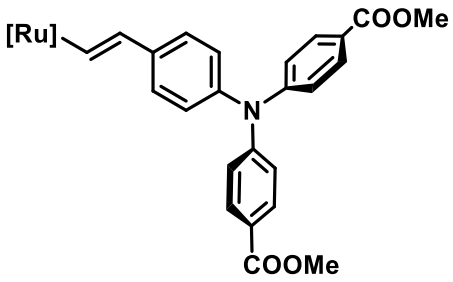

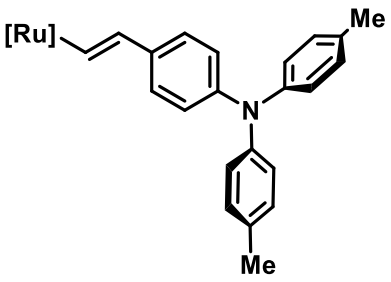

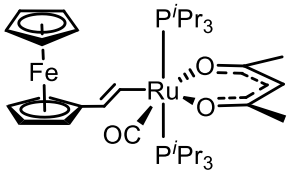

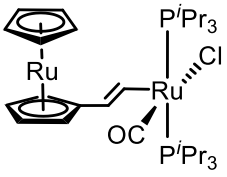

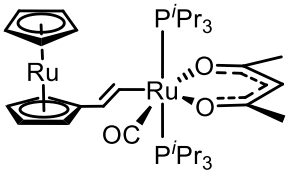

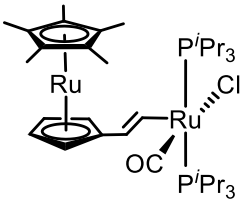

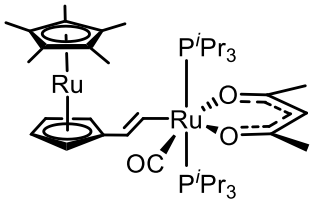

Other synthesized final compounds, which will be published soon:

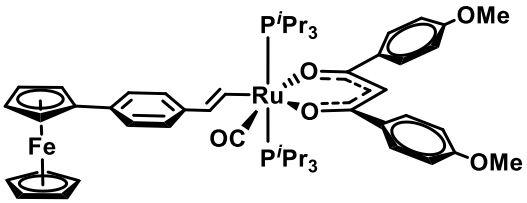

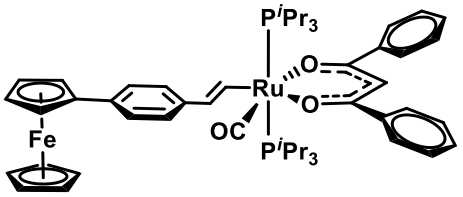

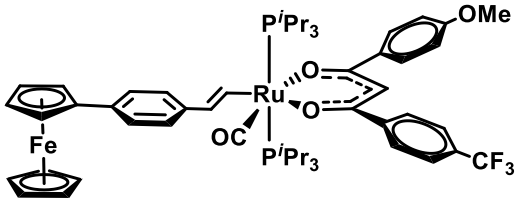

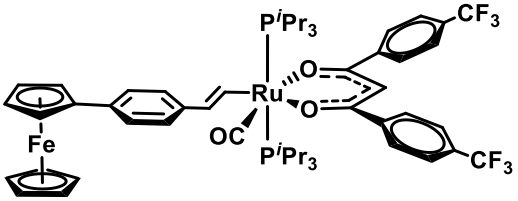

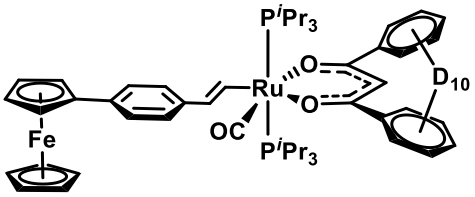

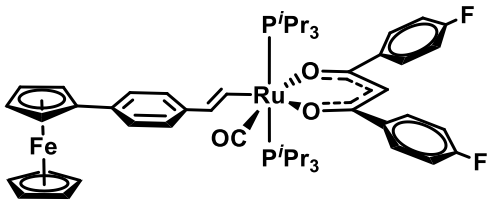

1. Introduction

1.1. The Origins of Organometallic Chemistry

In the early 19th to 20th century, the first advances in „Organometallic Chemistry" had essentially occurred in England, the USA and Germany. It was in a small pharmacy in Paris in 1760, however, where LOUIS CLAUDE CADET worked on cobalt-containing dyes, using arsenic-containing salts for their preparation. Ultimately, "Cadet's fuming liquid" tetramethyldiarsine marked the birth of Organometallic Chemistry, which was systematically investigated by ROBERT BUNSEN in 1835. Yet, most of today's chemists would rather avoid to be close to this toxic compound also known as "cacodyl" derived from the Greek words kakodes (evil-smelling) and hyle (matter).[1]

The "Zeise salt" $K[PtCl_3(\mu^2\text{-}C_2H_4)]$, which represents the first π-complex in history, followed in 1827.[2] Noteworthy are also EDWARD FRANKLAND's diethyl- and dimethylzinc (1846) or VICTOR GRIGNARD's organomagnesium compounds (1900).[3,4] A process for purifying Nickel, which is still used today, was created by LUDWIG MOND in 1890, where carbon monoxide reacts reversibly with Ni(0) forming the nickel carbonyl complex $Ni(CO)_4$.[5]

The most interesting and groundbreaking discovery, rendering "Organometallic Chemistry" an independent and distinct discipline in chemistry, was made in 1951 by THOMAS KEALY, PETER PAUSON and SAMUEL MILLER by reacting cyclopentadienyl magnesium bromide with $FeCl_3$.[6] The scientists expected a conversion to fulvalene, but isolated an orange solid instead later to be named "ferrocene" (Fig. 1.1), with respect to the bound iron as well as its aromatic behavior similar or even superior to benzene.

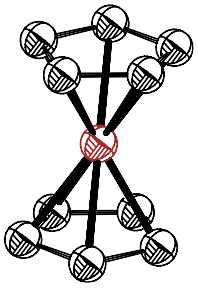

Fig. 1.1: "Ferrocene", bis(η^5-cyclopentadienyl)iron^{II} (protons omitted for clarity).[7]

For groundbreaking research on "metallocenes", i.e. complexes consisting of two cyclopentadienide anions (Cp^-) η^5-coordinated to a metal center, and the structural identification of ferrocene, ERNST FISCHER and GEOFFREY WILKINSON were awarded the Nobel Prize in 1973.[8] At the time of its discovery, the structure and properties of

ferrocene were both unexpected and unusual. Ferrocene is air stable to up to 400 °C, it reacts like an activated superarene with respect to the ease with which it undergoes electrophilic substitution reactions, and it displays a reversible oxidation at around 400 mV *vs*. a saturated calomel electrode.[9] The structure of ferrocene results from the various metal-ring interactions of σ-, π- and δ-symmetry. The orientation of the two Cp ligands (staggered vs. eclipsed) does not critically affect the bonding. The energy barrier for rotation along the Cp-Fe-Cp axis is very low with only 10.2 kJ/mol. Considering the nodal planes, it is quite easy to demonstrate the relative energies of the five π-molecular orbitals (MOs) of a cyclopentadienide ligand (Fig. 1.2). Combining these MOs with the iron(II) orbitals results in the MO diagram shown in Fig. 1.3.

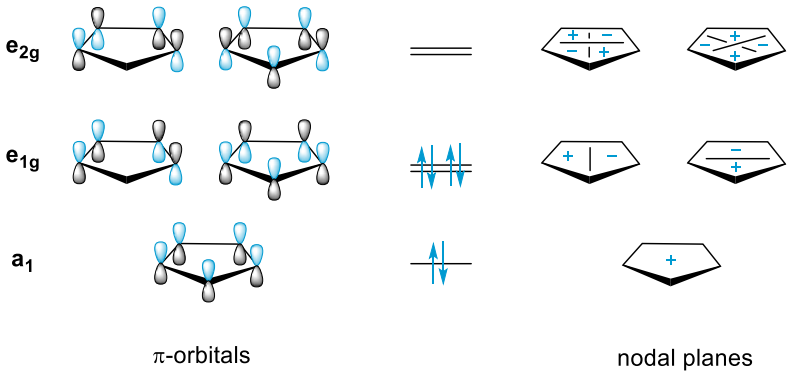

Fig. 1.2: π-Orbitals and nodal planes of a Cp^- ligand.

The iron atom provides nine atomic orbitals (one *s*-, three *p*- and five *d*-orbitals) to the MO diagram, whereas the two Cp-ligands contribute each five molecular orbitals (a_1, e_{1g} and e_{2g}, Fig. 1.2) . Thus, the MO scheme of ferrocene must consist of 19 molecular orbitals. In a sandwich complex like ferrocene, two orbitals of the Cp-ligands must be combined to form “symmetry-adapted linear combinations” (SALCs). The MOs with σ-symmetry in ferrocene originate from the overlap of two SALC a_1 Cp- orbitals (a_{2g} and a_{2u}) and the *s*-, p_z-, and d_{z^2} -orbitals of the iron atom. These combine to the occupied a_{1g} and a_{2u} MOs lowest in energy and the non-bonding a_{1g} orbital, which forms the HOMO of ferrocene as well as the antibonding σ*-orbitals a_{1g}* and a_{2u}*. The π-orbitals are generated by the overlap of the orbitals with one nodal plane. The iron atom provides the d_{yz}-, d_{xz}-, p_y-, and p_x- orbitals and the Cp-ligands each their two e_{1g}-orbitals contributing to their paired e_{1g}- and e_{1u}-MOs. In the MO diagram, the bonding π-orbitals are the two degenerate e_{1g}-, the two degenerate e_{1u}-, the antibonding degenerate e_{2u}*-, e_{2g}*- and the degenerate e_{1u}*-MOs. The δ-orbitals are finally formed by the orbitals with two nodal planes. The resulting δ–orbitals are the two degenerate e_{2g}- and the two degenerate e_{1g}*-orbitals. The two Cp-SALCs with e_{2u}-symmetry have no metal orbital of appropriate symmetry available. The HOMO-1 is thus formed by the two degenerate

bonding e_{2g} orbitals and on the other hand the LUMO by a strongly antibonding e^*_{1g} orbital. The strongly metal centered a_{1g} and e_{2g} orbitals are nearly nonbonding and are stabilized by the Cp π^* orbitals. These two may be reversed in energy, depending on the metal and oxidation state.[10]

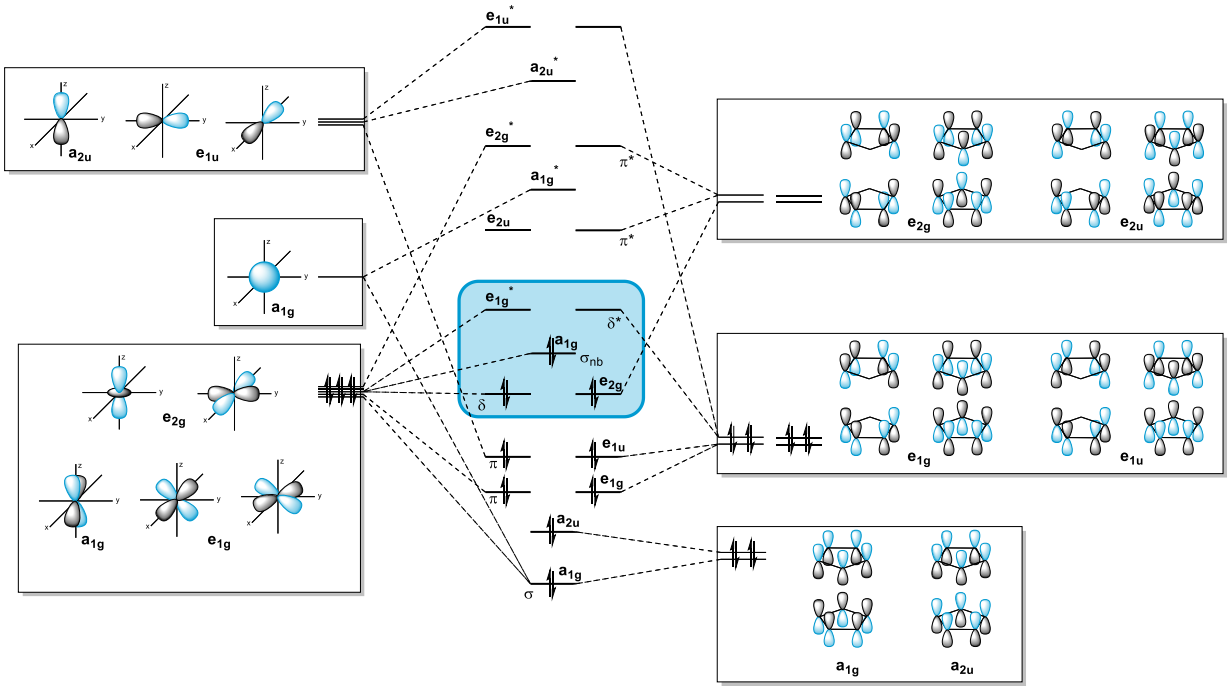

Fig. 1.3: Molecular orbital scheme of ferrocene.

Further, ferrocene's good solubility in a great variety of organic solvents rendered it the IUPAC recommended standard for electrochemical experiments in non-aqueous solvents. Due to the dependence of ferrocene's oxidation potential to the used solvent, its oxidation potential ranges from +583 mV in trifluoroethanol to +293 mV in water. Decamethylferrocene, consisting of two 1,2,3,4,5-pentamethylcyclopentadienide units (Cp*) and Fe^{II}, has been recognized as a better candidate for referencing as its half-wave potentials is much less affected because of its sterical demand. Moreover, it can also be utilized in easily oxidized solvents, e.g. in *N*-methylaniline or *N,N*-dimethylaniline, which is not possible for ferrocene.[11] Nevertheless, ferrocene is well established and still withstands any other complex to take its place in electrochemistry.

Although ferrocene's discovery is more than 65 years back in time, the cover picture of issue 8 of the journal *Science* from 2016 demonstrates that ferrocene and its many derivatives are still of high current interest.[12] Oligomeric rings consisting only of ferrocene (Fig. 1.4) exemplify how the beauty and versatility of ferrocene still fascinates chemists all over the world in nearly all fields of research, from traditional organometallic chemistry over catalysis to biological applications in drugs.[13]

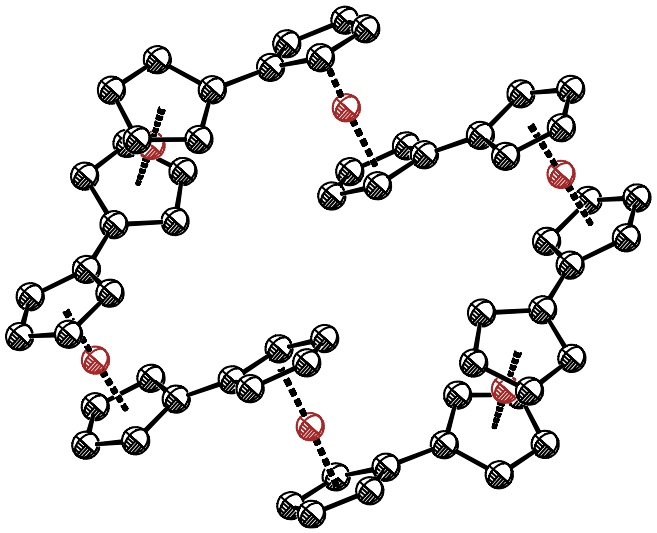

Fig. 1.4: Six-membered ring consisting of 1,1' connected ferrocenes (protons omitted for clarity).[12]

Until today, a great variety of metallocenes has been synthesized. These congeners of ferrocene differ in their physical and chemical properties due to their deviating valence electron counts.

Only one year after the discovery of ferrocene, ruthenocene, bis(cyclopentadienyl)Ru^{II}, the higher homologue of ferrocene was published.[14] It displays similar chemical behavior like its lighter congener ferrocene. Ruthenocene exhibits even higher thermal stability and stronger bonding interactions between the Ru atom and the two Cp^- ligands.[15] Peculiar is, however, that the oxidation potential of ruthenocene is surprisingly high with 560 mV positive of that of the ferrocene/ferrocenium couple. In addition, the ruthenocene cation tends to form dimers and is highly reactive towards even weak nucleophiles. Dimerization to a Ru-Ru bonded dimer can be circumvented by introducing bulky substitutents at the Cp ring whereas follow reaction to $[Cp_2Ru(L)]^+ X^-$ or Cp_2RuX, (X= anionic ligand or counterion) can only be suppressed when using very weakly coordinating anions and solvents.[16]

Cobaltocene, bis(cyclopentadienide)Co^{II}, has also attracted a lot of attention. Like ferrocene, cobaltocene is electroactive. It is reversibly oxidized to 18 valence electron cobaltocenium cation, and, under strictly anaerobic and aprotic conditions, reversibly reduced to the 20 valence electron cobaltocenide anion. In particular, the chemistry of the 18 valence electron cobaltocenium ion, which is isoelectronic to ferrocene, has been well explored. The variety of reactions with the cobaltocenium cation rage from typical organic substitution reactions to copper catalyzed “click” reactions. Still, chemical reactions on cobaltocenium ions are much less developed in comparison to ferrocene

chemistry. The main reason is the deactivating nature of the positive charge of the cobaltocenium moiety, which suppresses some established methods in organic or ferrocene chemistry. The reviews of SHEATS and TANG give an overview over the developed reaction library, which is still expanding today.[17,18]

Monosubstituted cobaltocenium ions can be synthesized using an S_N2-type reaction, e.g. with lithiated trimethylsilyl acetylene, yielding in an η^5/η^4 Co(I) complex containing the nucleophile in the exo position. The final product is then formed by selective hydride abstraction (Fig. 1.5).

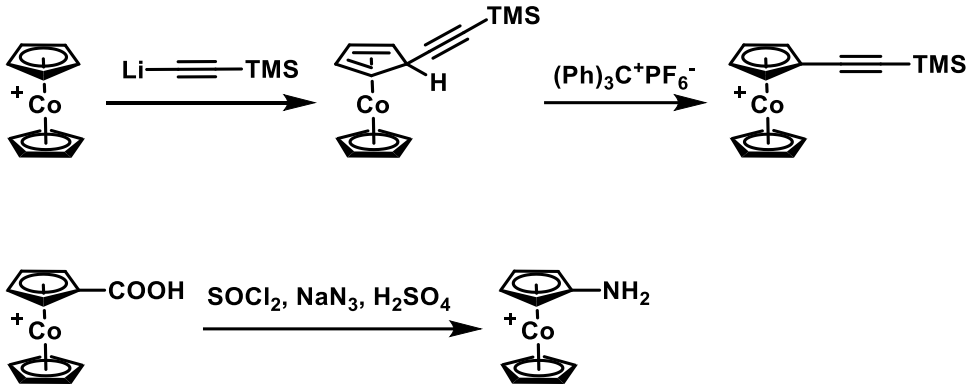

Fig. 1.5: Synthesis of a monosubstituted cobaltocenium derivative (top) and CURTIUS rearrangement from cobaltocenium carboxylic acid to the respective amine (bottom).[19,20]

Valuable cobaltocenium derivatives like aminocobaltocenium hexafluorophosphate, which is synthesized from the respective carboxylic acid by CURTIUS rearrangement (Fig. 1.5), can also undergo some typical organic syntheses like acylation- or SCHIFF-base reactions for ligand design or biorthogonal chemistry.[19,20] Cobaltocenium salts may also be synthetically derivatized to halogenated chloro-, bromo-, iodo- and azidocobaltocenium by a dediazoniation reaction of cobaltoceniumdiazonium bis(hexafluorophosphate).[20] This starting material can also give rise to a remarkable electron rich mesoionic metalloceno carbene, which is able to stabilize Au^{III} (Fig. 1.6).

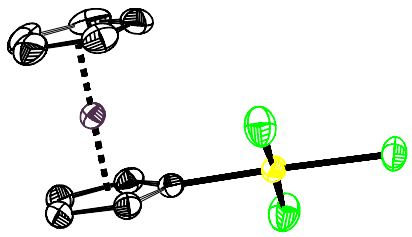

Fig. 1.6: Cobaltocenylidene Au^{III} complex by BENNO BILDSTEIN (protons omitted for clarity).[21]

This cobaltocenylidene demonstates electronic properties like cyclic (amino)(alkenyl/aryl)carbenes, but exhibits stronger basicity and polarity.[21]

1.2. Mixed-Valent Compounds

Chemists all over the world have always been intrigued by compounds that are strongly colored or electrically conductive. Many colorful compounds found in geology and in inorganic chemistry belong to the class of “mixed-valent compounds”. The first artificial mixed-valent compound, i.e. a compound containing an element which is present in more than just one oxidation state, was $K[Fe^{II}Fe^{III}(CN)_6]$. It was first synthesized long before ferrocene in 1706 by JOHANN JACOB DIESBACH and given the name “Prussian Blue.[22] Today, mixed-valent compounds are still a major topic in organic, inorganic and organometallic chemistry with over 1300 publications related to mixed-valency just in the past 10 years.

The late 1960s witnessed a moment of glory for mixed-valent complexes. HENRY TAUBE as the experimental chemist and NOEL HUSH as the theoretical chemist contributed greatly. They analyzed the paradigmatic mixed-valent complex $[(NH_3)_5Ru(\mu\text{-pyrazine})Ru(NH_3)_5]^{5+}$, that became known as the “Creutz-Taube Ion”. This complex is now considered as the archetype of mixed-valency and is still the most cited compound of this class (Fig. 1.7).[23-26] The originary Creutz-Taube ion was soon followed by a host of congeners with other bridging ligands than pyrazine.

The Creutz-Taube ion was intended as a model system for answering fundamental questions about intervalence charge transfer (IVCT), its intensity and the connection between IVCT band shape and the electron transfer rate. The anticipated IVCT band, meaning a band originating from a charge transfer from one metal atom to the other across the bridge, was much narrower than expected. Also its shape was rather asymmetric and not Gaussian-line shaped and characterized by a greater oscillator strength. Today, it is generally accepted that these unexpected properties are due to valence delocalization (vide infra). Mixed-valent compounds are thus quite complex systems that yearn for a thorough investigation and understanding.

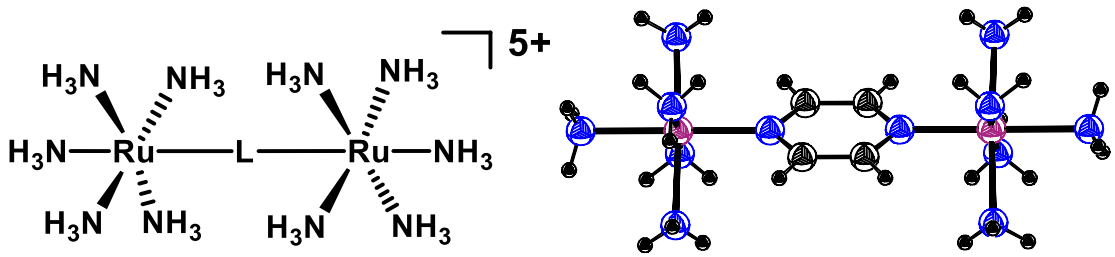

Fig. 1.7: The Creutz-Taube Ion and its chemical and crystal structure (counter ions are omitted for clarity).[27]

The classical Ru-L-Ru motif was later also augmented in terms of asymmetric substitution with osmium and rhodium, providing insight into asymmetrically substituted

analogs of the Creutz-Taube ion.[28] Still, the Creutz-Taube Ion is not an organometallic complex as there are no metal-carbon bonds present.

The first organometallic mixed-valent complex was the biferrocenium monocation, published in 1970 by DWAINE COWAN: (Fig. 1.8).[29]

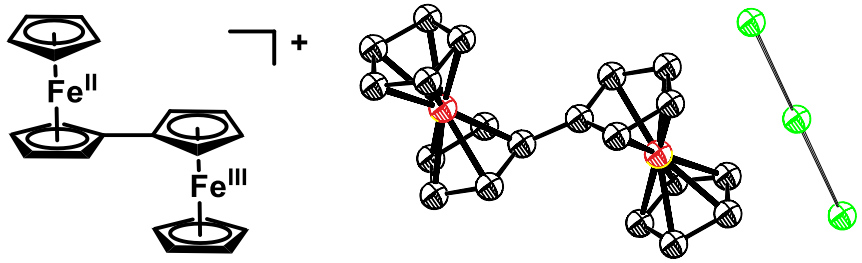

Fig. 1.8: The first organometallic mixed-valent compound: The diferrocenium cation (left) and the crystal structure of the biferrocenium triiodide salt (right, protons omitted for clarity).[30]

This mixed-valent state and the delocalization of the charge and the unpaired spin is very important in order to understand the electronic communication between the redox sites. In 1967, MELVIN B. ROBIN and PETER DAY[31] established a classification system for mixed-valent compounds according to the degree of electronic coupling and ground-state delocalization. This classification is discussed in the following section.

1.3. Classification System by ROBIN and DAY

Background research on oxidation and reduction mechanisms, both experimental and theoretical, was mainly performed in the 1950's to 1975's. The theories established by ARTHUR MARCUS and NOEL HUSH were dominant in this period of time.[32-35] ROBIN and DAY introduced a classification system, which subdivides mixed-valent compounds into three different classes (Fig. 1.9).[31]

Class I: The charge is fully localized at one redox site. No interaction or resonance between both redox moieties is possible. In fact, a distinct charge separation is observed.
Class II: Key attribute of molecules within this class is the partial charge localization with the possibility of sharing the charge among the subunits due to moderate electronic coupling through the bridge.
Class III: Characteristic for this class is the complete charge delocalization amongst all subunits of the mixed-valent system, which makes both metal centers indistinguishable in spectroscopic measurements on all time scales. The frontier molecular orbitals extend across the entire molecule and contain dominant contributions from all major redox subunits.

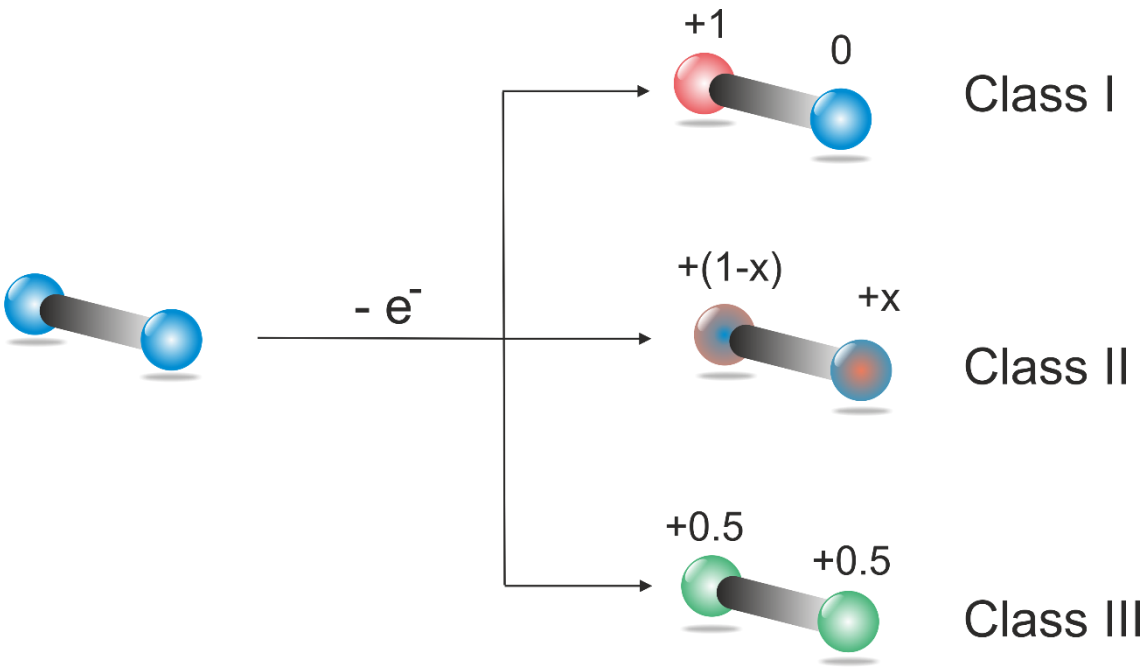

Fig. 1.9: Two redox sites symbolized as spheres, connected by a bridge (stick), form upon oxidation the ROBIN and DAY Classes, from localized Class I to charge delocalized Class III.

Later on, MEYER extended this classification by a borderline Class II/III, which represents a hybrid subdivision with characteristics of mixed-valent systems of Class II as well as Class III.[36,37] For systems belonging to this class, the electronic coupling is sufficiently strong to maintain full charge and ground-state delocalization in solvents of low polarity and the absence of strong ion-pairing. Highly polar solvents or ion-pairing effects, however, stabilize a polar ground state with charge localization at one side, thus driving these systems into the Class II regime.

The major aspect of charge and spin delocalization in the electronic ground state of a mixed-valent system is the ratio between the electronic matrix element H_{AB}, which describes the electronic coupling between the two sites, and the reorganization energy λ, which is the sum of inner and outer reorganization energy: $\lambda = \lambda_i + \lambda_o$.

The inner reorganization energy λ_i can be described as the sum of all energies necessary to change the bond lengths and angles during electron transfer (Eq. 1.1). It is determined by force constants and bond lengths of the interacting states, which can be gathered by crystallographic data or by theoretical modeling.[38] One should mention, however, that the accuracy of the computations decrease the more bonds are involved.

$$\lambda_i = \sum_j \left(\frac{f_i(D-A)_j \cdot f_i(D^{+\cdot} - A^{-\cdot})_j}{f_i(D-A)_j + f_i(D^{+\cdot} - A^{-\cdot})_j} \right) \cdot (\Delta q_i)^2$$

Eq. 1.1: Inner reorganization energy λ_i: f_i describes the force constant of the lattice vibrations i in the vibronic state j of the mixed-valent compound and Δq_i the change in bond length before and after the electron transfer.

λ_o, the outer reorganization energy, describes the energy needed for the adaption of a new solvent orientation during the electron transfer process. This energy can be calculated from the donor and acceptor radii, their distance and the optical dielectric constant (refractory index) and the dielectric constant (Eq. 1.2) of the respective solvent.

$$\lambda_o = \frac{(\Delta e)^2}{4\pi\varepsilon_0}\left[\frac{1}{2a_1} + \frac{1}{2a_2} + \frac{1}{r}\right]\left[\frac{1}{n^2} - \frac{1}{\varepsilon}\right]$$

Eq.1.2: Outer reorganization energy λ_o: a_1 and a_2 are the equilibrium radii of the two interacting redox sites including their solvent environment, r is their distance in the associate, n is the refractory index and ε is the dieelctric constant, Δe stands for the differnce in charge between the donor and acceptor.

Approximating the charge transfer geometry by ideal potential wells, so-called potential hypersurfaces can be obtained (Fig. 1.10). In a Class I system, the two diabatic (non-interacting) hypersurfaces of donor and acceptor cross, but no electron transfer may occur. In Class II, the two potential hypersurfaces combine to a bonding and an antibonding adiabatic (interacting) hypersurface by the avoided crossing at a value of 0 for the reaction coordinate. The electronic coupling is described by the aforementioned matrix element H_{AB}. The electron transfer can now occur thermally by overcoming the energy barrier ΔG from x to -x or by absorption of an electromagnetic wave of the energy λ. The system is then excited to the antibonding potential hypersurface and may relax to the ground state of the coordinate -x. The energy for this “intervalence charge-transfer” (IVCT) absorption typically resides in the near infrared (NIR) region of the spectrum. For systems of Class III, a so-called “charge resonance” (CR) band is observed. Here, no charge is transferred from one moiety to the other and there is no change of the equilibrium geometry along the electron transfer coordinate x.

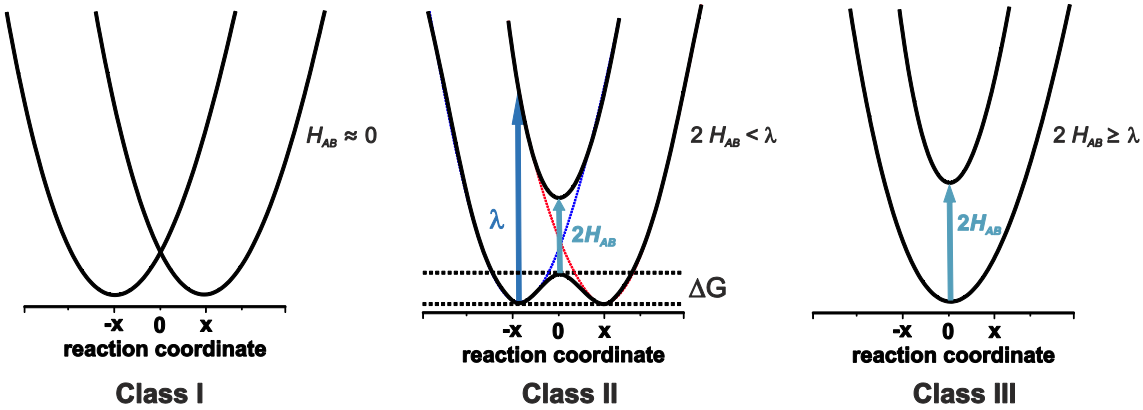

Fig. 1.10. Potential hypersurfaces by electronic coupling of two diabatic potential hypersurfaces for the three limiting classes of mixed-valent compounds, depending on the magnitudes of H_{AB} and λ.

There are several experimental methods available for determining the degree of electronic coupling on different timescales. Small electronic changes may lead to large differences in terms of charge and spin density distribution. This is the major topic of this thesis.

The electronic coupling matrix element H_{AB} can be obtained by analyzing the IVCT or CR band of mixed-valent compounds. Important parameters are the charge transfer energy and the extinction coefficient ($\tilde{\upsilon}_{max}$ and ε_{max}), the bandwidth ($\Delta\tilde{\upsilon}_{1/2}$) of the IVCT band at half height, and the electron or charge transfer distance r_{AB} (Eq. 1.3). The delocalization parameter α may vary between α = 0 for a Class I system to α = 0.5 for a fully delocalized system of Class III (Eq. 1.4).

$$H_{AB} = \frac{0.0206 \cdot \sqrt{\tilde{\nu}_{max} \cdot \varepsilon_{max} \cdot \Delta\tilde{\upsilon}_{1/2}}}{r_{AB}} \qquad \text{Eq. 1.3}$$

$$\alpha = \frac{H_{AB}}{\tilde{\upsilon}_{max}} \qquad \text{Eq. 1.4}$$

$$H_{AB} = \frac{\tilde{\upsilon}_{max}}{2} \qquad \text{Eq. 1.5}$$

$$\Gamma = 1 - (\Delta\tilde{\upsilon}_{1/2,exp}/\Delta\tilde{\upsilon}_{1/2,theo}) \quad \text{with } \Delta\tilde{\upsilon}_{1/2,theo} = \sqrt{2310 \cdot \tilde{\upsilon}_{max}} \qquad \text{Eq. 1.6}$$

Equation 1.3 strictly holds only for mixed-valent systems of Class II. For delocalized Class III systems, equation 1.5 must be used. The major drawback of this analysis method is the determination of the charge transfer distance r_{AB}. In organometallic complexes r_{AB} is set equal to the spatial distance of the two metal centers. Due to the orbital overlap of the metal ions with the organic linker (the bridge), the effective charge transfer distance is much smaller. Setting the spatial separation between the nominal redox centers leads therefore to unreliable results as the electronic coupling matrix H_{AB} will be underestimated.[39]

A good qualitative measure distinguishing between Class II, Class II/III and Class III mixed-valent systems is provided by equation 1.6, which was introduced by BRUNSCHWIG, CREUTZ and SUTIN, who calculated the coupling by analysis of the IVCT band using the theoretical and experimental halfwidth of the absorption band. For Γ < 0.5 a mixed-valent system belongs to Class II, whereas a value of Γ = 0.5 is typical for Class II/III borderline cases. For genuine systems of Class III, Γ assumes a value that is larger than 0.5. For some mixed-valent systems at the Class II/III borderline or just beyond the Class III limit, a skewing of the IVCT band, which is often denoted as a “low-energy cutoff”, has been observed.[41-43]

Besides electronic transitions in the vis/NIR, vibrational spectroscopy can also be applied to determine the extent of ground-state delocalization. This requires that charge-sensitive IR markers are present at the corresponding redox sites, whose vibrational energies change with the local charge at each of these sites.[44]

This culminated in the definition of the so-called charge distribution parameter $\Delta\rho$ as defined by Geiger. The parameter $\Delta\rho$ provides a quantitative measure of ground state

(a)symmetry based on the shifts and band patterns of the marker bands during the sequential one-electron transfer processes that connect the two isovalent states R-bridge-R and R^+-bridge-R^+ via the intermediate mixed-valent state R^+-bridge-R. This method operates at a time scale of 10^{-12} to 10^{-11} s. Other experimental techniques with a slower inherent time scale of 10^{-8} to 10^{-9} s are EPR and Mößbauer spectroscopy.

The potential hypersurfaces of Fig. 1.10 apply only if the two redox active subunits are chemically identical. If the two redox sites are chemically different and have different intrinsic redox potentials, the hypersurfaces of Class I and II systems show a vertical displacement of the two local minima as displayed in Fig. 1.11. The presence of an energy barrier ΔG^*, separating two energetically inequivalent minima, implies the possibility that two different isomers might coexist, which differ with respect to how charge or spin densities are distributed over the redox sites. These isomers are called "valence tautomers". If this energy barrier decreases, the relative ratio of the valence tautomers changes in favor of the less stable one. If the ΔG^* is negligibly small, a Class III behavior is to be expected with a CR band in the electronic spectrum.

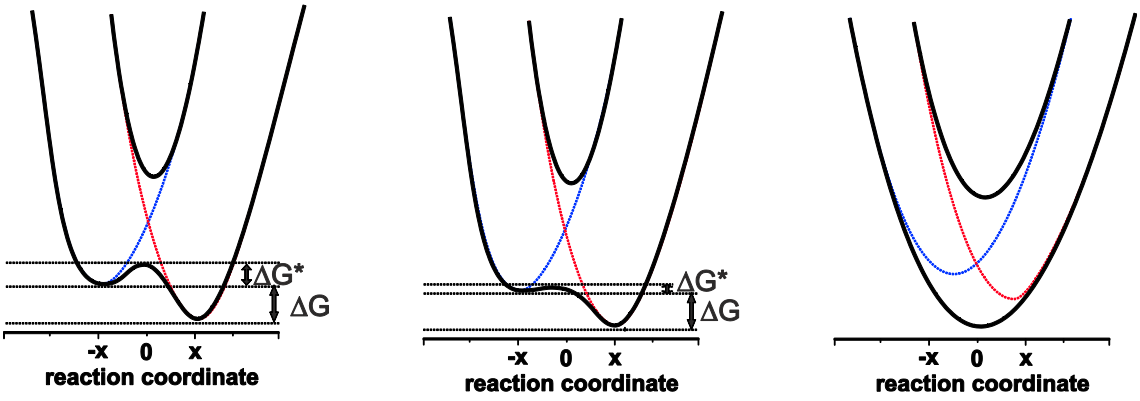

Fig. 1.11: Two diabatic potentials (red and blue lines) and adiabatic potential hypersurfaces for mixed-valent systems of Class II and III with two chemically different redox sites.

The only examples for valence tautomerism in unsymmetric mixed-valent molecules are summarized in the following, and in a selection which is presented in Fig. 1.12:

- pyrazine-bridged bis(triruthenium) clusters with unsymmetrical bridging ligands or slightly varied triruthenium units[45,46]
- diimine-bridged complexes $[\{Cl(bipy)_2Os\}\{bis(imine)\}\{Ru(NH_3)_5\}]^{4+}$ [47-49]
- protonated ferrocenyl or triarylamine substituted anthraquinones or pyrylium salts[50-52]
- 4-[(ferrocenylvinyl)tetrachlorophenyl}-{bis(pentachlorophenyl)}methyl-radicals[53,54]

- heterobimetallic amide-bridged Ru{bis(terpyridine)}(bipyridine)rhenium complexes[55]
- 1,4-diethynylphenylene bridged Fe-Mo complexes[56]
- 1',1''-bis(ethynyl)biferrocenyl bridged Fe-Ru and Fe-Os complexes[57,58]

Simultaneous occurrence of three different valence tautomers were observed by our group in *meso*-vinylruthenium-modified zinc porphyrin radical cations (vide infra).[59]

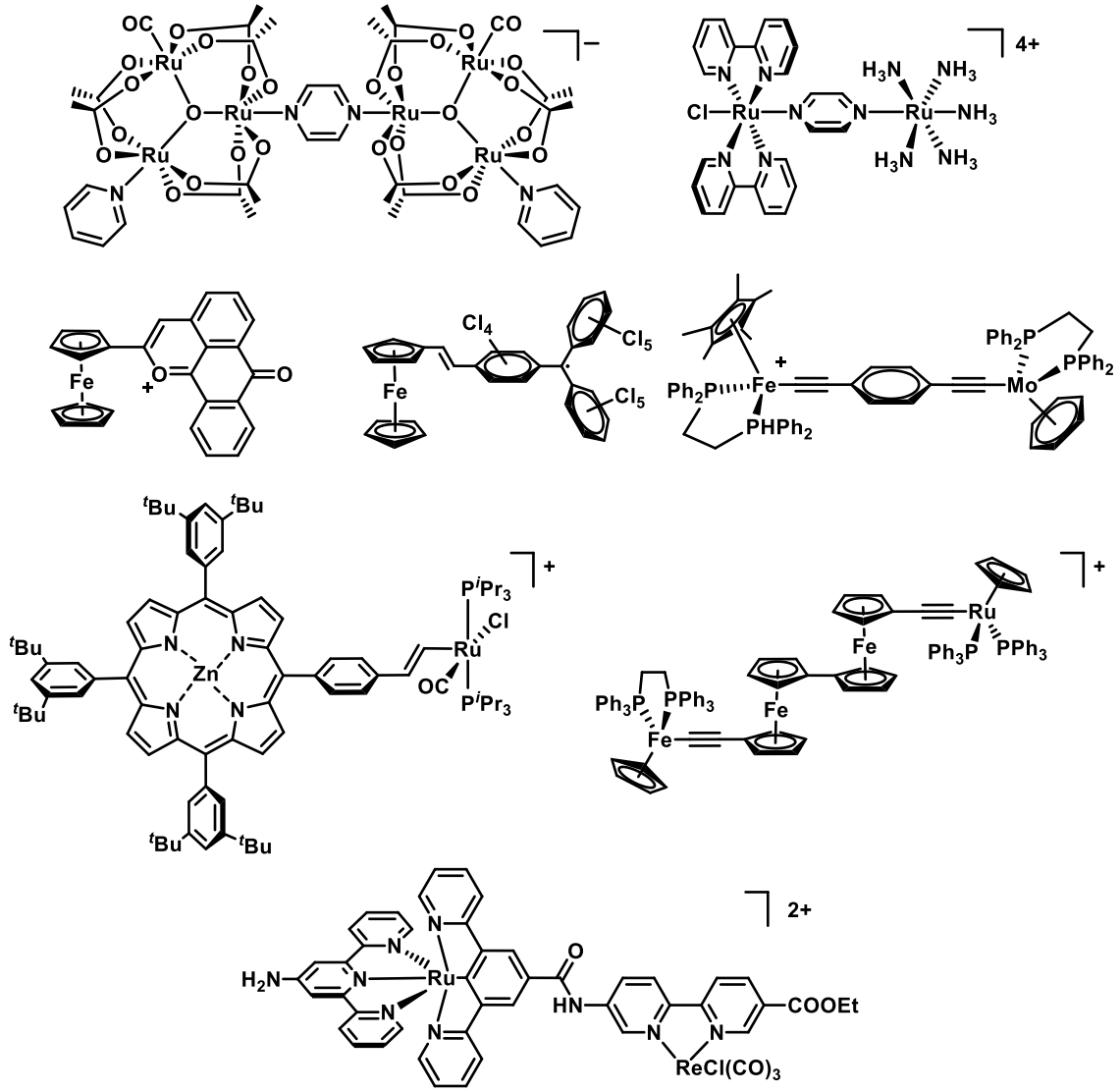

Fig. 1.12: A selection of complexes forming equilibria of valence tautomerism.

In order to observe valence tautomerism, many electronic and steric prerequisites must be fulfilled. The energy barrier ΔG^* must not be prohibitively high or low and the free enthalpy difference ΔG must therefore also be of sufficient height. Valence tautomerism is therefore difficult to realise and the interconversion of asymmetric Class II into

Class III-type systems resembles still a challenging task for chemists seeking to induce such behavior in already known complexes.

1.4. Alkenylruthenium Complexes

A structural motif, which is capable of effectively transporting charge within a molecule, is the styryl-ruthenium unit (Fig. 1.13). This has been intensively studied by our working group.[60-66]

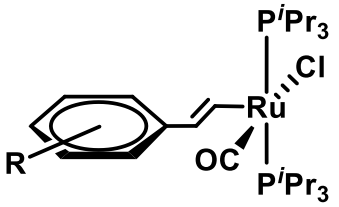

Fig. 1.13: Structural motif of the styryl-ruthenium unit.

The first ruthenium and osmium complexes of the type M(CO)Cl(CH=CH-R)(PR_3)$_2$(L), with L being a free coordination site, PR_3, MeCN or pyridine, were synthesized in 1986 by TORRES and WERNER.[67-69] The main reaction underlying the synthesis of these complexes is the stereo- and regioselective *cis*-insertion of a terminal alkyne into the Ru-H bond of the precursor complex HRu(CO)Cl(PR_3)$_2$(L).

The facile synthetic access to vinylruthenium complexes is a huge benefit. The insertion of a terminal alkyne into the ruthenium-hydride bond of complexes HRu(CO)Cl(PR_3)$_n$ (n = 3: R = Ph, Et, Me; n = 2: R = ^{i}Pr, cyclohexyl), called hydrometallation, proceeds in nearly quantitative yields and occurs with complete regio- and stereoselectivity.

The underlying mechanism was postulated by WERNER (Scheme 1.1).[70] First, the ligand L in trans-position to the hydrido ligand dissociates, providing space for the alkyne in a η^2-coordination fashion. After an isomerization step to a *cisoid* conformation of the hydrido and alkyne ligands, a four-membered metallacycle leads to the insertion into the Ru-H bond. The isomerization process could not be proven experimentally, but in 2001, CAULTON and EISENSTEIN were able to prove this postulate, as the insertion does not proceed from a transoid η^2-coordination of the alkyne to the vacant coordination site trans to the hydride ligand.[71]

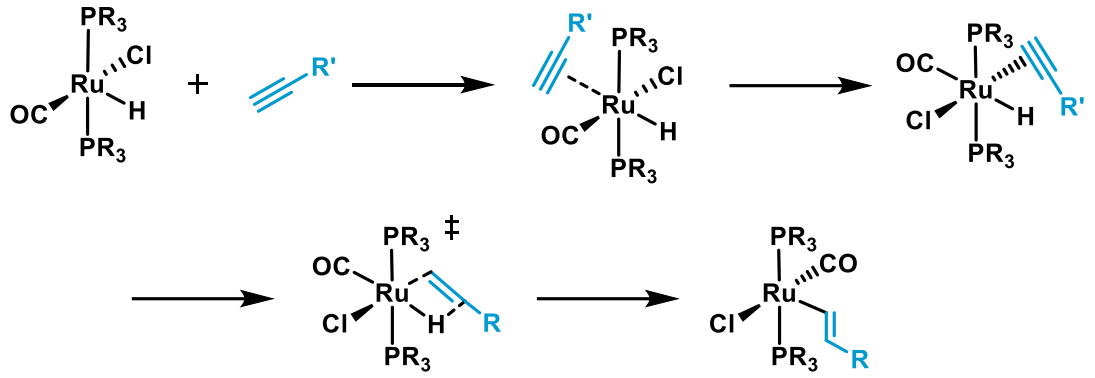

Scheme 1.1 Hydroruthenation reaction mechanism by insertion of a terminal alkyne into the ruthenium-hydride bond.

Whether a free coordination site is present or not in the final complex is determined by the bulkiness of the used phosphine ligand, i.e. the Tolman cone angle Θ. The Tolman cone angle increases in the order: $P(OEt)_3$ (Θ=109°) < PMe_3 (Θ=118°) < $P(O\text{-}p\text{-}Tol)_3$ (Θ=128°) < $P(O\text{-}^iPr)_3$ (Θ=130°) < PEt_3 (Θ=132°) < $PMePh_2$ (Θ=136°) < PPh_3 (Θ=145°) < P^iPr_3 (Θ=160°). If the angle is small the complex tends to adopt a hexa-coordinated structure with 18 valence electrons, as it is for example the case for PMe_3. The free coordination site can also be occupied by weak binding σ-donor ligands like pyridine or acetonitrile as listed in Table 1.1.

Table 1.1: Addition of different ligands to the vinylruthenium motif, table adapted from WUTTKE.[72]

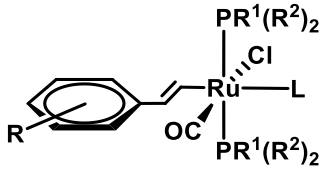

M	L	R^1	R^2	reference
Ru, Os	CO	Me	^{t}Bu	[70]
Os	CNMe	Me	^{t}Bu	[70]
Ru	CNBenzyl	^{i}Pr	^{i}Pr	[70]
Ru, Os	CO	^{i}Pr	^{i}Pr	[69]
Ru, Os	$HN{=}CPh_2$	^{i}Pr	^{i}Pr	[73]
Ru	CO	Ph	Ph	[70,74]
Ru	CNMe	Ph	Ph	[70]
Ru	NC_5H_4R'	Ph	Ph	[75-77,60,78,63,79]
Ru	CNR''	Ph	Ph	[76,80,81]
Ru	Me_2HPz	Ph	Ph	[82]
Ru	PPh_3	Ph	Ph	[83]
Ru	PMe_3	Ph	Ph	[77,84-88,79]
Ru	$CNC_6H_3Me_2$	Cy	Cy	[76]

R' = COOEt, H, Ph, Py; R'' = C_6Me_4NC, ^{t}Bu, Cy

Five- and six-coordinated vinylruthenium complexes of this type can be modified by substituting the chloro or the chloro and one neutral ligand by a bidentate monoanionic β-ketoenolate or a carboxylate ligand. Vinyl complexes with PPh_3 and bidentate ligands can also be synthesized starting from hydridocarboxylato

complexes, whereas this is not feasible for P^iPr_3 complexes. A list of six-coordinated vinylruthenium compounds with bidentate ligands is provided in Table 1.2.

Table 1.2: Coordination of bidentate ligands to vinylmetal complexes.[72]

M	bidentate ligand	PR_3	reference
Ru	$^{\ominus}O_2CR$	PPh_3	[89]
Ru	$^{\ominus}MI$	PPh_3	[74]
Ru	$^{\ominus}O_2CC_6H_4CCH$	P^iPr_3	[90]
Ru, Os	$^{\ominus}OAc$	P^iPr_3	[69]
Ru, Os	$^{\ominus}acac$	P^iPr_3	[69]
Ru	$^{\ominus}OAc$	PCy_3	[91]

R = Ph, C_6H_4Me, C_6H_4OMe, MI = 1-methylimidazol-2-thiolate

Independent of the ligand count and the number of valence electrons, the HOMO of the styrylruthenium unit extends over the metal ion and the alkenyl ligand as shown in Fig. 1.14. The alkenyl ligand is thus to be termed as “redox non-innocent”, i.e. actively taking part in the oxidation process. The other frontier orbitals in Fig. 1.14, like the LUMO as well as the HOMO-1 constitute metal-centered orbitals with only minor contributions from the alkenyl ligand. One should bear in mind that the occupied frontier molecular orbitals of the alkenylruthenium complexes of this type have strong ligand character. Not only alkenyl- but also alkynyl-complexes demonstrate a non-innocent character of the coordinated π-system. This was at first not considered but has been discussed later on.[92-94]

This pattern is also retained in divinylphenylene-bridged diruthenium complexes. This leads to an extraordinary communication between the redox termini (vide infra).

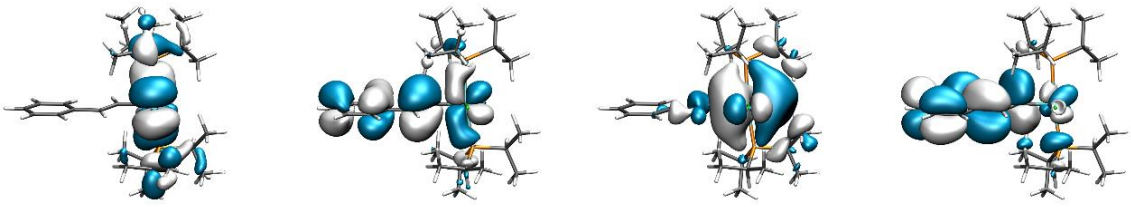

Fig. 1.14: Frontier orbitals of the complex $Ru(CO)Cl(P^iPr_3)_2(CH=CH-Ph)$ (pbe1pbe/6-31G(d)/PCM level of theory).

These alkenyl complexes exhibit several favorable properties:[61] First, they show excellent electron transfer abilities, as the redox orbitals are delocalized over the styryl- or, in the homobimetallic case, over the divinylarylene bridge. Secondly, they offer chemically and electrochemically reversible redox processes at low potentials that can be probed by voltammetric methods like cyclic voltammetry or square-wave voltammetry.

Another important feature of this system, however, is the charge sensitive CO ligand. This ligand represents one of the most important ligands in organometallic chemistry. The ability to act as a σ-donor as well as a strong π-acceptor makes it a perfect tool to investigate the electronic properties of the bound metal. The metal M receives electron density by the overlap of the populated σ-orbital of the CO ligand while electron density is withdrawn from M into the π*-orbital of the carbonyl ligand (Fig. 1.15). Upon oxidation, π-backbonding from populated metal-d-orbitals is diminished, resulting in a higher bond order of the CO bond, thus increasing the streching frequency. This vibrational band shift is a sensitive measure of the change of electron density at the metal ion during a redox reaction.

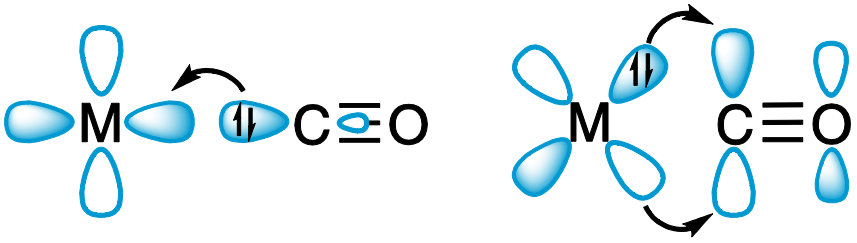

Fig. 1.15: Schematic drawing of a σ-bond and π-backbonding in a metal carbonyl complex.

Not only in the vibrational range of the electromagnetic spectrum but also in the near infrared (NIR) range, this family of complexes displays a distinct feature. Intense NIR-bands in the oxidized state are found, which are sensitive to the electronic coupling and conjugation length of the organometallic π-system. In homo- and heterobimetallic complexes, these absorptions can be of IVCT or CR origin (vide infra). In addition to the IVCT or CR NIR bands, mono- and divinylarylene-bridged diruthenium complexes also display an intense band in the visible part of the electronic spectrum, which also results from the open-shell metalorganic chromophore.

Upon oxidation, these complexes therefore change their color, which is generally denoted as “electrochromism”. In the case of a simple styrylruthenium complex, a color change from red to blue can be observed by the naked eye.

During oxidation, one electron is withdrawn from the HOMO, leaving one unpaired electron behind. This unpaired electron resides in a spin orbital (SO) and can thus be detected by Electron Paramagnetic Resonance (EPR) spectroscopy. The phosphorus atoms in the PR_3 ligands provide information about the spin (de)localization, because their nuclei magnetic moments couple to that of the unpaired spin. These $A(^{31}P)$ hyperfine splittings are often observed in fluid solution spectra and their magnitude increases with increasing metal contribution to the singly occupied molecular orbital (SOMO).

As already discussed, the redox orbitals are delocalized over the aryl moiety. Thus, the alkenyl ligand is involved in the oxidation process and can therefore tune the oxidation potential. The influence of 4-substituents in complexes Ru(CO)Cl(CH=CH-C_6H_4R-4)(P^iPr_3)$_2$ or *mer*-Ru(CO)Cl(CH=CH-C_6H_4R-4)(PMe_3)$_3$ was found to scale with their Hammett-parameter of the chosen substituent and provides control over the HOMO energy. When an electron donator is attached to the aryl group, the energy of the HOMO increases leading to a cathodic shift to lower potential in cyclic voltammetry. This is valid vice-versa for electron withdrawing substituents.

1.5. Asymmetric Dinuclear Complexes with π-Conjugated Bridging Ligands

Introducing chemically different redox sites to both ends of a bridged dinuclear complex leads to unsymmetrical heterobimetallic systems. In literature, a large number of such compounds can be found. Especially interesting are metal alkynyl complexes e.g. Ru-Os homo- or heterobimetallic complexes as demonstrated by YOUNUS, HUMPHREY, LOW and LAPINTE (Fig. 1.16).[57,95,96]

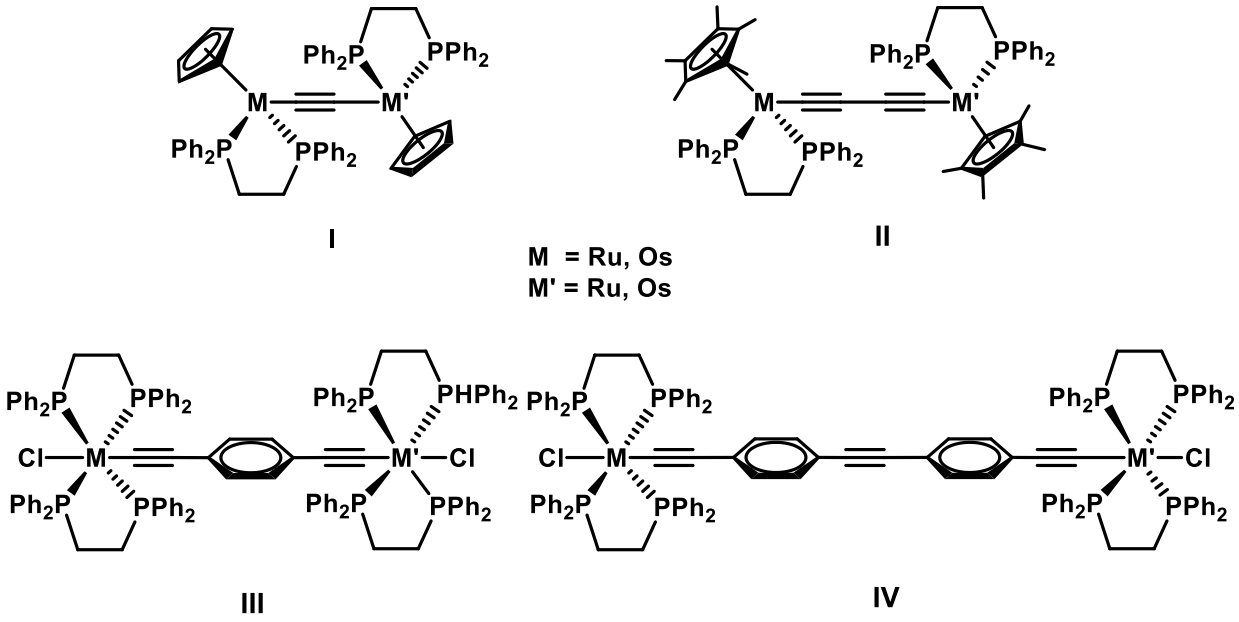

Fig. 1.16: Heterobimetallic ruthenium-osmium alkynediyl complexes.

These complexes have been synthesized by reacting the respective metal chlorides with terminal alkynes under chloride abstraction conditions ($NaPF_6$ in DCM) and the addition of a base. The synthesis of heterodinuclear complexes requires two separate synthesis steps with first the formation of a mononuclear alkynyl complex with a terminal ethynyl functionality. The homo- and heterobimetallic complexes are all electrochromic as electronic transitions in the visible grow in upon oxidation. The two redox centers in the

heterobimetallic case are oxidized in a (nominal) $Ru^{II}Os^{II} \rightarrow Ru^{II}Os^{III} \rightarrow Ru^{III}Os^{III}$ manner with distinct optical signatures for each of the states. As for divinylarylene-bridged dinuclear complexes, density functional theory (DFT) calculations revealed a strongly non-innocent behavior of the organic linker, resulting in a delocalized HOMO and strong electronic communication between the two centers.[97] One has to point out one peculiarity in the case of the homobimetallic complexes **I-III**. When both redox moieties are based on iron, a Class II behavior can be observed, however with ruthenium and osmium, the charge becomes delocalized denoting a Class III behavior.[98] The Class II behavior in homobimetallic Fe complexes has been mainly studied by LONG, LAPINTE and others.[99-101]

In the mixed-valent forms of **III** and **IV**, the communication between the two redox end groups depends on the torsion angle of the phenylene bridge. A detailed analysis of the IVCT bands of diethynylphenylene-bridged diruthenium complexes revealed that several rotamers with different degrees of electronic coupling coexist in fluid solution. Analysis of the charge and spin delocalization in the one-electron oxidized state is limited by the lack of a suitable marker apart from the transitions in the near infrared region of the spectrum. It is to note that the non-innocent behavior of the organic linkers increases upon substitution of Ru with Os. This goes along with an increase in electron density as observed by the cathodic shift of their oxidation potentials of around 200 mV as compiled in Table 1.3.[102,101,100,97,57,95,103,96]

Table 1.3: Oxidation potentials of homo- and heterobimetallic Ru-Os alkynyl complexes.[a)][72]

complex	M, M'	$E_{1/2}^{0/+}$	$E_{1/2}^{+/2+}$	$\Delta E_{1/2}$
I	Ru, Ru [b)]	- 610	210	820
	Ru, Os [b)]	- 670	90	760
II	Ru, Ru [a)]	- 430	220	650
	Os, Os [b)]	- 620	- 10	610
III	Ru, Ru [b)]	300	0	300
	Os, Ru [c)]	- 340	- 50	290
	Os, Os [b)]	- 510	- 210	300
IV	Ru, Os [c)]	- 150	60	210

a) all potentials given in mV vs. $Fc^{0/+}$ b) in DCM c) in THF

In literature, various attempts were made to correlate the half-wave potential splitting $\Delta E_{1/2}$ to the electronic coupling between two electronically connected redox groups.[104-107] This potential difference reflects the thermodynamic stabilities of both neighboring redox states, that is the extent to which the doubly oxidized and the neutral forms undergo comproportionation to the mixed-valent state. The comproportionation constant K_{comp} is given by the Arrhenius-type equation 1.7, from which the free enthalpy change of this reaction can be determined (Eq. 1.8).

$$K_{comp} = e^{n \cdot F \cdot \Delta E_{1/2} / R \cdot T} \quad \text{Eq. 1.7}$$

$$\Delta G_{comp} = -R \cdot T \cdot lnK_{comp} \quad \text{Eq. 1.8}$$

$$\Delta G_{comp} = \Delta G_{stat} + \Delta G_{ind} + \Delta G_{exc} + \Delta G_{el} + \Delta G_{res} + \Delta G_0 \quad \text{Eq. 1.9}$$

The free enthalpy change ΔG_{comp} is not only determined by the electronic coupling, which is represented by the resonance contribution ΔG_{res}, but has several more contributors, as given in Eq. 1.9.[104,108-110] The other factors having an impact on $\Delta E_{1/2}$ are:

- the statistical term, ΔG_{stat}, which amounts to 36 mV (arising from 2·ln2·RT/F)
- the inductive term ΔG_{ind}, which describes the change in bonding energy that accompanies the first oxidation
- ΔG_{exc}, which denotes the antiferromagnetic exchange term
- ΔG_{el}, which quantifies the electrostatic contribution, that is a shift of the second oxidation/ reduction potential due to the charge repulsion after the first oxidation/ reduction
- ΔG_0, describing the difference of the intrinsic redox potentials of the redox sites which increases with increasing “redox asymmetry” as is detailed in the next chapters.

Due to the many contributing factors, there is sometimes no direct relation between ΔG_{comp} and ΔG_{res}. Different examples of such “non-conformistic” behavior can be found in the literature.[106] In some cases, strong electronic coupling and charge delocalization despite contrasting small half-wave potential splittings are observed, but the opposite behavior with no or weak electronic coupling despite appreciable values of $\Delta E_{1/2}$ is also known.

Divinylarylene-bridged dinuclear transition metal complexes constitute another intriguing family of homo- and heterodimetallic compounds with π-conjugated, σ-bonded bridging ligands. The first diruthenium complexes of this type were published in 1994.[111,76] Still, the first electrochemical analysis was only performed ten years later.[60,77] In our research group, this structural motif has been studied with respect to the charge and spin delocalization, using the CO ligand as charge sensitive label and employing EPR spectroscopy (Fig. 1.17).[103,112] The divinylphenylene-bridged complexes in Fig. 1.17 undergo two reversible, consecutive one-electron oxidations, which can be addressed separately by electrolysis in an optically transparent thin layer electrolysis cell.

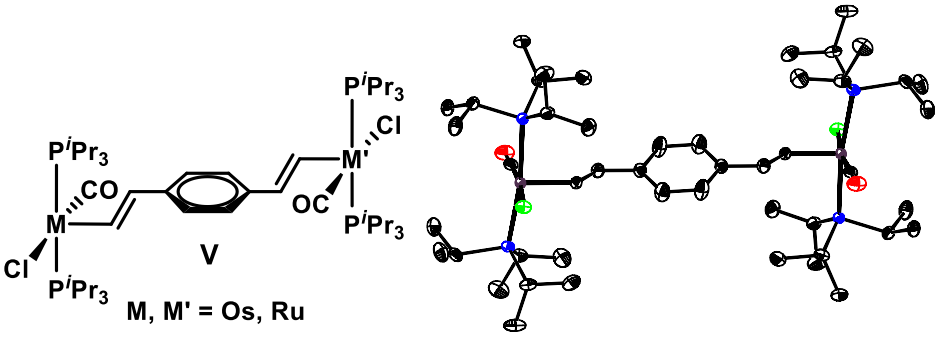

Fig. 1.17: Homo- and heterobimetallic alkenyl complexes and the crystal structure of the homobimetallic divinylenphenylene-bridged Ru complex **V** by MAURER (protons omitted for clarity).[112]

The homobimetallic diruthenium complex **V** of Fig. 1.17 (M, M'= Ru) was prepared by JÖRG MAURER and assigned as a charge and spin delocalized Class III system with strong non-innocent behavior of the ligand. The one-electron oxidation of this complex leads to the stable mixed-valent form, which is readily formed by either chemical oxidation or electrochemical means. The first oxidation changes the initial spectrum with one strong Ru(CO) band at 1910 cm^{-1} to a pattern of one strong band at 1934 $cm^{-1}$and a weaker shoulder at 1950 cm^{-1}. This pattern arises from the overlap of the stronger band of the asymmetric and a weaker band of the symmetric combination of the two Ru(CO) units (Fig. 1.18).

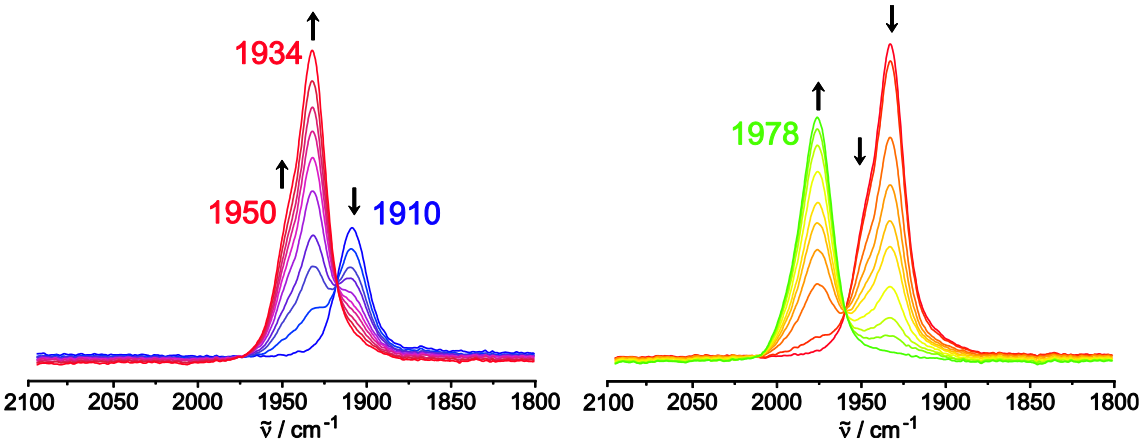

Fig. 1.18: IR spectroscopic changes during oxidation of the homobimetallic divinylenphenylene-bridged complex **V** by MAURER. Neutral form is depicted in blue, cationic form in red and dicationic in green.

The *meta*-substituted divinylphenylene-bridged diruthenium complex was also investigated and identified as a Class II system on the IR timescale. In order to investigate the changes in the electronic structure upon asymmetric substitution, the homobimetallic Ru-Ru and Os-Os complexes have been compared to the mixed Ru-Os complex (M, M' = Os and M = Ru, M' = Os, Fig. 1.17).[103]

In the divinylphenylene-bridged complexes, the electron density increases by substitution of Ru with Os, which was probed by cyclic voltammetry. For the homobimetallic vinylosmium complexes, oxidation potentials of -270 and -50 mV were

found, whereas the biruthenium complex oxidizes at -90 and 170 mV. For the mixed Os-Ru complex, oxidation waves at -200 and 60 mV indicate an average electron density (Table 1.4). The strongly delocalized character of the mixed-valent species is here demonstrated as both oxidation sites are influenced by the substitution with shifts of around 70 and 110 mV when compared to the homobimetallic analogs.

Table 1.4: Oxidation potentials of bimetallic divinylphenylene-bridged complexes of Ru and Os.[a)][103]

M, M'	$E_{1/2}^{0/+}$	$E_{1/2}^{+/2+}$	$\Delta E_{1/2}$
Ru, Ru	- 90	170	260
Ru, Os	- 200	60	350
Os, Os	- 270	- 50	320

a) Probed in DCM, $TBAPF_6$ (0.1 M) as supporting electrolyte, scan rate: 100 mV/s

IR spectroelectrochemistry (Fig. 1.19) also indicated a delocalized Class III system despite the two inequivalent redox sites. This conclusion is supported by the CR band in the NIR. In Fig. 1.19, the two CO vibrational signal sets of the neutral form arise from the Ru-CO and the Os-CO ligands, which are electronically inequivalent. The band lower in energy within one oxidation state can be assigned to the carbonyl ligand coordinated to the osmium atom. During oxidation, the vibrational energies increase from 1896 and 1911 cm^{-1} in the neutral state to 1913 and 1926 cm^{-1} in the cationic form to 1960 and 1973 cm^{-1} in the dicationic oxidation state.[103] EPR spectroscopy on the mixed-valent species revealed that the *g*-value of the heterobimetallic complex is intermediate to both homobimetallic systems.

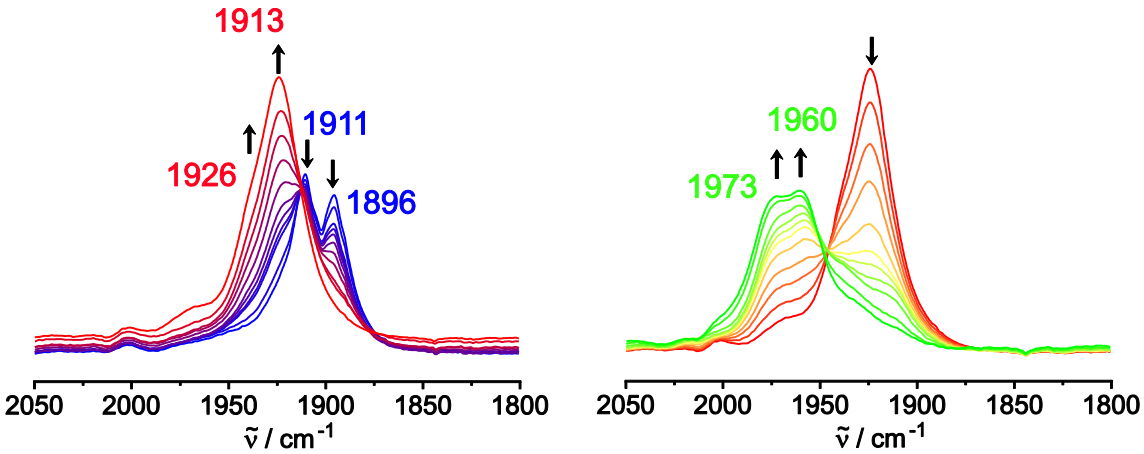

Fig. 1.19: IR spectroelectrochemistry in the CO vibrational region of the heterombimetallic Ru-Os divinylphenylene-bridged complex. Blue color represents the neutral, red the cationic, and green the dicationic species.[103]

Besides divinylenphenylene-bridged complexes of this type divinylanthracenyl-bridged complexes **VI** have also been investigated to probe the general difference of ruthenium to osmium alkenyl complexes (Fig. 1.20). Again, the substitution of Ru by Os increased the electron density in the system as could be concluded from the lower CO vibration

energy (1898 cm^{-1} for the diosmium *vs*. 1911 cm^{-1} in the biruthenium case) and cyclic voltammetric measurements of the two reversible waves (-60 and 190 mV *vs.* 90 and 370 mV). The characterization of the electronic structure was, however, problematic because two isomers – the *cisoid* and *transoid* forms coexist in solution. Both exhibit different sets of Ru(CO) bands which precludes a detailed analysis. Further, the conversion to the radical cations during the spectroelectrochemical experiment were incomplete, rendering a deconvolution of the bands problematic. Nevertheless, the redox potentials and changes in the vibrational and electronic spectra during oxidation point to a rather localized charge at the more electron-rich Os site and a generally lower electronic coupling of the metal alkenyl moieties to the π-system. The latter is due to a strong torsion of at least one of these moieties to the anthracene plane caused by their close spatial proximity.

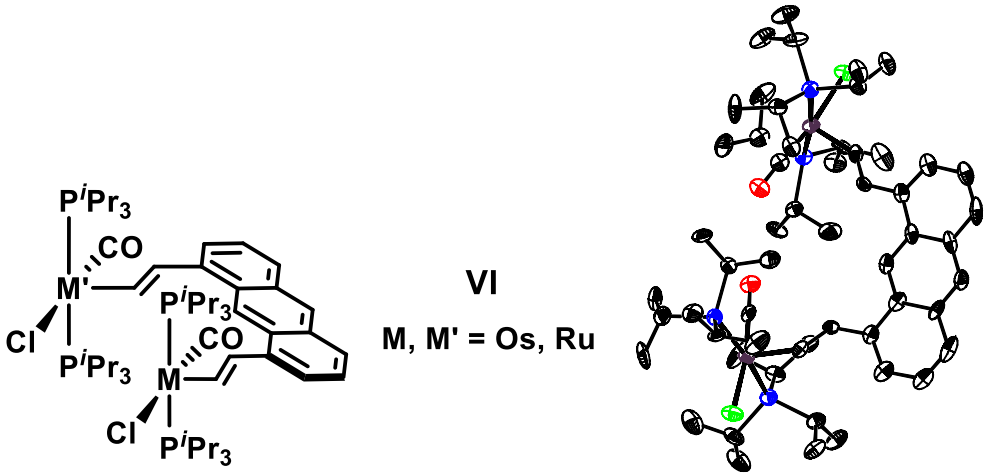

Fig. 1.20: Homo- and heterobimetallic divinylanthracenyl-bridged complexes of Ru and Os (left) of **VI** and the crystal structure of the homobimetallic diruthenium complex (right, protons omitted for clarity).

1.6. Heterobimetallic Complexes derived from Ethynyl-Metallocenes

In 1994 and 1997, SATO synthesized the first heterobimetallic mixed-valent complexes combining metallocenes and metal-alkynyl complexes (Fig. 1.21).[113,114]

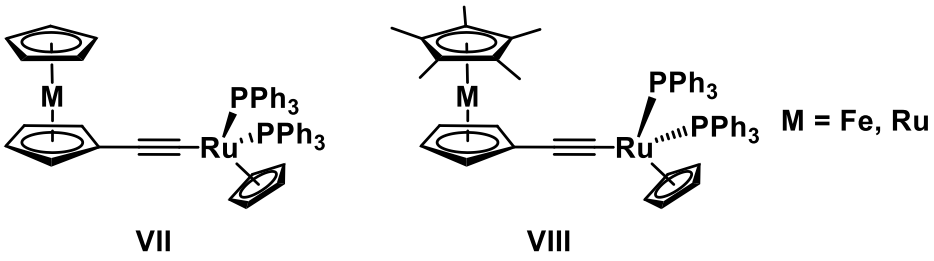

Fig. 1.21: Heterobimetallic metallocenyl alkynylruthenium complexes **VII** and **VIII** by SATO.[113,114]

These complexes are characterized by a reversible oxidation process at a half-wave potential in between -550 and -310 mV. Most of these compounds undergo a second oxidation at a distinctly higher oxidation potential, but this process may suffer from limited chemical reversibility. The potentials of these oxidations depend on the central metal atom of the metallocene and the phosphine ligands. During IR spectroelectrochemistry, an intense vibration at 1980 cm^{-1} was observed and assigned as a cumulene-type vibration of the oxidized form. This vibration falls energetically in between the C≡C stretching frequency of similar, neutral ethynyl complexes (ca. 2070 cm^{-1}) and the C=C=C-stretching frequencies of allenylidene complexes (ca. 1920 cm^{-1}) (Fig. 1.22). These complexes were assigned to the Class II regime in the ROBIN and DAY classification system.[113,114]

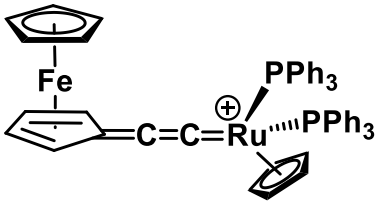

Fig. 1.22: Cumulene-type bonding mode in the ferrocenyl alkynylruthenium cation.

In 2010, LANG and LAPINTE published complexes combining the already mentioned biferrocene moiety as well as the metal-alkynyl substituents at the 1- and 1''-positions. The 1,1''-bis(ethynyl)biferrocenyl bridged Fe-Ru and Fe-Os complexes Type **IX** of Fig. 1.23 show up to four reversible one-electron oxidations. Spectroelectrochemical studies suggest that direct electron transfer between the redox termini does not occur.

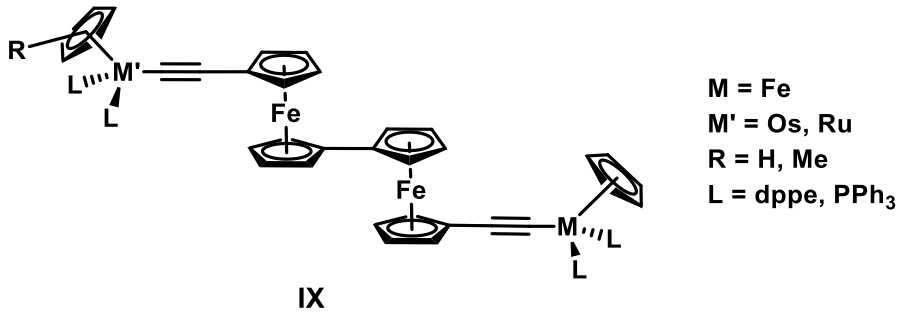

IX

Fig. 1.23: 1,1''-Bis(ethynyl)biferrocenyl-bridged Fe-Ru and Fe-Os complexes **IX** by LANG and LAPINTE.[57,58]

It was found that intramolecular electron transfer results from a strong interaction between the metal-alkynyl termini and the adjacent ferrocene units of the biferrocene moiety and a weak but notable interaction between the ferrocenyl units of the biferrocene. Further, multistep charge exchange processes between the redox termini were disclosed by EPR studies. In summary, these molecules are suitable examples of unsymmetrically built ROBIN and DAY Class II systems based on ferrocene and alkynylmetal moieties.

Combining ferrocene with the vinylruthenium moiety of our research group results in the rather small heterobimetallic complex synthesized by KONRAD KOWALSKI (Fig. 1.24).[115]

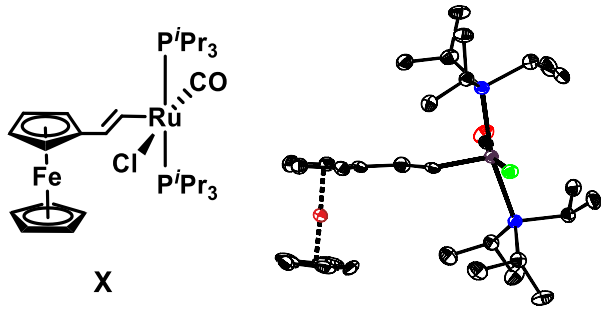

X

Fig. 1.24: Ferrocene vinylruthenium complex **X** and its crystal structure (protons omitted for clarity).[115]

The complex **X** was formed by using HRuCl(CO)(P^{i}Pr$_3$)$_2$ and ethynylferrocene for the hydroruthenation reaction. The created system benefits from the electronic properties and stabilities of both intrinsic complex halves. Due to the carbonyl ligand, the spectroscopic investigation of the electronic situation at the ruthenium center was feasible.[116]

KOWALSKI found a charge distribution of 60:40 between the ferrocene and the vinylruthenium moieties, respectively. The author extrapolated this from the CO vibrational shift from 1908 to 1932 cm^{-1} ($\Delta\nu$ = 24 cm^{-1}) during oxidation and the vibrational shift of the Cp protons (3096 to 3110 cm^{-1}) (Fig. 1.25). He compared these with the CO vibrational shifts in a simple styrylruthenium complex (Ph-CH=CH-Ru(CO)Cl(P^{i}Pr$_3$)$_2$), which amounts to 65 cm^{-1}, and the shifts of the Cp protons of ferrocene during oxidation (26 cm^{-1}).

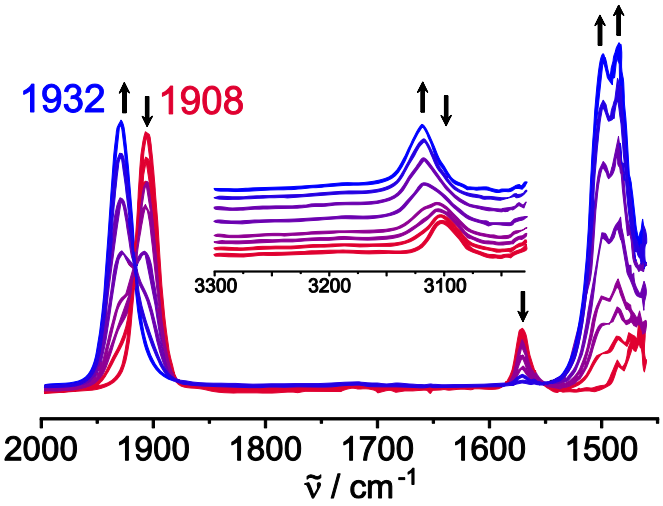

Fig. 1.25: IR spectroscopic changes of the ferrocene vinylruthenium complex **X** upon the first oxidation.[115]

EPR studies on the chemically oxidized radical monocationic species revealed an iron centered spin with an axial signal ($g_{\parallel}$ = 2.80 and $g_{\perp}$= 1.984) at 110 K in a frozen DCM matrix and no signal at room temperature. All these results indicated a Class II/Class III borderline mixed-valent complex with 60 % charge stabilization by the ferrocene moiety. The electronic coupling between ferrocene and the vinylruthenium part is strong as the very short "bridge" is an integral part of both redox centers. The question whether this behavior is also present for ruthenocene, the heavier congener of ferrocene, constitutes one topic to be addressed in the present thesis.

Our research group also succeeded in expanding the π-conjugated bridge of KOWALSKI's ferrocene vinylruthenium complex by inserting a phenyl, an ethynylphenyl, or a vinylphenyl entity.

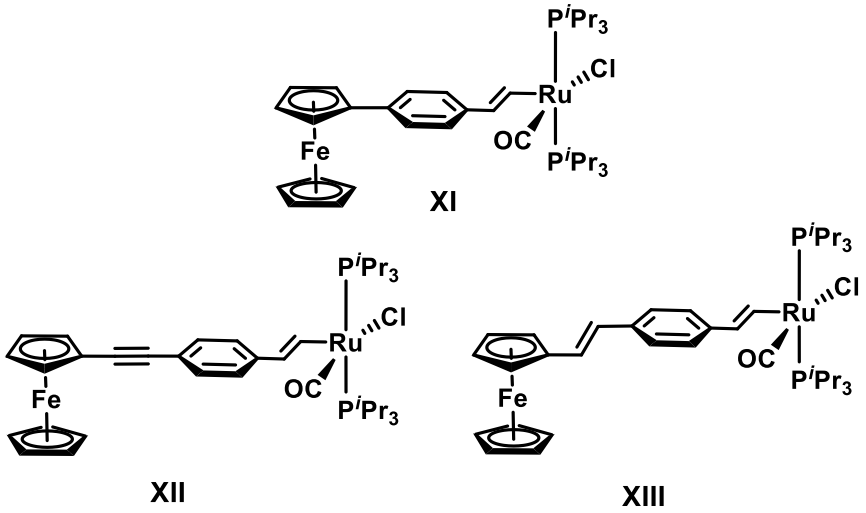

Fig. 1.26: Heterobimetallic ferrocenyl vinylruthenium complexes **XI** – **XIII** with larger π-conjugated bridges by MÜCKE.[117]

All obtained heterobimetallic complexes **XI**, **XII** and **XIII** undergo two reversible oxidations (Table 1.5). For the complexes **XI** and **XIII**, the vinylruthenium moiety increases the energy of the HOMO, which leads to a rather low oxidation potential of -31 or -29 mV *vs*. the ferrocene/ferrocenium couple. Complex **XII**, however, does not display this behavior and the oxidation potential of the first oxidation is more than 130 mV higher. This could be due to the electron accepting character of the alkynyl group as well as the smaller electronic coupling to the vinylruthenium site.

Table 1.5: Oxidation potentials of ferrocenyl vinylruthenium complexes by MÜCKE.[a) [117]]

complex	$E_{1/2}^{0/+}$	$E_{1/2}^{+/2+}$	$\Delta E_{1/2}$
XI	- 31	369	400
XII	107	366	259
XIII	-29	262	291

a) measured at room temperature, in DCM, scan rate 100 mV/s, $TBAPF_6$ (0.1 M) as supporting electrolyte.

IR spectroelectrochemistry reveals that the first oxidation for all complexes occurs, as expected, to a high extent at the ferrocene site with only small contributions from the vinylruthenium moiety. This is indicated by the very small vibrational shift of the CO ligands during the first oxidation of only 7 cm^{-1} (Fig. 1.27). During the second oxidation, the carbonyl shift of 60 cm^{-1} for **XI** and **XII**, and 56 cm^{-1} for **XIII** is substantially larger.

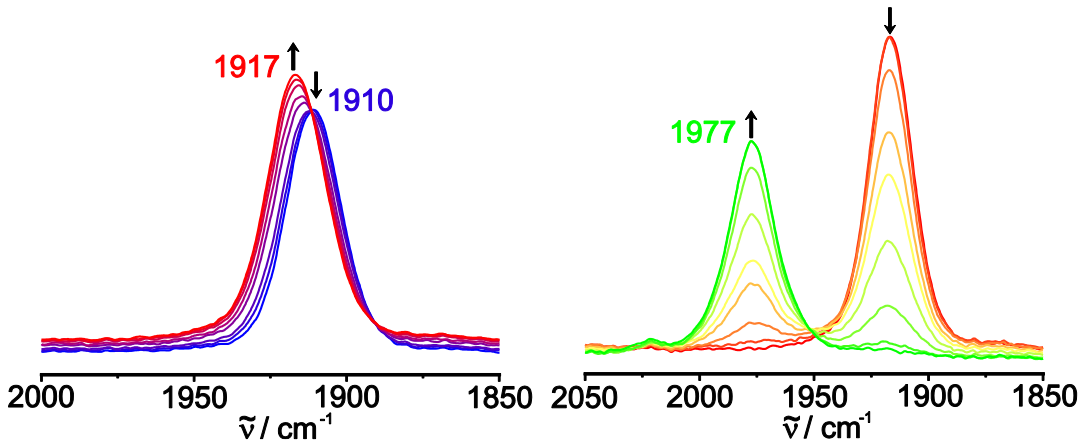

Fig. 1.27: The CO ligand's vibrational shift during the first and second oxidation of complex **XI** (blue neutral, red monocation and green dication).

The radical cations of all these compounds exhibit an IVCT band in the NIR with a moderate extinction coefficient (4950, 1391 and 1900 M^{-1} cm^{-1}). This band represents the electronic communication between the two redox centers, which leads to a Class II behavior. From the intensity of this band one can conclude that the communication in complex **XI** is the strongest and further elongation of the bridge reduces the communication. The weakest electronic coupling is observed in II^+.

Within this thesis, we reached out to investigate the change in the electronic structure upon coordination of a β-ketoenolato ligand to the vinylruthenium moiety of KOWALSKI's

complex **X** and complex **XI**, increasing the electron density at the vinylruthenium site (vide supra).

1.7. Mixed-Valent Triarylamine-Compounds

Besides organometallic compounds and metallocenes, also purely organic compounds are of interest when it comes to electrochemical properties. Triarylamines and their many derivatives are of high importance in organic electrochemistry. Their oxidized forms may undergo benzidine-type rearrangements[118-121] or cyclization to carbazoles,[122] if the para-positions are not appropriately blocked. Appropriately substituted, functionalized triarylamines are easily accessible from Vilsmeier-Haack reaction, Ullman or Buchwald-Hartwig coupling. Their oxidation potential is prone to the electron-withdrawing or donating capabilities of their substituents and may be tuned over a considerable range.[123-130] This becomes evident from the calculated highest occupied molecular orbital (HOMO), which is not only nitrogen-based but delocalized with high contributions of the aryl groups (Fig. 1.28).

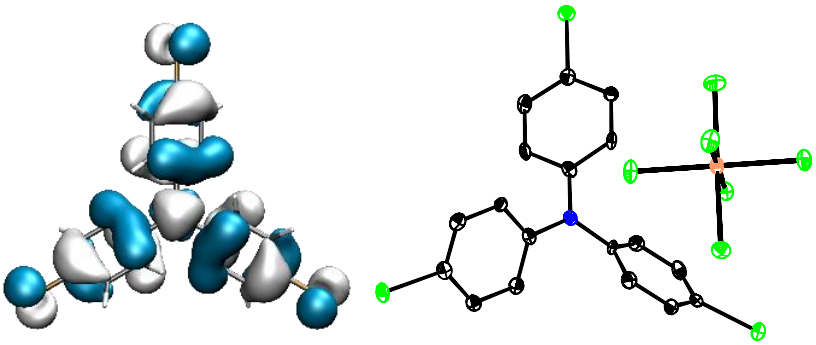

Fig. 1.28: Left: Highest occupied molecular orbital of tris(4-bromophenyl)amine (pbe1pbe/6-31G-D/ PCM level of theory); right: the crystallographic structure of tris(4-bromophenyl)aminium hexachloroantimonate ("Magic Blue"), an amine-based oxidant. [131]

Triarylamine derivatives are therefore widely used as one-electron oxidants. The most important is “Magic Blue”, tris(4-bromophenyl)aminium hexachloroantimonate (Fig. 1.28).[131] A strong absorption in the visible at 727 nm is responsible for its intense blue coloration. The degradation of “Magic Blue” generates a whole family of bromo-substituted triarylamines, which are often dubbed as the “Blues Brothers”. “Magic Blue” must therefore always be tested for purity prior to use.

Triphenylamine and its derivatives are of high interest in photovoltaics,[132] photophysics,[133] and electroluminescence.[134] Particular advantages are the facile derivatization of triarylamines to tune their optical and chemical properties. Triarylamines are easily prepared or commercially available and undergo a large variety of efficient substitution reactions like the Vilsmeier-Reaction, due to their electron-rich aryl rings.[135]

Furthermore, triarylamines exhibit a highly reversible redox behavior. They are therefore widely used as selective one-electron oxidants and electrocatalysts.[9,136,137]

Multiple investigations have been performed on bis(triarylamine)s and have provided deep insight into their charge transfer properties as well as the effects of the linking bridges and solvents on their electronic coupling or their matrix-dependent inner and outer reorganization energies (λ_{in} and λ_o).[138,139,42,140-146,41,147-152]

Most mixed-valent triarylamines feature two identical redox-active moieties. In the context of the present thesis, we, however, focus on asymmetric mixed-valent compounds featuring one triarylamine entity. There are some prominent examples of asymmetric mixed-valent compounds featuring purely organic triarylamines and perchlorinated trityl radicals by LAMBERT,[153-155] or of [Ru(2,2'-bipyridine)$_2$(N^C)]$^{2+}$ and [Ru(terpy)-(N^C^N)]$^{2+}$ complexes by YAO, where the triarylamine is an entity of the coordinating ligand (Fig. 1.29).[156,157]

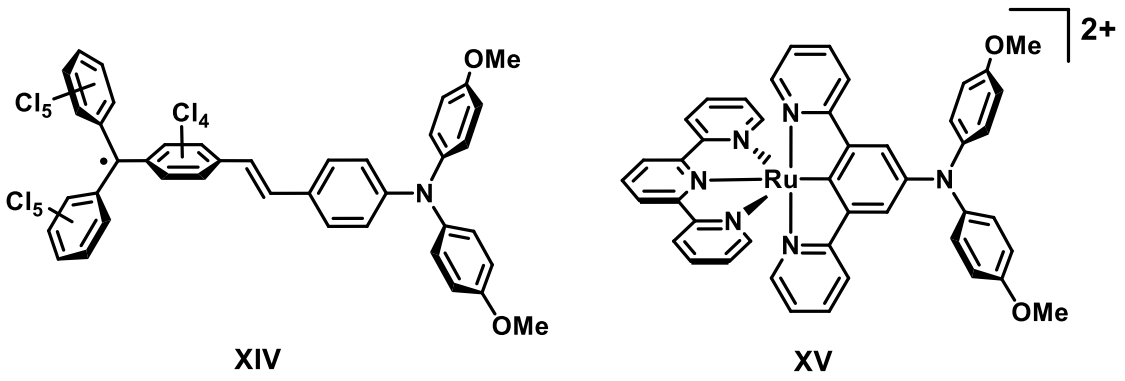

Fig. 1.29: Neutral and charged mixed-valent triarylamine-derived asymmetric redox-active compounds **XIV** and **XV** by LAMBERT and YAO.[141,158]

As expected for a neutral radical, in the perchlorinated trityl derivative **XIV** of Fig. 1.29, the spin is localized at the triphenylmethanyl unit. This is also indicated by the ^{13}C hyperfine splittings in an EPR experiment. As a consequence, the weakly but nonsystematic solvatochromic IVCT band at around 800 nm can be expected to arise from a charge transfer from the electron rich triarylamine to the radical moiety. This could be confirmed by DFT calculations. This model system was then used by the authors to calculate the inner and outer reorganization energies as well as the energy difference between the two possible redox isomers (triarylamine-trityl and triarylaminium-trityl anion) along the adiabatic potential hypersurface.[141]

The 1,4-bridged covalent hybrid of a triarylamine and a cyclometalated N^C^N ruthenium complex **XV** is a stable open-shell system, where the spin is mainly located at the triarylamine site. This is indicated by room temperature EPR spectroscopy with a sharp isotropic signal at $g = 2.0348$. A Ru(III)-based EPR signal would be expected to be rhombic or axial and would be characterized by a g-value more different from g_e. DFT

calculations supported this interpretation. A strong IVCT band at 1050 nm (ε = 20000 M^{-1} cm^{-1}) was found, which is only slightly solvatochromic, suggesting a strong coupling between the Ru(N^C^N) entity and the triarylamine unit, where the metal acts as the donor (Fig. 1.30).

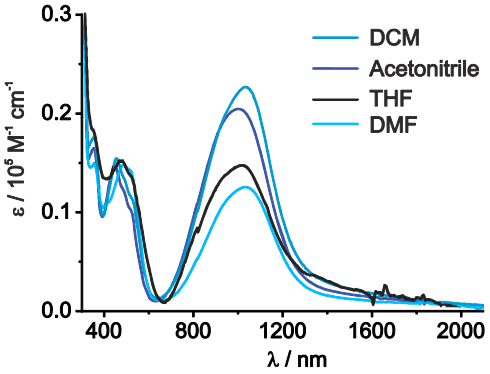

Fig. 1.30: Weakly solvatochromic bands in the UV/vis/NIR spectrum of the oxidized mixed-valent (terpyridine)Ru(N^C^N)-triarylaminium complex **XV** from Fig. 1.29.[152]

A perplexing similarity to triarylamines has been noted for our vinylruthenium conjugates of the type R-CH=CH-Ru(CO)Cl(P^iPr_3)$_2$ by investigation of vinylruthenium and triarylamine functionalized squaraines.[159] Herein, the attachment of triarylamines or vinylruthenium entities results in the same absorption properties in spectroelectrochemistry. Our research group then sought to combine triarylamines with vinylruthenium moieties. To this end, triarylamines with one to three vinylruthenium "substituents" were investigated by WALTHER POLIT during his doctoral thesis. Remarkably intense NIR absorptions of these compounds in their mixed-valent states were observed. The number of the NIR absorbing mixed-valent states increases from one to three on stepwise introduction of a further vinylruthenium moiety (Fig. 1.31).[160,161]

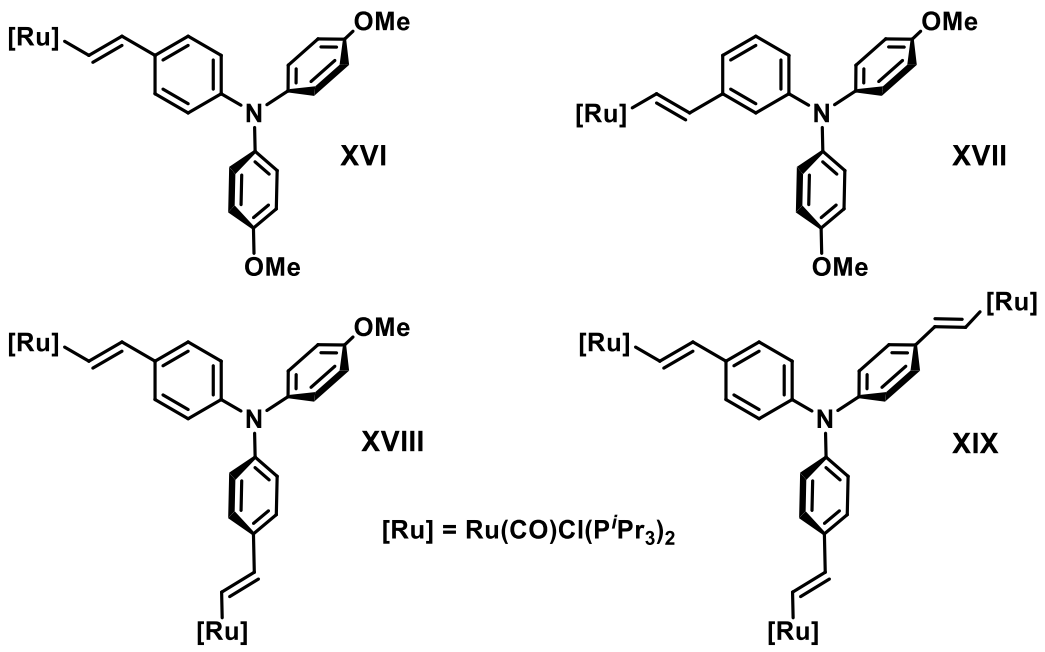

Fig. 1.31: Triarylamine vinylruthenium complexes with one to three ruthenium entities by POLIT.[160,161]

Further, DFT calculations of these complexes have indicated a highly delocalized π-system, which extends over the entire molecule, and a fully delocalized spin density. IR spectroelectrochemistry of complex **XVI** demonstrated a shift of the carbonyl vibration during the two oxidations from 1910 over 1944 to 1985 cm^{-1} (Fig. 1.32). The vinylruthenium moiety contributes thus roughly with *ca.* 45 % ($\Delta\tilde{\nu}$ = 34 cm^{-1}) to the first oxidation and with *ca.* 55 % ($\Delta\tilde{\nu}$ = 41 cm^{-1}) to the second, which let the authors assume a delocalized Class III behavior. For a Class III compound, a band in the NIR is expected with the characteristics of a charge resonance (CR) absorption. This is indeed the case as depicted on the right of Fig. 1.32. The complexes **XVIII** and **XIX** also display Class III behavior in their respective mixed-valent states. The investigations have proven that the charge and spin of these radical cations is equally shared by the triarylamine as well as by the vinylruthenium moieties.

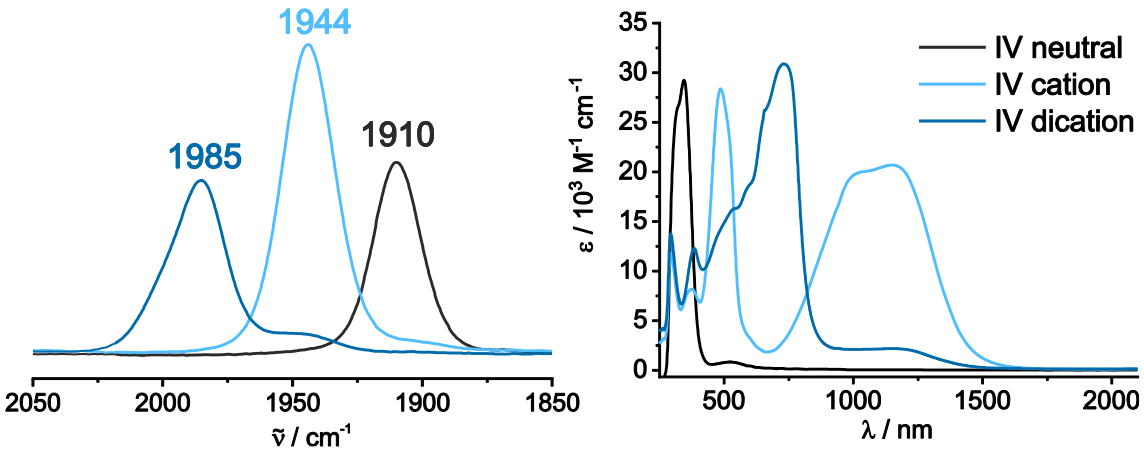

Fig. 1.32: Ru(CO) vibrational spectra (left) and UV/vis/NIR spectra of complex **XVI, XVI^{+} and XVI^{2+}** in DCE/ $TBAPF_6$ (0.2 M) as supporting electrolyte.[161]

The authors also synthesized complex **XVII**, which differs from **XVI** only by the site of attachment of the vinylruthenium group to the triarylamine group. The connection by the *meta*-position of the common aryl ring led to charge and spin localization at the triarylamine site as confirmed by IR and EPR spectroscopy, DFT calculations and comparison with complex **XVI^{+}**. In particular, the blue shift of the Ru(CO) stretch of 11 cm^{-1} was significantly smaller than in **XVI**. Consequently, the low-energy absorptions in the UV/vis/NIR spectrum were assigned as IVCT transitions and of much less intensity than the CR bands of complexes **XVI^{+}**, **XVIII^{+}** and **XIX^{+}**.

Now the question arises, if the degree of charge and spin delocalization in **XVI^{+}** can be tuned by simple chemical modifications at the triarylamine site. Here, electron withdrawing substituents should bias the HOMO more toward the vinylruthenium moiety and affect their redox potentials and charge as well as spin density distributions. This is one of the topics of this thesis.

1.8. Valence Tautomerism

The mixed-valent vinylruthenium ferrocene and triarylamine compounds can be used to explore the borderline regime between Class II, II/III or III behavior of mixed-valent systems with chemically different redox sites. These cases require that the redox sites are electronically coupled. An alternative electronic situation of such systems is the coexistence of two different isomers, so called “valence tautomers”, which differ with respect to the charge and spin (de)localization. As already mentioned in the introduction, the prerequisite for valence tautomerism is the presence of an energy barrier ΔG^{*}, separating the two inequivalent but distinct ground state minima on the potential hypersurface combined with a sufficiently small ground state energy difference ΔG (Fig. 1.11 in Chapter 1.3). An excellent example of valence tautomerism is given by

LAPINTE and WHITELEY[56], who found that the 1,4-diethynylbenzene-bridged Fe-Mo complex **XX** (Fig. 1.33) undergoes two reversible one-electron oxidations. DFT calculations indicated that the frontier orbitals in the mono-oxidized species are evenly distributed over both metal termini and the bridge whereas the HOMO in the neutral complex is rather heavily localized on the Mo ion with 48 % molybdenum d-orbital contribution in contrast to only 3 % from the iron atom.

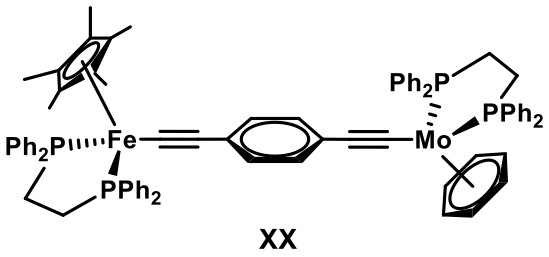

XX

Fig. 1.33: 1,4-Diethynylphenylene-bridged Fe-Mo complex **XX** by LAPINTE and WHITELEY.[56]

The spin density distribution was investigated by IR and EPR studies and found to be located on either the Mo or on the Fe center. This is graphically displayed in Fig. 1.34, where the individual contributions of the two tautomers add to the experimental EPR spectrum. Thus, the valence tautomeric equilibrium can be described by the two resonance structures of Fig. 1.35.

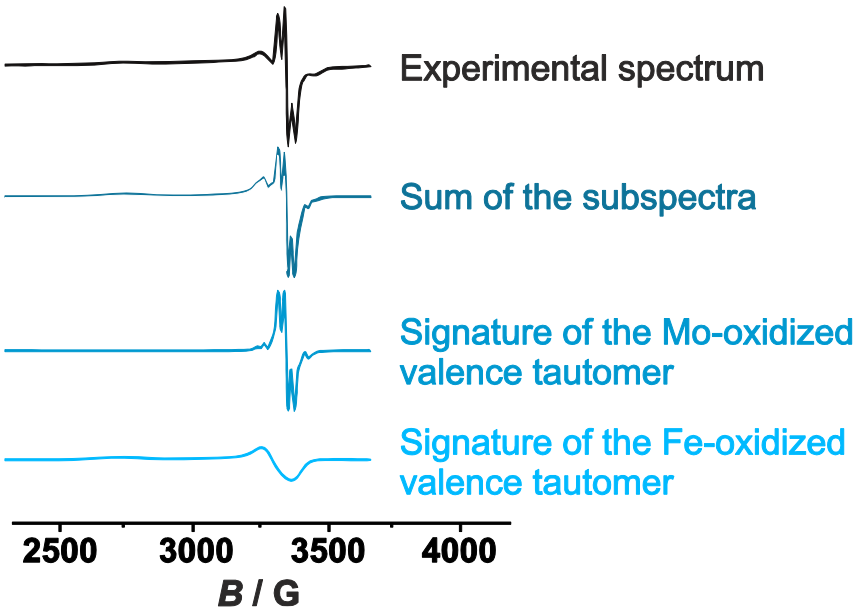

Fig. 1.34: EPR simulation of 1,4-diethynylphenylene-bridged Fe-Mo radical cationic complex **XX**$^+$, dividing the experimental data in Fe and Mo contributions.[56]

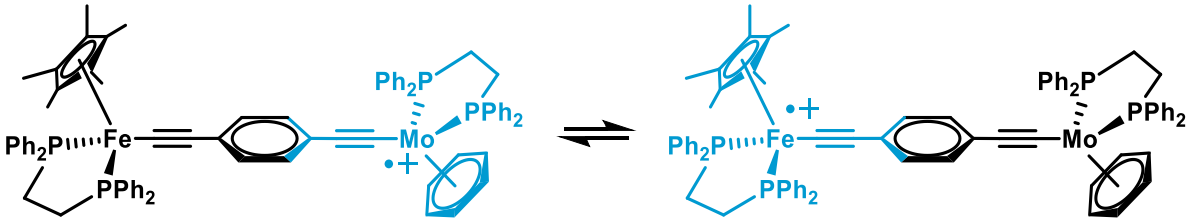

Fig. 1.35: Valence tautomerism observed in the heterobimetallic complex **XX**$^+$ by LAPINTE and WHITELEY.[56]

In this complex, small atomic displacements like the torsion of one terminal end group induce a redistribution of the spin density. Therefore, in this system the spin density distribution is highly dependent on environmental and conformational factors. That conformational factors can lead to two equilibrating spin density distributions was also observed by KATJA HEINZE in heterobimetallic amide-bridged Ru{bis(terpyridine)}(bipyridine)rhenium complexes, where the rotation around an C-N bond leads to the reorganization of the spin density.[55]

Veciana and his coworkers have published an impressive series of papers on neutral valence tautomers that combine a ferrocene or pentamethylferrocene or tetrathiafulvalene (TTF) and a polychlortriphenyl radical.[53,162-168] By external stimuli like a change in temperature or solvent polarity, a change in the equilibrium distribution between the zwitterionic or carbon-based radical forms can be triggered (Fig. 1.36).

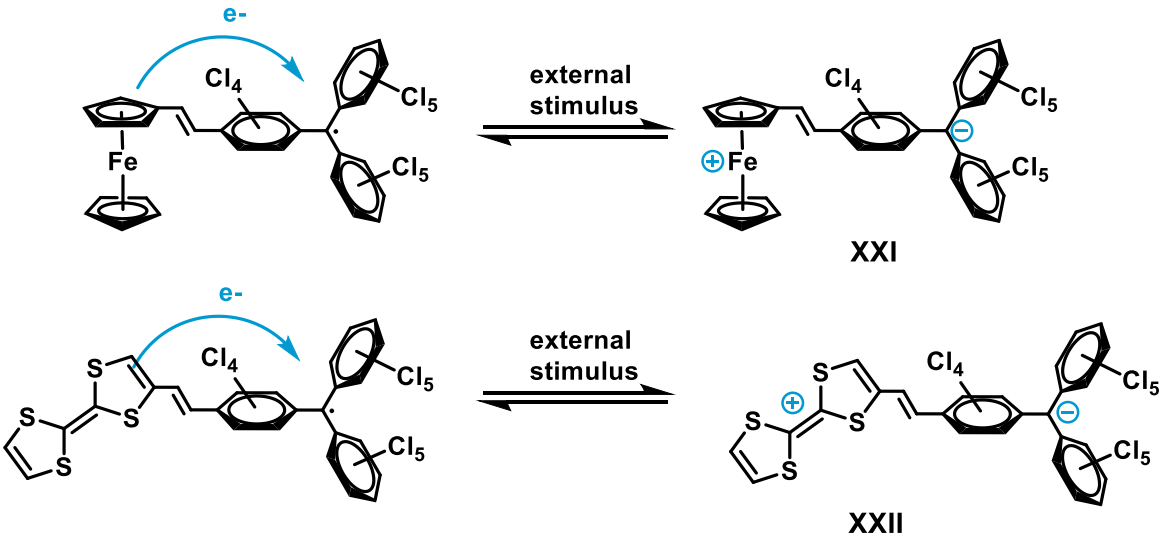

Fig. 1.36: Valence tautomeric equilibria in a ferrocene-triphenylmethyl **XXI** and a TTF-triphenylmethyl radical diad **XXII**.[168]

Mößbauer spectroscopic analysis of the ferrocene moiety in **XXI** can probe the ratio between the two states. Temperature dependent spectra revealed that the fraction of the Fe^{II} valence tautomer increases from 63 % at room temperature gradually to nearly 100 % at 4 K (Fig. 1.37). Here, the typical ferrocene doublet with an isomer shift of 0.542 mm s^{-1} and a rather large quadrupole splitting of ΔE_Q = 2.337 mm s^{-1}, but also one doublet with a smaller quadrupole splitting of ΔE_Q = 0.514 mm s^{-1} can be detected at high temperature. At 4 K, only the ferrocene Fe^{II}-trityl isomer persists.

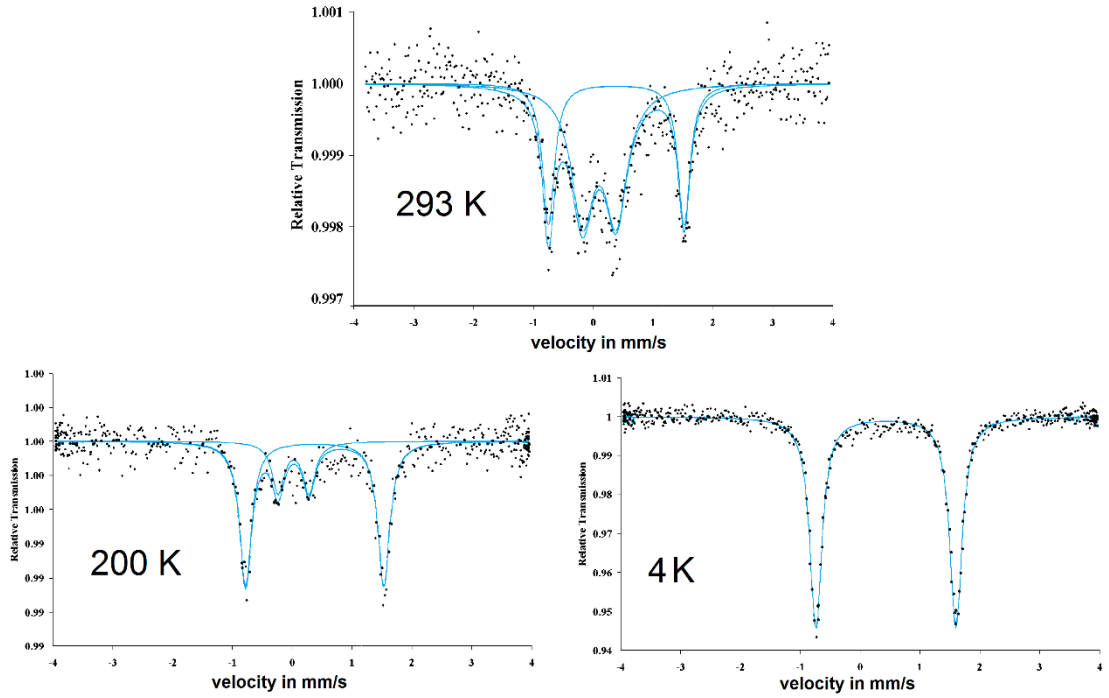

Fig. 1.37: Temperature-dependent Mößbauer spectra of the ferrocene-substituted triphenylmethyl radical **XXI** in Fig. 1.36. The valence tautomer equilibrium is influenced by temperature.[53]

An extraordinary example of valence tautomerism has been found by JING CHEN in our research group. A redox-active zink-porphyrin was combined with a five- or six-coordinated vinylruthenium fragment (Fig. 1.38).[59]

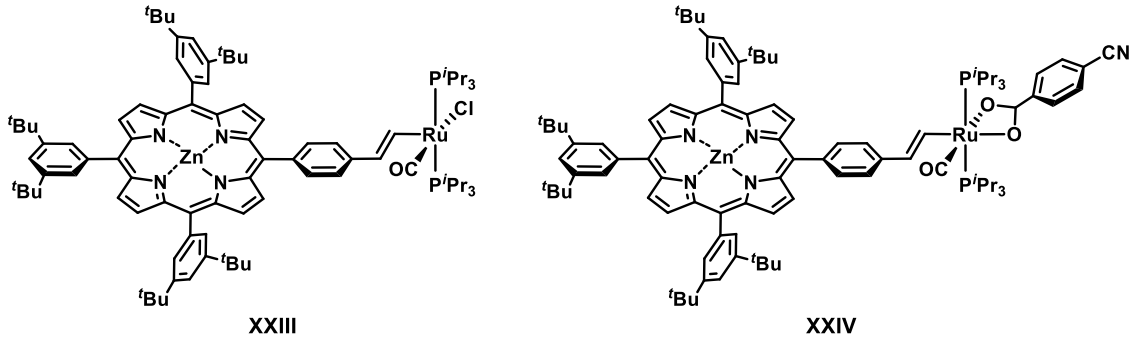

Fig. 1.38: Zink porphyrin vinylruthenium conjugates **XXIII** and **XXIV** displaying valence tautomerism in the mixed-valent state.[59]

The radical cations of those complexes were prepared by chemical oxidation with acetylferrocenium hexafluoroantimonate as a stoichiometric oxidant. The oxidized alkynyl precursor displays the typical sharp isotropic EPR signal at $g = 1.999$ of a porphyrin radical cation. The vinylruthenium Zn porphyrin complex **XXIII**$^+$, however, is characterized by separate EPR signals that coexist in a temperature dependent equilibrium. The individual components display a sharp isotropic signal for the porphyrin unit but also a resolved triplet at $g = 2.029$ with phosphorus hyperfine splittings ($A(^{31}P) = 15.6$ G). The second signal is due to the valence tautomer with an oxidized

styrylruthenium unit. With decreasing temperature, the intensity of the Zn-porphyrin signal decreases reversibly while that of the vinylruthenium signal increases (Fig. 1.39).

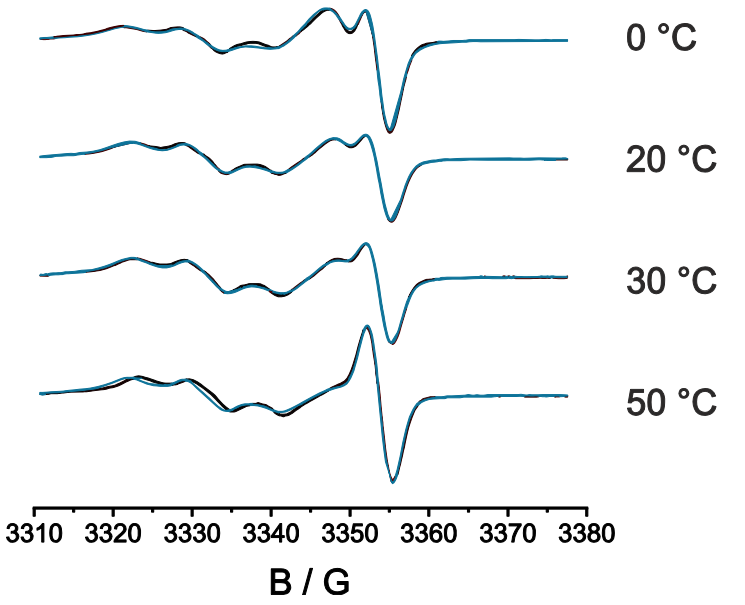

Fig. 1.39: EPR spectra of porphyrin vinylruthenium radical cation **XXIII**$^{+}$ at various temperatures. Overlay of experimental (black lines) and simulated spectra (blue lines).[59]

On first sight, these findings were supported by IR spectroscopy. After careful deconvolution of the CO vibration pattern, a satisfactory fit was only achieved when using three Gaussian lines instead of two. Temperature-dependent IR spectroscopy then revealed that a third species with an IR band of an intermediate position is present as well (Fig. 1.40).

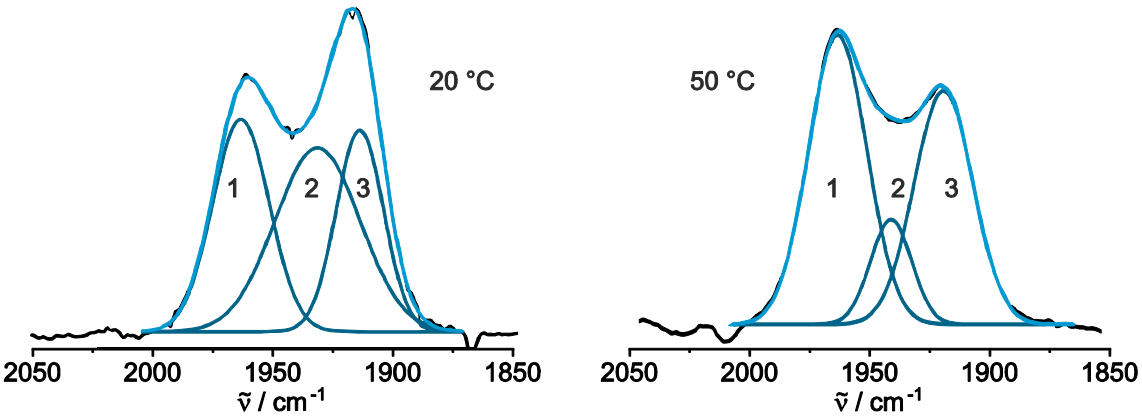

Fig. 1.40: IR deconvolution of the carbonyl stretching region of the zink porphyrine vinylruthenium radical cation **XXIII**$^{+}$. [59]

EPR spectra recorded at temperatures in between -110 and +50 °C also revealed a third signal, which is only slightly displaced from the *g*-value of the free electron g_e. UV/vis/NIR spectroscopy finally left no doubt that three different isomers coexist in solution, as low

energy bands were detected at *ca.* 6000 and 4900 cm^{-1} that are absent in solid state, where only the Zn-porphyrin tautomer is present.

The authors concluded that the three thermally equilibrating isomers must consist of two nearly degenerate valence tautomers where the charge and spin are either confined to the Zn porphyrin or the styrylruthenium unit, and an additional valence tautomer, where the charge and the spin density are delocalized over both redox-active entities (Fig. 1.41).

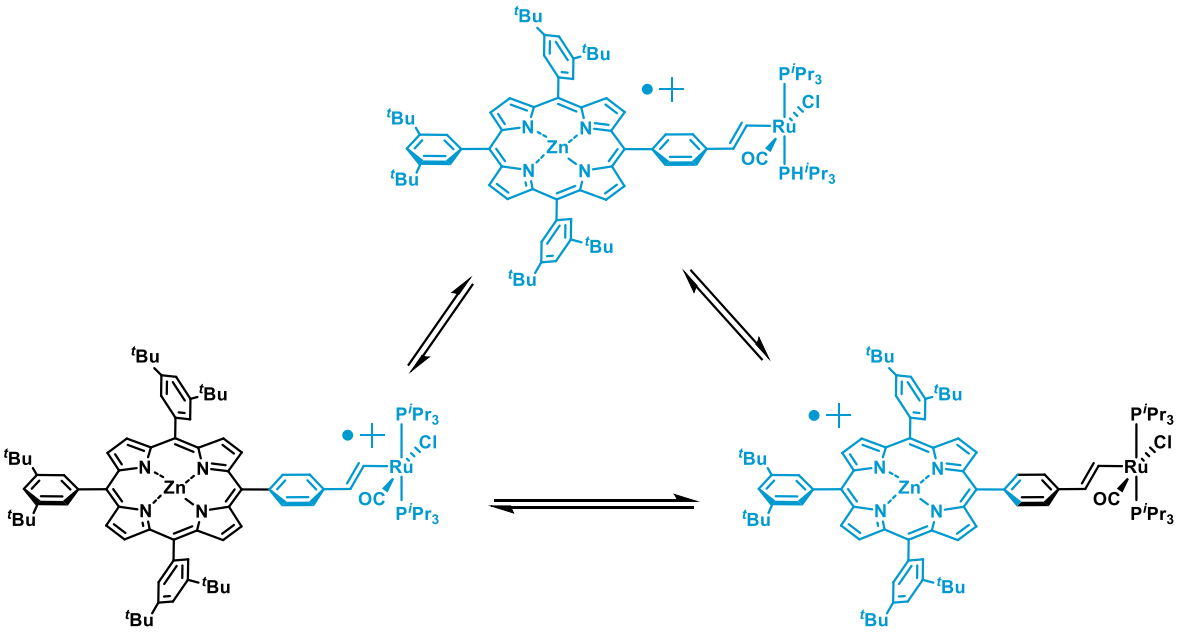

Fig. 1.41: Three equilibrating valence tautomers of a zink-porphyrin styrylruthenium radical cation **XXIII**$^+$ in solution.[59]

In general, small changes in the ground state energy and in the degree of electronic communication could lead to profound changes in terms of charge and spin (de)localization or the occurrence of valence tautomerism. The mentioned Class II systems by MÜCKE in Fig. 1.26 on page 41 are perfect starting points to evaluate possible valence tautomers due to their moderate electronic coupling and the facile detection by the CO vibrational band. This will be one further topic within this thesis.

2. Objectives

The goal of this thesis is the systematic exploration of the borderline regime between partial and complete charge and spin delocalization in asymmetric mixed-valent compounds with different redox-active moieties.

The analysis of the mixed-valent states of this type of complexes is of high interest as we need to learn how we can influence the charge and spin density distribution in radical cations upon oxidation of their neutral forms.

In particular, we were interested to explore whether the behavior of Class II/III borderline systems with identical redox sites also holds for similar compounds with different redox-active entities or if there are differences. This issue is only little explored in chemistry.

In doing so, we also sought out to answer the following basic questions which are still open in the literature:

- How do the intrinsic potentials of two redox-active active moieties correspond to the spin and charge density (de)localization in the mixed-valent state of a compound which combines these different redox sites?
- How does the IVCT- or CR-band of such systems respond to the gradual differences in electronic coupling?
- What are the basic requirements leading from charge localization to a delocalized behavior or from (de)localized behavior to valence tautomerism?
- How sensitive are the charge and spin density distributions of such compounds to environmental effects such as the solvent, counterion and temperature?

To this end, we selected ferrocene vinylruthenium, ruthenocene vinylruthenium and triarylamine vinylruthenium conjugates, as these allow for rather facile tuning of their intrinsic redox potentials by electron-withdrawing or electron-donating substituents (Fig. 2.1).

Another possibility to influence the intrinsic redox potentials of the target compounds is to increase the electron count of the vinylruthenium moiety by coordination of different β-ketoenolato ligands.

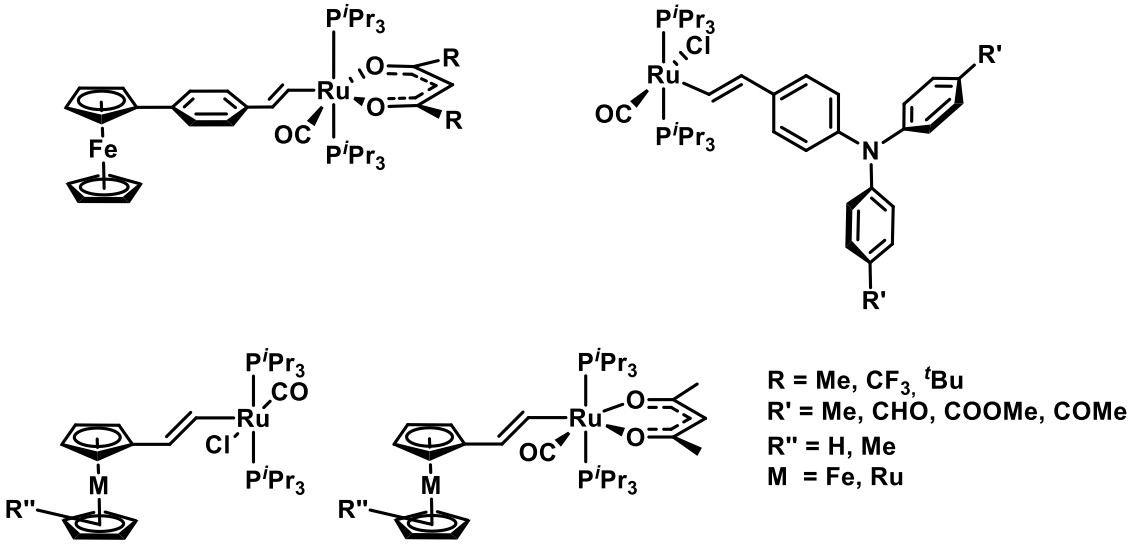

Fig. 2.1: Target compounds for the quantitative assessment of charge and spin delocalization in their one-electron oxidized forms: metallocenyl and triarylamine vinylruthenium conjugates.

This thesis is built on of three publications, where different structural motifs were realized and discussed in order to answer these questions. First, ferrocenyl vinylruthenium conjugates with varying donor capabilities of the β-ketoenolato ligand at the ruthenium moiety are presented. Second, triarylamine vinylruthenium complexes with varying electron withdrawing or donating substituents of the triarylamine moiety are discussed. The final chapter deals with ruthenocenyl vinylruthenium conjugates, where the electron density on either the vinylruthenium or the ruthenocenyl moiety is altered.

In addition to experimental data (NMR, CV, IR, UV/vis/NIR, EPR), density functional theory (DFT) calculations and their time-dependent quantum chemical extension TD-DFT of all compounds in their neutral, mixed-valent and, for selected compounds, in their dioxidized states provide further insight into their charge and spin distributions. These can be visualized either by graphical orbital representations or by summarizing the orbital coefficients and spin contributions of each atom to the respective orbitals.

3. Publications

3.1. Record of Contributions

The results in Chapter 3.2 have been published in *European Journal of Inorganic Chemistry*, **2017**, *2*, 401-411. The syntheses of the discussed complexes have been performed by myself as well as the NMR characterization, cyclic voltammetric measurements, IR spectroelectrochemistry, UV/vis/NIR spectroelectrochemistry and EPR spectroscopy. Mößbauer spectroscopy was performed by Dr. SERHIY DEMESHKO, University of Göttingen, and the acquisition and refinement of the crystallographic data was performed by BERHARD WEIBERT in our working group. The co-author PHILIPP MÜCKE provided the synthetic procedure of the 16 valence electron starting compound **1** as well as its analysis and the co-author JOHANNA SCHECK provided its crystal structure. The manuscript was written by PROF. WINTER and myself.

The results in Chapter 3.3 have been published in *Inorganic Chemistry*, **2017**, *56*, 13517-13529.The syntheses of the discussed complexes have been performed by myself. I also performed the NMR characterization, cyclic voltammetric measurements, IR spectroelectrochemistry, UV/vis/NIR spectroelectrochemistry, temperature dependent NIR spectroscopy, EPR spectroscopy and the quantum chemical calculations (DFT and TD-DFT). The manuscript was written by Prof. WINTER and myself.

The results in Chapter 3.4 have been published in *Inorganic Chemistry*, **2019**, *58*, 4, 2695-2707. The syntheses of the complexes **Rc-Ru^{Cl}** and **Rc-Ru^{acac}** as well as its NMR characterization, cyclic voltammetric measurements, IR spectroelectrochemistry, UV/vis/NIR spectroelectrochemistry and EPR spectroscopy were performed by ANDRÉ MANG during his Bachelor thesis under my supervision. The complexes **Fc-Ru^{acac}**, **Rc*-Ru^{Cl}** and **Rc*-Ru^{acac}** were synthesized by myself. I was also solely responsible for their complete analysis and all electrochemical and spectroscopic investigations. All quantum chemical calulations (DFT and TD-DFT) were performed by myself. The manuscript was written by Prof. WINTER and by myself.

In addition to the publications, which we post at the present thesis, the following articles have been published with me as a co-author.

1. Vanicek, S.; Kopacka, H.; Wurst, K.; Müller, T.; Hassenrück, C.; Winter, R. F.; Bildstein, B. *Organometallics* **2016,** *35*, 2101-2109 doi: 10.1021/acs.organomet.6b00329.

2. Wilson, L. E.; Hassenrück, C.; Winter, R. F.; White, A. J. P.; Albrecht, T.; Long, N. J. *Angew. Chem.* **2017,** *129*, 6942-6946, doi: 10.1002/ange.201702006.

3. Wilson, L. E.; Hassenrück, C.; Winter, R. F.; White, A. J. P.; Albrecht, T.; Long, N. J. *Eur. J. Inorg. Chem.* **2017,** *2017*, 496-504, doi: 10.1002/ange.201702006.

4. Vanicek, S.; Podewitz, M.; Hassenrück, C.; Pittracher, M.; Kopacka, H.; Wurst, K.; Müller, T.; Liedl, K. R.; Winter, R. F.; Bildstein, B. *Chemistry – A European Journal* **2018,** *24*, 3165-3169, doi: 10.1002/ejic.201601036.

5. Weststrate, N.-a.; Bouwer, S.; Hassenrück, C.; van Jaarsveld, N. A.; Liles, D. C.; Winter, R. F.; Lotz, S. *J. Organomet. Chem.* **2018,** *869*, 54-66, doi: 10.1016/j.jorganchem.2018.05.022.

6. Inge Schlapp-Hackl, Christopher Hassenrück, Klaus Wurst, Holger Kopacka, Thomas Müller, Rainer F. Winter,* Benno Bildstein*, *Eur. J. Inorg. Chem*. **2018**, 4434-4441, doi: 10.1002/ejic.201800774

7. Stefan Vanicek, Markus Jochriem, Christopher Hassenrück, Souvik Roy , Holger Kopacka, Klaus Wurst, Thomas Müller, Rainer F. Winter* , Erwin Reisner*, and Benno Bildstein*, *Organometallics*, Article ASAP, doi: 10.1021/acs.organomet.8b00681

To those papers, I contributed the spectroelectrochemical analyses and (TD-)DFT calculations and to paper 1), 4), 6) and 7) also the electrochemical measurements.

3.2. Paper 1: Oxidized Styrylruthenium-Ferrocene Conjugates: From Valence Localization to Valence Tautomerism

Christopher Hassenrück,[a] Philipp Mücke,[a], [b] Johanna Scheck[a], Serjihy Demeshko[c] and Rainer F. Winter*[a]

[a] Fachbereich Chemie der Universität Konstanz, Universitätsstraße 10, D-78457 Konstanz, Germany
[b] Present address: Infineon Technologies AG, Wernerwerkstraße 2, D-93049 Regensburg, Germany
[c] Dr. Serjihy Demeshko, Institut für Anorganische Chemie, Georg-August-Universität Göttingen, Tammannstraße 4, D-37077 Göttingen, Germany

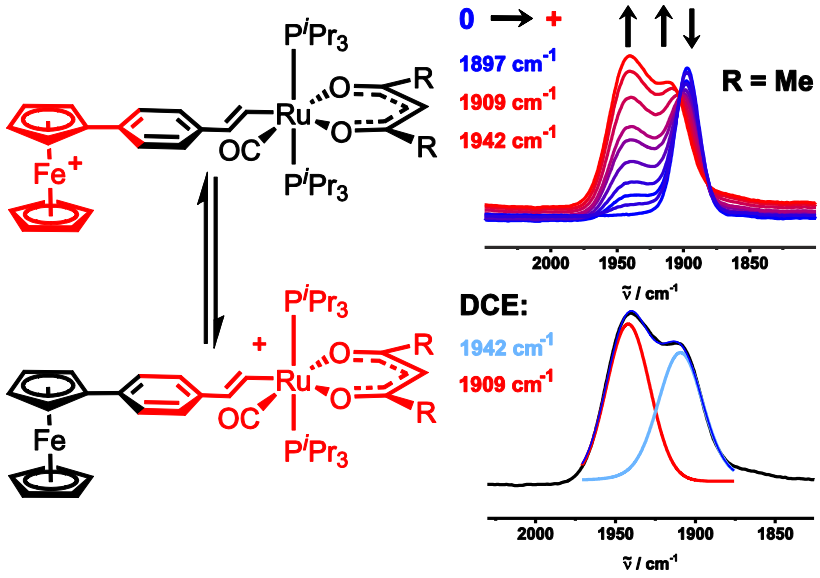

Reprinted with permission from *Eur. J. Inorg. Chem*, **2017**, pp. 401-411 Copyright 2017 John Wiley and Sons, License Number 4510830529468.

ChemPubSoc Europe

DOI: 10.1002/ejic.201600776

EurJIC European Journal of Inorganic Chemistry

Full Paper

Valence Tautomers | *Very Important Paper* | CLUSTER ISSUE

VIP

Oxidized Styrylruthenium–Ferrocene Conjugates: From Valence Localization to Valence Tautomerism

Christopher Hassenrück,[a] Philipp Mücke,[a][‡] Johanna Scheck,[a] Serhiy Demeshko,[b] and Rainer F. Winter*[a]

Abstract: We report on ferrocenyl–styrylruthenium conjugates Fc–C_6H_4–CH=CH–Ru(CO)($PiPr_3$)$_2$(L) in which the electron density at the alkenylruthenium site is modified by the variation of the coligand L [L = Cl, acetylacetonate (acac), hexafluoroacetylacetonate (hfac), or dipivaloylmethane (dpvm); Fc = ferrocenyl]. Crystallographic studies on three derivatives provide snapshots of the conformational degrees of freedom for rotation around the vinyl–phenylene and phenylene–ferrocenyl linkages. All four complexes undergo two consecutive, reversible one-electron oxidations, the potentials of which depend on the ligand L. On the basis of IR spectroelectrochemistry results, the first oxidations of the less electron-rich chlorido and hfac complexes are biased strongly towards the ferrocenyl site. However, the radical cation of the acac complex exists as two equilibrating valence tautomers (VTs) Fc^+–C_6H_4–CH=CH–{Ru^{acac}} ⇌ Fc–[C_6H_4–CH=CH–{Ru^{acac}}]$^+$ [{Ru^{acac}} = Ru(CO)($PiPr_3$)$_2$(acac)], in which the positive charge is either localized at the ferrocenyl site or delocalized over the styrylruthenium moiety. Variable-temperature electron paramagnetic resonance (EPR) and Mössbauer spectroscopy reveal that the ferrocenium valence tautomer dominates at low temperature. A marked solvent dependence on the position and relative intensities of the separate Ru(CO) bands in the IR spectra reveals environmental effects on the relative stabilities of the two VTs, whereas the strong negative solvatochromism of the prominent near-IR band of the radical cation of the acac complex argues for a sizable (intervalence) charge-transfer component of the underlying excitation.

Introduction

Mixed-valent (MV) radical cations of compounds featuring an alkenylruthenium entity and a second, chemically different redox site with a similar intrinsic redox potential can display different kinds of behavior: (1) complete charge and spin delocalization as in the 1,4-divinylphenylene-bridged heterodinuclear Ru/Os complex [(iPr_3P)$_2$Cl(CO)Ru–CH=CH–C_6H_4–CH=CH–Os(CO)Cl($PiPr_3$)$_2$]$^+$ (**A**; Figure 1),[1] the 1,4-ethynylvinylphenylene-bridged di- and triruthenium complexes *trans*-[X(dppe)$_2$Ru–C≡C–C_6H_4–CH=CH–Ru(CO)Cl($PiPr_3$)$_2$]$^+$[2] [X = Cl, –C≡CPh; dppe = 1,2-bis(diphenylphosphanyl)ethane; **B**] and *trans*-[(dppe)$_2$Ru{–C≡C–C_6H_4–CH=CH–Ru(CO)Cl($PiPr_3$)$_2$}$_2$]$^{n+}$ (*n* = 1–4; **C**),[3] or the alkenylruthenium–triarylamine conjugates *para*-[(iPr_3P)$_2$Cl(CO)Ru–CH=CH–$C_6H_4N(C_6H_4OMe\text{-}4)_2$]$^+$ (**D**) with a *para* disubstitution motif at the central phenylene ring;[4] (2) partial charge delocalization as in [Fc–CH=CH–Ru(CO)Cl($PiPr_3$)$_2$]$^+$ [Fc = ferrocenyl, (η^5-C_5H_5)Fe(η^5-C_5H_4), Ru-Fc$^+$]; and (3) predominant charge localization on just one of the two available redox sites as in *meta*-[(iPr_3P)$_2$Cl(CO)Ru–CH=CH–$C_6H_4N(C_6H_4OMe\text{-}4)_2$]$^+$[5] (**E**) or the radical cation of the squaraine bis(vinylruthenium) conjugate (**F**; Figure 1).[6] The attachment of a 16- or 18-valence-electron (VE) styrylruthenium moiety to a *meso*-tetraaryl-substituted zinc–porphyrin in complex **G** (Figure 1) has finally unearthed examples of MV radical cations that coexist as three thermally equilibrating redox isomers (valence tautomers, VTs), two of which exhibit charge localization on either the zinc porphyrin or the styrylruthenium subunit, and one with extensive delocalization of the positive charge and the unpaired spin density over both subunits.[7]

For Ru-Fc$^+$, the close proximity and intimate connection between the individual redox sites renders a partitioning somewhat arbitrary, as the vinyl "bridge" constitutes an integral part of both. We mused that the insertion of a phenyl ring into the nominal bridge might serve the purpose of spatially separating and partially decoupling the ferrocenyl and vinylruthenium moieties (note, however, that the phenyl ring will nevertheless constitute an integral part of the alkenylruthenium redox system[8]) and, possibly, also induce similar effects to those in the zinc porphyrin conjugate. We note in this respect that the insertion of an additional phenyl or styryl unit into the conjugated pathway that interconnects two vinylruthenium entities leads to a gradual decrease of the ground-state charge delocalization as measured by the Geiger charge-distribution parameter $\Delta\varrho$[9] from 0.50 in [{Ru}–1,4-CH=CH–C_6H_4–CH=CH–{Ru}]$^+$, which indicates a fully symmetrical charge-density distribution and a fully

[a] *Fachbereich Chemie der Universität Konstanz, Universitätsstraße 10, 78457 Konstanz, Germany*
E-mail: rainer.winter@uni-konstanz.de
https://cms.uni-konstanz.de/ag-winter/gruppe/
[b] *Institut für Anorganische Chemie, Georg-August-Universität Göttingen, Tammannstraße 4, 37077 Göttingen, Germany*
[‡] Current address: Infineon Technologies AG, Wernerwerkstraße 2, 93049 Regensburg, Germany

Supporting information and ORCID(s) from the author(s) for this article are available on the WWW under http://dx.doi.org/10.1002/ejic.201600776.

© 2017 Wiley-VCH Verlag GmbH & Co. KGaA, Weinheim

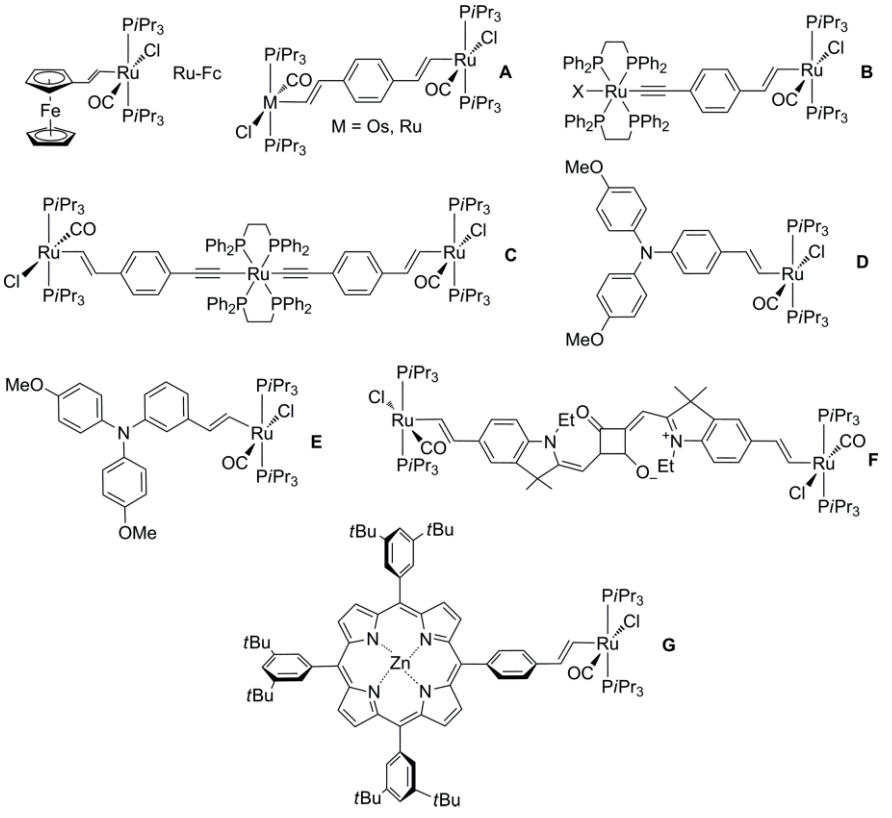

Figure 1. Examples of alkenylruthenium complexes with an additional, chemically different redox-active moiety.

symmetrical ground-state electronic structure of this radical cation, to 0.25 in the biphenyl-bridged [{Ru}–1,4-CH=CH–C_6H_4–C_6H_4–CH=CH–{Ru}]$^+$[10] and 0.19 in the all-*trans* stilbenyl-bridged [{Ru}–1,4-CH=CH–C_6H_4–CH=CH–C_6H_4–CH=CH–{Ru}]$^+$ [{Ru} = Ru(CO)Cl(P*i*Pr$_3$)$_2$].[11] In the latter systems, 75 or 81 % of the surplus positive charge is concentrated on one side, and the electronic ground state of the corresponding radical cation becomes increasingly asymmetric. Likewise, MV radical cations of bridged diferrocenes also reveal a steady decrease of the electronic coupling parameter H_{AB} with increasing bridge length, for example, from 490–665 cm^{-1} in the radical cation of *trans*-1,2-diferrocenylethene[12] to 350–380 cm^{-1} for 1,4-diferrocenylbenzene[12c,13] and 320 cm^{-1} for the radical cation of 1,4-divinylphenylene-bridged diferrocene.[12c] Within the boundaries of the Hush theory, H_{AB} denotes the energy splitting between the bonding and nonbonding adiabatic potential hypersurfaces of an MV system at the point of the avoided crossing of the diabatic, localized hypersurfaces; H_{AB} increases with the strength of the electronic interaction between these states.[14]

As an added complexity over compounds with equivalent redox sites, the energy minima of MV compounds with two differing redox sites are no longer isoenergetic but separated by an energy difference ΔG^0, which relates to the difference in the intrinsic redox potentials of the two unequal redox-active subunits (Figure 2).[15] The local electron density of the Ru(CO)Cl(P*i*Pr$_3$)$_2$ moiety can be altered in a straightforward way through the substitution of the chlorido ligand, for example, by a bidentate monoanionic ligand to increase the valence-electron (VE) count from 16 to 18. Such modification has already been found to influence the relative amounts of the different valence tautomers (VTs) of zinc-porphyrin–styrylruthenium conjugates.[7] Although ligand substitution at the ruthenium center will affect the positioning of the minima of both diabatic hypersurfaces, its effects will be stronger on the alkenylruthenium site. Thus, the intrinsic energy difference ΔG^0 between the local minima of the diabatic hypersurfaces can be varied.[16] This opens the possibility to realize, within the same basic system, the bordering situations of valence delocalization, of predominant valence localization at one site or the other, or to achieve electronic bistability, that is, the phenomenon of valence tautomerism. The latter kind of behavior can result if the local minima representing the different possibilities of charge distribution are similar in energy and are separated by an energy barrier ΔG^* of sufficient height (Figure 2, right). We note here that the energy ordering of different VTs may also depend on the solvent or counterion if specific solvation effects (e.g., strong hydrogen bonding) or ion pairing (de)stabilize one VT with respect to the other.[15b,15c,17]

For our present study, we chose β-keto enolato ligands as they are readily available, provide stable bidentate coordination, and their donor strengths can be adjusted by the variation of the substituents at the peripheral carbon atoms. We here compare the styrylruthenium–ferrocene conjugates **1**, **2**-hfac, **2**-acac, and **2**-dpvm [Scheme 1; hfac = hexafluoroacetylacetonate, acac = acetylacetonate, dpvm = dipivaloylmethane] with CF_3-, CH_3-, or *t*Bu-substituted β-keto enolato ligands,

© 2017 Wiley-VCH Verlag GmbH & Co. KGaA, Weinheim

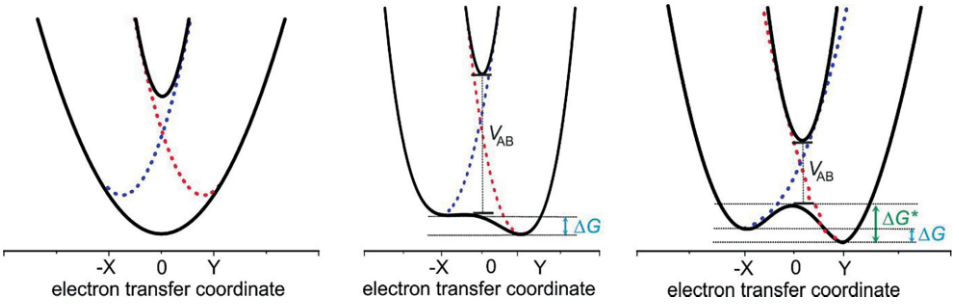

Figure 2. Schematic drawings of potential hypersurfaces representing full (left) or partial (middle) charge delocalization of a mixed-valent (MV) system with unequal redox sites or two coexisting valence tautomers (right).

respectively, and with a 16 or 18 VE count at the ruthenium center and show that the coligand indeed exerts a remarkable effect on the electronic ground states of these compounds.

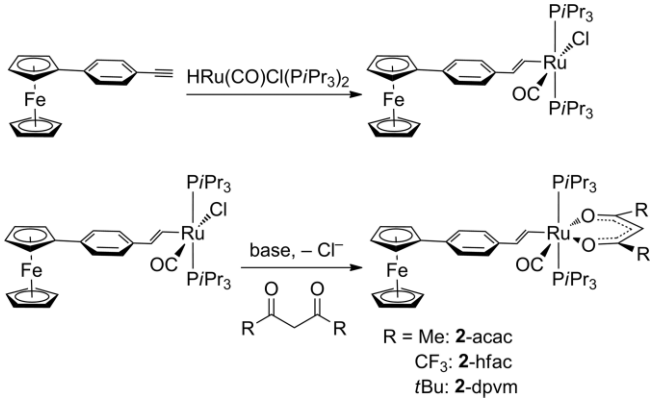

Scheme 1. Complexes of the present study and their synthesis.

Results and Discussion

Synthesis and Characterization

The ferrocenyl–styrylruthenium conjugate **1** (Scheme 1) was readily prepared from the known 1-ferrocenyl-4-ethynylbenzene[18] by insertion of the ethynyl function into the Ru–H bond of the hydrido complex $HRu(CO)Cl(PiPr_3)_2$.[19] In spite of the considerable complexities of the underlying mechanism,[20] this hydroruthenation reaction proceeds with complete regio- and stereoselectivity to afford alkenyl complexes with a *trans*-1,2-disubstitution pattern at the double bond and with the ruthenium ion bonded to the terminal carbon atom of the previous alkyne.[21] Thus, **1** was obtained in quantitative yield after simple washing. The substitution of the chlorido ligand for the corresponding β-keto enolate was achieved in a CH_2Cl_2/CH_3OH solvent mixture with sodium carbonate as the base and afforded the 18 VE substitution products **2**-hfac, **2**-acac, and **2**-dpvm in high to quantitative yields as deep-red (**2**-hfac) or orange-yellow solids (Scheme 1). The latter were duly characterized by multinuclear NMR, IR, and UV/Vis spectroscopy. The ^1H NMR spectra feature the characteristic doublets of triplets (owing to resolved $^2J_{H,P}$ or $^3J_{H,P}$ coupling) for the vinylic protons at the CH=CH linkage with $^3J_{H,H}$ coupling constants of 13.4 Hz for the 16 VE complex **1** and ca. 16 Hz for the 18 VE complexes as well as the resonances for a monosubstituted ferrocene, the 1,4-phenylene linker, and the two phosphine ligands with diastereotopic *i*Pr substituents in their correct integration ratios. The corresponding resonances were also observed in the ^{13}C NMR spectra with resolved $^2J_{C,P}$ or $^3J_{C,P}$ coupling to carbon atoms C^1 and C^2 of the alkenyl ligand and to that of the CO ligand of ca. 12, 3, and 15 Hz, respectively (for the spectra, see Figures S1–S13 in the Supporting Information). The most pertinent NMR spectroscopy data are compiled in Table 1 and illustrate that the VE count at the ruthenium center and the donor capacities of the keto enolato ligand influence the chemical shifts of the vinylic protons H^1 and H^2, the C atom of the CO ligand, and the carbon atoms of the styryl linker apart from that directly connected to the ferrocene moiety (see Scheme 2 for generic atomic numbering).

The CO stretching vibration ν(CO) of the carbonyl ligand provides a diagnostic marker for the electron density at the ruthenium center. Owing to the superior donor capabilities of the acac and dpvm ligands, the energy of the CO stretch decreases from $\tilde{\nu}$ = 1910 cm^{-1} in **1** to $\tilde{\nu} \approx$ 1896 cm^{-1} in **2**-acac and **2**-dpvm. Thus, the energy of the Ru–C≡O stretch is lower than in similar benzoato complexes ($\tilde{\nu} \approx$ 1902 cm^{-1}).[3a] Of particular

Table 1. Selected ^1H and ^{13}C NMR chemical shifts (δ [ppm]) for the complexes.[a]

	H^1	H^2	C^1	C^2	C^3	C^4	C^5	C^6	C^{11}
1	8.56	5.98	150.6	134.6	137.3	124.3	126.8	134.8	203.5
2-hfac	8.67	6.36	158.1	134.8	138.8	126.2	123.8	134.1	208.8
2-acac	8.96	6.40	166.3	134.3	140.6	126.8	124.1	133.5	210.5
2-dpvm	9.04	6.38	166.2	134.2	140.1	126.8	124.0	133.5	210.5

[a] Recorded in CD_2Cl_2 at room temperature, referenced against the signal of the non-deuterated solvent.

© 2017 Wiley-VCH Verlag GmbH & Co. KGaA, Weinheim

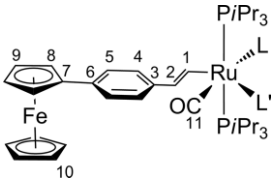

Scheme 2. Atomic numbering scheme for Table 1.

note is the position of the Ru–CO band of **2**-hfac at $\tilde{\nu}$ = 1917 cm^{-1}, which shows that the hfac ligand is a poorer donor than the simple chlorido ligand in spite of the increased VE count of 18. The poorer donor/stronger acceptor qualities of the hfac ligand compared with those of the other keto enolates is also manifest from the position of the visible absorption band, which, albeit of rather weak intensity, is responsible for the coloration of the complexes. By inference from several other complexes of this kind, this band corresponds to a ligand-to-metal charge-transfer (LMCT) band in the 16 VE complex **1** involving a transition from the delocalized styrylruthenium highest occupied molecular orbital (HOMO) to a metal–phosphine-centered lowest unoccupied molecular orbital (LUMO).[8] In the 18 VE complexes featuring a bidentate, π-conjugated donor ligand, a coligand-based π*-orbital usually lies energetically below the corresponding Ru d-orbital such that the character of this transition changes to a metal/alkenyl-to-coligand (LM→L') charge-transfer band.[3a,22]

Single crystals of **1**, **2**-hfac, and **2**-acac allowed the determination of their molecular structures by X-ray crystallography. Plots of the structures along with the atom-numbering schemes are displayed in Figures 3 (**1** and **2**-hfac) and S14 (**2**-acac), and the most pertinent bond lengths and angles are provided in Table 2 (for more details of the data collection and structure refinement, see Table S1). The structures offer different "snapshots" of the torsional degrees of freedom around the C_5H_4–phenylene–CH=CH–Ru(CO)LL' linkages. Thus, in **2**-hfac, the entire π-conjugated backbone is essentially planar with torsion angles of less than 3° between the equatorial coordination plane of the metal ion and the phenyl ring (2.8°), between the phenyl ring and the attached cyclopentadienide (Cp) ligand (2.9°), and between the coordination plane and that of the respective Cp ligand (2.6°). In **1** and **2**-acac, these interplanar angles increase to 23.9/4.7/28.4 and 14.1/24.7/34.2°, respectively (see also Table 2). The larger torsion angle is between the {Ru}–CH=CH moiety and the phenyl ring in **1** or between the phenyl ring and the Cp ligand in **2**-acac. Nevertheless, these values are still indicative of a conjugated pathway that interlinks the individual redox-active subunits. The cyclopentadienide ligands of each ferrocenyl substituent are coplanar and in a close to ecliptic conformation or a conformation between eclipsed and staggered, as measured by the average C–$Cp_{centroid}$–$Cp_{centroid}$–C dihedral angles of 4.8° for **1**, 7.0° for **2**-hfac, and 13.2° for **2**-acac.

The other metrical data are unremarkable compared to those of closely related structures of five-[5,8,10,11,23] and six-coordinate[3a,24] alkenylruthenium complexes with the Ru(CO)-($PiPr_3$)$_2$(L) moiety and warrant no further discussion. Owing to the strong σ-*trans* influence of the alkenyl ligand, the Ru–O

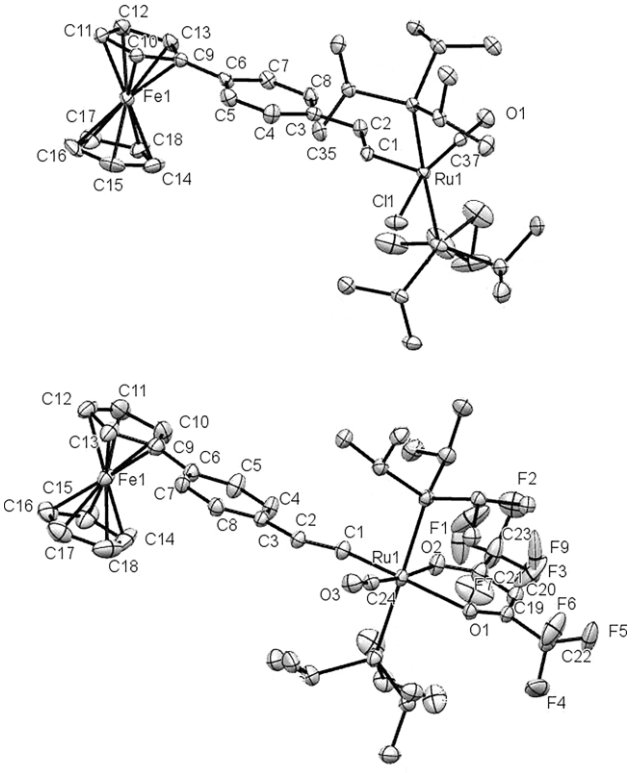

Figure 3. Crystal structures of **1** (top) and **2**-hfac (bottom) with atom-numbering schemes. Ellipsoids are drawn at the 50 % probability level. Hydrogen atoms are removed for clarity.

Table 2. Selected bond lengths [Å] and angles [°] for **1**, **2**-acac, and **2**-hfac.

	1	**2**-hfac	**2**-acac
Ru–C^1	1.983(4)	2.022(2)	2.040(3)
C^1–C^2	1.346(6)	1.335(4)	1.340(4)
C^2–C^{Ph}	1.472(6)	1.482(3)	1.476(4)
C^{Ph}–C^{Cp}	1.486(6)	1.479(3)	1.476(4)
Ru–C^{CO}	1.802(4)	1.809(3)	1.806(3)
C–O (CO)	1.147(5)	1.165(3)	1.166(4)
Ru–P	2.4060(14)	2.4490(6)	2.4488(8)
	2.4083(14)	2.4370(7)	2.4183(8)
Ru–Cl/Ru–O	2.433(1)	2.2118(16)	2.182(2)
		2.1669(17)	2.126(2)
P–Ru–P	173.01(4)	175.71(2)	177.79(3)
Cl–Ru–C^{CO}/	162.8(1)	100.17(9)	97.87(11)
O–Ru–C^{CO}	–	174.57(9)	175.91(12)
Cl–Ru–C^1/	108.41(13)	166.89(9)	170.97(19)
O–Ru–C^1	–	85.31(9)	85.83(10)
O–Ru–O	–	82.60(6)	85.28(8)
C^{CO}–Ru–C^1	88.77(18)	92.30(11)	91.11(13)
Ru–C^1–C^2	135.4(4)	137.0(2)	134.8(2)
C^1–C^2–C^{Ph}	126.4(4)	125.7(2)	127.5(3)
P–Ru–C^1	95.81(13)	91.27(7)	89.66(8)
	90.47(13)	89.95(7)	92.22(8)
{Ru}–C/phenyl[a]	23.9	2.8	14.1
Phenyl/Cp[b]	4.7	2.9	24.7
{Ru}–C/Cp[c]	28.4	2.6	34.2
Cp/Cp[d]	3.7	1.2	0.8

[a] Interplanar angle between the equatorial coordination plane at the Ru center and the phenyl ring of the styryl linker. [b] Interplanar angle between the phenyl ring and the attached Cp ring. [c] Interplanar angle between the coordination plane at the Ru center and the Cp ring. The Ru coordination plane is defined as the best plane through atoms Ru1, C1, Cl1, and C37 for **1**; atoms Ru1, C1, C24, O1, and O2 for **2**-hfac; and Ru1, C1, C42, O1, and O2 for **2**-acac. [d] Tilt angle between the Cp rings.

© 2017 Wiley-VCH Verlag GmbH & Co. KGaA, Weinheim

bond opposite the latter ligand is longer than that opposite the carbonyl ligand by ca. 0.04 Å. As is routinely observed in other complexes of this type, the alkenyl ligand is rotated towards the CO ligand. Such orientation has been ascribed to stabilizing interactions between occupied Ru t_{2g}-orbitals and the C=C and C≡O π*-orbitals of the alkenyl and CO ligands, and these interactions become most effective when the two unsaturated ligands are coplanar.[25]

Cyclic and square-wave voltammetric studies in CH_2Cl_2/nBu$_4$NPF$_6$ (0.1 M) as the supporting electrolyte show that, like Ru-Fc, every complex is oxidized in two consecutive, reversible one-electron waves with close to ideal parameters in terms of the peak current ratios $i_{p,reverse}/i_{p,forward}$, peak potential differences ΔE_p, and half-widths of the forward peaks. Representative voltammograms of **2**-hfac and **2**-dpvm are shown in Figure 4, and those of the other two complexes are shown in Figures S15 and S16. The pertinent data from these voltammograms are provided in Table 3.

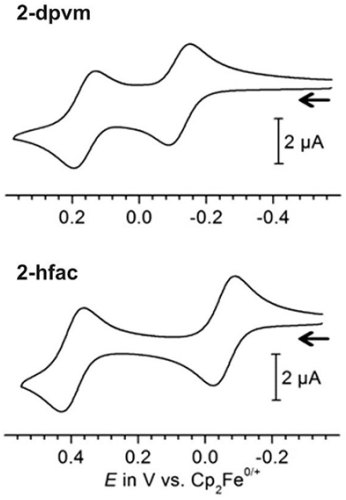

Figure 4. Cyclic voltammograms of **2**-dpvm (top) and **2**-hfac (bottom) in CH_2Cl_2/nBu$_4$NPF$_6$ at v = 0.1 V/s at r.t.

Table 3. Electrochemical properties of the complexes of this study[a] and of the vinyl-bridged Ru-Fc.[b]

Complex	$E_{1/2}^{0/+}$ (ΔE_p) [mV]	$E_{1/2}^{+/2+}$ (ΔE_p) [mV]	$\Delta E_{1/2}$ [mV]
Ru-Fc[c]	–235 (58)	580 (60)	815
1	–43 (57)	355 (63)	398
2-hfac	–52 (63)	400 (66)	452
2-acac	–114 (58)	166 (57)	280
2-dpvm	–107 (64)	178 (64)	285

[a] Data in CH_2Cl_2/nBu$_4$NPF$_6$ (0.1 M) at r.t. and at a scan rate v = 100 mV/s. [b] Ru-Fc = (η^5-C_5H_5)Fe(η^5-C_5H_4)–CH=CH–Ru(CO)Cl(PiPr$_3$)$_2$. [c] Data from ref.[23]

From these data, it becomes evident that the insertion of a phenylene linker into the conjugated pathway, which connects the {Ru}–CH=CH entity to the ferrocenyl redox system, leads to a reduction in the half-wave potential splitting $\Delta E_{1/2}$ for the two consecutive one-electron steps from 815 mV in Ru-Fc to ca. 400 mV in **1**. Secondly, although the identity of the coligand at the ruthenium center influences both half-wave potentials, it has a larger impact on the potential of the second redox process, such that $\Delta E_{1/2}$ decreases with increasing electron-donating capability of the coligand. Therefore, one might be drawn to assign the first redox process as ferrocene-based and the second one as more centered on the alkenylruthenium redox site. However, as detailed in the following section, spectroscopic studies on the radical cations of these complexes reveal this view as too simplistic. Thirdly, the electrochemical data also support the notion of less electron donation by the hfac ligand, even compared with the simple chlorido ligand. Thus, the half-wave potentials of the 18 VE complex **2**-hfac are higher on average than those of the 16 VE complex **1**.

Spectroscopic Studies on the Oxidized Forms

IR spectroscopy is particularly useful to elucidate the electron loss from the alkenylruthenium site on oxidation. Owing to the large contributions of the styryl ligand to the occupied frontier molecular orbitals (MOs, the so-called redox orbitals relevant for an oxidation process),[8,26] the blueshift of the Ru(CO) band of 50–70 cm^{-1} is significantly smaller than the displacement of 100–150 cm^{-1} expected for a metal-centered oxidation.[27] Benchmark systems related to the present complexes are the trigonal-bipyramidal mixed phosphine/carbonyl complexes *trans*-Ru(PR$_3$)$_2$(CO)$_3$ (R = Ph, benzyl, cyclohexyl), for which the CO band shifts amount to 120 cm^{-1} on the removal of one electron from an orbital with predominant Ru 4d-character.[28] For extensive series of 4-substituted styryl complexes {Ru}–CH=CH–C$_6$H$_4$–4-R with {Ru} = Ru(CO)Cl(PiPr$_3$)$_2$ or *mer*-Ru(CO)Cl(PMe$_3$)$_3$, a strong dependence of the oxidation-induced displacement of the CO band on the Hammett σ_p parameter of the substituent R has been noted, and the contribution of the styryl ligand to the HOMO increases with electron donation from R.[24,26c,29] Owing to the rather similar σ_p values of the methoxy (σ_p = –0.27) and ferrocenyl substituents (σ_p = –0.18),[30] the $\Delta\nu$(CO) value of 57 cm^{-1} observed for Ru(CO)Cl(PiPr$_3$)$_2$–CH=CH–C$_6$H$_4$–4-OMe provides a suitable point of comparison for the expected CO band shift for a styrylruthenium-based oxidation, that is, for the extreme situation in which the ferrocenyl entity acts merely by inductive and resonance effects.[24] On the other hand, much smaller CO band shifts of only 6–8 cm^{-1} are usually observed when a redox process occurs at a remote redox site of an alkenylruthenium conjugate. The bis(alkenylruthenium)-appended squaraine **F** or the radical cation and anion of the styrylruthenium-modified zinc porphyrin **G** (Figure 1) with a porphyrin-centered oxidation/reduction provide prototypical examples of this other extreme case.[6,7]

According to our IR spectroscopic studies performed under the in situ conditions of spectroelectrochemistry, this latter scenario adequately describes the situation for the first oxidation of the less electron-rich **1** and **2**-hfac (see Figures 5 and S17 and Table 4 for a compilation of the relevant data). Thus, during this process, the CO band shifts by only 7 or 3 cm^{-1}, respectively. For these complexes, the intrinsic redox potential of the styrylruthenium moiety is clearly so high and its contribution to the singly occupied molecular orbital (SOMO) so small that the unipositive charge resulting from one-electron oxidation largely resides on the ferrocenyl entity. This is also indicated

© 2017 Wiley-VCH Verlag GmbH & Co. KGaA, Weinheim

by the absence of intense C=C stretching and =C–H bending vibrations in the spectra of the radical cations. The latter are typical assets of oxidized styrylruthenium complexes.[8,24] In contrast, the shift of 60 or 63 cm^{-1} during the second oxidation matches that expected for the one-electron oxidation of a simple styrylruthenium complex bearing a slightly electron-withdrawing 4-substituent (note that the second oxidation of **2**-hfac is accompanied by an irreversible chemical process, which leads to additional CO-containing species; see Figure S17).

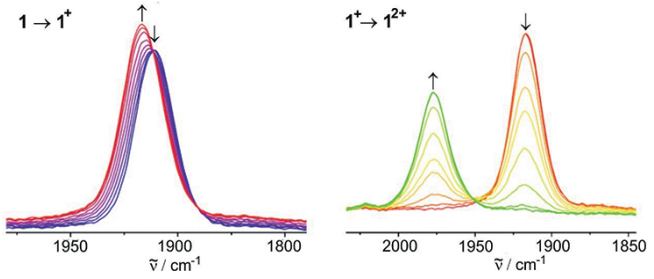

Figure 5. IR spectroscopic changes of ν(CO) during the first (left) and the second (right) oxidation of **1** (1,2-$C_2H_4Cl_2$/nBu$_4$NPF$_6$, 0.1 M, r.t.).

Table 4. Changes in the ν(CO) region [cm^{-1}] of the IR spectra of the complexes.[a]

Complex	Neutral	Cation	Dication
1	1910	1917	1977
2-hfac	1917	1920	1983
2-acac	1897	1909, 1942	1969

[a] In 1,2-$C_2H_4Cl_2$/0.1 M nBu$_4$NPF$_6$ at r.t.

Complex **2**-acac shows a different behavior. As is illustrated in Figure 6, the single Ru(CO) band evolves during the first oxidation into a pattern of overlapping bands with different intensities. The Ru–CO band region of the spectrum obtained after the full conversion to the corresponding radical cation is readily deconvoluted into two separate bands at $\tilde{\nu}$ = 1909 and 1942 cm^{-1}. On the second oxidation, the two bands merge and give way to a single Ru–CO band at $\tilde{\nu}$ = 1969 cm^{-1}. A graphical account for this latter process is shown in Figure S18. These results point to the coexistence of two equilibrating species (isomers) at the radical cation stage that differ in terms of the charge at the alkenylruthenium (and, by inference, also at the ferrocenyl) site. This is the typical fingerprint for the phenomenon of valence tautomerism. In keeping with the considerable fraction of the valence tautomer with an oxidized styryl-

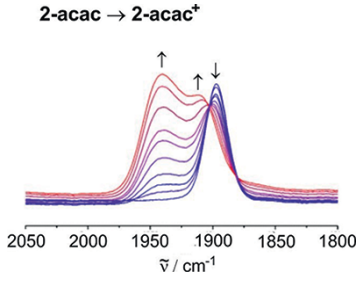

Figure 6. IR spectroscopic changes of ν(CO) during the first oxidation of **2**-acac in 1,2-$C_2H_4Cl_2$/nBu$_4$NPF$_6$, 0.1 M at r.t.

ruthenium moiety in the equilibrium, the IR spectrum of **2**-acac$^+$ shows rather intense bands at $\tilde{\nu}$ = 1585, 1576, 1483, and 1173 cm^{-1} that arise from the vibrations of the conjugated linker, which strongly participates in the oxidation of a styrylruthenium complex.

In further keeping with a sizable proportion of the latter VT, the electron paramagnetic resonance (EPR) spectrum of **2**-acac$^+$ in CH_2Cl_2 solution shows a strong isotropic signal at g = 2.0542.[3a,8,11,22,24] As the temperature decreases, the intensity of the signal decreases gradually until it almost vanishes at –120 °C (see Figure 7). This indicates that the VT with the oxidized ferrocenyl moiety is the thermodynamically more favored one and that the other VT with an oxidized styrylruthenium moiety becomes increasingly populated on warming.

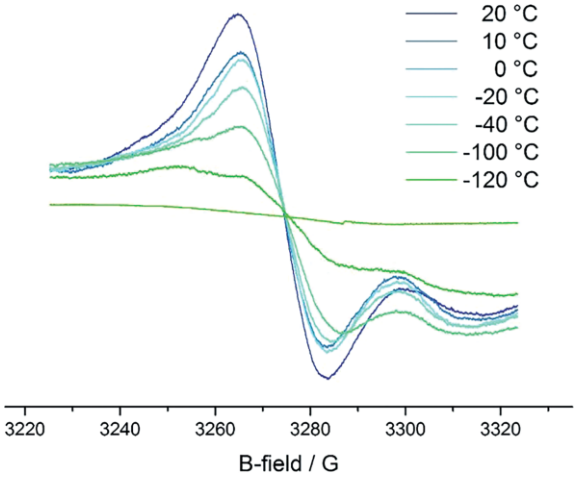

Figure 7. Temperature-dependent EPR spectra of chemically generated **2**-acac$^+$ (oxidation with FcHPF$_6$) in CH_2Cl_2 solution.

Similarly, the Mössbauer spectrum of a solid sample of **2**-acac$^+$ recorded at T = 80 K shows only one doublet signal with an isomer shift of 0.53 mm s^{-1} and a quadrupole splitting ΔE_Q of 0.42 mm s^{-1} (see Figure 8). We note here that the isomer shifts of ferrocenes are nearly invariant to the oxidation state and that the quadrupole splittings of simple ferrocenium ions are usually too small to be resolved ($\Delta E_Q \leq$ 0.20 mm s^{-1}),[31] even if the ferrocenium ion is covalently linked to an extended π-conjugated substituent.[32] Nevertheless, some ferrocenium ions with charge delocalization onto an appended, secondary redox site such as in charge-localized diferrocenium cations,[33] an oxidized bis(ferrocene)-appended protonated bis(vinylene)tetrathiafulvalene (ΔE_Q = 0.42 mm s^{-1}),[34] or the oxidized (ferrocenylethynyl)ruthenium complexes Cp(PPh$_3$)$_2$Ru–C≡C–Fc$^+$ and [1,1′-{Cp(PPh$_3$)$_2$Ru–C≡C–(η^5-C_5H_4)$_2$}$_2$Fe]$^+$ (ΔE_Q = 0.77 or 0.952 mm s^{-1})[34,35] have shown significantly larger quadrupole splittings. Notably, situations similar to that in **2**-acac$^+$ have been found in other ferrocene–electron-acceptor conjugates that engage in VT equilibria such as ferrocenylvinyl–polychlorotriphenyl radicals (ΔE_Q = 0.514 mm s^{-1} for the ferrocenyl and 0.594 mm s^{-1} for the octamethylferrocenyl derivative)[36] or ferrocenyl-appended pyrylium ions (ΔE_Q = 0.54 mm s^{-1}).[37] Thus, the Mössbauer parameters of **2**-acac$^+$ can be safely assigned to the VT with the charge localized at the ferrocenyl site. We note here that the oxidized ferrocene–vinylruthenium complex

© 2017 Wiley-VCH Verlag GmbH & Co. KGaA, Weinheim

Ru-Fc$^+$, in which ca. 20 % of the charge density resides at the alkenylruthenium moiety, has an even larger ΔE_Q value of 0.92 mm s^{-1}.[23]

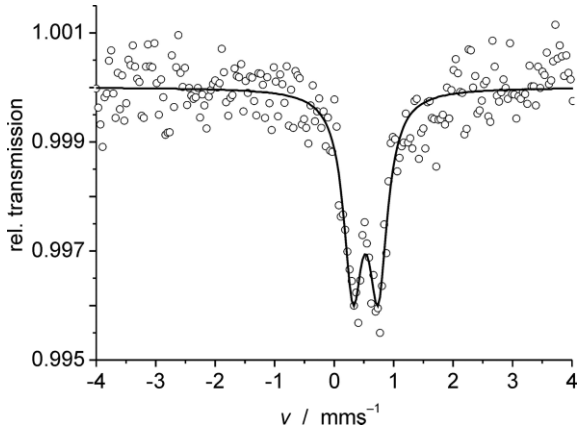

Figure 8. Mössbauer spectrum of [**2**-acac][SbF_6] generated by oxidation with N(C_6H_4Br-4)$_3SbF_6$, diluted with BN at T = 80 K.

As was previously found for other valence-tautomeric systems,[15b,15e,36b,37,38] the distribution of the different VTs of the **2**-acac$^+$ radical cation is affected by its environment. As is illustrated in Figure 9, the positions and relative intensities of the ν(CO) bands change in different solvents. At present, we can only make the obvious statement that a more polar solvent seems to increase charge localization at the individual redox sites. This follows from the increasing separation of the ν(CO) values for the different VTs from chlorobenzene [Δν(CO) = 20 cm^{-1}] and CH_2Cl_2 [Δν(CO) = 21 cm^{-1}] to 1,2-dichlorobenzene [$C_6H_4Cl_2$, Δν(CO) = 31 cm^{-1}], the 1,2-$C_2H_4Cl_2$/Bu_4NPF_6 (0.1 M) supporting electrolyte [Δν(CO) = 33 cm^{-1}] and acetone [Δν(CO) = 41 cm^{-1}]. Additional studies of the effect of solvent and counterion are clearly warranted to investigate these effects for **2**-acac$^+$ more closely. Unfortunately, attempts to study the radical cation of **2**-dpvm have been thwarted by an unexpected reactivity that results in irreversible changes in the IR spectra.

The oxidation of the styrylruthenium–ferrocene conjugates **1**, **2**-hfac, and **2**-acac is also accompanied by profound changes in the electronic spectra. Irrespective of whether the radical cations exist as valence-localized Fc$^+$–C_6H_4–CH=CH–{Ru^L} species (**1**$^+$ and **2**-hfac$^+$) or as equilibrating Fc$^+$–C_6H_4–CH=CH–{Ru^L} ⇌ Fc–[C_6H_4–CH=CH–{Ru^L}]$^+$ (**2**-acac$^+$) VTs [{Ru^L} = Ru(CO)(P*i*Pr$_3$)$_2$L, L = Cl or the respective β-keto enolato ligand], the oxidation of the neutral complexes results in the growth of fairly intense bands in the visible and near-infrared (NIR) regions. The results of a UV/Vis/NIR spectroelectrochemical experiment on **2**-acac are shown in Figure 10, and those of **1** and **2**-hfac are shown in Figures S19 and S20; the relevant data are compiled in Table 5. Both oxidized styrylruthenium complexes and ferrocenium ions usually show bands in the visible region. For the

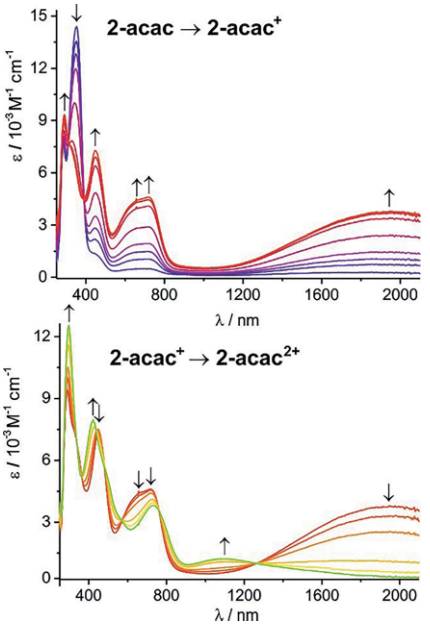

Figure 10. Spectroscopic changes during the first (top) and the second (bottom) oxidations of **2**-acac in 1,2-$C_2H_4Cl_2$/Bu_4NPF_6 (0.1 M) at r.t.

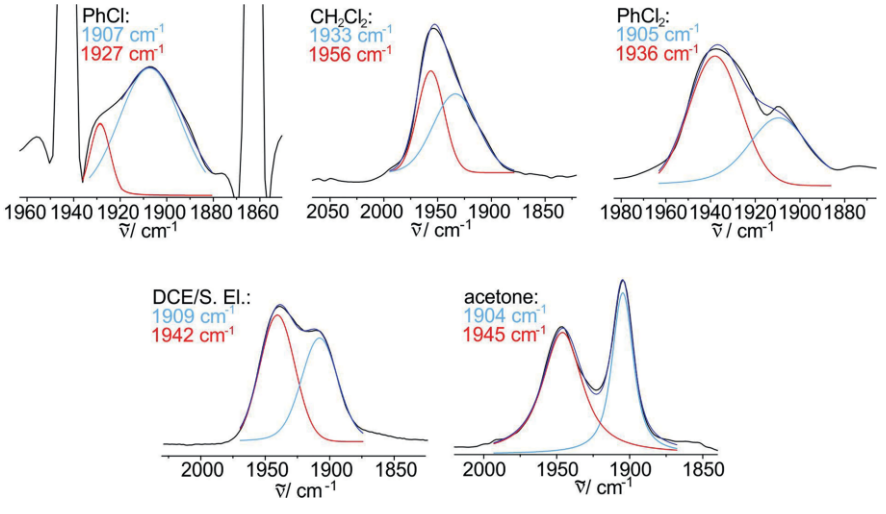

Figure 9. Experimental and deconvoluted IR spectra in the region of the ν(CO) stretching vibrations of chemically generated (oxidation with $FcHPF_6$) [**2**-acac][PF_6] in various solvents.

© 2017 Wiley-VCH Verlag GmbH & Co. KGaA, Weinheim

Ru-Fc$^+$ cation, the visible bands are most probably caused by ferrocene-to-cyclopentadienide CT within the oxidized ferrocene nucleus and CT from the styrylruthenium moiety to the ferrocenium moiety.[23] The latter assignment would also explain the sizable redshift of this band from $\lambda \approx 570$ nm in **1**$^+$ and **2**-hfac$^+$ to 718 nm in **2**-acac$^+$ by the energy increase of occupied MOs close to the HOMO level with more substantial contributions from the styrylruthenium entity induced by the electron-rich acac coligand.

Table 5. Spectroscopic UV/Vis/NIR data for **1**, **2**-hfac, and **2**-acac in their accessible oxidation states.[a]

	λ [nm] (ε [10^{-3} M^{-1} cm^{-1}])
1	281 (12.1), 344 (33.0), 465 (0.8)
1$^+$	302 (19.5), 347 (20.7), 471 (7.2), 571 (10.3), 1518 (3.9), 2520(–)
1^{2+}	290 (23.7), 426 (13.2), 654 (6.7), 1007 (1.5)
2-hfac	283 (11.4), 338 (19.0), 465 (1.1)
2-hfac$^+$	285 (14.4), 341 (12.0), 476 (4.2), 565 (6.0), 1520 (2.4), 2470 (–)
2-hfac^{2+}	286 (19.4), 448 (13.2), 709 (8.0), 970 (2.3)
2-acac	285 (14.4), 353 (14.4), 448 (1.3)
2-acac$^+$	290 (9.3), 448 (7.3), 655 (4.4), 718 (4.6), 1951 (3.8), 2551(–)
2-acac^{2+}	297 (12.5), 422 (7.9), 732 (3.8), 1101 (1.3)

[a] Measured in 1,2-$C_2H_4Cl_2$/nBu$_4$NPF$_6$, 0.1 M, r.t.

The radical cations of the present complexes feature low-energy NIR bands at $\tilde{\nu} \approx 4000$ cm^{-1} ($\lambda = 2500$ nm), which were observed in the low-energy region of the IR spectra but are outside the detector range of our Vis/NIR equipment (Figure S21). The near invariance of the band position with respect to the identity of the coligand at the {Ru} site and, for **2**-acac$^+$, also on the solvent let us assign this band as the ligand-field transition of the ferrocenium ion.[23,39] An equivalent transition was observed for Ru-Fc$^+$ at $\lambda = 2150$ nm and assigned to an excitation between the Fe $3d_{xy}$- and $3d_{x^2-y^2}$-δ-orbitals on the basis of DFT calculations.[23,39] In contrast, the position and intensity of the other NIR band clearly depends on the nature of the ruthenium moiety, as is shown by its redshift of 1540 cm^{-1} from $\lambda \approx 1520$ nm in **1**$^+$ and **2**-hfac$^+$ to 1951 nm for the acac complex. Further studies on **2**-acac$^+$ revealed that the band is solvatochromic with a shift from $\tilde{\nu} = 6090$ cm^{-1} ($\lambda = 1642$ nm) in acetone to 5400 cm^{-1} (1850 nm) in chlorobenzene, 4955 cm^{-1} (2018 nm) in CH_2Cl_2, and 4680 cm^{-1} (2135 nm) in 1,2-dichlorobenzene (see Figure S21). Taken together, these results indicate that the underlying excitation involves at least some degree of charge transfer between the different redox-active subunits. Again, the redshift of this band in the electron-rich **2**-acac$^+$ hints at charge transfer from the styrylruthenium moiety to the ferrocenium acceptor, that is, a CT band that would be more specific for the Fc$^+$–C_6H_4–CH=CH–{Ru} VT. However, this assignment awaits further proof, for example, through the monitoring of the Vis/NIR absorption profiles as a function of T.

The spectroscopic changes during the second oxidation include the bleaching of the aforementioned NIR band and the accompanying growth of another weaker band peaking at $\lambda =$ 970–1100 nm as well as a redshift of the prominent Vis band from $\lambda \approx 570$ to 700 nm. Both of these bands are characteristic of oxidized styrylruthenium complexes.[3a,8,22,24,40]

Conclusions

In the present paper, we have demonstrated that seemingly minor variations in the redox potentials of the local redox sites of a compound featuring two different redox-active entities can have a profound impact on the electronic ground state of the associated mixed-valent (MV) form generated by the oxidation or reduction of one of these sites. Here, a cathodic displacement of the redox potential at the styrylruthenium site of ca. 200 mV in **2**-acac is sufficient to drive the MV radical cation of ferrocenyl–styrylruthenium conjugates from valence localization at the ferrocenium site, as observed for the chlorido and hfac complexes **2** and **2**-hfac, to electronic bistability, that is, to an equilibrium Fc$^+$–C_6H_4–CH=CH–{Ru^{acac}} ⇌ Fc–[C_6H_4–CH=CH–{Ru^{acac}}]$^+$ between different valence tautomers (VTs).

This equilibrium situation is demonstrated by the observation of two separate Ru(CO) bands for the MV radical cation, one with only a modest shift with respect to that of the neutral complex and one with a larger shift, which is characteristic of an oxidized alkenylruthenium complex with charge delocalization onto an extended π-conjugated substituent. This VT gives rise to a strong isotropic EPR signal. Its strong intensity decrease as T decreases indicates that the Fc$^+$–C_6H_4–CH=CH–{Ru} valence tautomer is thermodynamically preferred with an increasing population of the more delocalized Fc–[C_6H_4–CH=CH–{Ru^{acac}}]$^+$ VT on warming. This is also in line with Mössbauer studies on solid **2**-acac$^+$ at $T = 80$ K, which shows the characteristics of a ferrocenium ion with some charge delocalization onto the periphery.

The relative stabilities of the two VTs also depend on the environment. Thus, we note shifts in the band positions and relative band intensities on variation of the solvent. More detailed studies to discriminate the influence of solvent polarity from more specific solvation effects such as hydrogen bonding or π-interactions and the impact of the ion-pairing capabilities of the associated counterion are clearly warranted and will be the subject of further work. Our present investigations also indicate a strong negative solvatochromism of the prominent NIR band of **2**-acac$^+$ and, thus, provide compelling evidence that the underlying excitation is associated with sizable charge transfer between the different redox sites.

Experimental Section

Experimental Methods and Materials: All syntheses were performed under purified nitrogen with dry, distilled, and nitrogen-saturated solvents. Reagents were purchased from commercial sources and used without further purification. ^{1}H (400 MHz) and ^{31}P NMR (162 MHz) spectra were recorded with a Bruker Avance III 400 spectrometer, and ^{1}H (600 MHz), ^{13}C (151 MHz), and ^{31}P (243 MHz) NMR spectra were recorded with a Bruker Avance III 600 spectrometer. Combustion analyses (C, H) were performed at in-house facilities with an Elementar Analyzer Vario MICRO Cube from Heraeus. HRuCl(CO)(PiPr$_3$)$_2$[19b] and (4-ethynylphenyl)ferrocene[18] were prepared according to literature methods. Single crystals suitable for X-ray crystallography were grown by layering a saturated CH_2Cl_2 solution of the respective complex with methanol to yield dark-red (**1** and **2**-acac) or black (**2**-hfac) platelike crystals. X-ray diffraction analysis was performed with a STOE IPDS-II diffractometer

© 2017 Wiley-VCH Verlag GmbH & Co. KGaA, Weinheim

equipped with a graphite-monochromated radiation source (λ = 0.71073 Å) and an image-plate detection system at 100 K. The structures were solved by direct methods (SHELXS-97), completed with difference Fourier syntheses, and refined with full-matrix least-squares techniques with SHELXL-97[42] to minimize $\omega(F_o^2 - F_c^2)^2$. CCDC 919530 (for **1**), 1483115 (for **2**-dpvm), and 1483116 (for **2**-hfac) contain the supplementary crystallographic data for this paper. These data can be obtained free of charge from The Cambridge Crystallographic Data Centre.

Electrochemical and Spectroscopic Measurements: Cyclic voltammetry was performed in a home-built cylindrical vacuum-tight one-compartment cell. A spiral-shaped Pt wire and an Ag wire as the counter and reference electrodes were sealed into glass capillaries that were introduced through Quickfit screws at opposite sides of the cell. A platinum electrode (diameter 1.6 mm, from BASi) was first polished with 1 μm and then with 0.25 μm diamond paste (Buehler–Wirtz) and introduced as the working electrode through the top central port through a Teflon screw cap with a suitable fitting. CH_2Cl_2/Bu_4NPF_6 (0.1 M) was used as the supporting electrolyte. Referencing was done with the addition of equimolar decamethylferrocene (Cp^*_2Fe) as an internal standard to the analyte solution after all data of interest had been acquired. Representative sets of scans were repeated with the added standard. Final referencing was done against the ferrocene/ferrocenium ($Cp_2Fe^{0/+}$) couple with $E_{1/2}(Cp^*_2Fe^{0/+})$ = –550 mV versus $Cp_2Fe^{0/+}$. Electrochemical data were acquired with a computer-controlled BASi potentiostat. The optically transparent thin-layer electrochemical (OTTLE) cell was also home-built and comprised a Pt mesh working and counter electrode and a thin silver wire as a pseudoreference electrode sandwiched between the CaF_2 windows of a conventional liquid IR cell. The working electrode was positioned in the center of the spectrometer beam. The FTIR spectra were recorded with Thermo IS10 or Bruker TENSORII instruments. The UV/Vis/NIR spectra were obtained with a TIDAS fiber optic diode array spectrometer (combined MCS UV/NIR and PGS NIR instrumentation) from J&M in HELLMA quartz cuvettes with 0.2 cm optical path lengths. Electron paramagnetic resonance (EPR) studies were performed with a table-top X-band spectrometer MiniScope MS 400 from Magnettech. The Mössbauer spectra were recorded with a ^{57}Co source in a rhodium matrix with an alternating constant acceleration Wissel Mössbauer spectrometer operated in the transmission mode and equipped with a Janis closed-cycle helium cryostat. The isomer shifts are given relative to iron metal at ambient temperature. The simulation of the experimental data was performed with the Mfit program using Lorentzian line doublets.[41]

Complex 1: $HRu(CO)Cl(PiPr_3)_2$ (106.3 mg, 0.21 mmol) and (4-ethynylphenyl)ferrocene (0.21 mmol, 62.6 mg) were dissolved in dichloromethane (DCM, abs.; 10 mL) under nitrogen and stirred at r.t. for 1 h. The solution turned immediately from orange to deep-red. The solvent was evaporated, and the resulting solid was washed with dry hexane (3 × 3 mL). The product (167 mg, quantitative) was isolated as a deep-red solid after drying. ^{1}H NMR (400 MHz, CD_2Cl_2, 25 °C): δ = 8.56 (d, $^3J_{H,H}$ = 13.4 Hz, 1 H, H^1), 7.29 (d, $^3J_{H,H}$ = 8.2 Hz, 2 H, H^5), 6.96 (d, $^3J_{H,H}$ = 8.2 Hz, 2 H, H^4), 5.98 (dt, $^3J_{H,H}$ = 13.4, $^3J_{H,P}$ = 1.9 Hz, 1 H, H^2), 4.56 (t, $^3J_{H,H}$ = 1.7 Hz, 2 H, H^8), 4.26 (t, $^3J_{H,H}$ = 1.7 Hz, 2 H, H^9), 4.03 (s, 5 H, H^{10}), 2.82–2.70 {m, 6 H, P[CH(CH$_3$)$_2$]$_3$}, 1.32–1.28 {m, 36 H, P[CH(CH_3)$_2$]$_3$} ppm. ^{13}C NMR (101 MHz, CD_2Cl_2): δ = 203.5 (t, $^2J_{C,P}$ = 9.8 Hz, C^{11}), 150.6 (t, $^2J_{C,P}$ = 10.9 Hz, C^1), 137.3 (s, C^3), 134.8 (s, C^6), 134.6 (t, $^3J_{C,P}$ = 3.3 Hz, C^2), 126.8 (s, C^5), 124.3 (s, C^4), 86.9 (s, C^7), 69.9 (s, C^9), 69.0 (s, C^8), 66.7 (s, C^{10}), 25.0 {vt, ^3J = 9.8 Hz, P[CH(CH$_3$)$_2$]$_3$}, 20.3 {s, P[CH(CH$_3$)$_2$]$_3$}, 20.0 {s, P[CH(CH$_3$)$_2$]$_3$} ppm. ^{31}P NMR (162 MHz, CD_2Cl_2): δ = 38.1 (s) ppm. $C_{37}H_{57}ClFeOP_2Ru$ (772.16): calcd. C 57.55, H 7.44; found C 57.21, H 7.18.

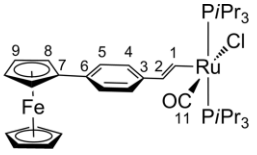

Complex 2-hfac: Complex **1** (100 mg, 0.13 mmol) was dissolved in DCM (abs.; 10 mL) under nitrogen. Sodium carbonate (20 mg, 0.19 mmol) was suspended in methanol (abs.; 5 mL), and hexafluoroacetylacetone (83 mg, 0.4 mmol) was added. The resulting mixture was warmed to 50 °C and stirred until the solution became clear and then added to **1**. After 30 min at 40 °C, the mixture had turned from red to light-red. The solvents were evaporated, and the resulting solid was dissolved in DCM (abs.; 5 mL). The solution was filtered to remove the insoluble salts. The solvent was evaporated, and the solids were washed once with methanol. The product (130 mg, quantitative) was isolated as a deep-red solid after drying. ^{1}H NMR (400 MHz, CD_2Cl_2, 25 °C): δ = 8.67 (dt, $^3J_{H,H}$ = 16.2, $^3J_{H,P}$ = 1.7 Hz, 1 H, H^1), 7.36–7.31 (m, 2 H, H^4), 7.10–7.06 (m, 2 H, H^5), 6.36 (dt, $^3J_{H,H}$ = 16.2, $^3J_{H,P}$ = 2.0 Hz, 1 H, H^2), 6.06 (s, 1 H, H^{12}), 4.57 (t, $^3J_{H,H}$ = 1.9 Hz, 2 H, H^8), 4.27 (t, $^3J_{H,H}$ = 1.9 Hz, 2 H, H^9), 4.05 (s, 5 H, H^{10}), 2.39 {m, 6 H, P[CH(CH$_3$)$_2$]$_3$}, 1.29, 1.24 {m, 36 H, P[CH(CH_3)$_2$]$_3$} ppm. ^{13}C NMR (101 MHz, CD_2Cl_2): δ = 208.8 (t, $^2J_{C,P}$ = 15.0 Hz, C^{11}), 175.5 (q, $^2J_{C,F}$ = 34.1 Hz), 174.3 (q, $^2J_{C,F}$ = 33.7 Hz, C^{13}, C^{15}), 158.1 (t, $^2J_{C,P}$ = 11.7 Hz, C^1), 138.8 (s, C^3), 134.8 (t, $^3J_{C,P}$ = 2.7 Hz, C^2), 134.1 (s, C^6), 126.2 (s, C^4), 123.8 (s, C^5), 117.6 (q, $^1J_{C,F}$ = 286.12 Hz), 117.1 (q, $^1J_{C,F}$ = 286.6 Hz, C^{14}, C^{16}), 91.5 (s, C^{12}), 86.5 (s, C^7), 69.3 (s, C^{10}), 68.4 (s, C^9), 66.1 (s, C^8), 24.2 {vt, $J_{C,P}$ = 9.1 Hz, P[CH(CH$_3$)$_2$]$_3$}, 19.3, 19.1 {s, P[CH(CH_3)$_2$]$_3$} ppm. ^{31}P NMR (162 MHz, CD_2Cl_2): δ = 35.0 (s) ppm. ^{19}F NMR (376 MHz, CD_2Cl_2): δ = –75.38 (s), –76.72 (s, F^{14} and F^{16}) ppm. $C_{42}H_{58}F_6FeO_3P_2Ru$ (943.76): calcd. C 53.45, H 6.19; found C 53.43, H 6.16.

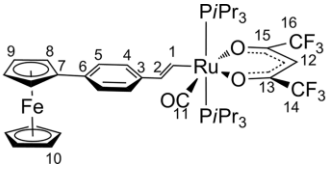

Complex 2-acac: Complex **1** (100 mg, 0.13 mmol) was dissolved in DCM (abs.; 10 mL) under nitrogen. Sodium carbonate (20 mg, 0.19 mmol) was suspended in methanol (abs.; 5 mL), and acetylacetone (73 mg, 0.73 mmol) was added. The resulting mixture was warmed to 50 °C and stirred until the solution became clear. This solution was then added to **1**. After 30 min at 40 °C, the mixture had turned from orange to yellow. The solvents were evaporated, and the resulting solid was dissolved in DCM (abs.; 5 mL). The solution was filtered to remove the insoluble salts. The solvent was evaporated, and the solid was washed once with methanol. The product (100 mg, 92 %) was isolated as an orange-yellow solid after drying. ^{1}H NMR (400 MHz, CD_2Cl_2, 25 °C): δ = 8.96 (dt, $^3J_{H,H}$ = 16.6, $^3J_{H,P}$ = 1.7 Hz, 1 H, H^1), 7.35–7.26 (m, 2 H, H^4), 7.12–7.02 (m, 2 H, H^5), 6.40 (dt, $^3J_{H,H}$ = 16.6, $^3J_{H,P}$ = 1.9 Hz, 1 H, H^2), 5.37 (s, 1 H, H^{12}), 4.56 (t, $^3J_{H,H}$ = 1.9 Hz, 2 H, H^8), 4.25 (t, $^3J_{H,H}$ = 1.9 Hz, 2 H, H^9), 4.05 (s, 5 H, H^{10}), 2.42–2.27 {m, 6 H, P[CH(CH$_3$)$_2$]$_3$}, 1.94, 1.79 (s, 6 H, H^{14}, H^{16}), 1.31, 1.24 {m, 16 H, P[CH(CH_3)$_2$]$_3$} ppm. ^{13}C NMR (101 MHz, CD_2Cl_2): δ = 210.5 (t, $^2J_{C,P}$ = 14.9 Hz, C^{11}) 189.1, 187.2 (s, C^{13}, C^{15}), 166.3 (t, $^2J_{C,P}$ = 11.9 Hz, C^1) 140.6 (s, C^3), 134.3 (s, C^2), 133.5 (s, C^6), 126.8 (s, C^4), 124.1 (s, C^5), 100.6 (s, C^{12}), 87.6 (s, C^7), 69.9 (s, C^{10}), 68.9 (s, C^9), 66.7 (s, C^8), 28.9, 28.9 (s, C^{14}, C^{16}), 24.9 {vt, $J_{C,P}$ = 8.7 Hz, P[CH(CH$_3$)$_2$]$_3$}, 20.1, 19.9 {s, P[CH(CH$_3$)$_2$]$_3$} ppm. ^{31}P NMR (162 MHz,

© 2017 Wiley-VCH Verlag GmbH & Co. KGaA, Weinheim

CD_2Cl_2): δ = 35.6 (s) ppm. $C_{42}H_{64}FeO_3P_2Ru$ (835.82): calcd. C 60.35, H 7.72; found C 60.37, H 7.70.

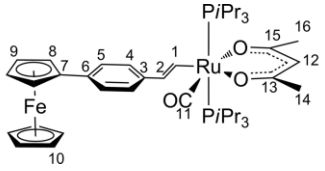

Chemical Oxidation of 2-acac: The chemical oxidation of **2**-acac was achieved by treatment of the neutral complex with either $FcHPF_6$ (for EPR studies) or tris(4-bromophenyl)aminium hexafluoroantimonate (iron-free oxidant necessary for Mössbauer spectroscopy). To a vigorously stirred mixture of **2**-acac (100 mg, 0.12 mmol), $FcHPF_6$ (40 mg, 0.12 mmol) in dichloromethane (abs.; 5 mL) or an equimolar amount of tris(4-bromophenyl)aminium hexafluoroantimonate was added. Upon the addition of the solvent, the reaction mixture became dark blue and was stirred at room temperature for 10 min. The solvent was evaporated to dryness, and the resulting solid was washed three times with *n*-hexane (abs.; 3 × 5 mL). The purity of the product was confirmed by attenuated total reflectance IR (ATR-IR) and solution IR spectroscopy. Spectral deconvolutions of the IR spectra of **2**-acac$^+$ were performed with the Origin2015 software using Voigt functions.

Complex 2-dpvm: Complex **1** (100 mg, 0.13 mmol) was dissolved in DCM (abs.; 5 mL) under nitrogen. KOH (15 mg, 0.26 mmol) was suspended in methanol (abs.; 5 mL), and dipivaloylmethane (74 mg, 0.4 mmol) was added. The resulting mixture was warmed to 50 °C for 1 h. This solution was then added to **1**. After 30 min at 40 °C, the mixture had changed from red to yellow. The solvents were evaporated, and the resulting solid was dissolved in DCM (abs.; 5 mL). The solution was filtered to remove the insoluble salts. The solvent was evaporated, and the solids were washed once with methanol. The product (130 mg, quantitative) was isolated as a deep-red solid after drying. ^{1}H NMR (400 MHz, CD_2Cl_2, 25 °C): δ = 9.04 (dt, $^3J_{H,H}$ = 16.6, $^3J_{H,P}$ = 1.6 Hz, 1 H, *H*^{1}), 7.34–7.27 (m, 2 H, *H*^{4}), 7.12–7.03 (m, 2 H, *H*^{5}), 6.38 (dt, $^3J_{H,H}$ = 16.6, $^3J_{H,P}$ = 2.0 Hz, 1 H, *H*^{2}), 5.69 (s, 1 H, *H*^{12}), 4.56 (t, $^3J_{H,H}$ = 1.9 Hz, 2 H, *H*^{9}), 4.25 (t, $^3J_{H,H}$ = 1.9 Hz, 2 H, *H*^{8}), 4.05 (s, 5 H, *H*^{10}), 2.39 {m, 6 H, P[C*H*(CH$_3$)$_2$]$_3$}, 1.28 {m, 36 H, P[CH(C*H*$_3$)$_2$]$_3$}, 1.22, 1.07 (s, 18 H, *H*^{15}, *H*^{17}) ppm. ^{13}C NMR (101 MHz, CD_2Cl_2): δ = 210.5 (t, $^2J_{C,P}$ = 16.1 Hz, *C*^{11}), 197.9, 196.4 (s, *C*^{13}, *C*^{16}), 166.2 (d, $^2J_{C,P}$ = 12.4 Hz, *C*^{1}), 140.1 (s, *C*^{3}), 134.2 (t, $^3J_{C,P}$ = 2.5 Hz, *C*^{2}), 133.5 (s, *C*^{6}), 126.8 (s, *C*^{4}), 124.0 (s, *C*^{5}), 93.7 (s, *C*^{12}), 87.5 (s, *C*^{7}), 69.9 (s, *C*^{10}), 68.9 (s, *C*^{9}), 66.7 (s, *C*^{8}), 42.1, 41.3 (s, *C*^{14}, *C*^{17}), 29.3, 28.9 (s, *C*^{15}, *C*^{18}), 24.5 {vt, $J_{C,P}$ = 8.7 Hz, P[CH(CH$_3$)$_2$]$_3$}, 20.3 {s, P[CH(CH$_3$)$_2$]$_3$}, 19.9 {s, P[CH(CH$_3$)$_2$]$_3$} ppm. ^{31}P NMR (162 MHz, CD_2Cl_2): δ = 35.6 (s) ppm. $C_{48}H_{76}FeO_3P_2Ru$ (919.98): calcd. C 62.67, H 8.33; found C 62.58, H 8.20.

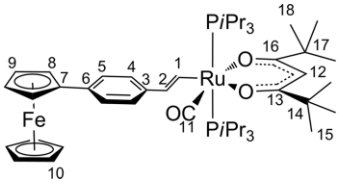

Supporting Information (see footnote on the first page of this article): Tables pertaining to the data collection and structure refinement for X-ray crystallography; ^{1}H, ^{13}C, ^{31}P{^{1}H}, and ^{19}F NMR (**2**-hfac) spectra; cyclic voltammograms; IR spectroelectrochemical results for **2**-hfac and for the second oxidation of **2**-acac; Mössbauer spectrum of **2**-acac$^+$ at 80 K; UV/Vis/NIR spectroelectrochemical results for **1** and **2**-hfac; NIR spectra of **2**-acac$^+$ in various solvents.

Acknowledgments

This work was financially supported by the Deutsche Forschungsgemeinschaft (DFG) (grant WI1262/13-1). We also thank Bernhard Weibert for X-ray data collection and structure refinement.

Keywords: Sandwich complexes · Ruthenium · Valence tautomerism · Spectroelectrochemistry · Heterometallic complexes

[1] E. Wuttke, D. Fink, P. Anders, A.-L. M. Hoyt, W. Polit, M. Linseis, R. F. Winter, *J. Organomet. Chem.* **2016**, DOI: 10.1016/j.jorganchem.2016.02.031.
[2] F. Pevny, E. Di Piazza, L. Norel, M. Drescher, R. F. Winter, S. Rigaut, *Organometallics* **2010**, *29*, 5912–5918.
[3] a) E. Wuttke, Y.-M. Hervault, W. Polit, M. Linseis, P. Erler, S. Rigaut, R. F. Winter, *Organometallics* **2014**, *33*, 4672–4686; b) E. Wuttke, F. Pevny, Y.-M. Hervault, L. Norel, M. Drescher, R. F. Winter, S. Rigaut, *Inorg. Chem.* **2012**, *51*, 1902–1915.
[4] W. Polit, T. Exner, E. Wuttke, R. F. Winter, *Bioinorg. React. Mech.* **2012**, *8*, 85–105.
[5] W. Polit, P. Mücke, E. Wuttke, T. Exner, R. F. Winter, *Organometallics* **2013**, *32*, 5461–5472.
[6] J. Chen, R. F. Winter, *Chem. Eur. J.* **2012**, *18*, 10733–10741.
[7] J. Chen, E. Wuttke, W. Polit, T. Exner, R. F. Winter, *J. Am. Chem. Soc.* **2013**, *135*, 3391–3394.
[8] J. Maurer, M. Linseis, B. Sarkar, B. Schwederski, M. Niemeyer, W. Kaim, S. Záliš, C. Anson, M. Zabel, R. F. Winter, *J. Am. Chem. Soc.* **2008**, *130*, 259–268.
[9] a) C. G. Atwood, W. E. Geiger, *J. Am. Chem. Soc.* **2000**, *122*, 5477–5485; b) M. E. Stoll, S. R. Lovelace, W. E. Geiger, H. Schimanke, I. Hyla-Kryspin, R. Gleiter, *J. Am. Chem. Soc.* **1999**, *121*, 9343–9351.
[10] S. Scheerer, N. Rotthowe, O. S. Abdel-Rahman, X. He, S. Rigaut, H. Kvapilová, S. Záliš, R. F. Winter, *Inorg. Chem.* **2015**, *54*, 3387–3402.
[11] M. Linseis, S. Záliš, M. Zabel, R. F. Winter, *J. Am. Chem. Soc.* **2012**, *134*, 16671–16692.
[12] a) F. Delgado-Pena, D. R. Talham, D. O. Cowan, *J. Organomet. Chem.* **1983**, *253*, C43–C46; b) A.-C. Ribou, J.-P. Launay, M. L. Sachtleben, H. Li, C. W. Spangler, *Inorg. Chem.* **1996**, *35*, 3735–3740; c) F. Ding, H. Wang, Q. Wu, T. Van Voorhis, S. Chen, J. P. Konopelski, *J. Phys. Chem. A* **2010**, *114*, 6039–6046.
[13] C. Patoux, C. Coudret, J. P. Launay, C. Joachim, A. Gourdon, *Inorg. Chem.* **1997**, *36*, 5037.
[14] a) G. C. Allen, N. S. Hush, *Prog. Inorg. Chem.* **1967**, *8*, 357–389; b) N. S. Hush, *Prog. Inorg. Chem.* **1967**, *8*, 391–444; c) C. Creutz, "Mixed Valence Complexes of d^5–d^6 Metal Centers" in *Progress in Inorganic Chemistry*, vol. 30 (Ed.: S. J. Lippard), John Wiley and Sons, New York, **1983**, pp. 1–73; d) J. R. Reimers, N. S. Hush, *J. Photochem. Photobiol. A* **1994**, *82*, 31–46; e) B. S. Brunschwig, N. Sutin, *Coord. Chem. Rev.* **1999**, *187*, 233–254.
[15] a) R. A. Marcus, *Annu. Rev. Phys. Chem.* **1964**, *15*, 155–196; b) P. Chen, T. J. Meyer, *Chem. Rev.* **1998**, *98*, 1439–1477; c) Y. J. Chen, C.-H. Kao, S. J. Lin, C.-C. Tai, K. S. Kwan, *Inorg. Chem.* **2000**, *39*, 189–194; d) S. Barlow, *Inorg. Chem.* **2001**, *40*, 7047–7053; e) I. Ratera, C. Sporer, D. Ruiz-Molina, N. Ventosa, J. Baggerman, A. M. Brouwer, C. Rovira, J. Veciana, *J. Am. Chem. Soc.* **2007**, *129*, 6117–6129.
[16] F. Salaymeh, S. Berhane, R. Yusof, R. de la Rosa, E. Y. Fung, R. Matamoros, K. W. Lau, Q. Zheng, E. M. Kober, J. C. Curtis, *Inorg. Chem.* **1993**, *32*, 3895–3908.
[17] a) J. T. Hupp, G. A. Neyhart, T. J. Meyer, *J. Am. Chem. Soc.* **1986**, *108*, 5349–5350; b) J. C. Curtis, J. A. Roberts, R. L. Blackbourn, Y. Dong, M. Massum, C. S. Johnson, J. T. Hupp, *Inorg. Chem.* **1991**, *30*, 3856–3860; c) G. A. Neyhart, J. T. Hupp, J. C. Curtis, C. J. Timpson, T. J. Meyer, *J. Am. Chem. Soc.* **1996**, *118*, 3724–3729.

© 2017 Wiley-VCH Verlag GmbH & Co. KGaA, Weinheim

[18] H. Schottenberger, J. Lukassser, E. Reichel, A. G. Müller, G. Steiner, H. Kopacka, K. Wurst, K. H. Ongania, K. Kirchner, *J. Organomet. Chem.* **2001**, *637–639*, 558–576.
[19] a) M. A. Esteruelas, H. Werner, *J. Organomet. Chem.* **1986**, *303*, 221–231; b) H. Werner, M. A. Esteruelas, H. Otto, *Organometallics* **1986**, *5*, 2295–2299.
[20] a) A. V. Marchenko, H. Gérard, O. Eisenstein, K. G. Caulton, *New J. Chem.* **2001**, *25*, 1244–1255; b) A. V. Marchenko, H. Gérard, O. Eisenstein, K. G. Caulton, *New J. Chem.* **2001**, *25*, 1382–1388.
[21] a) H. Werner, U. Meyer, K. Peters, H. G. von Schnering, *Chem. Ber.* **1989**, *122*, 2089–2107; b) M. A. Esteruelas, A. V. Gómez, F. M. Lahoz, A. M. López, E. Oñate, L. A. Oro, *Organometallics* **1996**, *15*, 3423–3435; c) H. Werner, W. Stüer, B. Weberndörfer, J. Wolf, *Eur. J. Inorg. Chem.* **1999**, 1707–1713; d) M. L. Buil, M. A. Esteruelas, *Organometallics* **1999**, *18*, 1798–1800.
[22] F. Pevny, R. F. Winter, B. Sarkar, S. Záliš, *Dalton Trans.* **2010**, *39*, 8000–8011.
[23] K. Kowalski, M. Linseis, R. F. Winter, M. Zabel, S. Záliš, H. Kelm, H.-J. Krüger, B. Sarkar, W. Kaim, *Organometallics* **2009**, *28*, 4196–4209.
[24] O. S. Abdel-Rahman, J. Maurer, S. Záliš, R. F. Winter, *Organometallics* **2015**, *34*, 3611–3628.
[25] S.-H. Choi, I. Bytheway, Z. Lin, G. Jia, *Organometallics* **1998**, *17*, 3974–3980.
[26] a) W. Y. Man, J.-L. Xia, N. J. Brown, J. D. Farmer, D. S. Yufit, J. A. K. Howard, S. H. Liu, P. J. Low, *Organometallics* **2011**, *30*, 1852–1858; b) J.-L. Xia, W. Y. Man, X. Zhu, C. Zhang, G.-J. Jin, P. A. Schauer, M. A. Fox, J. Yin, G.-A. Yu, P. J. Low, S. H. Liu, *Organometallics* **2012**, *31*, 5321–5333; c) S. Záliš, R. F. Winter, W. Kaim, *Coord. Chem. Rev.* **2010**, *254*, 1383–1396.
[27] P. Mücke, M. Linseis, S. Záliš, R. F. Winter, *Inorg. Chim. Acta* **2011**, *374*, 36–50.
[28] S. J. Sherlock, D. C. Boyd, B. Moasser, W. L. Gladfelter, *Inorg. Chem.* **1991**, *30*, 3626–3632.
[29] X. Wu, T. Weng, S. Jin, J. Liang, R. Guo, G.-a. Yu, S. H. Liu, *J. Organomet. Chem.* **2009**, *694*, 1877–1883.
[30] C. Hansch, A. Leo, R. W. Taft, *Chem. Rev.* **1991**, *91*, 165–195.
[31] a) G. K. Wertheim, R. H. Herber, *J. Chem. Phys.* **1963**, *38*, 2106–2111; b) R. L. Collins, *J. Chem. Phys.* **1965**, *42*, 1072–1075; c) N. N. Greenwood, T. C. Gibb, *Mössbauer Spectroscopy*, Chapman and Hall, London, **1971**.
[32] a) H. Schottenberger, M. R. Buchmeiser, R. H. Herber, *J. Organomet. Chem.* **2000**, *612*, 1–8; b) T. Yamamoto, T. Morikita, T. Maruyama, K. Kubota, M. Katada, *Macromolecules* **1997**, *30*, 5390–5396.
[33] a) W. H. Morrison, D. N. Hendrickson, *Inorg. Chem.* **1975**, *14*, 2331–2346; b) J. A. Kramer, D. N. Hendrickson, *Inorg. Chem.* **1980**, *19*, 3330–3337; c) M. F. Moore, S. R. Wilson, M. J. Cohn, T. Y. Dong, U. T. Mueller-Westerhoff, D. N. Hendrickson, *Inorg. Chem.* **1985**, *24*, 4559–4565.
[34] M. C. B. Colbert, J. Lewis, N. J. Long, P. R. Raithby, A. J. P. White, D. J. Williams, *J. Chem. Soc., Dalton Trans.* **1997**, 99–104.
[35] M. Sato, H. Shintate, Y. Kawata, M. Sekino, M. Katada, S. Kawata, *Organometallics* **1994**, *13*, 1956–1962.
[36] a) I. Ratera, D. Ruiz-Molina, F. Renz, J. Ensling, K. Wurst, C. Rovira, P. Gütlich, J. Veciana, *J. Am. Chem. Soc.* **2003**, *125*, 1462–1463; b) J. Guasch, L. Grisanti, S. Jung, D. Morales, G. D'Avino, M. Souto, X. Fontrodona, A. Painelli, F. Renz, I. Ratera, J. Veciana, *Chem. Mater.* **2013**, *25*, 808–814.
[37] M. Kondo, M. Uchikawa, K. Namiki, W.-W. Zhang, S. Kume, E. Nishibori, H. Suwa, S. Aoyagi, M. Sakata, M. Murata, Y. Kobayashi, H. Nishihara, *J. Am. Chem. Soc.* **2009**, *131*, 12112–12124.
[38] a) E. Evangelio, D. Ruiz-Molina, *C. R. Chim.* **2008**, *11*, 1137–1154; b) G. D'Avino, L. Grisanti, J. Guasch, I. Ratera, J. Veciana, A. Painelli, *J. Am. Chem. Soc.* **2008**, *130*, 12064–12072.
[39] a) M. Lohan, P. Ecorchard, T. Rüffer, F. Justaud, C. Lapinte, H. Lang, *Organometallics* **2009**, *28*, 1878–1890; b) J. M. Speck, D. Schaarschmidt, H. Lang, *Organometallics* **2012**, *31*, 1975–1982; c) J. M. Speck, R. Claus, A. Hildebrandt, T. Rüffer, E. Erasmus, L. van As, J. C. Swarts, H. Lang, *Organometallics* **2012**, *31*, 6373–6380.
[40] P. Mücke, M. Zabel, R. Edge, D. Collison, S. Clément, S. Záliš, R. F. Winter, *J. Organomet. Chem.* **2011**, *696*, 3186–3197.
[41] E. Bill, *Mfit*, Max-Planck Institute for Chemical Energy Conversion, Mülheim an der Ruhr, **2008**.
[42] G. M. Sheldrick, *SHELXL-97*, University of Göttingen, **1997**.

Received: June 30, 2016
Published Online: November 10, 2016

© 2017 Wiley-VCH Verlag GmbH & Co. KGaA, Weinheim

Eur. J. Inorg. Chem. **2016** · ISSN 1099–0682

SUPPORTING INFORMATION

DOI: 10.1002/ejic.201600776
Title: Oxidized Styrylruthenium–Ferrocene Conjugates: From Valence Localization to Valence Tautomerism
Author(s): Christopher Hassenrück, Philipp Mücke, Johanna Scheck, Serhiy Demeshko, Rainer F. Winter*

I. NMR spectra of the complexes

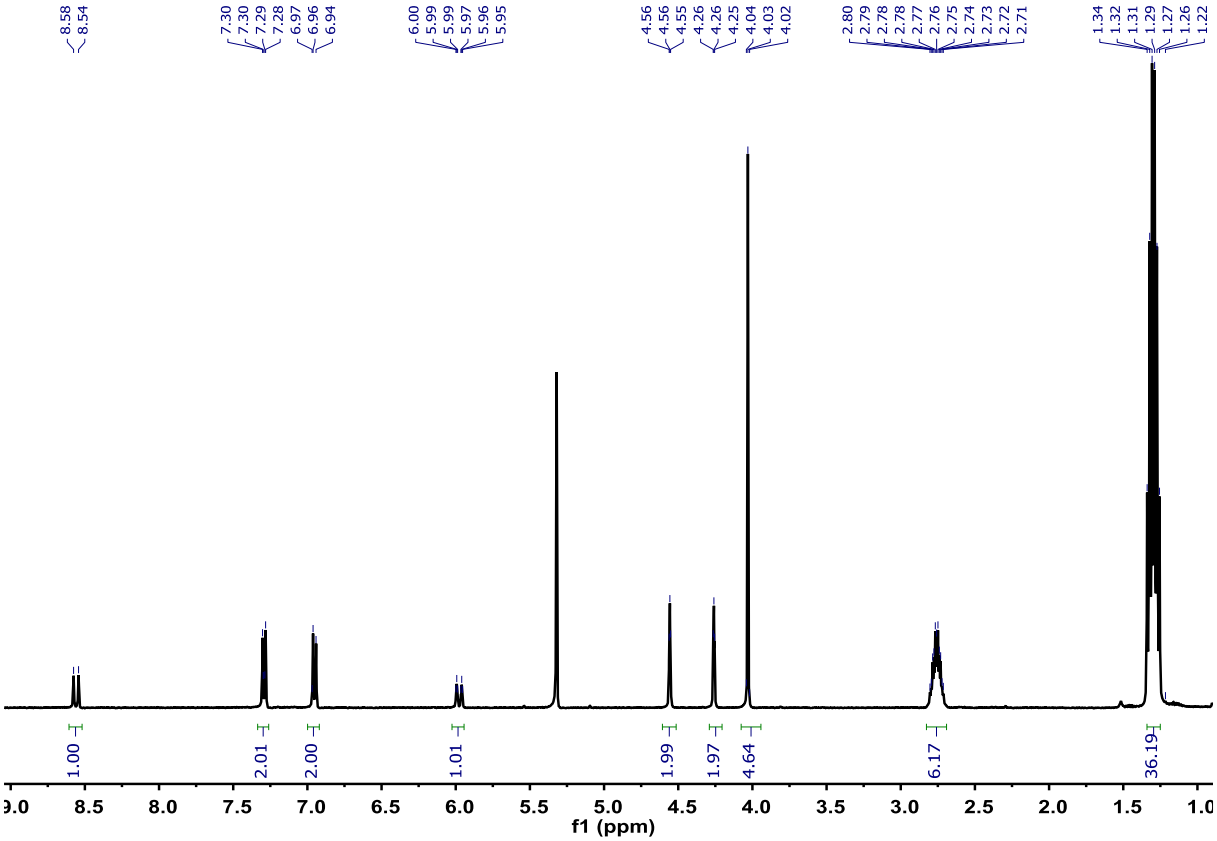

Figure S1. ^{1}H NMR spectrum of complex **1**.

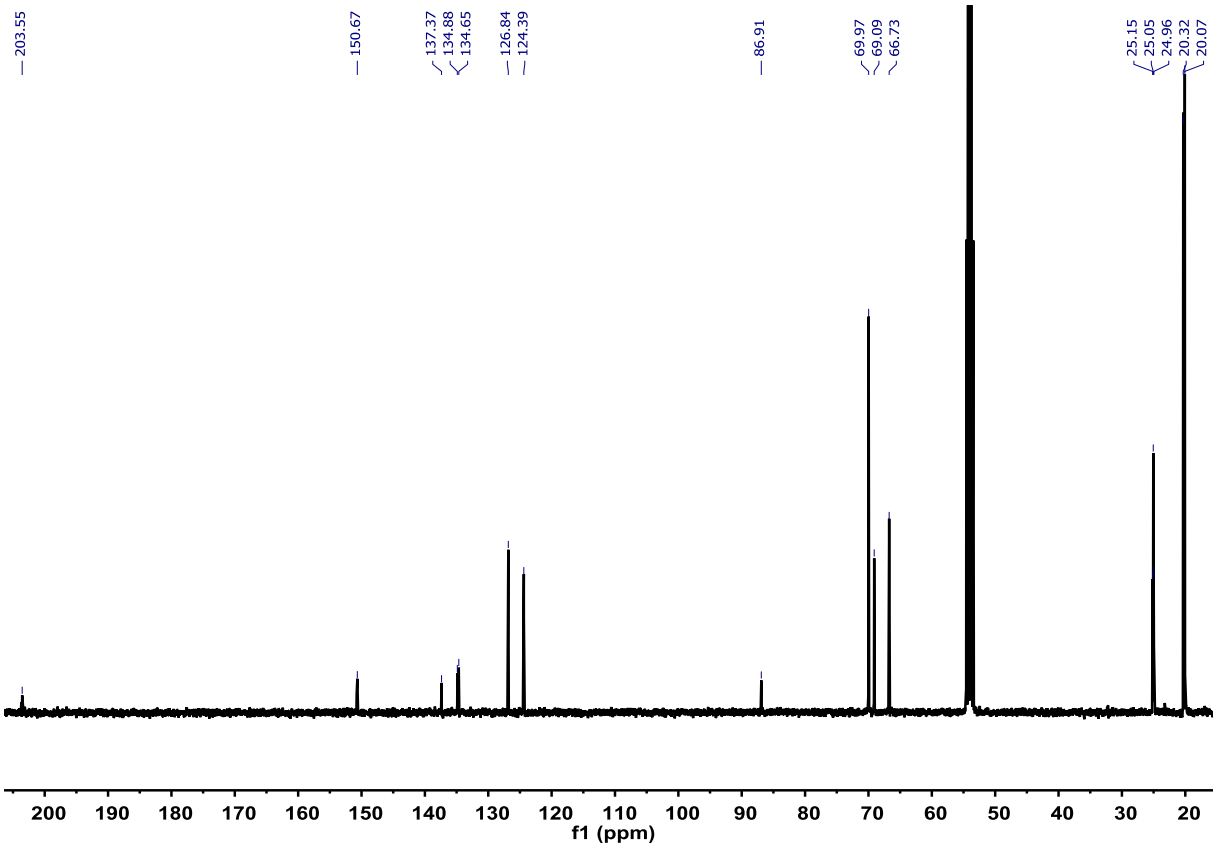

Figure S2. ^{13}C NMR spectrum of complex **1**.

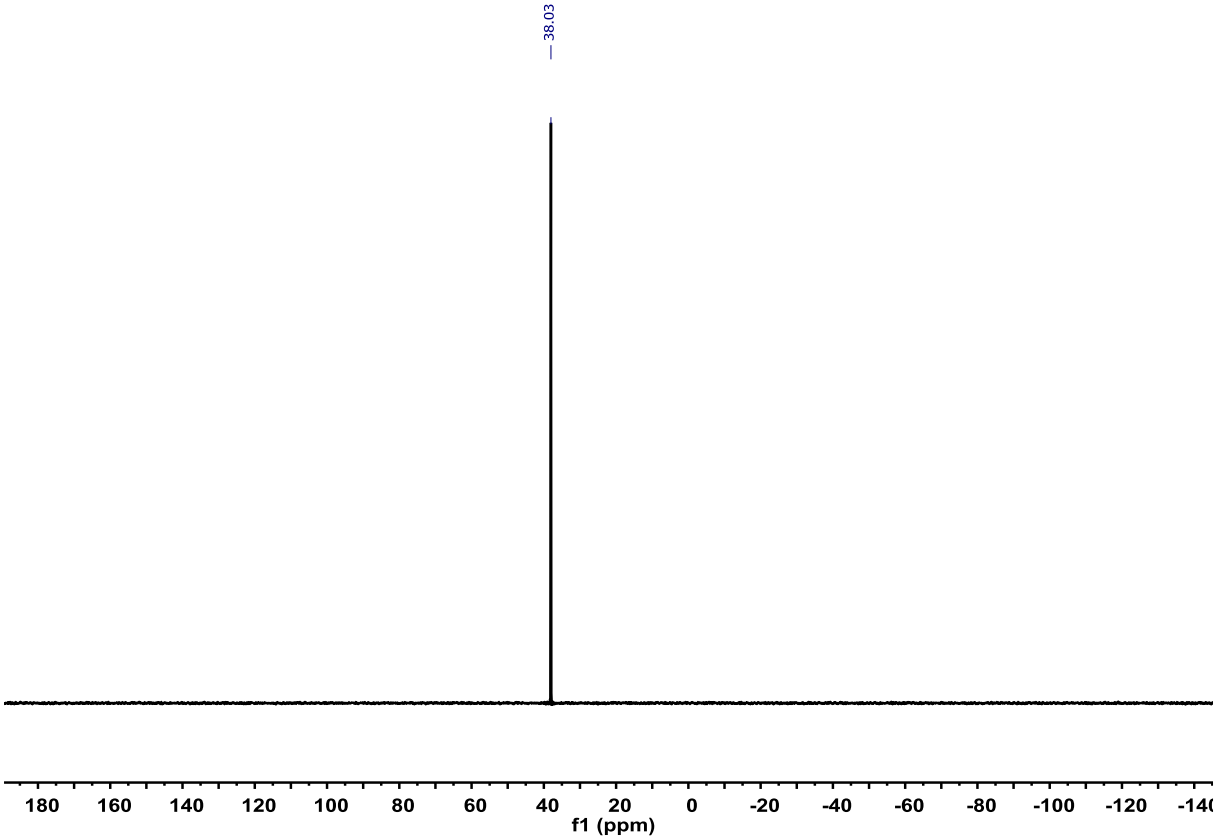

Figure S3. ^{31}P NMR spectrum of complex **1**.

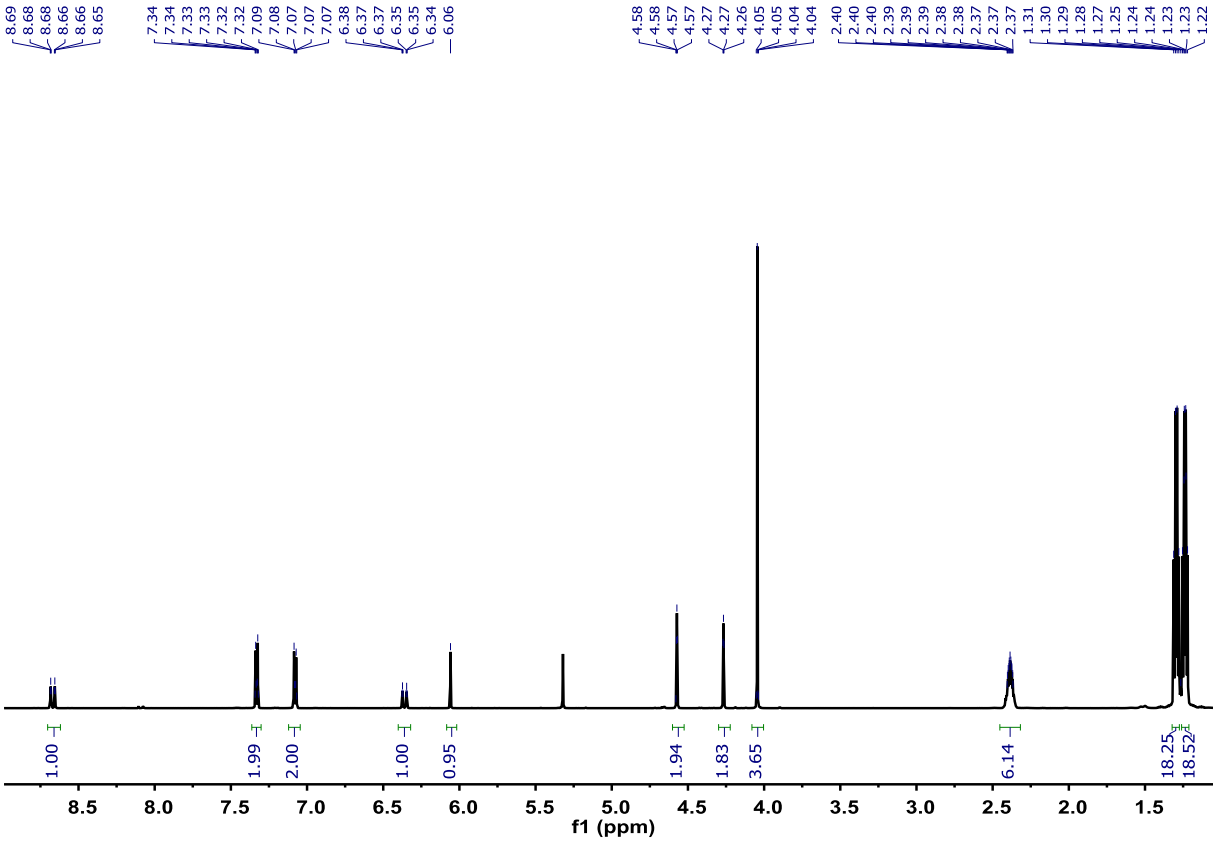

Figure S4. ^{1}H NMR spectrum of complex **2-hfac**.

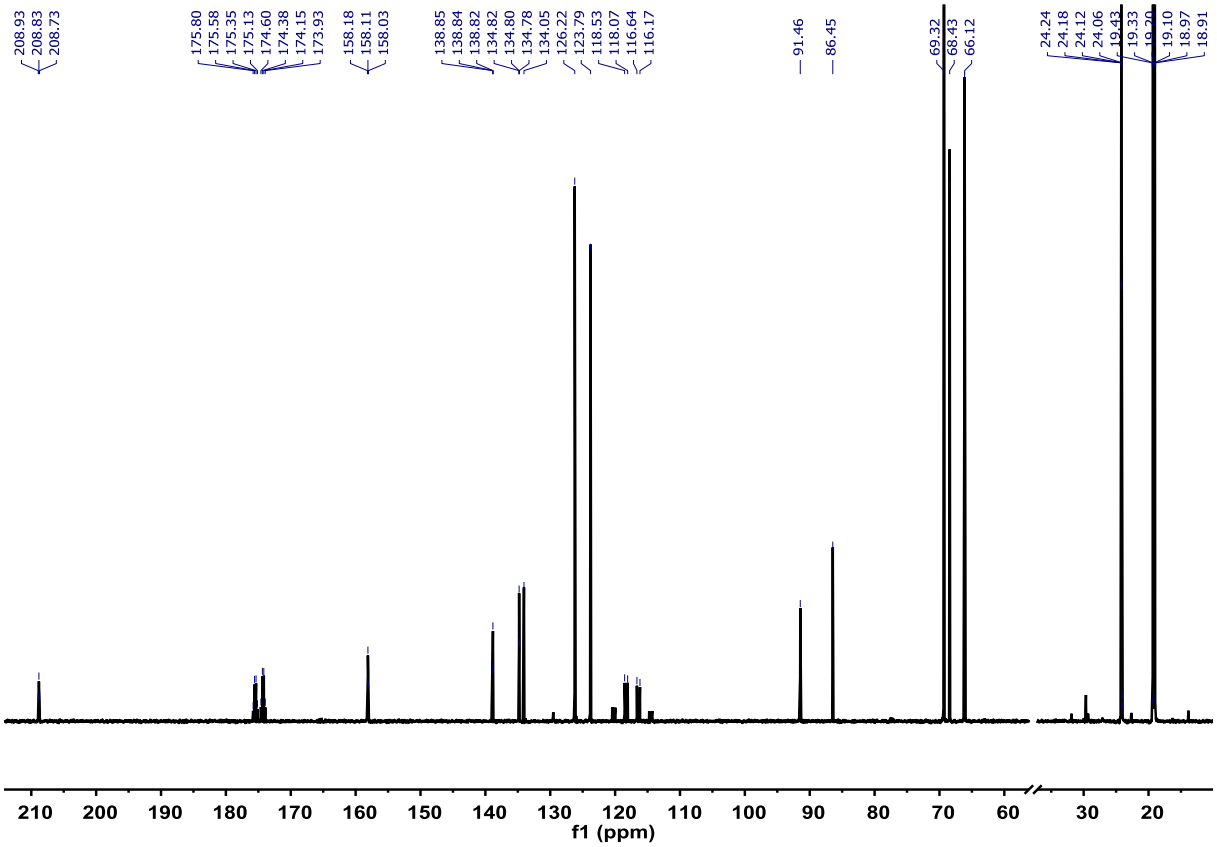

Figure S5. ^{13}C NMR spectrum of complex **2-hfac**.

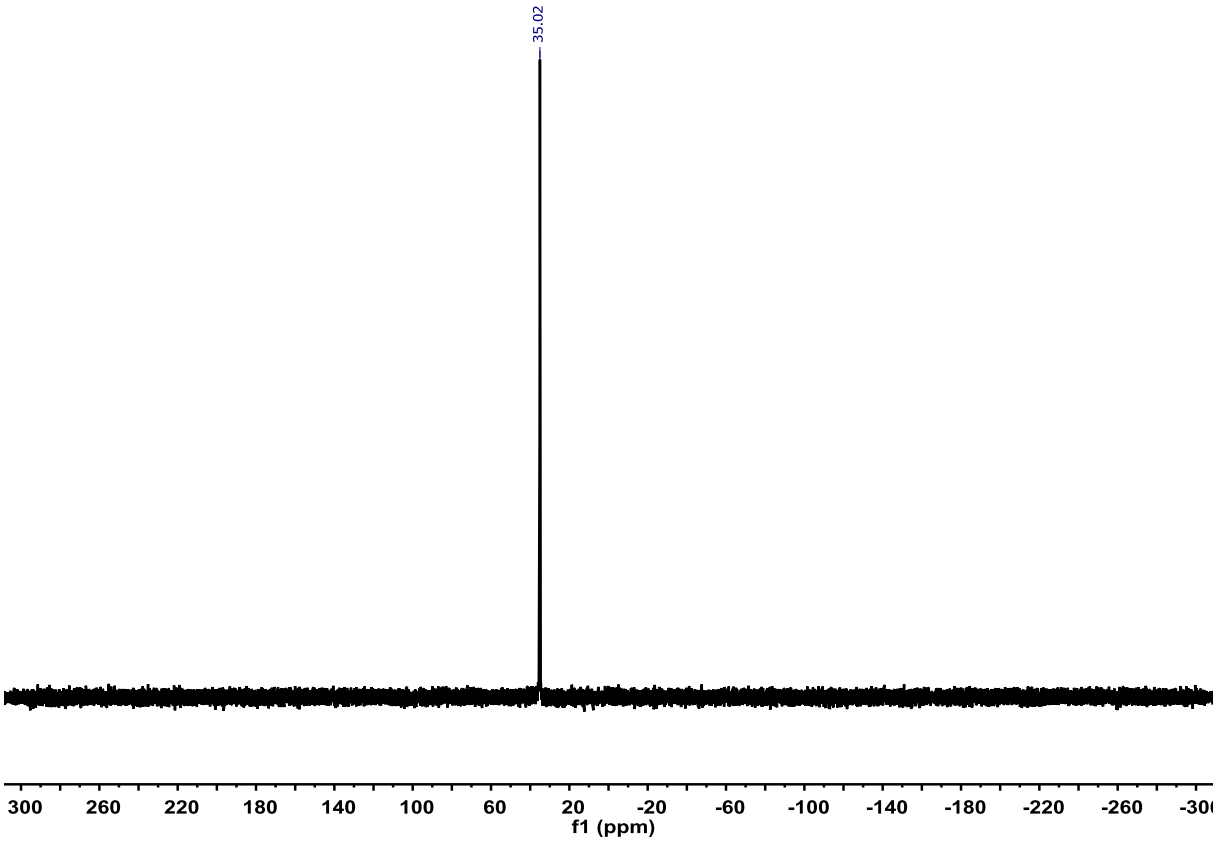

Figure S6. ^{31}P NMR spectrum of complex **2-hfac**.

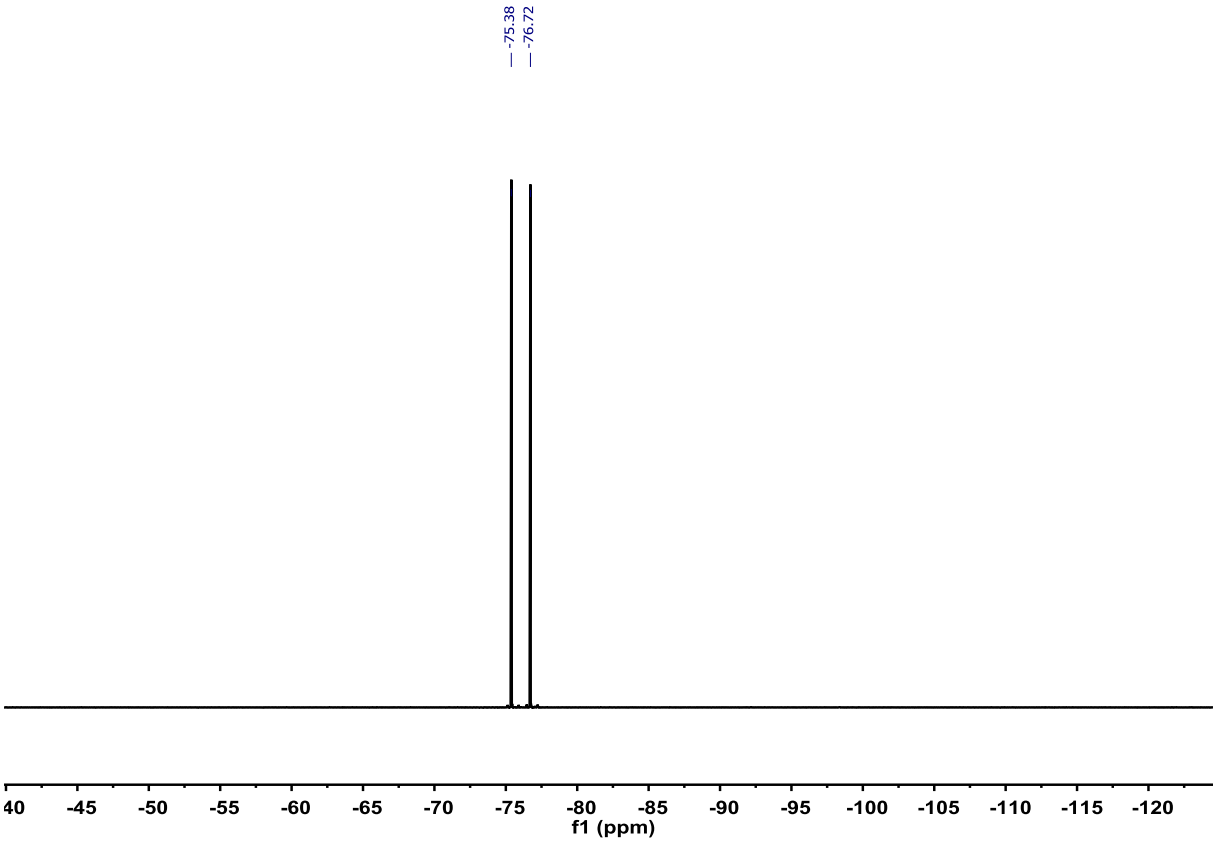

Figure S7. ^{19}F NMR spectrum of complex **2-hfac**.

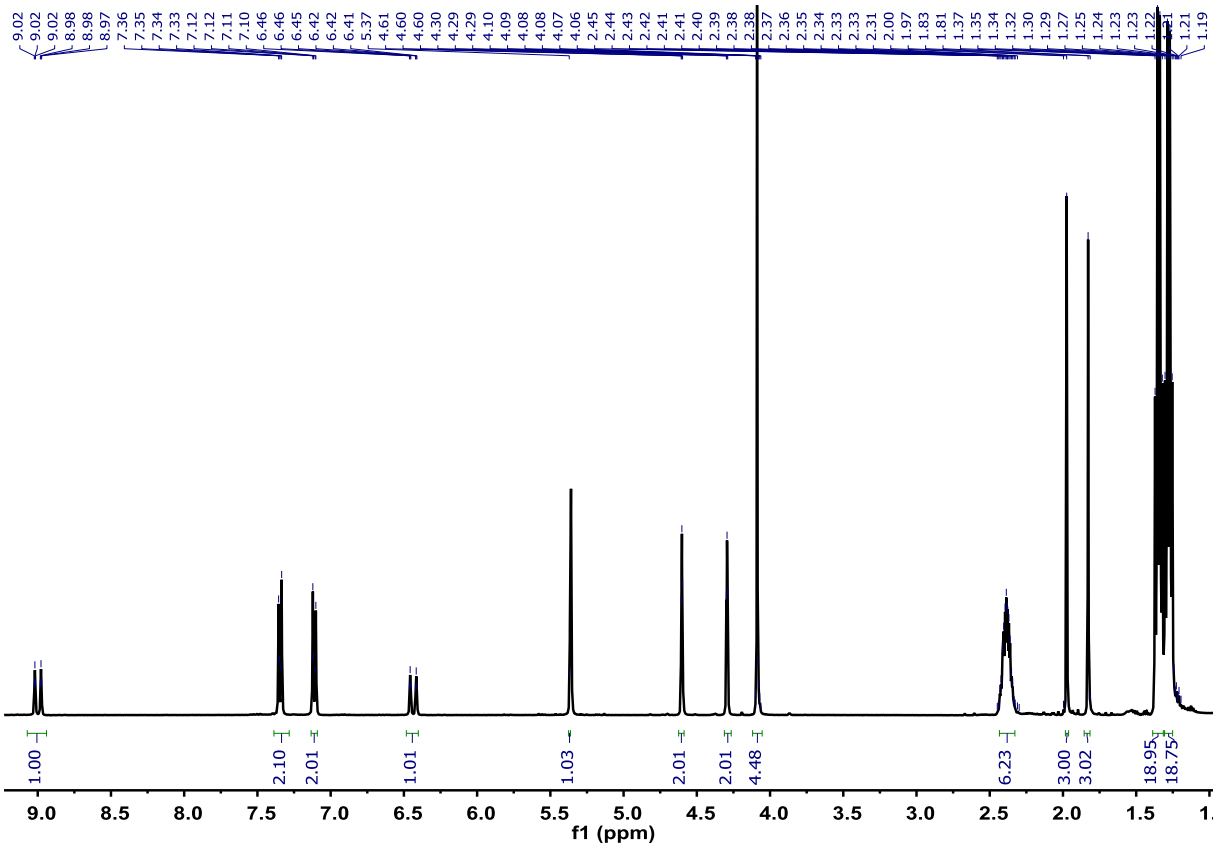

Figure S8. ^{1}H NMR spectrum of complex **2-acac**.

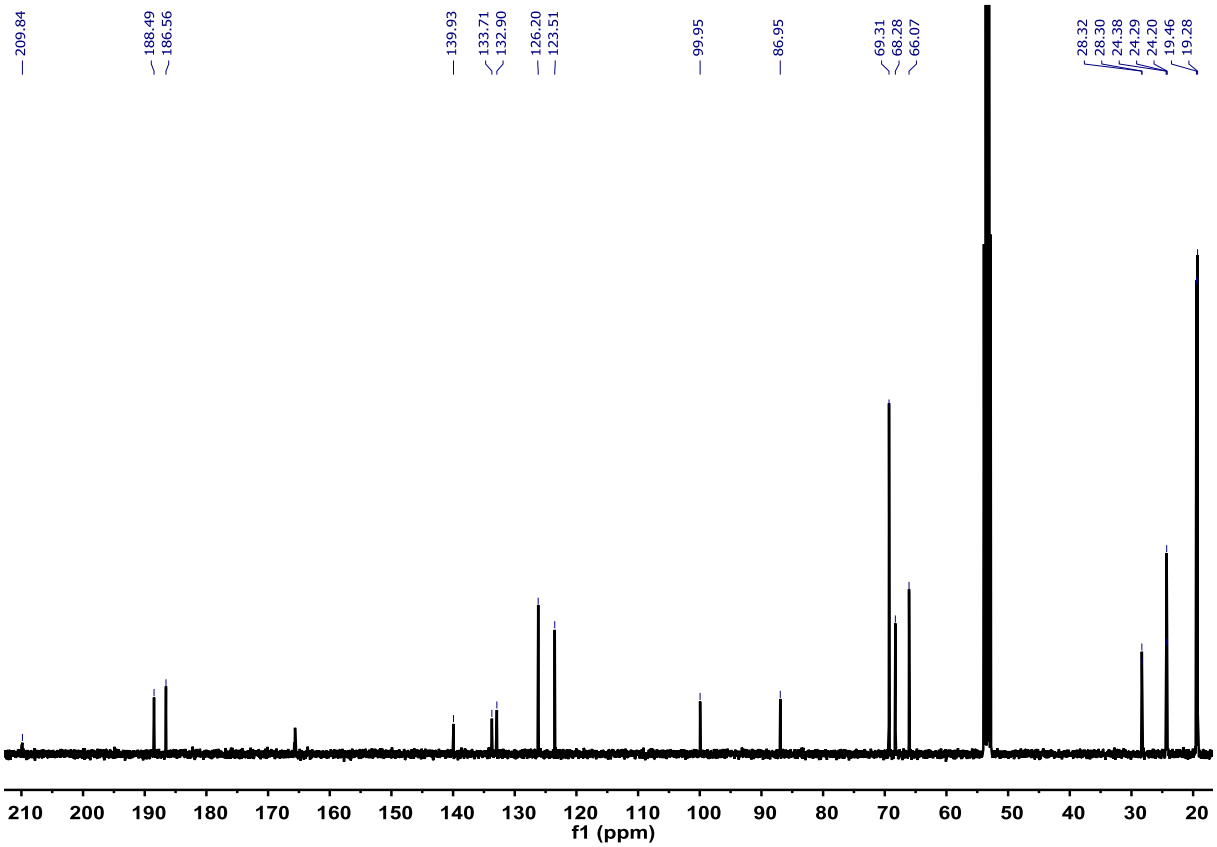

Figure S9. ^{13}C NMR spectrum of complex **2-acac**.

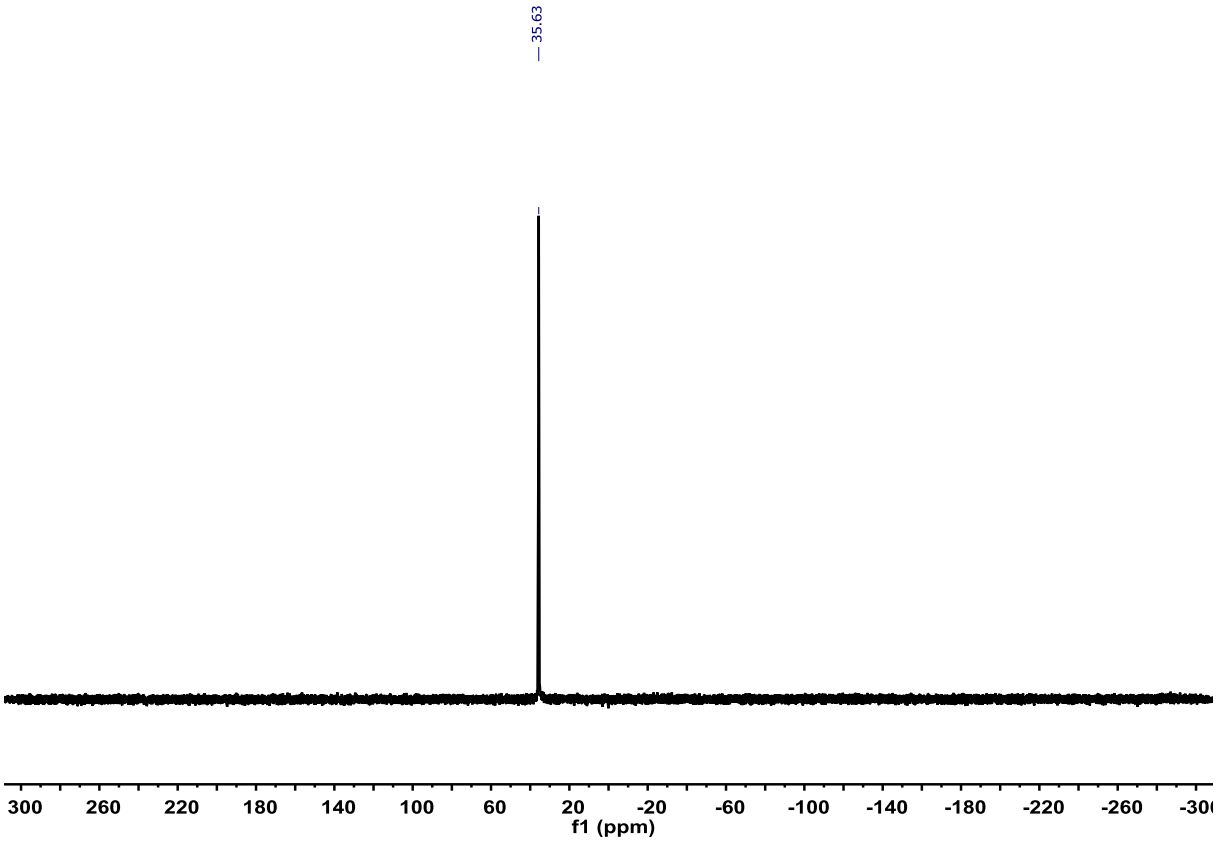

Figure S10. ^{31}P NMR spectrum of complex **2-acac**.

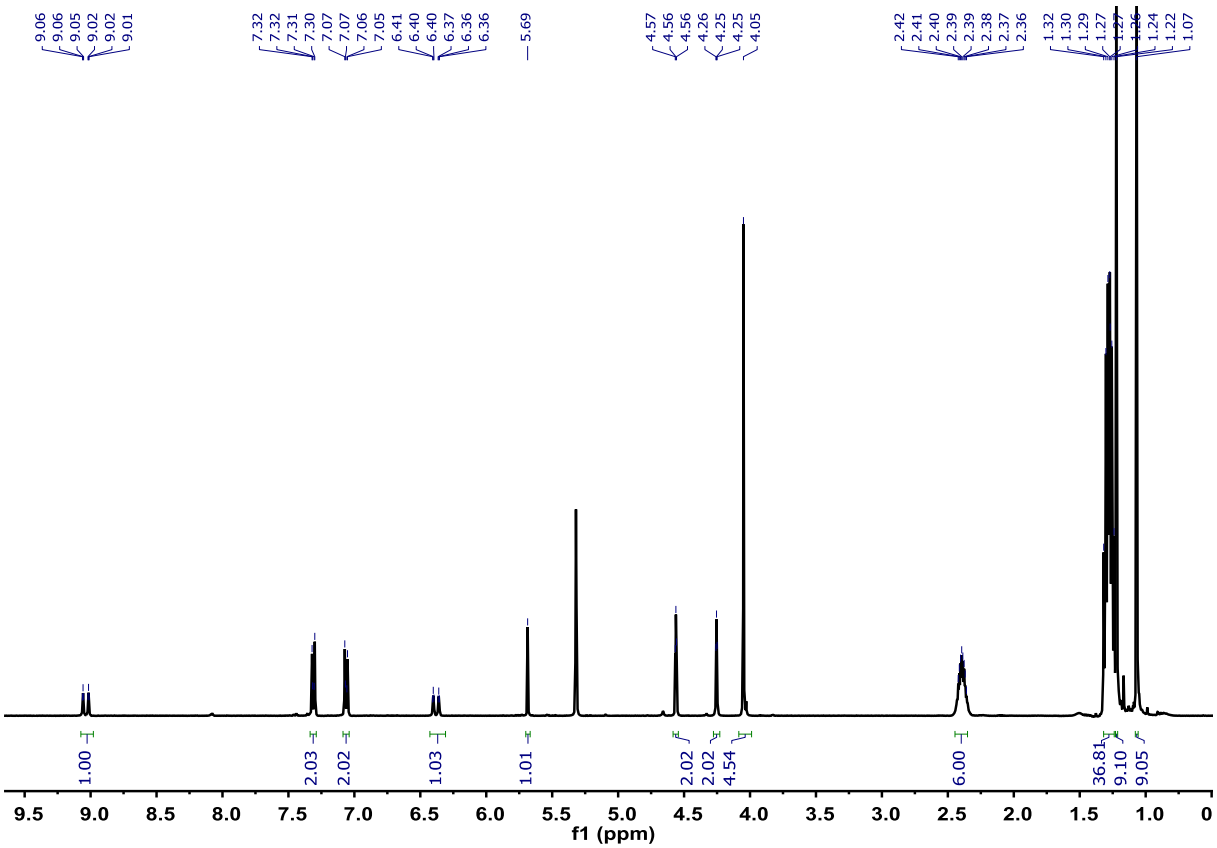

Figure S11. ^{1}H NMR spectrum of complex **2-dpvm**.

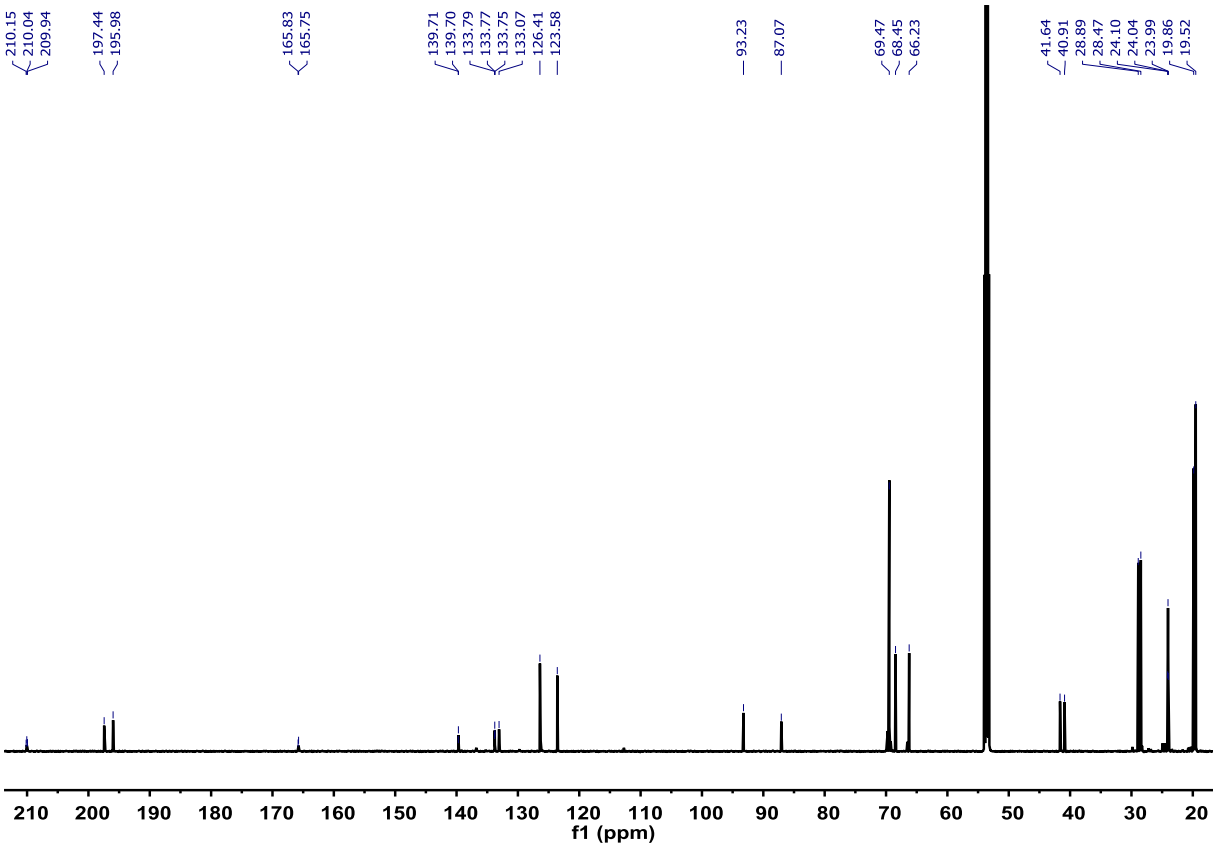

Figure S12. ^{13}C NMR spectrum of complex **2-dpvm**.

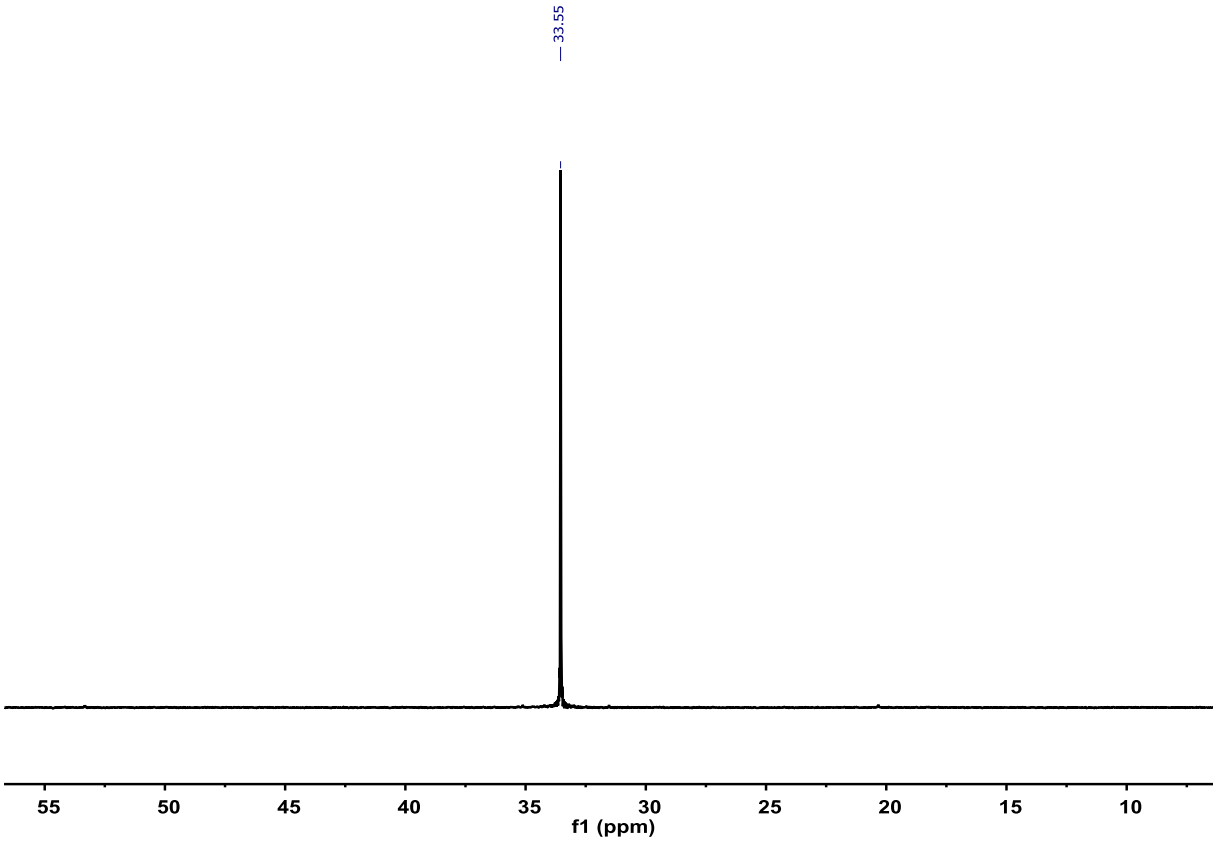

Figure S13. ^{31}P NMR spectrum of complex **2-dpvm**.

II: X-ray crystallography

Table S1. Crystal and refinement data for complexes **1**, **2-hfac** and **2-acac**.

	1	2-hfac	2-acac
emp. formula / f. wt. (g mol^{-1})	$C_{37}H_{57}ClFeOP_2Ru$ / 772.14	$C_{42}H_{58}F_6FeO_3P_2Ru$ / 943.74	$C_{42}H_{64}FeO_3P_2Ru$ / 835.79
Temperature (K)	100(2)	100(2)	100(2)
Crystal system	triclinic	monoclinic	triclinic
Space group	*P*1	$P2_1/c$	*P*1
a, *b*, *c* (Å)	8.5707(17), 13.420(3), 17.115(3)	10.8221(4), 15.1660(7), 26.5208(10)	8.8224(5), 14.4821(9), 16.7357(10)
α, β, γ (deg)	106.29(3), 94.53(3), 99.53(3)	90, 97.591(3), 90	104.757(5), 99.567(5), 101.887(5)
V (Å^3)	1846.9(6)	4314.7(3)	1968.6(2)
Z	2	4	2
ρ_{calcd} (g cm^{-3})	1.388	1.453	1.410
Abs. coefficient (mm^{-1})	0.988	0.823	0.871
θ range for data collection (deg)	1.72 to 26.82	1.549 to 26.855	1.666 to 26.818
Limiting Indices	$-10 \le h \le 10$, $-16 \le k \le 16$, $-21 \le l \le 21$	$-13 \le h \le 12$, $-19 \le k \le 19$, $-33 \le l \le 33$	$-11 \le h \le 11$, $-18 \le k \le 18$, $-21 \le l \le 21$
Reflections collected / unique ($> 2\sigma(I)$)	25085 /7804 [R(int) = 0.1082]	62407 / 9171 [R(int) = 0.0584]	27597 / 8323 [R(int) = 0.0378]
Data / Restraints / Parameter	7804 / 0 / 398	9171 / 0 / 536	8323 / 0 / 467
R ($I > 2\sigma(I)$)	R_1 = 0.0555, wR_2 = 0.0773	R_1 = 0.0302, wR_2 = 0.0837	R_1 = 0.0424, wR_2 = 0.0956
R_w (all data)	R_1 = 0.0999, wR_2 = 0.0860	R_1 = 0.0471, wR_2 = 0.0942	R_1 = 0.0499, wR_2 = 0.0989
GooF (all Data)	0.989	0.680	1.047
Max. and min. res. dens. (eÅ^{-3})	0.635 and -0.684	0.616 and -0.566	2.605 and -0.922

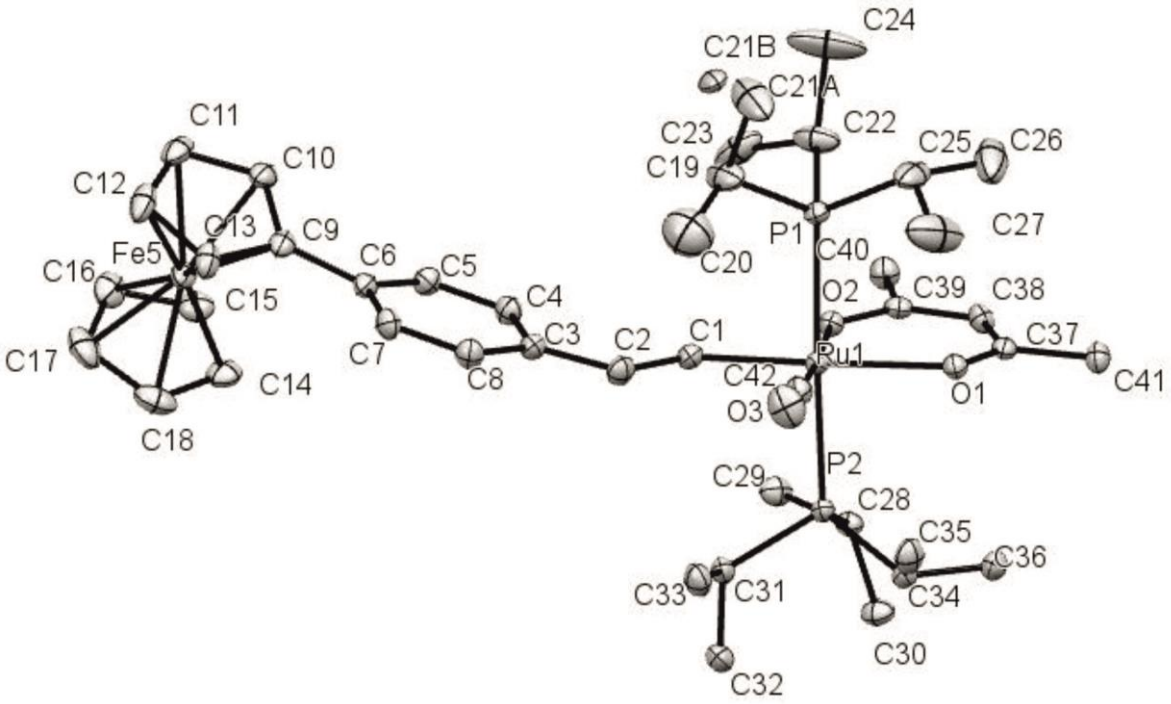

Figure S14. Molecule structure of complex **2-acac** in the crystal with atomic numbering scheme. Ellipsoids are drawn at a 50% probability level.

III. Cyclic Voltammetry

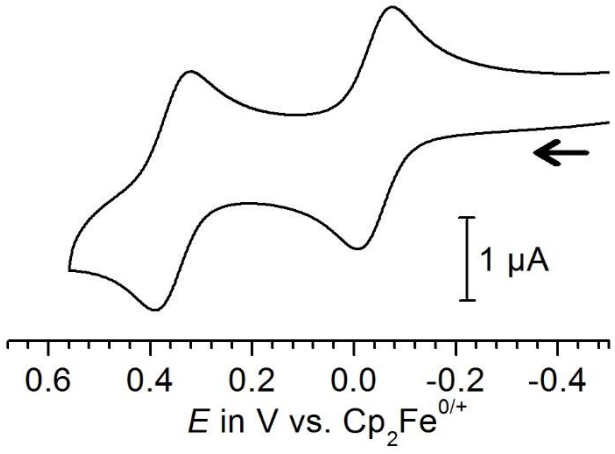

Figure S15. Cyclic voltammogram of complex **1** in CH_2Cl_2/nBu$_4$NPF$_6$ at v = 0.1 V/s at r. t.

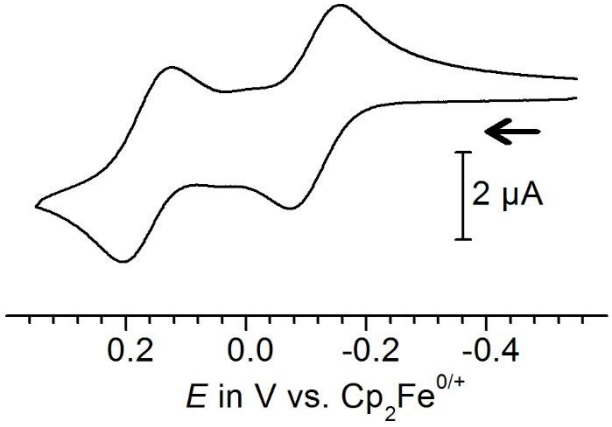

Figure S16. Cyclic voltammogram of **2-acac** in CH_2Cl_2/*n*Bu_4NPF_6 at *v* = 0.1 V/s at r. t.

IV IR spectroelectrochemistry

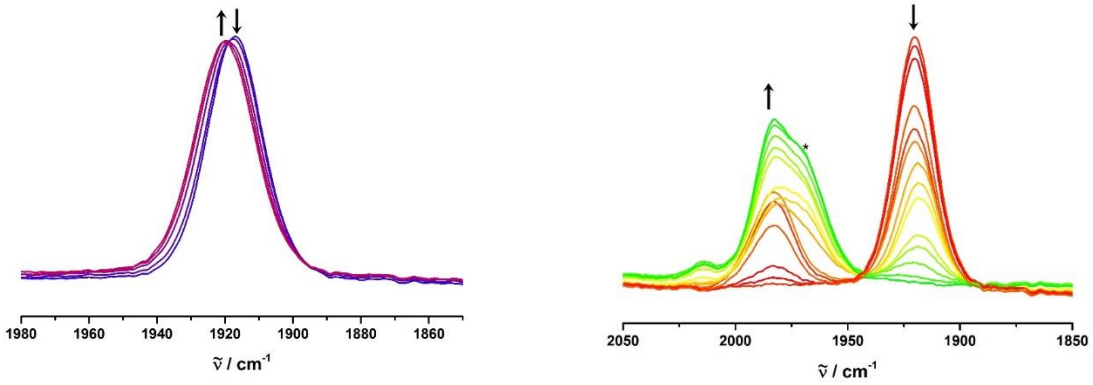

Figure S17. IR spectroscopic changes of ν(CO) during the first (left) and the second (right) oxidation of complex **2-hfac** (1,2-$C_2H_4Cl_2$/nBu_4NPF_6, 0.2 M, at r. t.). The star symbol denotes a decomposition product which is formed upon prolonged electrolysis.

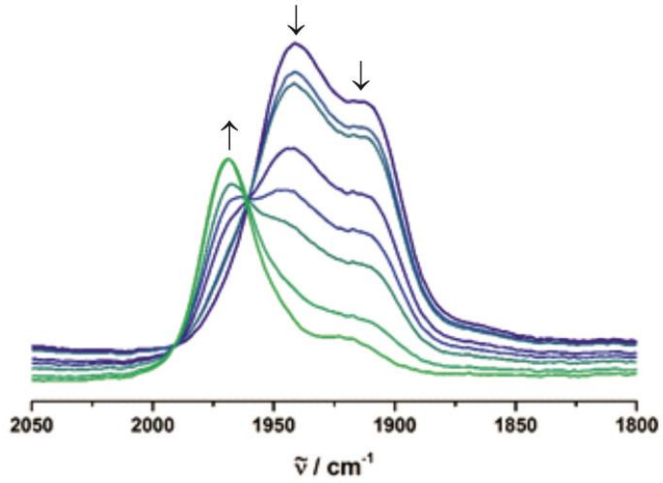

Figure S18. IR spectroscopic changes of ν(CO) during the second oxidation of complex **2-acac** ($1,2\text{-}C_2H_4Cl_2/nBu_4NPF_6$, 0.2 M, at r. t.).

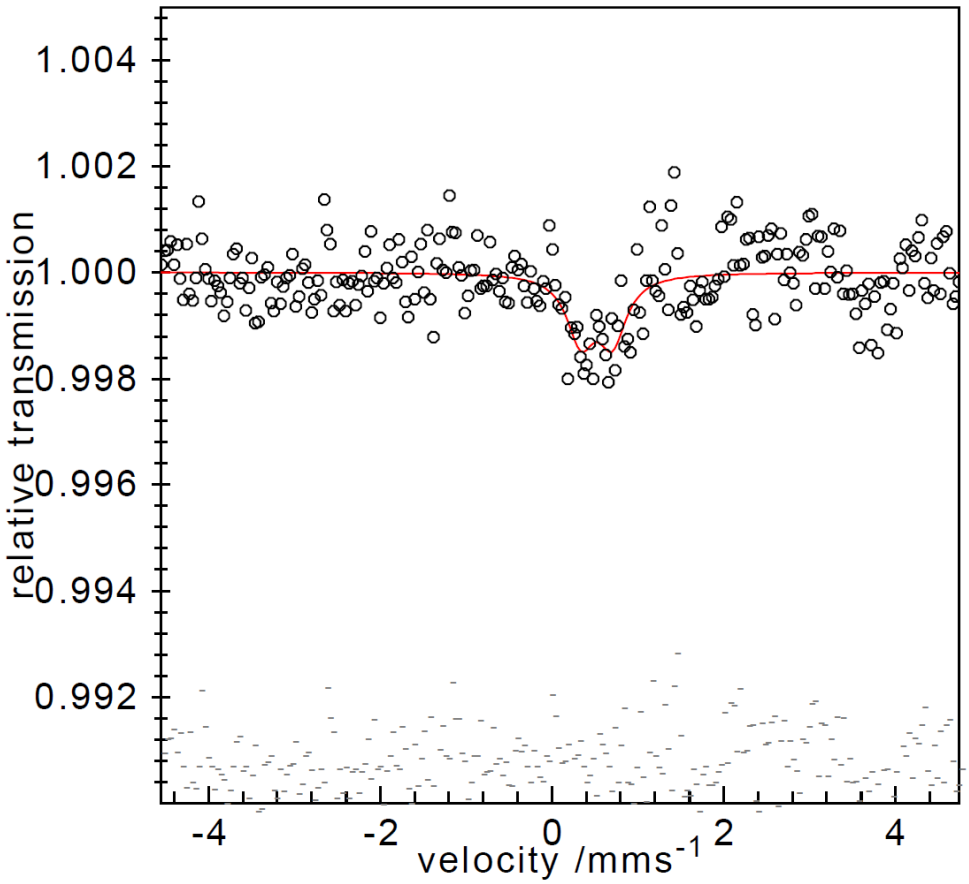

Figure S19. Mößbauer spectrum of pristine **2-acac**$^+$ **SbF$_6$**$^-$ at T = 80 K.

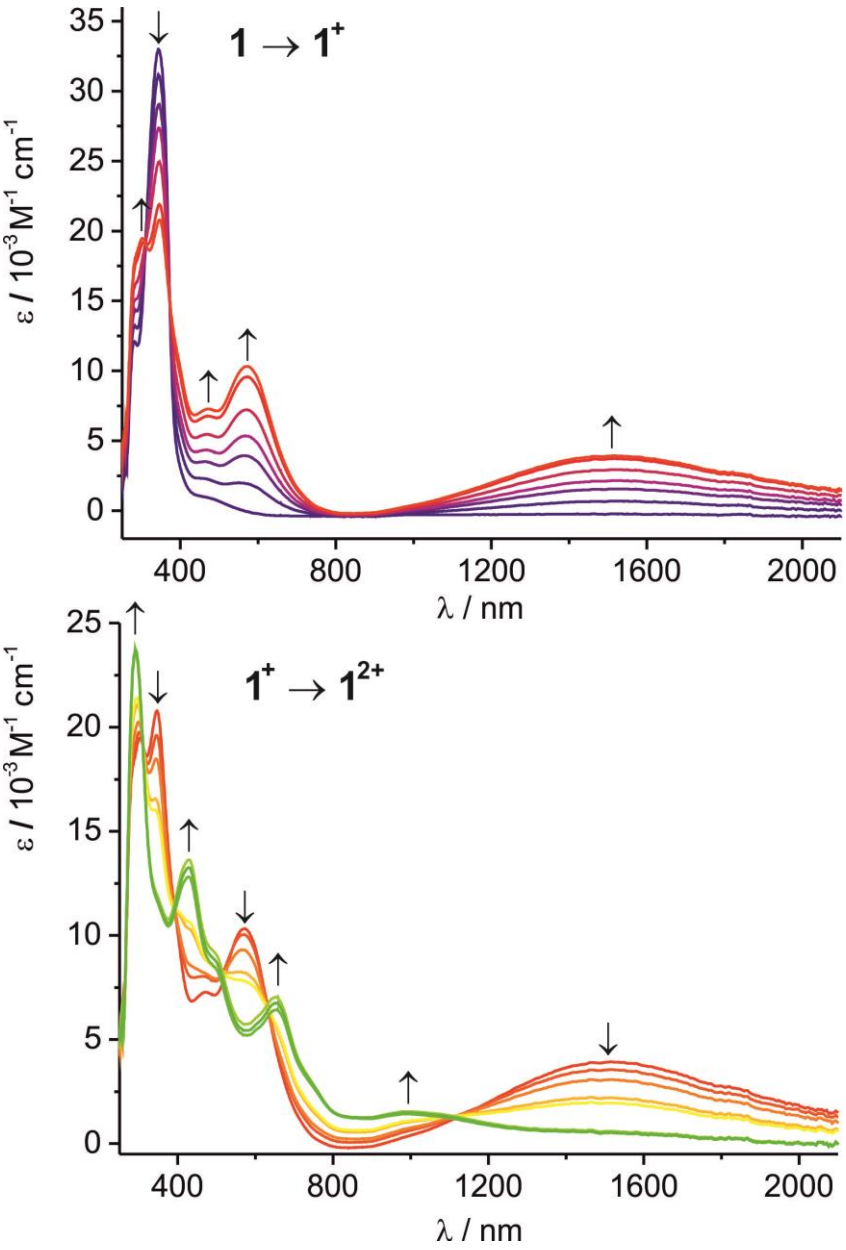

Figure S 20. Spectroscopic changes during the first (top) and the second (bottom) oxidation of complex **1** in 1,2-$C_2H_4Cl_2$/NBu_4^+ PF_6^- (0.2 M) at r. t.

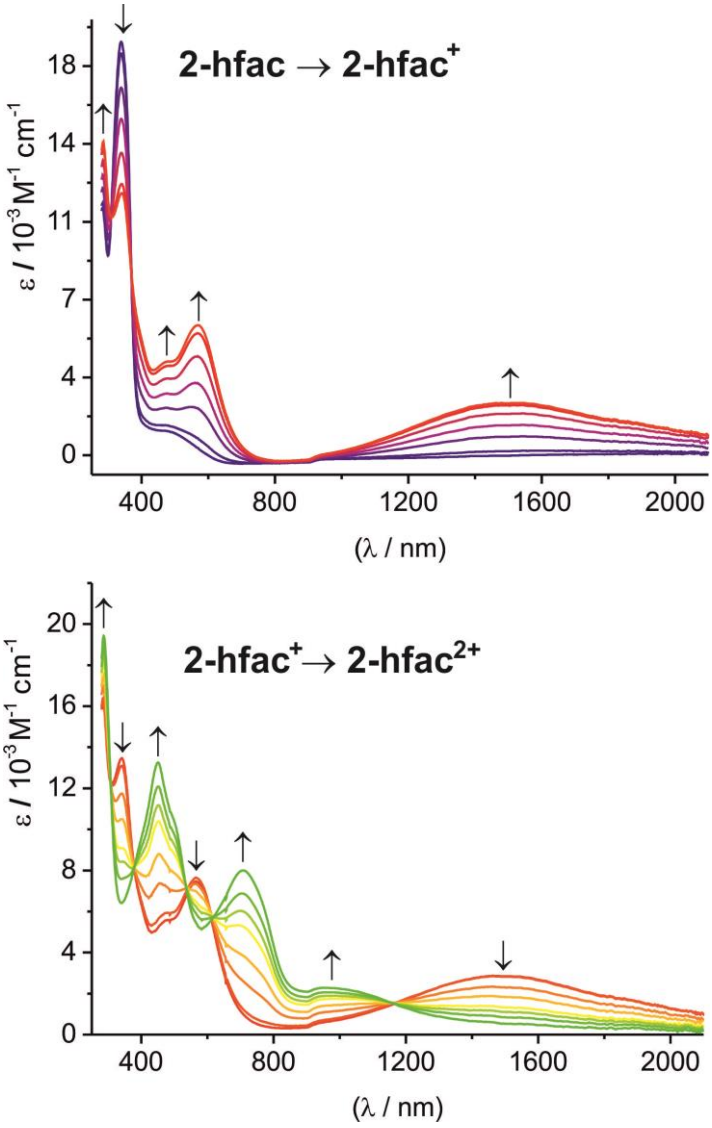

Figure S21. Spectroscopic changes during the first (top) and the second (bottom) oxidation of complex **2-hfac** in 1,2-$C_2H_4Cl_2$/NBu_4^+ PF_6^- (0.2 M) at r. t.

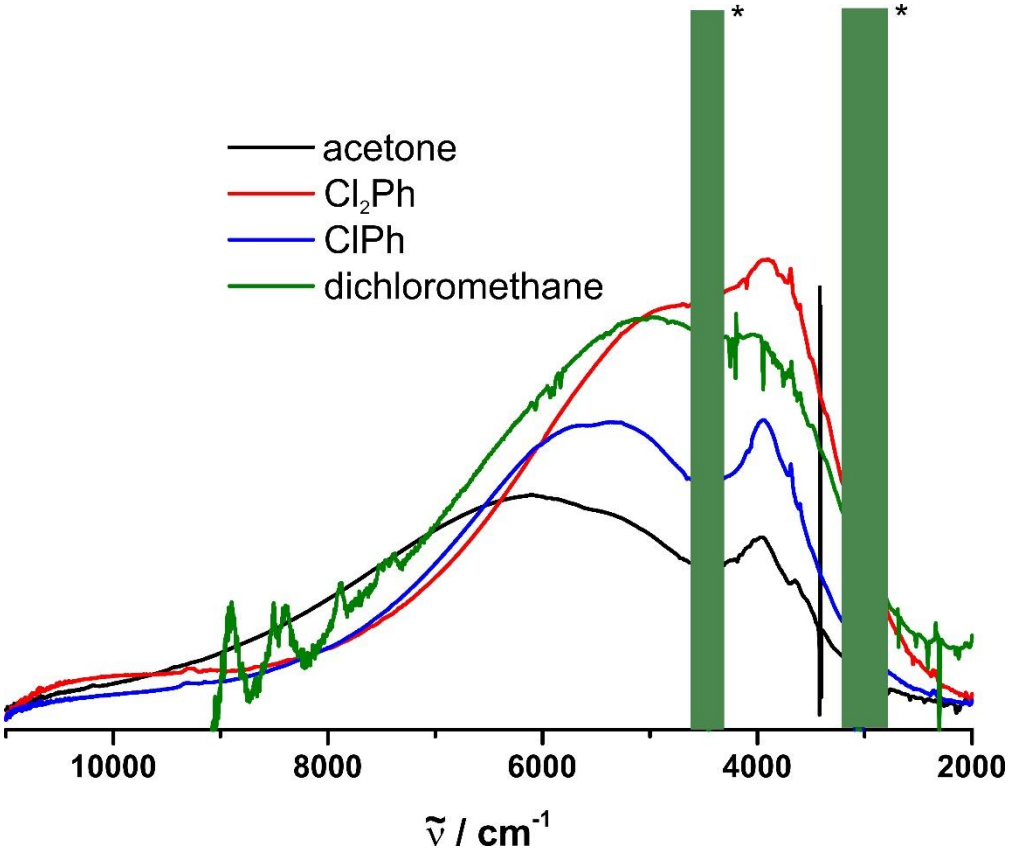

Figure S22. NIR spectra of **2-acac**$^{+}$ in different solvents.

3.3. Paper 2: Manipulation and Asessment of Charge and Spin Delocalization in Mixed-Valent Triarylamine Vinylruthenium Conjugates

Christopher Hassenrück and Rainer F. Winter*

University of Konstanz, Universitätstraße 10, D-78457 Konstanz, Germany

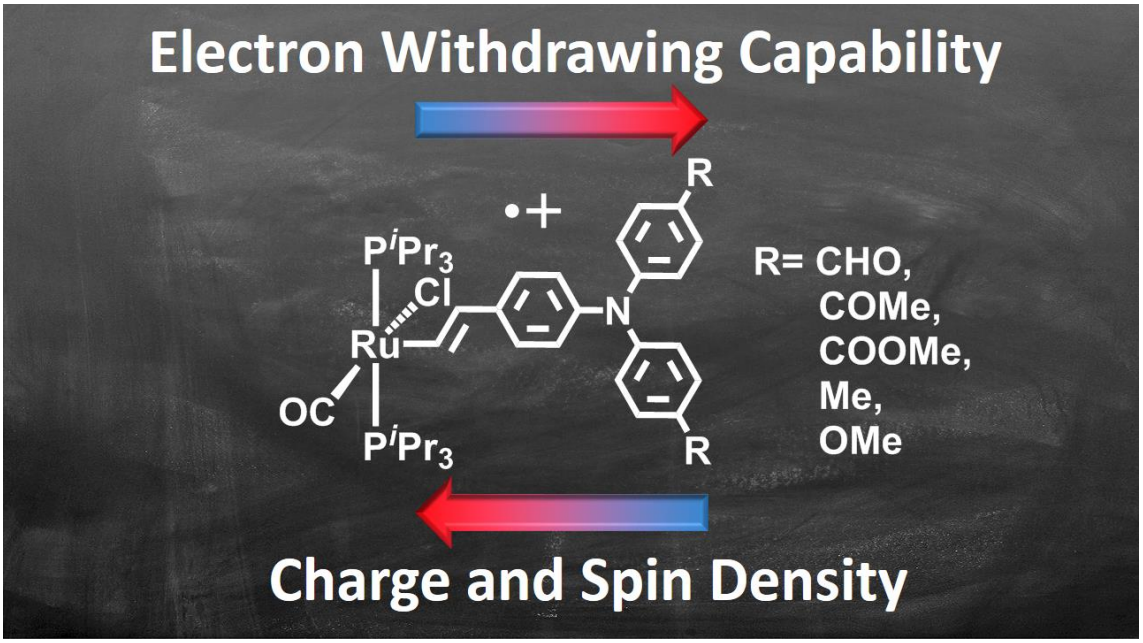

Reprinted with permission from *Inorg. Chem*, **2017**, *56* (21), pp. 13517-13529 Copyright 2017 American Chemical Society.

Inorganic Chemistry

Article

Cite This: Inorg. Chem. 2017, 56, 13517-13529

pubs.acs.org/IC

Manipulation and Assessment of Charge and Spin Delocalization in Mixed-Valent Triarylamine−Vinylruthenium Conjugates

Christopher Hassenrück and Rainer F. Winter*

University of Konstanz, Universitätsstraße 10, D-78457 Konstanz, Germany

Supporting Information

ABSTRACT: Triarylamine−vinylruthenium conjugates (4-$RC_6H_4)_2N\{C_6H_4$-4-CH=CHRu(CO)Cl($P^iPr_3)_2\}$, with R = CHO (**1-CHO**), C(=O)Me (**1-Ac**), COOMe (**1-E**), and Me (**1-Me**), have been prepared and investigated in their neutral, mono- and dioxidized states by cyclic voltammetry, IR, and UV/vis/near-infrared spectroelectrochemistry, electron paramagnetic resonance spectroscopy, and quantum-chemical calculations. Electron-withdrawing substituents at the triarylamine moiety shift the charge and spin density toward the more electron-rich vinylruthenium site in comparison to the 4-OMe-substituted triarylamine−vinylruthenium conjugate **1-OMe**. A more asymmetric charge distribution changes the intense vibrationally structured intervalence charge-transfer (IVCT) band of completely delocalized, mixed-valent (MV) **1-OMe**$^+$ to a weaker, highly asymmetric, nonsolvatochromic band with significantly smaller bandwidth at the low-energy side. The temperature dependence of the IVCT band of the formyl derivative **1-CHO**$^+$ proves that vibrational coupling of the IVCT transition to a symmetrical vibration is the underlying reason for band skewing. All of our results indicate that the MV radical cations remain electronically strongly coupled despite an increasingly stronger bias of the highest occupied molecular orbital to the vinylruthenium entity. Moreover, the dications of these complexes were found to be paramagnetic, which makes them rare examples of compounds that combine strong electronic coupling in the cationic MV state with paramagnetism of the dications.

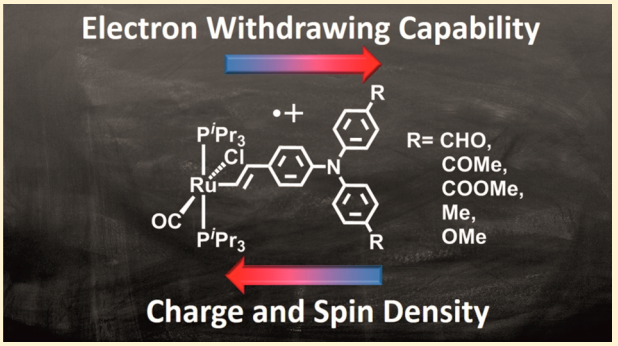

Downloaded by UNIV KONSTANZ at 04:13:37:017 on June 17, 2019
from https://pubs.acs.org/doi/10.1021/acs.inorgchem.7b02186.

INTRODUCTION

Triphenylamine and its many derivatives are of pivotal importance in organic electrochemistry. If appropriately substituted in the para positions in order to prevent benzidine formation[1−4] or cyclization to carbazoles,[5] triarylamines (TAAs) usually exhibit highly reversible redox behavior and are easily oxidized to persistent triarylaminium radical cations TAA$^+$.[6] Efficient methods of synthesis and derivatization, e.g., by Ullman or Buchwald−Hartwig coupling, halogenation, or the Vilsmeier−Haack reaction, offer access to a huge variety of TAAs with identical or nonidentical aryl rings. In this manner, redox potentials can be readily tuned over a considerable range.[5,7−13] TAAs are therefore widely used as selective one-electron oxidants and electrocatalysts. This is exemplified by the family of oxidized, brominated triphenylamines (the so-called "Blues-Brothers"),[6,14] which are widely used stoichiometric one-electron oxidants.[7]

Bis(triarylamine)s and their associated radical cations constitute a cornerstone of organic mixed-valent (MV) chemistry. They have provided valuable insight into the impact of the interconnecting bridges, solvent, and counteranion on their charge-transfer (CT) properties, the degree of electronic coupling in the MV state, and the rates of intramolecular electron transfer (ET), as well as the inner and outer reorganization energies λ_{in} and λ_o involved in these processes.[15−41] While the vast majority of these compounds feature two identical redox sites, some unsymmetrical TAA derivatives, which, nevertheless, form electronically strongly coupled MV radical cations, have also been reported. Prominent examples are neutral MV compounds featuring TAA and a perchlorinated trityl (PCT) radical,[37,42,43] and $[Ru(bipy)_2(N^\wedge C)]^{2+}$ (bipy = 2,2′-bipyridine) or $[Ru(terpy)(N^\wedge C^\wedge N)]^{2+}$ complexes featuring a TAA-derived cyclometalating phenylpyridine or phenyl-2,6-di(2-pyridyl) ligand.[44,45]

Aryl-substituted vinylruthenium complexes of the type ArCH=CHRu(CO)Cl($P^iPr_3)_2$ (ArCH=CH{Ru}) have properties astoundingly similar to those of TAAs.[46−48] Just like the latter, they exhibit a reversible one-electron oxidation whose half-wave potential strongly depends on the aryl substituent and delocalized frontier orbitals with large contributions of the arylalkenyl ligand.[47,49−55] As a consequence of large styryl contributions to the highest occupied molecular orbital (HOMO) and HOMO−1, their associated radical cations usually display intense electron paramagnetic resonance (EPR) signals in a fluid solution with resolved hyperfine splittings (hfs's) to the ^{31}P nuclei of the phosphine coligands. The latter trace the metal contribution to the overall spin density. In

Received: August 30, 2017
Published: October 16, 2017

ACS Publications © 2017 American Chemical Society

DOI: 10.1021/acs.inorgchem.7b02186
Inorg. Chem. 2017, 56, 13517−13529

addition, the carbonyl ligand, by virtue of its characteristic and intense CO stretching vibration, provides information on redox-induced changes of the electron density at the Ru atom. Depletion of the electron density from the metal ion decreases the π back-donation into the CO π^* orbitals and induces a blue shift of the Ru(CO) band. The magnitude of this shift of ca. 40−70 cm^{-1} is, however, much lower than that of ca. 125 cm^{-1} for similar carbonylphosphine complexes with a mainly metal-centered HOMO.[56] Both have shown to be extremely useful in elucidating the degree of charge and spin delocalization in arylene-bridged, MV bis(vinylruthenium) complexes.[48−52,54,57−72]

Blending the vinylruthenium and TAA entities together in one compound has led to strongly coupled, intrinsically delocalized MV systems if the vinylruthenium moiety attaches to the phenylene linker in the para position to the amine N atom.[73,74] This is opposed to the situation where a redox process (predominantly) involves either the metal ion or a redox-active, noninnocent ligand of the inner coordination sphere with only a little electron delocalization between them but strongly resembles the situation in the other delocalized, unsymmetrical MV systems such as PCT-TAAs, *N,N,N′,N′*-tetraarylphenylenediamines with different aryl substituents at the N and N′ atoms,[75,76] a heterobimetallic divinylphenylene-bridged ruthenium/osmium complex,[77] and the alkenyl/alkynyl complexes {Ru}CH=$CHC_6H_4C{\equiv}CRu(dppe)_2(L)$ (L = Cl or C≡CPh).[78,79] Their associated oxidized forms absorb strongly in the near-infrared (NIR) with stepwise blue shifts of the underlying intervalence charge transfer (IVCT)/$\pi \rightarrow \pi^*$ bands upon further oxidation.[73] In particular, the charge and spin density of the MV radical cation of the bis(anisyl)amine complex {Ru}CH=$CHC_6H_4N(C_6H_4$-4-OMe$)_2$ (**1-OMe** of Scheme 1) is equally distributed over the TAA and vinyl-

Scheme 1. Synthesis of Vinylruthenium−TAA Complexes

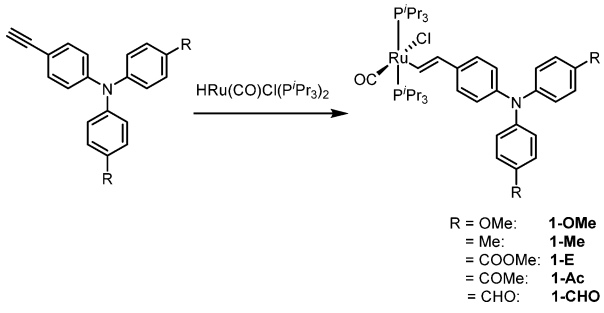

ruthenium moieties. That radical cation thus constitutes a rare example of an intrinsically delocalized MV system despite the presence of two chemically different redox sites.[37,42,77−80] We mused that substitution of the methoxy substituents of **1-OMe** by less electron-donating or electron-accepting substituents should lead to a less symmetrical charge and spin density distribution in the MV state. These modifications serve to increase the difference between the intrinsic redox potentials of the TAA and vinylruthenium sites from 0.165 V for **1-OMe** to 0.285 V for **1-Me** and 0.615 V for **1-CHO** when compared to the 4-methoxy-substituted styryl complex {Ru}CH=CHC_6H_4OMe-4.[4,53,81] This would then allow us to probe for the consequences of such increasing imbalance on the ^{31}P and ^{14}N hfs constants in their EPR spectra, the Ru(CO) band shifts on stepwise oxidation, and the shape and intensity of the IVCT bands of the MV radical cations. The results of this study are reported herein.

RESULTS AND DISCUSSION

Synthesis and Characterization. The TAA substituents chosen for our study are methyl, methyl acetate, acetyl, and formyl. The latter three were also chosen to provide an additional IR-sensitive label as an independent probe for electronic changes at the TAA site. The corresponding ethynyl-substituted amines $(4\text{-}HC{\equiv}CC_6H_4)N(C_6H_4\text{-}4\text{-}R)_2$ were prepared according to literature procedures.[73,82−85] Details of the syntheses and characterization can be found in the Supporting Information (SI; see also Figures S1−S3). The target complexes were then obtained in high to quantitative yields by the regio- and stereoselective cis insertion of the ethynyl function into the Ru−H bond of $HRu(CO)Cl(P^iPr_3)_2$ (Scheme 1).[86−89]

^1H, ^{31}P, and ^{13}C NMR spectra proved the purity of the complexes (see Figures S4−S15 in the SI). Selected NMR data are collected in Table 1 with the numbering scheme in Figure 1.

Table 1. Selected ^1H and ^{13}C NMR Chemical Shifts (δ in ppm) of the Complexes[a]

	H_1/H_2	H_4/H_5	H_8/H_9	C_1/C_2
1-OMe	8.28/5.89	6.85/6.74	6.79/6.98	147.6/134.3
1-Me	8.35/5.92	6.82/6.90	6.90/7.03	148.6/134.3
1-E	8.61/6.00	6.95/7.01	7.07/7.87	152.9/134.6
1-Ac	8.64/6.01	7.03/6.95	7.10/7.82	152.6/133.9
1-CHO	8.69/6.02	7.05/6.97	7.18/7.74	153.2/133.9

[a]NMR spectra recorded in CD_2Cl_2 at room temperature.

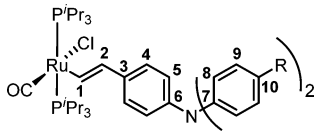

Figure 1. Atomic numbering scheme for Table 1.

Particularly characteristic of vinylruthenium complexes are the CH=CH doublet resonances of the vinylic protons with a $^3J_{HH}$ coupling constant of 13.4 Hz. In line with previous observations, decreasing electron donation by the 4-substituted phenyl ring and lesser electron density at the styrylruthenium moiety shifts the resonances of the vinylic proton H_1 and of the phenyl protons to lower field, while affecting the neighboring proton H_2 only to a minor extent.[53,65,66] Similar trends are observed for the ^{13}C resonances of the vinylic C atoms. ^{31}P NMR spectra showed just one sharp singlet resonance in a very narrow shift range of 37.9−38.7 ppm.

Electrochemistry. All vinylruthenium−TAA conjugates exhibit two consecutive one-electron oxidations in their cyclic voltammograms (CVs). Both waves comply with the requirements of a chemically and electrochemically reversible Nernstian process over the range of sweep rates from 50 mV s^{-1} to 1 V s^{-1}, attesting to the rapid ET kinetics and stabilities of the oxidized forms on the experimental time scale. Figure 2 shows the CVs of complexes **1-Me** and **1-Ac**, while those of the other complexes can be found as Figures S16 and S17 in the SI. The most important parameters derived from the experimental CVs are collected in Table 2.

As one would expect for a strongly delocalized system, increasing the electron-withdrawing or decreasing the electron-

DOI: 10.1021/acs.inorgchem.7b02186
Inorg. Chem. 2017, 56, 13517−13529

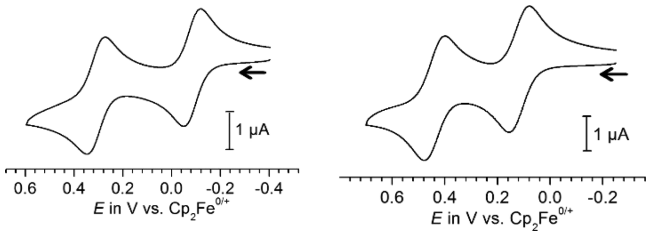

Figure 2. CVs of complexes **1-Me** (left) and **1-Ac** (right) in CH_2Cl_2/NBu_4PF_6 (0.1 M) supporting electrolyte at room temperature and ν = 0.1 V s^{-1}.

Table 2. Cyclic Voltammetry Data of the Complexes[a]

complex	$E_{1/2}^{0/+}$ (ΔE_p)	$r^{0/+}$[b]	$E_{1/2}^{+/2+}$ (ΔE_p)	$r^{+/2+}$[b]	$\Delta E_{1/2}$
1-CHO	151 (69)	1.00	461 (69)	0.98	310
1-Ac	118 (77)	1.00	439 (74)	1.00	321
1-E	104 (80)	0.98	433 (80)	0.98	329
1-Me	−84 (68)	1.00	310 (68)	0.99	394
1-OMe	−118 (80)	1.00	266 (84)	0.99	384

[a]All data in millivolts versus $Cp_2Fe^{0/+}$ in CH_2Cl_2/NBu_4PF_6 (0.1 M) at room temperature and ν = 0.1 V s^{-1}; data for **1-OMe** are from ref 73. [b]The reversibility coefficient $r = i_{p,rev}/i_{p,fw}$.

donating character of R shifts *both* waves to higher potentials. Similar observations have been previously reported for unsymmetrically substituted *N,N,N′,N′*-tetraarylphenylenediamines with different aryl substituents on the N and N′ atoms,[75,76] the heterobimetallic divinylphenylene-bridged ruthenium/osmium complex {Ru}CH═CHC_6H_4CH═CH-{Os} ({Os} = Os(CO)Cl(P^iPr_3)$_2$),[77] and the mixed alkenyl/alkynyl complexes {Ru}CH═CHC_6H_4C≡CRu$(dppe)_2$(L) (L = Cl or C≡CPh).[78,79] Because of the many parameters that influence the individual redox potentials and their splitting in compounds with multiple coupled redox sites, shifts of the half-wave potentials provide no direct information on the mutual involvement of the individual redox sites and the degree of electron delocalization of their corresponding MV radical cations.[90−93] This can, however, be probed with the aid of molecular spectroscopy by utilizing spectroscopic tags that are sensitive to the distribution of the charge and spin density in the oxidized forms.[94]

Charge and Spin Density Distributions As Probed by IR and EPR Spectroscopy and Quantum Chemistry. Oxidation of the styrylruthenium complex {Ru}CH═CHC_6H_4R-4 leads to a blue shift of the Ru(CO) band by ca. 40−70 cm^{-1}. When the positive charge is shared between two redox sites, as it is the case here, CO band shifts on one-electron oxidation are generally smaller. An increasingly unsymmetrical charge distribution in the vinylruthenium−TAA conjugates compared to **1-OMe** should manifest itself in a comparatively larger CO band shift during the first oxidation and, concomitantly, a smaller one for the second oxidation. Electrochemical oxidation of the complexes inside a transparent thin-layer electrolysis cell[95] occurred in two well-defined, separate processes with clean isosbestic points and with stepwise blue shifts of the Ru(CO) band. Figure 3 displays spectra recorded during the two consecutive oxidations of complex **1-E** as a representative example. The results for the other complexes can be found as Figures S18−S25 in the SI. Pertinent data to the IR spectroelectrochemical studies are collected in Table 3 together with the DFT-calculated energies of the Ru(CO) bands (vide infra).

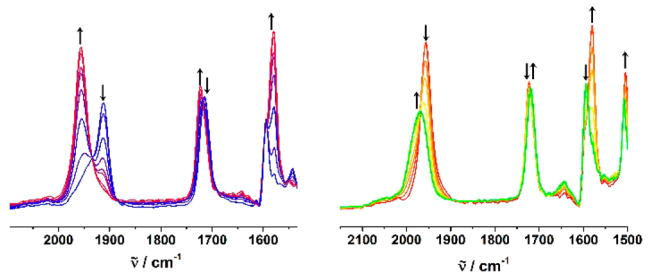

Figure 3. IR spectroscopic changes during the first (left) and second (right) oxidations of complex **1-E** (1,2-$C_2H_4Cl_2$/0.1 M NBu_4PF_6).

In compliance with the above expectations, the modest influence of substituent R on the energy of the Ru(CO) stretch of only 3 cm^{-1} amplifies to 13 cm^{-1} in the associated radical cations and to 17 cm^{-1} in the dications. Remarkably, the Ru(CO) band for the dications of the less electron-rich, acceptor-substituted complexes appears at lower energy than in the more electron-rich congeners **1-OMe**$^{2+}$ or **1-Me**$^{2+}$. Obviously, the propensity of, in particular, the ester substituent to delocalize the positive charge by resonance overrides its inductive effect. Our data also indicate that the normal ordering of oxidation-induced CO band shifts as $\Delta\nu_{CO}^{+/2+} > \Delta\nu_{CO}^{0/+}$ reverts as substituent R becomes an increasingly stronger electron acceptor. This is best seen from the ratio of the Ru(CO) band shift observed on the first oxidation to the total shift of the dicationic compared to the neutral complexes, $\Delta\nu(CO)^{+/0}/\Delta\nu(CO)^{2+/0}$ (Table 3). **1-OMe** can be regarded as a benchmark system with complete charge delocalization in the MV state.[73] All acceptor-substituted complexes show higher values for that ratio, which is in line with an increasing bias of the first oxidation to the vinylruthenium site and of the second oxidation to the TAA site.

By virtue of their carbonyl functional groups, complexes **1-CHO**, **1-Ac**, and **1-E** feature an additional IR label at the NAr_3-type redox site. Oxidizing the complexes by one electron produces the expected blue shift of the ester, acyl, or formyl C═O stretch. The second oxidation, however, has a smaller and, counterintuitively, an opposite effect, shifting the C═O band slightly to the red. While we have no ready explanation for this unexpected observation, it may still be seen as another token for the involvement of the conjugated functional groups in delocalizing the positive charge(s).

Our previous studies on **1-OMe**$^+$ have shown that the hfs constant $A(^{31}P)$ by the phosphorus nuclei of the P^iPr ligands of 10.4 G is very similar to that in [{Ru}-1,4-CH═CHC_6H_4CH═CH{Ru}]$^+$ [$A(^{31}P)$ = 9.7 G; note that the ^{31}P hfs was originally misinterpreted as ^1H hfs],[58] while the $A(^{14}N)$ hfs of 5.1 G closely resembles that of 5.75 G for [$(4\text{-}OMeC_6H_4)_2$N-1,4-C_6H_4N$(C_6H_4OMe\text{-}4)_2$]$^+$.[96] Because all of the parent symmetrical MV radical cations constitute completely delocalized systems, this should, by inference, also hold for **1-OMe**$^+$, at least on the EPR time scale of 10^{-8}−10^{-9} s. A larger contribution of the vinylruthenium moiety to the HOMO of the neutral complexes and the singly occupied molecular orbital (SOMO) of their corresponding radical cations should increase the $A(^{31}P)$ hfs constants and decrease the $A(^{14}N)$ hfs constants with respect to **1-OMe**$^+$.

Samples of the radical cations **1-Me**$^+$ to **1-CHO**$^+$ for EPR measurements were prepared by chemical oxidation of the neutral complexes with the acetylferrocenium ion in dichloromethane (CH_2Cl_2) at room temperature, and their identities

DOI: 10.1021/acs.inorgchem.7b02186
Inorg. Chem. 2017, 56, 13517−13529

Table 3. IR Data of the Vinylruthenium−TAA Complexes in Their Various Oxidation States[a]

	$\nu(CO)_{exp}$			$\nu(CO)_{calc}$[b]			$\Delta\nu(CO)$				$\nu(C{=}O)$[c]		
	$n = 0$	$n = 1$	$n = 2$	$n = 0$	$n = 1$	$n = 2$ (S/T)	+/0	2+/+	2+/0	$\Delta\nu(CO)^{+/0}/\Delta\nu(CO)^{2+/0}$	$n = 0$	$n = 1$	$n = 2$
1-CHO	1912	1957	1974	1906	1943	1977/1970	45	17	62	0.73	1693	1701	1698
1-Ac	1912	1956	1975	1906	1941	1978/1969	44	19	63	0.70	1674	1686	1680
1-E	1911	1956	1968	1906	1942	1976/1970	45	12	57	0.79	1714	1722	1718
1-Me	1910	1947	1989	1904	1932	1969/1967	37	41	78	0.47			
1-OMe[a]	1909	1944	1985	1913	1945	1971/1968	35	41	76	0.46			

[a]In 1,2-$C_2H_4Cl_2$/NBu_4PF_6 (0.2 M) at room temperature; the data for **1-OMe**$^{n+}$ are from ref 73. [b]DFT-calculated energies (S = singlet; T = triplet state). [c]CO stretch of substituent R.

were checked by comparing their IR spectra to those obtained from IR spectroelectrochemistry. All radical cations show well-resolved solution EPR spectra. This allowed us to extract individual hfs constants by digital simulation, as is exemplified by comparing the experimental and simulated spectra of **1-CHO**$^+$ in Figure 4. Experimental and simulated EPR spectra of the radical cations of the other complexes are displayed as Figures S26−S28 in the SI.

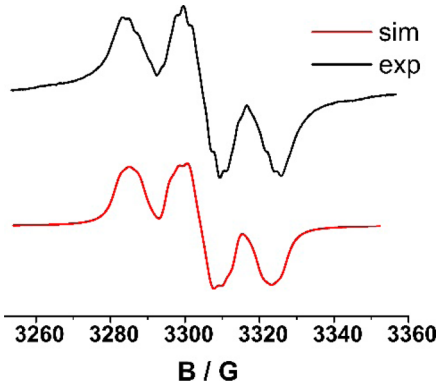

Figure 4. Experimental (black) and simulated (red) EPR spectra of **1-CHO**$^+$ (CH_2Cl_2, room temperature).

The corresponding data in Table 4 indicate an increasingly unsymmetrical spin-density distribution over the two conjoined

Table 4. EPR Data of the Paramagnetic Radical Cations and Dications

	radical cation			dication
	g_{iso}	$A(^{31}P)$[a]	$A(^{14}N)$[a]	g_{iso}
1-CHO[b]	2.039	13.6	4.1	2.020[d]
1-Ac[b]	2.037	12.8	3.6	2.020[d]
1-E[b]	2.038	14.3	3.2	2.022[d]
1-Me[c]	2.031	11.1	4.1	2.014[e]
1-OMe[c]	2.015	10.4	5.1	2.014[e]

[a]Hyperfine coupling constants in Gauss. [b]With acetylferrocenium hexafluoroantimonate as the oxidant. [c]With ferrocenium hexafluorophosphate as the oxidant. [d]With tris(4-bromophenyl)aminium hexafluoroantimonate as the oxidant. [e]With diacetylferrocenium hexafluoroantimonate as the oxidant.

redox sites. As the amine substituents change from electron-donating to electron-accepting, $A(^{31}P)$ increases with a concomitant decrease of $A(^{14}N)$. This is accompanied by an increase of the gyromagnetic ratio g from 2.015 in **1-OMe**$^+$ to 2.039 in **1-CHO**$^+$, again in line with a higher contribution of vinylruthenium (and, more specifically, the Ru 4d orbitals) to the SOMO. Also of note is the reduction of $A(^{14}N)$ from 4.1 to 3.2 G in the series **1-CHO**$^+$ > **1-Ac**$^+$ > **1-E**$^+$. This may be another token of an increasing ability of the π-conjugated functional groups at the amine-bonded aryl rings to delocalize the spin density at the TAA site and mirrors the substituent effects observed in IR spectroelectrochemistry. In spite of a larger metal contribution to the SOMO, the EPR signal remains isotropic even in frozen CH_2Cl_2 glass at 153 K. No hfs's were, however, resolved under these conditions (see Figures S29−S32 in the SI).

The dication of the 1,4-phenylene-bridged bis(vinylruthenium) complex {Ru}CH=CHC$_6$H$_4$CH=CH{Ru} has been found to be also paramagnetic,[64] thus defying the predictions of Ovchinnikov's rule.[97] According to those results, the resonance form **II** of Figure 5 with two noninteracting spin

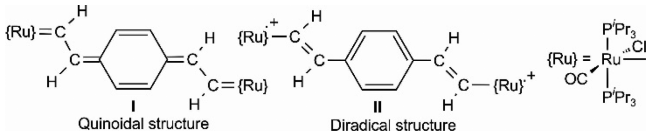

Figure 5. Resonance forms for the dications of the 1,4-phenylene-bridged bis(vinylruthenium) complex.

centers separated by an arylene spacer is probably more relevant than the resonance form **I**, where the six-membered ring adopts a quinoidal structure. The latter would support antiferromagnetic spin coupling. Furthermore, the good obedience to Curie's law over the temperature range from 103 to 4 K with increasing intensity of the EPR signal at decreasing T indicates that the paramagnetic triplet state constitutes the ground state and is not the thermally excited form of a singlet diradical ground state. Similar observations were recently reported for some arylene-bridged bis(triarylaminium) dications.[18,98,99] In these cases, unresolved EPR spectra with g values in the range of 2.04 were observed.

In light of these results, we also prepared the dications of the present complexes by chemically oxidizing their neutral parents with 2 equiv of 1,1′-diacetylferrocenium hexafluorophosphate or Magic Blue [$N(C_6H_4Br\text{-}4)_3^+SbF_6^-$] and investigated them by means of EPR spectroscopy. Indeed, strong isotropic signals at g values of ca. 2.02 were detected at room temperature and, with moderate broadening, in a frozen CH_2Cl_2 matrix. Figure 6 displays the spectra of **1-E**$^{2+}$ and **1-CHO**$^{2+}$ as representative examples; those of the other complexes as well as the spectra in a solid frozen matrix can be found as Figures S33−S38 in the SI.

The decreased g values compared to those of the corresponding radical cations agree with an enhanced organic spin density corresponding to strong involvement of the TAA site in the second oxidation. In addition, **1-Me**$^{2+}$ offered a richly

DOI: 10.1021/acs.inorgchem.7b02186
Inorg. Chem. 2017, 56, 13517−13529

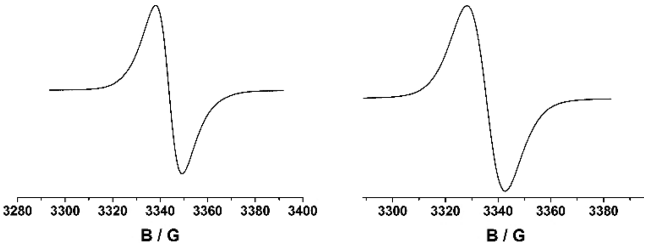

Figure 6. EPR spectra of chemically generated **1-E**$^{2+}$ (left) and **1-CHO**$^{2+}$ (right) in CH_2Cl_2 at room temperature.

structured spectrum with resolved hfs's to several H atoms. Its complexity, however, defied unambiguous interpretation by digital simulation. More work is clearly warranted in order to quantify the spin concentrations for these dications and their magnetic exchange interactions. We can, nevertheless, conclude at this point that the diactions of the vinylruthenium−TAA conjugates share with their 1,4-phenylene-bridged bis(vinylruthenium) counterpart the uncommon feature of a paramagnetic ground state with two ferromagnetically coupled or noninteracting spin centers despite strong electronic coupling in the MV state. Our failure to observe any half-field signal for the forbidden $\Delta m_s = 2$ transition supports the latter description of two noninteracting spin centers. The latter situation has been found in systems where two spin centers are separated by an extended aromatic spacer, which defies sacrificing the loss of resonance energy through quinoidal distortion.[100−102]

Quantum-chemical calculations using density functional theory (DFT) have documented shortcomings when applied to extended conjugated MV systems because of the problem of self-interaction (or "delocalization") errors. It has, however, been shown that functionals with appropriate admixtures of exact (Hartree−Fock) exchange and inclusion of solvation effects can overcome these problems and can often provide appropriate descriptions of the electron and spin density distributions.[37,50,103,104] Our present calculations at the pbe1pbe−DFT level of theory corroborate the experimental results (for details, see the Experimental Section). The good agreement between the calculated and experimental electronic spectra (vide infra) and energies of the CO stretching vibration of the carbonyl ligand (Table 3) lends further credibility to our computational results. Computed structure changes on consecutive one-electron oxidation as they are listed in Table S1 in the SI indicate an involvement of both sites in every redox process. Previous studies have revealed that the Ru−C, C═C, and ═C−$C_{phenylene}$ bond lengths at the vinyl group are particularly sensitive to oxidation of a styrylruthenium complex.[77] Calculated alterations of these parameters on the first oxidation increase slightly in the order **1-OMe** < **1-Me** < **1-CHO**, as exemplified by the compression of the Ru−C bond lengths by 0.053, 0.063, or 0.072 Å and of the ═C−$C_{phenylene}$ bond by 0.034, 0.041, or 0.039 Å. Simultaneous involvement of the NAr_2 site is evidenced by a shortening of the N−$C_{phenylene}$ bond by 0.029−0.039 Å and a rotation of the diarylamine moiety so as to attain a larger degree of coplanarity with the phenylene linker. That effect is particularly pronounced for **1-CHO**, where, contrary to **1-Me** and **1-OMe**, the NAr_2 plane adopts a higher degree of coplanarity with the peripheral aryl rings than with the phenylene bridge in the neutral state.

Figure 7 compiles the frontier molecular orbitals (MOs) of the full model of complex **1-CHO** as a representative example.

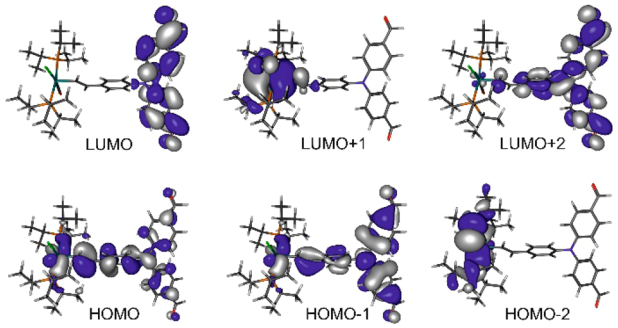

Figure 7. Contour plots of the frontier MOs of complex **1-CHO**.

The crucial "redox orbitals" HOMO and HOMO−1 are both delocalized over the entire {Ru}CH═$CHC_6H_4NAr_2$ array. They result from antibonding interactions between the appropriate Ru dπ orbital and the π orbital of the vinyl group and bonding/antibonding interactions between the vinyl group and phenylene bridge, as well as the phenylene bridge and the pπ orbital on the N atom. The HOMO receives stronger contributions from the vinylruthenium entity ({Ru}CH═CH/phenylene/NAr_2 = 55/25/20%), while the opposite is true for HOMO−1 ({Ru}CH═CH/phenylene/NAr_2 = 26/8/66%). Similar results are obtained for **1-Ac** and **1-E**. **1-Me** and **1-OMe** show an increasingly balanced situation (e.g., {Ru}CH═CH/phenylene/NAr_2 = 31/26/42% for the HOMO and 48/10/42% for the HOMO−1 of **1-Me**; for the fragment decomposition scheme and a complete listing, see Figures 8

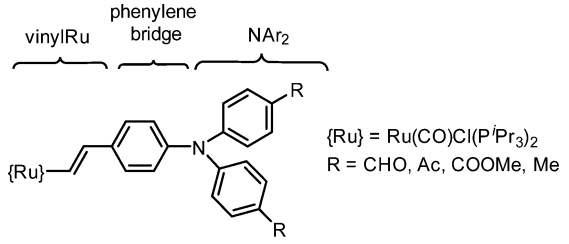

Figure 8. Fragment decomposition scheme for Table 5 and Figures S39−S42 in the SI.

and S39−S42 in the SI). This also supports the notion of a somewhat stronger bias of the first oxidation to the vinylruthenium site in an unsymmetrical, but still strongly delocalized, redox system composed of two different constituents. Occupied MOs below the HOMO−1 and unoccupied MOs tend to localize on just one of the two redox-active subunits and alternate between the TAA (HOMO−3 and LUMO+2) or the vinylruthenium (HOMO−2 and LUMO+1) sites.

The MO ordering of the neutral complexes remains unchanged upon one-electron oxidation; i.e., the HOMO of the neutral complexes resembles the α-HOSO and β-LUSO of the corresponding radical cations. A general involvement of both redox-active subunits in the first oxidation with an increasing bias toward the vinylruthenium moiety can also be derived from the computed charges, charge differences, and spin densities, which are summarized in Table 5 and graphically visualized in Figures 9 and S43 and S44 in the SI. Thus, changing R from the OMe donor to the CHO acceptor increases the charge loss from the vinylruthenium moiety by roughly 0.2 equiv of an elementary charge, while decreasing

DOI: 10.1021/acs.inorgchem.7b02186
Inorg. Chem. 2017, 56, 13517−13529

Table 5. Calculated Fragment Charges and Spin Densities for the Neutral Complexes (n = 0) and Radical Cations (n = 1)[a]

		charge			
complex	fragment	n = 0	n = 1	spin density	charge difference
1-CHO	NAr_2	−0.28	−0.06	0.17	0.22
	ph	0.23	0.49	0.24	0.26
	viRu	0.05	0.57	0.59	0.52
1-Ac	NAr_2	−0.28	−0.03	0.19	0.25
	ph	0.23	0.48	0.25	0.25
	viRu	0.05	0.55	0.57	0.50
1-E	NAr_2	−0.27	−0.03	0.19	0.24
	ph	0.22	0.49	0.25	0.26
	viRu	0.05	0.54	0.57	0.49
1-Me	NAr_2	−0.22	0.10	0.29	0.32
	ph	0.20	0.47	0.26	0.27
	viRu	0.02	0.44	0.45	0.41
1-OMe	NAr_2	−0.22	0.23	0.45	0.45
	ph	0.20	0.44	0.25	0.24
	viRu	0.02	0.33	0.31	0.31

[a]ph = phenylene bridge; viRu = vinylruthenium.

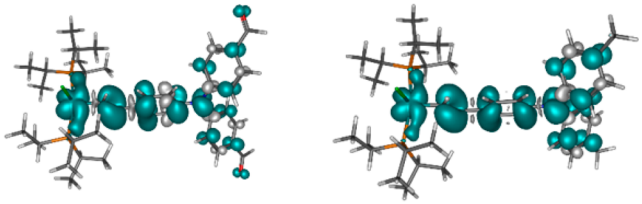

1-CHO$^+$ **1-Me$^+$**

Figure 9. Calculated spin-density maps of full models **1-CHO$^+$** (left) and **1-Me$^+$** (right).

that at the NAr_2 unit by almost the same amount. Similar alterations are observed for the spin densities.

As shown in Figures 10 and S45−S47 in the SI, the dicationic forms of the complexes in their triplet states have their spin

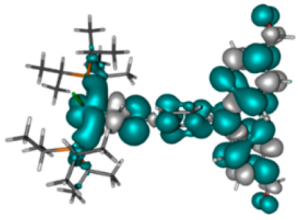

Figure 10. Calculated spin densities of dicationic **1-CHO^{2+}** in the triplet state.

densities uniformly distributed over the entire molecule. This matches with our experimental observations. We note, however, that the triplet states were consistently calculated to be ca. 10−12 kJ mol^{-1} higher in energy than the closed-shell singlet states. Similar failures of the DFT methods to correctly predict the energy ordering of different spin states have been noted on earlier occasions,[105,106] including [{Ru}CH═CHC_6H_4CH═CH{Ru}]$^{2+}$ and its 2,5-dibutoxy derivative [{Ru}CH═$CHC_6H_2OBu_2$CH═CH{Ru}]$^{2+}$.[64]

UV/Vis/NIR Spectroscopy and the Consequences of Increasing the Electronic Asymmetry. The electronic spectra of the neutral vinylruthenium−TAA conjugates are dominated by a strong band in the near-UV with an extinction coefficient ε of 28000−38400 M^{-1} cm^{-1} (Table 6). As a consequence of the lowering of the local symmetry from C_3 to C_2, that band is sometimes associated with a likewise intense shoulder at higher energy.[13] Time-dependent DFT (TD-DFT) calculations assign the underlying molecular excitation as the HOMO → LUMO+2 transition. With reference to Figure 7, it can thus be characterized as a $\pi \rightarrow \pi^*$ band associated with CT from the vinylruthenium site to the TAA site. In agreement with such character, this band red-shifts as the aryl substituents become more electron-withdrawing, e.g., from 342 nm in **1-Me** to 372 nm in **1-CHO** (ΔE = 2360 cm^{-1}). Weak transitions, which are often buried under the tail of the intense UV band, correspond to the HOMO−1 → LUMO and HOMO → LUMO+1 transitions.

Table 6. Spectroscopic Changes in the UV/vis/NIR Region on the First (n = 1) and Second (n = 2) Oxidation of the Complexes[a]

	n	λ_{max} (ε_{max}/10^{-3} M^{-1} cm^{-1})
1-CHO	0	302 (12.7), 372 (28.0)
	1+	274 (14.0), 366 (19.4), 512 (12.4), 984 (9.6)
	2+	274 (13.8), 378 (25.8), 573 (3.7), 714 (2.4), 793 (2.2)
1-Ac	0	303 (15.5), 369 (38.4)
	1+	269 (14.0), 353 (17.6), 508 (19.5), 987 (16.0)
	2+	269 (14.5), 371 (33.7), 527 (1.3)
1-E	0	298 (12.9), 357 (33.7)
	1+	274 (12.8), 346 (16.5), 502 (13.4), 987 (11.6)
	2+	273 (11.8), 352 (23.5), 388 (17.9), 536 (2.8), 755 (1.1)
1-Me	0	311 (24.8), 342 (29.8)
	1+	284 (12.5), 366 (7.8), 493 (22.7), 1007 (19.0)
	2+	285 (13.6), 397 (16.1), 609 (12.0), 663 (13.0)
1-OMe	0	322 (22.6), 343 (30.0)
	1+	365 (7.5), 487 (24.0), 516 (20.0), 1030 (19.6), 11160 (22.0)
	2+	380 (11.3), 482 (10.5), 535 (13.0), 595 (15.5), 664 (27.0), 730 (59.5)

[a]In 1,2-$C_2H_4Cl_2$/NBu_4PF_6 at room temperature.

The various oxidized forms of the complexes were again generated inside an optically transparent thin-layer electrolysis (OTTLE) cell.[95] Data from these experiments are gathered in Table 6 and displayed in Figures 11 and S48 and S49 in the SI. They demonstrate the polyelectrochromic behavior of this class of compounds like that already reported for **1-OMe** (for convenience, graphics showing the spectroscopic changes during the first and second oxidation of this complex are also included as Figure S50 in the SI).[73] Thus, the radical cations are characterized by a rather intense band in the NIR at ca. 1000 nm (see also Figures S18−S25 in the SI for their detection from the IR/NIR side), likewise intense vis absorption at ca. 500 nm, and a significantly reduced absorbance of the original UV band.

The transition near 500 nm is computed to originate from the α-HOSO → α-LUSO+2 and β-HOSO-3 → β-LUSO excitations. Contour plots of the corresponding MOs of **1-CHO$^+$** are shown in Figure 12, while Figures S51−S54 in the SI demonstrate the good match between the experimental and calculated spectra of the radical cations. The first of these excitations corresponds closely to the prominent UV band of the neutral complexes but with an enhanced delocalization of the receptor orbital, i.e., reduced CT character. The second

DOI: 10.1021/acs.inorgchem.7b02186
Inorg. Chem. 2017, 56, 13517−13529

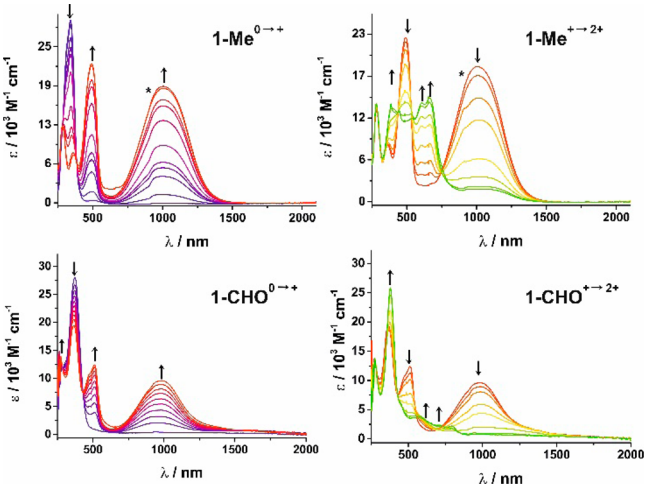

Figure 11. Spectroscopic changes in the UV/vis/NIR spectra on the first (top left) and second (top right) oxidation of complex **1-Me** and the first (bottom left) and second (bottom right) oxidation of complex **1-CHO** in an OTTLE cell (1,2-$C_2H_4Cl_2$/0.1 M NBu_4PF_6, room temperature). The asterisk marks a step due to an artifact of the instrumentation.

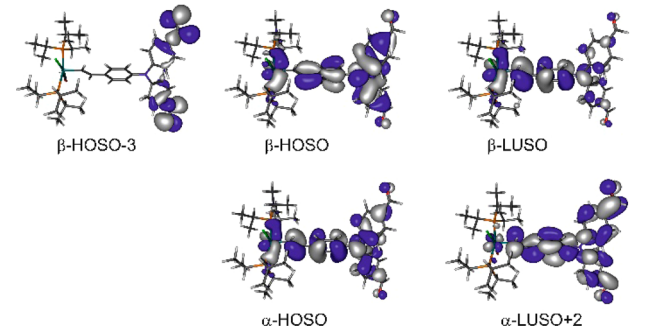

Figure 12. Graphical representations of the MOs involved in the major transitions of **1-CHO**$^+$.

component involves CT from TAA to the vinylruthenium/phenylene moiety.

While the spectra of the radical cations resemble each other rather closely, those of the dications show distinct differences. Those of the donor-substituted congeners **1-OMe**$^{2+}$ and **1-Me**$^{2+}$ feature a highly intense, structured vis absorption with considerable blue shifts from 730/664 nm for **1-OMe**$^{2+}$ to 663/609 nm for **1-Me**$^{2+}$ and a notable intensity decrease for the latter. The acceptor-substituted complexes have only weak absorption in the vis, while a band in the near-UV/vis borderline regime gains in intensity. We note that the TD-DFT-calculated spectra of the triplet dications match the experimental spectra of these dications much better than those calculated for their singlet states (see Figures S55–S58 in the SI). This further supports the notion of a paramagnetic ground state of the dioxidized complexes, as was already indicated by EPR spectroscopy.

A particularly interesting aspect of this study is to elaborate the consequences of an increasingly unsymmetrical charge distribution for the NIR transitions of the radical cations. Like for **1-OMe**$^+$, that band corresponds to the β-HOSO → β-LUSO transition (see Table S2 in the SI). These spin orbitals closely resemble the HOMO and HOMO−1 of the closed-shell neutral precursors and are both delocalized over the entire $[\{Ru\}C_6H_4NAr_2]^+$ array. Subtle differences between the individual complexes originate from an increasing bias of the donor orbital to the TAA site and of the acceptor orbital to the vinylruthenium site with an increasingly electron-withdrawing nature of the amine substituents. In other words, the characteristics of this band demonstrate the consequences of smoothly displacing the minima of the bonding and antibonding potential hypersurfaces toward the TAA (ground state) or vinylruthenium (excited state) sites within an intrinsically delocalized MV system with unequal redox sites.

In order to probe for the degree of CT involved in the IVCT transition, we investigated its solvatochromism by recording UV/vis/NIR spectra in CH_2Cl_2, chlorobenzene, tetrahydrofuran, and acetone. Spectra in these solvents can be found in Figures S59–S63 in the SI, and absorption wavelengths and energies are compiled in Table S3 in the SI. No spectra could be obtained in aliphatic solvents because of too low solubilities or in the more polar propylene carbonate or nitromethane due to rapid decomposition. In keeping with strong electronic coupling throughout the entire series, the NIR band of all complexes shows only a very modest negative solvatochromism of 380–570 cm^{-1}. This compares well with other strongly coupled bis(triarylamine)-type MV systems, where shifts in the order of 500–900 cm^{-1} have been observed.[19,24,30] Similar to radical cations of unsymmetrically substituted *N,N,N′,N′*-tetraarylphenylenediamines with two different diarylamine sites,[75] substituent R has hardly any influence on the exact positioning of the NIR peak.

Nelsen and others have pointed out that, in the class III limit, the vertical transition between ground and excited states will, besides band narrowing, also lead to vibrational structuring of the IVCT band.[22,107] This is what we see for **1-OMe**$^+$, where three individual bands are required to reconstruct the absorption envelope. For all other radical cations of this series, the NIR band shows no such splitting but clearly has a non-Gaussian shape with a considerably smaller bandwidth at the low-energy side. This is illustrated in Figures 13 and S64–S67

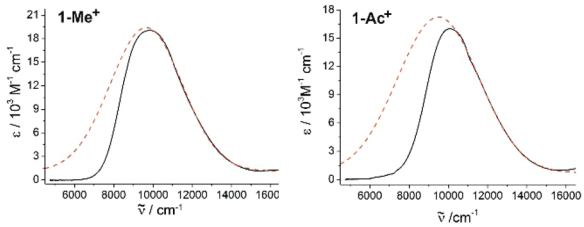

Figure 13. Demonstration of the asymmetry of the IVCT bands of radical cations **1-Me**$^+$ (left) and **1-Ac**$^+$ (right) in a CH_2Cl_2 solution. The experimental spectrum is shown as the black solid line and the low-energy portion of the NIR spectrum with the fitting parameters for the high-energy part of the band as the red dotted line.

in the SI. Such behavior has been observed previously for various strongly coupled MV systems of class III or at the class II/III borderline, including radical cations of tetraaryl-substituted arylene-bridged diamines.[18,19,25,29,32,98,108,109] Two Gaussians, one representing the high-energy and one the low-energy branch of the IVCT band, are therefore required to reconstruct the band shape, as indicated in Figures S64–S67 in the SI.

Table 7 lists the IVCT band positions, the two bandwidths derived from digital simulations and their ratios as a measure of truncation. The ratios $\Delta\tilde{\nu}_{1/2,high}/\Delta\tilde{\nu}_{1/2,low}$ are similar or even

DOI: 10.1021/acs.inorgchem.7b02186
Inorg. Chem. 2017, 56, 13517–13529

Table 7. Data for the IVCT Bands of the Radical Cations in CH_2Cl_2 and Acetone

	solvent	$\tilde{\nu}_{max}$ (cm^{-1})	ε_{max} (M^{-1} cm^{-1})	f	$\Delta\tilde{\nu}_{1/2,high}$ (cm^{-1})	$\Delta\tilde{\nu}_{1/2,low}$ (cm^{-1})	$\Delta\tilde{\nu}_{1/2,theo}$ (cm^{-1})	$\frac{\Delta\tilde{\nu}_{1/2,high}}{\Delta\tilde{\nu}_{1/2,low}}$
1-CHO$^+$	CH_2Cl_2	10173	9560	0.17	4330	2198	4848	1.97
	acetone	10537	8440	0.15	4396	2504	4934	1.76
1-Ac$^+$	CH_2Cl_2	10050	11590	0.19	4411	2250	4818	1.81
	acetone	10438	9220	0.16	4436	2442	4910	1.82
1-E$^+$	CH_2Cl_2	10132	11585	0.19	4530	2149	4837	2.11
	acetone	10515	9340	0.17	4333	2360	4928	1.84
1-Me$^+$	CH_2Cl_2	9833	19050	0.24	4325	2286	4766	1.89
	acetone	10373	16910	0.23	4405	2479	4895	1.78
1-OMe$^+$	CH_2Cl_2	8255/9456	23000/20000	0.36	n.a.	1138/2045[a]		n.a.
	acetone	8524/9891	19700/19100	0.34	n.a.	n.a.	n.a.	n.a.

[a]Bandwidths at half-height of the two prominent components of the NIR band envelope of **1-OMe**$^+$.

larger than those for the radical cations of *N,N,N′,N′*-tetraanisylphenylenediamine (1.76), which, after some dispute, has been recognized as a genuine class III MV system,[103] or of 2,6-bis(di-4-anisylamino)naphthalene (1.73).[25] We also note that the bandwidth at the high-energy side is by ca. 500 cm^{-1} smaller than the theoretical IVCT bandwidth $\Delta\tilde{\nu}_{1/2,theo}$ of a MV class II system in the high-temperature limit, as given by the familiar expression in eq 1.[110,111] (Note, however, that the $\Delta\tilde{\nu}_{1/2,theo}$ value of an unsymmetrical MV system of class II is most probably smaller than that of a symmetrical one because $\tilde{\nu}_{max}$ is larger than the reorganization energy λ.)

$$\Delta\tilde{\nu}_{1/2,theo} = \sqrt{2310\tilde{\nu}_{max}} \quad (1)$$

Two different possible origins of such band asymmetry have been discussed in the literature. One is a shallow ground-state hypersurface with a vanishing barrier for thermal intramolecular ET ΔG^*.[25,112] This so-called low-energy cutoff is typically found in MV systems at the class II/III borderline with still localized electronic ground states. Another possible reason is coupling to symmetric vibrational modes, which has been observed for some intrinsically delocalized MV systems.[22,112,113] These two alternatives can be distinguished by the dependence of the band asymmetry on temperature. As Coropceanu et al. have pointed out, the band asymmetry is expected to increase with increasing T in the case of a low-energy cutoff, i.e., if the skewing of the band is due to thermal population at the top of the barrier for ET. The opposite is, however, true for vibronic coupling of the IVCT band to symmetric modes.[112] In agreement with the vibronic coupling model, the ratio $\Delta\tilde{\nu}_{1/2,high}/\Delta\tilde{\nu}_{1/2,low}$ of **1-CHO**$^+$ as an exemplary representative increases from 1.97 at T = 298 K to 2.26 at T = 253 K and to 2.38 at T = 213 K. This is accompanied by a sharpening of the band and a red shift of the peak by ca. 500 cm^{-1} as T decreases within the indicated temperature range. Graphical accounts of this experiment can be found as Figure S68 in the SI, while the relevant data are summarized in Table S4 in the SI.

Table 7 also lists the oscillator strengths f of the IVCT band in CH_2Cl_2 and acetone, as determined from the area under the NIR band (the integral term) according to eq 2 (m_e is the mass of an electron, c the vacuum speed of light, e the electron charge, and N_A Avogadro's constant).[114] It is evident that f decreases from **1-OMe**$^+$ to **1-Me**$^+$ and the acceptor-substituted congeners **1-E**$^+$, **1-OAc**$^+$, and **1-CHO**$^+$ with only minor variations for the latter.

$$f = \frac{2303 m_e c^2}{\pi N_A e^2} \int \varepsilon(\tilde{\nu})\, d\tilde{\nu} = 4.33 \times 10^{-9} \int \varepsilon(\tilde{\nu})\, d\tilde{\nu} \quad (2)$$

All of our results thus support the notion that decreasing the electron density at the TAA site by replacing the 4-methoxy donors by more weakly donating Me groups or formyl, methyl acetate, or acetyl acceptors increases the contribution of the vinylruthenium site to the HOMO and renders the electronic ground state less well-balanced. The corresponding radical cations are, nevertheless, electronically strongly coupled MV systems as shown by the stepwise blue shifts of the Ru(CO) stretching vibrations upon oxidation, the EPR hfs constants to the ^{31}P and ^{14}N nuclei, the highly asymmetric shape of their IVCT band, and the near-invariance of their positions to solvent polarity.

CONCLUSIONS

Vinylruthenium−TAA conjugates, where the electronic properties of the TAA-type subunit were systematically varied from electron-donating to electron-withdrawing, have been synthesized. All complexes are oxidized in two reversible, consecutive one-electron steps. In keeping with the intrinsically delocalized nature of the occupied frontier MOs (the "redox orbitals"), both waves are rather uniformly displaced anodically as the 4-substituents at the amine-bonded phenyl rings change from electron-donating to electron-accepting. As a consequence of these alterations, the HOMO of the neutral complexes and the SOMO of their associated radical cations become more biased toward the vinylruthenium moiety. Starting from an essentially balanced charge and spin density distribution over the two different redox sites in **1-OMe**$^+$,[73] larger blue shifts of the Ru(CO) stretching band of the ruthenium-bonded carbonyl ligand in the IR and increasing $A(^{31}P)$ and decreasing $A(^{14}N)$ hfs constants in the EPR spectra are clear tokens of an increasingly unsymmetrical electronic ground state of the associated MV radical cations with a larger charge loss from and increased spin density at the vinylruthenium moiety. This is also supported by quantum-chemical calculations.

These radical cations thus allow one to probe for the consequences of increasing the electronic asymmetry in intrinsically delocalized MV systems with two different redox sites. Thus, the vibrationally structured IVCT band of **1-OMe**$^+$ with resolved individual peaks changes its appearance to a highly unsymmetrical, skewed shape with a characteristic sharpening at the low-energy side. T-dependent measurements have revealed vibronic coupling of the IVCT transition to symmetric modes as the underlying reason for band skewing.

DOI: 10.1021/acs.inorgchem.7b02186
Inorg. Chem. 2017, 56, 13517−13529

This is accompanied by a significant reduction of the overall oscillator strength and a blue shift of the NIR absorption. Interestingly though, none of the present radical cations show enhanced solvatochromism of the IVCT band.

Like the 1,4-divinylphenylene-bridged bis(vinylruthenium) complexes {Ru}1,4-CH═CH-$C_6H_2R_2$CH═CH{Ru} (R = H, OMe, OBu),[64] but contrary to the majority of arylene-bridged bis(diarylamines) with electronically strongly coupled MV states, among them the immediate organic parent $[(4\text{-}OMeC_6H_4)_2NC_6H_4N(C_6H_4OMe\text{-}4)_2]^{2+}$,[48] the dications of the present complexes are also EPR-active and display intense, isotropic signals. In keeping with enhanced "organic" spin densities, their g values are closer to the free-electron value g_e than those of the radical cations. The present complexes are thus rare examples that combine the treats of strong electronic coupling in the MV states and paramagnetism of the higher oxidized forms.

EXPERIMENTAL SECTION

General Procedures. All syntheses were performed using standard Schlenk techniques under a nitrogen atmosphere. The solvents used for synthesis and characterization were dried over appropriate drying agents, distilled, and stored under a nitrogen atmosphere. The purities of the complexes were determined by NMR spectroscopy and combustion analyses. All chemicals were obtained from commercial suppliers and used without further purification. Details to the synthesis of the required triarylamines (TAAs) and their characterization can be found in the SI. ^{1}H and ^{13}C NMR spectra were recorded on a Bruker AVANCE III 400 (B_H = 400 MHz, B_C = 100.6 MHz, and B_P = 162 MHz) spectrometer at room temperature. The spectra were referenced to the residual signal of the protonated solvents or, for ^{31}P NMR spectroscopy, to H_3PO_4 as an external standard. Coupling constants are given in hertz.

Cyclic voltammetry was performed in a one-compartment cell with 5−7 mL of CH_2Cl_2 as the solvent and NBu_4PF_6 (0.1 M) as the supporting electrolyte. A platinum electrode (⌀ = 1.1 mm, BASI) was used as the working electrode. It was polished with diamond pastes (1.5 and 1 μm particle size) from Buehler and Wirtz. A computer-controlled BASi EPSILON potentiostat was used for recording of the voltammograms. An Ag/AgCl wire pseudoreference electrode and a platinum wire auxiliary electrode were used in the measurements. The cell was connected to an argon gas bottle. Potential calibration was performed by adding the appropriate quantities of decamethylferrocene (Cp^*_2Fe) after all scans of interest had been acquired. Potentials are reported against the ferrocene/ferrocenium ($Cp_2Fe^{0/+}$) couple, which is 550 mV positive of the $Cp^*_2Fe^{0/+}$ couple under our conditions.

IR and UV/vis/NIR spectroelectrochemistry was performed in a self-built OTTLE cell according to the design of Hartl et al.[95] A platinum minigrid as the working and counter electrodes and a thin silver foil as the reference electrode are welded in a polyethylene spacer, incorporated into a Teflon housing with electrical connectors and sandwiched between the CaF_2 plates of a conventional liquid IR cell. 1,2-$C_2H_4Cl_2$/0.1 M NBu_4PF_6 was used as the supporting electrolyte. IR/NIR spectra were recorded on a FT-IR Bruker Tensor II instrument. The UV/vis/NIR measurements were performed on a diode-array unit TIDAS by J&M ANALYTIK AG with a spectroscopic window of 250−2100 nm. A computer-controlled potentiostat WENKING POS3 was used for controlled electrolysis.

EPR spectroscopy was performed with an X-band benchtop spectrometer of the type MINISCOPE400MS by Magnettech GmBH. Low-temperature work was conducted by cooling with liquid nitrogen. As the thermostat, a temperature controller by the same manufacturer was used. The magnet was cooled using a Thermo Fischer Scientific Inc. HAAKE A10 cooling unit. The complexes were chemically oxidized with appropriate amounts of ferrocenium hexafluorophosphate, 1,1′-diacetylferrocenium hexafluoroantimonate, or tris(*p*-bromophenyl)aminium hexafluoroantimonate in a CH_2Cl_2 solution at room temperature prior to the measurements. Simulations of the measured spectra was performed using the MATLAB *Easyspin* program.[115]

DFT calculations were performed on the full model complexes using the *Gaussian 09* program package.[116] Geometry optimizations were performed without any symmetry constraints. Electronic transitions were calculated by the TD-DFT method. Within *Gaussian 09* calculations, quasirelativistic effective core pseudopotentials and the corresponding optimized set of basis functions for ruthenium were used.[117] Polarized double-ζ basis sets [6-31G(d), geometry optimization] were employed together with the pbe1pbe functional.[118] Solvation effects were modeled by the polarizable continuum model[119] in TD-DFT calculations.

Hydroruthenation Procedure. To a mixture of the respective deprotected alkyne and 1 equiv of $HRu(CO)Cl(P^iPr_3)_2$ was added 5 mL of dry CH_2Cl_2, and the solution was stirred at room temperature for 30 min. The resulting dark-red mixture was then evaporated to dryness and washed with hexane. The corresponding red to red-brown products were isolated in high yields (82−99%) by drying in vacuum.

$(4\text{-}CHOC_6H_4)_2N(C_6H_4\text{-}3\text{-}CH{=}CHRu(CO)Cl(P^iPr_3)_2)$ ***(1-CHO)***. Yield: 82%. ^{1}H NMR (400 MHz, CD_2Cl_2; Figure 14): δ 9.86 (s, 2H, C*H*O),

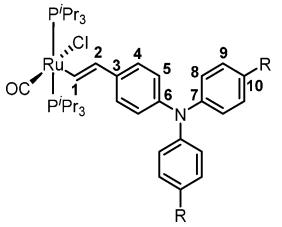

Figure 14. Atomic numbering for NMR characterization.

8.69 (d, $^3J_{HP}$ = 13.4 Hz, 1H, H_1), 7.74 (d, $^3J_{HH}$ = 8.6 Hz, 4H, H_9), 7.18 (d, $^3J_{HH}$ = 8.6 Hz, 4H, H_8), 7.05 (d, $^3J_{HH}$ = 8.5 Hz, 2H, H_4), 6.97 (d, $^3J_{HH}$ = 8.5 Hz, 2H, H_5), 6.02 (dt, $^3J_{HH}$ = 13.5 Hz, $^4J_{HP}$ = 2.3 Hz, 1H, H_2), 2.77 (m, 6H, P(C*H*$(CH_3)_2)_3$, 1.30 (m, 36H, P(CH(C*H*$_3)_2)_3$). ^{31}P NMR (162 MHz, CD_2Cl_2): δ 38.7. ^{13}C NMR (101 MHz, CD_2Cl_2): δ 203.4 (t, $^2J_{CP}$ = 13.0 Hz, CO), 190.9 (s, CHO), 153.2 (t, $^2J_{CP}$ = 10.4 Hz, C_1), 152.7 (s, C_{10}), 141.5 (s, C_6), 137.7 (s, C_3), 133.9 (t, $^3J_{CP}$ = 3.4 Hz, C_2), 131.7 (s, C_7), 131.7 (s, C_7), 131.6 (s, C_9), 127.8 (s, C_5), 125.7 (s, C_4), 123.0 (s, C_8), 25.1 (vt, $^{1/3}J_{CP}$ = 9.9 Hz, P(CH$(CH_3)_2)_3$), 20.1 and 20.3 (s, P(CH$(CH_3)_2)_3$). Anal. Calcd for $C_{41}H_{58}ClNO_3P_2Ru$: C, 60.69; H, 7.21; N, 1.73. Found: C, 60.63; H, 7.15; N, 1.77.

$(4\text{-}C(O)CH_3C_6H_4)_2N(C_6H_4\text{-}3\text{-}CH{=}CHRu(CO)Cl(P^iPr_3)_2)$ ***(1-Ac)***. Yield: quantitative. ^{1}H NMR (400 MHz, CD_2Cl_2): δ 8.64 (dt, $^3J_{HH}$ = 13.4 Hz, $^3J_{HP}$ = 1.2 Hz, 1H, H_1), 7.82 (d, $^3J_{HH}$ = 8.73 Hz, 4H, H_9), 7.10 (d, $^3J_{HH}$ = 8.73 Hz, 4H, H_8), 7.03 (d, $^3J_{HH}$ = 8.6 Hz, 2H, H_4), 6.95 (d, $^3J_{HH}$ = 8.6 Hz, 2H, H_5), 6.01 (dt, $^3J_{HH}$ = 13.4 Hz, $^4J_{HP}$ = 2.3 Hz, 1H, H_2), 2.76 (m, 6H, P((C*H*$(CH_3)_2)_3$), 2.51 (s, 6H, Ac), 1.30 (m, 36H, P((CH(C*H*$_3)_2)_3$). ^{31}P NMR (162 MHz, CD_2Cl_2): δ 38.2. ^{13}C NMR (101 MHz, CD_2Cl_2): δ 203.5 (t, $^2J_{CP}$ = 13.1 Hz, CO), 152.6 (t, $^3J_{CP}$ = 10.8 Hz, C_1), 151.7 (s, C_{10}), 141.9 (s, C_6), 137.3 (t, $^4J_{CP}$ = 2.0 Hz, C_3), 133.9 (t, $^3J_{CP}$ = 3.3 Hz, C_2), 132.0 (s, C_7), 130.3 (s, C_9), 127.5 (s, C_5), 125.6 (s, C_4), 122.6 (s, C_8), 26.7 (s, Ac), 25.1 (vt, $^{1/3}J_{CP}$ = 9.9 Hz, P(C*H*$(CH_3)_2)_3$), 20.1 and 20.3 (s, P(CH$(CH_3)_2)_3$). Anal. Calcd for $C_{43}H_{62}ClNO_3P_2Ru$: C, 61.53; H, 7.44; Cl, 4.22; N, 1.67; O, 5.72; P, 7.38; Ru, 12.04. Found: C, 61.43; H, 7.40; N, 1.70.

$(4\text{-}COOMeC_6H_4)_2N(C_6H_4\text{-}3\text{-}CH{=}CHRu(CO)Cl(P^iPr_3)_2)$ ***(1-E)***. Yield: 89%. ^{1}H NMR (400 MHz, CD_2Cl_2): δ 8.61 (dt, $^3J_{HH}$ = 13.4 Hz, $^3J_{HP}$ = 1.2 Hz, 1H, H_1), 7.87 (m, 4H, H_9), 7.07 (m, 4H, H_8), 7.01 (d, $^3J_{HH}$ = 8.6 Hz, 2H, H_5), 6.95 (d, $^3J_{HH}$ = 8.6 Hz, 2H, H_4), 6.00 (dt, $^3J_{HH}$ = 13.4 Hz, $^4J_{HP}$ = 3.1 Hz, 1H, H_2), 3.85 (s, 6H, COO*Me*), 2.76 (m, 6H, P(C*H*$(CH_3)_2)_3$), 1.30 (m, 36H, P(CH(C*H*$_3)_2)_3$). ^{31}P NMR (162 MHz, CD_2Cl_2): δ 38.2. ^{13}C NMR (101 MHz, CD_2Cl_2): δ 204.1 (t, $^2J_{CP}$ = 13.1 Hz, CO), 167.7 (s, C_{11}), 152.9 (t, $^2J_{CP}$ = 10.9 Hz, C_1), 152.3 (s, C_7), 142.7 (t, $^4J_{CP}$ = 3.6 Hz, C_3), 137.8 (s, C_6), 134.6 (t, $^3J_{CP}$ = 3.1 Hz, C_2), 131.9 (s, C_9), 128.0 (s, C_4), 126.2 (s, C_5), 124.4 (s, C_{10}), 123.2 (s, C_8), 52.9 (s, COO*Me*), 25.7 (vt, $^{1/3}J_{CP}$ = 9.9 Hz,

DOI: 10.1021/acs.inorgchem.7b02186
Inorg. Chem. 2017, 56, 13517−13529

$P(CH(CH_3)_2)_3$), 20.7 and 21.0 (s, $P(CH(CH_3)_2)_3$). Anal. Calcd for $C_{43}H_{62}ClNO_5P_2Ru$: C, 59.27; H, 7.17; N, 1.61. Found: C, 59.24; H, 7.20; N, 1.65.

$(4\text{-}MeC_6H_4)_2N(C_6H_4\text{-}3\text{-}CH{=}CHRu(CO)Cl(P^iPr_3)_2)$ (1-Me). Yield: quantitative. ^1H NMR (400 MHz, CD_2Cl_2 δ 8.35 (d, $^3J_{HH}$ = 13.3 Hz, 1H, H_1), 7.03 (d, $^3J_{HH}$ = 8.2 Hz, 4H, H_9), 6.93−6.86 (m, 6H, H_8 + H_5), 6.82 (d, $^3J_{HH}$ = 8.4 Hz, 2H, H_4), 5.92 (d, $^3J_{HH}$ = 13.3 Hz, 1H, H_2), 2.75 (m, 6H, $P(CH(CH_3)_2)_3$), 2.28 (s, 6H, Me), 1.29 (m, 36H, $P(CH(CH_3)_2)_3$). ^{31}P NMR (162 MHz, CD_2Cl_2): δ 37.9. ^{13}C NMR (101 MHz, CD_2Cl_2): δ 203.6 (t, $^2J_{CP}$ = 13.2 Hz, CO), 148.6 (t, $^2J_{CP}$ = 10.9 Hz, C_1), 146.3 (s, C_{10}), 144.8 (s, C_6), 134.4 (s, C_3), 134.3 (t, $^3J_{CP}$ = 2.2 Hz, C_2), 134.3 (s, C_7), 130.2 (s, C_9), 125.1 (s, C_5), 124.5 (s, C_8), 124.1 (s, C_4), 25.0 (vt, $^{1/3}J_{CP}$ = 9.9 Hz, $P(CH(CH_3)_2)_3$), 21.0 (s, Me), 20.1 and 20.3 (s, $P(CH(CH_3)_2)_3$). Anal. Calcd for $C_{41}H_{62}ClNOP_2Ru$: C, 62.86; H, 7.98; N, 1.79. Found: C, 62.80; H, 8.02; N, 1.83.

■ ASSOCIATED CONTENT

Supporting Information

The Supporting Information is available free of charge on the ACS Publications Web site. The Supporting Information is available free of charge on the ACS Publications website at DOI: 10.1021/acs.inorgchem.7b02186.

Additional data of cyclic voltammetry, NMR spectra of all new compounds, IR and UV/vis/NIR spectroelectrochemistry, EPR spectroscopy, DFT and TD-DFT calculations, the solvent dependence and spectral deconvolutions of the NIR bands, and synthetic procedures of the starting materials (PDF)

■ AUTHOR INFORMATION

Corresponding Author

*E-mail: rainer.winter@uni-konstanz.de.

ORCID

Rainer F. Winter: 0000-0001-8381-0647

Notes

The authors declare no competing financial interest.

■ ACKNOWLEDGMENTS

We dedicate this paper to Prof. John A. Gladysz on the occasion of his 65th birthday. This work was financially supported by the Deutsche Forschungsgemeinschaft (Grant WI1262/13-1). We thank the State of Baden-Württemberg for providing us access to the bwHPC computational facilities at the Karlsruhe Institute of Technology. We also thank Markus Maier for the synthesis of complex **1-E**. In addition, we are indebted to the reviewers for their insightful comments and suggestions.

■ REFERENCES

(1) Bruning, W. H.; Nelson, R. F.; Marcoux, L. S.; Adams, R. N. The structure of the iodine-triphenylamine charge-transfer complex. *J. Phys. Chem.* **1967**, *71*, 3055−3057.

(2) Nelson, R. R.; Adams, R. N. Anodic oxidation pathways of substituted triphenylamines. II. Quantitative studies of benzidine formation. *J. Am. Chem. Soc.* **1968**, *90*, 3925−3930.

(3) Debrodt, H.; Heusler, K. E. Oxidation von Triphenylamin in Acetonitril an rotierenden Scheibenelektroden. *Z. Phys. Chem.* **1981**, *125*, 35−40.

(4) Sreenath, K.; Suneesh, C. V.; Ratheesh Kumar, V. K.; Gopidas, K. R. Cu(II)-Mediated Generation of Triarylamine Radical Cations and Their Dimerization. An Easy Route to Tetraarylbenzidines. *J. Org. Chem.* **2008**, *73*, 3245−3251.

(5) Reynolds, R.; Line, L. L.; Nelson, R. F. Electrochemical generation of carbazoles from aromatic amines. *J. Am. Chem. Soc.* **1974**, *96*, 1087−1092.

(6) Eberson, L.; Larsson, B.; Maartmann-Moe, K.; Sæbø, J.; Fischer, G. W. Reactions of 4-Substituted Triarylaminium Radical Cations With Nucleophiles; Polar versus Electron Transfer Pathways. *Acta Chem. Scand.* **1987**, *41b*, 367−378.

(7) Connelly, N. G.; Geiger, W. E. Chemical Redox Agents for Organometallic Chemistry. *Chem. Rev.* **1996**, *96*, 877−910.

(8) Dapperheld, S.; Steckhan, E.; Brinkhaus, K.-H. G.; Esch, T. Organic Electron Transfer Systems, II Substituted Triarylamine Cation-Radical Redox Systems − Synthesis, Electrochemical and Spectroscopic Properties, Hammet Behavior, and Suitability as Redox Catalysts. *Chem. Ber.* **1991**, *124*, 2557−2567.

(9) Walter, R. I. Substituent Effects on the Properties of Stable Aromatic Free Radicals. The Criterion for Non-Hammett Behavior1. *J. Am. Chem. Soc.* **1966**, *88*, 1923−1930.

(10) Steckhan, E. Indirect Electroorganic Syntheses—A Modern Chapter of Organic Electrochemistry [New Synthetic Methods (59)]. *Angew. Chem., Int. Ed. Engl.* **1986**, *25*, 683−701.

(11) Steckhan, E. Organic Syntheses with Electrochemically Regenerable Redox Systems. *Top. Curr. Chem.* **1987**, *142*, 1−69.

(12) Bender, T. P.; Graham, J. F.; Duff, J. M. Effect of Substitution on the Electrochemical and Xerographic Properties of Triarylamines: Correlation to the Hammett Parameter of the Substituent and Calculated HOMO Energy Level. *Chem. Mater.* **2001**, *13*, 4105−4111.

(13) Amthor, S.; Noller, B.; Lambert, C. UV/Vis/NIR spectral properties of triarylamines and their corresponding radical cations. *Chem. Phys.* **2005**, *316*, 141−152.

(14) Talipov, M. R.; Hossain, M. M.; Boddeda, A.; Thakur, K.; Rathore, R. A search for blues brothers: X-ray crystallographic/spectroscopic characterization of the tetraarylbenzidine cation radical as a product of aging of solid magic blue. *Org. Biomol. Chem.* **2016**, *14*, 2961−2968.

(15) Hankache, J.; Wenger, O. S. Organic Mixed Valence. *Chem. Rev.* **2011**, *111*, 5138−5178.

(16) Heckmann, A.; Lambert, C. Organic Mixed-Valence Compounds: A Playground for Electrons and Holes. *Angew. Chem., Int. Ed.* **2012**, *51*, 326−392.

(17) Coropceanu, V.; Gruhn, N. E.; Barlow, S.; Lambert, C.; Durivage, J. C.; Bill, T. G.; Nöll, G.; Marder, S. R.; Brédas, J.-L. Electronic Coupling in Organic Mixed-Valence Compounds: The Contribution of Photoelectron Spectroscopy. *J. Am. Chem. Soc.* **2004**, *126*, 2727−2731.

(18) Barlow, S.; Risko, C.; Chung, S.-J.; Tucker, N. M.; Coropceanu, V.; Jones, S. C.; Levi, Z.; Brédas, J.-L.; Marder, S. R. Intervalence Transitions in the Mixed-Valence Monocations of Bis(triarylamines) Linked with Vinylene and Phenylene−Vinylene Bridges. *J. Am. Chem. Soc.* **2005**, *127*, 16900−16911.

(19) Barlow, S.; Risko, C.; Coropceanu, V.; Tucker, N. M.; Jones, S. C.; Levi, Z.; Khrustalev, V. N.; Antipin, M. Y.; Kinnibrugh, T. L.; Timofeeva, T.; Marder, S. R.; Brédas, J.-L. A mixed-valence bis(diarylamino)stilbene: crystal structure and comparison of electronic coupling with biphenyl and tolane analogues. *Chem. Commun.* **2005**, 764−766.

(20) Zheng, S.; Barlow, S.; Risko, C.; Kinnibrugh, T. L.; Khrustalev, V. N.; Jones, S. C.; Antipin, M. Y.; Tucker, N. M.; Timofeeva, T. V.; Coropceanu, V.; Brédas, J.-L.; Marder, S. R. Isolation and Crystal Structures of Two Singlet Bis(Triarylamine) Dications with Non-quinoidal Geometries. *J. Am. Chem. Soc.* **2006**, *128*, 1812−1817.

(21) Odom, S. A.; Lancaster, K.; Beverina, L.; Lefler, K. M.; Thompson, N. J.; Coropceanu, V.; Brédas, J.-L.; Marder, S. R.; Barlow, S. Bis[bis-(4-alkoxyphenyl)amino] Derivatives of Dithienylethene, Bithiophene, Dithienothiophene and Dithienopyrrole: Palladium-Catalysed Synthesis and Highly Delocalised Radical Cations. *Chem. - Eur. J.* **2007**, *13*, 9637−9646.

(22) Risko, C.; Coropceanu, V.; Barlow, S.; Geskin, V.; Schmidt, K.; Gruhn, N. E.; Marder, S. R.; Brédas, J.-L. Trends in Electron-Vibration and Electronic Interactions in Bis(dimethylamino) Mixed-Valence

Systems: A Joint Experimental and Theoretical Investigation. *J. Phys. Chem. C* **2008**, *112*, 7959−7967.
(23) Lancaster, K.; Odom, S. A.; Jones, S. C.; Thayumanavan, S.; Marder, S. R.; Brédas, J.-L.; Coropceanu, V.; Barlow, S. Intramolecular Electron-Transfer Rates in Mixed-Valence Triarylamines: Measurement by Variable-Temperature ESR Spectroscopy and Comparison with Optical Data. *J. Am. Chem. Soc.* **2009**, *131*, 1717−1723.
(24) Kaafarani, B. R.; Risko, C.; El-Assaad, T. H.; El-Ballouli, A. a. O.; Marder, S. R.; Barlow, S. Mixed-Valence Cations of Di(carbazol-9-yl) Biphenyl, Tetrahydropyrene, and Pyrene Derivatives. *J. Phys. Chem. C* **2016**, *120*, 3156−3166.
(25) Lambert, C.; Noell, G. The Class II/III Transition in Triarylamine Redox Systems. *J. Am. Chem. Soc.* **1999**, *121*, 8434−8442.
(26) Coropceanu, V.; Malagoli, M.; André, J. M.; Brédas, J. L. Charge-Transfer Transitions in Triarylamine Mixed-Valence Systems: A Joint Density Functional Theory and Vibronic Coupling Study. *J. Am. Chem. Soc.* **2002**, *124*, 10519−10530.
(27) Lambert, C.; Nöll, G. Tuning of intervalence charge transfer energies by substituents in one-dimensional bis(triarylamine) systems. *J. Chem. Soc, Perkin Trans. 2* **2002**, 2039−2043.
(28) Lambert, C.; Nöll, G.; Schelter, J. Bridge-mediated hopping or superexchange electron-transfer processes in bis(triarylamine) systems. *Nat. Mater.* **2002**, *1*, 69−73.
(29) Low, P. J.; Paterson, M. A. J.; Puschmann, H.; Goeta, A. E.; Howard, J. A. K.; Lambert, C.; Cherryman, J. C.; Tackley, D. R.; Leeming, S.; Brown, B. Crystal, Molecular and Electronic Structure of N,N′-Diphenyl-N,N′-bis(2,4-dimethylphenyl)-(1,1′-biphenyl)-4,4′-diamine and the Corresponding Radical Cation. *Chem. - Eur. J.* **2004**, *10*, 83−91.
(30) Szeghalmi, A. V.; Erdmann, M.; Engel, V.; Schmitt, M.; Amthor, S.; Kriegisch, V.; Nöll, G.; Stahl, R.; Lambert, C.; Leusser, D.; Stalke, D.; Zabel, M.; Popp, J. How delocalized is the N,N,N′,N′-Tetraphenylphenylenediamine Radical Cation? An Experimental and Theoretical Study on the Electronic and Molecular Structure. *J. Am. Chem. Soc.* **2004**, *126*, 7834−7845.
(31) Lambert, C.; Amthor, S.; Schelter, J. From Valence Trapped to Valence Delocalized by Bridge State Modification in Bis(triarylamine) Radical Cations: Evaluation of Coupling Matrix Elements in a Three-Level System. *J. Phys. Chem. A* **2004**, *108*, 6474−6468.
(32) Lambert, C.; Risko, C.; Coropceanu, V.; Schelter, J.; Amthor, S.; Gruhn, N. E.; Durivage, J. C.; Brédas, L.-L. Electronic Coupling in Tetraanisylarylenediamine Mixed-Valence Systems: The Interplay between Bridge Energy and Geometric Factors. *J. Am. Chem. Soc.* **2005**, *127*, 8508−8516.
(33) Heckmann, A.; Amthor, S.; Lambert, C. Mulliken−Hush analysis of a bis(triarylamine) mixed-valence system with a NN distance of 28.7 Å. *Chem. Commun.* **2006**, 2959−2961.
(34) Amthor, S.; Lambert, C. [2.2]Paracyclophane-Bridged Mixed-Valence Compounds: Application of a Generalized Mulliken-Hush Three-Level Model. *J. Phys. Chem. A* **2006**, *110*, 1177−1189.
(35) Seibt, J.; Schaumloeffel, A.; Lambert, C.; Engel, V. Quantum Study of the Absorption Spectroscopy of Bis(triarylamine) Radical Cations. *J. Phys. Chem. A* **2008**, *112*, 10178−10184.
(36) Kattnig, D. R.; Mladenova, B.; Grampp, G.; Kaiser, C.; Heckmann, A.; Lambert, C. Electron Paramagnetic Resonance Spectroscopy of Bis(triarylamine) Paracyclophanes as Model Compounds for the Intermolecular Charge-Transfer in Solid State Materials for Optoelectronic Applications. *J. Phys. Chem. C* **2009**, *113*, 2983−2995.
(37) Kaupp, M.; Renz, M.; Parthey, M.; Stolte, M.; Wuerthner, F.; Lambert, C. Computational and spectroscopic studies of organic mixed-valence compounds: where is the charge? *Phys. Chem. Chem. Phys.* **2011**, *13*, 16973−16986.
(38) Mladenova, B.; Kattnig, D. R.; Kaiser, C.; Schäfer, J.; Lambert, C.; Grampp, G. Investigations of the Degenerate Intramolecular Charge Exchange in Symmetric Organic Mixed Valence Compounds: Solvent Dynamics of Bis(triarylamine)paracyclophane Redox Systems. *J. Phys. Chem. C* **2015**, *119*, 8547−8553.
(39) Schäfer, J.; Holzapfel, M.; Mladenova, B.; Kattnig, D.; Krummenacher, I.; Braunschweig, H.; Grampp, G.; Lambert, C. Hole Transfer Processes in meta- and para-Conjugated Mixed Valence Compounds: Unforeseen Effects of Bridge Substituents and Solvent Dynamics. *J. Am. Chem. Soc.* **2017**, *139*, 6200−6209.
(40) Nie, H.-J.; Yang, W.-W.; Zheng, R.-H.; Shi, Q.; Chen, H.; Yao, J.; Zhong, Y.-W. Metal Chelation-Assisted Amine−Amine Electronic Coupling through the 4,4′-Positions of 2,2′-Bipyridine. *Inorg. Chem.* **2015**, *54*, 1272−1282.
(41) Jahnke, A. C.; Proppe, J.; Spulber, M.; Palivan, C. G.; Herrmann, C.; Wenger, O. S. Charge Delocalization in an Organic Mixed Valent Bithiophene Is Greater Than in a Structurally Analogous Biselenophene. *J. Phys. Chem. A* **2014**, *118*, 11293−11303.
(42) Heckmann, A.; Lambert, C. Neutral Organic Mixed-Valence Compounds: Synthesis and All-Optical Evaluation of Electron-Transfer Parameters. *J. Am. Chem. Soc.* **2007**, *129*, 5515−5527.
(43) Kanal, F.; Ruetzel, S.; Lu, H.; Moos, M.; Holzapfel, M.; Brixner, T.; Lambert, C. Measuring Charge-Separation Dynamics via Oligomer Length Variation. *J. Phys. Chem. C* **2014**, *118*, 23586−23598.
(44) Yao, C.-J.; Zheng, R.-H.; Shi, Q.; Zhong, Y.-W.; Yao, J. 1,4-Benzene-bridged covalent hybrid of triarylamine and cyclometalated ruthenium: a new type of organic-inorganic mixed-valent system. *Chem. Commun.* **2012**, *48*, 5680−5682.
(45) Tang, J.-H.; Wu, S.-H.; Shao, J.-Y.; Nie, H.-J.; Zhong, Y.-W. Ruthenium-Amine Electronic Coupling Bridged through Phen-1,3-diyl Versus Phen-1,4-diyl: Reverse of the Charge Transfer Direction. *Organometallics* **2013**, *32*, 4564−4570.
(46) Chen, J.; Winter, R. F. Studies on a Vinyl Ruthenium-Modified Squaraine Dye: Multiple Vis/NIR Absorbance Switching through Dye and Substituent-Based Redox Processes. *Chem. - Eur. J.* **2012**, *18*, 10733−10741.
(47) Linseis, M.; Záliš, S.; Zabel, M.; Winter, R. F. Ruthenium Stilbenyl and Diruthenium Distyrylethene Complexes: Aspects of Electron Delocalization and Electrocatalyzed Isomerization of the *Z*-Isomer. *J. Am. Chem. Soc.* **2012**, *134*, 16671−16692.
(48) Oßwald, S.; Breimaier, S.; Linseis, M.; Winter, R. F. Polyelectrochromic Vinyl Ruthenium-Modified Tritylium Dyes. *Organometallics* **2017**, *36*, 1993−2003.
(49) Maurer, J.; Linseis, M.; Sarkar, B.; Schwederski, B.; Niemeyer, M.; Kaim, W.; Záliš, S.; Anson, C.; Zabel, M.; Winter, R. F. Ruthenium Complexes with Vinyl, Styryl, and Vinylpyrenyl Ligands: A Case of Non-Innocence in Organometallic Chemistry. *J. Am. Chem. Soc.* **2008**, *130*, 259−268.
(50) Záliš, S.; Winter, R. F.; Kaim, W. Quantum chemical interpretation of redox properties of ruthenium complexes with vinyl and TCNX type non-innocent ligands. *Coord. Chem. Rev.* **2010**, *254*, 1383−1396.
(51) Mücke, P.; Linseis, M.; Záliš, S.; Winter, R. F. Vinyl-ruthenium entities as markers for intramolecular electron transfer processes. *Inorg. Chim. Acta* **2011**, *374*, 36−50.
(52) Wuttke, E.; Hervault, Y.-M.; Polit, W.; Linseis, M.; Erler, P.; Rigaut, S.; Winter, R. F. Divinylphenylene- and Ethynylvinylphenylene-Bridged Mono-, Di-, and Triruthenium Complexes for Covalent Binding to Gold Electrodes. *Organometallics* **2014**, *33*, 4672−4686.
(53) Abdel-Rahman, O. S.; Maurer, J.; Záliš, S.; Winter, R. F. Ruthenium Styryl Complexes with Ligands Derived from 2-Hydroxy- and 2-Mercaptopyridine and 2-Hydroxy- and 2-Mercaptoquinoline. *Organometallics* **2015**, *34*, 3611−3628.
(54) Man, W. Y.; Xia, J.-L.; Brown, N. J.; Farmer, J. D.; Yufit, D. S.; Howard, J. A. K.; Liu, S. H.; Low, P. J. Spectroscopic and Computational Studies of the Ligand Redox Non-Innocence in Mono- and Binuclear Ruthenium Vinyl Complexes. *Organometallics* **2011**, *30*, 1852−1858.
(55) Xia, J.-L.; Man, W. Y.; Zhu, X.; Zhang, C.; Jin, G.-J.; Schauer, P. A.; Fox, M. A.; Yin, J.; Yu, G.-A.; Low, P. J.; Liu, S. H. Synthesis and Characterization of Dithia[3.3]paracyclophane-Bridged Binuclear Ruthenium Vinyl and Alkynyl Complexes. *Organometallics* **2012**, *31*, 5321−5333.

DOI: 10.1021/acs.inorgchem.7b02186
Inorg. Chem. 2017, 56, 13517−13529

(56) Sherlock, S. J.; Boyd, D. C.; Moasser, B.; Gladfelter, W. L. Homogeneous Catalytic Carbonylation of Nitroaraomatics. 4. Preparation and Characterization of Ruthenium Radical Cations. *Inorg. Chem.* **1991**, *30*, 3626−3632.
(57) Maurer, J.; Winter, R. F.; Sarkar, B.; Fiedler, J.; Záliš, S. Bridge dominated oxidation of a diruthenium 1,3-divinylphenylene complex. *Chem. Commun.* **2004**, 1900−1901.
(58) Maurer, J.; Sarkar, B.; Schwederski, B.; Kaim, W.; Winter, R. F.; Záliš, S. Divinylphenylene bridged diruthenium complexes bearing $Ru(CO)Cl(PiPr_3)_2$ entities. *Organometallics* **2006**, *25*, 3701−3712.
(59) Linseis, M.; Winter, R. F.; Sarkar, B.; Kaim, W.; Záliš, S. Multistep Electrochromic Behaviour from an Organometallic Tetranuclear Complex of a Tetradonor-Substituted Olefin. *Organometallics* **2008**, *27*, 3321−3324.
(60) Mücke, P.; Zabel, M.; Edge, R.; Collison, D.; Clément, S.; Záliš, S.; Winter, R. F. Electron delocalization in vinyl ruthenium substituted cyclophanes: Assessment of the through-space and the through-bond pathways. *J. Organomet. Chem.* **2011**, *696*, 3186−3197.
(61) Scheerer, S.; Rotthowe, N.; Abdel-Rahman, O. S.; He, X.; Rigaut, S.; Kvapilová, H.; Záliš, S.; Winter, R. F. Vinyl Ruthenium-Modified Biphenyl and 2,2′-Bipyridines. *Inorg. Chem.* **2015**, *54*, 3387−3402.
(62) Fink, D.; Weibert, B.; Winter, R. F. Redox-active tetraruthenium metallacycles: reversible release of up to eight electrons resulting in strong electrochromism. *Chem. Commun.* **2016**, *52*, 6103−6106.
(63) Pfaff, U.; Hildebrandt, A.; Korb, M.; Oßwald, S.; Linseis, M.; Schreiter, K.; Spange, S.; Winter, R. F.; Lang, H. Electronically Strongly Coupled Divinylheterocyclic-Bridged Diruthenium Complexes. *Chem. - Eur. J.* **2016**, *22*, 783−801.
(64) Scheerer, S.; Linseis, M.; Wuttke, E.; Weickert, S.; Drescher, M.; Tröppner, O.; Ivanović-Burmazović, I.; Irmler, A.; Pauly, F.; Winter, R. F. Redox-Active Tetraruthenium Macrocycles Built from 1,4-Divinylphenylene-Bridged Diruthenium Complexes. *Chem. - Eur. J.* **2016**, *22*, 9574−9590.
(65) Wu, X.; Weng, T.; Jin, S.; Liang, J.; Guo, R.; Yu, G.-a.; Liu, S. H. Synthesis, characterization, and substituent effects of mononuclear ruthenium complexes $[RuCl(CO)(PMe_3)_3(CHCH\text{-}C_6H_4\text{-}R\text{-}p)]$ (R = H, CH_3, OCH_3, NO_2, NH_2, NMe_2). *J. Organomet. Chem.* **2009**, *694*, 1877−1883.
(66) Wu, X. H.; Jin, S.; Liang, J. H.; Li, Z. Y.; Yu, G.-a.; Liu, S. H. Synthesis, Characterization, and Substituent Effects of Binuclear Ruthenium Vinyl Complexes $[RuCl(CO)(PMe_3)_3]_2(\mu\text{-}CHCH\text{−}Ar\text{−}CHCH)$. *Organometallics* **2009**, *28*, 2450−2459.
(67) Ou, Y.-P.; Jiang, C.; Wu, D.; Xia, J.; Yin, J.; Jin, S.; Yu, G.-A.; Liu, S. H. Synthesis, Characterization, and Properties of Anthracene-Bridged Bimetallic Ruthenium Vinyl Complexes $[RuCl(CO)(PMe_3)_3]_2(\mu\text{-}CH{=}CH\text{-anthracene-}CH{=}CH)$. *Organometallics* **2011**, *30*, 5763−5770.
(68) Tian, L. Y.; Liu, Y. M.; Tian, G.-X.; Wu, X. H.; Li, Z.; Kou, J.-F.; Ou, Y.-P.; Liu, S. H.; Fu, W.-F. Bimetallic ruthenium complexes bridged by divinylphenylene bearing oligo(ethylene glycol)-methylether: synthesis, (spectro)electrochemistry and the lithium cation effect. *Dalton Trans.* **2014**, *43*, 4093−4101.
(69) Xia, J.; Ou, Y.-P.; Meng, X.-G.; Yin, J.; Yu, G.-a.; Liu, S. H. Synthesis and Characterization of Dithia[3.3]metaparacyclophane-Bridged Dimetallic Ruthenium Acetylide Complexes. *Eur. J. Inorg. Chem.* **2014**, *2014*, 247−255.
(70) Zhang, J.; Ou, Y.; Xu, M.; Sun, C.; Yin, J.; Yu, G.-A.; Liu, S. H. Synthesis and Characterization of Dibenzoheterocycle-Bridged Dinuclear Ruthenium Alkynyl and Vinyl Complexes. *Eur. J. Inorg. Chem.* **2014**, *2014*, 2941−2951.
(71) Kong, D.-D.; Xue, L.-S.; Jang, R.; Liu, B.; Meng, X.-G.; Jin, S.; Ou, Y.-P.; Hao, X.; Liu, S.-H. Conformational Tuning of the Intramolecular Electronic Coupling in Molecular-Wire Biruthenium Complexes Bridged by Biphenyl Derivatives. *Chem. - Eur. J.* **2015**, *21*, 9895−9904.
(72) Zhang, J.; Sun, C.-F.; Wu, X.-H.; Zhang, M.-X.; Yin, J.; Yu, G.-A.; Liu, S. H. Bimetallic Ruthenium Vinyl Complexes Bridged by Electronic Substituent Phenylenes: Spectroelectrochemical and Computational Studies. *Int. J. Electrochem. Sci.* **2016**, *11*, 7875−7889.
(73) Polit, W.; Exner, T.; Wuttke, E.; Winter, R. F. Vinylruthenium-Triarylamine Conjugates as Electroswitchable Polyelectrochromic NIR Dyes. *BioInorg. React. Mech.* **2012**, *8*, 85−105.
(74) Polit, W.; Mücke, P.; Wuttke, E.; Exner, T.; Winter, R. F. Charge and Spin Confinement to the Amine Site in 3-Connected Triarylamine Vinyl Ruthenium Conjugates. *Organometallics* **2013**, *32*, 5461−5472.
(75) Chiu, K. Y.; Su, T.-H.; Huang, C. W.; Liou, G.-S.; Cheng, S.-H. Substituent effects on the electrochemical and spectral characteristics of N,N,N′,N′-tetraaryl-p-phenylenediamine derivatives. *J. Electroanal. Chem.* **2005**, *578*, 283−287.
(76) Yano, M.; Ishida, Y.; Aoyama, K.; Tatsumi, M.; Sato, K.; Shiomi, D.; Ichimura, A.; Takui, T. Synthesis and Electronic Properties of Tetraaryl p- and m-Phenylenediamines. *Synth. Met.* **2003**, *137*, 1275−1276.
(77) Wuttke, E.; Fink, D.; Anders, P.; Maria Hoyt, A.-L.; Polit, W.; Linseis, M.; Winter, R. F. Homo- and heterobimetallic 1,4-divinylphenylene- and naphthalene-1,8-divinyl-bridged diruthenium, diosmium and ruthenium osmium complexes. *J. Organomet. Chem.* **2016**, *821*, 4−18.
(78) Pevny, F.; Di Piazza, E.; Norel, L.; Drescher, M.; Winter, R. F.; Rigaut, S. Fully delocalized (ethynyl)(vinyl)phenylene bridged diruthenium radical complexes. *Organometallics* **2010**, *29*, 5912−5918.
(79) Wuttke, E.; Pevny, F.; Hervault, Y.-M.; Norel, L.; Drescher, M.; Winter, R. F.; Rigaut, S. Fully Delocalized (Ethynyl)(vinyl)phenylene Bridged Triruthenium Complexes in up to Five Different Oxidation States. *Inorg. Chem.* **2012**, *51*, 1902−1915.
(80) Hupp, J. T.; Neyhart, G. A.; Meyer, T. J. Solvent control of oxidation state distribution and electronic delocalization in an osmium-ruthenium, mixed-metal dimer. *J. Am. Chem. Soc.* **1986**, *108*, 5349−5350.
(81) Ott, I.; Kowalski, K.; Gust, R.; Maurer, J.; Mücke, P.; Winter, R. F. Comparative biological evaluation of two ethylene linked mixed binuclear ferrocene/ruthenium organometallic species. *Bioorg. Med. Chem. Lett.* **2010**, *20*, 866−869.
(82) Planells, M.; Abate, A.; Hollman, D. J.; Stranks, S. D.; Bharti, V.; Gaur, J.; Mohanty, D.; Chand, S.; Snaith, H. J.; Robertson, N. Diacetylene bridged triphenylamines as hole transport materials for solid state dye sensitized solar cells. *J. Mater. Chem. A* **2013**, *1*, 6949−6960.
(83) Chowdhury, A.; Mukherjee, P. S. Electron-Rich Triphenylamine-Based Sensors for Picric Acid Detection. *J. Org. Chem.* **2015**, *80*, 4064−4075.
(84) Kim, C.; Choi, H.; Paek, S.; Kim, J.-J.; Song, K.; Kang, M.-S.; Ko, J. Molecular engineering of thia-bridged triphenylamine heterohelicenes as novel organic dyes for dye-sensitized solar cells. *J. Photochem. Photobiol., A* **2011**, *225*, 17−25.
(85) Li, Z. a.; Ye, T.; Tang, S.; Wang, C.; Ma, D.; Li, Z. Triphenylamine-based [small pi]-conjugated dendrimers: convenient synthesis, easy solution processability, and good hole-transporting properties. *J. Mater. Chem. C* **2015**, *3*, 2016−2023.
(86) Werner, H.; Esteruelas, M. A.; Otto, H. Insertion Reactions of the 16-Electron Complexes $MHCl(CO)(P\text{-}i\text{-}Pr_3)_2$ (M = Ru, Os) with Alkynes. The X-ray Crystal Structure of $Os((E)CH{=}CHPh)Cl(CO)(P\text{-}i\text{-}Pr_3)_2$. *Organometallics* **1986**, *5*, 2295−2299.
(87) Hill, A. F. In *Comprehensive Organometallic Chemistry II*; Shriver, D. E., Bruce, M. I., Eds.; Pergamon: Oxford, U.K., 1995; Vol. 7, pp 399−411.
(88) Marchenko, A. V.; Gérard, H.; Eisenstein, O.; Caulton, K. G. A comprehensive view of M-H addition across the RCCH bond: frustration culminating in ultimate union. *New J. Chem.* **2001**, *25*, 1244−1255.
(89) Marchenko, A. V.; Gérard, H.; Eisenstein, O.; Caulton, K. G. A comparative study of olefin or acetylene insertion into Ru−H or Os−H of $MHCl(CO)(phosphine)_2$. *New J. Chem.* **2001**, *25*, 1382−1388.
(90) Richardson, D. E.; Taube, H. Mixed-valence molecules: Electronic delocalization and stabilization. *Coord. Chem. Rev.* **1984**, *60*, 107−129.

DOI: 10.1021/acs.inorgchem.7b02186
Inorg. Chem. 2017, 56, 13517−13529

(91) D'Alessandro, D. M.; Keene, F. R. A cautionary warning on the use of electrochemical measurements to calculate comproportionation constants for-mixed-valence compounds. *Dalton Trans.* **2004**, 3950−3954.
(92) Winter, R. F. Half-Wave Potential Splittings ΔE1/2 as a Measure of Electronic Coupling in Mixed-Valent Systems: Triumphs and Defeats. *Organometallics* **2014**, *33*, 4517−4536.
(93) Santi, S.; Bisello, A.; Cardena, R.; Donoli, A. Key multi-(ferrocenyl) complexes in the interplay between electronic coupling and electrostatic interaction. *Dalton Trans.* **2015**, *44*, 5234−5257.
(94) Hassenrück, C.; Mücke, P.; Scheck, J.; Demeshko, S.; Winter, R. F. Oxidized Styrylruthenium−Ferrocene Conjugates: From Valence Localization to Valence Tautomerism. *Eur. J. Inorg. Chem.* **2017**, *2017*, 401−411.
(95) Krejcik, M.; Danek, M.; Hartl, F. Simple construction of an infrared optically transparent thin-layer cell: Applications to the redox reactions of ferrocene, $Mn_2(CO)_{10}$ and $Mn(CO)_3$(3,5-di-t-butyl-catecholate)$^-$. *J. Electroanal. Chem. Interfacial Electrochem.* **1991**, *317*, 179−187.
(96) Selby, T. D.; Blackstock, S. C. Preparation of a Redox-Gradient Dendrimer. Polyamines Designed for One-Way Electron Transfer and Charge Capture. *J. Am. Chem. Soc.* **1998**, *120*, 12155−12156.
(97) Ovchinnikov, A. A. Multiplicity of the ground state of large alternant organic molecules with conjugated bonds (do organic ferromagnets exist?). *Theor. Chim. Acta* **1978**, *47*, 297−304.
(98) Barlow, S.; Risko, C.; Odom, S. A.; Zheng, S.; Coropceanu, V.; Beverina, L.; Brédas, J.-L.; Marder, S. R. Tuning Delocalization in the Radical Cations of 1,4-Bis[4-(diarylamino)styryl]benzenes, 2,5-Bis[4-(diarylamino)styryl]thiophenes, and 2,5-Bis[4-(diarylamino)styryl]-pyrroles through Substituent Effects. *J. Am. Chem. Soc.* **2012**, *134*, 10146−10155.
(99) Nie, H.-J.; Yao, C.-J.; Shao, J.-Y.; Yao, J.; Zhong, Y.-W. Oligotriarylamines with a Pyrene Core: A Multicenter Strategy for Enhancing Radical Cation and Dication Stability and Tuning Spin Distribution. *Chem. - Eur. J.* **2014**, *20*, 17454−17465.
(100) Koide, T.; Furukawa, K.; Shinokubo, H.; Shin, J.-Y.; Kim, K. S.; Kim, D.; Osuka, A. A Stable Non-Kekulé Singlet Biradicaloid from meso-Free 5,10,20,25-Tetrakis(Pentafluorophenyl)-Substituted [26]-Hexaphyrin(1.1.1.1.1.1). *J. Am. Chem. Soc.* **2010**, *132*, 7246−7247.
(101) Li, Y.; Heng, W.-K.; Lee, B. S.; Aratani, N.; Zafra, J. L.; Bao, N.; Lee, R.; Sung, Y. M.; Sun, Z.; Huang, K.-W.; Webster, R. D.; López Navarrete, J. T.; Kim, D.; Osuka, A.; Casado, J.; Ding, J.; Wu, J. Kinetically Blocked Stable Heptazethrene and Octazethrene: Closed-Shell or Open-Shell in the Ground State? *J. Am. Chem. Soc.* **2012**, *134*, 14913−14922.
(102) Abe, M. Diradicals. *Chem. Rev.* **2013**, *113*, 7011−7088.
(103) Renz, M.; Theilacker, K.; Lambert, C.; Kaupp, M. A Reliable Quantum-Chemical Protocol for the Characterization of Organic Mixed-Valence Compounds. *J. Am. Chem. Soc.* **2009**, *131*, 16292−16302.
(104) Parthey, M.; Kaupp, M. Quantum-chemical insights into mixed-valence systems: within and beyond the Robin-Day scheme. *Chem. Soc. Rev.* **2014**, *43*, 5067−5088.
(105) Völker, S. F.; Renz, M.; Kaupp, M.; Lambert, C. Squaraine Dyes as Efficient Coupling Bridges between Triarylamine Redox Centres. *Chem. - Eur. J.* **2011**, *17*, 14147−14163.
(106) Carlson, R. K.; Odoh, S. O.; Tereniak, S. J.; Lu, C. C.; Gagliardi, L. Can Multiconfigurational Self-Consistent Field Theory and Density Functional Theory Correctly Predict the Ground State of Metal−Metal-Bonded Complexes? *J. Chem. Theory Comput.* **2015**, *11*, 4093−4101.
(107) Nelsen, S. F.; Konradsson, A. E.; Weaver, M. N.; Telo, J. P. Intervalence Near-IR Spectra of Delocalized Dinitroaromatic Radical Anions. *J. Am. Chem. Soc.* **2003**, *125*, 12493−12501.
(108) Nelsen, S. F. "Almost Delocalized" Intervalence Compounds. *Chem. - Eur. J.* **2000**, *6*, 581−588.
(109) Low, P. J.; Paterson, M. A. J.; Goeta, A. E.; Yufit, D. S.; Howard, J. A. K.; Cherryman, J. C.; Tackley, D. R.; Brown, B. The molecular structures and electrochemical response of "twisted" tetra(aryl)benzidenes. *J. Mater. Chem.* **2004**, *14*, 2516−2523.
(110) Sutin, N. *Prog. Inorg. Chem.* **1983**, *30*, 441−499.
(111) Brunschwig, B. S.; Creutz, C.; Sutin, N. *Chem. Soc. Rev.* **2002**, *31*, 168.
(112) Coropceanu, V.; Lambert, C.; Nöll, G.; Brédas, J. L. Charge-transfer transitions in triarylamine mixed-valence systems: the effect of temperature. *Chem. Phys. Lett.* **2003**, *373*, 153−160.
(113) Coropceanu, V.; André, J. M.; Malagoli, M.; Brédas, J. L. The role of vibronic interactions on intramolecular and intermolecular electron transfer in π-conjugated oligomers. *Theor. Chem. Acc.* **2003**, *110*, 59−69.
(114) Creutz, C.; Newton, M. D.; Sutin, N. *J. Photochem. Photobiol., A* **1994**, *82*, 47.
(115) Stoll, S.; Schweiger, A. EasySpin, a comprehensive software package for spectral simulation and analysis in EPR. *J. Magn. Reson.* **2006**, *178*, 42−55.
(116) Frisch, M. J.; Trucks, G.; Schlegel, H. B.; Scuseria, G. E.; Robb, M. A.; Cheeseman, J. R.; Scalmani, G.; Barone, V.; Mennucci, B.; Petersson, G. A.; Nakatsuji, H.; Caricato, M.; Li, X.; Hratchian, H. P.; Izmaylov, A. F.; Blonio, J.; Zheng, G.; Sonnenberg, J. L.; Hada, M.; Ehara, M.; Toyota, K.; Fukuda, R.; Hasegawa, J.; Ishida, M.; Nakajima, T.; Honda, Y.; Kitao, O.; Nakai, H.; Vreven, T.; Montgomery, J. A., Jr.; Peralta, J. E.; Ogliaro, F.; Bearpark, M.; Heyd, J. J.; Brothers, E.; Kudin, K. N.; Staroverov, V. N.; Keith, T.; Kobayashi, R.; Normand, J.; Raghavachari, K.; Rendell, A.; Burant, J. C.; Iyengar, S. S.; Tomasi, J.; Cossi, M.; Rega, N.; Millam, J. M.; Klene, M.; Knox, J. E.; Cross, J. B.; Bakken, V.; Adamo, C.; Jaramillo, J.; Gomperts, R.; Stratmann, R. E.; Yazyev, O.; Austin, A. J.; Cammi, R.; Pomelli, C.; Ochterski, J. W.; Martin, R. L.; Morokuma, K.; Zakrzewski, V. G.; Voth, G. A.; Salvador, P.; Dannenberg, J. J.; Dapprich, S.; Daniels, A. D.; Farkas, Ö.; Foresman, J. B.; Ortiz, J. V.; Cioslowski, J.; Fox, D. J. *Gaussian 09*, revision B.01; Gaussian Inc.: Wallingford, CT, 2010.
(117) Andrae, D.; Haeussermann, U.; Dolg, M.; Stoll, H.; Preuss, H. Energy-adjusted ab initio pseudopotentials for the second and third row transition elements. *Theor. Chim. Acta* **1990**, *77*, 123−141.
(118) Perdew, J. P.; Burke, K.; Ernzerhof, M. Generalized Gradient Approximation Made Simple. *Phys. Rev. Lett.* **1996**, *77*, 3865−3868.
(119) Cossi, M.; Rega, N.; Scalmani, G.; Barone, V. Energies, structures, and electronic properties of molecules in solution with the C-PCM solvation model. *J. Comput. Chem.* **2003**, *24*, 669−681.

DOI: 10.1021/acs.inorgchem.7b02186
Inorg. Chem. 2017, 56, 13517−13529

Supporting Information

Manipulation and Assessment of Charge and Spin Delocalization in Mixed-Valent Triarylamine-Vinylruthenium Conjugates

Christopher Hassenrück, Rainer F. Winter*

Fachbereich Chemie Universität Konstanz, Universitätsstraße 10, D-78457 Konstanz, Germany

Contents:

1. **Synthetic procedures and spectroscopic characterization of triarylamine precursors**
2. **^{1}H-, ^{13}C- ^{31}P-NMR spectra of 1 to 4**
3. **Cyclic Voltammetry**
4. **IR-Spectroelectrochemistry**
5. **EPR spectra of the radical cations and dications at room temperature and in frozen DCM glass**
6. **Fragment contributions to selected MOs and calculated structure parameters of 1-CHO^{n,} 1-Me^{n+}, and 1-OMe^{n+}**
7. **Spin density plots of the radical cations and dications**
8. **UV/vis/NIR Spectroelectrochemistry**
9. **TD-DFT calculated transitions and spectra**
10. **Vis/NIR spectra of the radical cations in various solvents**
11. **Gaussian analysis of the experimental NIR spectra**

1. Synthetic procedures and spectroscopic characterization of triarylamine precursors 1a to 4a

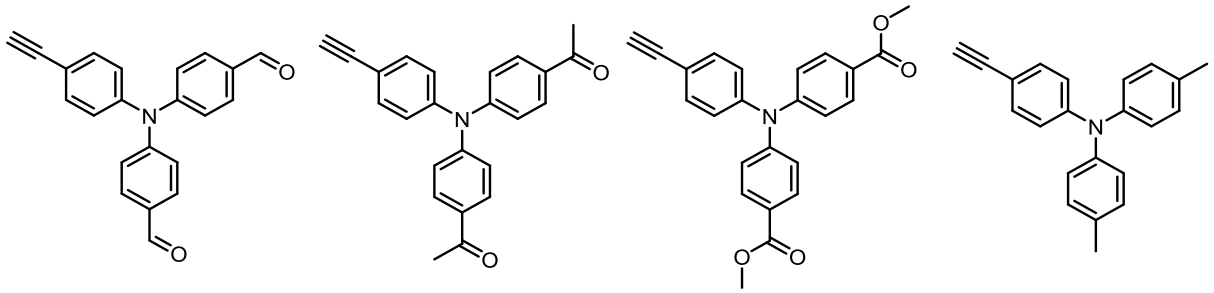

1a **2a** **3a** **4a**

1a was synthesized following a literature known iodination of di(paraformyl)triphenylamine[1] followed by standard Sonogashira Coupling methodology and subsequent deprotection using K_2CO_3 in a 1:1 mixture of methanol and tetrahydrofuran. ^{1}H-NMR (400 MHz, $CDCl_3$): d 9.91 (s, 2H), 7.80 (d, *J* = 8.6 Hz, 4H), 7.49 (d, *J* = 8.5 Hz, 2H), 7.19 (d, *J* = 8.6 Hz, 4H), 7.10 (d, *J* = 8.5 Hz, 2H), 3.12 (s, 1H).

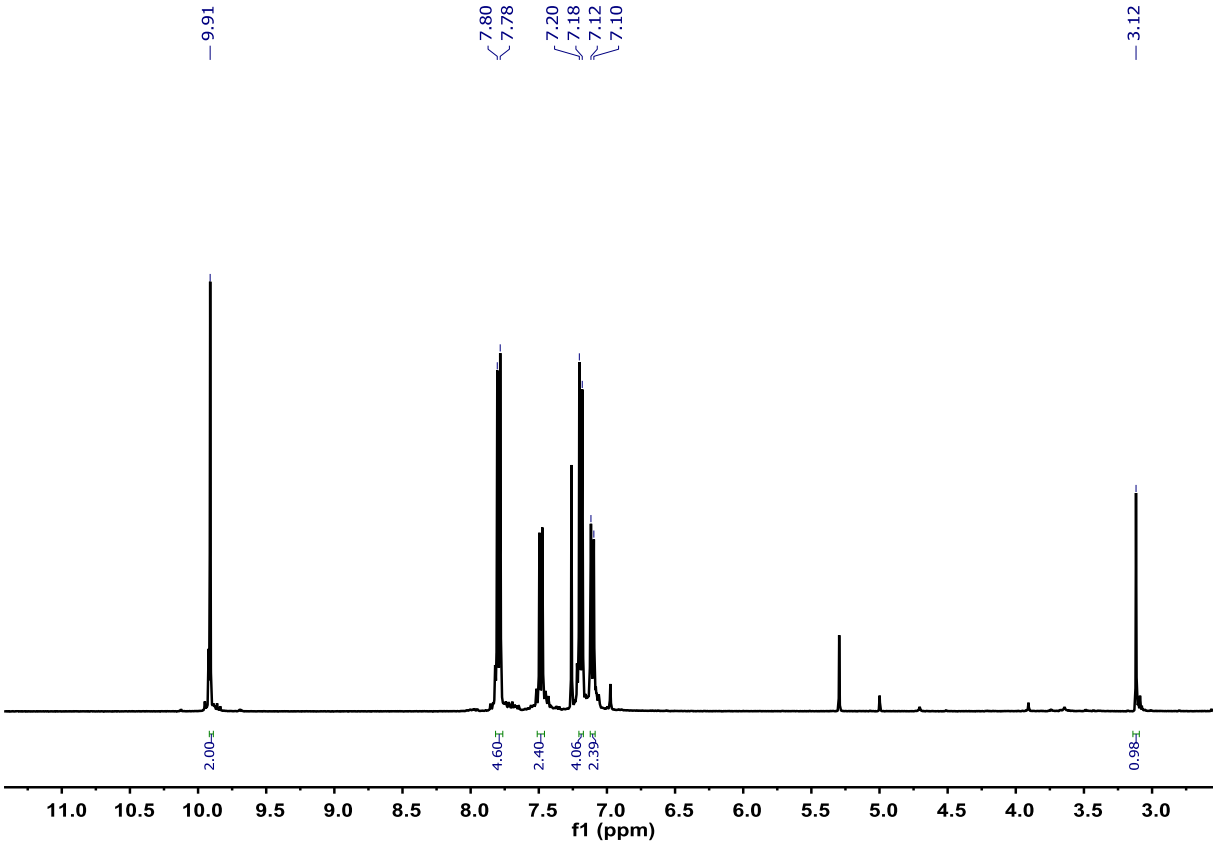

Figure S1. ^{1}H-NMR spectrum of **1a** recorded in $CDCl_3$ at room temperature.

2a was synthesized by adaption of a literature-known method.[2]

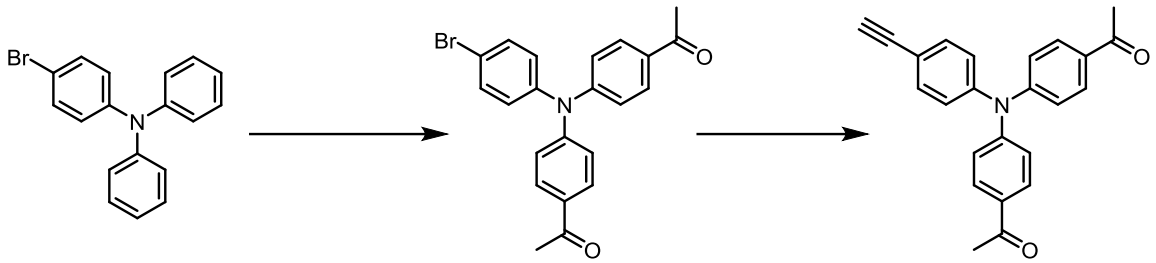

2aa **2a**

First, 4-bromotriphenylamine was acetylated under Friedel-Crafts acylation conditions. $AlCl_3$ (7 g, 50.3 mmol) was dissolved in dichloromethane (90 mL) at 0 °C. Acetyl chloride (2.91 mL, 40.7 mmol) was added over 30 minutes and, after warming to room temperature, 4-bromo-*N*,*N*-diphenylaniline (6 g, 18.5 mmol) in dichloromethane (60 mL) was added. The resulting suspension was stirred at 60 °C for 10 hours. The reaction was quenched with ice/ 10% hydrochloric acid and the aqueous phase was extracted with dichloromethane (3 x 50 mL). The product was isolated by silica column chromatography (10:1 diethylether/ethyl acetate) as a light yellow solid.^{1}H-NMR (400 Mhz, $CDCl_3$): d 7.87 (d, *J* = 8 Hz, 4H), 7.47 (d, *J* = 12 Hz, 2H), 7.10 (d, *J* = 8 Hz, 4H), 7.03 (d, *J* = 12 Hz, 2H), 2.56 (s, 6H).

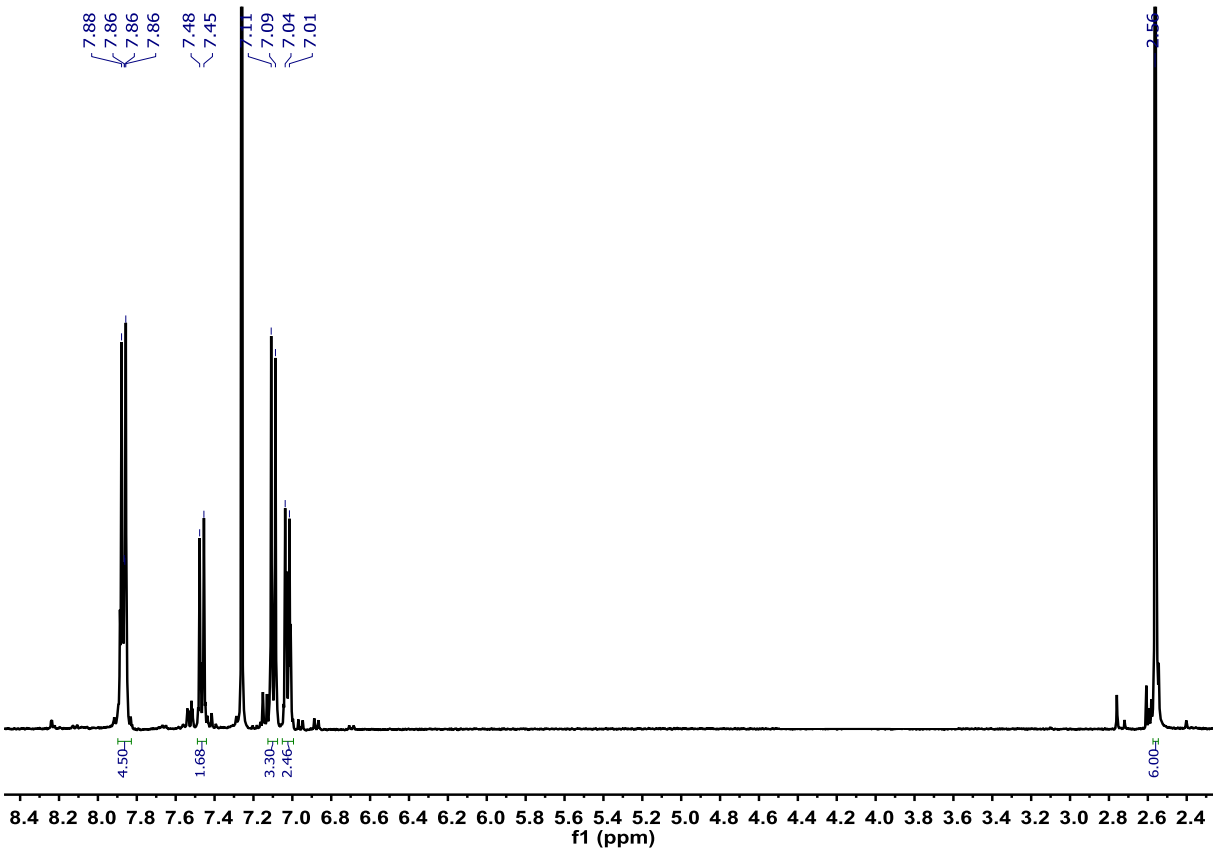

Figure S2. ^{1}H-NMR spectrum of **2aa** recorded in $CDCl_3$ at room temperature.

Second, the 4-bromo-4'4'-diacetyltriphenylamine **2aa** was reacted under standard Sonogashira reaction conditions. Subsequent deprotection using K_2CO_3 in a methanol/THF 1:1 mixture yielded **2a** in 55 % yield. ^{1}H-NMR (400 MHz, $CDCl_3$): δ 7.88 (d, *J* = 8 Hz, 4H), 7.45 (d, *J* = 12 Hz, 2H), 7.12 (d, *J* = 8 Hz, 4H), 7.08 (d, *J* = 12 Hz, 2H), 3.10 (s, 1H), 2.57 (s, 6H).

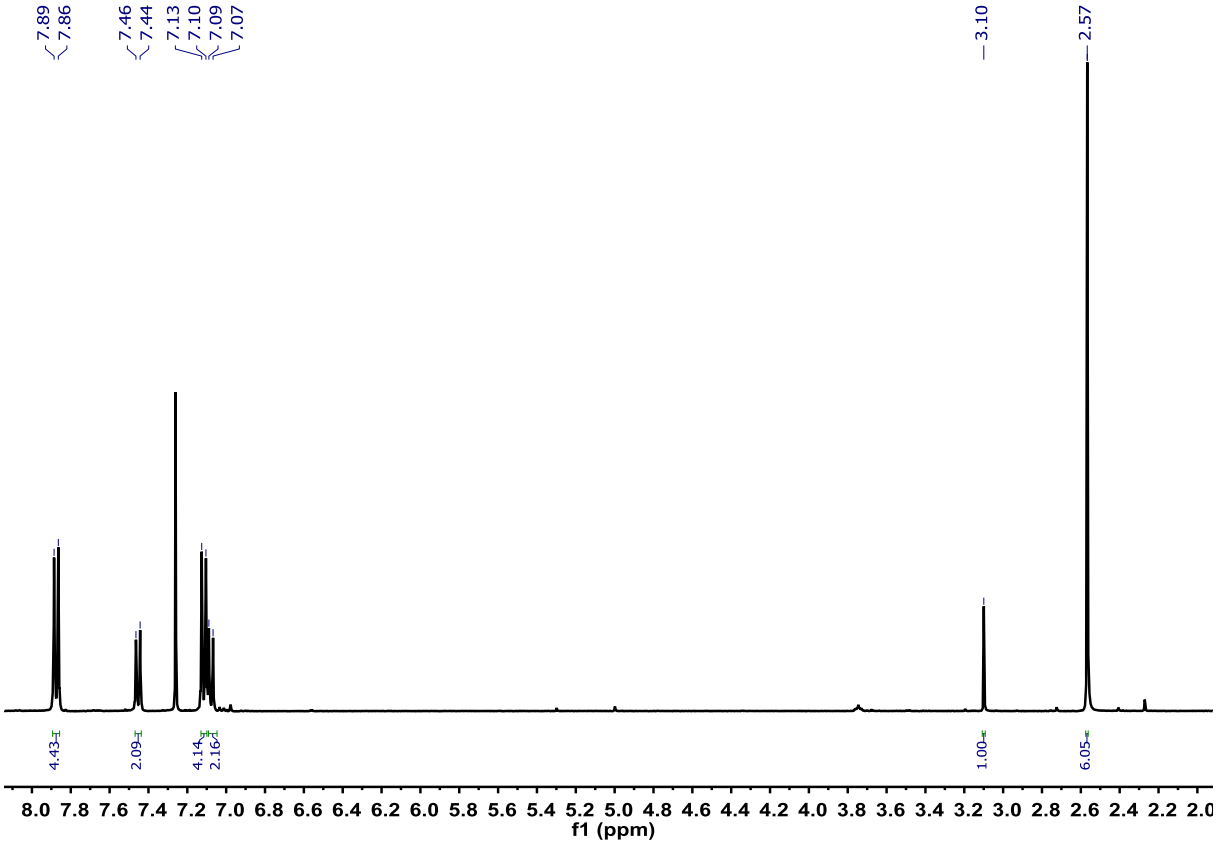

Figure S3. ^{1}H-NMR spectrum of **2a** recorded in $CDCl_3$ at room temperature.

3a and **4a** were synthesized following literature known methods.[3, 4]

2. ^{1}H-, ^{13}C- ^{31}P-NMR spectra of the complexes

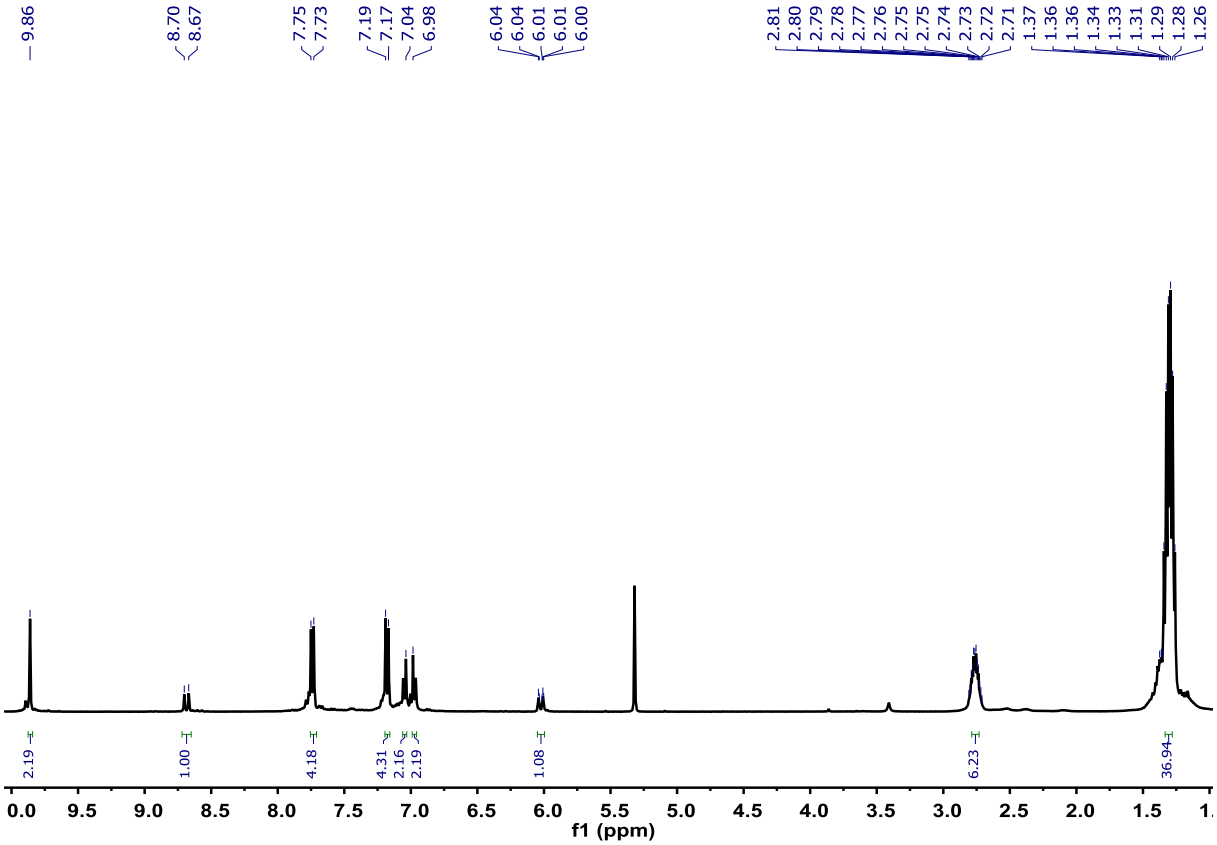

Figure S4. ^{1}H-NMR spectrum of **1-CHO**, recorded in CD_2Cl_2 at room temperature.

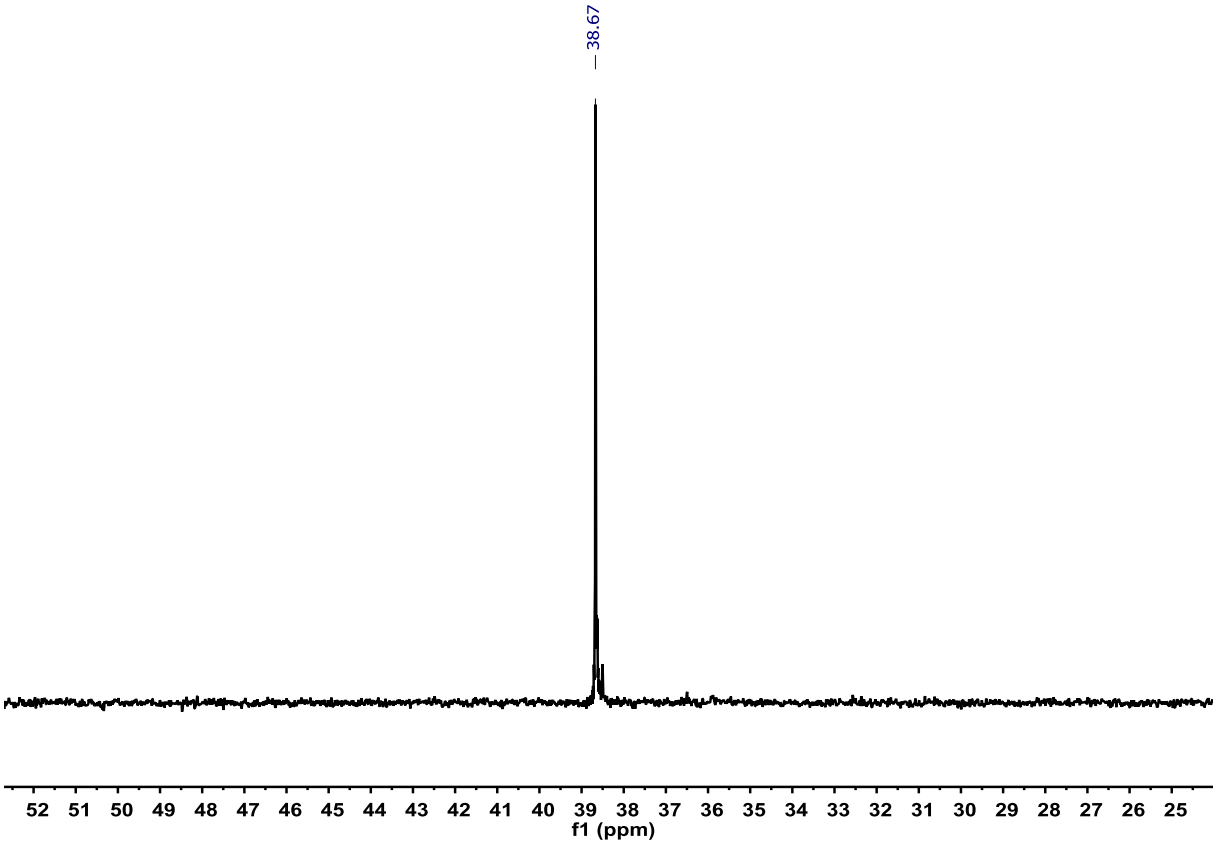

Figure S5. ^{31}P-NMR spectrum of **1-CHO**, recorded in CD_2Cl_2 at room temperature.

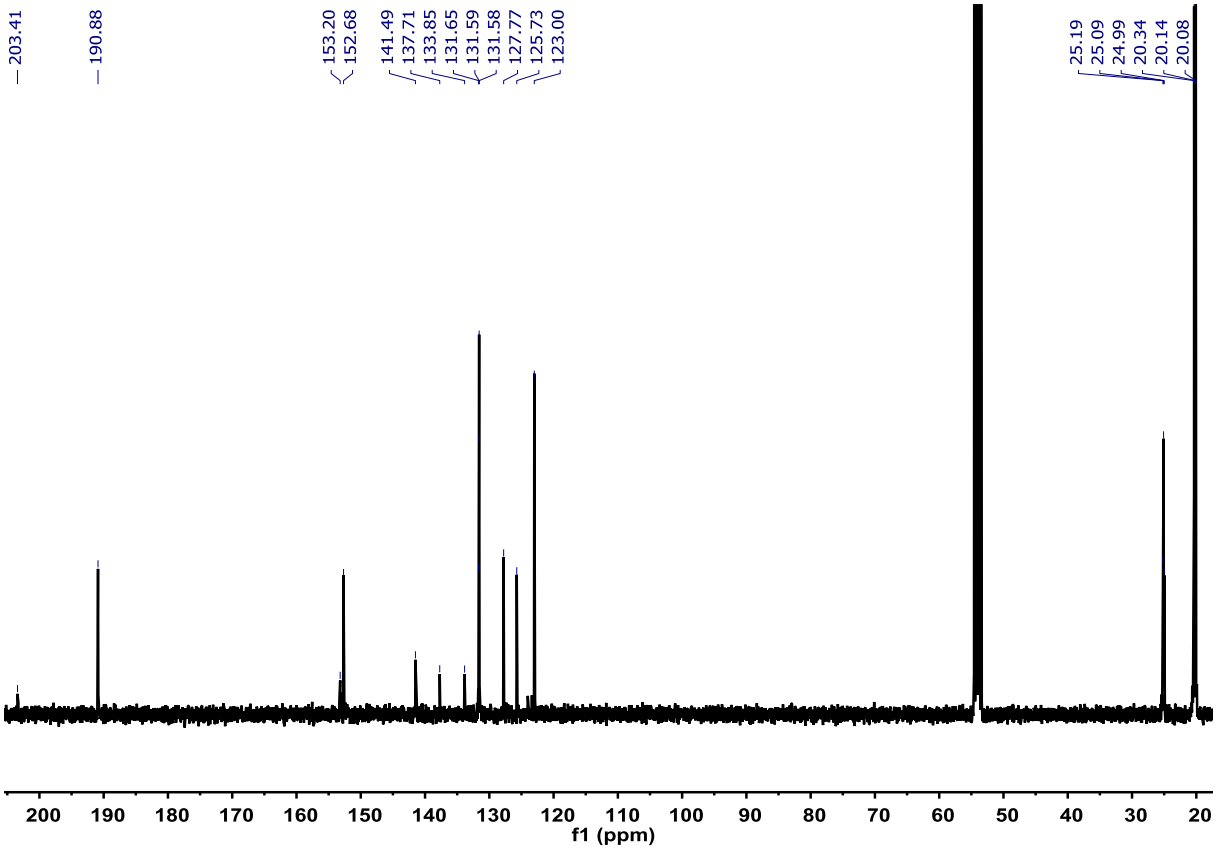

Figure S6. ^{13}C-NMR spectrum of **1-CHO**, recorded in CD_2Cl_2 at room temperature.

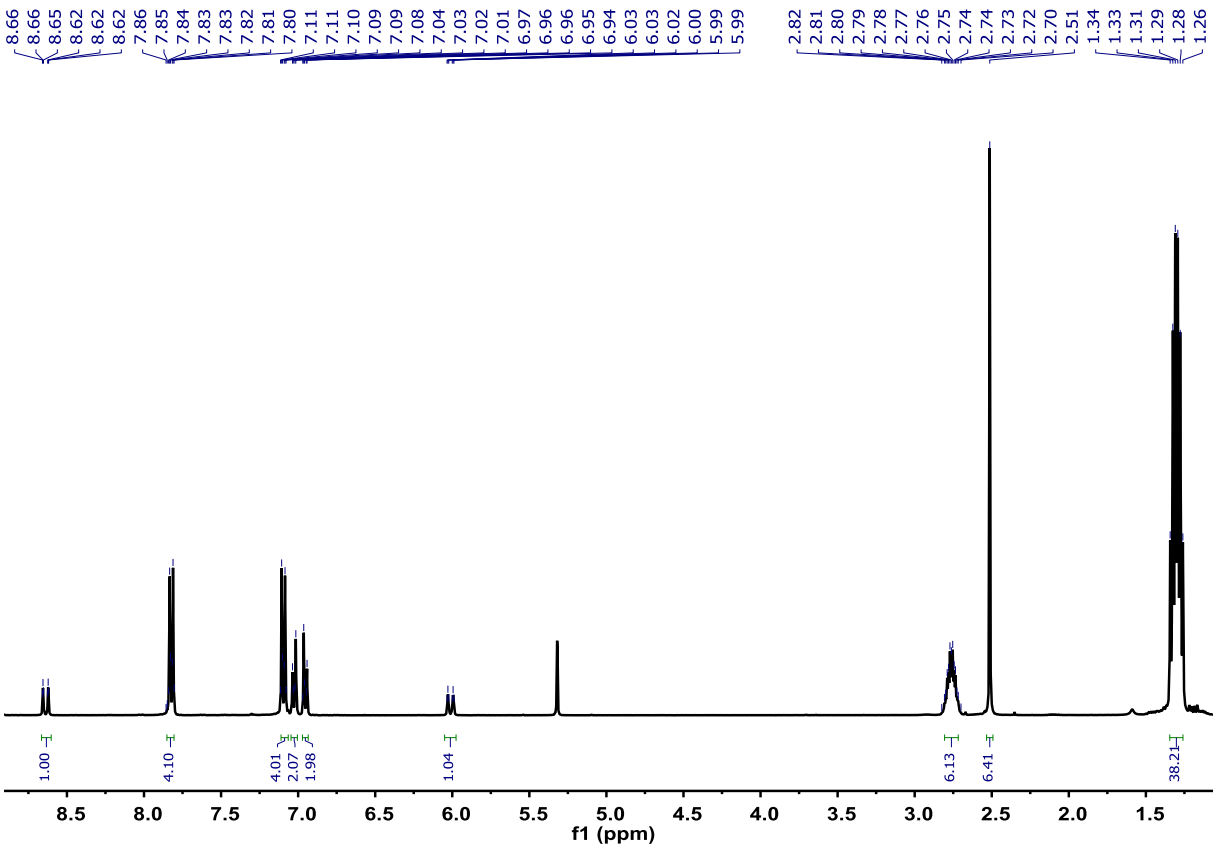

Figure S7. ^{1}H-NMR spectrum of **1-Ac**, recorded in CD_2Cl_2 at room temperature.

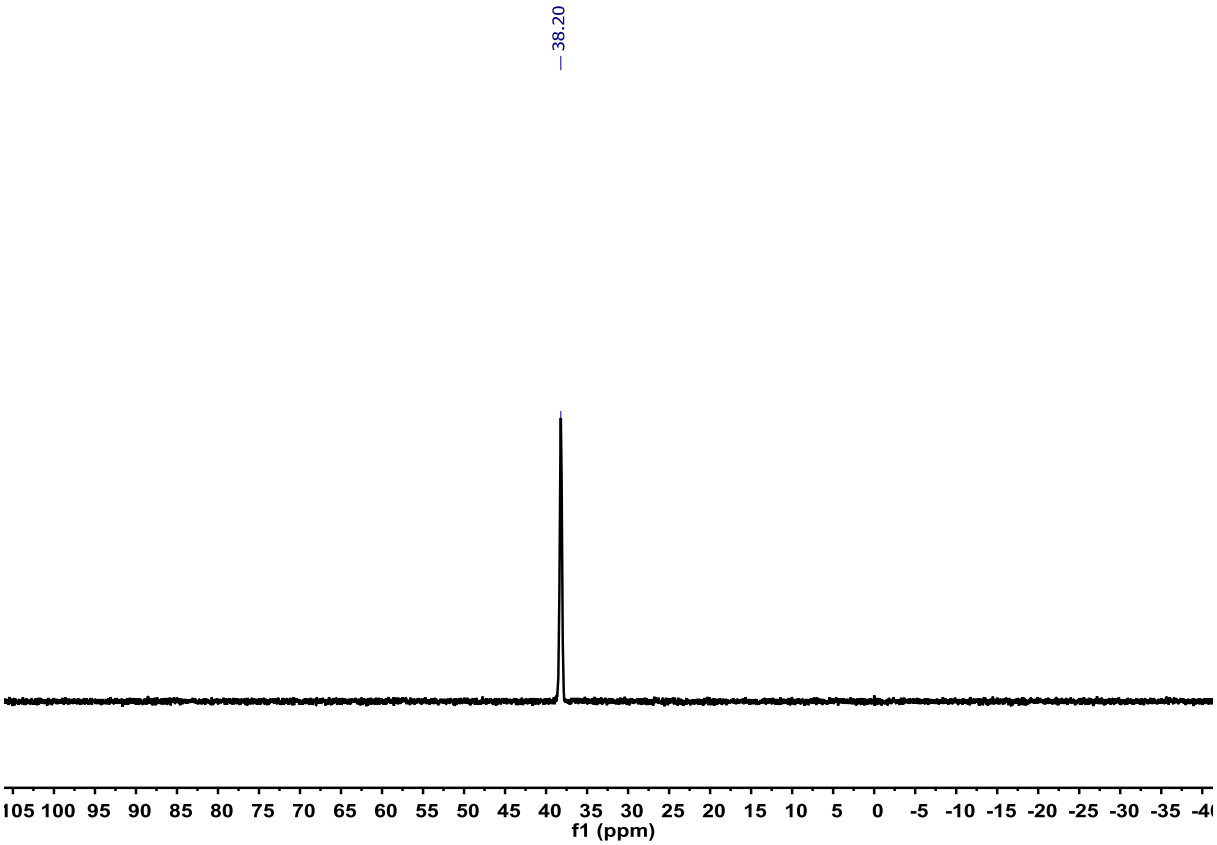

Figure S8. ^{31}P-NMR spectrum of **1-Ac**, recorded in CD_2Cl_2 at room temperature.

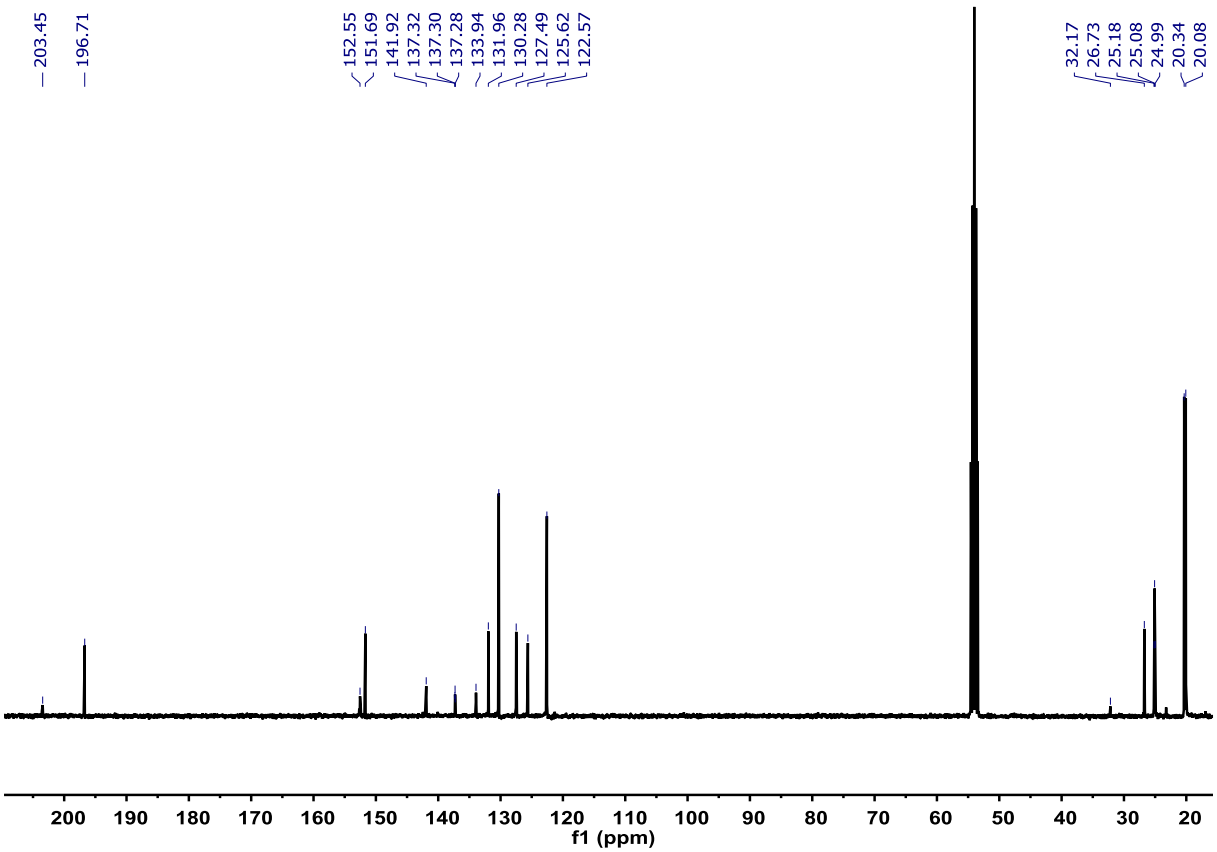

Figure S9. ^{13}C-NMR spectrum of **1-Ac**, recorded in CD_2Cl_2 at room temperature.

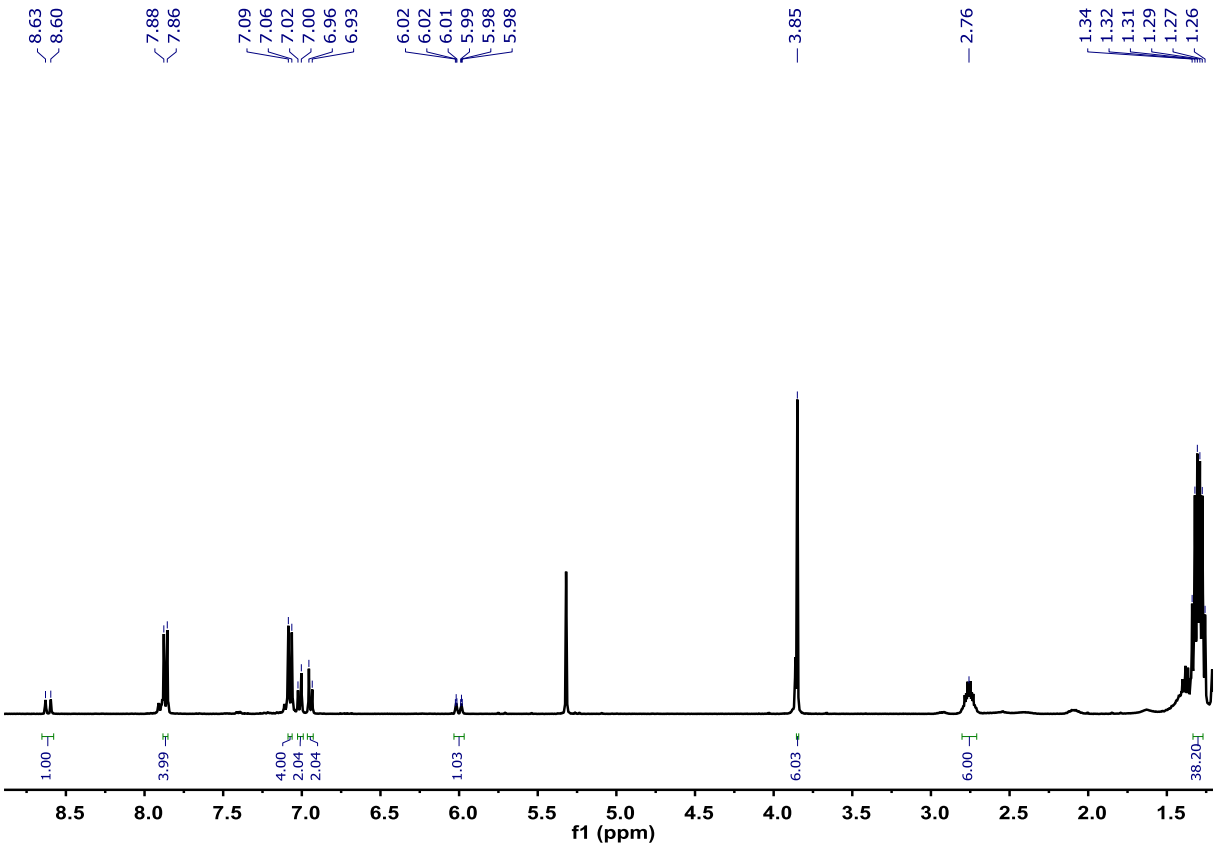

Figure S10. ^{1}H-NMR spectrum of **1-E**, recorded in CD_2Cl_2 at room temperature.

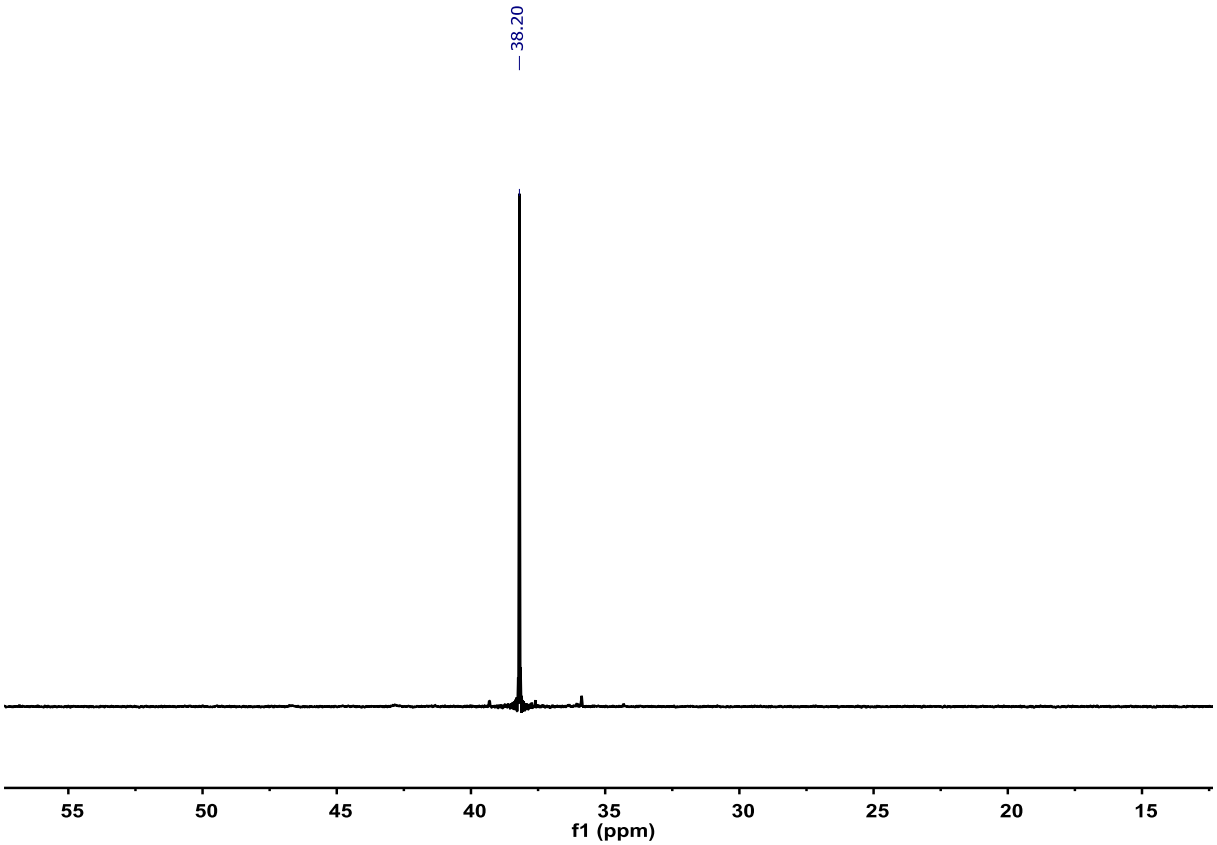

Figure S11. ^{31}P-NMR spectrum of **1-E**, recorded in CD_2Cl_2 at room temperature.

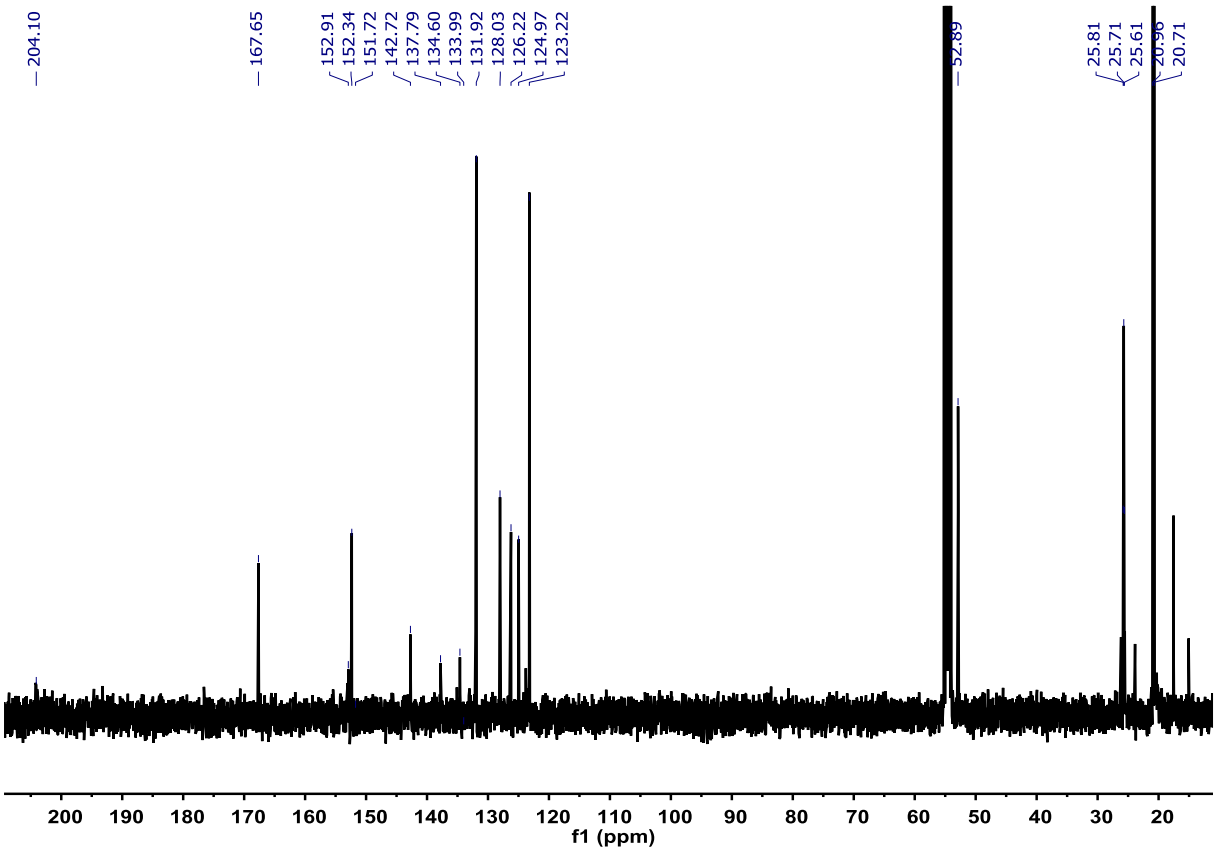

Figure S12. ^{13}C-NMR spectrum of **1-E**, recorded in CD_2Cl_2 at room temperature.

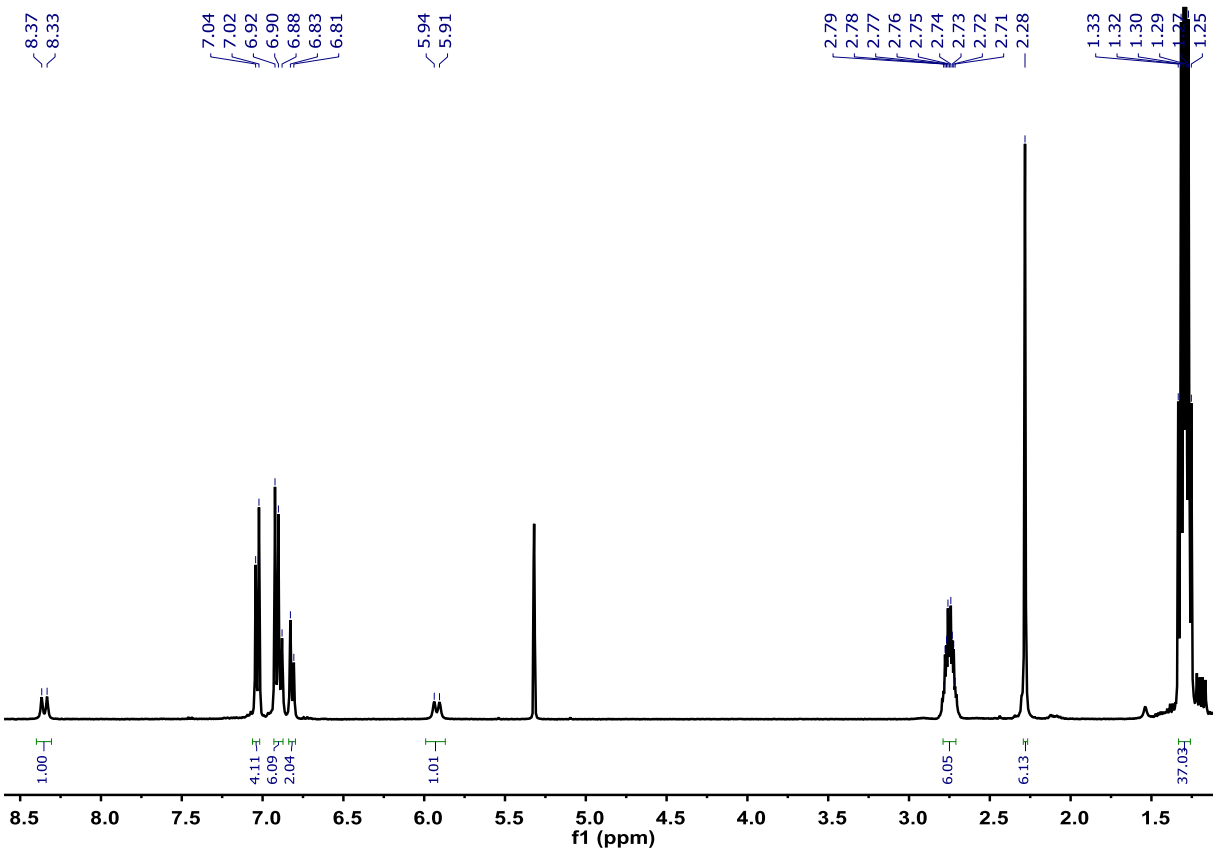

Figure S13. ^{1}H-NMR spectrum of **1-Me**, recorded in CD_2Cl_2 at room temperature.

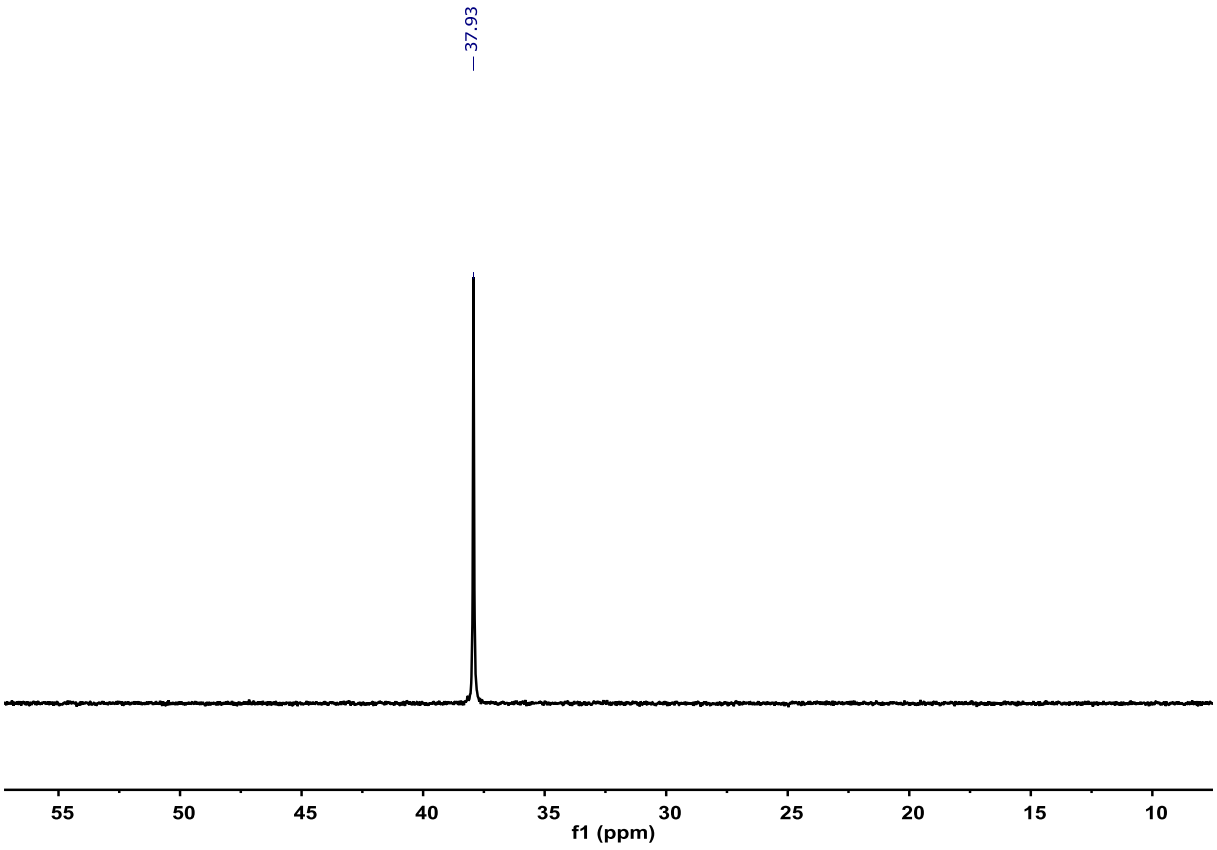

Figure S14. ^{31}P-NMR spectrum of **1-Me**, recorded in CD_2Cl_2 at room temperature.

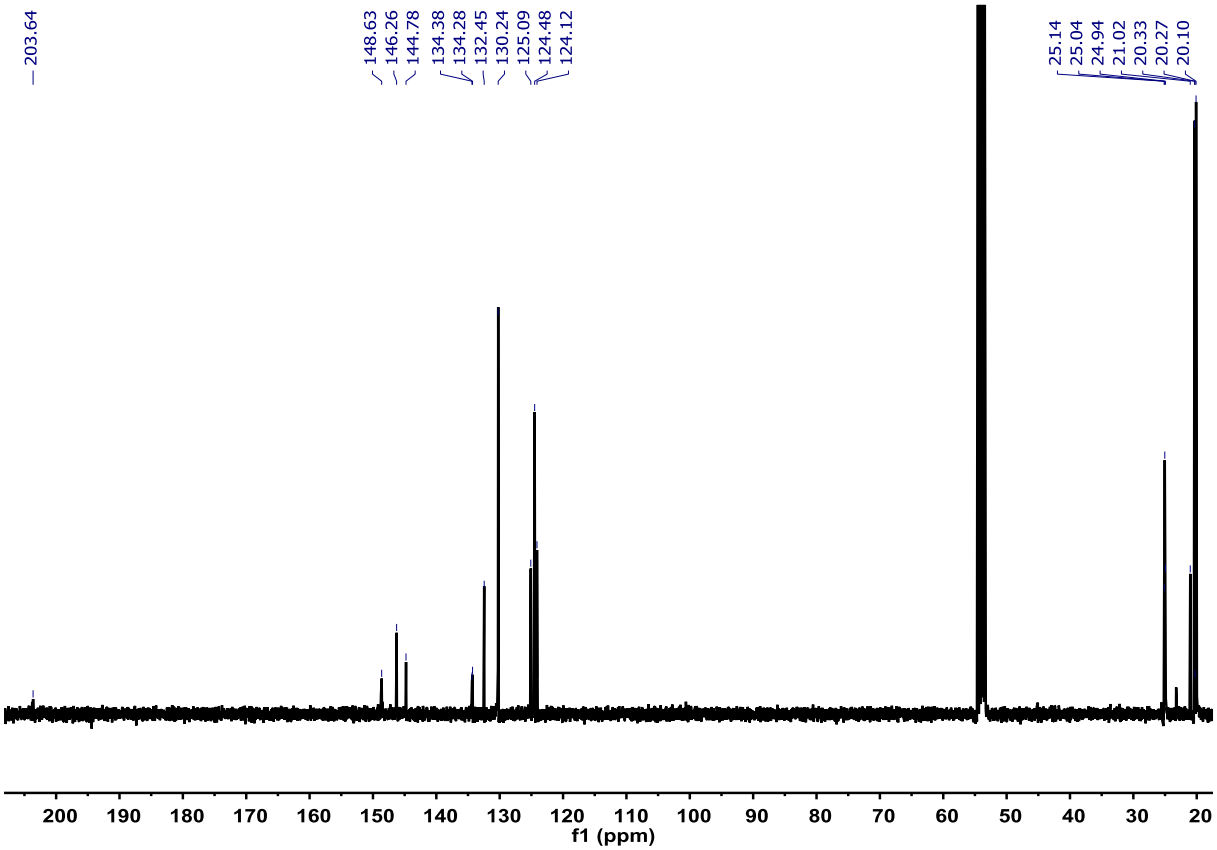

Figure S15. ^{13}C-NMR spectrum of **1-Me**, recorded in CD_2Cl_2 at room temperature.

3. Cyclic Voltammetry

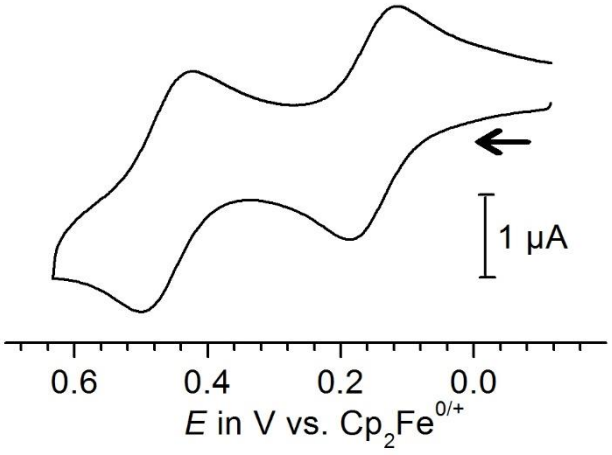

Figure S16. Cyclic Voltammetry of **1-CHO**, measured in DCM, NBu_4PF_6 (0.1 M) as supporting electrolyte.

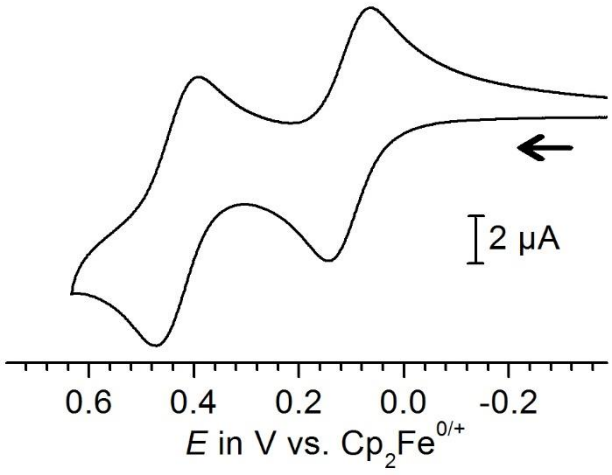

Figure S17. Cyclic Voltammetry of **1-E**, measured in DCM, NBu_4PF_6 (0.1 M) as supporting electrolyte.

4. IR-Spectroelectrochemistry

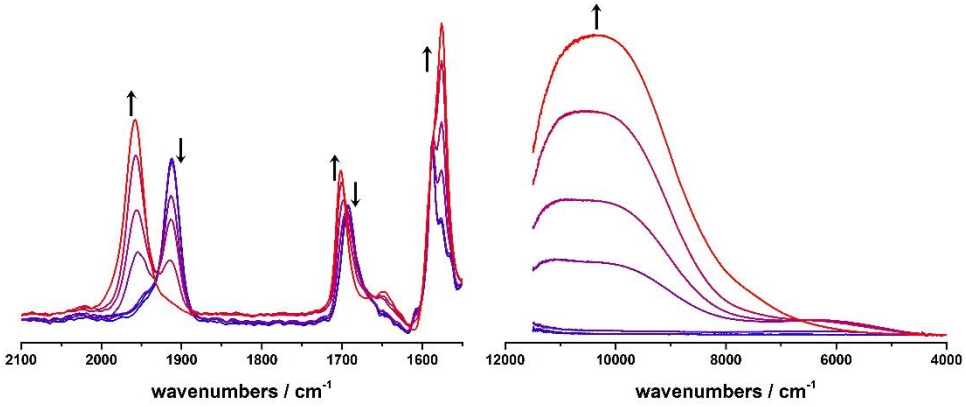

Figure S18. IR-Spectroelectrochemistry of **1-CHO** during the first oxidation; blue neutral and red first oxidation; spectra obtained in 1,2-dichloroethane/ NBu_4PF_6 (0.1M) as supporting electrolyte.

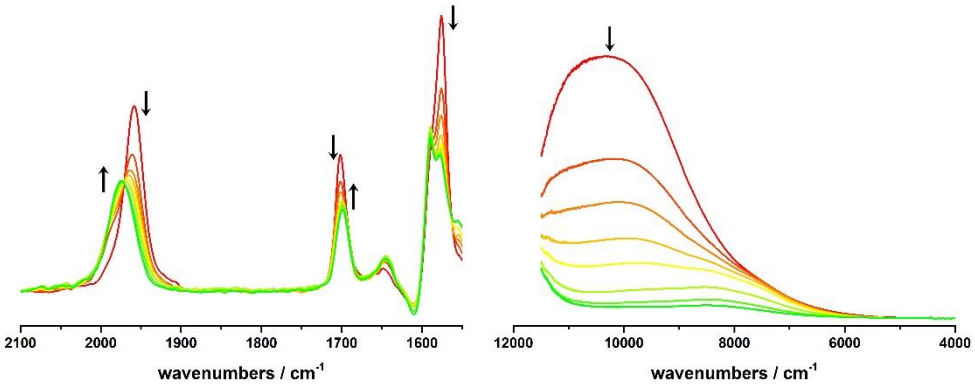

Figure S19. IR-Spectroelectrochemistry of **1-CHO** during the second oxidation; red first oxidation and green second oxidation; spectra obtained in 1,2-dichloroethane/ NBu_4PF_6 (0.1M) as supporting electrolyte.

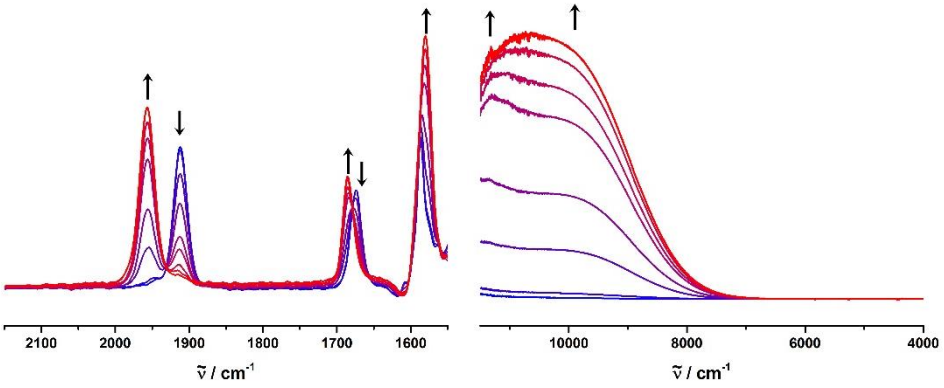

Figure S20. IR-Spectroelectrochemistry of **1-Ac** during the first oxidation; blue neutral and red first oxidation; spectra obtained in 1,2-dichloroethane/ NBu_4PF_6 (0.1M) as supporting electrolyte.

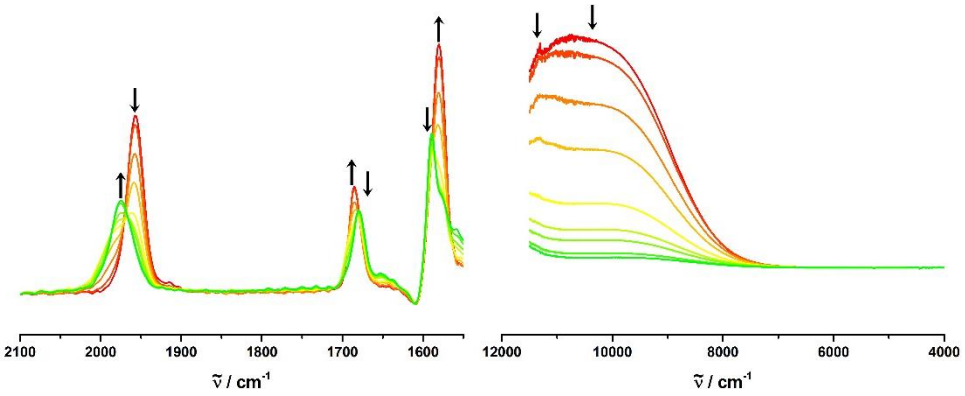

Figure S21. IR-Spectroelectrochemistry of **1-Ac** during the second oxidation; red first oxidation and green second oxidation; spectra obtained in 1,2-dichloroethane/ NBu_4PF_6 (0.1M) as supporting electrolyte.

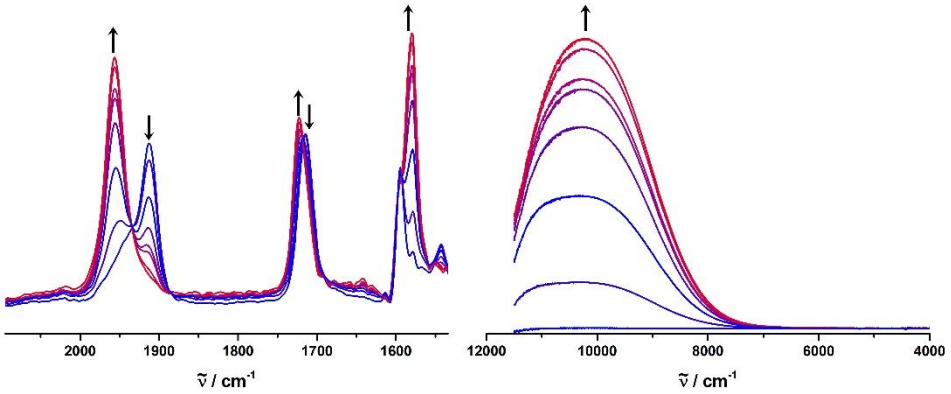

Figure S22. IR-Spectroelectrochemistry of **1-E** during the first oxidation; blue neutral and red first oxidation; spectra obtained in 1,2-dichloroethane/ NBu_4PF_6 (0.1M) as supporting electrolyte.

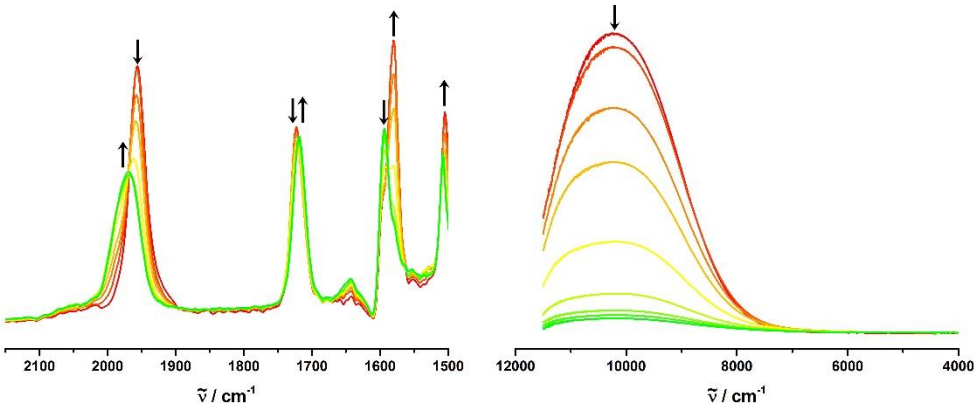

Figure S23. IR-Spectroelectrochemistry of **1-E** during the first oxidation; red first oxidation and green second oxidation; spectra obtained in 1,2-dichloroethane/ NBu_4PF_6 (0.1M) as supporting electrolyte.

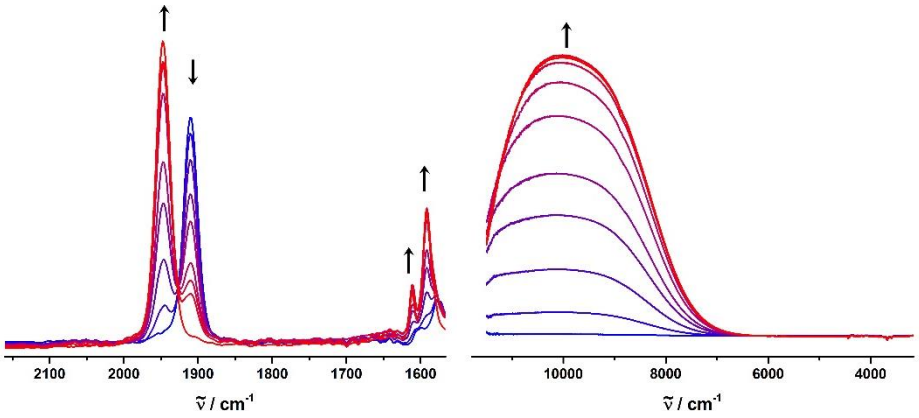

Figure S24. IR-Spectroelectrochemistry of **1-Me** during the first oxidation; blue neutral and red first oxidation; spectra obtained in 1,2-dichloroethane/ NBu_4PF_6 (0.1M) as supporting electrolyte.

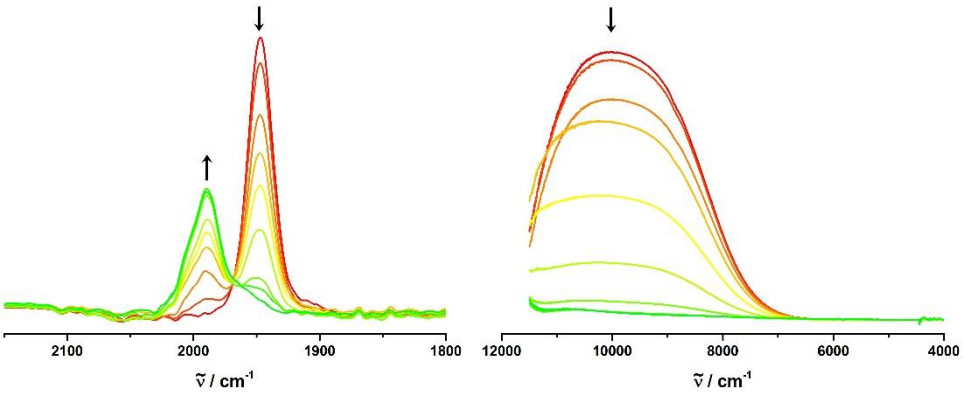

Figure S25. IR-Spectroelectrochemistry of **1-Me** during the second oxidation; red first oxidation and green second oxidation; spectra obtained in 1,2-dichloroethane/ NBu_4PF_6 (0.1M) as supporting electrolyte.

5. EPR spectra of the radical cations and dications at room temperature and in frozen DCM glass

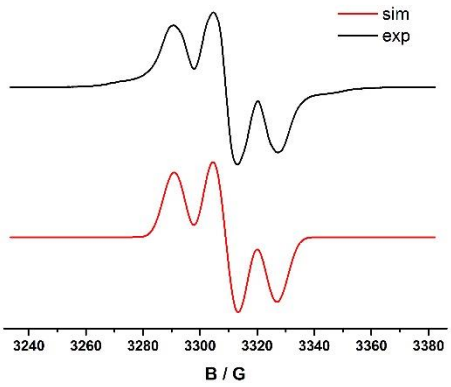

Figure S26. EPR spectrum of **1-Ac**$^{\bullet+}$ measured in dichloromethane at room temperature, black: experimental spectrum, red: simulated spectrum.

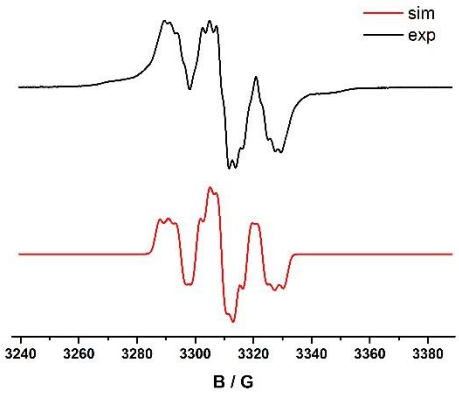

Figure S27. EPR spectrum of **1-E**$^{\bullet+}$ measured in dichloromethane at room temperature, black: experimental spectrum, red: simulated spectrum.

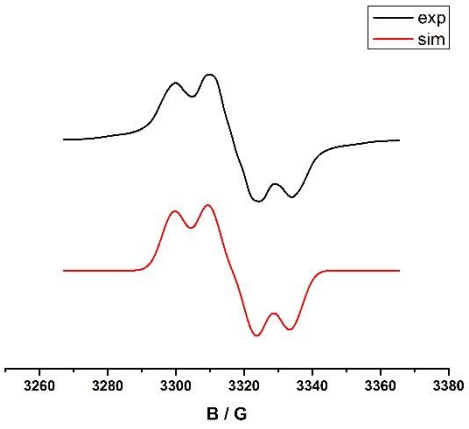

Figure S28. EPR spectrum of **1-Me**$^{\bullet+}$ measured in dichloromethane at room temperature, black: experimental spectrum, red: simulated spectrum.

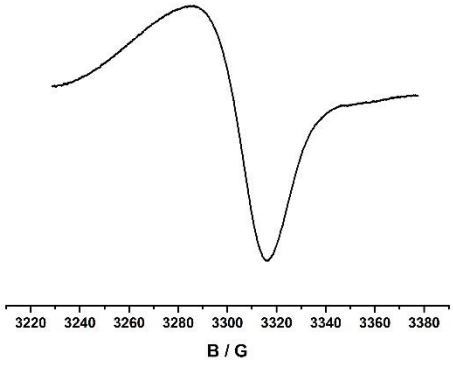

Figure S29. EPR spectrum of **1-CHO**$^{+}$ measured in dichloromethane in frozen dichloromethane glass (-120 °C).

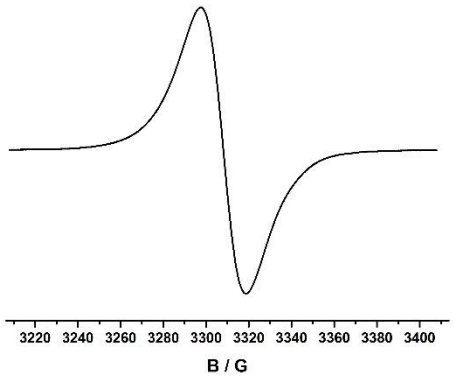

Figure S30. EPR spectrum of **1-Ac**$^{\bullet+}$ measured in dichloromethane in frozen dichloromethane glass (-120 °C).

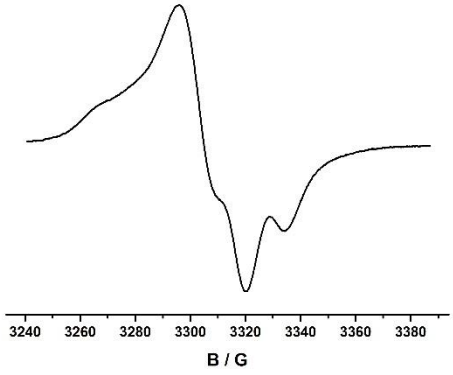

Figure S31. EPR spectrum of **1-E**$^{\bullet+}$ measured in dichloromethane in frozen dichloromethane glass (-120 °C).

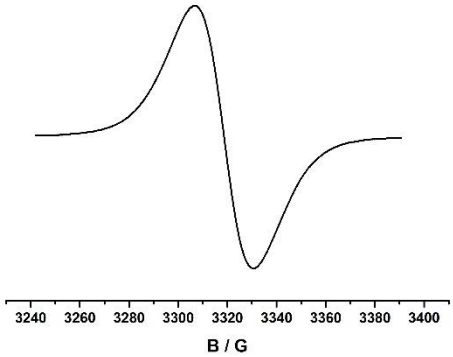

Figure S32. EPR spectrum of **1-Me**$^{\bullet+}$ measured in dichloromethane in frozen dichloromethane glass (-120 °C).

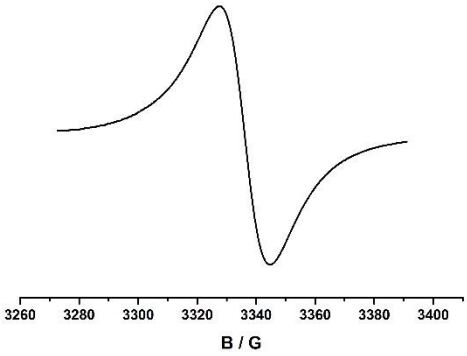

Figure S33. EPR spectrum of **1-CHO**$^{2\bullet+}$ in dichloromethane in frozen dichloromethane glass (-120 °C).

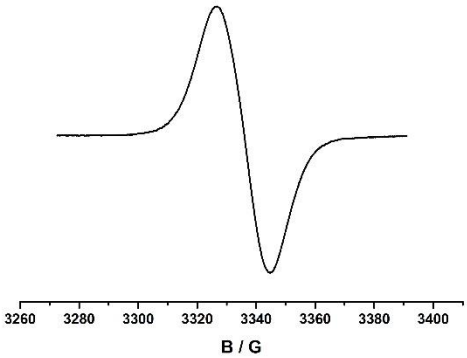

Figure S34. EPR spectrum of **1-Ac**$^{2\bullet+}$ measured in dichloromethane at room temperature.

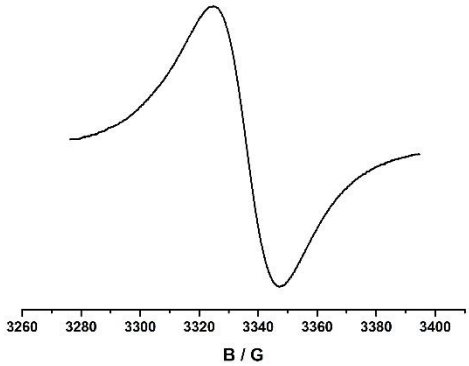

Figure S35. EPR spectrum of **1-Ac**$^{2\bullet+}$, measured in dichloromethane in frozen dichloromethane glass (-120 °C).

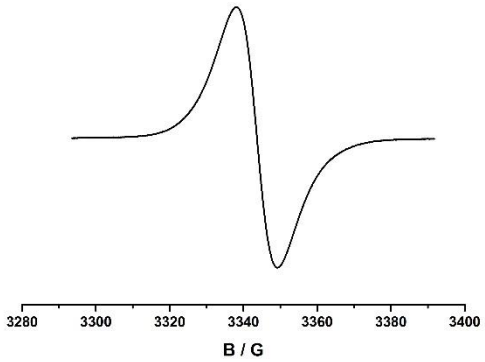

Figure S36. EPR spectrum of **1-E**$^{2\bullet+}$, measured in dichloromethane in frozen dichloromethane glass (-120 °C).

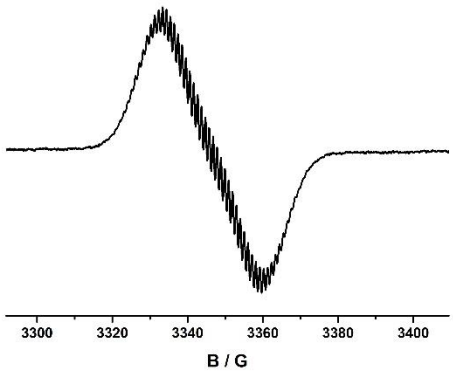

Figure S37. EPR spectrum of **1-Me**$^{2\bullet+}$, measured in dichloromethane at room temperature.

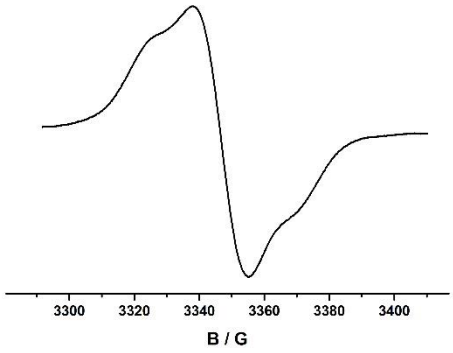

Figure S38. EPR spectrum of **1-Me**$^{2\bullet+}$, measured in dichloromethane in frozen dichloromethane glass (-120 °C).

6. **Fragment contributions to selected MOs and calculated structure parameters of 1-CHO^{n,} 1-Me^{n+}, and 1-OMe^{n+}**

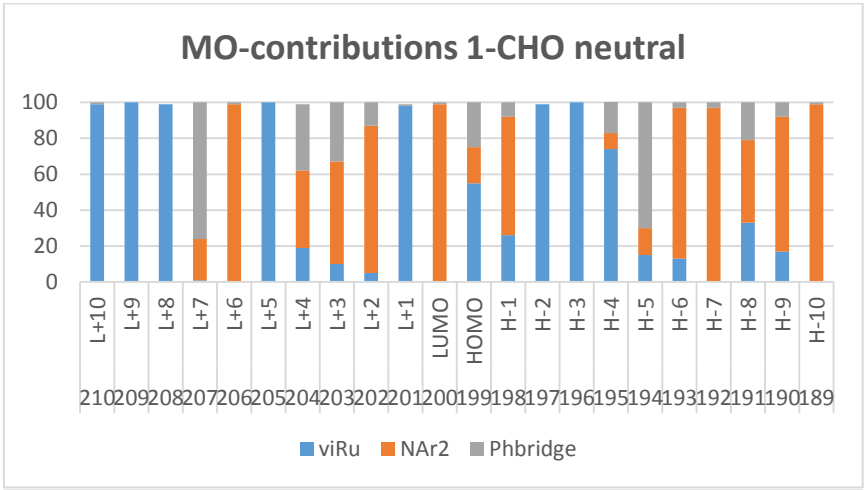

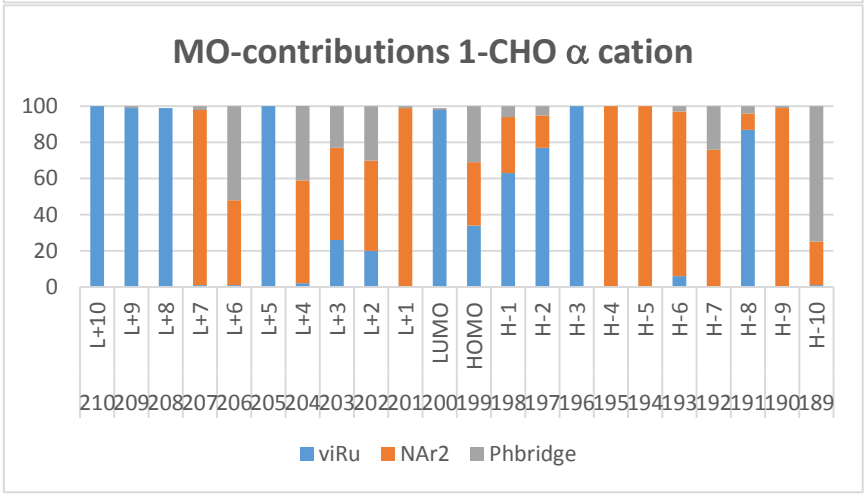

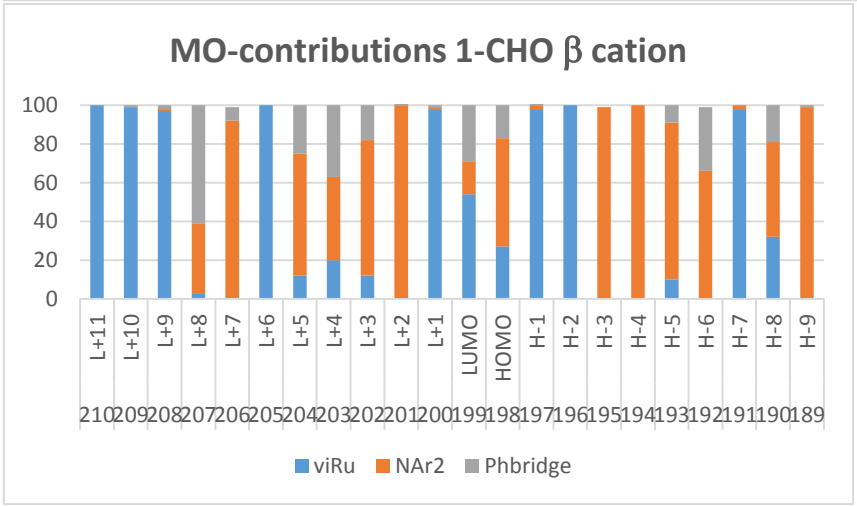

Figure S39. Molecular orbital contributions of the individual fragments to the frontier orbitals of complex **1-CHO** in its various oxidation states.

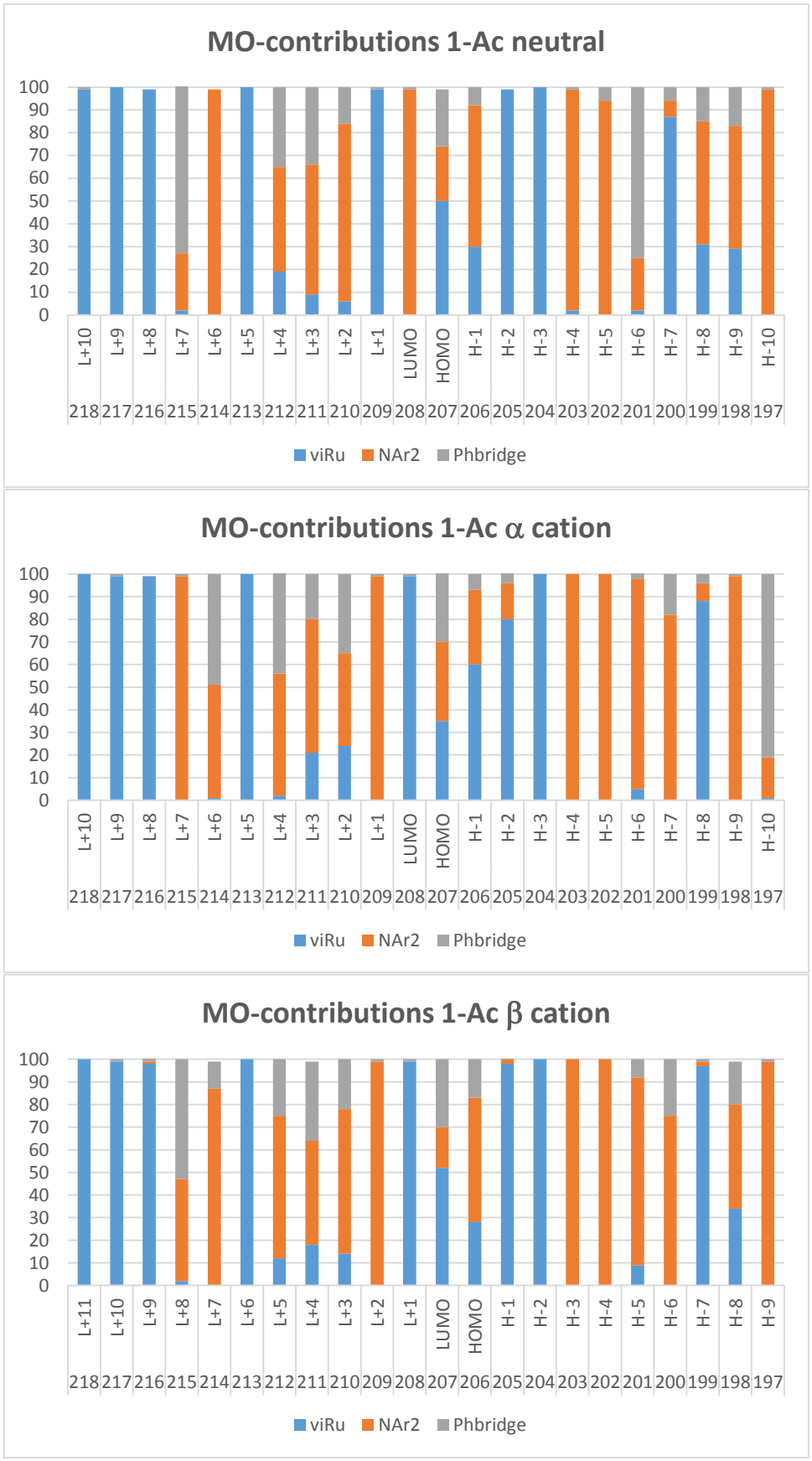

Figure S40. Molecular orbital contributions of the individual fragments to the frontier orbitals of complex **1-Ac** in its various oxidation states.

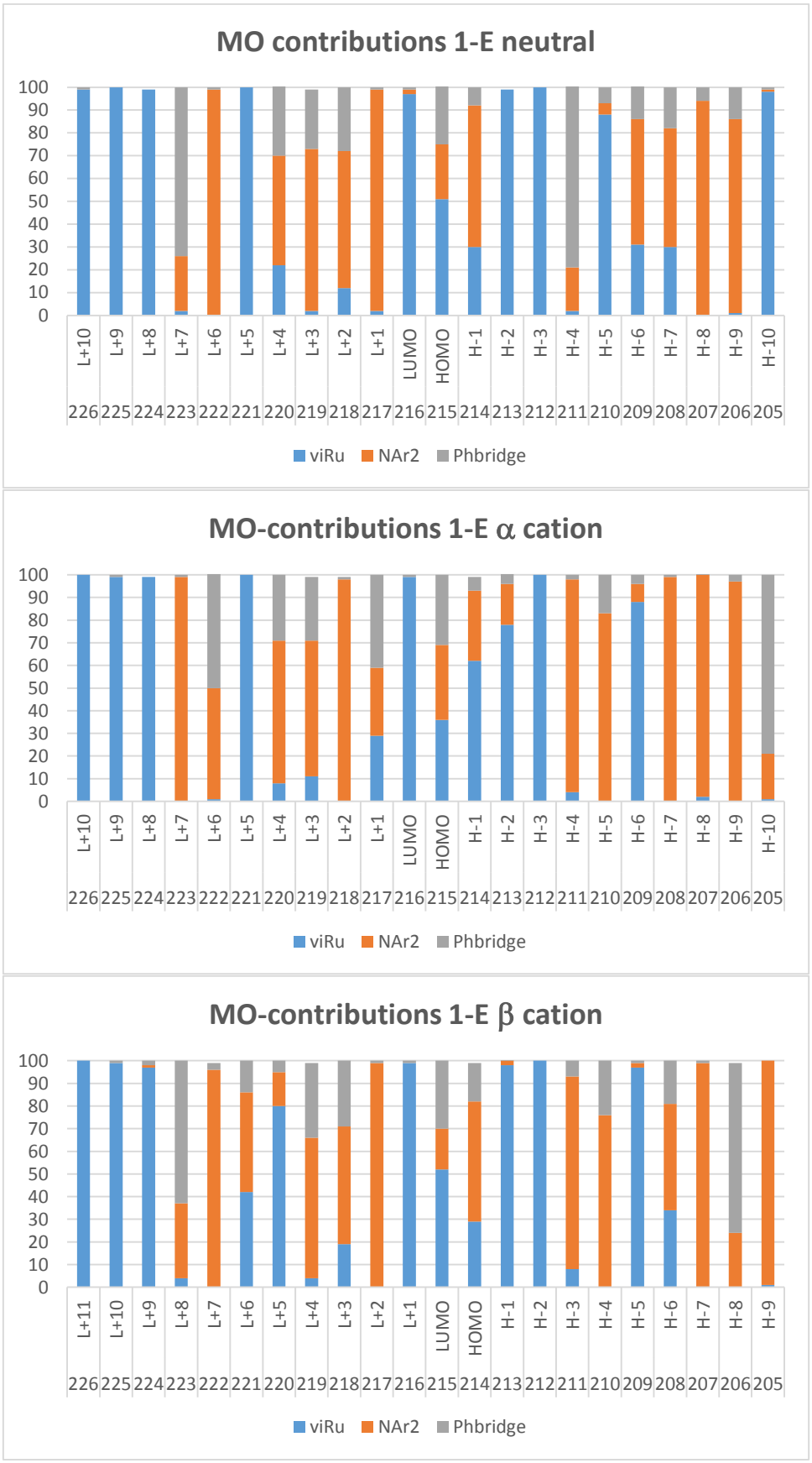

Figure S41. Molecular orbital contributions of the individual fragments to the frontier orbitals of complex **1-E** in its various oxidation states.

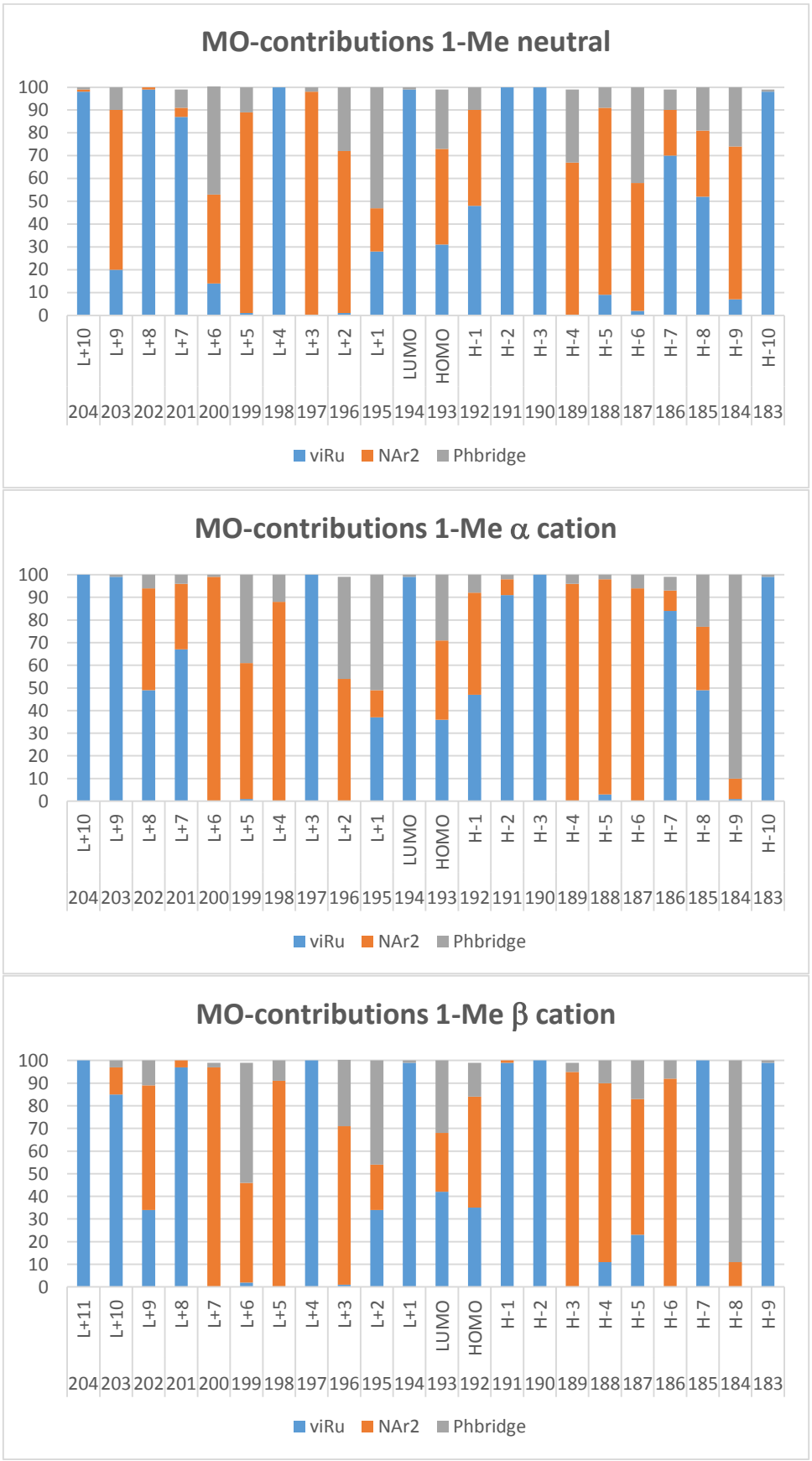

Figure S42. Molecular orbital contributions of the individual fragments to the frontier orbitals of complex **1-Me** in its various oxidation states..

Table S1. Calculated structure parameters of complexes 1-CHO^{n}, 1-Me^{n+}, and 1-OMe^{n+} [a]

	1-CHO	**1-CHO^{+}**	**1-CHO^{2+}**	**1-Me**	**1-Me^{+}**	**1-Me^{2+}**	**1^{Me}-OMe**	**1^{Me}-OMe^{+}**	**1^{Me}-OMe^{2+}**
Ru-Cl	2.448	2.417	2.395	2.450	2.423	2.400	2.449	2.432	2.411
Ru-P	2.420, 2.425	2.444, 2.445	2.460, 2.460	2.416, 2.421	2.440, 2.442	2.460, 2.457	2.363	2.379	2.394
Ru-C_{CO}	1.805	1.826	1.840	1.803	1.819	1.838	1.807	1.820	1.839
Ru-C_{vi}	1.973	1.901	1.904	1.979	1.916	1.899	1.985	1.932	1.871
C=C	1.349	1.388	1.381	1.349	1.381	1.384	1.348	1.372	1.409
=C-$C_{phenylene}$	1.465	1.426	1.453	1.467	1.426	1.451	1.468	1.434	1.397
N-$C_{phenylene}$	1.425	1.386	1.419	1.413	1.374	1.423	1.407	1.378	1.355
N-C_{aryl1}	1.402	1.417	1.397	1.412	1.422	1.395	1.414	1.416	1.412
N-C_{aryl2}	1.402	1.418	1.395	1.413	1.424	1.396	1.415	1.418	1.413
Ru[b] vs phenylene[c]	10.1	3.4	5.0	14.5	3.4	2.9			
NC_3[d] vs phenylene[c]	53.3	28.8	45.2	39.8	24.0	47.6	34.9	26.7	26.2
NC_3[d] vs $Aryl_1$[e]	33.2	45.1	35.2	39.3	48.2	28.5	44.4	45.8	44.3
NC_3[d] vs $Aryl_2$[e]	33.4	44.5	34.3	67.9	47.8	34.0	43.2	44.5	43.2

[a]Calculated on the pbe1pbe/ 6-31G(d), Ru: MWB28 level of theory; distances in Å and angles in degrees; data for complexes **1^{Me}-OMe^{n+}** with PMe_3 instead of P^iPr_3 lignds from ref. 5. [b]Best planes containing the Ru and the Cl atoms, the CO ligand, and the vinylic carbon atoms. [c]Best plane through the carbon atoms of the phenylene linker. [d]Plane containing the nitrogen and the immediately attached carbon atoms of the phenyl rings. [e]Planes of the peripherally appended aryl rings.

7. Spin Density Plots of Radical Cations and Dications

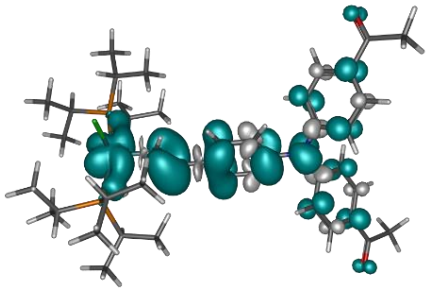

Figure S43. Calculated spin density map of **1-Ac**$^{\bullet+}$

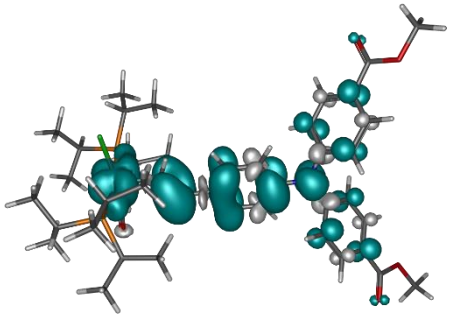

Figure S44. Calculated spin density of map **1-E**$^{\bullet+}$

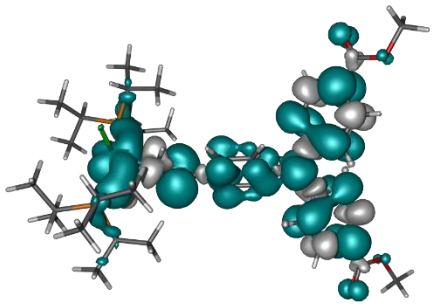

Figure S45. Calculated spin density of **1-E**$^{2\bullet+}$

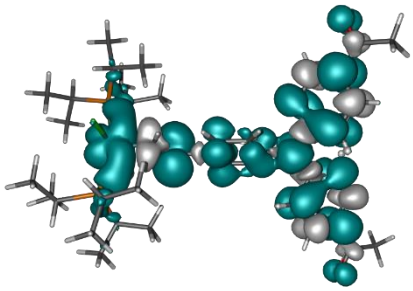

Figure S46. Calculated spin density of **1-Ac**$^{2\bullet+}$

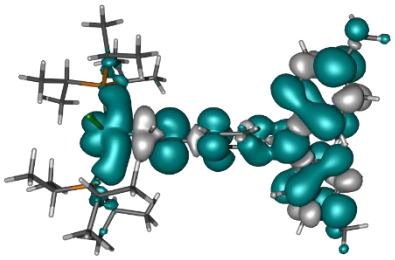

Figure S47. Calculated spin density of **1-Me**$^{2\bullet+}$

8. UV/vis/NIR Spectroelectrochemistry

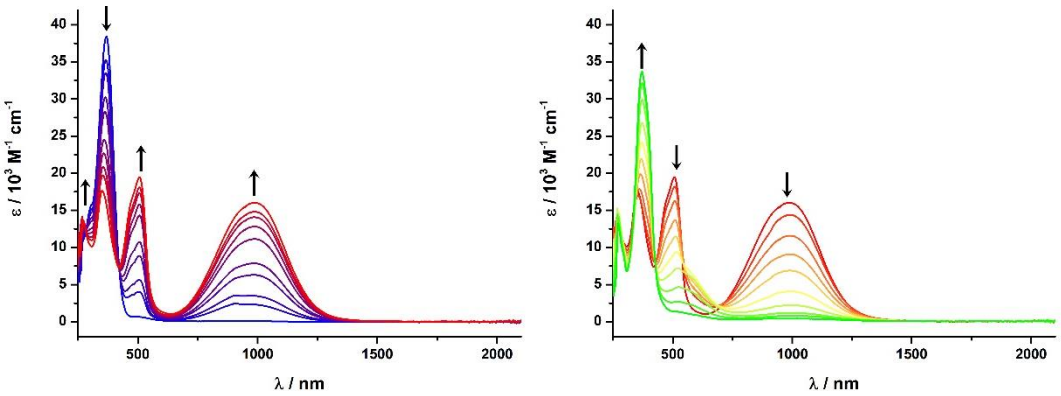

Figure S48. UV/vis/NIR-Spectroelectrochemistry of **1-Ac** during the first and second oxidation; blue neutral, red first oxidation, green second oxidation; spectra obtained in 1,2-dichloroethane/ NBu_4PF_6 (0.1M) as supporting electrolyte.

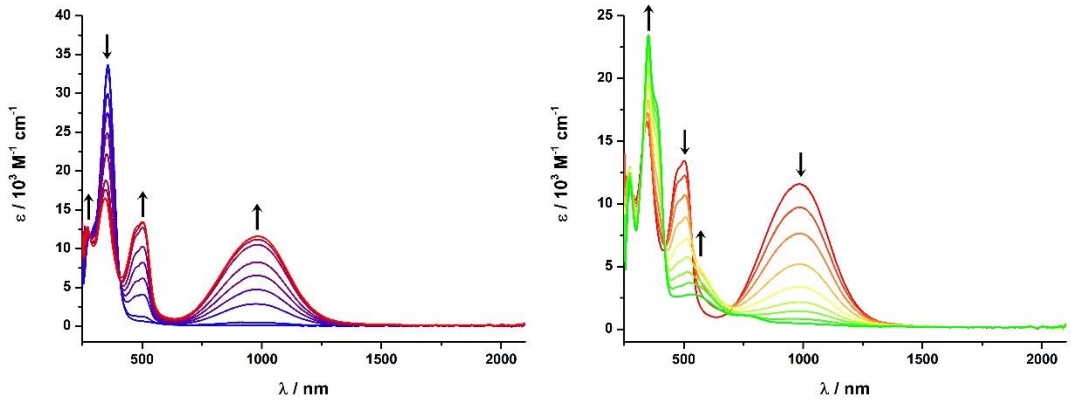

Figure S49. UV/vis/NIR-Spectroelectrochemistry of **1-E** during the first and second oxidation; blue neutral, red first oxidation, green second oxidation; spectra obtained in 1,2-dichloroethane/ NBu_4PF_6 (0.1M) as supporting electrolyte.

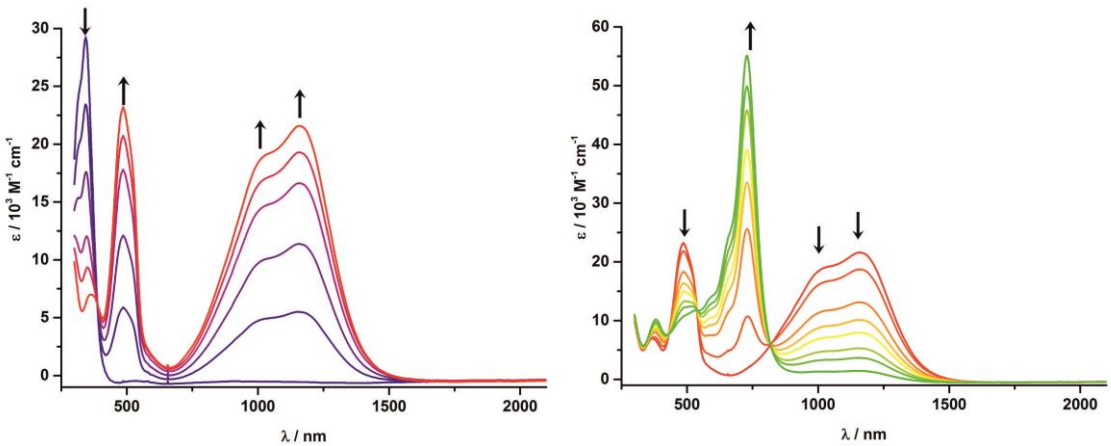

Figure S50. UV/vis/NIR-Spectroelectrochemistry of **1-OMe** during the first and second oxidation; blue neutral, red first oxidation, green second oxidation; spectra obtained in 1,2-dichloroethane/ NBu_4PF_6 (0.1M) as supporting electrolyte.

9. TD-DFT calculated transitions and spectra

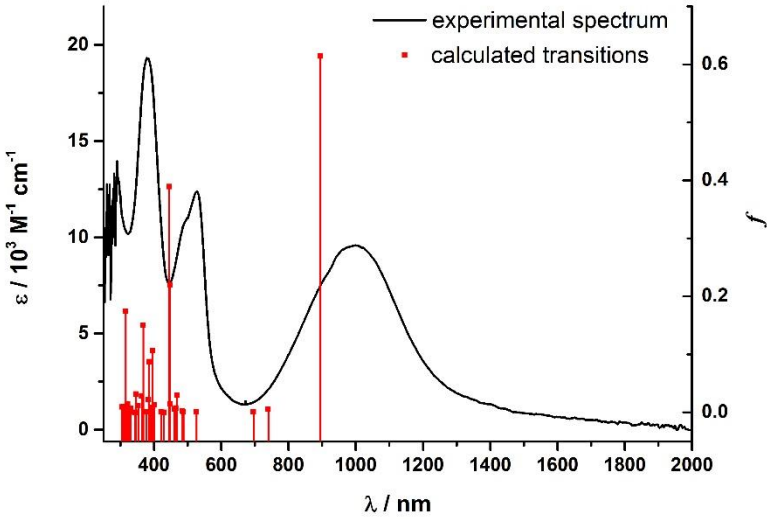

Figure S51. Overlay of experimental UV/vis/NIR spectrum of **1-CHO**$^{\bullet+}$ (black) and its calculated transitions (red).

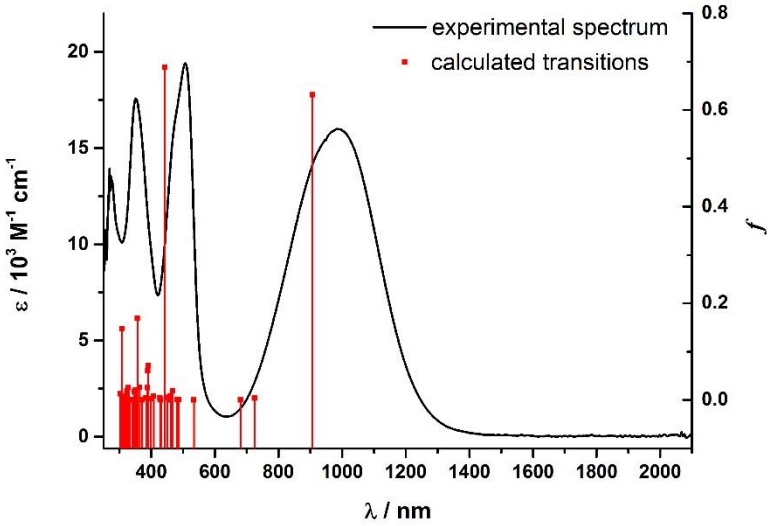

Figure S52. Overlay of experimental UV/vis/NIR spectrum of **1-Ac**$^{\bullet+}$ (black) and its calculated transitions (red).

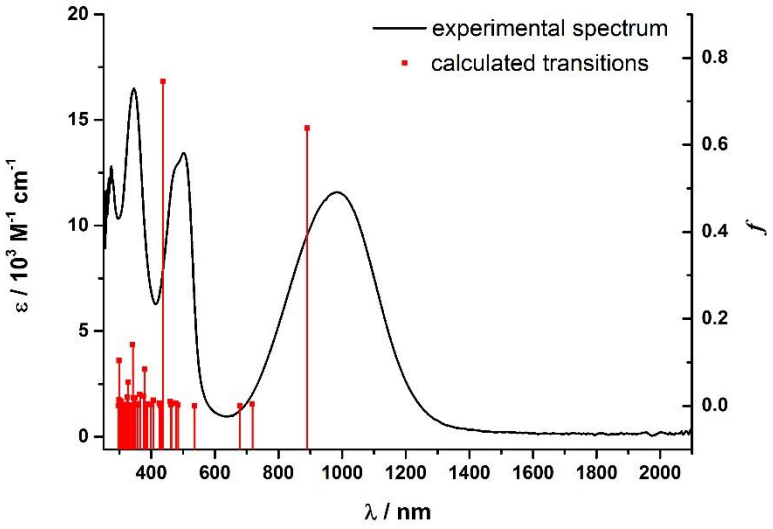

Figure S53. Overlay of experimental UV/vis/NIR spectrum of **1-E**$^{\bullet+}$ (black) and its calculated transitions (red).

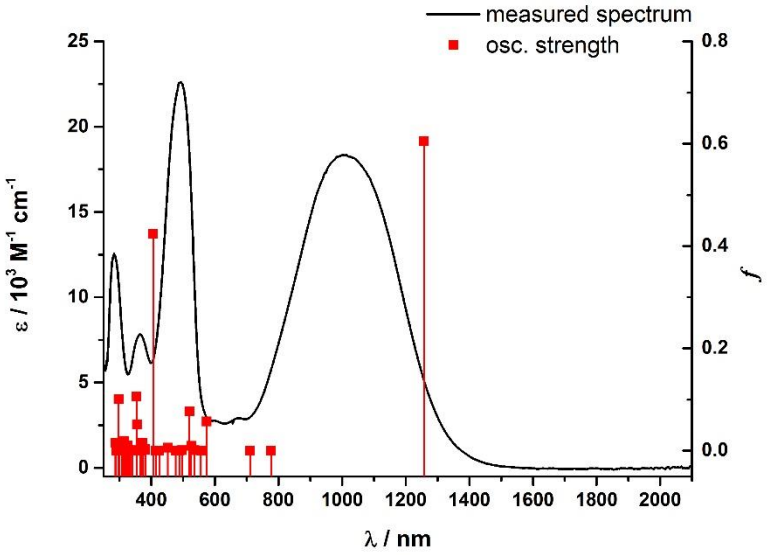

Figure S54. Overlay of experimental UV/vis/NIR spectrum of **1-Me**$^{\bullet+}$ (black) and its calculated transitions (red).

Table S2. Calculated electronic transitions for the complexes in their neutral and radical cation states.

Calculated transitions for 1-CHO

transition	energy/ cm^{-1}	wavelength / nm	osc. strength	major contribution	minor contribution
1	23004	435	0.264	HOMO→ LUMO (98%)	--
2	26327	380	0.781	HOMO→L+2 (87%)	H-3→ L+1 (8%)
3	28767	348	0.465	H-1→ LUMO (97%)	--

Calculated transitions for 1-CHO^+

transition	energy/ cm^{-1}	wavelength / nm	osc. strength	major contribution	minor contribution
1	11167	896	0.614	HOMO(B) →LUMO(B) (96%)	
2	22321 4	448	0.220	HOMO(A) →L+2(A) (28%), H-4(B) →LUMO(B) (12%), H-3(B) → LUMO(B) (36%)	H-5(A) → L+1(A) (2%), H-5(B) → LUMO(B) (2%), H-4(B) →L+2(B) (5%), H-3(B→ L+3(B) (2%)
3	22349	447	0.015	H-4(B) → LUMO(B) (65%), H-3(B) → LUMO(B) (11%)	H-4(A) → L+1(A) (2%), HOMO(A) → L+2(A) (2%), H-6(B) → LUMO(B) (2%), H-4(B) → L+3(B) (4%), H-3(B) → L+2(B) (8%)
4	22432	446	0.389	HOMO(A) → L+2(A) (48%), H-3(B) → LUMO(B) (24%)	HOMO(A) → L+3(A) (3%), H-5(B) → LUMO(B) (5%), H-4(B) → L+2(B) (3%), H-3(B) → L+3(B) (2%)

Calculated transitions for 1-Ac

transition	energy/ cm^{-1}	wavelength / nm	osc. strength	major contribution	minor contribution
1	24049	416	0.314	HOMO→ LUMO (97%)	-
2	27011	370	0.406	H-3→ L+1 (37%), HOMO→L+2 (57%)	
3	29812	335	0.390	H-1→ LUMO (96%)	

Calculated transitions for 1-Ac^+

transition	energy/ cm^{-1}	wavelength / nm	osc. strength	major contribution	minor contribution
1	11031	906.50974	0.632	HOMO(B)→ LUMO(B) (96%)	-
2	22603	442	0.688	HOMO(A) → L+2(A) (81%)	HOMO(A) → L+3(A) (2%)
3	28042	3567	0.168	HOMO(A) → L+1(A) (42%), HOMO(B) → L+2(B) (39%)	H-9(B) → LUMO(B) (2%), H-9(B) → L+3(B) (2%)

Calculated transitions for 1-E

selected transition	energy/ cm^{-1}	wavelength / nm	osc. strength	major contribution	minor contribution
1	18839	531	0.005	H-1-→ LUMO (13%), HOMO→ LUMO (79%)	-
2	25535	392	0.340	HOMO→ L+1 (95%)	H-1→ L+1 (3%)
3	27964	358	0.971	HOMO→ L+2 (93%)	H-3→ LUMO (2%)

Calculated transitions for 1-E^+

selected transition	energy/ cm^{-1}	wavelength / nm	osc. strength	major contribution	minor contribution
1	11227	891	0.638	HOMO(B) → LUMO(B) (96%)	-
3	23297	429	0.003	HOMO(A) → L+2(A) (34%), H-7(B) → LUMO(B) (12%), HOMO(B) → L+2(B) (12%)	H-2(A) → L+2(A) (3%), H-1(A) → L+2(A) (7%), H-8(B) → LUMO(B) (7%), H-7(B) → L+3(B) (2%), H-6(B) → L+2(B) (2%), H-4(B) → LUMO(B) (4%)
2	22880	437	0.745	HOMO(A) → L+1(A) (84%)	-

Calculated transitions for 1-Me

selected transition	energy/ cm^{-1}	wavelength / nm	osc. strength	major contribution	minor contribution
1	17998	556	0.005	H-1→LUMO (23%), HOMO→LUMO (72%)	-
2	28526	351	0.977	HOMO→L+1 (96%)	-
3	31568	317	0.300	HOMO→L+3 (95%)	H-1->L+3 (3%)

Calculated transitions for 1-Me^+

selected transition	energy/ cm^{-1}	wavelength / nm	osc. strength	major contribution	minor contribution
1	7953	1257	0.605	HOMO(B) →LUMO(B) (98%)	
2	22138	452	0.006	HOMO(A) →LUMO(A) (21%), HOMO(B) →L+1(B) (57%)	H-1(A) →LUMO(A) (5%), H-7(B) →L+1(B) (3%), H-4(B) →L+1(B) (3%), H-1(B) →L+1(B) (6%)
3	24598	407	0.424	HOMO(A) →L+1(A) (67%), HOMO(B) →L+2(B) (10%)	H-1(A) →L+1(A) (2%), H-12(B) →LUMO(B) (4%), H-7(B) →L+2(B) (2%)

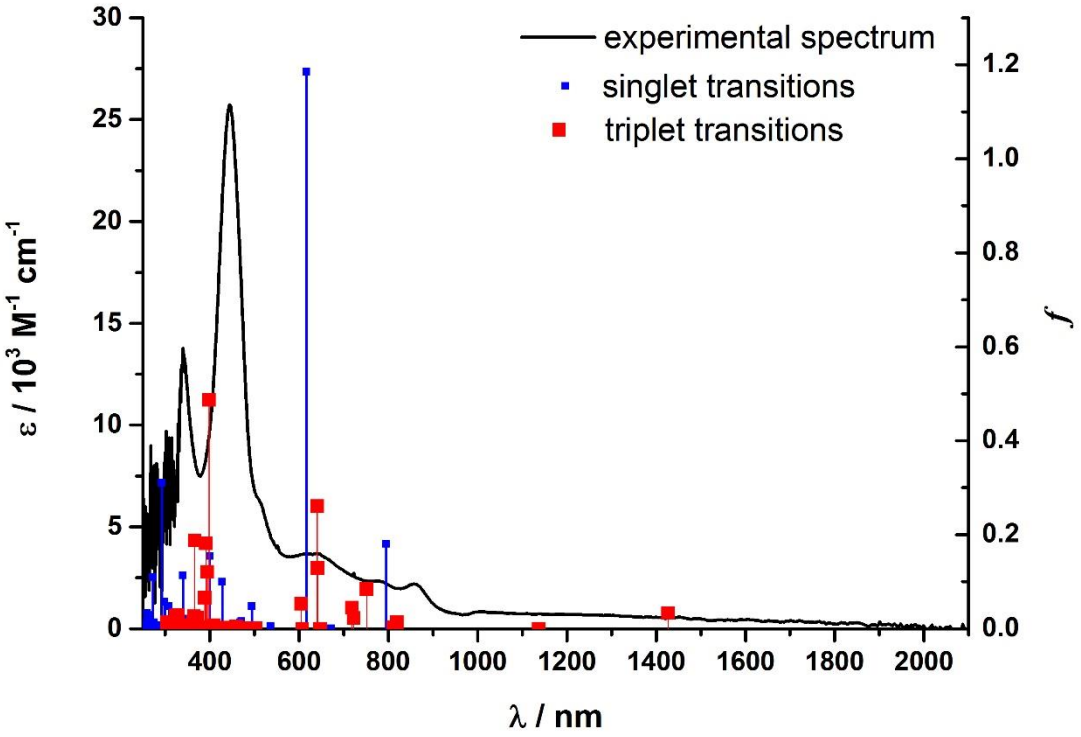

Figure S55. Comparison between calculated and experimental UV/vis/NIR spectra of **1-CHO**$^{2+}$ (black) in its singlet state (blue bars) and its triplet state (red bars).

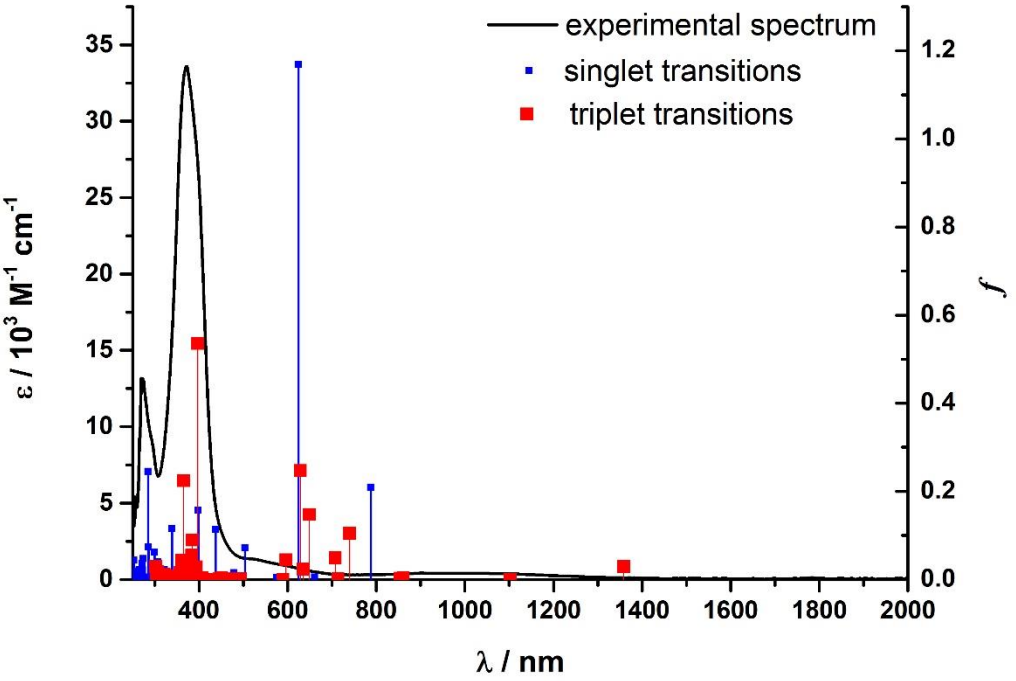

Figure S56. Comparison between calculated and experimental UV/vis/NIR spectra of **1-Ac**$^{2+}$ (black) in its singlet state (blue bars) and its triplet state (red bars).

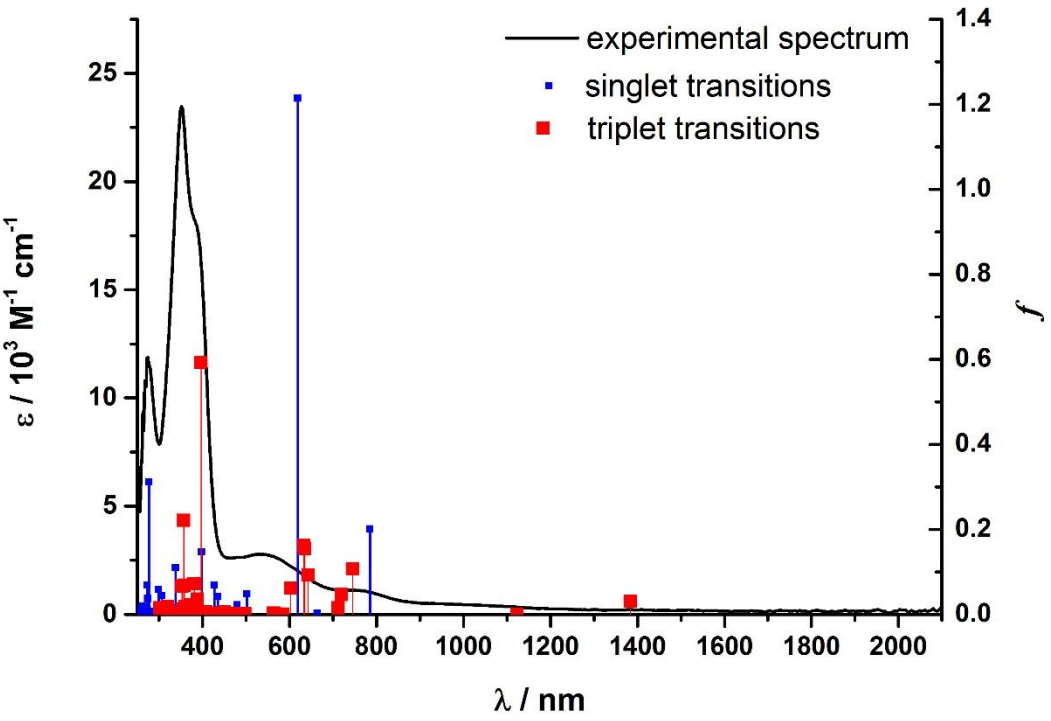

Figure S57. Comparison between calculated and experimental UV/vis/NIR spectra of **1-E**$^{2+}$ (black) in its singlet state (blue bars) and its triplet state (red bars).

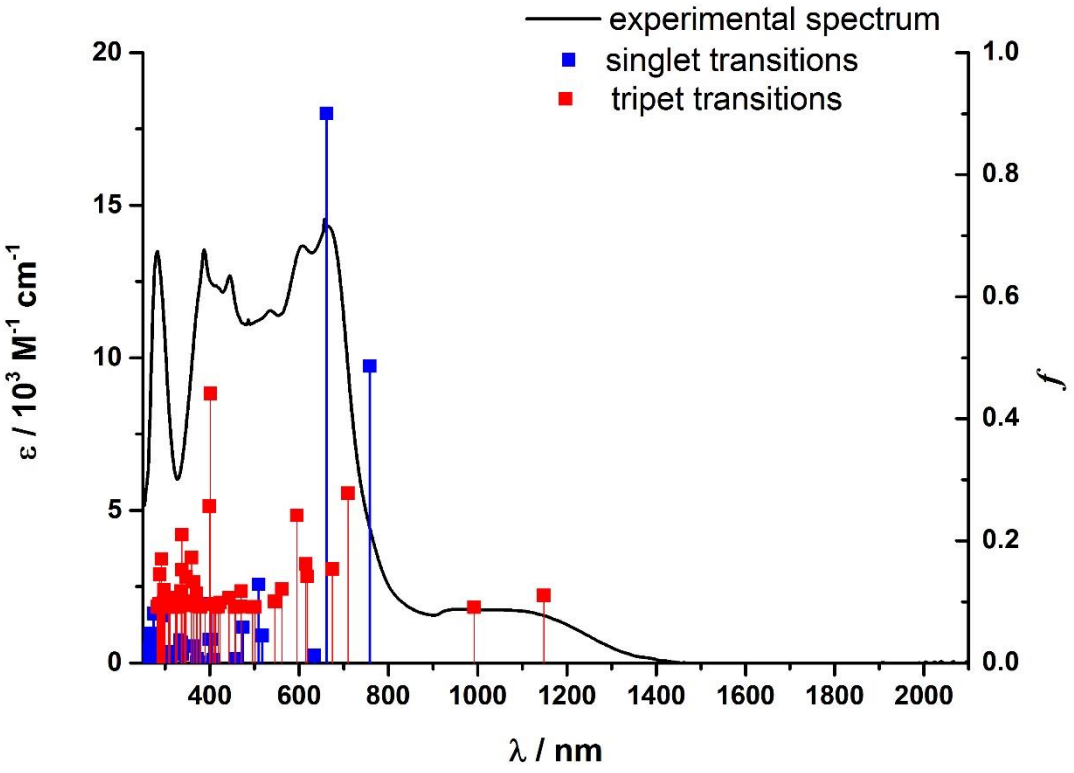

Figure S58. Comparison between calculated and experimental UV/vis/NIR spectra of **1-Me**$^{2+}$ (black) in its singlet state (blue bars) and its triplet state (red bars).

10. Vis/NIR spectra of the radical cations in various solvents

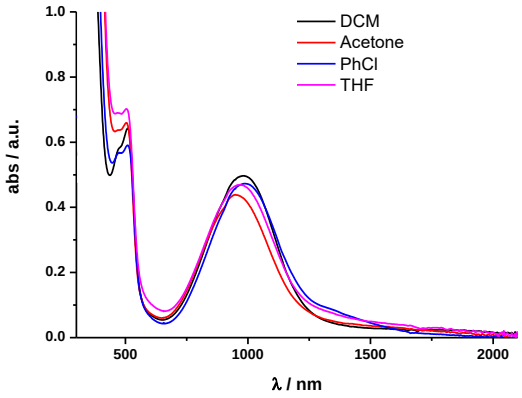

Figure S59. Vis/NIR spectra of **1-CHO**$^{\bullet+}$ in dichloromethane, acetone, chlorobenzene and THF.

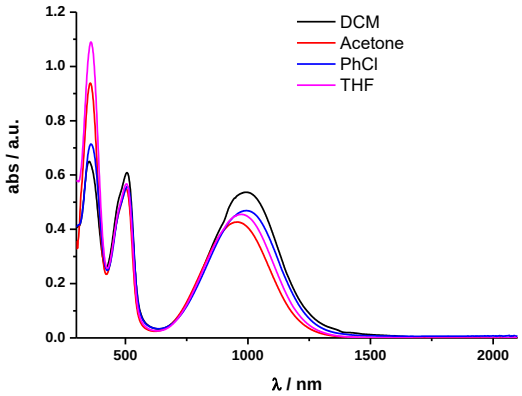

Figure S60. Vis/NIR spectra of **1-Ac**$^{\bullet+}$ in dichloromethane, acetone, chlorobenzene and THF.

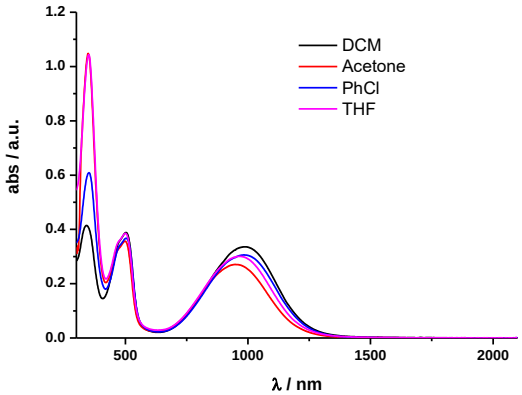

Figure S61. Vis/NIR spectra of **1-E**$^{\bullet+}$ in dichloromethane, acetone, chlorobenzene and THF.

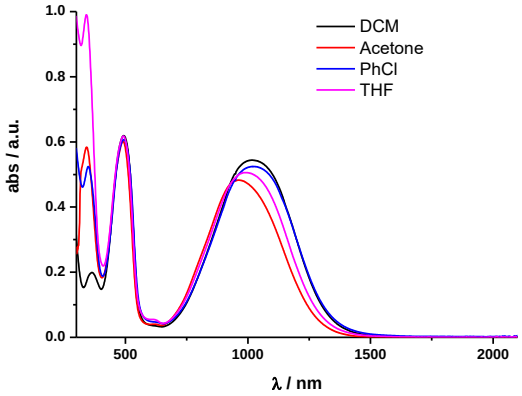

Figure S62. Vis/NIR spectra of **1-Me**$^{\bullet+}$ in dichloromethane, acetone, chlorobenzene and THF.

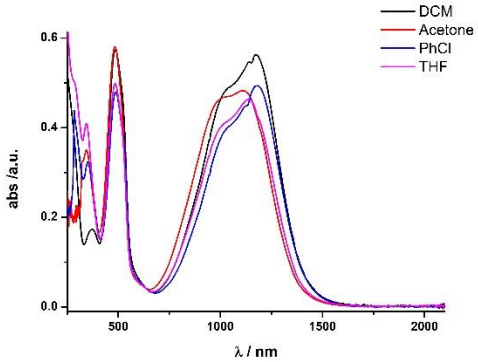

Figure S63. Vis/NIR spectra of **1-OMe**$^{\bullet+}$ in dichloromethane, acetone, chlorobenzene and THF.

Table S3. Absorption wavelengths of the chemically oxidized complexes in various solvents

	solvent	$\tilde{\nu}_{max}$/ nm	$\tilde{\nu}_{max}$ / cm^{-1}	ε_{max} / M^{-1} cm^{-1}
1-CHO	chlorobenzene	988	10121	9096
	dichloromethane	983	10173	9560
	THF	967	10341	9024
	acetone	949	10537	8440
1-Ac	chlorobenzene	995	10050	10126
	dichloromethane	995	10050	11590
	THF	973	10277	9823
	acetone	958	10438	9220
1-E	chlorobenzene	983	10173	10559
	dichloromethane	987	10132	11585
	THF	965	10363	10380
	acetone	951	10515	9340
1-Me	chlorobenzene	1020	9804	18373
	dichloromethane	1017	9833	19050
	THF	990	10101	17713
	acetone	964	10373	16910
1-OMe	chlorobenzene	1216 1057	8225 9456	20100 16600
	dichloromethane	1211 1052	8255 9502	23000 20000
	THF	1187 1026	8426 9745	18700 16800
	acetone	1173 1011	8524 9891	19700 19100

Equation used for calculating the oscillator strength:

$$f = \frac{4\,\varepsilon_0\,c\,m_e \ln 10}{N_A\,e^2} \int \varepsilon(v)dv = (4.6 * 10^{-9})\varepsilon_{max}\Delta\nu_{1/2}$$

11. Gaussian analysis of the experimental NIR spectra

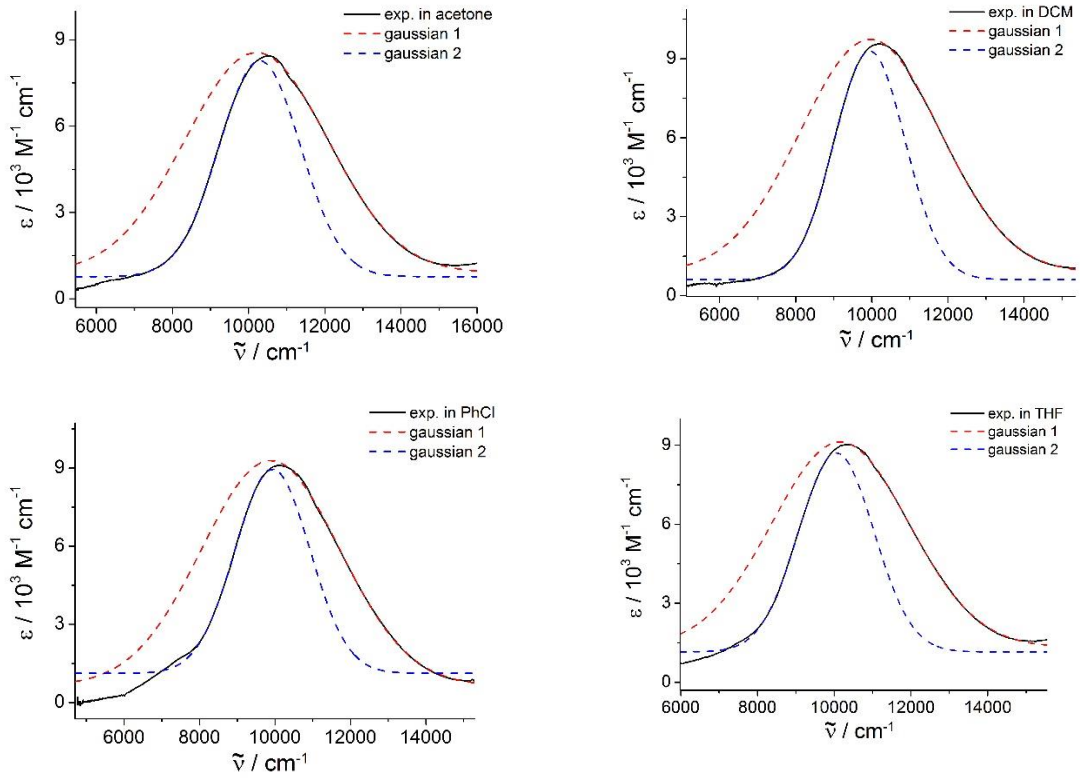

Figure S64. Simulation of the high and low-energy portions of the IVCT band of **1-CHO**$^{+}$ in different solvents demonstrating the low energy cutoff.

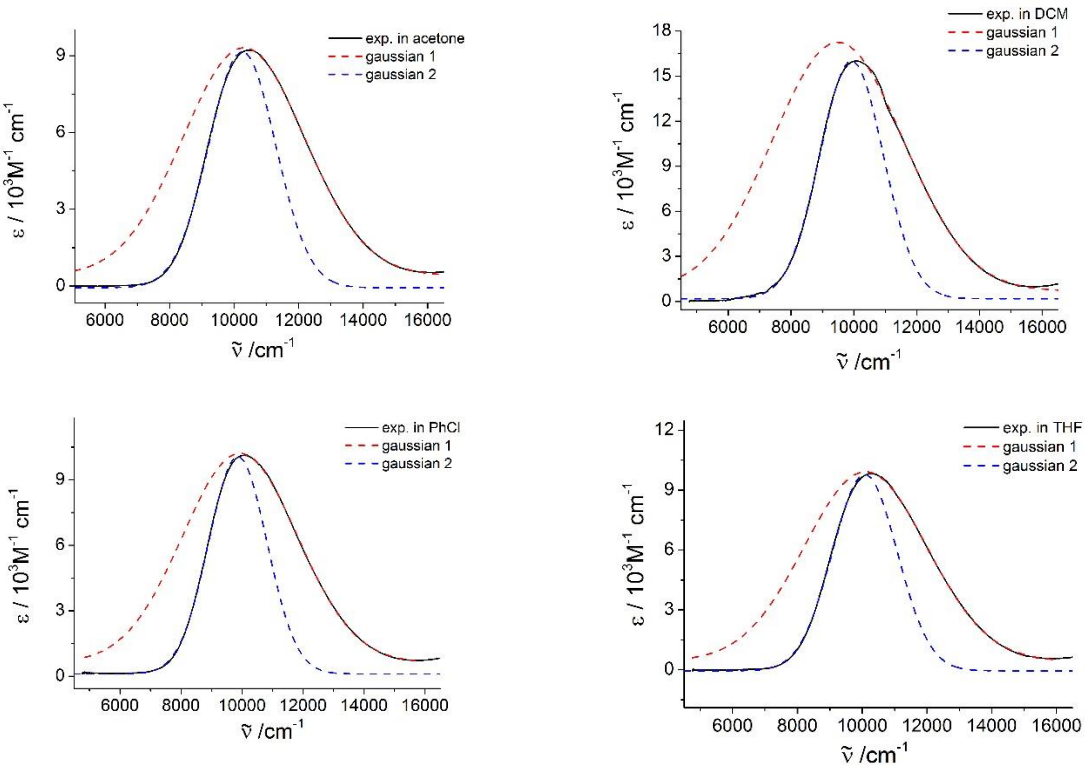

Figure S65. Simulation of the high and low-energy portions of the IVCT band of **1-Ac**$^{+}$ in different solvents demonstrating the low energy cutoff.

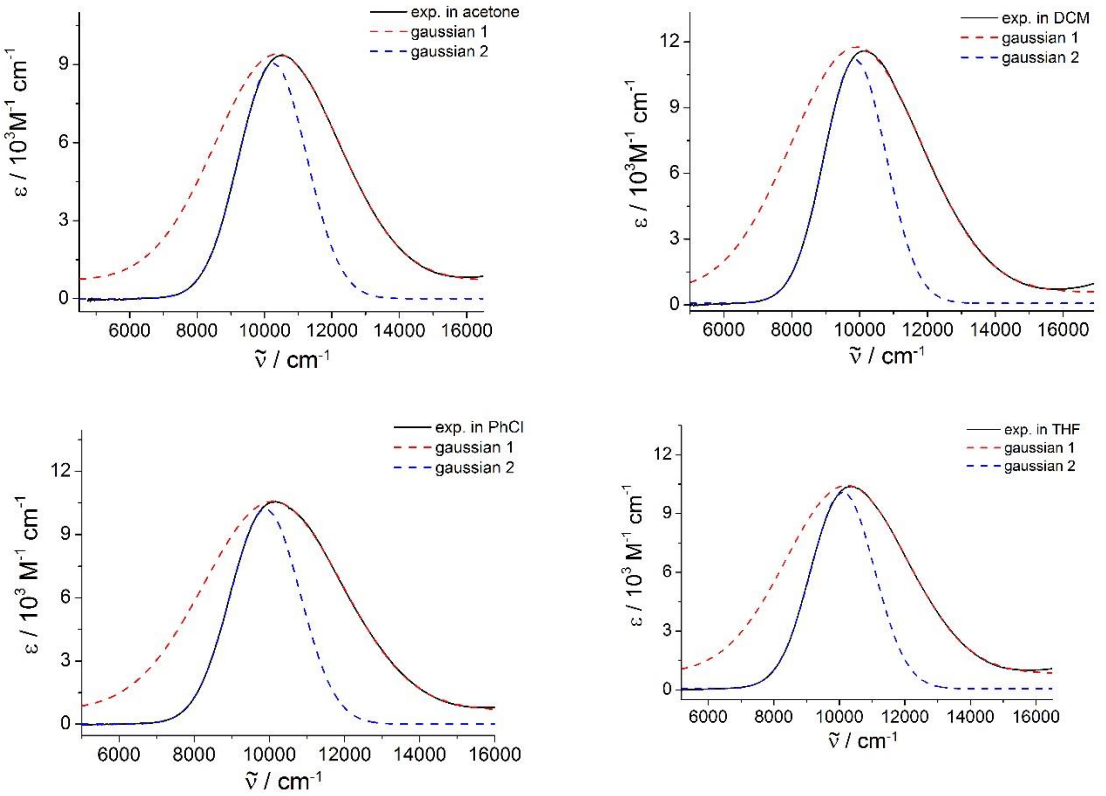

Figure S66. Simulation of the high and low-energy portions of the IVCT band of **1-E**$^{+}$ in different solvents demonstrating the low energy cutoff.

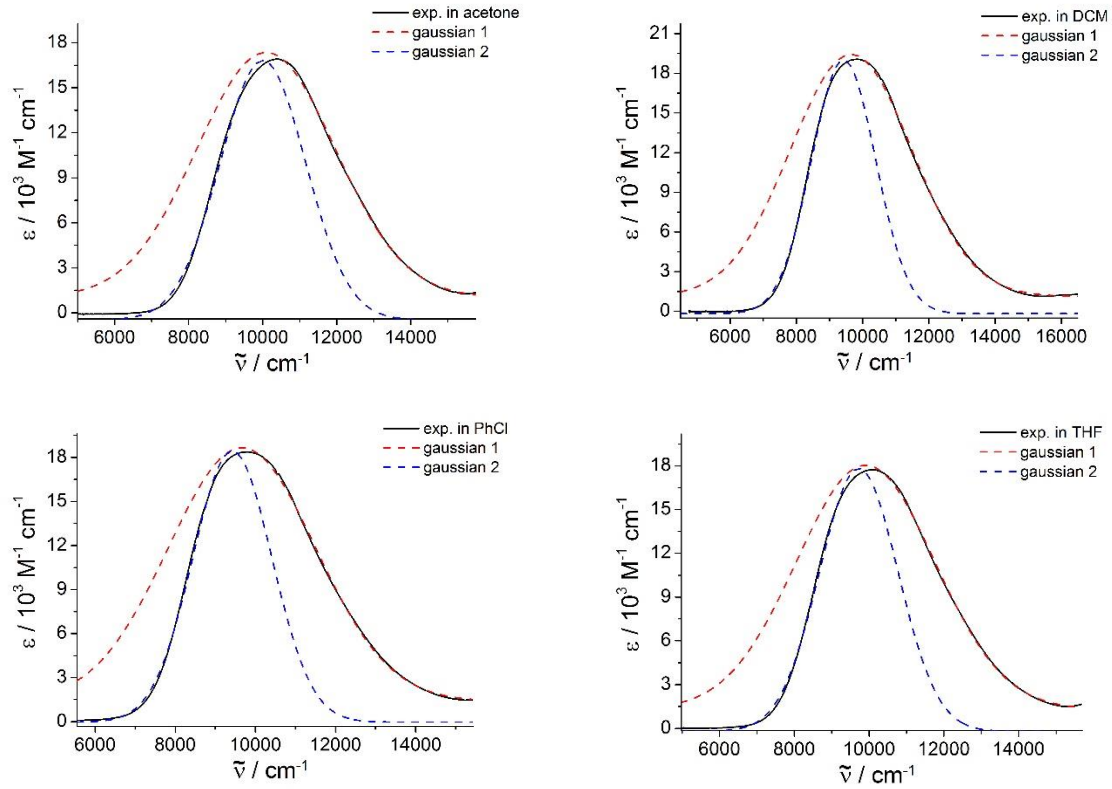

Figure S67. Simulation of the high and low-energy portions of the IVCT band of **1-Me**$^{+}$ in different solvents demonstrating the low energy cutoff.

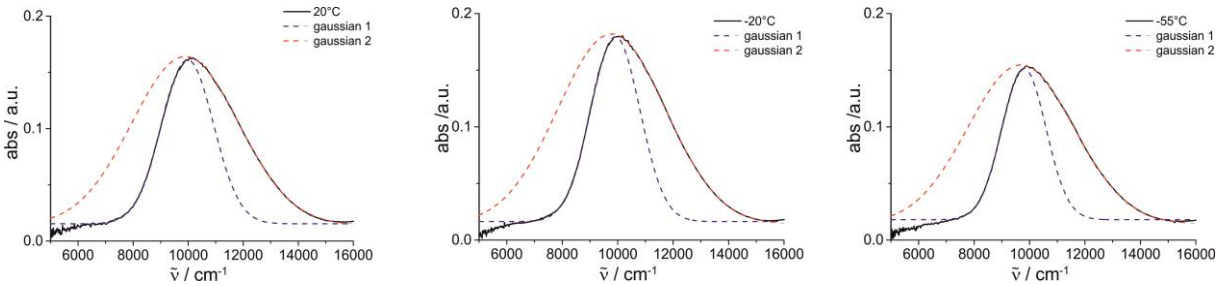

Figure S68. Variation of the IVCT band of **1-CHO**$^+$ with *T* in CH_2Cl_2 and spectral fits by Gaussian functions for the high and low energy branch demonstrating the band asymmetry.

Table S4. Variation of the IVCT band of 1-CHO$^+$ with *T* in CH_2Cl_2.

***T* (°C)**	$\tilde{\nu}_{max}$(cm^{-1})	$\Delta\tilde{\nu}_{1/2,high}$(cm^{-1})	$\Delta\tilde{\nu}_{1/2,low}$(cm^{-1})	$\frac{\Delta\tilde{\nu}_{1/2,high}}{\Delta\tilde{\nu}_{1/2,low}}$
25	10173	4330	2198	1.97
10	9874	4541	2184	2.08
0	9835	4569	2151	2.12
-10	9828	4520	2099	2.15
-20	9782	4560	2021	2.26
-30	9762	4553	2022	2.25
-40	9750	4523	1975	2.29
-50	9723	4518	1911	2.36
-55	9688	4514	1900	2.38

Literature:

1. Li, Z. a.; Ye, T.; Tang, S.; Wang, C.; Ma, D.; Li, Z. Triphenylamine-based [small pi]-conjugated dendrimers: convenient synthesis, easy solution processability, and good hole-transporting properties. *J. Mat. Chem. C* **2015**, *3*, 2016-2023.
2. Kim, C.; Choi, H.; Paek, S.; Kim, J.-J.; Song, K.; Kang, M.-S.; Ko, J. Molecular engineering of thia-bridged triphenylamine heterohelicenes as novel organic dyes for dye-sensitized solar cells. *J. Photochem. Photobiol. A* **2011**, *225*, 17-25.
3. Planells, M.; Abate, A.; Hollman, D. J.; Stranks, S. D.; Bharti, V.; Gaur, J.; Mohanty, D.; Chand, S.; Snaith, H. J.; Robertson, N. Diacetylene bridged triphenylamines as hole transport materials for solid state dye sensitized solar cells. *J. Mat. Chem. A* **2013**, *1*, 6949-6960.
4. Chowdhury, A.; Mukherjee, P. S. Electron-Rich Triphenylamine-Based Sensors for Picric Acid Detection. *J. Org. Chem.* **2015**, *80*, 4064-4075.
5. Polit, W.; Exner, T.; Wuttke, E.; Winter, R. F. Vinylruthenium-Triarylamine Conjugates as Electroswitchable Polyelectrochromic NIR Dyes. *Bioinorg. React. Mech.* **2012**, *8*, 85-105.

3.4. Paper 3: Mixed-Valent Ruthenocene-Vinylruthenium Conjugates: Valence Delocalization Despite Chemically Different Redox Sites

Christopher Hassenrück, André Mang and Rainer F. Winter*

University of Konstanz, Universitätstraße 10, D-78457 Konstanz, Germany

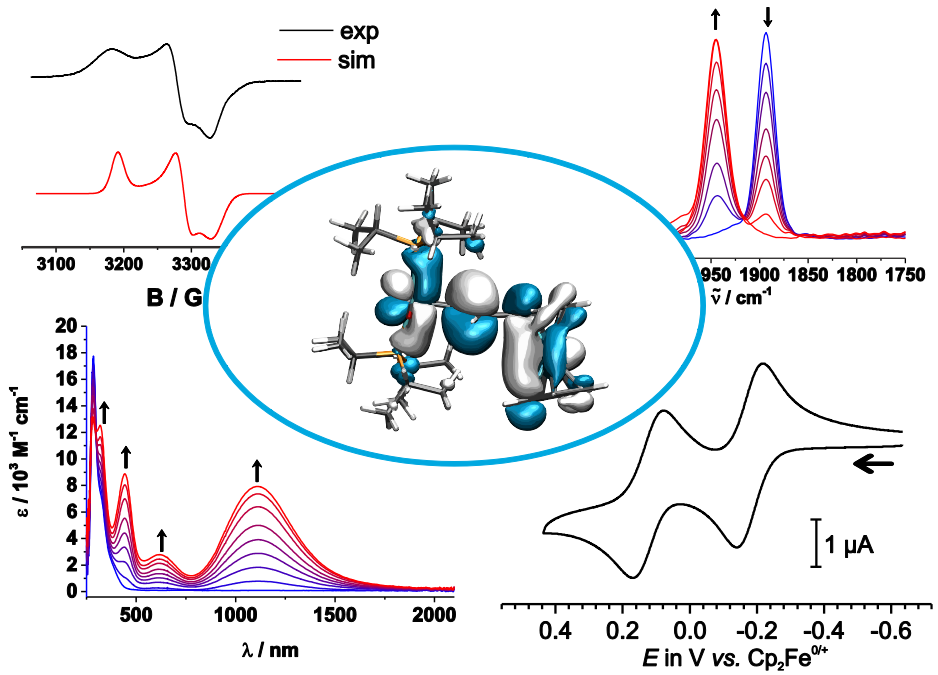

Reprinted with permission from *Inorg. Chem*, **2019**, *58*, 4, 2695-2707. Copyright 2019.

Inorganic Chemistry
Article
Cite This: Inorg. Chem. 2019, 58, 2695−2707
pubs.acs.org/IC

Mixed-Valent Ruthenocene−Vinylruthenium Conjugates: Valence Delocalization Despite Chemically Different Redox Sites

Christopher Hassenrück, André Mang, and Rainer F. Winter*

University of Konstanz, Department of Chemistry, Universitätsstraße 10, 78457 Konstanz, Germany

Supporting Information

ABSTRACT: Ruthenocene−vinylruthenium conjugates Rc/Rc*−CH═CH−Ru(CO)(L)(P^iPr_3)$_2$ (Rc = (η^5-C_5H_5)Ru(η^5-C_5H_4); Rc* = (η^5-C_5Me_5)Ru(η^5-C_5H_4); L = Cl or $\kappa O,O'$-acetylacetonato) have been prepared and investigated in their neutral, mono-, and dioxidized states by cyclic voltammetry, IR and UV/vis/NIR spectroelectrochemistry, and EPR spectroscopy. Their corresponding radical cations are (almost) completely delocalized mixed-valent systems as indicated by the low half-widths, the absence of solvatochromism, and the low-energy cutoff of their IVCT bands in the near-infrared (NIR) and their IR and EPR spectroscopic signatures. The degree of electronic coupling even exceeds that of their ferrocene analogs despite comparable differences between the intrinsic half-wave potentials of the vinylruthenium and the metallocenyl entities and substantially smaller half-wave potential splittings, $\Delta E_{1/2}$, in the ruthenocene congeners. All experimental results are backed by quantum chemical calculations.

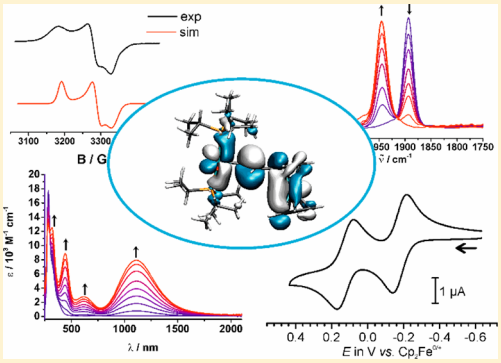

INTRODUCTION

Due to their ease of synthesis and highly favorable redox properties, ferrocene and its many derivatives are widely used in studies of inter- and intramolecular electron transfer. Biferrocenium and biferrocenyleneium radical cations as well as their 1,2-diferrocenylethyne, 1,4-diferrocenylbutadiyne, and [2.2]ferrocenophane-1,13-diyne ethynylogues are paradigmatic examples of mixed-valent di-/biferrocenes with chemically identical redox sites. Detailed studies on their mixed-valent (MV) radical cations provided detailed insight on how intramolecular electron transfer rates depend on the environment.[1−6] Interest in such compounds continues until today, as highlighted by the use of biferrocenylene/-ium bridges as conduits in linear and macrocyclic architectures.[7−12] Later on, the MV radical cations of heterodimetallic ethynylferrocene complexes of the type {M}−C≡C−Fc (Fc = ferrocenyl, (η^5-C_5H_5)Fe(η^5-C_5H_4)) with M = $CpFe(CO)_2$, CpFe(CO)(PPh_3), $CpFe\{P(OMe)_3\}_2$, CpFe(dppe), CpFe(dmpe),[13,14] $CpRuL_2$ (L_2 = 2 PPh_3, dppe, dppf),[15] or *trans*-$Cl(dppm)_2Ru$ or Os[16] (dppm = bis(diphenylphosphino)methane, dppe = 1,2-bis(diphenylphosphino)ethane, dppf = 1,1′-bis(diphenylphosphino)ferrocene, and dmpe = 1,2-bis(dimethylphosphino)ethane) were scrutinized by Sato, Long, and their co-workers and were found to exhibit valence delocalization between the disparate redox sites.

Similar studies were also extended to ruthenium acetylide derivatives of ruthenocenes.[17,18] Despite the notoriously complicated redox behavior of ruthenocenes,[19−23] most of these complexes exhibit two consecutive, chemically reversible one-electron oxidations with redox splittings $\Delta E_{1/2}$ of 200−460 mV.

Two-electron oxidation of ruthenium σ-alkynyl complexes of ethynyl ruthenocene was found to induce a remarkable structural rearrangement to vinylidene complexes [CpRu(η^6:η^1-C_5R_4═C═C)═Ru(η^5-Cp^R)L_2]$^{2+}$ (R = H, Me; Cp^R = Cp, Cp* (Cp* = C_5Me_5)) or the fulvene vinylidene complex (η^6-C_5Me_4═CH_2)Ru(η^5-C_5H_4CH═C═)RuCp(PPh_3)$_2$]$^{2+}$ formed by hydrogen transfer from a methyl group of the Cp* ligand to the α-ethynyl carbon atom (Figure 1).[17,18] All attempts to generate and characterize their one-electron oxidized MV intermediates led only to the isolation of products such as Cp*Ru(η^5-C_5H_4═CH═C═)RuCp(PPh_3)$_2$]$^+$ resulting from hydrogen atom abstraction from the solvent (Figure 1).

We have recently demonstrated that mixed-valent vinylruthenium complexes [(RA−CH═CH)Ru(CO)Cl(P^iPr_3)$_2$]$^+$ with a chemically different redox-active substituent RA may either display charge localization at one of the two redox sites[24] corresponding to class I systems according to Robin and Day's classification scheme,[25] partial charge localization at one site,[26] complete charge delocalization over the dislike redox sites,[27−31] or exist as thermally equilibrating mixtures of valence tautomers.[32,33] Most relevant to the present work is the ferrocene−vinylruthenium conjugate CpFe(η^5-C_5H_4−CH═CH−){Ru^{Cl}}]$^+$ (**Fc-Ru**$^{Cl+}$, {Ru^{Cl}} = Ru(CO)Cl(P^iPr_3)$_2$). The combined results of IR, EPR and Mössbauer spectroscopic studies on its associated radical cation allowed us to estimate the ratio of contributions of the Fc and the {Ru^{Cl}}(CH═CH)

Received: November 27, 2018
Published: February 7, 2019

ACS Publications © 2019 American Chemical Society

DOI: 10.1021/acs.inorgchem.8b03253
Inorg. Chem. 2019, 58, 2695−2707

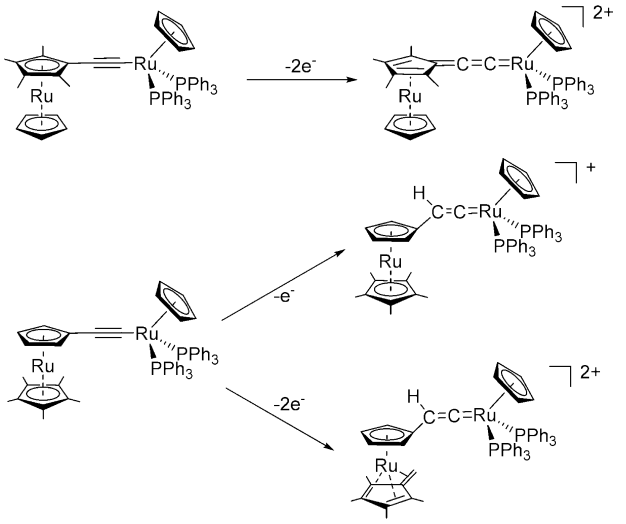

Figure 1. Products isolated from oxidation of σ-ethynylruthenocene half-sandwich ruthenium complexes.

entities to one-electron oxidation as ca. 80:20 in the solid state.[26]

The reversible electrochemical behavior of resonance-stabilized metal-alkynyl complexes of ethynylruthenocenes[17,18,34−36] prompted us to explore ruthenocene derivatives of **Fc-Ru^{Cl}**. To these ends we prepared and studied the four ruthenocene−vinylruthenium conjugates of Scheme 1. By

Scheme 1. Ferrocene− and Ruthenocene−Vinylruthenium Conjugates of This Study

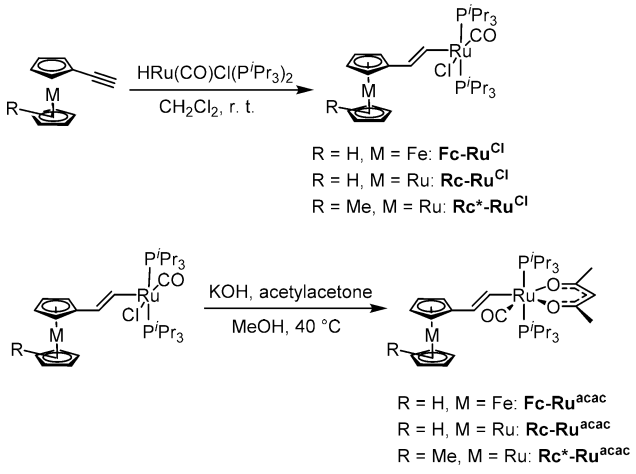

combining either ruthenocene (**Rc**) or pentamethylruthenocene (**Rc***) and the 16 valence electron (VE) (Ru(CO)Cl(P^iPr_3)$_2$ ({Ru^{Cl}}) or the more electron-rich 18 VE Ru(acac)(CO)(P^iPr_3)$_2$ ({Ru^{acac}}, acac = κ*O*,*O*′-acetylacetonato) entities, we were able to alter the electron richness of both redox sites independently and to study the impact on the electrochemical and spectroscopic properties. The new acac derivatives **Fc-Ru^{acac}** and **Ph-Ru^{acac}** of the ferrocenyl-vinylruthenium complex **Fc-Ru^{Cl}** and the simple styryl complex Ph−CH═CH−Ru(CO)Cl(P^iPr_3)$_2$ (**Ph-Ru^{Cl}**) were also included to provide further couples of compounds that illustrate the effects of a higher electron density at the vinylruthenium site. The results of this study are presented in the following.

SYNTHESIS AND CHARACTERIZATION

Ethynylruthenocene and (1-ethynylcyclopentadienyl)(pentamethylcyclopentadienyl)ruthenocene were synthesized according to the procedures published by Sato.[17,18] The target complexes were obtained in moderate to high yields by hydroruthenation, i.e., the regio- and stereoselective *cis*-insertion of the ethynyl function into the Ru−H bond of HRu(CO)Cl(P^iPr_3)$_2$ (Scheme 1).[37−40] Substitution of the Cl$^-$ ligand by acetylacetonate (acac$^-$) provided derivatives **Rc-Ru^{acac}**, **Rc*-Ru^{acac}** and **Fc-Ru^{acac}**.

All complexes were characterized by multinuclear (^{1}H, ^{31}P, ^{13}C) NMR and by IR spectroscopy as well as by combustion analysis (see Figures S1−S17 of the Supporting Information). Selected NMR data are collected in Table 1 and compared to those of the respective ferrocene analogue **Fc-Ru^{Cl}** (see also the numbering scheme in Figure 2). Particularly characteristic

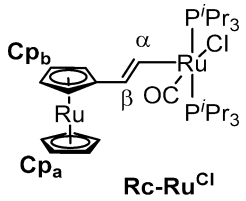

Figure 2. Atomic numbering scheme for Table 1.

are the C*H*═C*H* doublet resonances of the vinylic protons with a $^3J_{HH}$ coupling constant of 16.6 Hz. For all three pairs of complexes, replacing the Cl$^-$ by the acac$^-$ ligand shifts the resonances of both vinylic protons as well as the Ru−C_α and the Ru−*C*O resonances to lower field. Despite the less electron-donating character of the Rc as compared to the Fc substituent, corresponding resonances of **Rc-Ru^{Cl}** and **Rc-Ru^{acac}** fall close to those of their ferrocene analogues. ^{31}P NMR spectra display the expected sharp singlet resonance of the *trans*-disposed P^iPr_3 ligands in a narrow shift range of 37.9−38.3 ppm for the 16 VE Ru^{Cl} and of 35.0 to 36.3 ppm for the 18 VE Ru^{acac} complexes.

Table 1. Selected ^{1}H and ^{13}C NMR Chemical Shifts (δ in ppm) of the Complexes[a]

	$H_{\alpha/\beta}$	$C_{\alpha/\beta}$	Cp[b]	Cp^{sub}	CO	^{31}P
Fc-Ru^{Cl}	7.62/5.52	143.3/129.6	4.02	4.00/3.98	203.0	38.3
Rc-Ru^{Cl}	7.64/5.39	144.0/129.3	4.42	4.44/4.36	203.5	38.3
Rc*-Ru^{Cl}	7.39/5.29	143.6/129.3	1.87	3.94/3.90	203.7	37.9
Fc-Ru^{acac}	8.10/5.90	161.2/128.9	4.03	4.06/3.97	210.7	35.9
Rc-Ru^{acac}	8.07/5.74	160.6/128.0	4.43	4.52/4.35	210.6	36.3
Rc*-Ru^{acac}	7.84/5.67	161.2/127.9	1.91	3.96/3.92	210.7	35.0

[a]NMR spectra recorded in CD_2Cl_2 at room temperature. [b]Proton resonance of the unsubstituted Cp or methyl resonance of the Cp* ligand.

DOI: 10.1021/acs.inorgchem.8b03253
Inorg. Chem. 2019, 58, 2695−2707

The complex **Ph-Ru^{acac}** was also characterized by X-ray crystallography. Figure 3 provides a view of the molecular

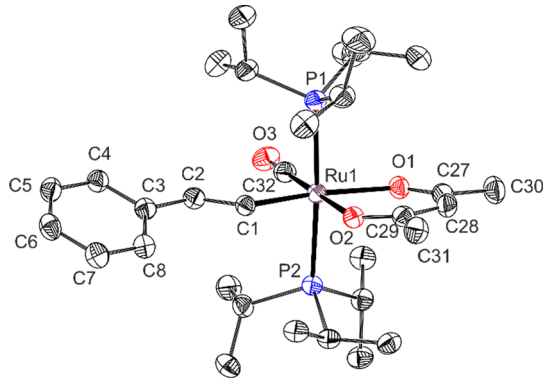

Figure 3. Crystallographically determined structure of the complex **Ph-Ru^{acac}** with the atomic numbering. Thermal ellipsoids are provided at the 50% probability level and protons are omitted for reasons of clarity. Selected bond lengths [Å] and interatomic angles [deg]: Ru−P1, 2.4416(7), Ru−P2, 2.4188(6); Ru−O1, 2.1838(18); Ru−O2, 2.1276(17); Ru−C1, 2.030(3); Ru−C32, 1.813(3); P1−Ru−P2, 176.44(2); O1−Ru−O2, 85.14(7), O1−Ru−C32, 95.44(10); O2−Ru−C1, 86.13(8); C32−Ru−C1, 93.31(11); C1−Ru−O1, 170.96(8); C32−Ru−O2, 179.18(9).

structure along with the most pertinent bond lengths and angles. Full listings together with the crystal, structure refinement, and solution data are provided as Tables S1 to S4 in the Supporting Information. As a consequence of the strong *σ-trans* influence of the styryl ligand, the Ru−O1 bond of 2.1838(18) Å to the *trans*-disposed acac donor atom is appreciably longer than the Ru−O2 bond of 2.1276(17) Å to the O atom opposite the carbonyl ligand. Owing to the formation of an unstrained six-membered chelate ring all cis-angles between the equatorial acac, CO and styryl donor atoms fall in a narrow range of 85.14(7) to 95.44(10)° and show only minor distortions from an ideal octahedral coordination geometry.[33] The Ru−C32 and the Ru−C1 bond lengths of 1.813(3) and 2.030(3) Å comply with sp and sp^2 hybridization of the corresponding carbon donor atom, and the C1−C2 bond of 1.339(3) Å is in the typical range of C = C bonds. As usual, the vinyl group is oriented toward the CO ligand.[41] The phenyl ring of the styryl ligand is rotated by 27.5° out of the equatorial coordination plane.

■ ELECTROCHEMISTRY

All complexes were studied by cyclic voltammetry and found to undergo two consecutive one-electron oxidations. We first used $NBu_4[B\{C_6H_3(CF_3)_2\text{-}3,5\}_4]$ in CH_2Cl_2 as the supporting electrolyte, which had proven to render the $Cp_2Ru^{0/+}$ couple reversible.[42] Under these conditions, the first wave fulfilled all criteria of chemical and electrochemical reversibility while the second oxidation was electrochemically only quasireversible at low sweep rates and close to irreversible at higher ones. Quite curiously, the nonideal behavior of the second wave improved considerably after adding cobaltocenium hexafluorophosphate ($CcH^+PF_6^-$) as internal redox standard, while the presence of decamethylferrocene had no such effect. Figure S18 of the Supporting Information provides exemplary voltammograms of **Rc-Ru^{acac}** under different conditions. In the presence of roughly equimolar amounts of CcH^+ PF_6^-, half-wave potentials $E_{1/2}$ of **Rc-Ru^{acac}** are −275 mV for the first and +260 mV for the second oxidation. Replacing the $[B\{C_6H_3(CF_3)_2\text{-}3,5\}_4]^-$ counterion of the supporting electrolyte by PF_6^- brought further improvement. Under these conditions, the second oxidation is associated with an only ∼10 mV larger peak potential splitting than the first one. Half-wave potentials amount to −179 and +124 mV, respectively, thus diminishing the half-wave potential splitting $\Delta E_{1/2}$ from 535 to 303 mV, obviously as a result of enhanced ion-pairing. Large medium and counterion effects on half-wave potentials, particularly of redox couples that produce higher charged species, have been well described in the literature,[43,44] and our observations are in line with these earlier comprehensive reports.

In view of the less ideal responses in the presence of the $[B\{C_6H_3(CF_3)_2\text{-}3,5\}_4]^-$ anion, we used the CH_2Cl_2/NBu_4PF_6 electrolyte in all further (spectro)electrochemical studies. Under these conditions all dinuclear complexes exhibit two consecutive, chemically reversible one-electron oxidations with an only moderate broadening of the second wave. Figure 4

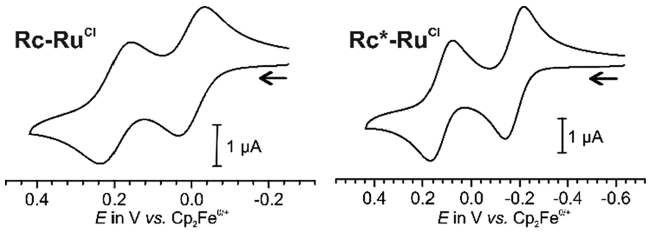

Figure 4. Cyclic voltammograms of **Rc-Ru^{Cl}** (left) and **Rc*-Ru^{Cl}** (right), vs FcH/FcH^+ in CH_2Cl_2/NBu_4PF_6 (0.1 M) at r.t. and ν = 100 mV/s.

displays representative voltammograms of the complexes **Rc-Ru^{Cl}** and **Rc*-Ru^{Cl}**; those of all other complexes can be found as Figure S19 in the Supporting Information. Pertinent data are compiled in Table 2.

Table 2. Cyclic Voltammetry Data[a]

	$E_{1/2}{}^{0/+}$ (ΔE_p)	$r^{0/+}$[b]	$E_{1/2}{}^{+/2+}$ (ΔE_p)	$r^{+/2+}$[b]	$\Delta E_{1/2}$
Fc-Ru^{Cl}	−235 (69)	1.00	580 (69)	0.98	815
Fc-Ru^{acac}	−362 (77)	1.00	417 (79)	1.00	779
Rc-Ru^{Cl}	−1 (66)	0.98	199 (78)	0.98	200
Rc-Ru^{acac}	−179 (76)	1.00	124 (90)	0.99	303
Rc*-Ru^{Cl}	−175 (78)	1.00	184 (87)	0.97	359
Rc*-Ru^{acac}	−335 (80)	0.97	79 (91)	0.80	414
Ph-Ru^{Cl}	280 (76)	0.96	850[c]	–	–
Ph-Ru^{acac}	22 (74)	0.97	948[c]		
Rc[d]	560	1.0			
Rc*[e]	230	0.55			

[a]All data in mV vs FcH/FcH^+ in CH_2Cl_2/NBu_4PF_6 (0.1 M) at room temperature, ν = 50 mV/s; data for **Fc-Ru^{Cl}** from ref 26 and data for **Ph-Ru^{Cl}** from ref 45. [b]Reversibility coefficient $r = i_{p,rev}/i_{p,fw}$. [c]Peak potential of a chemically irreversible process. [d]In $CH_2Cl_2/NBu_4[B\{C_6F_5\}_4]$ according to ref 42. [e]In CH_2Cl_2/NBu_4ClO_4 according to ref 46.

Comparison of these data reveals some interesting details: (i) Substitution of ruthenocene (Rc) for pentamethylruthenocene (Rc*) has a large impact on the half-wave potential $E_{1/2}{}^{0/+}$ of the first oxidation, but induces only smaller shifts of that of the second oxidation, $E_{1/2}{}^{+/2+}$ (**Rc-Ru^{Cl}**/**Rc*-Ru^{Cl}**: $\Delta E_{1/2}{}^{0/+}$ = 174 mV; $\Delta E_{1/2}{}^{+/2+}$ = 15 mV; **Rc-Ru^{acac}**/**Rc*-Ru^{acac}**: $\Delta E_{1/2}{}^{0/+}$ = 156 mV; $\Delta E_{1/2}{}^{+/2+}$ = 45 mV). (ii) Replacing the

DOI: 10.1021/acs.inorgchem.8b03253
Inorg. Chem. 2019, 58, 2695−2707

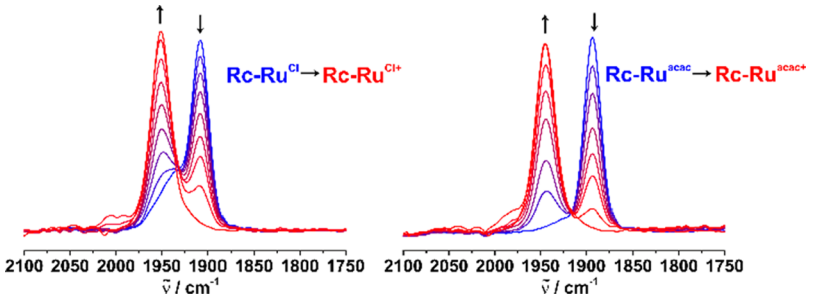

Figure 5. IR spectral changes of the Ru(CO) stretching vibration during electrolysis from neutral **Rc-Ru^{Cl}** (blue, top) and **Rc-Ru^{acac}** (blue, bottom) to their radical cations (red), in 1,2-$C_2H_4Cl_2$/NBu_4PF_6 (0.2 M) at room temperature.

Table 3. ν(CO) Values of the Metallocene−Vinylruthenium Complexes in Their Various Oxidation States[a]

	$\nu(CO)^{exp}$ [cm^{-1}]			$\nu(CO)^{calc,b}$ [cm^{-1}]			$\Delta\nu(CO)$ [cm^{-1}]			
	n = 0	n = 1	n = 2	n = 0	n = 1	+/0	+/0	2+/+	2+/0	$\Delta\nu(CO)^{+/0}$/ $\Delta\nu(CO)^{2+/0}$
Fc-Ru^{Cl}	1908	1932	2004	1895	1913	18	24	72	96	0.25
Rc-Ru^{Cl}	1908	1952	2004	1899	1936	37	44	52	96	0.46
Rc*-Ru^{Cl}	1908	1940	1999	1902	1932	30	32	59	91	0.35
Fc-Ru^{acac}	1893	1921	1966	1882	1904	22	28	45	73	0.38
Rc-Ru^{acac}	1893	1945	1987	1891	1934	43	52	42	94	0.55
Rc*-Ru^{acac}	1893	1932	1981	1890	1922	32	39	49	88	0.44
Ph-Ru^{Cl}	1904	1976	–	1900	1964	64	72	–	–	–
Ph-Ru^{acac}	1897	1968	–	1896	1954	58	71	–	–	–

[a]In 1,2-$C_2H_4Cl_2$, NBu_4PF_6 (0.2 M) at room temperature. [b]DFT-calculated values

two-electron donor Cl^- coligand at the vinylruthenium site by the four-electron donor $acac^-$ causes more uniform cathodic shifts of $E_{1/2}{}^{0/+}$ and $E_{1/2}{}^{+/2+}$ (**Rc-Ru^{Cl}**/**Rc-Ru^{acac}**: $\Delta E_{1/2}{}^{0/+}$ = −178 mV; $\Delta E_{1/2}{}^{+/2+}$ = −75 mV; **Rc*-Ru^{Cl}**/**Rc*-Ru^{acac}**: $\Delta E_{1/2}{}^{0/+}$ = −160 mV; $\Delta E_{1/2}{}^{+/2+}$ = −105 mV). Quite revealingly, the sum of both shifts (−253 mV or −265 mV, respectively) matches with the $\Delta E_{1/2}$ of −258 mV for the styryl complexes **Ph-Ru^{Cl}** and **Ph-Ru^{acac}**. These observations point to electronic coupling between the vinylruthenium and the ruthenocene sites via the common cyclopentadienide ligand while substitution of the other Cp ring seems to exert an only minor, inductive effect. (iii) Replacing ferrocene (Fc) by ruthenocene (Rc) increases $E_{1/2}{}^{0/+}$ by ca. 200 mV while decreasing $E_{1/2}{}^{+/2+}$ by an even larger amount (**Fc-Ru^{Cl}**/**Rc-Ru^{Cl}**: $\Delta E_{1/2}{}^{0/+}$ = 234 mV; $\Delta E_{1/2}{}^{+/2+}$ = −381 mV; **Fc-Ru^{acac}**/**Rc-Ru^{acac}**: $\Delta E_{1/2}{}^{0/+}$ = 183 mV; $\Delta E_{1/2}{}^{+/2+}$ = −293 mV). As a consequence, the half wave potential differences $\Delta E_{1/2}$ of **Fc-Ru^{Cl}** and **Fc-Ru^{acac}** of 779 mV and 815 mV are much larger than those of 200 mV and 303 mV of their ruthenocene analogs. This might be viewed as indication, that the one-electron oxidized ruthenocene−vinylruthenium radical cations are electronically less strongly coupled than their ferrocene analogs. As we will show in the following, this is, however, not the case.

IR-SPECTROELECTROCHEMISTRY

The charge-sensitive ν(CO) label has proven highly useful for determining the degree of charge and spin delocalization in mixed-valent (MV) dinuclear, ligand-bridged bis(alkenylruthenium) complexes,[27−29,31−33,47−58] and metallamacrocycles derived from them.[59−61] In complexes RA−CH=CH−Ru^{Cl} with a chemically different secondary redox site RA, including **Fc-Ru^{Cl}**,[26] the ratio between the CO-band shift after one-electron oxidation to the total shift between the neutral and dicationic forms of a complex, $\Delta\nu(CO)^{+/0}$/$\Delta\nu(CO)^{2+/0}$, provides a good measure of the charge distribution in the one-electron oxidized MV state.[24,26,30,31]

With this in mind, all complexes have been subjected to infrared (IR) spectroelectrochemistry in an optically transparent thin layer electrolysis (OTTLE) cell following the design of Hartl et al.[62] Generally, oxidation of the neutral complexes to their one-electron oxidized radical cations commenced without problems as seen by the isosbestic points and the basically quantitative recovery of the neutral starting complex on rereduction. Further conversion to the associated dications was however accompanied by some decomposition, which leads to additional bands and some intensity loss of the original Ru(CO) band after a full oxidation−reduction cycle. Still, the band of the respective dication did revert to that of the radical cation or the neutral starting compound, making its assignment unambiguous. Spectroscopic changes in the ν(CO) region during the first oxidation of complexes **Rc-Ru^{Cl}** and **Rc-Ru^{acac}** are shown in Figure 5 while Figures S20−S24 of the Supporting Information give a full account of our results. Experimental IR data as well as the energies derived from quantum chemical calculations are compiled in Table 3. Judging by the $\Delta\nu(CO)^{+/0}/\Delta\nu(CO)^{2+/0}$ ratio, the charge distribution in **Fc-Ru^{Cl+}** amounts to 0.25, indicating that ca. 75% of the charge reside at the ferrocene and 25% on the vinyl ruthenium entity.[26] Increasing the electron richness at the Ru site by replacing the Cl^- by the $acac^-$ coligand increases the value of $\Delta\nu(CO)^{+/0}/\Delta\nu(CO)^{2+/0}$ to 0.38, in line with a more balanced charge distribution.

The same general behavior is also found for the ruthenocene derivatives. Similar to the **Fc-Ru^{Cl}**/**Fc-Ru^{acac}** pair of complexes, the contribution of the vinylruthenium site to the first oxidation (and hence to stabilizing the positive charge) increases as it is rendered more electron rich. Replacing the Cp by the Cp* ligand at the Rc site has the opposite effect. The most remarkable finding is, however, that the $\Delta\nu(CO)^{+/0}$/

DOI: 10.1021/acs.inorgchem.8b03253
Inorg. Chem. 2019, 58, 2695−2707

$\Delta\nu(CO)^{2+/0}$ values of all ruthenocene derivatives except **Rc*-Ru^{Cl}** are in the range of 0.44 to 0.55 and hence close to the value of 0.5 expected for complete charge delocalization of the corresponding radical cation.

Our density functional theory (DFT) calculations on the neutral ruthenocene− and ferrocene−vinylruthenium conjugates and their associated radical cations corroborate the latter results. For every complex, the HOMO is distributed rather uniformly over both redox sites (Figure 6 and Figures S25−S30 of the Supporting Information). The results of natural population analyses as summarized in Table S5 of the Supporting Information provide a more quantitative account. The overall charge differences between the MV radical cations and their neutral precursors of 0.48/0.52 for the ruthenocene and the vinylruthenium sites of **Rc-Ru^{Cl+}**, of 0.41/0.59 for **Rc-Ru^{acac+}**, of 0.64/0.36 for **Rc*-Ru^{Cl+}**, and of 0.58/0.42 for **Rc*-Ru^{acac}** are in good general agreement with our IR spectroscopic data. One should, however, note that the full attribution of the vinyl linker to the vinylruthenium site and of the substituted Cp ring to the metallocene are certainly an oversimplification.

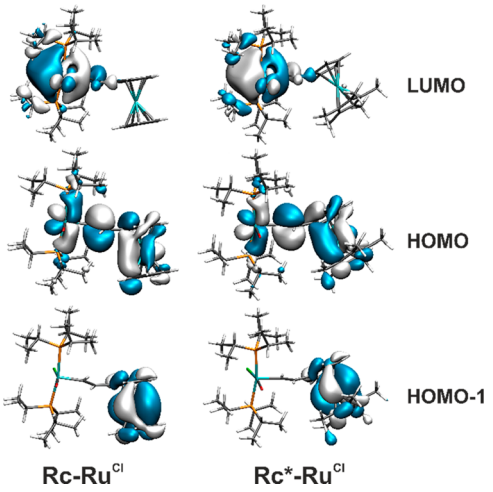

Figure 6. Graphical representation of the HOMO−1, HOMO, and LUMO of complexes **Rc-Ru^{Cl}** (left) and **Rc*-Ru^{Cl}** (right) at the pbe1pbe/6-31G(d) level of theory.

EPR SPECTROSCOPY

While IR spectroscopy probes the local charge at the vinylruthenium site, electron paramagnetic resonance (EPR) spectroscopy provides complementary information on the spin density distribution. EPR studies on generic ruthenocenium radical cations are extremely scarce. The only reported example known to us is the decamethylruthenocenium cation, $Cp^*_2Ru^+$. The latter exhibits an axial spectrum with $g_\perp = 2.008$ and $g_\parallel = 2.059$ ($g_{av} = 2.025$) and hence a rather small g anisotropy.[63] This contrasts sharply with the behavior of the parent ferrocenium or the penta- and decamethylferrocenium ions (Fc^+, $g_\perp = 1.26$, $g_\parallel = 4.35$, $g_{av} = 2.71$; $Cp^*_2Fe^+$, $g_\perp = 1.35$, $g_\parallel = 4.43$, $g_{av} = 2.79$; $CpCp^*Fe^+$, $g_\perp = 1.24$, $g_\parallel = 4.36$, $g_{av} = 2.71$).[64−66] All these metallocenium ions require low temperatures to become EPR active and provide no EPR signal in fluid solution. The previously investigated radical cation **Fc-Ru^{Cl+}** displays a ferrocenium-type EPR signal at 77 K, but with considerably reduced g anisotropy compared to ordinary ferrocenium ions. Both these observations are in line with delocalization of the unpaired spin density onto the vinylruthenium moiety.[26]

For EPR studies, the MV radical cations of the present complexes were generated by chemical oxidation of the neutral compounds with ferrocenium hexafluorophosphate in CH_2Cl_2 and investigated at room temperature and in frozen matrix at 123 K. Radical cation **Fc-Ru^{acac+}** reveals an axial EPR signal at 123 K with a lower anisotropy $\Delta g = 0.648$ than its **Fc-Ru^{Cl+}** counterpart ($\Delta g = 0.848$). This parallels the results from IR spectroscopy, which indicated an increased contribution of the vinylruthenium moiety of **Fc-Ru^{acac}** to the first oxidation process and a more uniform charge distribution over the conjoined redox sites.

In contrast, the one-electron oxidized ruthenocene conjugates give an intense isotropic EPR signal at room temperature with a g-value close to 2.06. When the samples are frozen to 123 K, the spectra change to the rhombic type as is exemplarily shown in Figure 7 for **Rc-Ru^{Cl+}**. Spectra of the other complexes are collected in Figures S31−S35 of the Supporting Information. On inspection of the data in Table 4 one finds that (i) g values and g tensor anisotropies of the ruthenocene vinylruthenium conjugates are larger than those of five-[29,45,67−70] and six-coordinated styrylruthenium complexes like **Ph-Ru^{Cl+}** and **Ph-Ru^{acac+}**, (ii) replacing the Cl^- by the $acac^-$ ligand decreases the g tensor anisotropy and the average g value, and (iii) replacing Rc by Rc* has the opposite effect. All these observations are in line with delocalization of the unpaired spin density over both redox sites and its shifting toward either the metallocene or the vinylruthenium site on replacing a less by a more strongly electron donating coligand at one of these sites.

Our quantum chemical calculations corroborate this view. Computed spin densities are represented graphically in Figure 8 and Figures S36 and S37 of the Supporting Information;

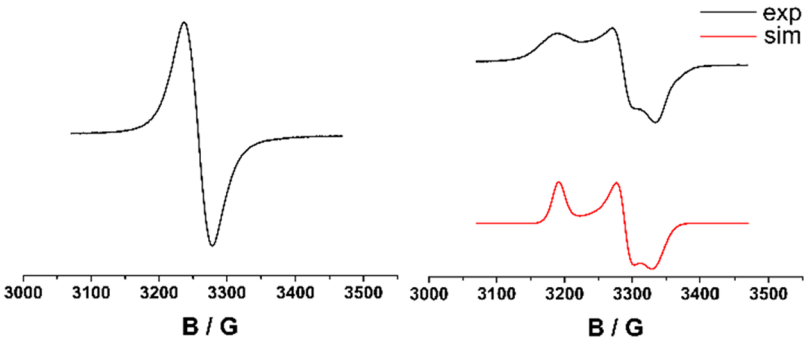

Figure 7. EPR spectrum of **Rc-Ru^{Cl+}** at room temperature (left) and in frozen CH_2Cl_2 matrix at −150 °C (right).

DOI: 10.1021/acs.inorgchem.8b03253
Inorg. Chem. 2019, 58, 2695−2707

Table 4. EPR Data of the Paramagnetic Radical Cations at Room Temperature and in Frozen Matrix

	g_{iso} [a]	g_x [b]	g_y [b]	g_z [b]	g_{av} [b,c]
Fc-Ru^{Cl+} [d]	–	2.800	1.984	1.984	2.289
Fc-Ru^{acac+}	–	2.600	1.952	1.952	2.189
Rc-Ru^{Cl+}	2.068	2.109	2.042	2.019	2.057
Rc-Ru^{acac+}	2.060	2.109	2.042	2.019	2.057
Rc*-Ru^{Cl+}	2.069	2.193	2.021	1.981	2.067
Rc*-Ru^{acac+}	2.059	2.151	2.059	2.027	2.080
Ph-Ru^{Cl+} [e]	2.045	2.071	2.034	2.023	2.043
Ph-Ru^{acac+}	2.040	2.069	2.032	2.015	2.039

[a]In CH_2Cl_2 at room temperature [b]In CH_2Cl_2 at 123 K. [c]$g_{av} = \{^1/_3(g_x^2 + g_y^2 + g_z^2)\}^{1/2}$. [d]From ref 26 at 110 K. [e]From ref 45.

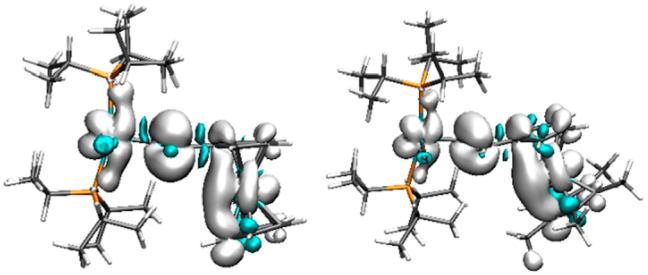

Figure 8. Spin density plots for **Rc-Ru^{Cl+}** and **Rc*-Ru^{Cl+}** (white color α- and cyan color β-spin density) at the pbe1pbe/6-31G(d) level of theory).

numerical values can be found in Table S5 of the Supporting Information. From the data in Table S5 it becomes evident that fragment contributions to hosting the unipositive charge and the unpaired spin density go in parallel. Thus the ruthenocene/vinylruthenium contributions of 0.42/0.58 for **Rc-Ru^{Cl+}**, 0.41/0.59 for **Rc-Ru^{acac+}**, 0.59/0.41 for **Rc*-Ru^{Cl+}** and of 0.51/0.49 for **Rc*-Ru^{acac+}** closely resemble the charge distributions.

UV/VIS/NIR SPECTROSCOPY

Electronic spectra of the neutral complexes are dominated by intense $\pi \rightarrow \pi^*$ absorptions of the π-conjugated backbone and the metallocenyl entities in the UV. As for the similar styrylruthenium complexes, the reddish coloration of the 16 VE complexes is due to a weakly allowed transition from the delocalized HOMO to the Ru-based d orbital, which is directed toward the vacant coordination site opposite the alkenyl donor. In the 18 VE complexes, the LUMO is higher in energy and resides on the chelating donor ligand. The increased HOMO−LUMO gap renders these 18 VE complexes pale yellow in color.[29,67] As can be inferred from the data in Table 5 and the MO plots of Figure 7 and Figures S25−S30 of the Supporting Information, the present complexes comply with this general behavior.

Of much higher interest are the spectra of the associated one-electron oxidized MV forms. Changes of the electronic spectra during oxidation of the neutral complexes to their corresponding radical cations were monitored by means of spectroelectrochemistry. The results of these studies are shown in Figure 9 for the **Rc*-Ru$^{acac\ 0\rightarrow+}$** process and in Figures S38−S42 of the Supporting Information for the remaining complexes. These figures also include the spectroscopic changes during further oxidation to the associated dications. All processes commenced cleanly except for the second

Table 5. Spectroscopic Changes in the UV/Vis/NIR on the First (n = 1) and Second (n = 2) Oxidation of the Complexes

	n	λ_{max} ($\varepsilon_{max}/10^{-3}$ $M^{-1}cm^{-1}$)
Fc-Ru^{Cl} [b]	0	300 (17), 381 (2.3), 455 (0.5), 529 (0.4)
	1	415 (3.2), 504 (3.3), 556 (5.0), 1371 (2.7)
	2	418 (13.5), 540 (sh)
Fc-Ru^{acac}	0	281 (14), 294 (13.6)
	1	281 (15.2), 431 (4.2), 577 (9.3), 1474 (4.0)
	2	281 (16.1), 402 (5.8), 522 (2.4), 1262 (0.6)
Rc-Ru^{Cl}	0	282 (sh), 372 (sh), 510 (0.5)
	1	433 (5.1), 515 (2.6), 1029 (3.0)
	2	371 (6.0), 489 (3.2)
Rc-Ru^{acac}	0	282 (sh), 319 (sh)
	1	433 (6.7), 592 (2.0), 1102 (4.4)
	2	324 (sh) 376 (7.0)
Rc*-Ru^{Cl}	0	369 (sh), 517 (0.2)
	1	369 (6.4), 465 (9.7), 639 (1.2), 1030 (4.9)
	2	369 (8.4), 495 (17.7)
Rc*-Ru^{acac}	0	317 (sh)
	1	321 (12.5), 443 (8.9), 615 (2.8), 1110 (7.9)
	2	400 (sh), 493 (7.3), 782 (1.5)

[a]In 1,2-$C_2H_4Cl_2$/NBu_4PF_6 at room temperature; sh = shoulder. [b]Data from ref 26.

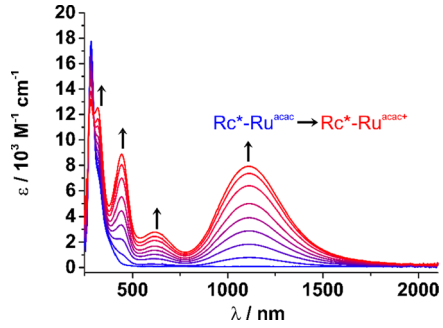

Figure 9. Spectroscopic changes in the UV/vis/NIR region upon oxidation of **Rc*-Ru^{acac}** in 1,2-$C_2H_4Cl_2$/0.2 M NBu_4PF_6 at room temperature.

oxidation of **Rc*-Ru^{acac}**, where slight deviations from isosbestic points were encountered.

UV/vis/NIR data for of all complexes in their different oxidation states are compiled in Table 5. The spectra of the radical cations resemble each other closely. The three common features are a fairly intense NIR band (ε = 3000 to 7900 $M^{-1}cm^{-1}$) at ca. 1000 to 1100 nm for the ruthenocene or at even lower energy for the ferrocene complexes, a less intense (ε = 1200 to 2800 $M^{-1}cm^{-1}$) vis band near 600 nm, and another intense (ε = 5100 to 9700 $M^{-1}cm^{-1}$) vis band at 433 to 465 nm. Comparisons between the TD-DFT computed transitions and the experimental spectra are provided in Tables S7−S12 and Figures S43−S47 of the Supporting Information. They demonstrate that our quantum chemical calculations reproduce the general appearance of the spectra and the band positions and intensities of the ruthenocene complexes very well with a particularly good match for the NIR transition. Less accurate agreement is found for the ferrocene-derived complexes, where the TD-DFT analysis overestimates the energies of the typical ligand-field/Cp → Fe CT NIR band of the ferrocenium cation[7,65] and the IVCT band (see Figure S47 of the Supporting Information).

DOI: 10.1021/acs.inorgchem.8b03253
Inorg. Chem. 2019, 58, 2695−2707

According to these calculations the vis band at ca. 600 nm can be assigned to Rc → vinylruthenium charge-transfer whereas the higher energy vis band is strongly mixed in character and involves MOs that are delocalized across the entire metal−organic π-system (for electron density difference maps see Figures S48−S53 of the Supporting Information). The suspicious NIR band of every complex is mainly due to the β-HOMO → β-LUMO excitation with some admixture from the lower-lying β-HOMO−1 or, in the case of **Rc*-Ru^{acac+}**, the β-HOMO−3 donor orbitals. The MO contributions of the individual components as listed in Table S6 of the Supporting Information and the electron density difference maps of Figure 10 (more comprehensive accounts can be found as Figures S54−S59 of the Supporting Information) provide useful entry points for discussing the origin of this band. In the ruthenocene-derived complexes, the underlying electronic transition involves only minor charge-transfer (CT) between the peripheral redox sites. It is rather associated with the shifting of electron density from the ruthenocene Ru atom and the Ru(CO)(L)(P^iPr_3)$_2$ (L = Cl^- or $acac^-$) entity at the vinylruthenium site to the central part of the molecules, in particular to the common vinyl linker. Such periphery → bridge CT character is known for IVCT bands in strongly coupled MV systems.[71,72] The absence of CT from one of the different redox sites to the other is also corroborated by the nearly identical positions of the NIR band in 1,2-dichlorobenzene, CH_2Cl_2 or 1,2-$C_2H_4Cl_2$/0.1 M NBu_4PF_6 solutions (Figure S60; unfortunately, the radical cations proved to be unstable in coordinating or more polar solvents and too insoluble in unpolar solvents, thus limiting the available ε_{DK} range in this study). In **Fc-Ru^{Cl+}** and in **Fc-Ru^{acac+}**, however, the IVCT band clearly involves CT from the vinylruthenium to the ferrocenyl site in line with a more ferrocenium-type character of these radical cations. In agreement with this notion we observe negative solvatochromism of this band, indicating a more polar ground state (Figure S61 of the Supporting Information).

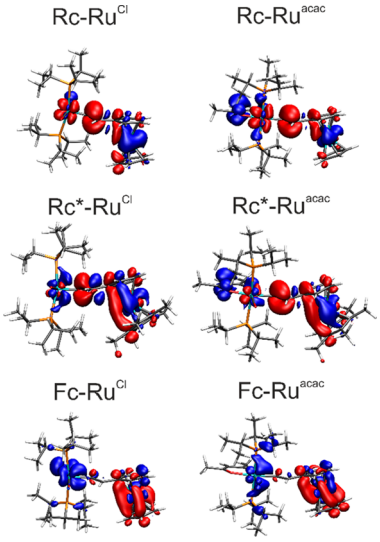

Figure 10. Electron density difference maps of the calculated NIR transition of the metallocene−vinylruthenium radical cations. Red and blue color represent increasing and decreasing electron density, respectively.

On further scrutinizing the NIR band we noted an asymmetric band shape for radical cations of the ruthenocene-derived complexes. No such effect was observed for the ferrocene derivatives (see Figure S62, Supporting Information). Thus, for **Rc-Ru^{acac+}** and, to a lesser degree, for **Rc-Ru^{Cl+}** and **Rc*-Ru^{acac+}**, the half-width at the low-energy side is distinctly smaller than that at the high-energy side. Two Gaussian half-bands with a common peak position but different half-widths are therefore necessary to reproduce the overall band shape adequately. Figure 11 demonstrates the good match between the convoluted band shape and the experiment and the hypothetical shape of the IVCT band when using the band widths derived for the high-energy (left-hand solid and blue broken line) or low-energy sides (right-hand solid and red dotted line). These data are collected in Table 6

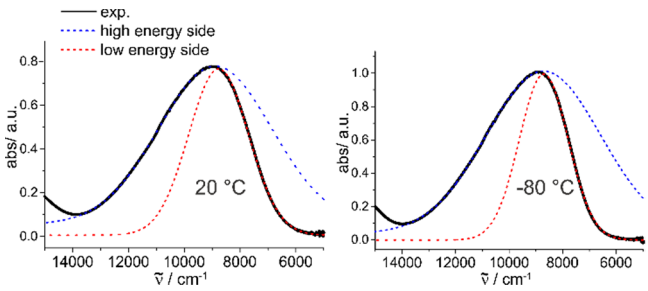

Figure 11. NIR band of **Rc-Ru^{acac+}** at +20 and −80 °C. The experimental spectrum is given by the solid black line. The red and blue dotted lines represent the hypothetical band shape when using the band widths for the low- and high-energy sides.

Table 6. Band Widths of the High- and Low-Energy Sides of the IVCT Band of the Complexes at +20 and −80 °C

	T [°C]	$\Delta\tilde{\nu}_{1/2,high}$	$\Delta\tilde{\nu}_{1/2,low}$	$\Delta\tilde{\nu}_{1/2,high}/\Delta\tilde{\nu}_{1/2,low}$	$\Delta\tilde{\nu}_{1/2,theo}$
Fc-Ru^{Cl+}	+20	2135[a]	2135[a]	1.00	4140
Fc-Ru^{acac+}	+20	2001[a]	2001[a]	1.00	3946
Rc-Ru^{Cl+}	+20	3635	3053	1.19	4738
	−80	3432	2985	1.15	
Rc-Ru^{acac+}	+20	4775	2529	1.89	4578
	−80	5029	2153	2.34	
Rc*-Ru^{Cl+}	+20	2615	2739	0.95	4736
	−80	2529	2558	0.99	
Rc*-Ru^{acac+}	+20	3188	2838	1.12	4562
	−80	3104	2574	1.21	

[a]Only one Gaussian shaped line needed for fitting, see Figure S62 of the Supporting Information.

along with the theoretical half-widths at the high-temperature limit of class II MV systems according to eq 1, which applies for electronically moderately coupled MV systems of class II with intrinsically localized ground states[73−75] (for a more detailed discussion of this issue see the Supporting Information). The ratio of band widths $\Delta\tilde{\nu}_{1/2,high}/\Delta\tilde{\nu}_{1/2,low}$ provides a measure for the band asymmetry.

$$\Delta\tilde{\nu}_{1/2,theo} = \sqrt{2310\tilde{\nu}_{max}} \quad (1)$$

Asymmetric shapes of IVCT bands have been observed for some electronically strongly coupled MV systems of class III or at the class II/III borderline.[71,72,76−80] The band asymmetry was initially ascribed to a very shallow ground-state potential

DOI: 10.1021/acs.inorgchem.8b03253
Inorg. Chem. 2019, 58, 2695−2707

hypersurface with a low energy barrier for thermally activated electron transfer, such that the top of the barrier becomes populated by thermal excitation of low-energy vibrations.[71,76] In this model the truncation of the IVCT band results from the fact that its energy cannot be smaller than twice the electronic coupling matrix element H_{AB}. This model does, however, not hold for some arylene-bridged bis(triarylamine) radical cations, where the band asymmetry was found to increase as the temperature is lowered.[77] In these cases, the band skewing was ascribed to the coupling of the electronic IVCT transition to symmetric high-energy vibrational bridge modes.[72,77,78,81]

With this in mind, we also probed the temperature dependence of band skewing by recording the IVCT band at room temperature and at −80 °C. Inspection of the data in Table 6 reveals that lowering the temperature notably increases the band asymmetry of **Rc-Ru^{acac+}** and, to a lesser extent, **Rc*-Ru^{acac+}** but has hardly any effect for the other compounds. From comparing the data it also becomes evident that for all metallocene-ruthenocene conjugates except **Rc-Ru^{acac+}** $\Delta\tilde{\nu}_{1/2,high}$ is significantly lower than $\Delta\tilde{\nu}_{1/2,theo}$. This is also a typical asset of strongly coupled MV systems close at or beyond the Class II/III limit.

■ $\Delta E_{1/2}$ AND THE ELECTRONIC COUPLING

The relation between $\Delta E_{1/2}$ and the strength of electronic coupling is a broadly discussed issue within the context of mixed-valent (MV) chemistry.[82−85] Generally speaking, $\Delta E_{1/2}$ mirrors the thermodynamic stability of the intermediate MV state of a two-step redox system with respect to the bordering isovalent states as expressed by the equilibrium constant K_{comp} for the comproportionation reaction of eq 3 and the associated free enthalpy change ΔG_{comp}, given by eq 4.

$$K_{comp} = \exp\{(n\cdot F\cdot \Delta E_{1/2})/(R\cdot T)\} \quad (2)$$

$$\Delta G_{comp} = -R\cdot T\cdot \ln K_{comp} \quad (3)$$

$$\Delta G_{comp} = -G_{stat} + \Delta G_{ind} + \Delta G_{exc} + \Delta G_{el} + \Delta G_{res} + \Delta G^{\circ} \quad (4)$$

In a two-step redox system with two chemically inequivalent redox sites, several factors contribute to ΔG_{comp} (eq 4).[82,86−88] Of these, the statistical term ΔG_{stat} of 36 mV,[89] the inductive term ΔG_{ind}[82,90,91] and the magnetic exchange term ΔG_{exc}[92,93] usually account for only some tens of millivolts. They can thus not explain the large differences of more than 400 mV of the $\Delta E_{1/2}$ values of related ferrocene and ruthenocene vinylruthenium complexes. The ΔG^0 contributor reflects the differences of the intrinsic redox potentials of the chemically different redox sites (the "redox asymmetry").[94−97] Considering the data in Table 2, one can identify several pairs of ferrocene/ruthenocene vinylruthenium complexes with identical or rather similar values of ΔG^0 but vastly different values of $\Delta E_{1/2}$. Thus, when using the parent styryl complexes **Ph-Ru^{Cl}** and **Ph-Ru^{acac}** as reference points for estimating the intrinsic redox potentials of the {Ru} site, the $E_{1/2}$ of **Ph-Ru^{Cl}** of 280 mV falls exactly in between those of the $Fc^{0/+}$ (0 mV) and the $Rc^{0/+}$ (560 mV) redox couples such that ΔG^0 for **Fc-Ru^{Cl}** and **Rc-RuCl** should be identical.[42] The same holds for the **Fc-Ru^{acac}** and **Rc*-Ru^{Cl}** and the **Fc-Ru^{Cl}** and the **Rc*-Ru^{acac}** pairs of complexes with similar differences between the intrinsic redox potentials of 22 mV and 50 mV, or 208 and 280 mV between the metallocenyl and the vinylruthenium sites. Their $\Delta E_{1/2}$ values differ nevertheless by 615, 420, or 401 mV.

Our results clearly indicate that the radical cations of the ruthenocene vinylruthenium conjugates even surpass their ferrocene counterparts in terms of charge and spin delocalization. The resonance term ΔG_{res}, which reflects the thermodynamic stabilization of the MV state due to charge delocalization over the two conjoined redox-active entities across the common connector, should therefore be even larger for the ruthenocene derivatives. This leaves us with the conclusion that the differences in $\Delta E_{1/2}$ arise mainly from the electrostatic contribution ΔG_{el}. ΔG_{el} indicates how the charge generated during the first redox process increases the free enthalpy change of the second electron transfer process owing to electrostatic repulsion. It therefore depends on the solvent−solute interactions and ion pairing effects between the solute and the counterion of the supporting electrolyte that accompany the solvation of charged versus uncharged and of charge-localized versus charge-delocalized MV species.[43,44,83,98−102]

Such large differences of ΔG_{el} on a seemingly minor variation of one redox site come as a surprise. A possible explanation assumes a different location of the PF_6^- counterion. In the ferrocene derivatives, the positive charge mainly resides on the metallocenium site while the vinylruthenium moiety remains rather electron rich. The PF_6^- anion may therefore be positioned close to the ferrocenium site and rather remote from the vinylruthenium one. The lesser shielding of the positive charge at the side of the vinylruthenium moiety would then account for a rather large electrostatic penalty for the second oxidation. In the more delocalized ruthenocene systems, where the positive charge is evenly spread over the entire molecule, a suitably sized anion may enter the cleft between the metallocene and the vinylruthenium entities and shield them from each other more efficiently, thus diminishing ΔG_{el} and $\Delta E_{1/2}$. In this vein we note that, in the presence of NBu_4^+ $[B\{C_6H_3(CF_3)_2\text{-}3,5\}_4]^-$ supporting electrolyte with its sterically much more demanding anion, the forward peaks of the first and the second oxidation of **Rc-Ru^{Cl}** and **Rc-Ru^{acac}** are separated by 630 and 720 mV, respectively (see Figure S18 of the Supporting Information). This hints at a decisive role of the counterion in determining $\Delta E_{1/2}$.

■ SUMMARY AND CONCLUSION

We have synthesized the four ruthenocene vinylruthenium conjugates **Rc-Ru^{Cl}**, **Rc*-Ru^{Cl}**, **Rc-Ru^{acac}** and **Rc*-Ru^{acac}** with either ruthenocene (Rc) or pentamethylruthenocene (Rc*), or with 16 valence electron (VE) Ru(CO)Cl(P^iPr_3) (Ru^{Cl}) or 18 VE Ru(CO)(acac)(P^iPr_3)$_2$, acac = κO,O′-acetylacetonato) alkenylruthenium entities. Our primary interest was to compare the electronic coupling between the chemically disparate redox sites in their mixed-valent (MV) state to that in their ferrocene congeners **Fc-Ru^{Cl}** and **Fc-Ru^{acac}**.

The combined results of our IR, EPR and UV/vis/NIR studies leave no doubt that the radical cations of the ruthenocene−vinylruthenium conjugates are rare examples of MV systems with two chemically different redox sites of class III or at the class III/II borderline. Strong electronic coupling in these systems is manifest through nearly uniform shifts of the carbonyl IR label at the Ru(CO) site on stepwise oxidation of the neutral complexes to the radical cations and the dications. Particularly revealing is the presence of an intense nonsolvatochromic IVCT band in the near IR (NIR) with a

DOI: 10.1021/acs.inorgchem.8b03253
Inorg. Chem. 2019, 58, 2695−2707

significantly smaller half-width compared to the high-temperature limit of a Class II MV system. For **Rc-Ru^{acac+}** and **Rc*-Ru^{Cl}**, which constitute the electronically most strongly coupled systems of this series, the IVCT band is skewed and has a distinctly smaller half-width at the low energy side. The low-energy cutoff becomes even more prominent at lower T. Such behavior is typical of (almost) delocalized MV systems of class III or at the class II/III borderline and is due to coupling of the electronic IVCT transition to symmetrical vibrational modes of the bridge. The present findings complement our previous study on the MV radical cations of vinylruthenium triarylamine conjugates $(4\text{-}RC_6H_4)_2N{-}C_6H_4{-}CH{=}CH{-}\{Ru^{Cl}\}$, where skewed IVCT bands were also observed for those congeners situated at the class II/III borderline.[31]

The MV radical cations of their ferrocene analogs **Fc-Ru^{Cl+}** and **Fc-Ru^{acac+}** are electronically less strongly coupled and their IVCT bands are adequately represented by a single Gaussian. Quite interestingly, the HOMO of the ferrocene vinyl ruthenium conjugates appears to be as delocalized as that of their ruthenocene analogs. This does, however, not pertain to their radical cations. For the ruthenocene derivatives, the β-LUSO of the associated radical cations has the same character as the HOMO of their neutral precursors. In the ferrocene analogs, however, the β-LUSO, which represents the spin orbital from where the electron is taken, is strongly biased toward the ferrocenyl entity.

Perhaps the most stunning finding of this study comes from the comparison between the ruthenocene derivatives and their ferrocene analogs. We have identified several pairs of ferrocene/ruthenocene vinylruthenium conjugates where the free enthalpy differences ΔG^0 for oxidation of the vinyl-ruthenium or the metallocene site are largely identical or very similar. Even in these cases, the $\Delta E_{1/2}$ values of the ruthenocene complexes are by 400 to over 600 mV smaller than for their ferrocene analogs despite the stronger electronic coupling of the former. A different positioning of the associated counterion either close to the metallocene site in the case of a more localized charge or within the cleft in between the metallocene and the vinylruthenium sites in the more delocalized congeners may explain these unexpected observations.

EXPERIMENTAL SECTION

General methods and procedures are detailed in the Supporting Information. Scheme 2 provides the atomic numbering used for the assignment of NMR signals.

Scheme 2. General Atomic Numbering for the Cp- and Cp*-Substituted Metallocenes−Vinyl Ruthenium Conjugates

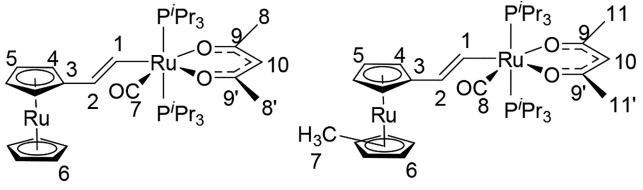

Synthesis and Characterization. *(η^5-C_5H_5)Ru(η^5-C_5H_4−CH═CH−){Ru(CO)Cl(P^{i}Pr$_3$)$_2$}*, ***Rc-Ru^{Cl}***. Ethynylruthenocene (151 mg, 0.59 mmol, 1 equiv) and HRu(CO)Cl(P^{i}Pr$_3$)$_2$ (287 mg, 0.59 mmol, 1 equiv) were put into a falcon tube and dissolved in 10 mL of dry CH_2Cl_2 under inert gas conditions. The solution was stirred for 30 min. After evaporating most of the solvent under nitrogen, the crude product was dried under reduced pressure. The residue was washed with dry pentane (10 mL), centrifuged and the washing solution was removed via decanting. After evaporating to dryness, compound **4** was isolated as reddish gray solid in 56% yield (250 mg, 0.34 mmol). ^{1}H NMR (400 MHz, CD_2Cl_2): δ 7.64 (dt, 1H, $^3J_{HH}$ = 13.3 Hz, *H*-1), 5.39 (dt, 1H, $^3J_{HH}$ = 13.3 Hz, $^3J_{HP}$ = 2.2 Hz, *H*-2), 4.44 (vt, 2H, $^3J_{HH}$ = 1.6 Hz, *H*-5), 4.42 (s, 5H, *H*-6), 4.36 (vt, 2H, $^3J_{HH}$ = 1.6 Hz, *H*-4), 2.66−2.78 (m, 6H, P(C*H*(CH$_3$)$_2$)$_3$), 1.25−1.32 (m, 36H, P(CH-(C*H*$_3$)$_2$)$_3$). ^{13}C NMR (100.6 MHz, CD_2Cl_2): δ 203.5 (t, $^2J_{CP}$ = 13.3 Hz, *C*-7), 144.0 (t, $^2J_{CP}$ = 10.8 Hz, *C*-1), 129.3 (t, $^3J_{CP}$ = 3.4 Hz, *C*-2), 93.2 (t, $^4J_{CP}$ = 1.7 Hz, *C*-3), 70.6 (s, *C*-6), 69.2 (s, *C*-4), 67.4 (s, *C*-5), 24.9 (t, $^1J_{CP}$ = 9.8 Hz, P(*C*H(CH$_3$)$_2$)$_3$), 20.3 (s, P(CH(*C*H$_3$)$_2$)$_3$), 20.2 (s, P(CH(*C*H$_3$)$_2$)$_3$). ^{31}P NMR (162 MHz, CD_2Cl_2): δ 38.3 (s, 2P, P^{i}Pr$_3$). Anal. Calcd for $C_{31}H_{53}ClOP_2Ru_2$: C, 50.23; H, 7.21. Found: C, 50.02; H: 7.11.

(η^5-C_5H_5)Ru(η^5-C_5H_4−CH═CH−){Ru(acac)(CO)(P^{i}Pr$_3$)$_2$}, ***Rc-Ru^{acac}***. To a solution of potassium hydroxide (20 mg, 0.36 mmol, 2.6 equiv) in dry methanol (10 mL) was added acetylacetone (0.08 mL, 74 mg, 0.74 mmol, 5.5 equiv). The mixture was stirred at 50 °C for 1.5 h. The resulting solution was added to a solution of **Rc-Ru^{Cl}** (100 mg, 0.14 mmol, 1 equiv) in dry CH_2Cl_2 (10 mL) at room temperature. The reaction mixture was stirred for 1 h at 40 °C. Then, the solvents were removed under reduced pressure. The residue was dissolved in CH_2Cl_2 and filtered via syringe filtration into a falcon tube under inert gas conditions. The solvent was removed and the crude product was dried under reduced pressure. The solid was washed with dry methanol (5 mL). After evaporating to dryness, compound **5** was obtained as yellow powder in 62% yield (67 mg, 0.08 mmol). ^{1}H NMR (400 MHz, CD_2Cl_2): δ 8.07 (dt, 1H, $^3J_{HH}$ = 16.6 Hz, $^3J_{HP}$ = 1.6 Hz, *H*-1), 5.74 (dt, 1H, $^3J_{HH}$ = 16.6 Hz, $^4J_{HP}$ = 1.8 Hz, *H*-2), 5.28 (s, 1H, *H*-10), 4.52 (vt, 2H, $^3J_{HH}$ = 1.6 Hz, *H*-5), 4.43 (s, 5H, *H*-6), 4.35 (vt, 2H, $^3J_{HH}$ = 1.6 Hz, *H*-4), 2.25−2.38 (m, 6H, P(C*H*(CH$_3$)$_2$)$_3$), 1.87 (s, 3H, *H*-8/8′), 1.76 (s, 3H, *H*-8/8′), 1.21−1.30 (m, 36H, P(CH(C*H*$_3$)$_2$)$_3$). ^{13}C NMR (100.6 MHz, CD_2Cl_2): δ 210.6 (t, $^2J_{CP}$ = 15.3 Hz, *C*-7), 188.9 (s, *C*-9/9′), 187.1 (s, *C*-9/9′), 160.6 (t, $^2J_{CP}$ = 11.9 Hz, *C*-1), 128.0 (t, $^3J_{CP}$ = 2.4 Hz, *C*-2), 100.4 (s, *C*-10), 97.4 (t, $^4J_{CP}$ = 1.4 Hz, *C*-3), 70.3 (s, *C*-6), 68.8 (s, *C*-4), 67.3 (s, *C*-5), 28.9 (s, *C*-8/8′), 24.7 (t, $^1J_{CP}$ = 8.7 Hz, P(*C*H(CH$_3$)$_2$)$_3$), 20.1 (s, P(CH(*C*H$_3$)$_2$)$_3$), 19.9 (s, P(CH(*C*H$_3$)$_2$)$_3$). ^{31}P NMR (162 MHz, CD_2Cl_2): δ 36.3 (s, 2P, P^{i}Pr$_3$). Anal. Calcd for $C_{36}H_{60}O_3P_2Ru_2$: C, 53.72; H, 7.51. Found: C, 53.60; H, 7.53.

C_6H_5CH═CH−){Ru(acac)(CO)(P^{i}Pr$_3$)$_2$}, ***Ph-Ru^{acac}***. Complex **Ph-Ru^{acac}** was prepared from the literature-known complex **Ph-Ru^{Cl}**[45] according to the procedure described for complex **Rc-Ru^{acac}**. ^{1}H NMR (400 MHz, CD_2Cl_2): δ 8.96 (dt, 1H, $^3J_{HH}$ = 16.6 Hz, $^3J_{HP}$ = 1.6 Hz, *H*-1), 7.20−7.11 (m, 4H, *H*-Ph), 6.98 (tt, 1H, $^3J_{HH}$ = 6.5, 2.1 Hz *H*-Ph), 6.40 (dt, 1H, $^3J_{HH}$ = 16.7 Hz,, $^3J_{HP}$ = 1.9 Hz, *H*-2), 5.33 (s, 1H, *H*-12), 2.34 (m, 6H, P(C*H*(CH$_3$)$_2$)$_3$), 1.93 (s, 3H, *H*-11/11′), 1.79 (s, 3H, *H*-11/11′), 1.35−1.16 (m, 36H, P(CH(C*H*$_3$)$_2$)$_3$). ^{13}C NMR (100.6 MHz, CD_2Cl_2): δ 210.5 (t, $^2J_{CP}$ = 15.4 Hz, *C*-7), 189.1 (s, C-9/C-9′), 187.2 (s, C-9/C-9′), 166.5 (t, $^2J_{CP}$ = 12.3 Hz, *C*-1), 142.5 (t, $^3J_{CP}$ = 1.50 Hz, C-*ipso*Ph), 134.4 (t, $^3J_{CP}$ = 2.3 Hz, C-2), 128.7 (s, C-*o*/*m*Ph), 124.2 (s, C-*o*/*m*Ph), 123.2 (s, C-*p*Ph), 100.6 (s, C-10), 28.9 (s, C-11/C-11′) 24.9 (t, $^1J_{CP}$ = 8.7 Hz, P(CH(CH$_3$)$_2$)$_3$), 20.0 (s, P(CH(*C*H$_3$)$_2$)$_3$), 19.9 (s, P(CH(*C*H$_3$)$_2$)$_3$. ^{31}P NMR (162 MHz, CD_2Cl_2): δ 35.6 (s, 2P, P^{i}Pr$_3$). Anal. Calcd for $C_{32}H_{56}O_3P_2Ru$: C, 58.97; H, 8.66. Found: C, 58.72; H, 8.42.

(η^5-C_5Me_5)Ru(η^5-C_5H_4−CH═CH−){Ru(CO)Cl(P^{i}Pr$_2$)$_2$}, ***Rc*-Ru^{Cl}***. 1-Ethynyl-1′,2′,3′,4′,5′-pentamethylruthenocene was prepared according to the literature.[103] Hydroruthenation was carried out as for complex **Rc-Ru^{Cl}**. Complex **Rc*-Ru^{Cl}** was isolated as a red solid in 57% yield (250 mg, 0.34 mmol). ^{1}H NMR (400 MHz, CD_2Cl_2): δ 7.39 (dt, 1H, $^3J_{HH}$ = 13.2 Hz, $^3J_{HP}$ = 1.6 Hz *H*-1), 5.29 (dt, 1H, $^3J_{HH}$ = 13.2 Hz, $^3J_{HP}$ = 1.9 Hz, *H*-2), 3.94 (vt, 2H, $^3J_{HH}$ = 1.7 Hz, *H*-5), 3.90 (vt, 2H, $^3J_{HH}$ = 1.7 Hz, *H*-4), 1.87 (s, 15H, C$_5$(*C*H$_3$)$_5$), 2.77−2.66 (m, 6H, P(C*H*(CH$_3$)$_2$)$_3$), 1.34−1.22 (m, 36H, P(CH(C*H*$_3$)$_2$)$_3$). ^{13}C NMR (100.6 MHz, CD_2Cl_2): δ 203.7 (t, $^2J_{CP}$ = 13.3 Hz, *C*-8), 143.7 (t, $^2J_{CP}$ = 10.5 Hz, *C*-1), 129.3 (t, $^3J_{CP}$ = 3.4 Hz, *C*-2), 93.2 (t, $^4J_{CP}$ = 1.70 Hz, *C*-3), 84.9 (s, C$_5$(CH$_3$)$_5$), 71.8 (s, *C*-4), 69.9 (s, *C*-5), 24.6 (t, $^1J_{CP}$ = 9.8 Hz, P(CH(CH$_3$)$_2$)$_3$), 20.2 (s, P(CH(*C*H$_3$)$_2$)$_3$), 20.2 (s, P(CH(*C*H$_3$)$_2$)$_3$), 12.4 (s, C$_5$(*C*H$_3$)$_5$). ^{31}P NMR (162 MHz, CD_2Cl_2):

DOI: 10.1021/acs.inorgchem.8b03253
Inorg. Chem. 2019, 58, 2695−2707

δ 37.9 (s, 2P, P^iPr_3). Anal. Calcd for $C_{36}H_{63}ClOP_2Ru_2$: C, 53.29; H, 7.83. Found: C, 53.31, H: 7.84.

(η^5-C_5Me_5)Ru(η^5-C_5H_4–CH=CH–){Ru(acac)(CO)(P^iPr_3)$_2$}, Rc-Ru^{acac}.* The synthesis was performed according to that used for complex **Rc-Ru^{acac}**. It was obtained as yellow powder in 60% yield (100 mg, 0.08 mmol). ^{1}H NMR (400 MHz, CD_2Cl_2): δ 7.84 (dt, 1H, $^3J_{HH}$ = 16.5 Hz, $^3J_{HP}$ = 1.6 Hz, *H*-1), 5.67 (dt, 1H, $^3J_{HH}$ = 16.5 Hz, $^4J_{HP}$ = 1.9 Hz, *H*-2), 5.26 (s, 1H, *H*-10), 3.96 (vt, 2H, $^3J_{HH}$ = 1.7 Hz, *H*-5), 3.92 (vt, 2H, $^3J_{HH}$ = 1.7 Hz, *H*-4), 2.39–2.30 (m, 6H, P(C*H*(CH$_3$)$_2$)$_3$), 1.91 (s, 15H, C$_5$(C*H*$_3$)$_5$), 1.84 (s, 3H, *H*-11/11′), 1.74 (s, 3H, *H*-11/11′), 1.30–1.20 (m, 36H, P(CH(C*H*$_3$)$_2$)$_3$). ^{13}C NMR (100.6 MHz, CD_2Cl_2): δ 210.7 (t, $^2J_{CP}$ = 15.2 Hz, *C*-8), 188.7 (s, *C*-9/9′), 187.2 (s, *C*-9/9′), 161.2 (t, $^2J_{CP}$ = 11.6 Hz, *C*-1), 127.9 (t, $^3J_{CP}$ = 2.5 Hz, *C*-2), 100.4 (s, *C*-10), 97.7 (t, $^4J_{CP}$ = 1.3 Hz, *C*-3), 84.6 (s, C$_5$(CH$_3$)$_5$), 71.2 (s, *C*-4), 70.0 (s, *C*-5), 28.9 (s, C-11/C-11′), 28.8 (s, C-11/C-11′), 24.6 (t, $^1J_{CP}$ = 8.6 Hz, P(CH(CH$_3$)$_2$)$_3$), 20.1 (s, P(CH(CH$_3$)$_2$)$_3$), 18.8 (s, P(CH(CH$_3$)$_2$)$_3$), 12.5 (s, C$_5$(CH$_3$)$_5$). ^{31}P NMR (162 MHz, CD_2Cl_2): δ 35.0 (s, 2P, P^iPr_3). Anal. Calcd for $C_{41}H_{69}O_3P_2Ru_2$: C, 56.34; H, 7.96. Found: C, 56.32, H, 8.13.

(η^5-C_5H_5)Fe(η^5-C_5H_4–CH=CH–){Ru(acac)(CO)(P^iPr_3)$_2$}, Fc-Ru^{acac}. Complex **Fc-Ru^{acac}** was prepared from the literature-known complex **Fc-Ru^{Cl}**[26] according to the procedure described for complex **Rc-Ru^{acac}**. ^{1}H NMR (400 MHz, CD_2Cl_2): δ 8.10 (dt, 1H, $^3J_{HH}$ = 16.5 Hz, $^3J_{HP}$ = 1.6 Hz, *H*-1), 5.90 (dt, 1H, $^3J_{HH}$ = 16.5 Hz, $^4J_{HP}$ = 1.8 Hz, *H*-2), 5.25 (s, 1H, *H*-10), 4.08 (vt, 2H, $^3J_{HH}$ = 1.6 Hz, *H*-5), 4.04 (s, 5H, *H*-6), 3.99 (vt, 2H, $^3J_{HH}$ = 1.6 Hz, *H*-4), 2.42–2.32 (m, 6H, P(C*H*(CH$_3$)$_2$)$_3$), 1.87 (s, 3H, *H*-8/8′), 1.76 (s, 3H, *H*-8/8′), 1.32–1.20 (m, 36H, P(CH(C*H*$_3$)$_2$)$_3$). ^{13}C NMR (100.6 MHz, CD_2Cl_2): δ 210.7 (t, $^2J_{CP}$ = 15.3 Hz, *C*-7), 188.7 (s, *C*-9/9′), 187.2 (s, *C*-9/9′), 161.21 (t, $^2J_{CP}$ = 12.0 Hz, *C*-1), 127.9 (t, $^3J_{CP}$ = 2.6 Hz, *C*-2), 100.4 (s, *C*-10), 97.7 (t, $^4J_{CP}$ = 1.1 Hz, *C*-3), 84.6 (s, *C*-6), 84.6 (s, *C*-5), 71.2 (s, *C*-4), 70.0 (s, *C*-8/8′), 24.6 (t, $^1J_{CP}$ = 8.5 Hz, P(CH(CH$_3$)$_2$)$_3$), 20.1 (s, P(CH(CH$_3$)$_2$)$_3$), 19.8 (s, P(CH(CH$_3$)$_2$)$_3$). ^{31}P NMR (162 MHz, CD_2Cl_2): δ 35.9 (s, 2P, P^iPr_3). Anal. Calcd for $C_{36}H_{60}FeO_3P_2Ru$: C, 56.91; H, 7.96. Found: C, 57.12; H, 8.03.

■ ASSOCIATED CONTENT

Supporting Information

The Supporting Information is available free of charge on the ACS Publications website at DOI: 10.1021/acs.inorgchem.8b03253.

General procedures, synthesis of starting compounds, NMR spectra, crystallographic data for **Ph-Ru^{acac}**, cyclic voltammograms, spectra obtained in IR and UV/vis/NIR spectroelectrochemical experiments, NIR spectra in different solvents, graphical MO representations, compositions of MOs from HOMO−10 to LUMO+10, and details of the TD-DFT analysis of the neutral complexes and their associated radical cations as well as electron density difference maps for the various transitions and spin density plots of the radical cations (PDF)

Accession Codes

CCDC 919534 contains the supplementary crystallographic data for this paper. These data can be obtained free of charge via www.ccdc.cam.ac.uk/data_request/cif, or by emailing data_request@ccdc.cam.ac.uk, or by contacting The Cambridge Crystallographic Data Centre, 12 Union Road, Cambridge CB2 1EZ, UK; fax: +44 1223 336033.

■ AUTHOR INFORMATION

Corresponding Author

*(R.F.W.) E-mail: rainer.winter@uni-konstanz.de.

ORCID

Rainer F. Winter: 0000-0001-8381-0647

Notes

The authors declare no competing financial interest.

■ ACKNOWLEDGMENTS

This work was supported by the Deutsche Forschungsgemeinschaft (Grant Wi1262/13-1). We also thank the State of Baden-Württemberg for providing us access to the bwHPC computational facilities at the Karlsruhe Institute of Technology.

■ REFERENCES

(1) LeVanda, C.; Bechgaard, K.; Cowan, D. O. Chemistry of π-bridged analogues of biferrocene and biferrocenylene. *J. Org. Chem.* **1976**, *41*, 2700–2704.

(2) Cowan, D. O.; LeVanda, C.; Park, J.; Kaufman, F. Organic solid state. VIII. Mixed-valence ferrocene chemistry. *Acc. Chem. Res.* **1973**, *6*, 1–7.

(3) Kramer, J. A.; Hendrickson, D. N. Electron transfer in mixed-valent diferrocenylacetylene and [2.2]ferrocenophane-1,13-diyne. *Inorg. Chem.* **1980**, *19*, 3330–3337.

(4) Hendrickson, D. N.; Oh, S. M.; Dong, T.-Y.; Kambara, T.; Cohn, M. J.; Moore, M. F. Effect of Lattice Dynamics on Intramolecular Electron-Transfer Rates in Mixed-Valence Complexes. *Comments Inorg. Chem.* **1985**, *4*, 329–349.

(5) Dong, T.-Y.; Kambara, T.; Hendrickson, D. N. Counterion effects on the intramolecular electron-transfer rate of mixed-valence biferrocenium salts: micromodulation and phase transitions. *J. Am. Chem. Soc.* **1986**, *108*, 4423–4432.

(6) Lowery, M. D.; Hammack, W. S.; Drickamer, H. G.; Hendrickson, D. N. Effects of ion aggregation on the intervalence transfer band of the mixed-valence biferrocenium cation in solution. *J. Am. Chem. Soc.* **1987**, *109*, 8019–8024.

(7) Lohan, M.; Ecorchard, P.; Rüffer, T.; Justaud, F.; Lapinte, C.; Lang, H. 1′,1‴-Bis(ethynyl)biferrocene as a Linking Group for Gold, Ruthenium, and Osmium Fragments: Synthesis, Solid State Structures, and Electrochemical, UV–Vis, and EPR Spectroscopical Studies. *Organometallics* **2009**, *28*, 1878–1890.

(8) Lohan, M.; Justaud, F.; Roisnel, T.; Ecorchard, P.; Lang, H.; Lapinte, C. 1′,1‴-Bis(ethynyl)biferrocenyl-Bridged Fe(dppe)Cp* Units: Synthesis, Solid-State Structures, and Electronic Couplings. *Organometallics* **2010**, *29*, 4804–4817.

(9) Lohan, M.; Justaud, F.; Lang, H.; Lapinte, C. Synthesis, Spectroelectrochemical, and EPR Spectroscopic Studies of Mixed Bis(alkynyl)biferrocenes of the Type (LnMC≡C)(LnM′C≡C)bfc. *Organometallics* **2012**, *31*, 3565–3574.

(10) Wilson, L. E.; Hassenrück, C.; Winter, R. F.; White, A. J. P.; Albrecht, T.; Long, N. J. Functionalised Biferrocene Systems towards Molecular Electronics. *Eur. J. Inorg. Chem.* **2017**, *2017*, 496–504.

(11) Wilson, L. E.; Hassenrück, C.; Winter, R. F.; White, A. J. P.; Albrecht, T.; Long, N. J. Ferrocene- and Biferrocene-Containing Macrocycles towards Single-Molecule Electronics. *Angew. Chem., Int. Ed.* **2017**, *56*, 6838–6842.

(12) Hoffmann, V.; le Pleux, L.; Häussinger, D.; Unke, O. T.; Prescimone, A.; Mayor, M. Deltoid versus Rhomboid: Controlling the Shape of Bis-ferrocene Macrocycles by the Bulkiness of the Substituents. *Organometallics* **2017**, *36*, 858–866.

(13) Sato, M.; Hayashi, Y.; Shintate, H.; Katada, M.; Kawata, S. Oxidized Fe^{II} ferrocenylacetylide complexes. A novel type of mixed-valence complex. *J. Organomet. Chem.* **1994**, *471*, 179–184.

(14) Sato, M.; Hayashi, Y.; Kumakura, S.; Shimizu, N.; Katada, M.; Kawata, S. Synthesis and Oxidation of Iron(II) Ferrocenylacetylide Diphosphine Complexes. A Novel Type of Mixed-Valence Complex. *Organometallics* **1996**, *15*, 721–728.

(15) Sato, M.; Shintate, H.; Kawata, Y.; Sekino, M.; Katada, M.; Kawata, S. Oxidized Ruthenium Ferrocenylacetylide Complexes, [(η^5-C_5H_5)L_2RuCCFc]PF_6 and [(η^5-C_5Me_5)L_2RuCCFc]PF_6 (L = Phosphines). Electron-Delocalized Heterobinuclear Mixed-Valence Complexes. *Organometallics* **1994**, *13*, 1956–1962.

(16) Colbert, M. C. B.; Lewis, J.; Long, N. J.; Raithby, P. R.; White, A. J. P.; Williams, D. J. Synthetic, structural, electrochemical and electronic chracterisation of heterobimetallic bis(acetylide) ferrocene complexes. *J. Chem. Soc., Dalton Trans.* **1997**, 99−104.
(17) Sato, M.; Kawata, Y.; Shintate, H.; Habata, Y.; Akabori, S.; Unoura, K. Novel Structural Rearrangements Induced by Metal-Metal-Interactions in Ruthenium(II) Ruthenocenyl- and (Pentamethylruthenocenyl)acetylide Complexes, RcCCRuL$_2$(η^5-C$_5$R$_5$) and Rc'CCRuL$_2$(η^5-C$_5$R$_5$) [Rc = Ruthenocenyl, Rc' = Pentamethylruthenocenyl, L$_2$ = 2 PPh$_3$ or Ph$_2$PCH$_2$CH$_2$PPh$_2$ (dppe), R = H or Me]. *Organometallics* **1997**, *16*, 1693−1701.
(18) Sato, M.; Iwai, A.; Watanabe, M. Synthesis and Redox Behavior of Ruthenium(II) 2,3,4,5-Tetramethylruthenocenylacetylide and Related Complexes. Formation of μ-[(Cyclopentadienylidene)-ethylidene]diruthenium Complexes Containing a Strong Metal-Metal Interaction. *Organometallics* **1999**, *18*, 3208−3219.
(19) Kuwana, T.; Bublitz, D. E.; Hoh, G. Chronopotentiometric Studies on the Oxidation of Ferrocene, Ruthenocene, Osmocene and Some of their Derivatives1. *J. Am. Chem. Soc.* **1960**, *82*, 5811−5817.
(20) Denisovich, L. I.; Zakurin, N. V.; Bezrukova, A. A.; Gubin, S. P. Chemical and electrochemical oxidation of metallocenes, reactions of metallocenes with mercury salts. *J. Organomet. Chem.* **1974**, *81*, 207−216.
(21) Sohn, Y. S.; Schlueter, A. W.; Hendrickson, D. N.; Gray, H. B. Synthesis, characterization, and molecular structure of halogen oxidation products of ruthenocene. *Inorg. Chem.* **1974**, *13*, 301−304.
(22) Kukharenko, S. V.; Strelets, V. V.; Kudinov, A. R.; Kreidlin, A. Z.; Peterleitner, M. G.; Denisovich, L. I.; Rybinskaya, M. I. Reactivity of 17- and 19-electron organometallic complexes. Formation of bent sandwich 19-electron radical cation complexes of osmium and ruthenium. *J. Organomet. Chem.* **1996**, *519*, 1−5.
(23) Swarts, J. C.; Nafady, A.; Roudebush, J. H.; Trupia, S.; Geiger, W. E. One-Electron Oxidation of Ruthenocene: Reactions of the Ruthenocenium Ion in Gentle Electrolyte Media. *Inorg. Chem.* **2009**, *48*, 2156−2165.
(24) Polit, W.; Mücke, P.; Wuttke, E.; Exner, T.; Winter, R. F. Charge and Spin Confinement to the Amine Site in 3-Connected Triarylamine Vinyl Ruthenium Conjugates. *Organometallics* **2013**, *32*, 5461−5472.
(25) Robin, M. B.; Day, P. Mixed Valence Chemistry - A survey and Classification. *Adv. Inorg. Chem. Radiochem.* **1968**, *10*, 247−422.
(26) Kowalski, K.; Linseis, M.; Winter, R. F.; Zabel, M.; Záliš, S.; Kelm, H.; Krüger, H.-J.; Sarkar, B.; Kaim, W. Charge Delocalization in a Heterobimetallic Ferrocene−(Vinyl)Ru(CO)Cl(P^{i}Pr$_3$)$_2$ System. *Organometallics* **2009**, *28*, 4196−4209.
(27) Pevny, F.; Di Piazza, E.; Norel, L.; Drescher, M.; Winter, R. F.; Rigaut, S. Fully delocalized (ethynyl)(vinyl)phenylene bridged diruthenium radical complexes. *Organometallics* **2010**, *29*, 5912−5918.
(28) Wuttke, E.; Fink, D.; Anders, P.; Maria Hoyt, A.-L.; Polit, W.; Linseis, M.; Winter, R. F. Homo- and heterobimetallic 1,4-divinylphenylene- and naphthalene-1,8-divinyl-bridged diruthenium, diosmium and ruthenium osmium complexes. *J. Organomet. Chem.* **2016**, *821*, 4−18.
(29) Wuttke, E.; Hervault, Y.-M.; Polit, W.; Linseis, M.; Erler, P.; Rigaut, S.; Winter, R. F. Divinylphenylene- and Ethynylvinylphenylene-Bridged Mono-, Di-, and Triruthenium Complexes for Covalent Binding to Gold Electrodes. *Organometallics* **2014**, *33*, 4672−4686.
(30) Polit, W.; Exner, T.; Wuttke, E.; Winter, R. F. Vinylruthenium-Triarylamine Conjugates as Electroswitchable Polyelectrochromic NIR Dyes. *BioInorg. React. Mech.* **2012**, *8*, 85−105.
(31) Hassenrück, C.; Winter, R. F. Manipulation and Assessment of Charge and Spin Delocalization in Mixed-Valent Triarylamine−Vinylruthenium Conjugates. *Inorg. Chem.* **2017**, *56*, 13517−13529.
(32) Chen, J.; Wuttke, E.; Polit, W.; Exner, T.; Winter, R. F. Simultaneous Occurrence of Three Different Valence Tautomers in meso-Vinylruthenium-Modified Zinc Porphyrin Radical Cations. *J. Am. Chem. Soc.* **2013**, *135*, 3391−3394.
(33) Hassenrück, C.; Mücke, P.; Scheck, J.; Demeshko, S.; Winter, R. F. Oxidized Styrylruthenium−Ferrocene Conjugates: From Valence Localization to Valence Tautomerism. *Eur. J. Inorg. Chem.* **2017**, *2017*, 401−411.
(34) Sato, M.; Kawata, Y.; Kudo, A.; Iwai, A.; Saitoh, H.; Ochiai, S. Synthesis, structure and redox chemistry of 1,2-bis(ruthenocenyl)-ethylene derivatives: a novel structural rearrangement to a (μ-η^6:η^6-pentafulvadiene)diruthenium complex upon two-electron oxidation. *J. Chem. Soc., Dalton Trans.* **1998**, 2215−2224.
(35) Sato, M.; Kubota, Y.; Kawata, Y.; Fujihara, T.; Unoura, K.; Oyama, A. Synthesis and Some Properties of Binuclear Ruthenocenes Bridged by Oligoynes: Formation of Bis(cyclopentadienylidene)-cumulene Diruthenium Complexes in the Two-Electron Oxidation. *Chem. - Eur. J.* **2006**, *12*, 2282−2292.
(36) Bruce, M. I.; Jevric, M.; Perkins, G. J.; Skelton, B. W.; White, A. H. Trimetallic complexes containing 1,1′-Rc′(CC)$_2$ units [Rc′ = ruthenocene-1,1′-diyl, Ru(η-C$_5$H$_4$)$_2$]. *J. Organomet. Chem.* **2007**, *692*, 1757−1765.
(37) Werner, H.; Esteruelas, M. A.; Otto, H. Insertion Reactions of the 16-Electron Complexes MHCl(CO)(P-i-Pr$_3$)$_2$ (M = Ru, Os) with Alkynes. The X-ray Crystal Structure of Os((E)CH = CHPh)Cl-(CO)(P-i-Pr$_3$)$_2$. *Organometallics* **1986**, *5*, 2295−2299.
(38) Hill, A. F. Mononuclear Complexes of Ruthenium and Osmium Containing η1 Carbon Ligands. *Comprehensive Organometallic Chemistry II* **1995**, *7*, 399−411.
(39) Marchenko, A. V.; Gérard, H.; Eisenstein, O.; Caulton, K. G. A comprehensive view of M-H addition across the RCCH bond: frustration culminating in ultimate union. *New J. Chem.* **2001**, *25*, 1244−1255.
(40) Marchenko, A. V.; Gérard, H.; Eisenstein, O.; Caulton, K. G. A comparative study of olefin or acetylene insertion into Ru−H or Os−H of MHCl(CO)(phosphine)$_2$. *New J. Chem.* **2001**, *25*, 1382−1388.
(41) Choi, S.-H.; Bytheway, I.; Lin, Z.; Jia, G. Understanding the Preference for the Coplanarity of Alkenyl and Carbonyl Ligands in η^1-Alkenyl Transition-Metal Complexes: A Simple Molecular Orbital Approach and *ab Initio* Calculations. *Organometallics* **1998**, *17*, 3974−3980.
(42) Hill, M. G.; Lamanna, W. M.; Mann, K. R. Tetrabutylammonium tetrakis[3,5-bis(trifluoromethyl)phenyl]borate as a noncoordinating electrolyte: reversible 1e$^-$ oxidations of ruthenocene, osmocene, and Rh$_2$(TM$_4$)$_4^{2+}$ (TM$_4$=2,5-diisocyano-2,5-dimethylhexane). *Inorg. Chem.* **1991**, *30*, 4687−4690.
(43) Barrière, F.; Camire, N.; Geiger, W. E.; Mueller-Westerhoff, U. T.; Sanders, R. Use of Medium Effects to Tune the DE$_{1/2}$ Values of Bimetallic and Oligometallic Compounds. *J. Am. Chem. Soc.* **2002**, *124*, 7262−7263.
(44) Barrière, F.; Geiger, W. E. Use of Weakly Coordinating Anions to Develop an Integrated Approach to the Tuning of DE$_{1/2}$ Values by Medium Effects. *J. Am. Chem. Soc.* **2006**, *128*, 3980−3989.
(45) Maurer, J.; Linseis, M.; Sarkar, B.; Schwederski, B.; Niemeyer, M.; Kaim, W.; Záliš, S.; Anson, C.; Zabel, M.; Winter, R. F. Ruthenium Complexes with Vinyl, Styryl, and Vinylpyrenyl Ligands: A Case of Non-Innocence in Organometallic Chemistry. *J. Am. Chem. Soc.* **2008**, *130*, 259−268.
(46) Gassman, P. G.; Sowa, J. R.; Hill, M. G.; Mann, K. R. Electrochemical Studies of Organometallic Complexes with Tetra-n-butylammonium Tetrakis[3,5-bis(trifluoromethyl)phenyl]borate as the Electrolyte. X-ray Crystal Structure of [C$_5$(CF$_3$)Me$_4$]Fe(C$_5$H$_5$). *Organometallics* **1995**, *14*, 4879−4885.
(47) Maurer, J.; Sarkar, B.; Schwederski, B.; Kaim, W.; Winter, R. F.; Záliš, S. Divinylphenylene bridged diruthenium complexes bearing Ru(CO)Cl(P^{i}Pr$_3$)$_2$ entities. *Organometallics* **2006**, *25*, 3701−3712.
(48) Linseis, M.; Winter, R. F.; Sarkar, B.; Kaim, W.; Záliš, S. Multistep Electrochromic Behaviour from an Organometallic Tetranuclear Complex of a Tetradonor-Substituted Olefin. *Organometallics* **2008**, *27*, 3321−3324.
(49) Wuttke, E.; Pevny, F.; Hervault, Y.-M.; Norel, L.; Drescher, M.; Winter, R. F.; Rigaut, S. Fully Delocalized (Ethynyl)(vinyl)phenylene

DOI: 10.1021/acs.inorgchem.8b03253
Inorg. Chem. 2019, 58, 2695−2707

Bridged Triruthenium Complexes in up to Five Different Oxidation States. *Inorg. Chem.* **2012**, *51*, 1902−1915.
(50) Scheerer, S.; Rotthowe, N.; Abdel-Rahman, O. S.; He, X.; Rigaut, S.; Kvapilová, H.; Záliš, S.; Winter, R. F. Vinyl Ruthenium-Modified Biphenyl and 2,2′-Bipyridines. *Inorg. Chem.* **2015**, *54*, 3387−3402.
(51) Pfaff, U.; Hildebrandt, A.; Korb, M.; Oßwald, S.; Linseis, M.; Schreiter, K.; Spange, S.; Winter, R. F.; Lang, H. Electronically Strongly Coupled Divinylheterocyclic-Bridged Diruthenium Complexes. *Chem. - Eur. J.* **2016**, *22*, 783−801.
(52) Abdel-Rahman, O. S.; Jan, M. T.; Oßwald, S.; Winter, R. F. Polyelectrochromism and electronic coupling in vinylruthenium-modified carbazoles. *J. Organomet. Chem.* **2017**, *849*−*850*, 98−116.
(53) Wu, X. H.; Jin, S.; Liang, J. H.; Li, Z. Y.; Yu, G.; Liu, S. H. Synthesis, Characterization, and Substituent Effects of Binuclear Ruthenium Vinyl Complexes $[RuCl(CO)(PMe_3)_3]_2(\mu$-CHCH−Ar−CHCH). *Organometallics* **2009**, *28*, 2450−2459.
(54) Ou, Y.-P.; Jiang, C.; Wu, D.; Xia, J.; Yin, J.; Jin, S.; Yu, G.-A.; Liu, S. H. Synthesis, Characterization, and Properties of Anthracene-Bridged Bimetallic Ruthenium Vinyl Complexes $[RuCl(CO)(PMe_3)_3]_2(\mu$-CH = CH-anthracene-CH = CH). *Organometallics* **2011**, *30*, 5763−5770.
(55) Tian, L. Y.; Liu, Y. M.; Tian, G.-X.; Wu, X. H.; Li, Z.; Kou, J.-F.; Ou, Y.-P.; Liu, S. H.; Fu, W.-F. Bimetallic ruthenium complexes bridged by divinylphenylene bearing oligo(ethylene glycol)-methylether: synthesis, (spectro)electrochemistry and the lithium cation effect. *Dalton Trans* **2014**, *43*, 4093−4101.
(56) Zhang, J.; Ou, Y.; Xu, M.; Sun, C.; Yin, J.; Yu, G.-A.; Liu, S. H. Synthesis and Characterization of Dibenzoheterocycle-Bridged Dinuclear Ruthenium Alkynyl and Vinyl Complexes. *Eur. J. Inorg. Chem.* **2014**, *2014*, 2941−2951.
(57) Kong, D.-D.; Xue, L.-S.; Jang, R.; Liu, B.; Meng, X.-G.; Jin, S.; Ou, Y.-P.; Hao, X.; Liu, S.-H. Conformational Tuning of the Intramolecular Electronic Coupling in Molecular-Wire Biruthenium Complexes Bridged by Biphenyl Derivatives. *Chem. - Eur. J.* **2015**, *21*, 9895−9904.
(58) Zhang, J.; Sun, C.-F.; Wu, X.-H.; Zhang, M.-X.; Yin, J.; Yu, G.-A.; Liu, S. H. Bimetallic Ruthenium Vinyl Complexes Bridged by Electronic Substituent Phenylenes: Spectroelectrochemical and Computational Studies. *Int. J. Electrochem. Sci.* **2016**, *11*, 7875−7889.
(59) Fink, D.; Weibert, B.; Winter, R. F. Redox-active tetraruthenium metallacycles: reversible release of up to eight electrons resulting in strong electrochromism. *Chem. Commun.* **2016**, *52*, 6103−6106.
(60) Fink, D.; Bodensteiner, M.; Linseis, M.; Winter, R. F. Macrocyclic Triruthenium Complexes Having Electronically Coupled Mixed-Valent States. *Chem. - Eur. J.* **2018**, *24*, 992−996.
(61) Fink, D.; Linseis, M.; Winter, R. F. Constitutional Isomers of Macrocyclic Tetraruthenium Complexes with Vastly Different Spectroscopic and Electrochemical Properties. *Organometallics* **2018**, *37*, 1817−1820.
(62) Krejcik, M.; Danek, M.; Hartl, F. Simple construction of an infrared optically transparent thin-layer cell: Applications to the redox reactions of ferrocene, $Mn_2(CO)_{10}$ and $Mn(CO)_3$(3,5-di-t-butylcatecholate)$^-$. *J. Electroanal. Chem. Interfacial Electrochem.* **1991**, *317*, 179−187.
(63) Koelle, U.; Salzer, A. Elektrochemie von Übergangsmetall-π-Komplexen: VI. Elektrochemische Oxidation von Decamethylruthenocen. *J. Organomet. Chem.* **1983**, *243*, C27−C30.
(64) Prins, R.; Korswagen, A. R. Substituent effects in the ESR spectra of ferricenium cations. *J. Organomet. Chem.* **1970**, *25*, C74−C76.
(65) Duggan, D. E. M.; Hendrickson, D. N. Electronic Structure of Various Ferricenium systems as Inferred from Raman, Infrared, Low-Temperature Electronic Absorption and EPR Measurements. *Inorg. Chem.* **1975**, *14*, 955−970.
(66) Miller, J. S.; Glatzhofer, D. T.; O'Hare, D. M.; Reiff, W. M.; Chakraborty, A.; Epstein, A. J. Ferromagnetic behavior in linear charge-transfer complexes. Structural and magnetic characterization of octamethylferrocene salts: $[Fe(C_5Me_4H)_2]^+$ $[A]^-$ (A = TCNE, TCNQ). *Inorg. Chem.* **1989**, *28*, 2930−2939.
(67) Pevny, F.; Winter, R. F.; Sarkar, B.; Záliš, S. How to elucidate and control the redox sequence in vinylbenzoate and vinylpyridine bridged diruthenium complexes. *Dalton Trans* **2010**, *39*, 8000−8011.
(68) Mücke, P.; Zabel, M.; Edge, R.; Collison, D.; Clément, S.; Záliš, S.; Winter, R. F. Electron delocalization in vinyl ruthenium substituted cyclophanes: Assessment of the through-space and the through-bond pathways. *J. Organomet. Chem.* **2011**, *696*, 3186−3197.
(69) Linseis, M.; Záliš, S.; Zabel, M.; Winter, R. F. Ruthenium Stilbenyl and Diruthenium Distyrylethene Complexes: Aspects of Electron Delocalization and Electrocatalyzed Isomerization of the *Z*-Isomer. *J. Am. Chem. Soc.* **2012**, *134*, 16671−16692.
(70) Abdel-Rahman, O. S.; Maurer, J.; Záliš, S.; Winter, R. F. Ruthenium Styryl Complexes with Ligands Derived from 2-Hydroxy- and 2-Mercaptopyridine and 2-Hydroxy- and 2-Mercaptoquinoline. *Organometallics* **2015**, *34*, 3611−3628.
(71) Coropceanu, V.; Malagoli, M.; André, J. M.; Brédas, J. L. Intervalence transition in triarylamine mixed-valence systems: A time-dependent density functional theory study. *J. Chem. Phys.* **2001**, *115*, 10409−10416.
(72) Barlow, S.; Risko, C.; Odom, S. A.; Zheng, S.; Coropceanu, V.; Beverina, L.; Brédas, J.-L.; Marder, S. R. Tuning Delocalization in the Radical Cations of 1,4-Bis[4-(diarylamino)styryl]benzenes, 2,5-Bis[4-(diarylamino)styryl]thiophenes, and 2,5-Bis[4-(diarylamino)styryl]-pyrroles through Substituent Effects. *J. Am. Chem. Soc.* **2012**, *134*, 10146−10155.
(73) Allen, G. C.; Hush, N. S. Intervalence Charge-Transfer Absorption. Part 1. *Prog. Inorg. Chem.* **2007**, *8*, 357−389.
(74) Hush, N. S. Intervalence Charge Transfer Absorption. Part 2. Theoretical Considerations and Spectroscopic Data. *Prog. Inorg. Chem.* **2007**, *8*, 391−444.
(75) Brunschwig, B.; Creutz, C.; Sutin, N. Optical transitions of symmetrical mixed-valence systems in the Class II-III transition regime. *Chem. Soc. Rev.* **2002**, *31*, 168−184.
(76) Lambert, C.; Nöll, G. The Class II/III Transition in Triarylamine Redox Systems. *J. Am. Chem. Soc.* **1999**, *121*, 8434−8442.
(77) Coropceanu, V.; Lambert, C.; Nöll, G.; Brédas, J. L. Charge-transfer transitions in triarylamine mixed-valence systems: the effect of temperature. *Chem. Phys. Lett.* **2003**, *373*, 153−160.
(78) Coropceanu, V.; Gruhn, N. E.; Barlow, S.; Lambert, C.; Durivage, J. C.; Bill, T. G.; Nöll, G.; Marder, S. R.; Brédas, J.-L. Electronic Coupling in Organic Mixed-Valence Compounds: The Contribution of Photoelectron Spectroscopy. *J. Am. Chem. Soc.* **2004**, *126*, 2727−2731.
(79) Coropceanu, V.; Malagoli, M.; André, J. M.; Brédas, J. L. Charge-Transfer Transitions in Triarylamine Mixed-Valence Systems: A Joint Density Functional Theory and Vibronic Coupling Study. *J. Am. Chem. Soc.* **2002**, *124*, 10519−10530.
(80) Cheng, T.; Tan, Y. N.; Zhang, Y.; Zhang, Y. Y.; Meng, M.; Lei, H.; Chen, L.; Liu, C. Y. Distinguishing the Strength of Electronic Coupling for Mo_2-Containing Mixed-Valence Compounds within the Class III Regime. *Chem. - Eur. J.* **2015**, *21*, 2353−2357.
(81) Bailey, S. E.; Zink, J. I.; Nelsen, S. F. Contributions of Symmetric and Asymmetric Normal Coordinates to the Intervalence Electronic Absorption and Resonance Raman Spectra of a Strongly Coupled p-Phenylenediamine Radical Cation. *J. Am. Chem. Soc.* **2003**, *125*, 5939−5947.
(82) Richardson, D. E.; Taube, H. Mixed-valence molecules: Electronic delocalization and stabilization. *Coord. Chem. Rev.* **1984**, *60*, 107−129.
(83) D'Alessandro, D. M.; Keene, F. R. Current trends and future challenges in the experimental, theoretical and computational analysis of intervalence charge transfer (IVCT) transitions. *Chem. Soc. Rev.* **2006**, *35*, 424−440.
(84) Winter, R. F. Half-Wave Potential Splittings $\Delta E_{1/2}$ as a Measure of Electronic Coupling in Mixed-Valent Systems: Triumphs and Defeats. *Organometallics* **2014**, *33*, 4517−4536.

DOI: 10.1021/acs.inorgchem.8b03253
Inorg. Chem. 2019, 58, 2695−2707

(85) Santi, S.; Bisello, A.; Cardena, R.; Donoli, A. Key multi-(ferrocenyl) complexes in the interplay between electronic coupling and electrostatic interaction. *Dalton Trans* **2015**, *44*, 5234−5257.
(86) Evans, C. E. B.; Naklicki, M. L.; Rezvani, A. R.; White, C. A.; Kondratiev, V. V.; Crutchley, R. J. An Investigation of Superexchange in Dinuclear Mixed-Valence Ruthenium Complexes. *J. Am. Chem. Soc.* **1998**, *120*, 13096−13103.
(87) Lin, Y.-C.; Chen, W.-T.; Tai, J.; Su, D.; Huang, S.-Y.; Lin, I.; Lin, J.-L.; Lee, M. M.; Chiou, M. F.; Liu, Y.-H.; Kwan, K.-S.; Chen, Y.-J.; et al. Tuning Through-Bond Fe(III)/Fe(II) Coupling by Solvent Manipulation of a Central Ruthenium Redox Couple. *Inorg. Chem.* **2009**, *48*, 1857−1870.
(88) Crutchley, R. J. Intervalence Charge Transfer and Electron Exchange Studies of Dinuclear Ruthenium Complexes. *Adv. Inorg. Chem.* **1994**, *41*, 273−325.
(89) Ammar, F.; Savéant, J. M. Thermodynamics of successive electron transfers: Internal and solvation enthalpy and entropy variations in a series of polynitro compounds. *J. Electroanal. Chem. Interfacial Electrochem.* **1973**, *47*, 115−125.
(90) Salaymeh, F.; Berhane, S.; Yusof, R.; de la Rosa, R.; Fung, E. Y.; Matamoros, R.; Lau, K. W.; Zheng, Q.; Kober, E. M.; Curtis, J. C. Electronic coupling in mixed-valence binuclear ruthenium ammine complexes as probed by an electrochemical method and an extension of Mulliken's theory of donor-acceptor interactions. *Inorg. Chem.* **1993**, *32*, 3895−3908.
(91) De la Rosa, R.; Chang, P. J.; Salaymeh, F.; Curtis, J. C. Redox asymmetry and metal-metal coupling in pyrazine-bridged ruthenium dimers. *Inorg. Chem.* **1985**, *24*, 4229−4231.
(92) Bertrand, P. Electron transfer between biological molecules coupled by an exchange interaction. *Chem. Phys. Lett.* **1985**, *113*, 104−107.
(93) Tuczek, F.; Solomon, E. I. Charge-transfer states of bridged transition metal dimers: mono- vs binuclear copper azide systems with relevance to oxy-hemocyanin. *Inorg. Chem.* **1993**, *32*, 2850−2862.
(94) Brunschwig, B. S.; Sutin, N. Energy surfaces, reorganization energies, and coupling elements in electron transfer. *Coord. Chem. Rev.* **1999**, *187*, 233−254.
(95) Barlow, S. Fe^{II}-to-Co^{III} Charge-Transfer Transitions in Methylene-Bridged Metallocene Salts. *Inorg. Chem.* **2001**, *40*, 7047−7053.
(96) Santi, S.; Orian, L.; Durante, C.; Bencze, E. Z.; Bisello, A.; Donoli, A.; Ceccon, A.; Benetollo, F.; Crociani, L. Metal-Metal Electronic Coupling in syn and anti Stereoisomers of Mixed-Valent $(FeCp)_2$-, $(RhL_2)_2$-, and $(FeCp)(RhL_2)$-as-Indacenediide Ions. *Chem. - Eur. J.* **2007**, *13*, 7933−7947.
(97) Santi, S.; Orian, L.; Durante, C.; Bisello, A.; Benetollo, F.; Crociani, L.; Ganis, P.; Ceccon, A. Tuning the Electronic Communication in Heterobimetallic Mixed-Valence Ions of (1-Ferrocenyl)- and (2-Ferrocenyl)indenyl Rhodium Isomers. *Chem. - Eur. J.* **2007**, *13*, 1955−1968.
(98) Chen, P.; Meyer, T. J. Medium Effects on Charge Transfer in Metal Complexes. *Chem. Rev.* **1998**, *98*, 1439−1477.
(99) Demadis, K. D.; Hartshorn, C. M.; Meyer, T. J. The Localized-to-Delocalized Transition in Mixed-Valence Chemistry. *Chem. Rev.* **2001**, *101*, 2655−2686.
(100) Lear, B. J.; Glover, S. D.; Salsman, C.; Londergan, C. H.; Kubiak, C. P. Solvent Dynamical Control of Ultrafast Ground State Electron Transfer: Implications for Class II-III Mixed Valency. *J. Am. Chem. Soc.* **2007**, *129*, 12772−12779.
(101) Glover, S. D.; Goeltz, J. C.; Lear, B. J.; Kubiak, C. P. Inter- or intramolecular electron transfer between triruthenium clusters: wéll cross that bridge when we come to it. *Coord. Chem. Rev.* **2010**, *254*, 331−345.
(102) Kubiak, C. P. Inorganic Electron Transfer: Sharpening a Fuzzy Border in Mixed Valency and Extending Mixed Valency across Supramolecular Systems. *Inorg. Chem.* **2013**, *52*, 5663−5676.
(103) Gassman, P. G.; Winter, C. H. Preparation, electrochemical oxidation, and XPS studies of unsymmetrical ruthenocenes bearing the pentamethylcyclopentadienyl ligand. *J. Am. Chem. Soc.* **1988**, *110*, 6130−6135.

DOI: 10.1021/acs.inorgchem.8b03253
Inorg. Chem. 2019, 58, 2695−2707

Supporting Information

Mixed-Valent Ruthenocene–Vinylruthenium Conjugates: Valence Delocalization Despite Chemically Different Redox Sites

Christopher Hassenrück, André Mang, Rainer F. Winter*

University of Konstanz, Department of Chemistry, Universitätsstraße 10, 78457 Konstanz, Germany

Table of Content

1. General Procedures S2
2. Synthesis S3
   Ruthenocene S3
   Formylruthenocene S3
   Ethynylruthenocene S4
3. NMR Spectra S5
4. Crystallographic data S14
5. Cyclic Voltammetry S18
6. IR Spectroelectrochemistry S19
7. (TD-)DFT calculations S21
   Molecular Orbitals and calculated transitions S21
   Fragment contributions to the charge and spin densities……S27
8. EPR spectra of the chemically mono-oxidized complexes S288
9. Spin Density Plots of the radical cations S30
   DFT-computed fragment contributions to the β-MOs……S31
10. UV/vis/NIR data S322
11. TD-DFT calculated UV/vis/NIR spectra S344
11. Electron Density Difference Maps (EDDM) for the calculated transitions ... S366
12. Molecular orbital contributions S422
13. Brief Discussion of the Relation Between the Shape of an IVCT Band and the Electronic Coupling…… S48
14. Solvatochromism of the IVCT Band…… S49
15. References S51

1. General Procedures

General Procedures. All syntheses were performed using standard Schlenk techniques under nitrogen atmosphere. The solvents used for synthesis and characterization were dried over appropriate drying agents, distilled and stored under nitrogen atmosphere. The purities of the complexes were determined by NMR spectroscopy and combustion analyses. All chemicals were obtained from commercial suppliers and used without further purification. Details to the synthesis of the required triarylamines and their characterization can be found in the Supporting Information. ^{1}H- and ^{13}C NMR spectra were recorded on a Bruker AVANCE III 400 (B_H = 400 MHz, B_C= 100.6 MHz, B_P = 162 MHz) spectrometer at room temperature. The spectra were referenced to the residual signal of the protonated solvents or, for ^{31}P NMR spectroscopy, to H_3PO_4 as an external standard. Coupling constants are given in Hz.

Cyclic voltammetry was performed in a one compartment cell with 5 to 7 mL of CH_2Cl_2 as the solvent and NBu_4PF_6 (0.1 M) as the supporting electrolyte. A platinum electrode (Ø = 1.1 mm, BASI) was used as the working electrode. It was polished with diamond pastes (1.5 µm and 1 µm particle size) from Buehler&Wirtz. A computer-controlled BASi EPSILON potentiostat was used for recording of the voltammograms. An Ag/AgCl wire pseudo reference electrode and a Pt-wire as auxiliary electrode were used in the measurements. The cell was connected to an argon gas bottle. Potential calibration was performed by adding appropriate quantities of decamethylferrocene (Cp^*_2Fe) after all scans of interest had been acquired. Potentials are reported against the ferrocene/ferrocenium couple, which is 550 mV positive of the $Cp^*_2Fe^{0/+}$ couple under our conditions.

IR and UV/vis/NIR spectroelectrochemistry was performed in a self-built Optically Transparent Thin Layer Electrolysis (OTTLE) cell according to the design of *F. Hartl*.[1] A platinum minigrid as the working and counter electrodes and a thin silver foil as reference electrode are welded in a polyethylene spacer, incorporated into a Teflon housing with electrical connectors and sandwiched in between the CaF_2 plates of a conventional liquid IR cell. 1,2-$C_2H_4Cl_2$ / 0.1 M NBu_4PF_6 was used as the supporting electrolyte. IR/NIR spectra were recorded on a FT-IR Bruker Tensor II instrument. The UV/vis/NIR-measurements were performed on a diode array unit TIDAS by j&m ANALYTIK AG with a spectroscopic window of 250 to 2100 nm. A computer-controlled potentiostat WENKING POS3 was used for controlled electrolysis.

Electron Paramagnetic Resonance (EPR) spectroscopy was performed with an X-Band benchtop spectrometer of the type MINISOPE400MS by Magnettech GmBH. Low-temperature work was conducted by cooling with liquid nitrogen. As thermostat, a temperature controller by the same manufacturer was used. The magnet was cooled using a Thermo Fischer Sci. Inc. HAAKE A10 cooling unit. The complexes were chemically oxidized with appropriate amounts of ferrocenium hexafluorophosphate, in dichloromethane solution at room temperature prior to the measurements. Simulations of the measured spectra was performed using the MATLAB Easyspin program.[2]

Density functional theory (DFT) calculations were performed on the full model complexes using the GAUSSIAN 09 program package.[3] Geometry optimizations were performed without any symmetry constraints. Electronic transitions were calculated by the time-dependent DFT (TD-DFT) method. Within G09 calculations the quasirelativistic effective core pseudopotentials and the corresponding optimized set of basis functions for Ru were used.[4] Polarized double-ζ basis sets (6-31G(d), geometry optimization) were employed together with the pbe1pbe functional.[5] The for the Fe atoms the Wachter basis set implemented in the 6-311G(d) basis sets for transition metals were applied in DFT and TD-DFT calculations.[6] Solvation effects were modeled by the polarizable continuum model (PCM).[7]

2. Synthesis

Ruthenocene[8]

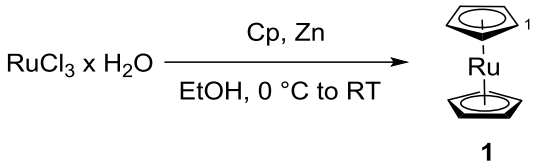

1

Ruthenium(III) chloride hydrate (17.4 g, 66 mmol, 1 eq) was dissolved in dry ethanol (180 mL). The solution was degassed with nitrogen for 10 min. After cooling to 0 °C, cyclopentadiene (85.6 mL, 68.5 g, 1036 mmol, 15 eq) was added. Zinc dust (45.0 g, 690 mmol, 10 eq) was added in small portions at the same temperature. After complete addition, the suspension was allowed to reach RT and was then stirred for 2 h. The reaction mixture was filtered over a short plug of diatomaceous earth and the filtrate was concentrated under reduced pressure. The residue was dissolved in toluene and filtered over a short column of silica. The solvent was removed under reduced pressure to give fine, slightly yellow crystals in 19 % yield (3.0 g, 13 mmol). **^{1}H-NMR** (400 MHz, $CDCl_3$) δ /ppm = 4.55 (s, 10H, *H*-1).

Formylruthenocene[9]

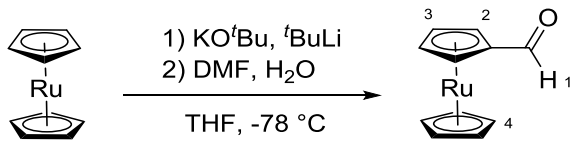

1 **2**

Ruthenocene (**1**) (1.0 g, 4.3 mmol, 1 eq) was dissolved in dry THF (100 mL). Subsequently, 0.5 mL of a 1 M KO^{t}Bu-solution in THF (0.5 mmol, 0.12 eq) were added and the reaction mixture was cooled to -78 °C. At this temperature, ^{t}BuLi in pentane (4.6 mL, 8.6 mmol, 1.9 M, 2 eq) was added dropwise over a period of 30 min. After 0.5 h at -78 °C, dry dimethylformamide (0.8 mL, 0.8 g, 10.9 mmol, 2.5 eq) was added slowly to the cooled reaction mixture. The solution was stirred for 10 min at -78 °C and then allowed to warm to approximately -40 °C for 10 min, whereon deionized water (50 mL) was added. The THF was removed under reduced pressure and DCM was added to the residue. The phases were separated and the organic layer was washed with deionized water (2 x 50 mL). The mixture was dried over magnesium sulfate and the solvent was removed under reduced pressure. The crude product was purified by silica column chromatography, using DCM as eluent. Compound **2** was isolated as lemony crystals in 74 % yield (0.83 g, 3.2 mmol).**^{1}H-NMR** (400 MHz, $CDCl_3$) δ / ppm = 9.72 (s, 1H, *H*-1), 5.08 (vt, 2H, $^3J_{HH}$ = 1.80 Hz, *H*-3), 4.86 (vt, 2H, $^3J_{HH}$ = 1.80 Hz, *H*-2), 4.65 (s, 5H, *H*-4).

Ethynylruthenocene[10]

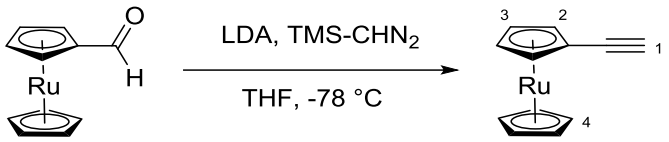

2 **3**

A prepared mixture of LDA (1.3 mL, 2 M in heptane/THF/ethylbenzene, 2.5 mmol, 1.2 eq) and dry THF (50 mL) was cooled to -78 °C. Subsequently, (trimethylsilyl)diazomethane (1.3 mL, 2 M solution in hexane, 2.5 mmol, 1.2 eq) was added slowly. The reaction was stirred for 10 min at -78 °C, whereon formylruthenocene (**2**) (0.55 g, 2.1 mmol, 1 eq), which was dissolved in dry THF (10 mL), was added dropwise. The mixture was stirred for 1 h at -78 °C, was allowed to reach RT and subsequently heated to 60 °C. The mixture was stirred at this temperature for 3 h before it was poured into a saturated solution of ammonium chloride. Organic compounds were extracted with diethyl ether and the resulting organic phase was washed with deionized water (2 x 25 mL). The organic layer was dried over magnesium sulfate and the solvents were removed under reduced pressure. The crude product was purified by silica column chromatography (hexane/benzene 2:1 *v/v*). Ethynylruthenocene was isolated as beige, sticky solid in quantitative yield (0.54 g, 2.1 mmol).**^{1}H-NMR** (400 MHz, $CDCl_3$) δ / ppm = 4.86 (vt, 2H, $^3J_{HH}$ = 1.7 Hz, *H*-3), 4.60 (s, 5H, *H*-4), 4.55 (vt, 2H, $^3J_{HH}$ = 1.7 Hz, *H*-2), 2.64 (s, 1H, *H*-1).

3. NMR Spectra

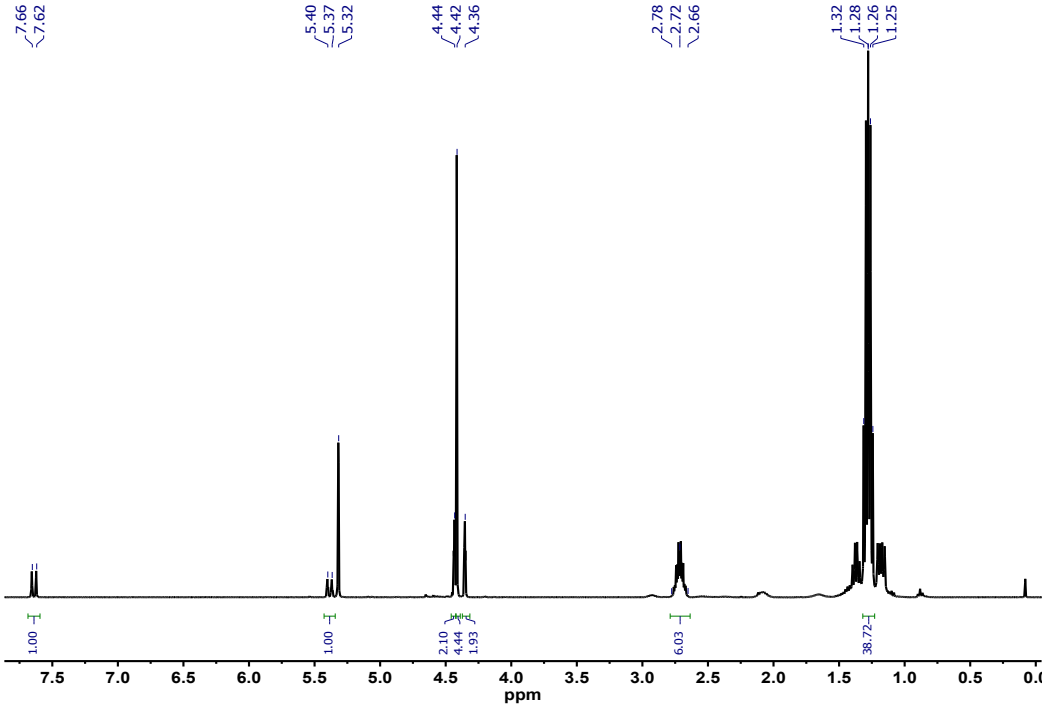

Figure S1: ^{1}H-NMR spectrum of **Rc-Ru^{Cl}** in DCM-d_2.

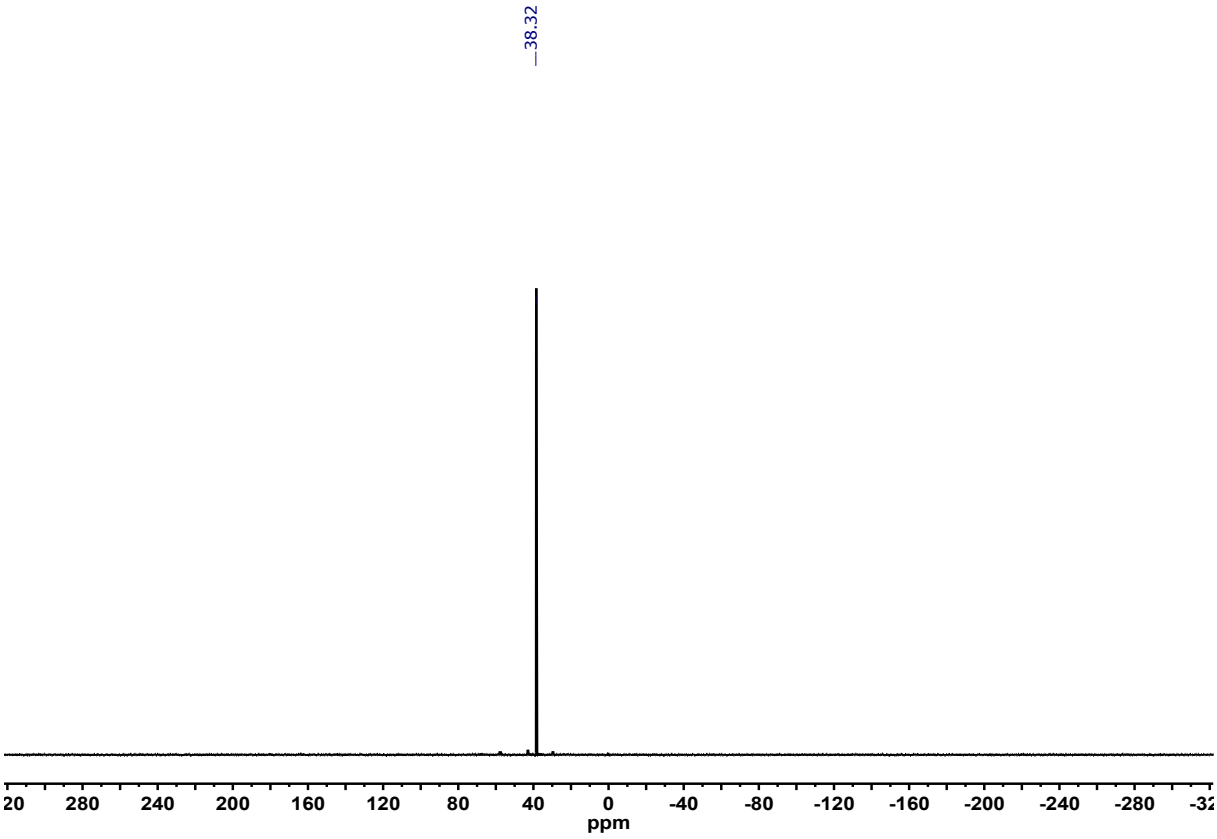

Figure S2: ^{31}P-NMR spectrum of **Rc-Ru^{Cl}** in DCM-d_2.

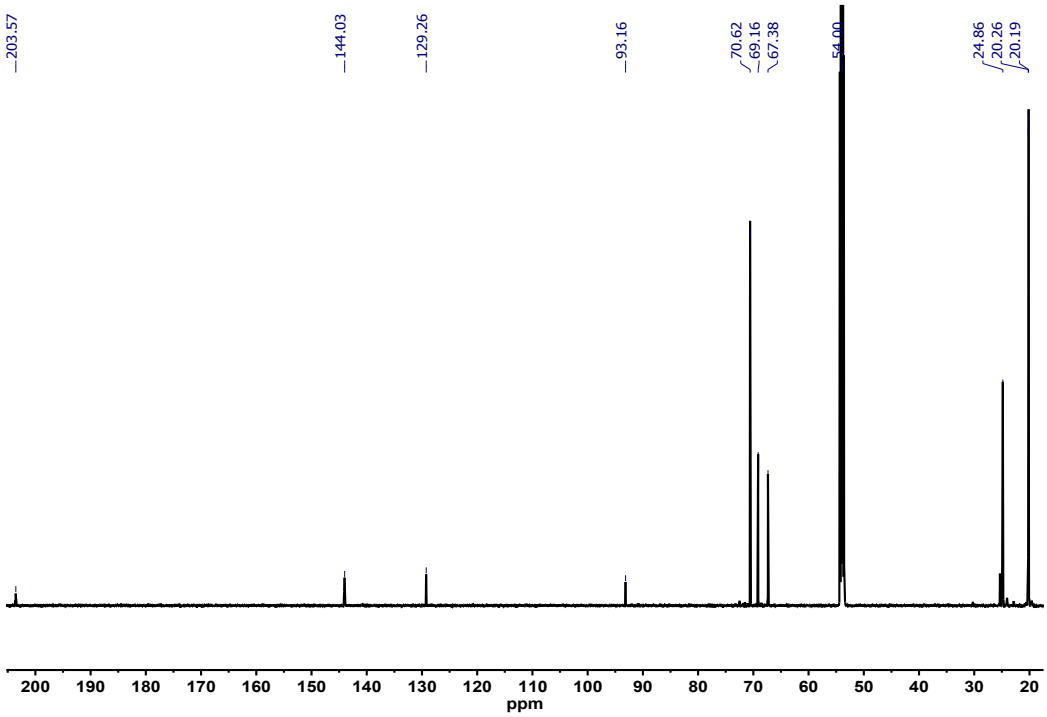

Figure S3: ^{13}C-NMR spectrum of **Rc-Ru^{Cl}** in DCM-d_2.

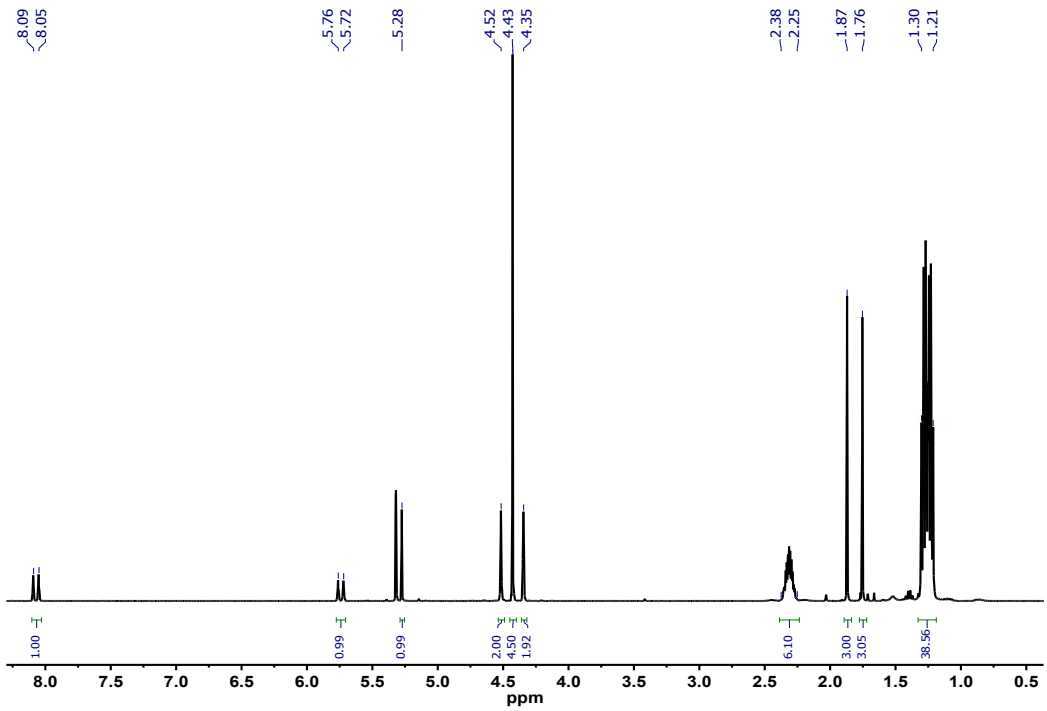

Figure S4: ^{1}H-NMR spectrum of **Rc-Ru^{acac}** in DCM-d_2.

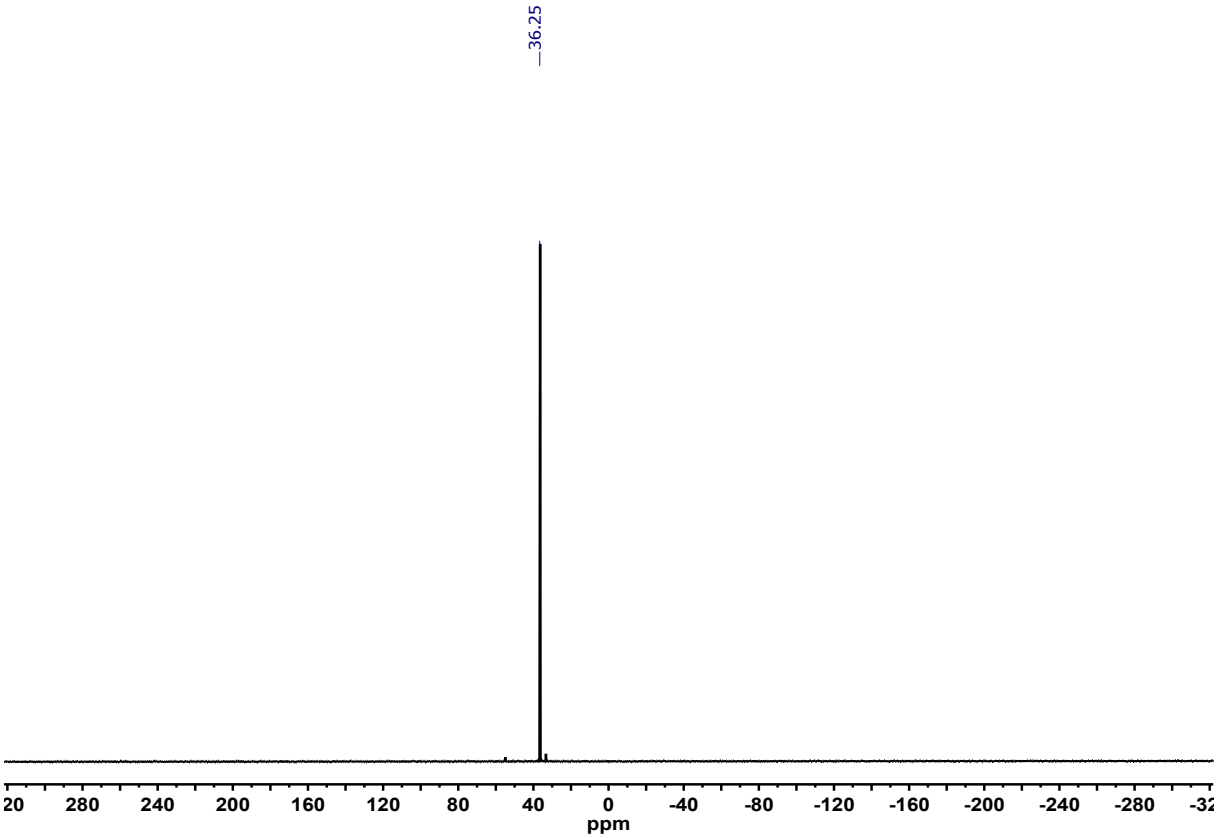

Figure S5: ^{31}P-NMR spectrum of **Rc-Ru^{acac}** in DCM-d_2.

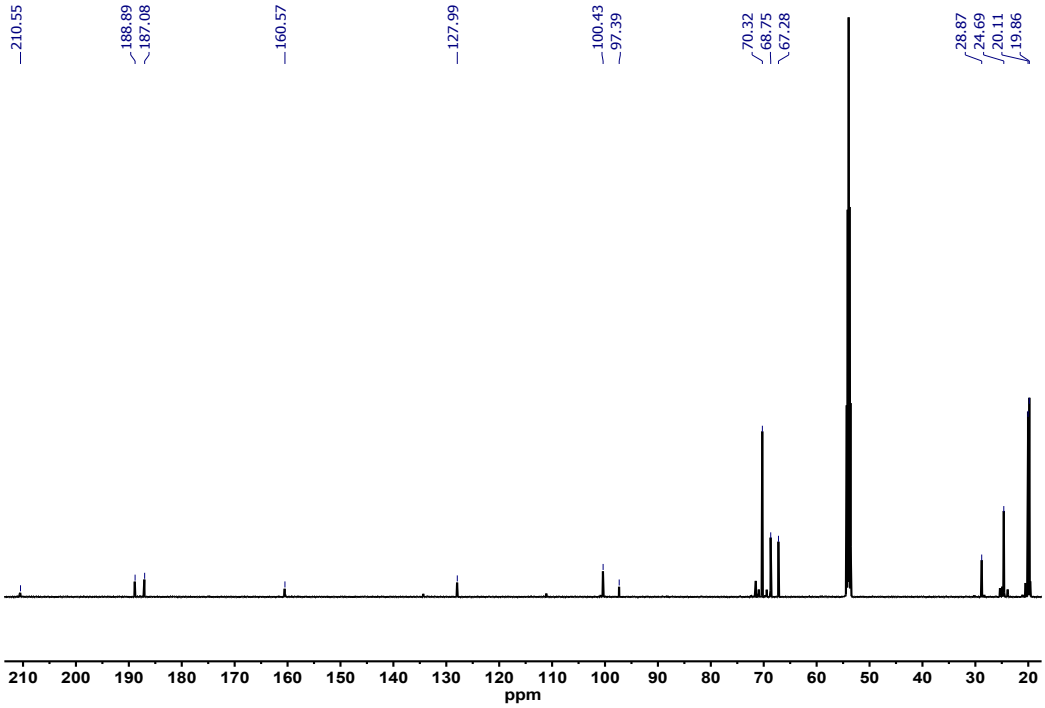

Figure S6: ^{13}C-NMR spectrum of **Rc-Ru^{acac}** in DCM-d_2.

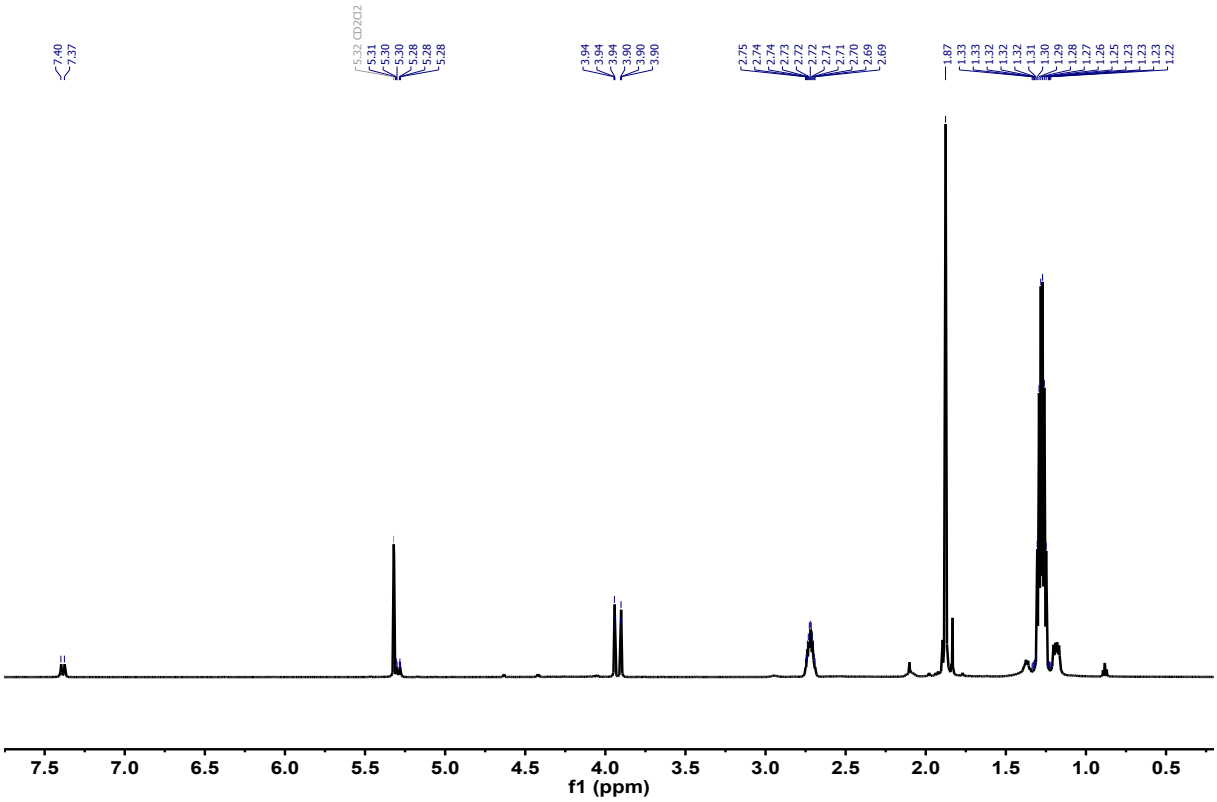

Figure S7: ^{1}H NMR of **Rc*-Ru^{Cl}** in DCM-d_2 at room temperature.

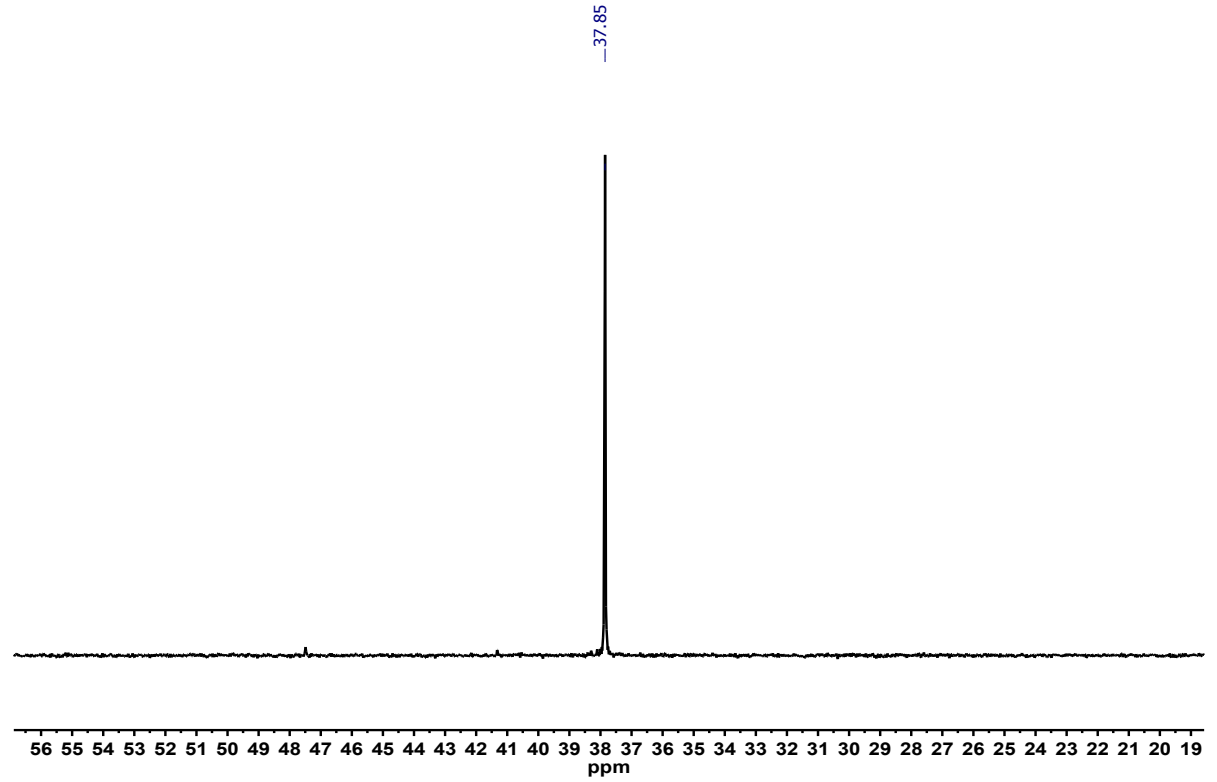

Figure S8: ^{31}P NMR of **Rc*-Ru^{Cl}** in DCM-d_2 at room temperature.

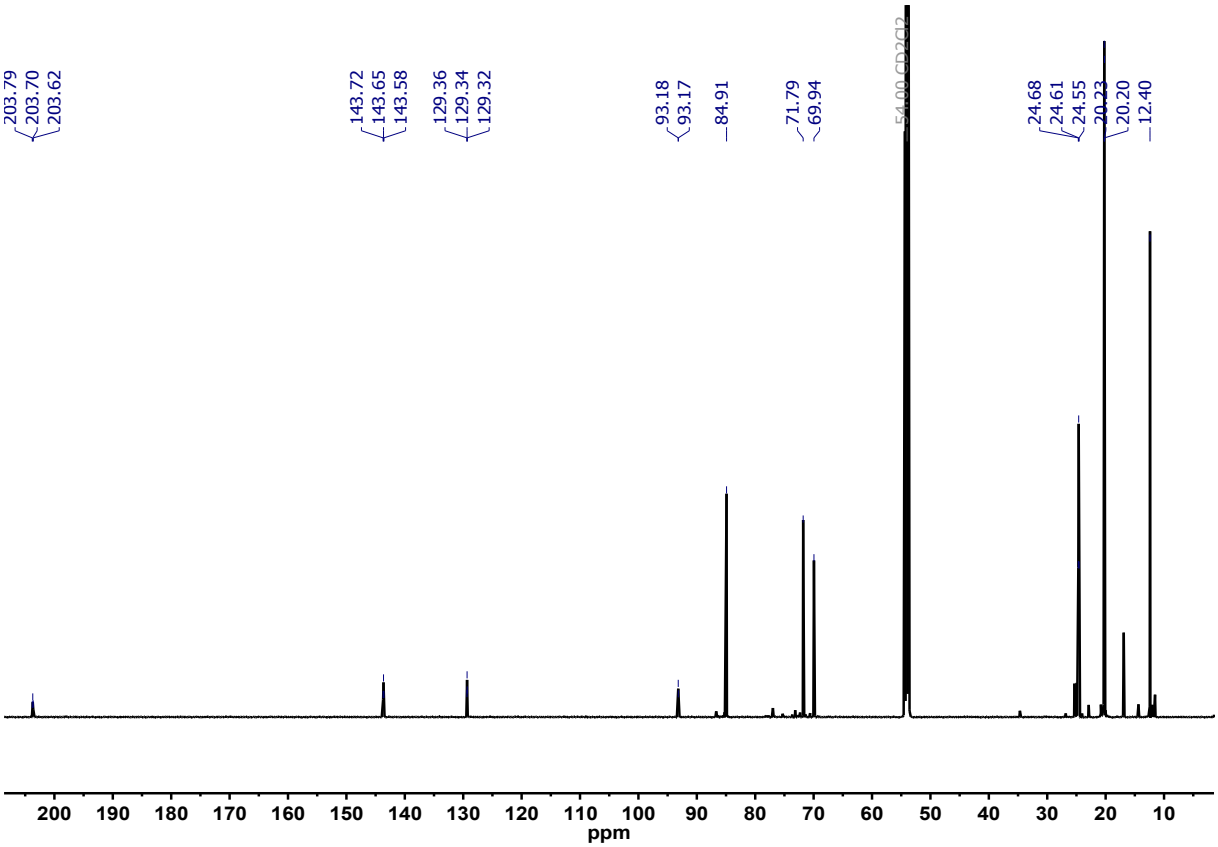

Figure S9: ^{13}C NMR of **Rc*-Ru^{Cl}** in DCM-d_2 at room temperature.

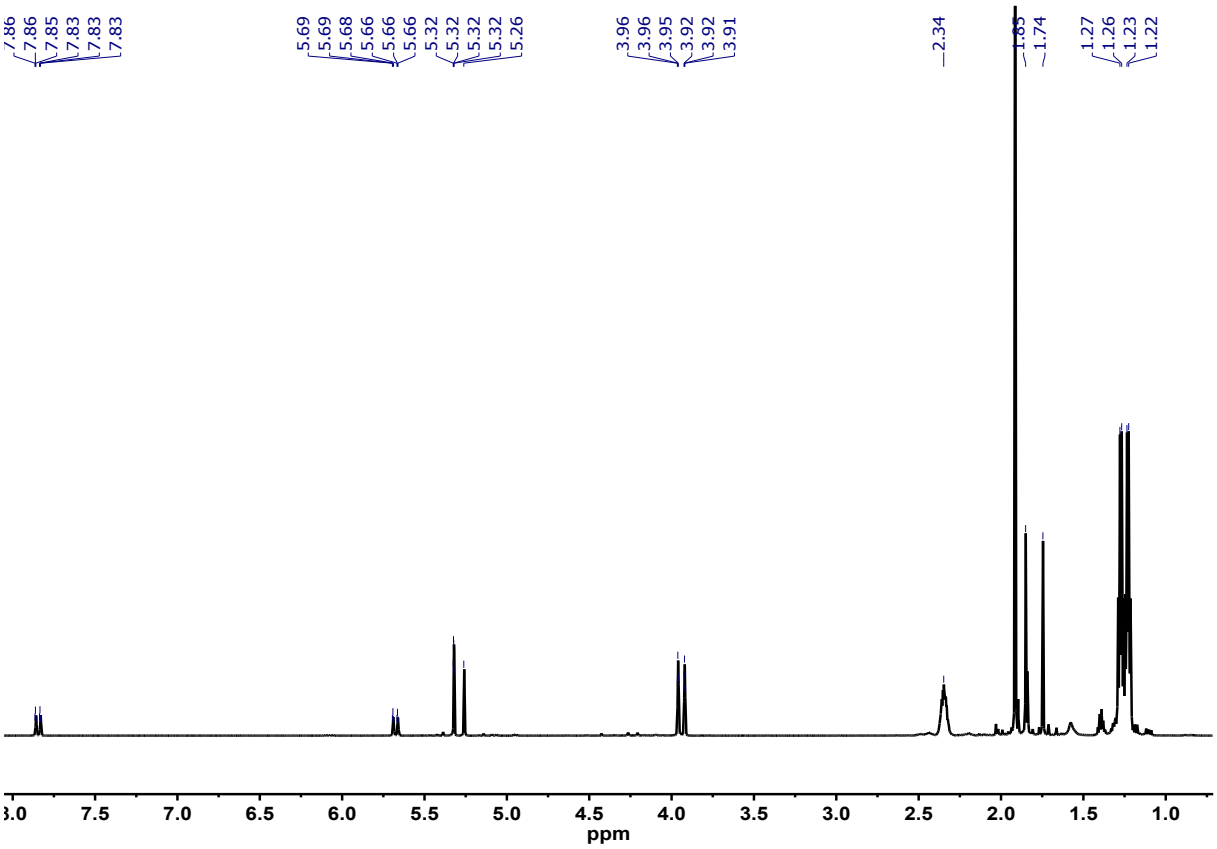

Figure S10: ^{1}H NMR of **Rc*-Ru^{acac}** in DCM-d_2 at room temperature.

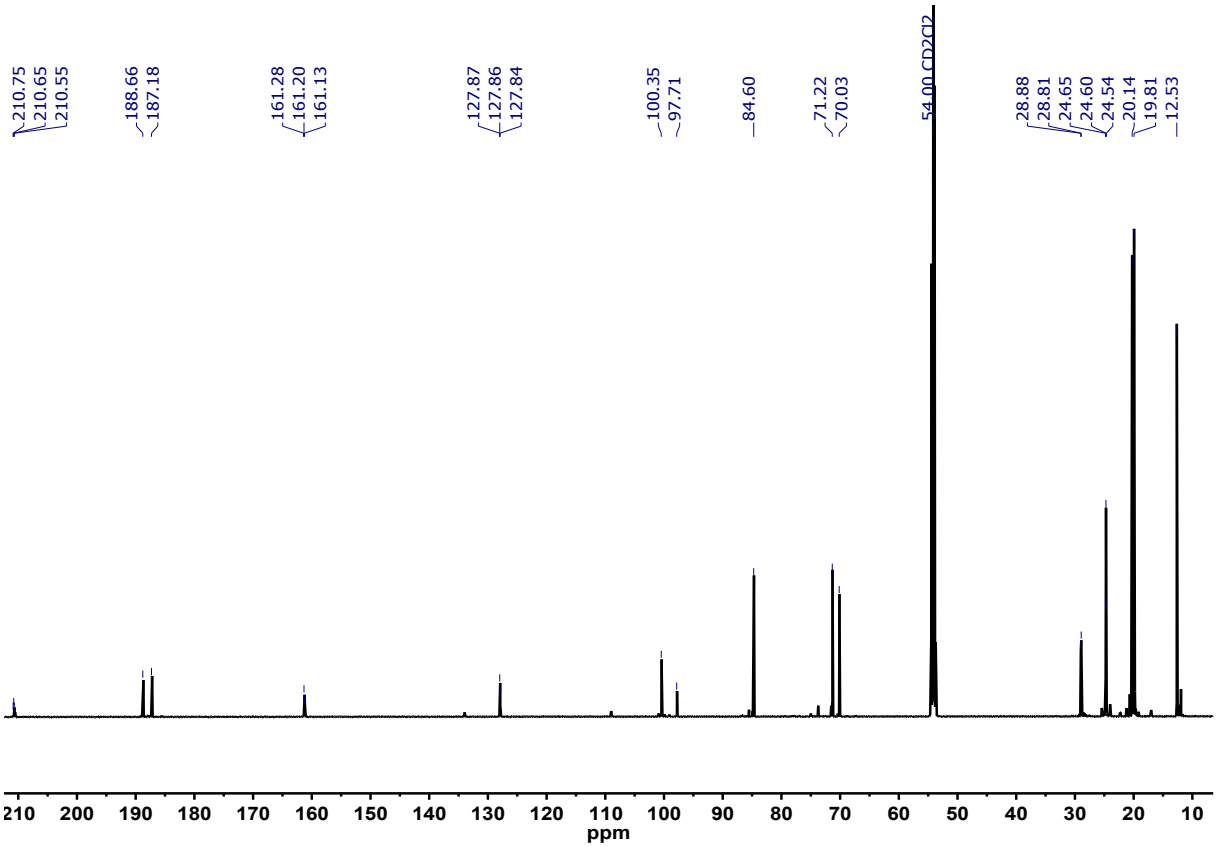

Figure S11: ^{13}C NMR of **Rc*-Ru^{acac}** in DCM-d_2 at room temperature.

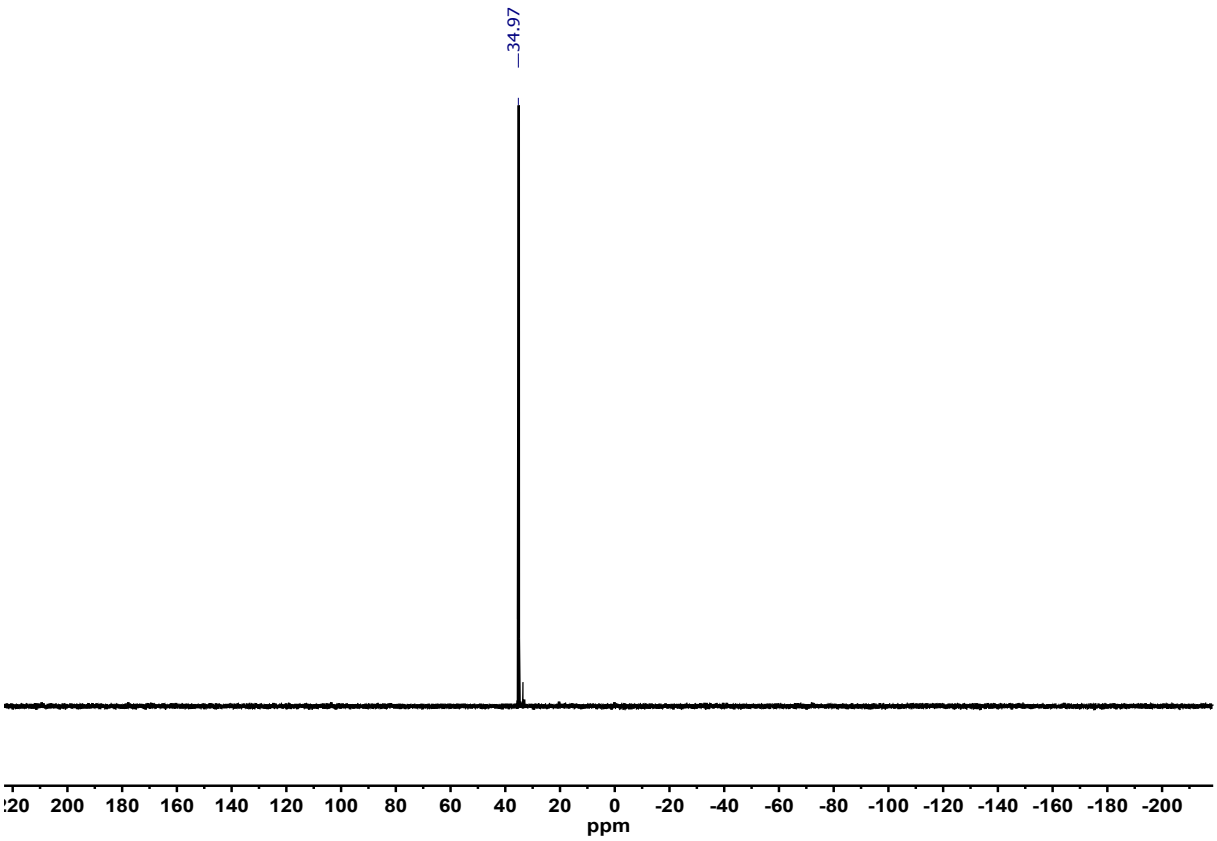

Figure S12: ^{31}P NMR of **Rc*-Ru^{acac}** in DCM-d_2 at room temperature.

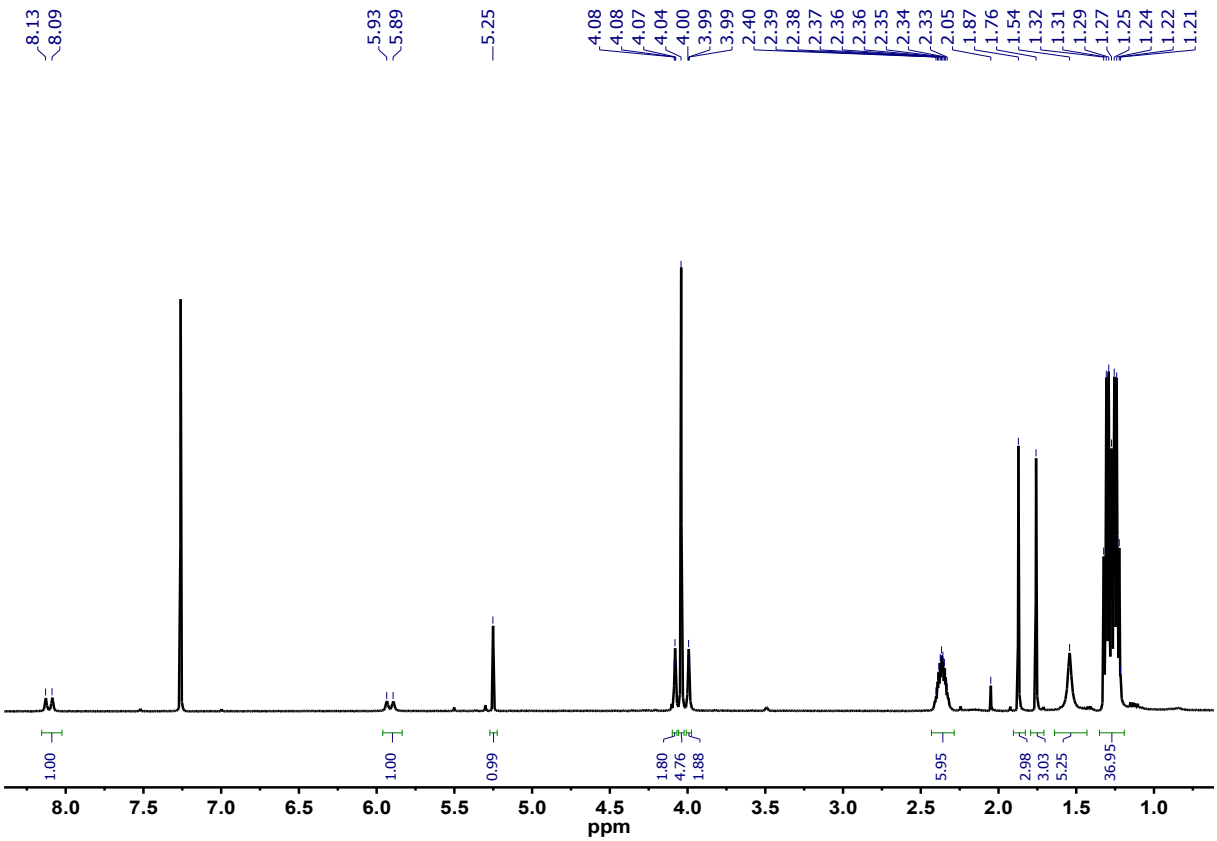

Figure S13: ^{1}H NMR of **Fc-Ru^{acac}** in $CDCl_3$ at room temperature.

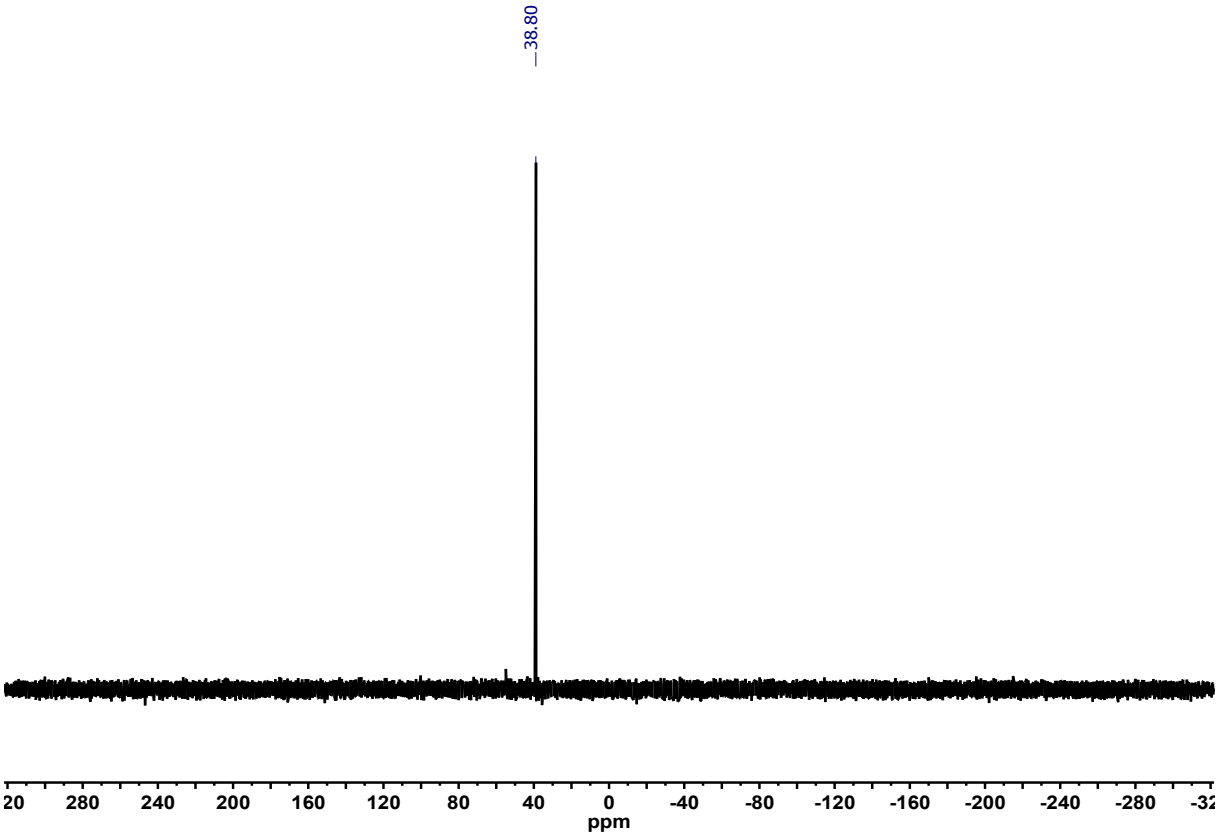

Figure S14: ^{31}P NMR of **Fc-Ru^{acac}** in $CDCl_3$ at room temperature.

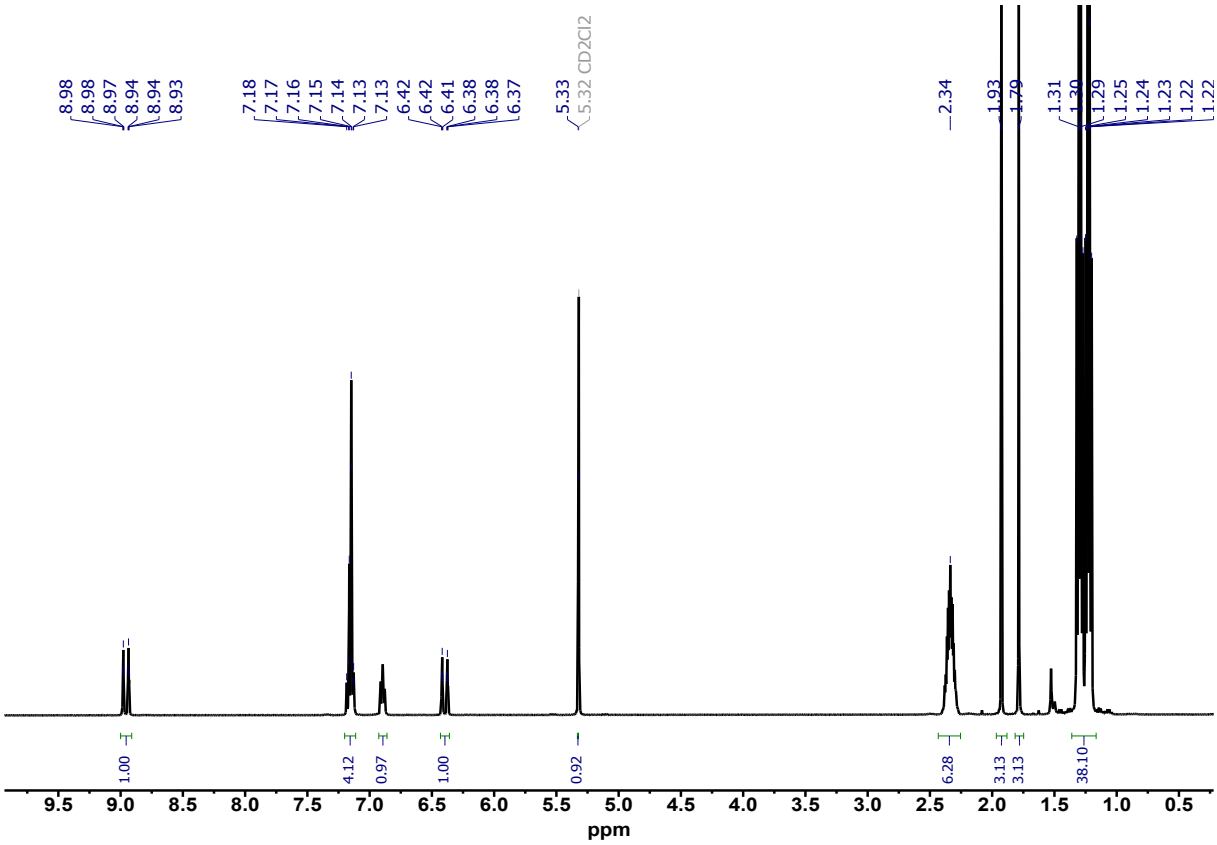

Figure S15: ^{1}H NMR of **Ph-Ru^{acac}** in $CDCl_3$ at room temperature.

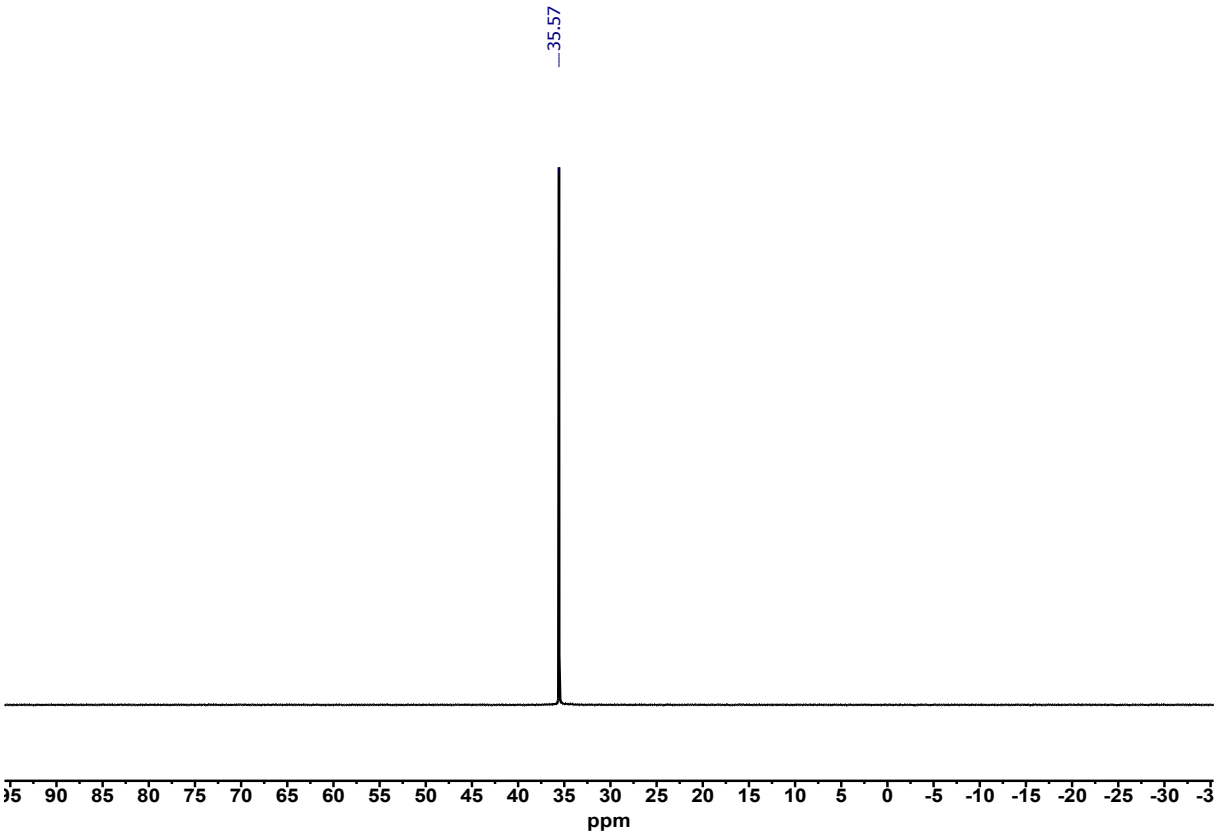

Figure S16: ^{31}P NMR of **Ph-Ru^{acac}** in $CDCl_3$ at room temperature.

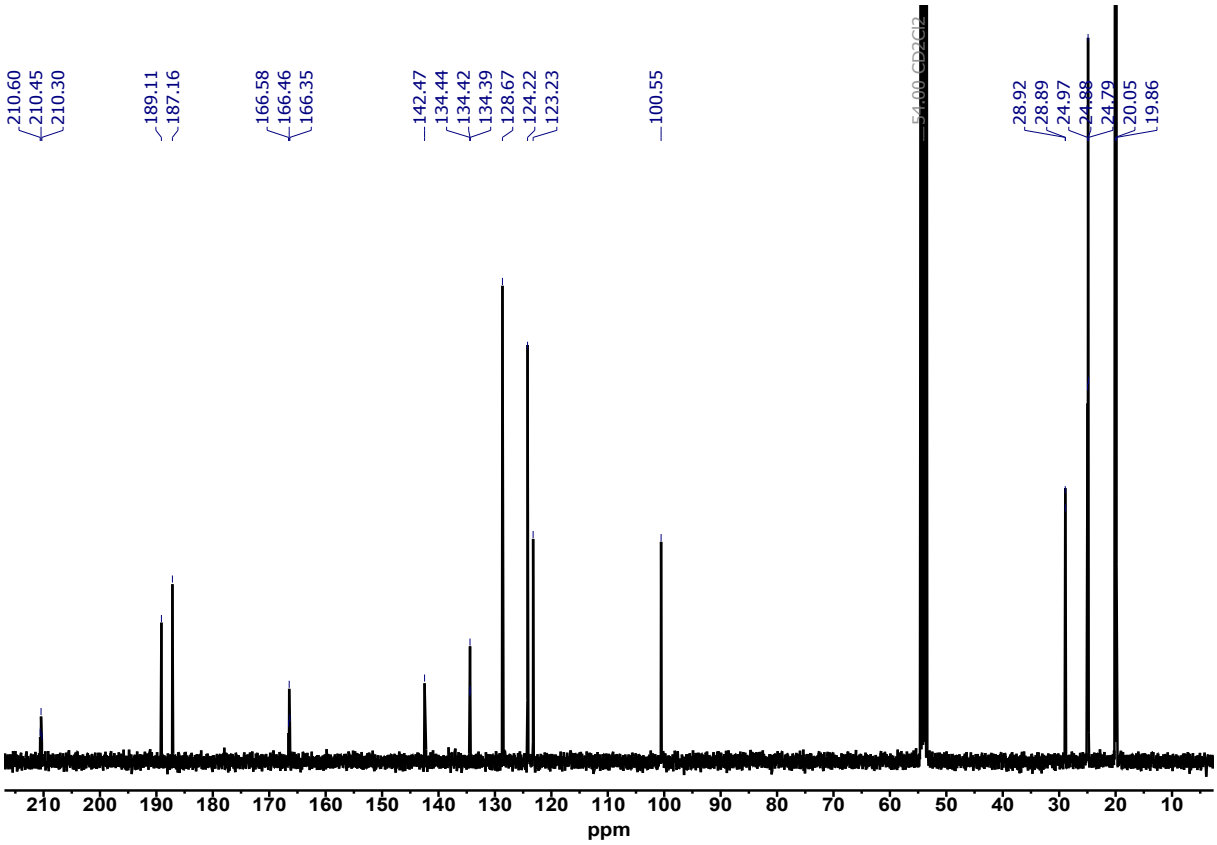

Figure S17: ^{13}C NMR of **Ph-Ru^{acac}** in $CDCl_3$ at room temperature.

4. Crystallographic data

Table S1: Crystal data and structure refinement for **Ph-Ru^{acac}**

Empirical formula	$C_{32}H_{56}O_3P_2Ru$
Formula weight	651.77
Temperature/K	100.15
Crystal system	triclinic
Space group	P-1
a/Å	10.5425(9)
b/Å	11.0929(9)
c/Å	14.8950(13)
α/°	91.934(7)
β/°	93.831(7)
γ/°	99.302(7)
Volume/Å^3	1713.4(3)
Z	2
ρ_{calc}g/cm^3	1.263
μ/mm^{-1}	0.579
F(000)	692.0
Crystal size/mm^3	0.01 × 0.2 × 0.3, light yellow plate
Radiation	MoKα (λ = 0.71073)
2Θ range for data collection/°	3.724 to 58.398
Index ranges	-14 ≤ h ≤ 14, -13 ≤ k ≤ 15, -20 ≤ l ≤ 20
Reflections collected	31843
Independent reflections	9227 [R_{int} = 0.0367, R_{sigma} = 0.0292]
Data/restraints/parameters	9227/0/358
Goodness-of-fit on F^2	1.036
Final R indexes [I>=2σ (I)]	R_1 = 0.0491, wR_2 = 0.1259
Final R indexes [all data]	R_1 = 0.0579, wR_2 = 0.1319
Largest diff. peak/hole / e Å^{-3}	1.29/-0.86

Table S2: Fractional Atomic Coordinates ($\times 10^4$) and Equivalent Isotropic Displacement Parameters ($Å^2 \times 10^3$) for Ph-Ru^{acac}. U_{eq} is defined as 1/3 of of the trace of the orthogonalised U_{IJ} tensor.

Atom	*x*	*y*	*z*	U(eq)
Ru1	7045.7(2)	7161.2(2)	7514.3(2)	23.78(8)
P1	8087.1(7)	5368.0(6)	7313.7(5)	29.63(14)
P2	6028.6(6)	8960.7(6)	7615.1(4)	25.28(13)
O1	6765.5(17)	6869.1(17)	8935.0(12)	29.8(4)
O2	8873.0(16)	8166.3(16)	7990.1(12)	26.9(3)
O3	4496.7(18)	5737.9(18)	6858.4(15)	38.1(4)
C1	7539(2)	7643(2)	6265.9(16)	25.7(4)
C2	6956(2)	7374(2)	5440.4(17)	29.1(5)
C3	7452(2)	7798(2)	4584.9(17)	28.4(5)
C4	7023(2)	7104(2)	3790.4(17)	30.9(5)
C5	7449(3)	7468(3)	2961.7(18)	34.8(5)
C6	8310(3)	8539(3)	2903.7(18)	36.3(6)
C7	8751(3)	9251(3)	3687.0(19)	35.8(5)
C8	8326(3)	8884(3)	4517.6(18)	32.5(5)
C9	7935(3)	4714(3)	6129.4(19)	35.8(5)
C10	6555(3)	4218(3)	5763(2)	44.7(7)
C11	8799(4)	3759(3)	5925(2)	48.5(7)
C12	7549(3)	4064(3)	8034(2)	38.6(6)
C13	6080(4)	3742(3)	8011(3)	51.5(8)
C14	8095(5)	4308(3)	9019(2)	58.7(10)
C15	9867(3)	5731(3)	7597(2)	38.5(6)
C16	10609(4)	4655(4)	7755(3)	60.0(10)
C17	10520(3)	6573(3)	6920(2)	43.9(7)
C18	5105(3)	9244(2)	6544.7(18)	32.4(5)
C19	3754(3)	8480(3)	6410(2)	41.3(6)
C20	5013(3)	10580(3)	6350(2)	38.2(6)
C21	7129(2)	10451(2)	7844.2(17)	28.7(5)
C22	8185(2)	10601(2)	7182.8(19)	32.5(5)
C23	7712(3)	10648(2)	8820.2(19)	33.7(5)
C24	4976(2)	8943(2)	8577.4(17)	29.5(5)
C25	4293(3)	10061(3)	8658(2)	35.4(5)
C26	4031(3)	7750(3)	8635(2)	35.9(5)
C27	7569(3)	7199(2)	9601.0(18)	32.7(5)
C28	8848(3)	7794(3)	9564.3(18)	34.4(5)
C29	9409(2)	8236(2)	8788.5(18)	30.9(5)
C30	7089(3)	6916(3)	10515.9(19)	41.9(6)
C31	10778(3)	8915(3)	8886(2)	38.4(6)
C32	5500(3)	6294(2)	7096.6(18)	30.8(5)

Table S3: Anisotropic Displacement Parameters ($Å^2 \times 10^3$) for Ph-Ru^{acac}. The Anisotropic displacement factor exponent takes the form: $-2\pi^2[h^2a^{*2}U_{11}+2hka^*b^*U_{12}+\ldots]$.

Atom	U_{11}	U_{22}	U_{33}	U_{23}	U_{13}	U_{12}
Ru1	23.49(11)	24.39(12)	23.77(11)	1.26(7)	2.60(7)	4.51(7)
P1	33.2(3)	27.7(3)	29.6(3)	1.4(2)	4.8(2)	8.5(2)
P2	22.8(3)	26.4(3)	27.1(3)	1.3(2)	2.8(2)	4.9(2)
O1	31.8(8)	33.3(9)	25.9(8)	4.1(7)	4.7(6)	8.2(7)
O2	22.2(7)	29.1(8)	28.9(8)	0.5(7)	-0.6(6)	3.9(6)
O3	29.7(9)	33.6(10)	48.3(12)	-6.5(8)	-0.7(8)	0.0(7)
C1	26.7(10)	27.4(11)	24.2(10)	2.7(8)	4.8(8)	6.0(8)
C2	27.7(11)	28.2(11)	31.0(12)	2.2(9)	2.4(9)	2.9(9)
C3	26.1(10)	31.5(12)	28.6(11)	2.3(9)	2.7(8)	7.4(9)
C4	31.9(12)	31.8(12)	29.2(12)	1.9(9)	3.2(9)	5.9(9)
C5	35.9(13)	42.2(14)	27.8(12)	-0.1(10)	2.5(9)	11.4(11)
C6	34.8(13)	48.4(15)	29.1(12)	9.2(11)	9.0(10)	12.5(11)
C7	31.3(12)	40.2(14)	35.7(13)	7.0(11)	5.7(10)	2.8(10)
C8	31.2(12)	36.0(13)	30.1(12)	3.1(10)	2.0(9)	5.0(10)
C9	45.3(14)	31.3(12)	32.1(13)	-1.4(10)	7.7(10)	9.1(11)
C10	46.7(16)	44.2(16)	41.7(15)	-9.2(13)	4.3(12)	5.1(13)
C11	62(2)	43.5(16)	44.4(16)	-4.7(13)	11.2(14)	21.3(15)
C12	52.0(16)	28.5(12)	38.9(14)	8.6(10)	10.8(12)	13.0(11)
C13	57.2(19)	41.6(16)	61(2)	17.0(15)	25.6(16)	10.7(14)
C14	103(3)	38.5(16)	37.7(16)	11.0(13)	6.6(17)	18.0(18)
C15	32.5(12)	40.9(15)	44.4(15)	-1.7(12)	-1.7(11)	16.1(11)
C16	51.8(19)	59(2)	76(3)	2.1(19)	-6.0(17)	32.4(17)
C17	30.5(13)	50.4(17)	50.9(17)	-3.5(14)	5.5(12)	7.0(12)
C18	32.9(12)	36.4(13)	29.3(12)	2.6(10)	-1.4(9)	11.2(10)
C19	35.4(13)	41.9(15)	45.0(16)	-1.1(12)	-12.4(11)	8.8(12)
C20	37.6(13)	38.4(14)	41.1(14)	9.4(11)	0.4(11)	13.4(11)
C21	27.9(11)	25.3(11)	34.0(12)	1.2(9)	4.2(9)	6.6(9)
C22	28.1(11)	29.6(12)	40.1(14)	3.6(10)	6.6(10)	3.7(9)
C23	32.1(12)	30.2(12)	37.8(13)	-5.1(10)	-0.5(10)	4.8(10)
C24	27.0(11)	32.3(12)	30.7(11)	0.8(9)	8.1(9)	7.1(9)
C25	32.4(12)	34.7(13)	41.2(14)	-0.2(11)	10.2(10)	9.4(10)
C26	29.8(12)	35.6(13)	42.8(14)	4.3(11)	9.0(10)	4.3(10)
C27	38.8(13)	32.7(12)	28.9(12)	3.5(10)	4.5(10)	11.3(10)
C28	38.1(13)	39.1(14)	26.8(11)	-0.6(10)	-3.5(10)	12.1(11)
C29	29.6(11)	30.3(12)	33.5(12)	-0.3(10)	-1.0(9)	9.4(9)
C30	47.7(16)	52.7(17)	28.8(13)	6.7(12)	6.7(11)	16.0(14)
C31	30.6(12)	44.8(15)	38.1(14)	-0.3(12)	-3.6(10)	4.1(11)
C32	33.9(12)	28.5(11)	31.5(12)	2.8(9)	5.4(9)	7.8(10)

Table S4: Bond Lengths and Bond Angles for **Ph-Ru^{acac} .**

Atom	Atom	Length/Å	Atom	Atom	Length/Å	Atom	Atom	Length/Å
Ru1	P1	2.4416(7)	O2	C29	1.276(3)	C12	C14	1.539(5)
Ru1	P2	2.4188(6)	O3	C32	1.162(3)	C15	C16	1.545(4)
Ru1	O1	2.1838(18)	C1	C2	1.339(3)	C15	C17	1.521(5)
Ru1	O2	2.1276(17)	C2	C3	1.473(4)	C18	C19	1.532(4)
Ru1	C1	2.030(2)	C3	C4	1.397(3)	C18	C20	1.537(4)
Ru1	C32	1.813(3)	C3	C8	1.404(4)	C21	C22	1.528(4)
P1	C9	1.871(3)	C4	C5	1.392(4)	C21	C23	1.535(4)
P1	C12	1.867(3)	C5	C6	1.383(4)	C24	C25	1.536(4)
P1	C15	1.871(3)	C6	C7	1.396(4)	C24	C26	1.531(4)
P2	C18	1.875(3)	C7	C8	1.395(4)	C27	C28	1.408(4)
P2	C21	1.866(3)	C9	C10	1.526(4)	C27	C30	1.510(4)
P2	C24	1.869(2)	C9	C11	1.541(4)	C28	C29	1.400(4)
O1	C27	1.264(3)	C12	C13	1.530(5)	C29	C31	1.512(4)

Atom	Atom	Atom	Angle/˚	Atom	Atom	Atom	Angle/˚
P2	Ru1	P1	176.44(2)	C8	C3	C2	123.5(2)
O1	Ru1	P1	94.00(5)	C5	C4	C3	121.4(3)
O1	Ru1	P2	89.56(5)	C6	C5	C4	120.5(3)
O2	Ru1	P1	88.32(5)	C5	C6	C7	119.2(3)
O2	Ru1	P2	92.05(5)	C8	C7	C6	120.2(3)
O2	Ru1	O1	85.14(7)	C7	C8	C3	121.1(2)
C1	Ru1	P1	88.10(7)	C10	C9	P1	114.6(2)
C1	Ru1	P2	88.39(7)	C10	C9	C11	109.0(2)
C1	Ru1	O1	170.96(8)	C11	C9	P1	116.2(2)
C1	Ru1	O2	86.13(8)	C13	C12	P1	112.3(2)
C32	Ru1	P1	91.06(8)	C13	C12	C14	109.0(3)
C32	Ru1	P2	88.53(8)	C14	C12	P1	112.3(2)
C32	Ru1	O1	95.44(10)	C16	C15	P1	118.1(2)
C32	Ru1	O2	179.18(9)	C17	C15	P1	111.1(2)
C32	Ru1	C1	93.31(11)	C17	C15	C16	110.1(3)
C9	P1	Ru1	114.17(9)	C19	C18	P2	114.1(2)
C12	P1	Ru1	115.69(9)	C19	C18	C20	108.8(2)
C12	P1	C9	106.14(13)	C20	C18	P2	117.13(19)
C12	P1	C15	103.76(14)	C22	C21	P2	110.64(17)
C15	P1	Ru1	111.92(9)	C22	C21	C23	110.9(2)
C15	P1	C9	103.99(13)	C23	C21	P2	113.78(18)
C18	P2	Ru1	113.42(8)	C25	C24	P2	114.38(19)
C21	P2	Ru1	116.31(8)	C26	C24	P2	114.32(18)
C21	P2	C18	101.91(12)	C26	C24	C25	111.3(2)
C21	P2	C24	101.50(11)	O1	C27	C28	126.2(3)
C24	P2	Ru1	112.62(8)	O1	C27	C30	115.8(3)
C24	P2	C18	110.00(12)	C28	C27	C30	118.0(2)
C27	O1	Ru1	127.40(18)	C29	C28	C27	125.6(2)
C29	O2	Ru1	127.82(17)	O2	C29	C28	126.9(2)
C2	C1	Ru1	133.1(2)	O2	C29	C31	114.8(2)
C1	C2	C3	126.5(2)	C28	C29	C31	118.2(2)
C4	C3	C2	119.0(2)	O3	C32	Ru1	177.7(2)
C4	C3	C8	117.6(2)				

5. Cyclic Voltammetry

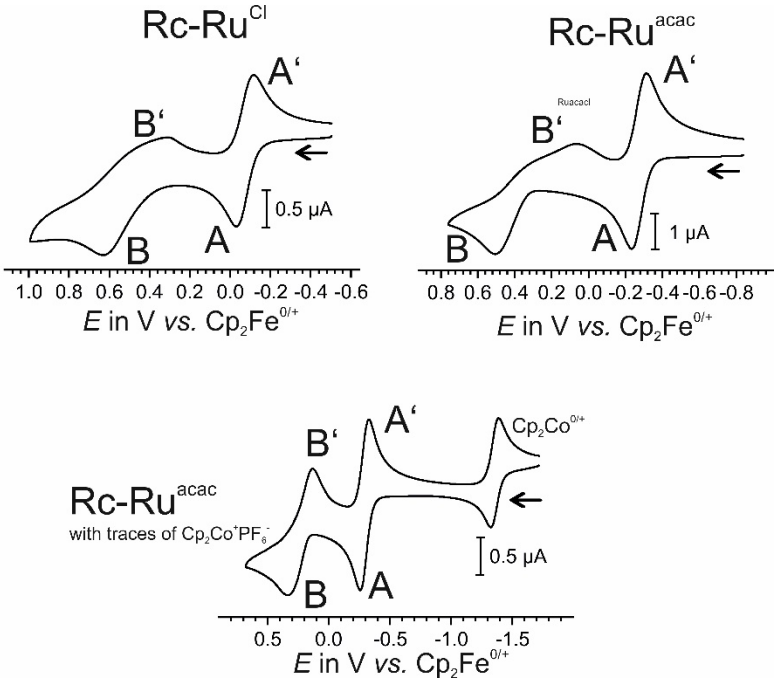

Figure S18: Cyclic voltammograms of **Rc-Ru^{Cl}** and **Rc-Ru^{acac}** in CH_2Cl_2 and NBu_4^+ $[B\{C_6H_3(CF_3)_2\text{-}3,5\}_4]^-$ as supporting electrolyte at room temperature.

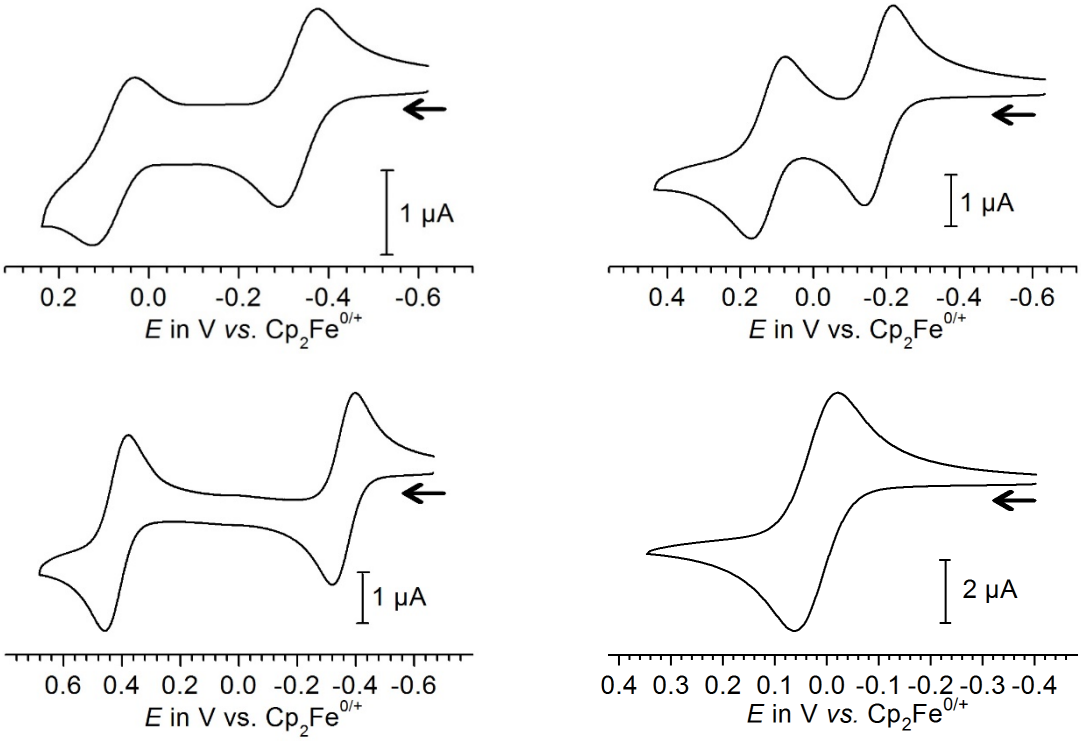

Figure S19: Cyclic voltammograms of **Rc*-Ru^{Cl}** (top left) and **Rc-Ru^{acac}** (top right) and **Fc-Ru^{acac}**(bottom left) and **Ph-Ru^{acac}** (bottom right), vs FcH/FcH+ in CH_2Cl_2/NBu_4PF_6 (0.1 M) at r.t. and v = 100 mV/s

6. IR Spectroelectrochemistry

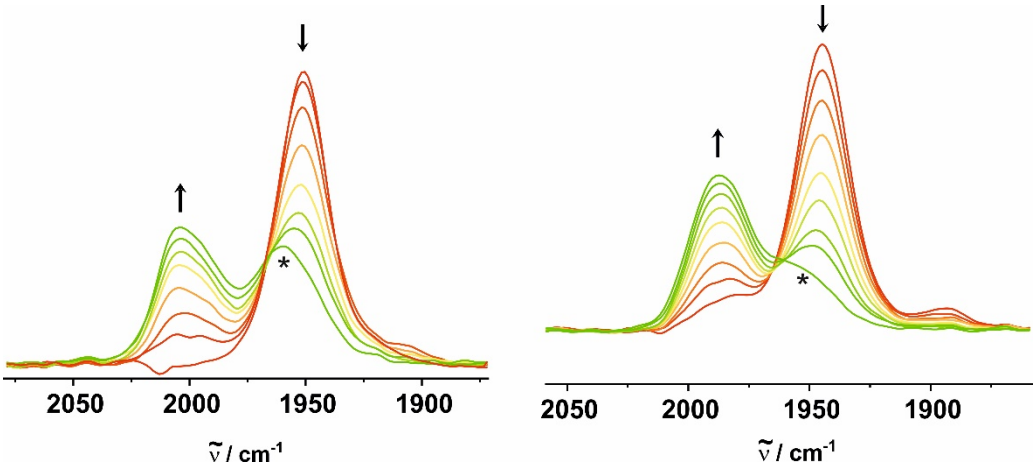

Figure S20: IR-spectroelectrochemical changes during oxidation of **Rc-Ru^{Cl}** and **Rc-Ru^{acac}** in dichloromethane and NBu_4PF_6 as supporting electrolyte (0.1 M) at room temperature red cationic and green dicationic form. The asterisk marks the decomposition product.

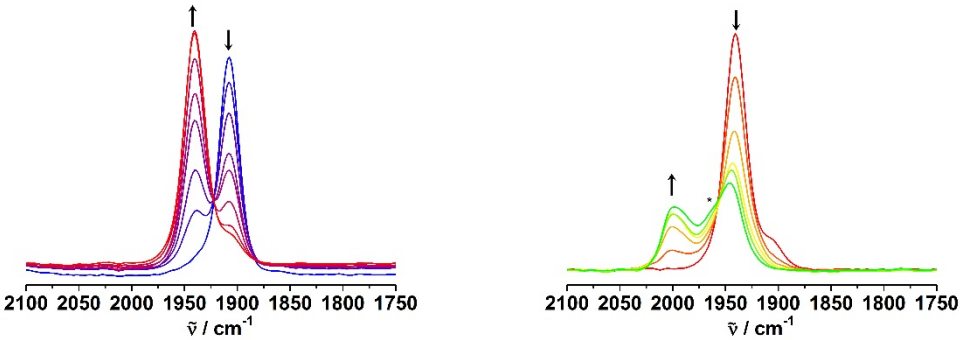

Figure S21: IR-spectroelectrochemical changes during oxidation of **Rc*-Ru^{Cl}** in dichloromethane and NBu_4PF_6 as supporting electrolyte (0.1 M) at room temperature, blue neutral, red cationic and green dicationic form. The asterisk marks the decomposition product.

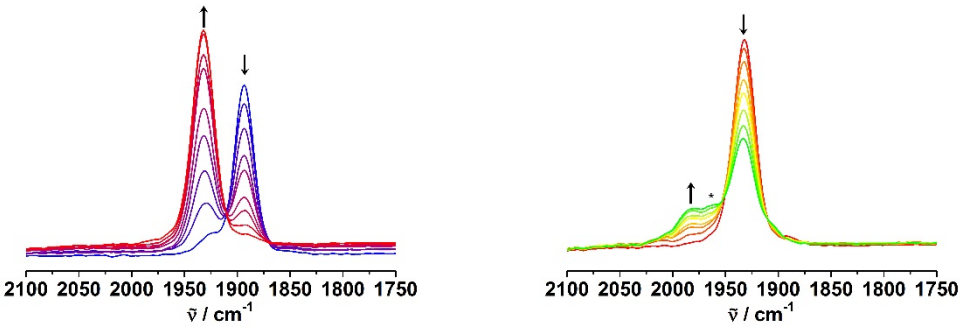

Figure S22. IR-spectroelectrochemical changes during oxidation of **Rc*-Ru^{acac}** in dichloromethane and NBu_4PF_6 as supporting electrolyte (0.1 M) at room temperature, blue neutral, red cationic and green dicationic form. The asterisk marks the decomposition product.

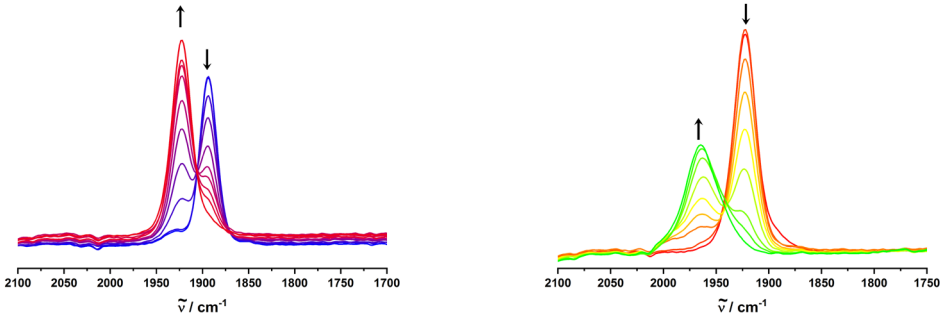

Figure S23: IR-spectroelectrochemical changes during oxidation of **Fc-Ru^{acac}** in dichloromethane and NBu_4PF_6 as supporting electrolyte (0.1 M) at room temperature, blue neutral, red cationic and green dicationic form.

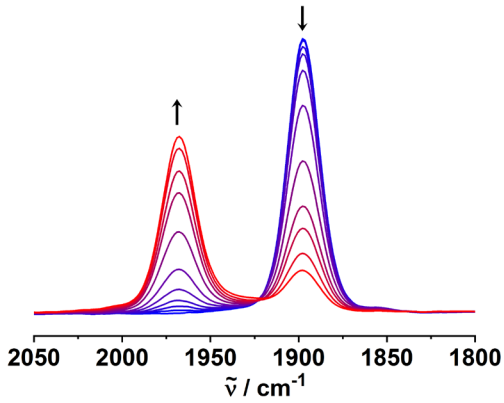

Figure S24: IR-spectroelectrochemical changes during oxidation of **Ph-Ru^{acac}** in dichloromethane and NBu_4PF_6 as supporting electrolyte (0.1 M) at room temperature, blue neutral, red cationic form.

7. (TD-)DFT calculations

Molecular Orbitals and calculated transitions

neutral state	oxidized state	
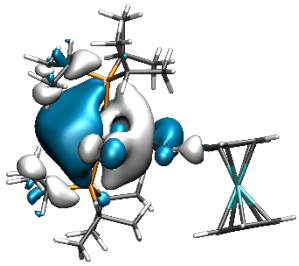	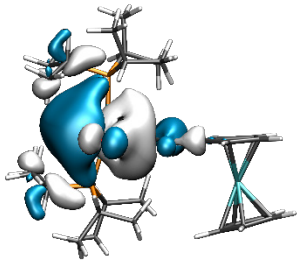	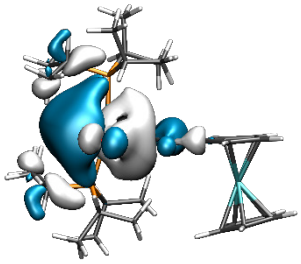
LUMO, E = -1.45 eV	α-LUSO, E = -2.42 eV	β-LUSO+1, E = -2.36 eV
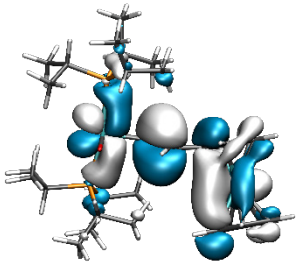	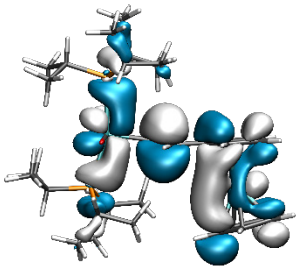	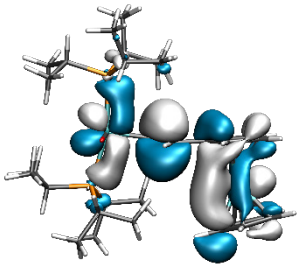
HOMO, E = -5.13 eV	α-HOSO, E = -6.19 eV	β-LUSO, E = -4.17 eV
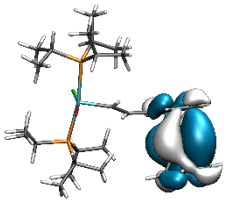		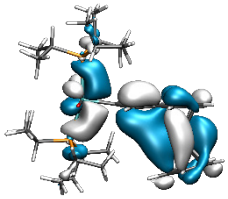
HOMO-1, E = -5.80 eV		β-HOSO, E = -6.62 eV
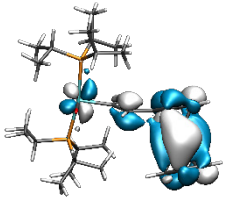		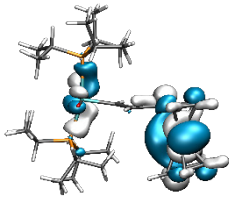
HOMO-2, E = -5.86 eV		β-HOSO-1, E = -6.93 eV
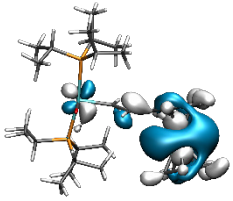		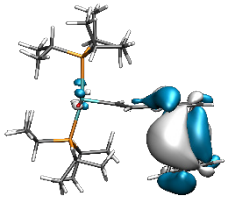
HOMO-3, E = -6.02 eV		β-HOSO-2, E = -6.97 eV

Figure S25: Molecular orbitals for **Rc-Ru^{Cl}** in its neutral and oxidized states.

neutral state	oxidized state	
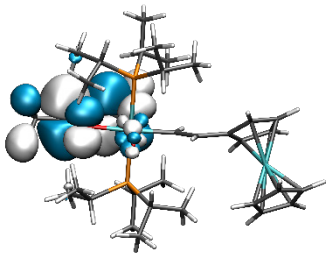	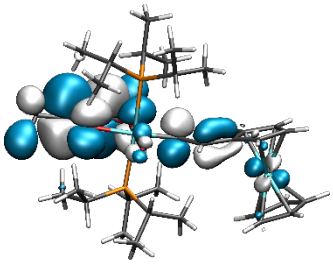	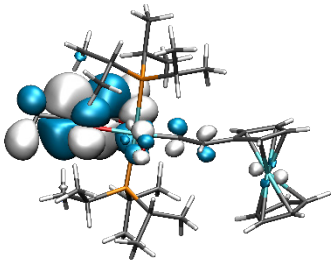
LUMO, E = -0.77 eV	α-LUSO, E = -1.38 eV	β-LUSO+1, E = -1.35eV
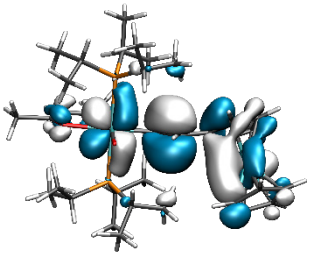	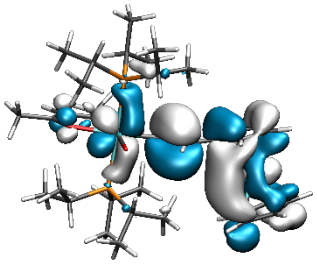	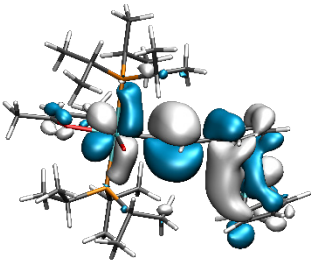
HOMO, E = -4.96eV	α-HOSO, E = -6.14 eV	β-LUSO, E = -4.06 eV
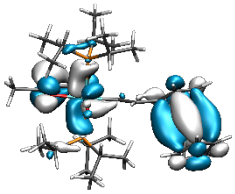	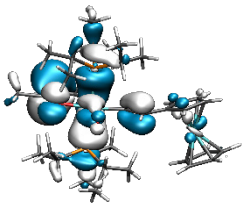	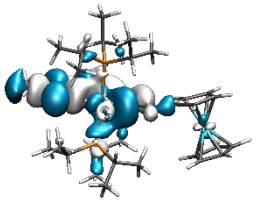
HOMO-1, E = -5.71 eV	β-HOSO-1, E = - eV	β-HOSO-5, E = - eV
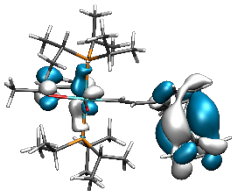	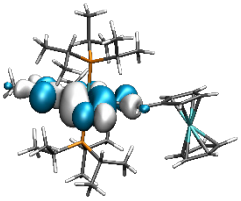	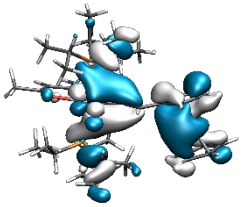
HOMO-2, E = -5.73 eV	β-HOSO-2, E = - eV	β-HOSO-6, E = - eV
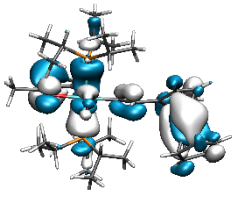	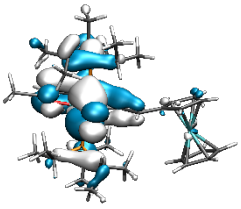	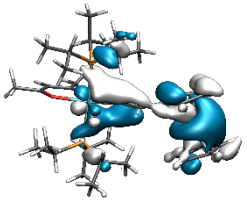
HOMO-3, E = -5.82 eV	β-HOSO-4, E = - eV	β-HOSO-7, E = - eV

Figure S26: Molecular orbitals for **Rc-Ru^{acac}** in its neutral and oxidized states.

neutral state	oxidized state	
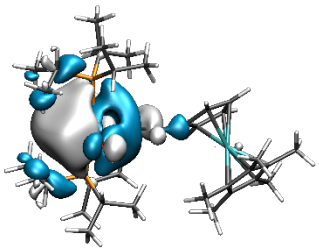	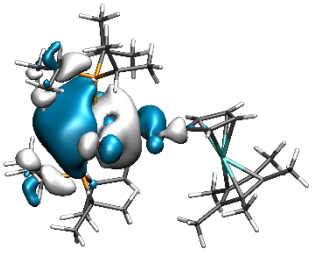	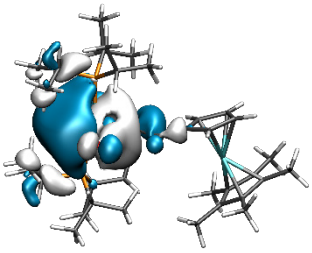
LUMO, E = -1.43 eV	α-LUSO, E = -2.21 eV	β-LUSO+1, E = -2.16 eV
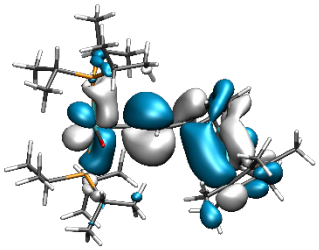	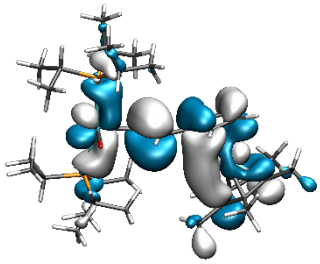	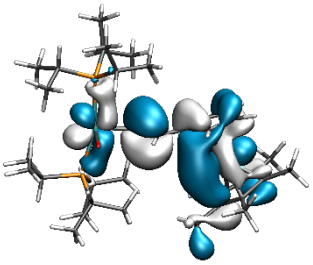
HOMO, E = -5.03 eV	α-HOSO, E = - 5.92eV	β-LUSO, E = -3.94 eV
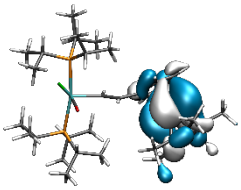		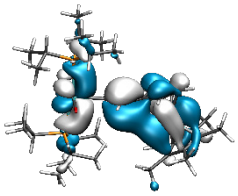
HOMO-1, E = -5.54 eV		β-HOSO, E = -6.37 eV
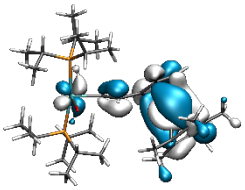		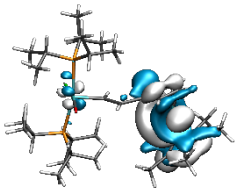
HOMO-2, E = -5.61 eV		β-HOSO-1, E = -6.73 eV
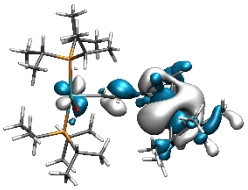		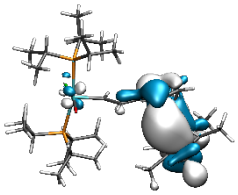
HOMO-3, E = -5.79 eV		β-HOSO-2, E = -6.76 eV

Figure S27: Molecular orbitals for **Rc*-Ru^{Cl}** in its neutral and oxidized states.

neutral state	oxidized state	
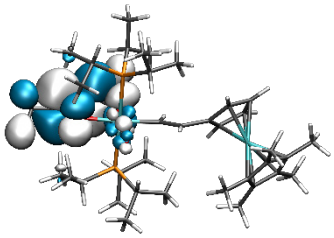 LUMO, E = -0-77 eV	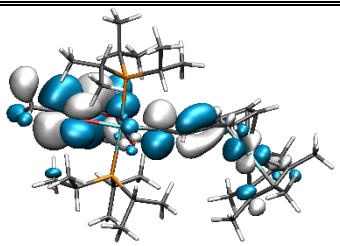 α-LUSO, E = --1-19 eV	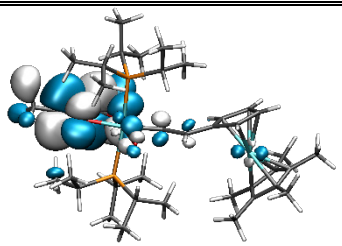 β-LUSO+1, E = -1.16 eV
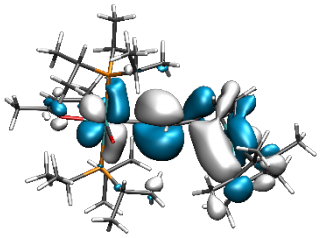 HOMO, E = -4.88eV	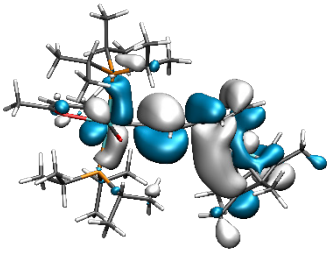 α-HOSO, E = -5.78 eV	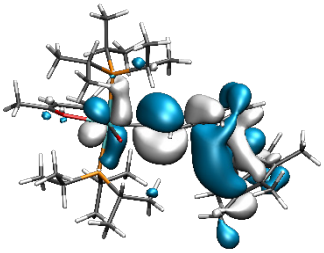 β-LUSO, E = -3.82 eV
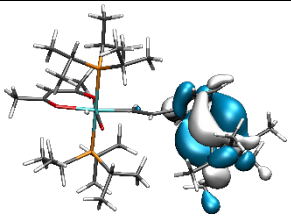 HOMO-1, E = -5.47 eV		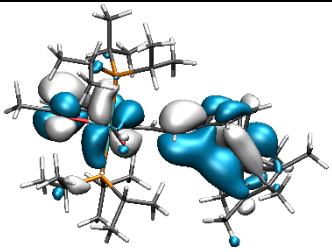 β-HOSO, E = -6.15 eV
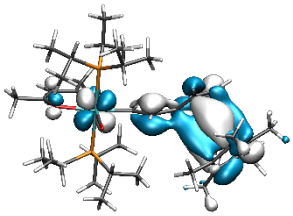 HOMO-2, E = -5.50 eV		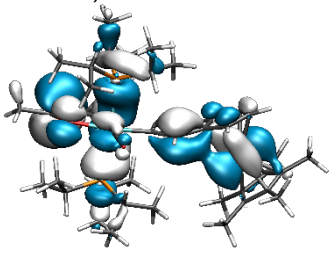 β-HOSO-1, E = -6.32 eV
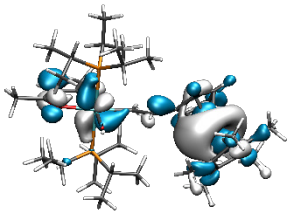 HOMO-3, E = -5.68 eV	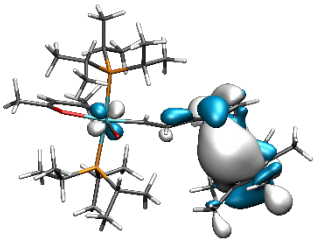 β-HOSO-3, E = -6.59 eV	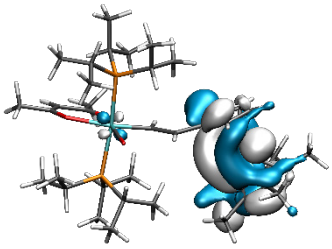 β-HOSO-2, E = -6.59 eV

Figure S28: Molecular orbitals for **Rc*-Ru^{acac}** in its neutral and oxidized states.

neutral state	oxidized state	
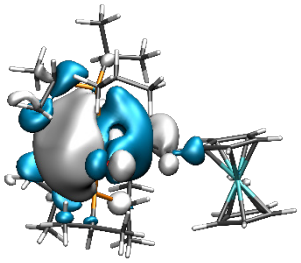	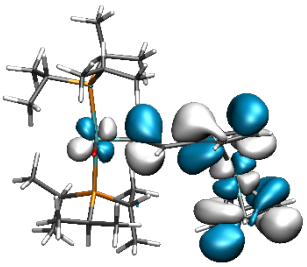	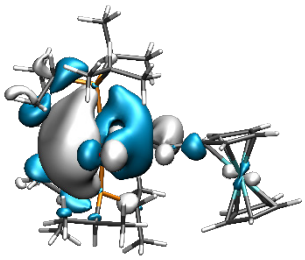
LUMO, E = -1.53 eV	α-LUSO, E = -1.19 eV	β-LUSO+1, E = -2.39 eV
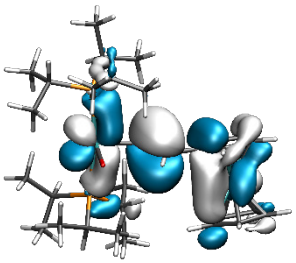	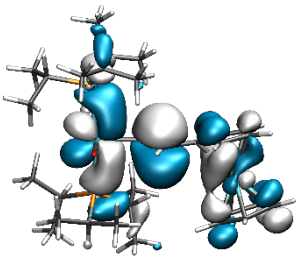	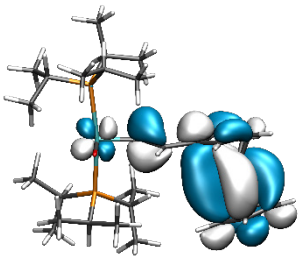
HOMO, E = -5.27 eV	α-HOSO, E = -5.78 eV	β-LUSO, E = -2.73 eV
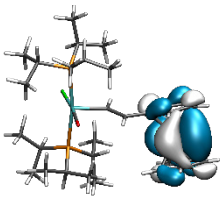	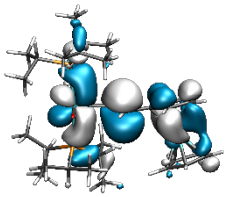	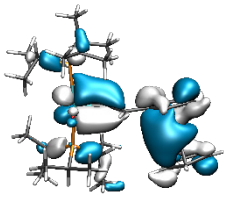
HOMO-1, E = -5.77 eV	β–HOSO, E = -6.24 eV	β–HOSO-4, E = -8.12 eV
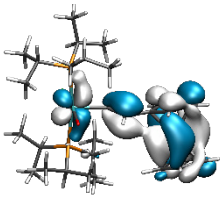	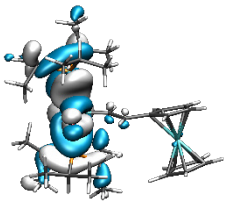	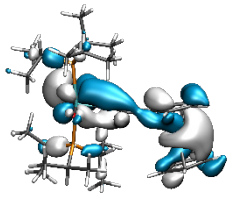
HOMO-2, E = -5.88 eV	β–HOSO-1, E = -6.90 eV	β–HOSO-5, E = -8.28 eV
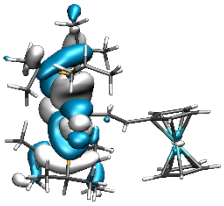	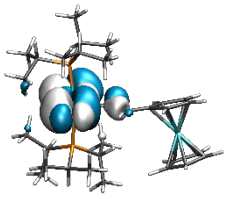	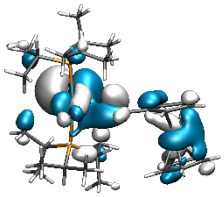
HOMO-3, E = -6.50 eV	β–HOSO-2, E = -7.13 eV	β–HOSO-6, E = -8.35 eV

Figure S29: Molecular orbitals for **Fc-Ru^{Cl}** in its neutral and oxidized states.

neutral state	oxidized state	
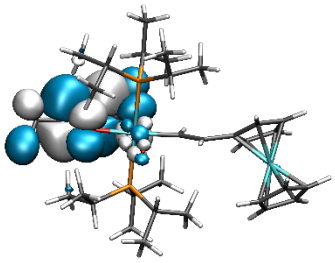	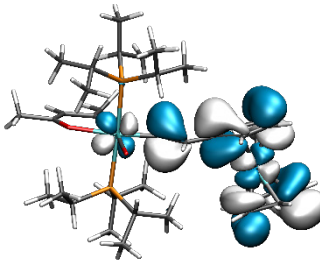	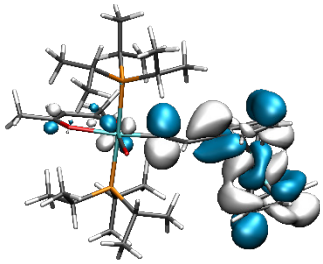
LUMO, E = -0.91 eV	α-LUSO, E = -2.66 eV	β-LUSO+1, E = -1.56 eV
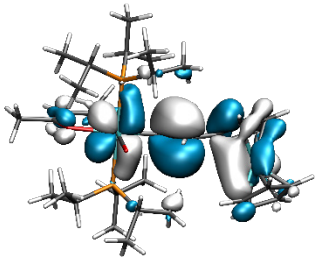	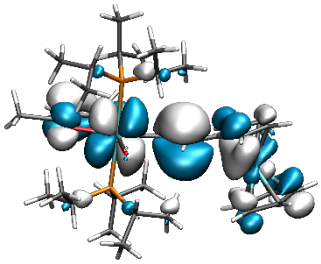	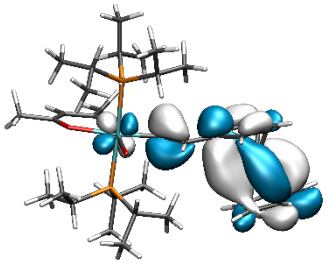
HOMO, E = -5.09 eV	α-HOSO, E = -5.99 eV	β-LUSO, E = -3.10 eV
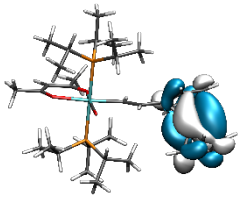	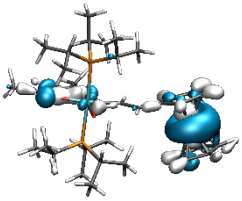	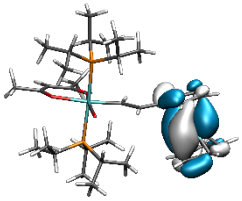
HOMO-1, E = -5.68 eV	α–HOSO-14, E = -8.86 eV	β–HOSO-8, E = -8.17 eV
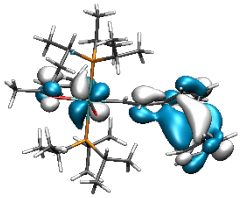	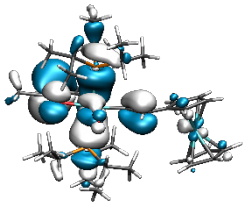	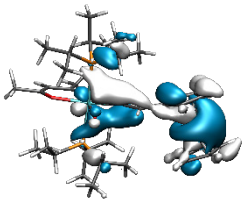
HOMO-2, E = -5.74 eV	α–HOSO-1, E = -6.28 eV	β–HOSO-7, E = -8.06 eV
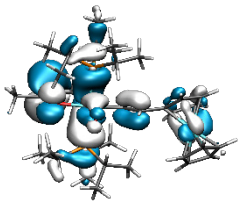		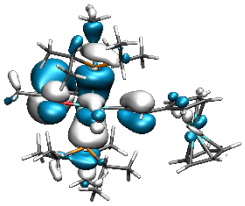
HOMO-3, E = -5.95 eV		β–HOSO-1, E = -6.28 eV

Figure S30: Molecular orbitals for **Fc-Ru^{acac}** in its neutral and oxidized states.

Table S5. Fragment contributions to the charge and spin densities according to analysis of the natural bond orbitals

complex	fragment	n = 0	n = 1		charge difference
		charge	charge	spin density	
Fc-Ru^{Cl}	{Ru^{Cl}}	0.10	0.12	0.01	0.02
	vinyl	-0.03	0.02	0.01	0.05
	Cp$^{vi\ a)}$	0.05	0.05	-0.12	0.00
	Fe	-0.21	0.72	1.29	0.93
	Cp$^{b)}$	0.09	0.09	-0.19	0.00
	SUM	0.00	1.00	1.00	1.00
Fc-Ru^{acac}	{Ru^{acac}}	0.24	0.19	0.00	-0.05
	vinyl	-0.15	-0.03	0.01	0.12
	Cp$^{vi\ a)}$	0.03	0.03	-0.19	0.00
	Fe	-0.20	0.73	1.30	0.93
	Cp $^{b)}$	0.08	0.08	-0.12	0.00
	SUM	0.00	1.00	1.00	1.00
Rc-Ru^{Cl}	{Ru^{Cl}}	0.10	0.35	0.28	0.25
	vinyl	-0.02	0.25	0.30	0.27
	Cp$^{vi\ a)}$	0.09	0.15	0.04	0.06
	Ru	-0.31	0.07	0.33	0.38
	Cp $^{b)}$	0.14	0.18	0.05	0.04
	SUM	0.00	1.00	1.00	1.00
Rc-Ru^{acac}	{Ru^{acac}}	0.23	0.47	0.23	0.24
	vinyl	-0.13	0.23	0.36	0.36
	Cp$^{vi\ a)}$	0.08	0.13	0.05	0.05
	Ru	-0.31	0.01	0.33	0.32
	Cp $^{b)}$	0.13	0.16	0.03	0.03
	SUM	0.00	1.00	1.00	1.00
Rc*-Ru^{Cl}	{Ru^{Cl}}	0.09	0.25	0.18	0.16
	vinyl	-0.02	0.18	0.23	0.20
	Cp$^{vi\ a)}$	0.02	0.15	0.07	0.13
	Ru	-0.26	0.18	0.45	0.44
	Cp* $^{b)}$	0.17	0.24	0.07	0.07
	SUM	0.00	1.00	1.00	1.00
Rc*-Ru^{acac}	{Ru^{acac}}	0.23	0.34	0.21	0.11
	vinyl	-0.13	0.18	0.28	0.31
	Cp$^{vi\ a)}$	0.02	0.13	0.07	0.11
	Ru	-0.26	0.13	0.38	0.39
	Cp* $^{b)}$	0.14	0.22	0.07	0.08
	SUM	0.00	1.00	1.00	1.00

[a]The bridging, vinyl substituted Cp ligand. [b]The appended, non-bridging Cp/Cp* ligand.

7. EPR spectra of the chemically mono-oxidized complexes

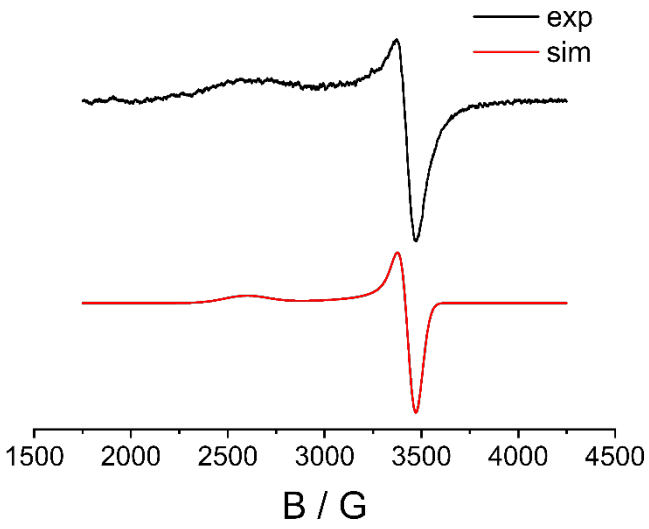

Figure S31: EPR spectra of **Fc-Ru^{acac+}** at -150°C in a frozen dichloromethane matrix.

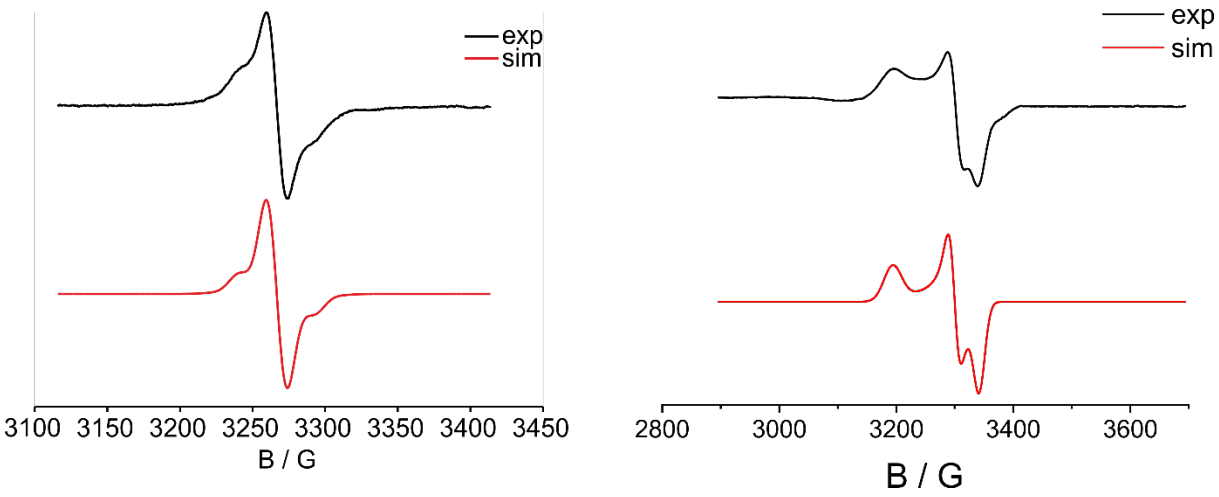

Figure S32: EPR spectra of **Rc-Ru^{acac+}** at room temperature (left) and at -150°C in a frozen dichloromethane matrix (right).

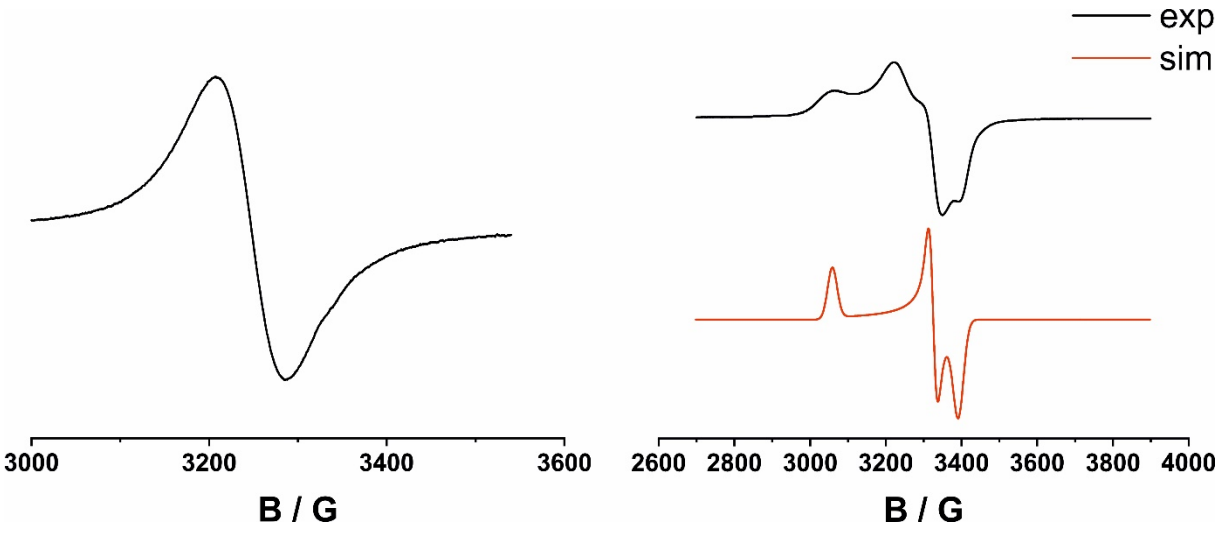

Figure S33: EPR spectra of **Rc*-Ru^{Cl+}** at room temperature (left) and at -150°C in a frozen dichloromethane matrix (right).

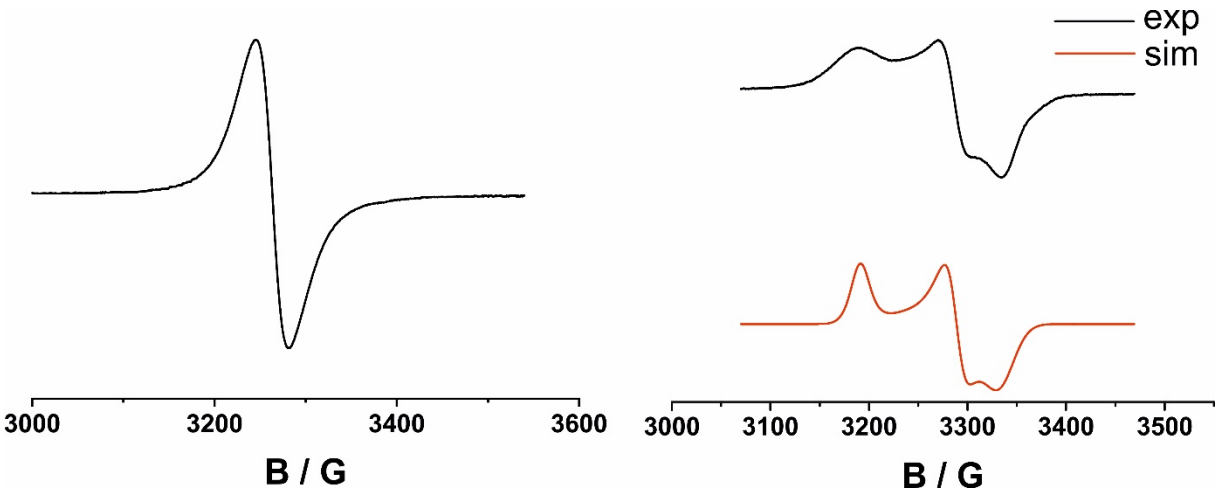

Figure S34: EPR spectra of **Rc*-Ru^{acac+}** at room temperature (left) and at -150°C in a frozen dichloromethane matrix (right).

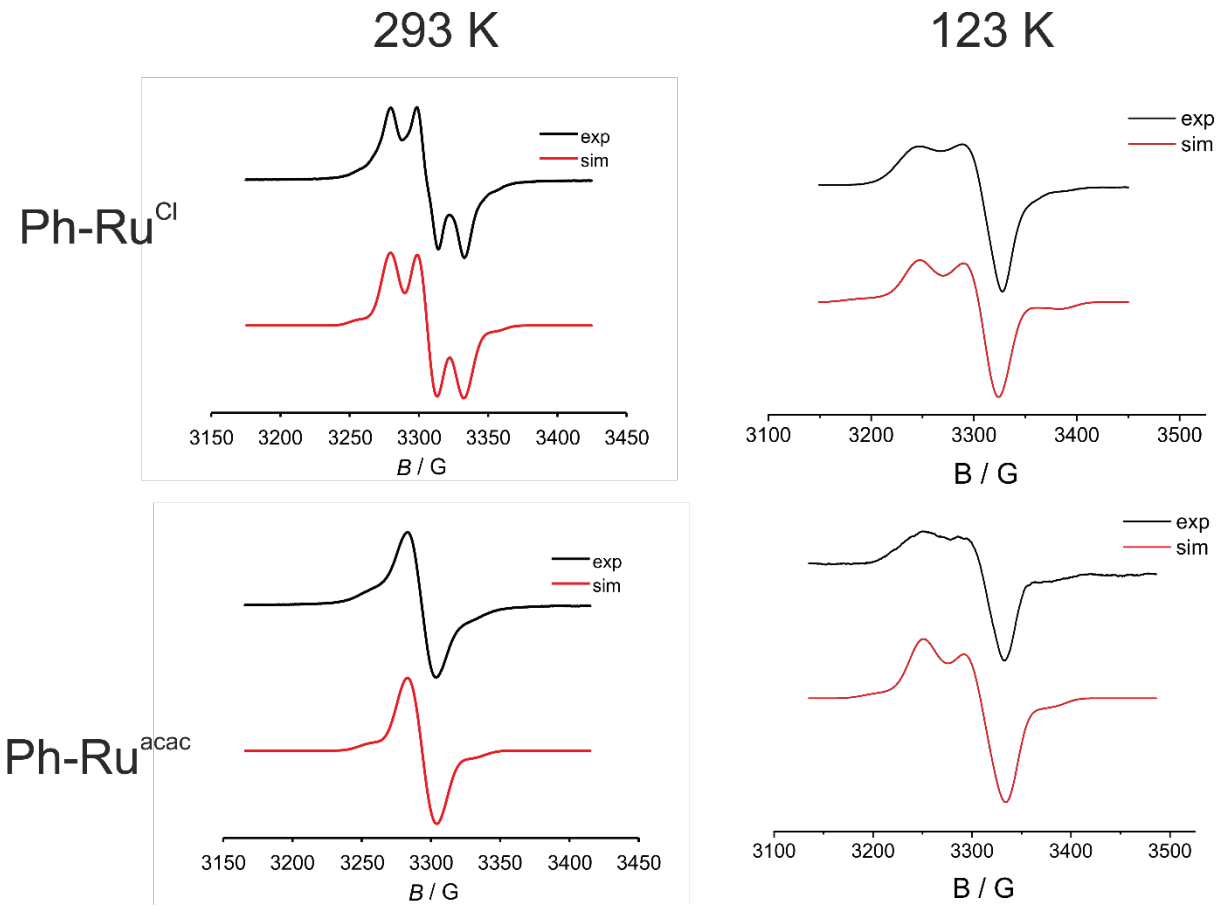

Figure S35: EPR spectra of **Ph-Ru^{Cl+}**and **Ph-Ru^{acac+}** at room temperature (left) and at -150°C in a frozen dichloromethane matrix (right).

8. Spin Density Plots of the radical cations

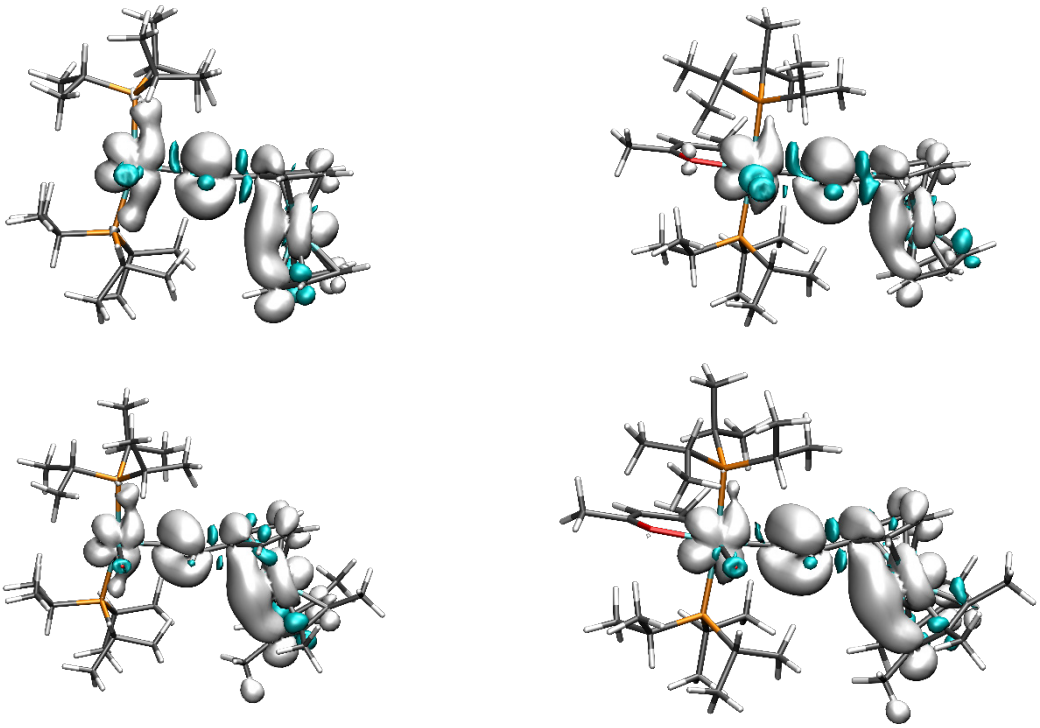

Figure S36: Spin density plots of **Rc-Ru^{Cl}** (upper left), **Rc-Ru^{acac}** (upper right), **Rc*-Ru^{Cl}** (bottom left), **Rc*-Ru^{acac}** (bottom right), white and cyan color positive (α) and negative (β) spin density, respectively (pbe1pbe/6-31G(d) level of theory).

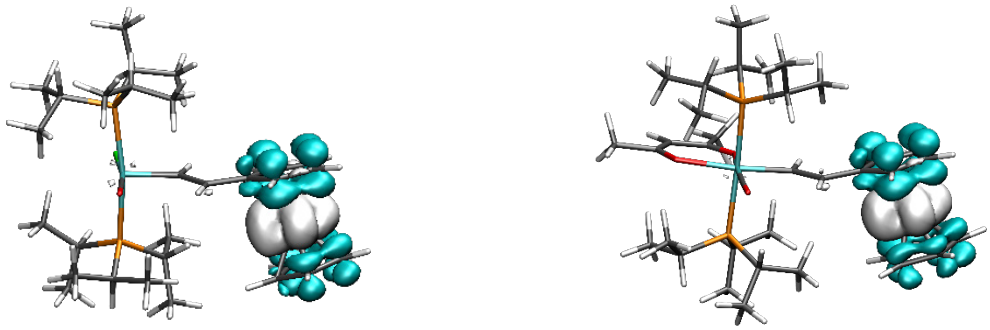

Figure S37: Spin density plots of **FcRu^{Cl}** (left), **Fc-Ru^{acac}** (right), white and cyan color positive (α) and negative (β) spin density, respectively (pbe1pbe/6-311G(d) level of theory).

Table S6. DFT-computed fragment contributions to the β-MOs relevant to the NIR band of the radical cations

		%[a]	Mc[b]	Cp[c]	vinyl	Ru[d]
Fc-Ru^{Cl+}	LUSO		37	50	9	4
	HOSO	56	7	16	31	46
	HOSO-1	22	0	0	2	98
Fc-Ru^{acac+}	LUSO		65	23	8	4
	HOSO	63	8	13	26	53
	HOSO-1	19	1	3	5	91
Rc-Ru^{Cl+}	LUSO		26	19	29	26
	HOSO	56	52	16	10	22
	HOSO-1	22	73	17	1	9
Rc-Ru^{acac+}	LUSO		20	16	32	32
	HOSO	61	22	6	2	70
	HOSO-1	24	42	12	4	42
Rc*-Ru^{Cl+}	LUSO		36	25	22	17
	HOSO	77	38	15	15	32
	HOSO-1	11	64	31	1	4
Rc*-Ru^{acac+}	LUSO		29	25	26	20
	HOSO	58	28	11	8	53
	HOSO-3	24	71	25	1	3

[a]Percent contribution of corresponding excitation. [b]Contribution of the Fe or Ru atom of the metallocene. [c]Combined contributions of the cyclopentadienyl ligands [d]Contribution of the Ru(CO)(L)(P^iPr_3)$_2$ (L = Cl^- or $acac^-$) entity.

9. UV/vis/NIR data

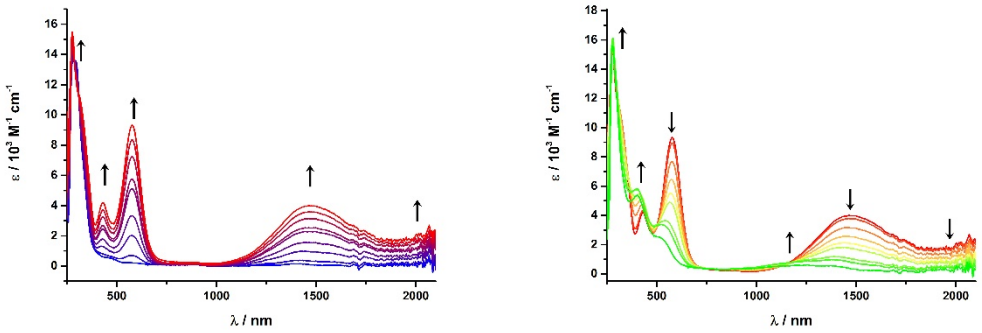

Figure S38: UV/vis/NIR spectroelectrochemistry during oxidation of **Fc-Ru^{acac}** in dichloromethane and NBu_4PF_6 as supporting electrolyte (0.1 M) at room temperature, blue neutral, red cationic and green dicationic form.

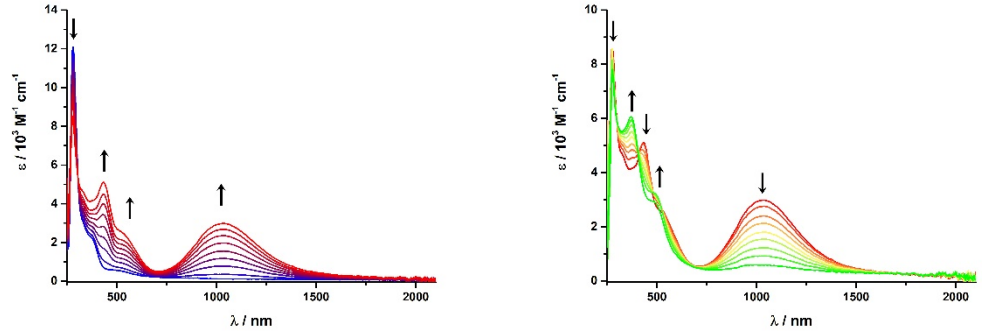

Figure S39: UV/vis/NIR spectroelectrochemistry during oxidation of **Rc-Ru^{Cl}** in dichloromethane and NBu_4PF_6 as supporting electrolyte (0.1 M) at room temperature, blue neutral, red cationic and green dicationic form.

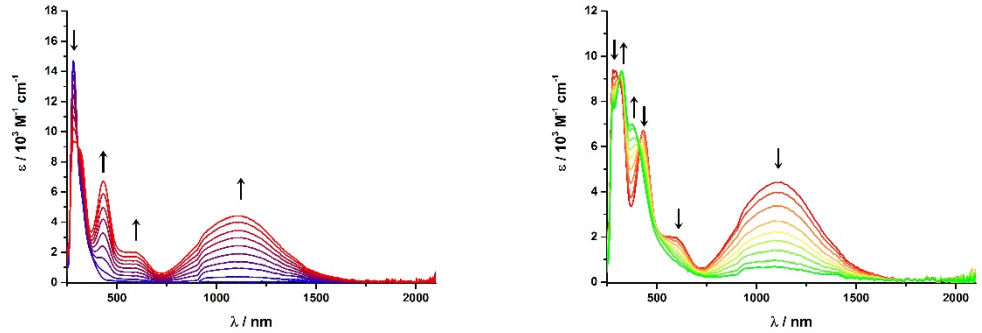

Figure S40: UV/vis/NIR spectroelectrochemistry during oxidation of **Rc-Ru^{acac}** in dichloromethane and NBu_4PF_6 as supporting electrolyte (0.1 M) at room temperature, blue neutral, red cationic and green dicationic form.

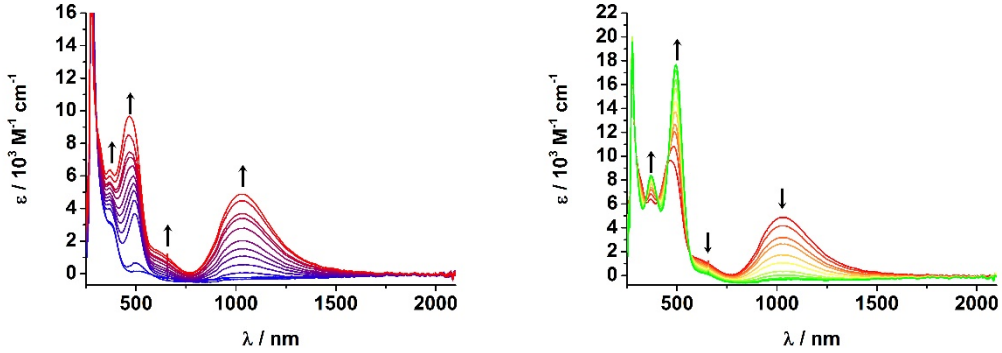

Figure S401: UV/vis/NIR spectroelectrochemistry during oxidation of **Rc*-Ru^{Cl}** in dichloromethane and NBu_4PF_6 as supporting electrolyte (0.1 M) at room temperature, blue neutral, red cationic and green dicationic form.

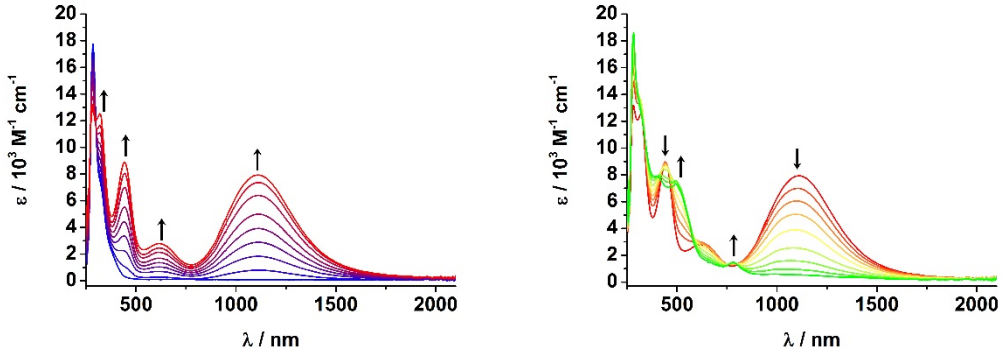

Figure S412: UV/vis/NIR spectroelectrochemistry during oxidation of **Rc*-Ru^{acac}** in dichloromethane and NBu_4PF_6 as supporting electrolyte (0.1 M) at room temperature, blue neutral, red cationic and green dicationic form.

10. TD-DFT calculated UV/vis/NIR spectra

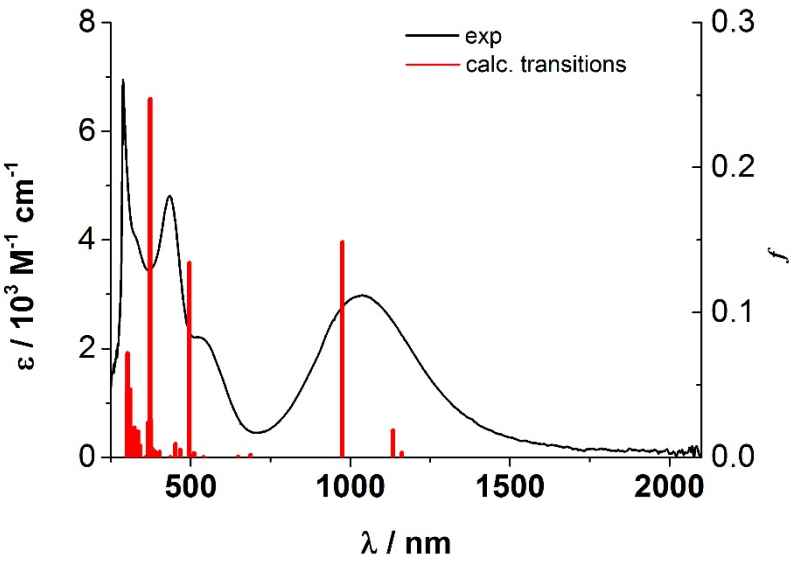

Figure S423: TD-DFT calculated transitions of **Rc-Ru^{Cl+}** (pbe1pbe/6-31G(d) level of theory)

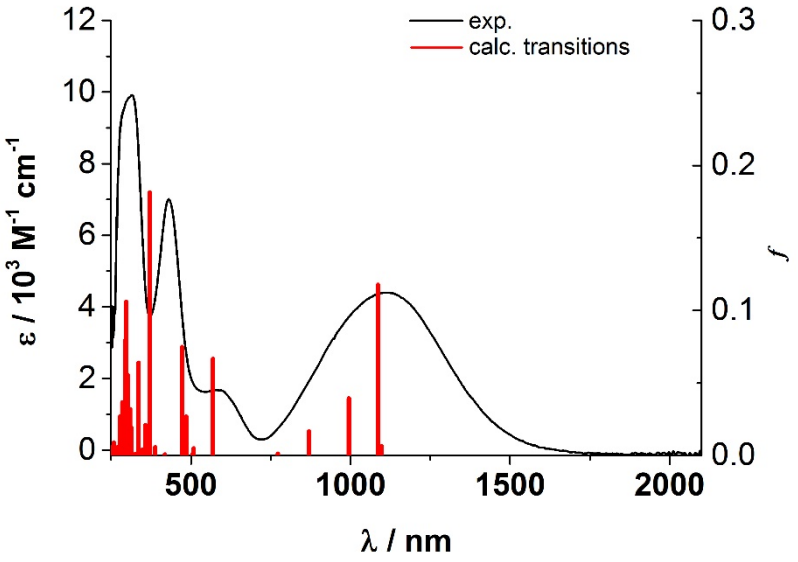

Figure S44: TD-DFT calculated transitions of **Rc-Ru^{acac+}** c (pbe1pbe/6-31G(d) level of theory)

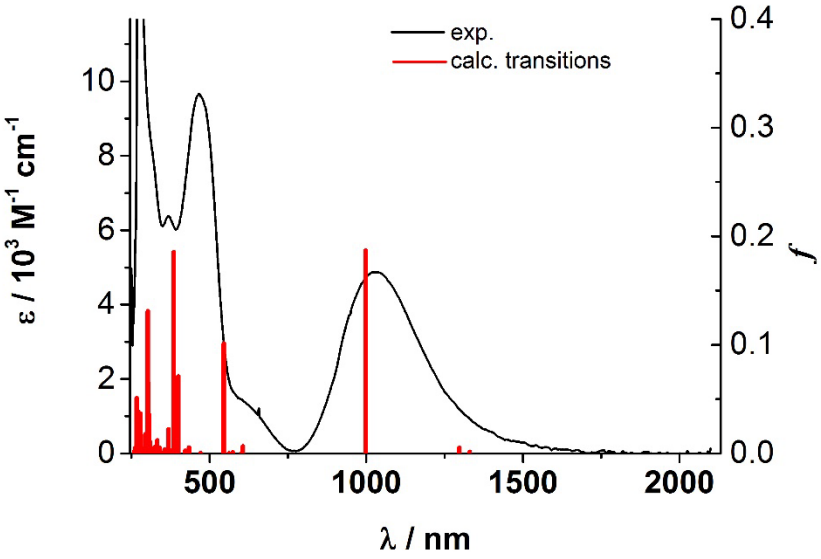

Figure S435: TD-DFT calculated transitions of **Rc*-Ru^{Cl+}** (pbe1pbe/6-31G(d) level of theory)

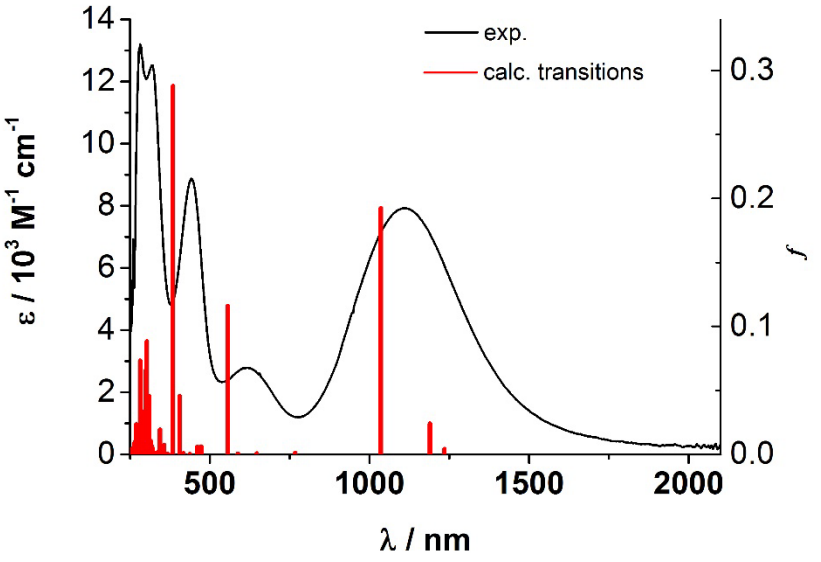

Figure S446: TD-DFT calculated transitions of **Rc*-Ru^{acac+}** (pbe1pbe/6-31G(d) level of theory)

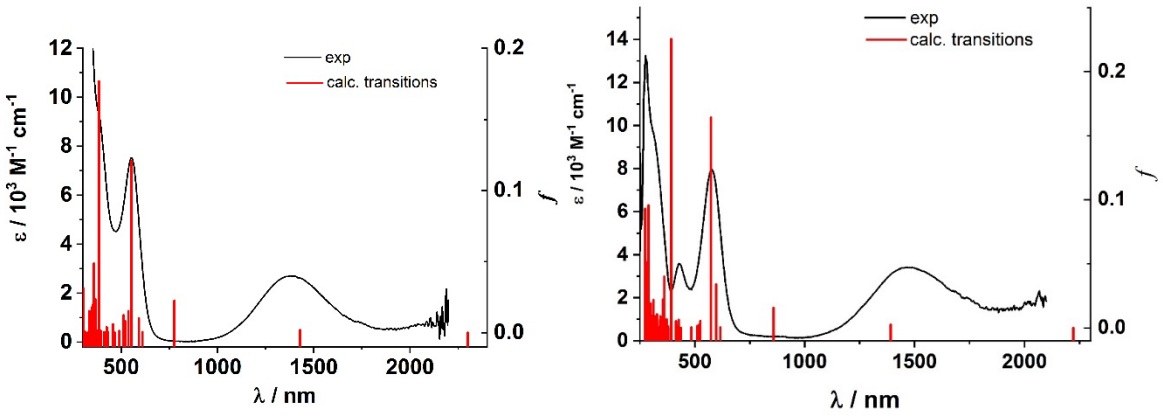

Figure S457: TD-DFT calculated transitions of **Fc-Ru^{Cl+}** (left) and **Fc-Ru^{acac+} (right)** (pbe1pbe/6-311G(d) level of theory)

11. Electron Density Difference Maps (EDDM) for the calculated transitions

Table S7. Selected calculated transition energies for **Fc-Ru^{Cl+}**.

transition number	calc. λ_{max}	major transition	oscillator strength
1	2299	HOSO-7(β)->LUSO(β) (86 %),	0.0
2	1428	HOSO-6(β) → LUSO(β) (10%) HOSO-5(β) → LUSO(β) (30%) HOSO-4(β) → LUSO(β) (46%)	0.0019
3	776	HOSO-2(β) → LUSO(β) (11%) HOSO-1(β) → LUSO(β) (22%) HOSO(β) → LUSO(β) (56%)	0.0227
6	554	HOSO-6(β) → LUSO(β) (83%)	0.1208
18	385	HOSO-19(α) → LUSO(α) (10%) HOSO(α) → LUSO(α) (14%), HOSO(β) → LUSO+2(β) (47%)	0.1769

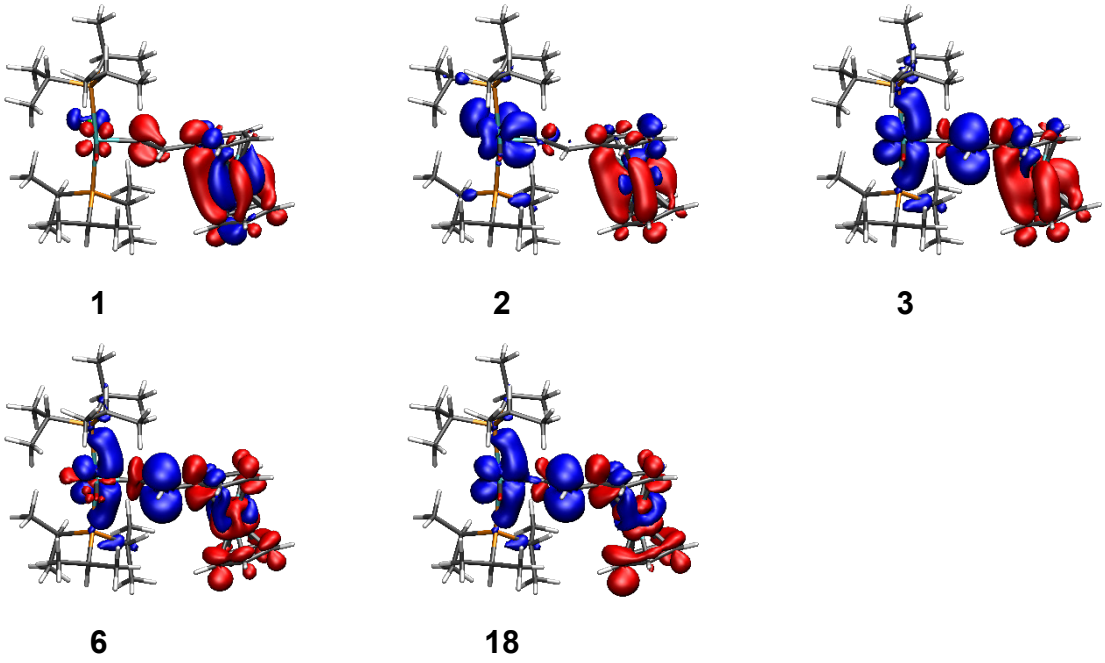

Figure S468: Electron density difference map for the selected transitions of **Fc-Ru^{Cl}**. Blue color indicates a decreasing and red color indicates an increasing electron density during the respective excitation.

Table S8. Selected calculated transition energies for **Fc-Ru^{acac+}**.

transition number	calc. λ_{max}	major transition	oscillator strength
1	2222	HOSO-8(β) → LUSO(β) (89 %),	0.0
2	1392	HOSO-7(β) → LUSO(β) (53%) HOSO-6(β) → LUSO(β) (29%)	0.0024
3	857	HOSO(β) → LUSO(β) (63%) HOSO-1(β) → LUSO(β) (19%)	0.0157
6	574	HOSO(α) → LUSO(α) (41%) HOSO-7(β) → LUSO+1(β) (38%) HOSO-6(β) → LUSO+2(β) (21%)	0.1642
16	393	HOSO-1(α) → LUSO(α) (47%)	0.2254

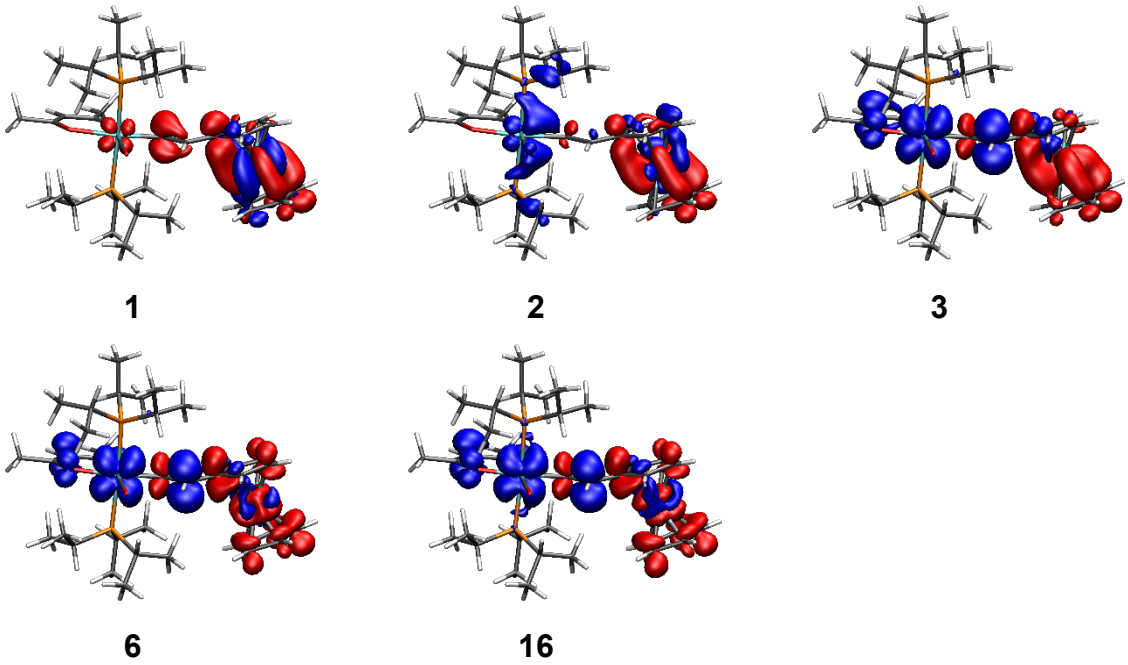

Figure S49: Electron density difference map for the selected transitions of **Fc-Ru^{acac+}**. Blue color indicates a decreasing and red color indicates an increasing electron density during the respective excitation.

Table S9. Selected calculated transition energies for **Rc-Ru^{Cl+}**.

transition number	calc. λ_{max}	major transition	oscillator strength
1	1160	HOSO-2(β) → LUSO(β) (31%) HOSO -1(β) → LUSO(β) (58%)	0.0031
2	1134	HOSO-2(β) → LUSO(β) (53%) HOSO-1(β) → LUSO(β) (11%) HOSO(β) → LUSO(β) (32%)	0.0186
3	975	HOSO-2(β) → LUSO(β) (11%) HOSO-1(β) → LUSO(β) (22%) HOSO(β) → LUSO(β) (56%)	0.1485
8	496	HOSO-6(β) → LUSO(β) (83%)	0.1342
16	373	HOSO(α) → L+1(α) (61%)	0.2472

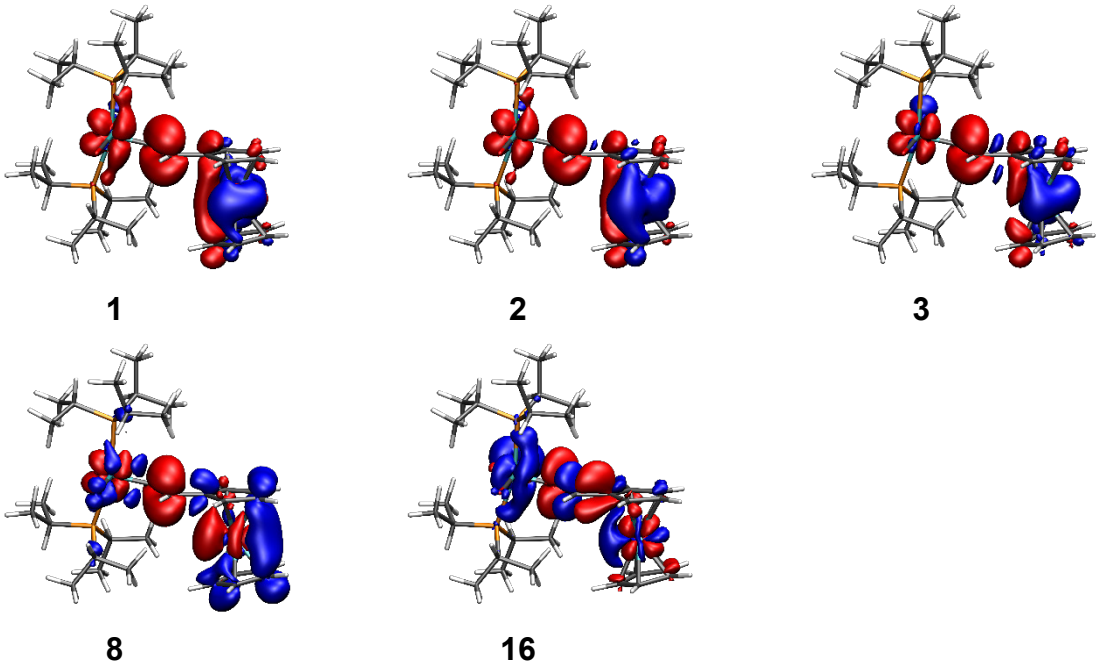

Figure S50: Electron density difference map for the selected transitions of **Rc-Ru^{Cl}**. Blue color indicates a decreasing and red color indicates an increasing electron density during the respective excitation.

Table S10. Selected calculated transition energies for **Rc-Ru^{acac+}**.

transition number	calc. λ_{max}	major transition	oscillator strength
1	1097	HOSO-2(β) → LUSO(β) (90%)	0.0064
2	1086	HOSO-1(β) → LUSO(β) (24%) HOSO(β) → LUSO(β) (61%)	0.1178
3	995	HOSO-3(β) → LUSO(β) (69%) HOSO(β) → LUSO(β) (18%)	0.0394
4	870	HOSO-3(β) → LUSO(β) (20%) HOSO-1(β) → LUSO(β) (59%), HOSO(β) → LUSO(β) (12%)	0.0165
6	569	HOSO-7(β) → LUSO(β) (32%), HOSO-5(β) → LUSO(β) (50%)	0.0666
10	473	HOSO-9(β) → LUSO(β) (38%) HOSO-8(β) → LUSO(β) (25%) HOSO-7(β) → LUSO(β) (23%) HOSO-5(β) → LUSO(β) (10%)	0.0748
13	371	HOSO(α) → L+1(α) (48%)	0.1815

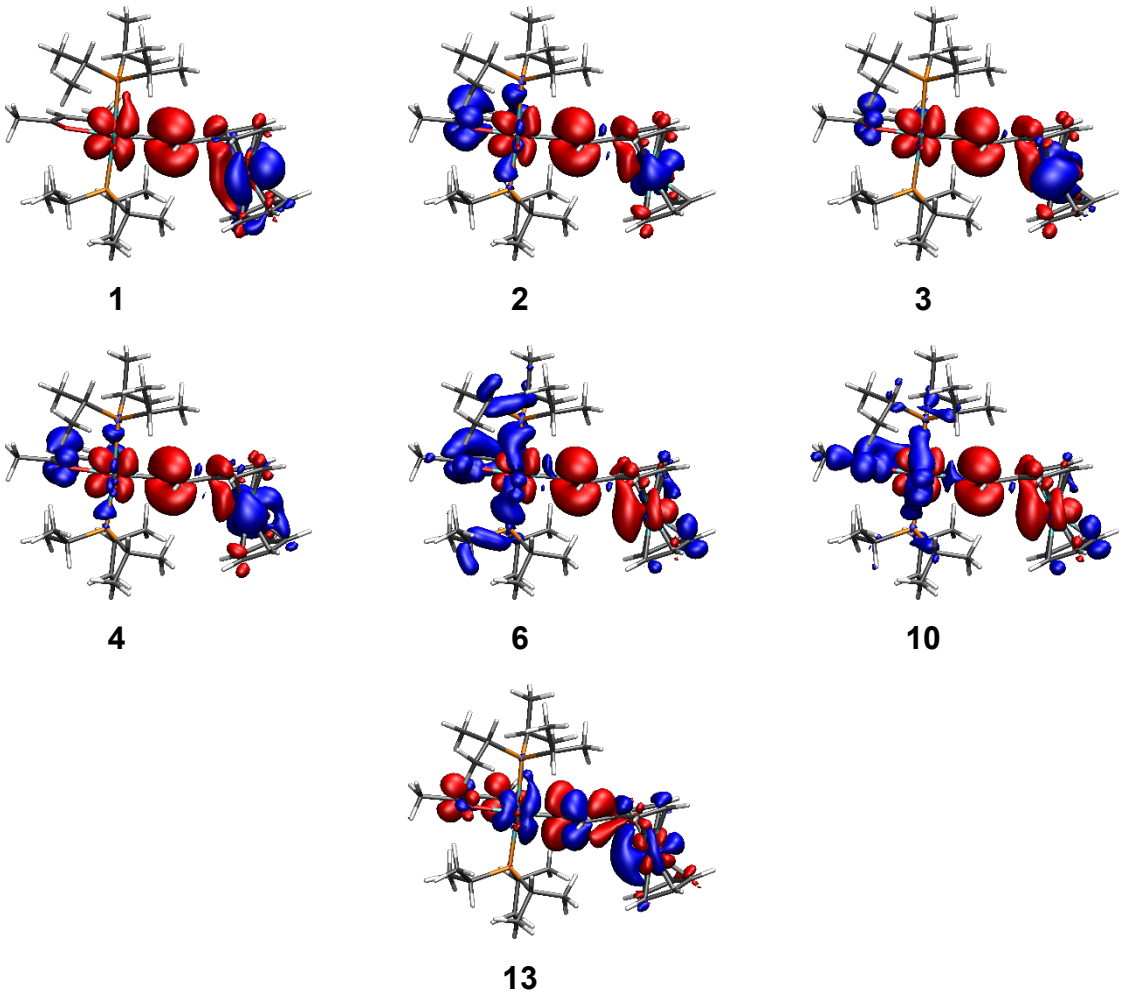

Figure S471: Electron density difference map for the selected transitions of **Rc-Ru^{acac}**. Blue color indicates a decreasing and red color indicates an increasing electron density during the respective excitation.

Table S11. Selected calculated transition energies for **Rc*-Ru^{Cl+}**.

transition number	calc. λ_{max}	major transition	oscillator strength
1	1331	HOSO-1(β)→LUSO(β) (84%)	0.0015
2	1298	HOSO-2(β)→LUSO(β) (77%), HOSO(β)→LUSO(β) (13%)	0.0054
3	998	HOSO(β)→LUSO(β) (77%)	0.187
8	545	HOSO-6(β)→LUSO(β) (90%)	0.1012
14	386	HOSO(α)→LUSO+1(α) (55%), HOSO-3(β)→LUSO+1(β) (11%)	0.1854

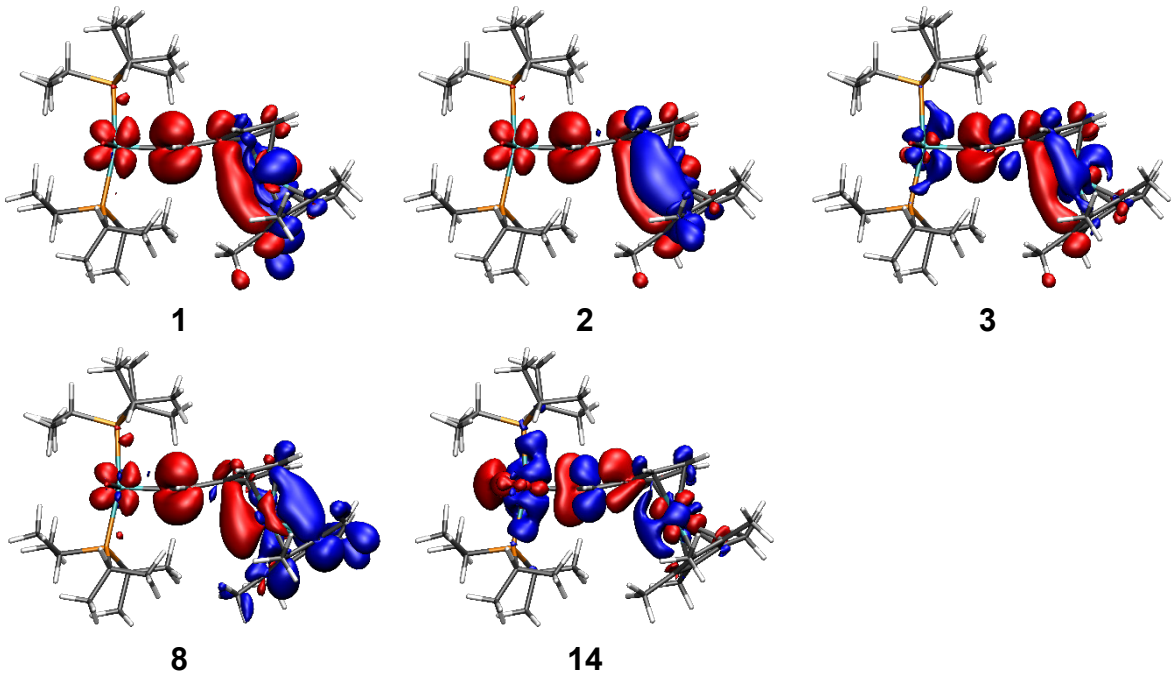

Figure S482: Electron density difference map for the selected transitions of **Rc*-Ru^{Cl}**. Blue color indicates a decreasing and red color indicates an increasing electron density during the respective excitation.

Table S12. Selected calculated transition energies for **Rc*-Ru^{acac+}**.

transition number	calc. λ_{max}	major transition	oscillator strength
1	1234	HOSO-2(β)→LUSO(β) (87%)	0.0042
2	1189	HOSO-3(β)→LUSO(β) (68%), HOSO-1(β)→LUSO(β) (10%), HOSO(β)→LUSO(β) (17%)	0.024
3	1036	HOSO-3(β)->LUSO(β) (24%), HOSO(β)→LUSO(β) (58%)	0.1925
7	556	HOSO-6(β)→LUSO(β) (87%)	0.1159
13	384	HOSO(α)→LUSO(α) (21%), HOSO(α)→LUSO+1(α) (57%)	0.2881

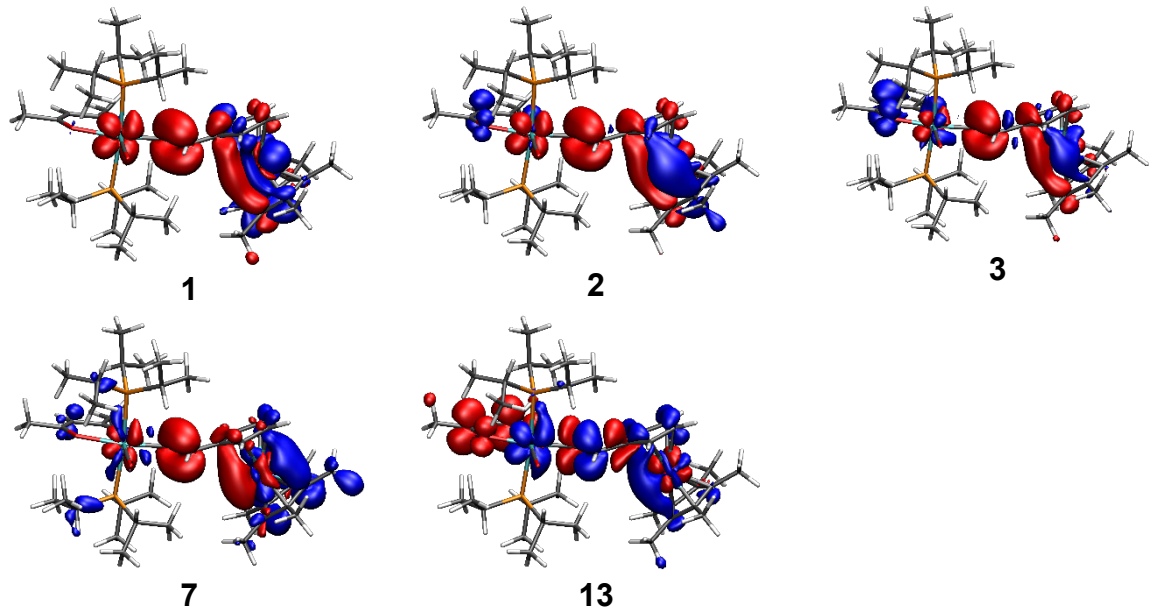

Figure S493: Electron density difference map for the selected transitions of **Rc*-Ru^{acac}**. Blue color indicates decreasing and red color increasing electron density during the respective excitation.

12. Molecular orbital contributions

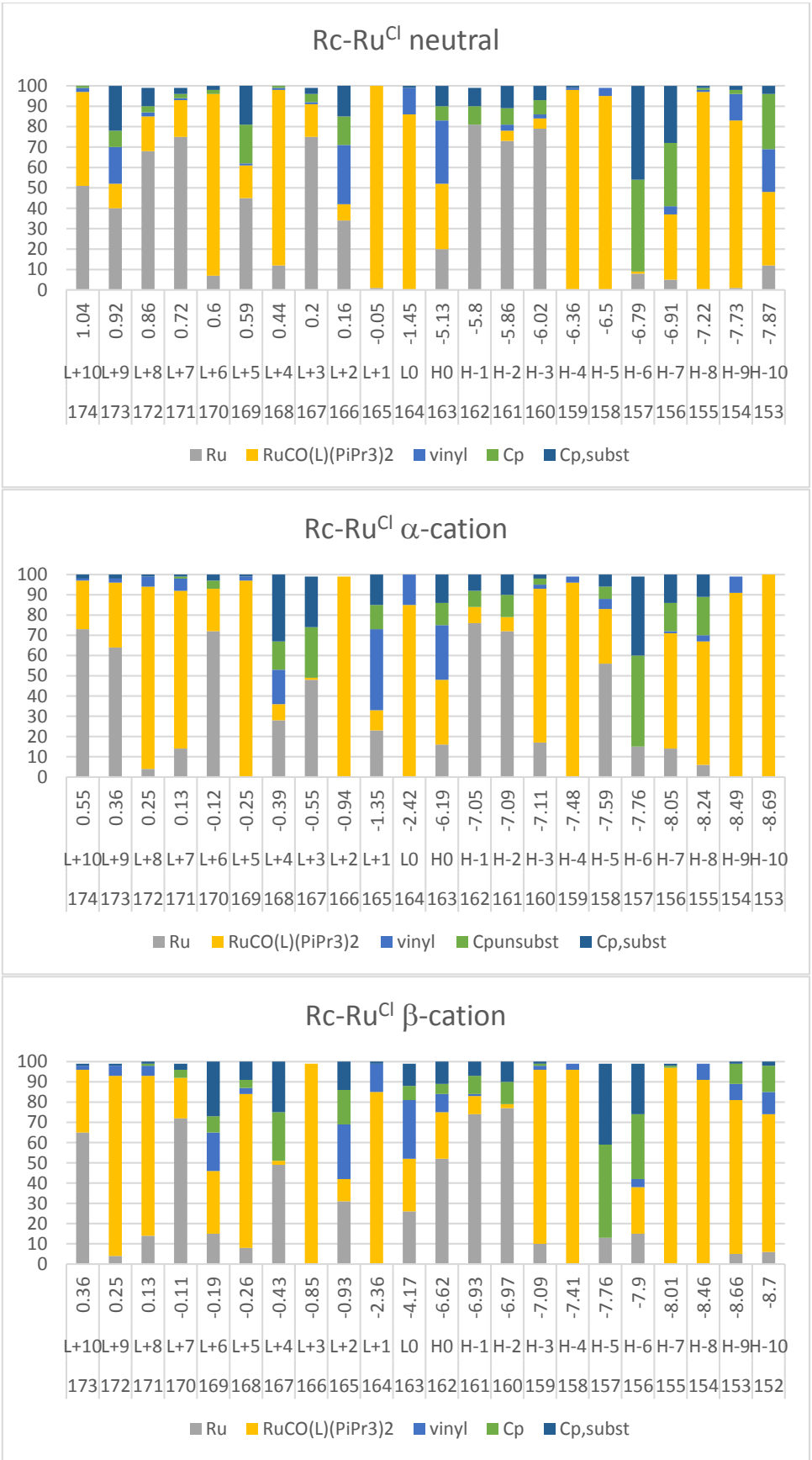

Figure S54: Fragment contributions to the frontier MOs in **Rc-Ru^{Cl}** and **Rc-Ru^{Cl+}**

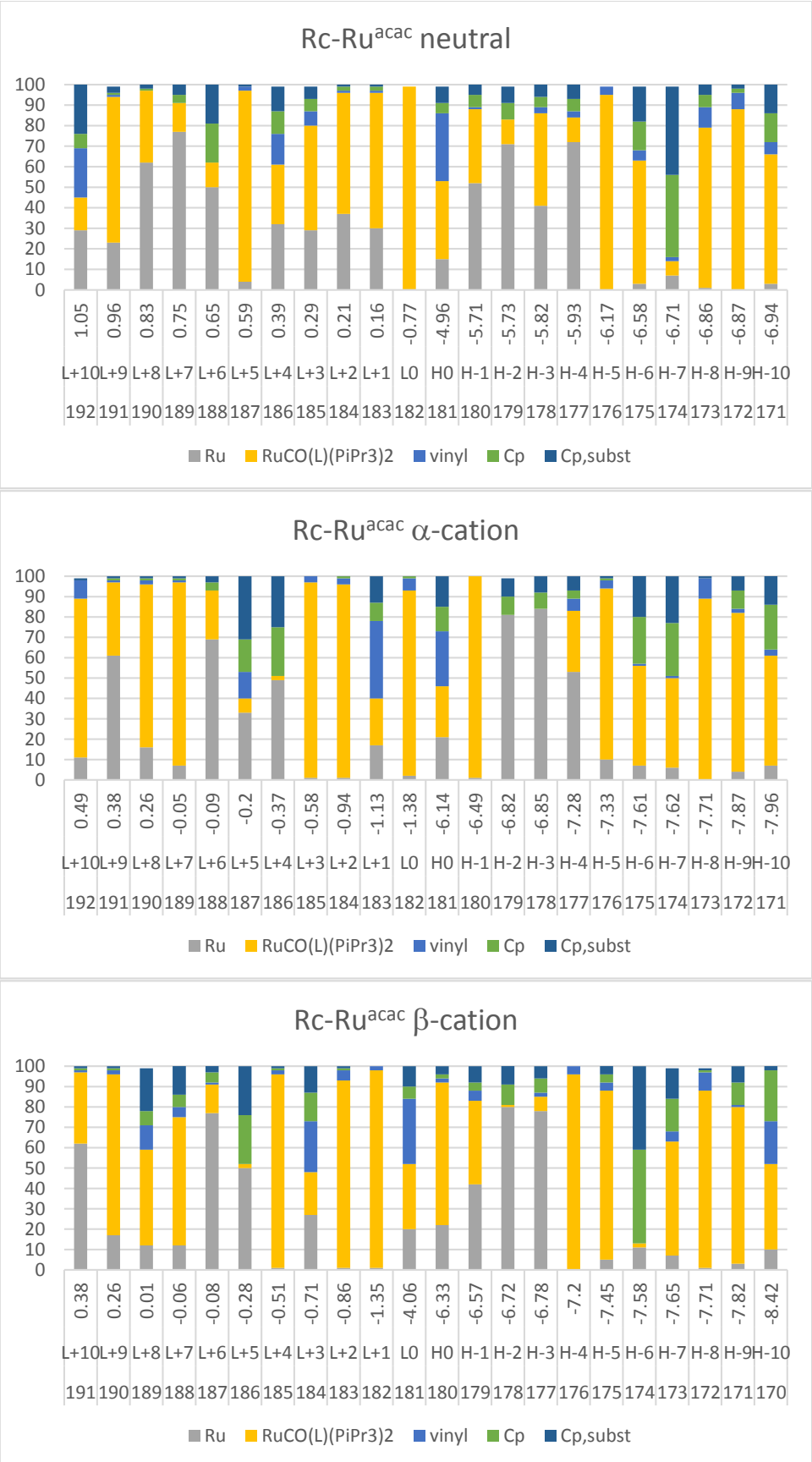

Figure S505: Fragment contributions to the frontier MOs in **Rc-Ru^{acac}** and **Rc-Ru^{acac+}**

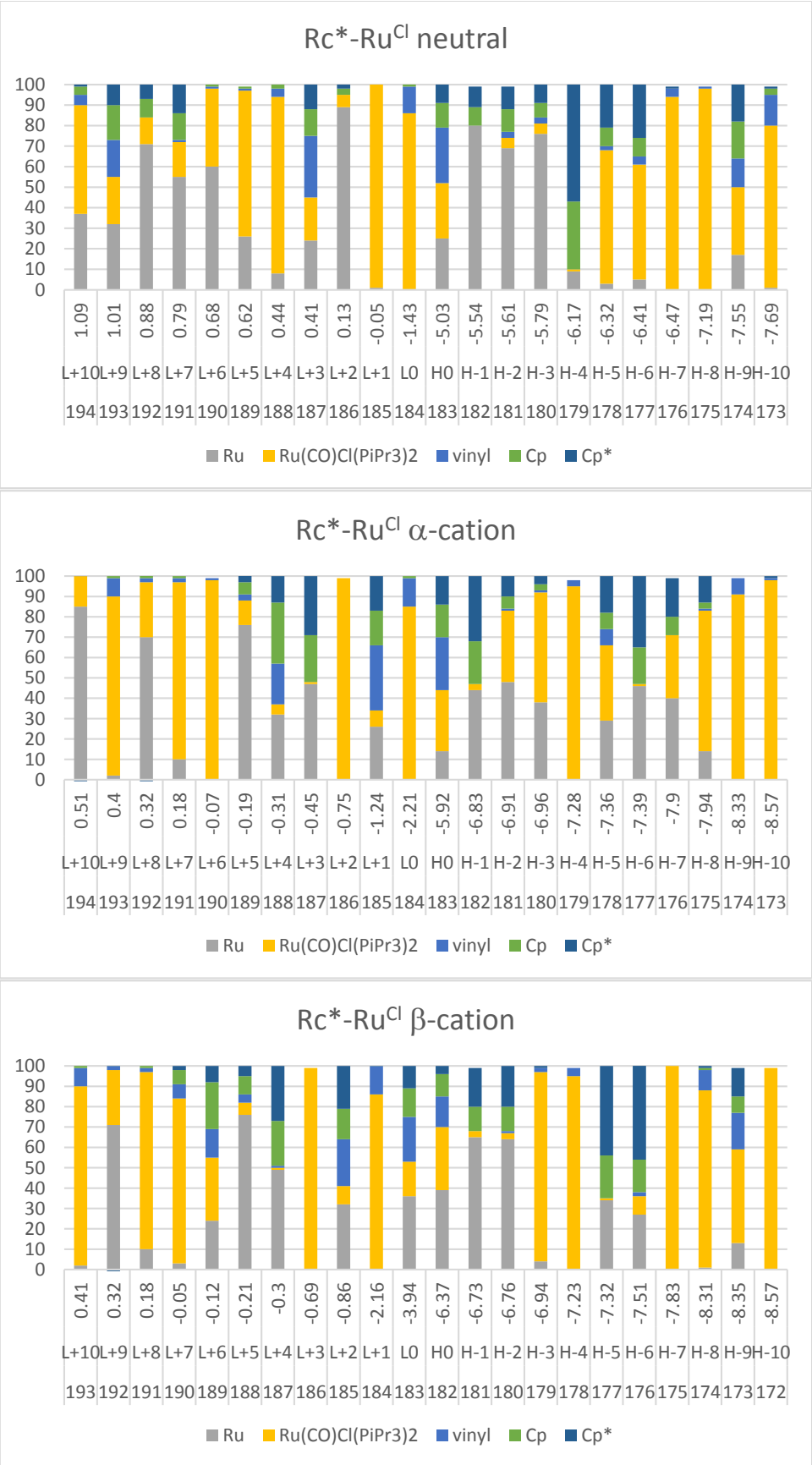

Figure S56: Fragment contributions to the frontier MOs in **Rc*-Ru^{Cl}** and **Rc*-Ru^{Cl+}**

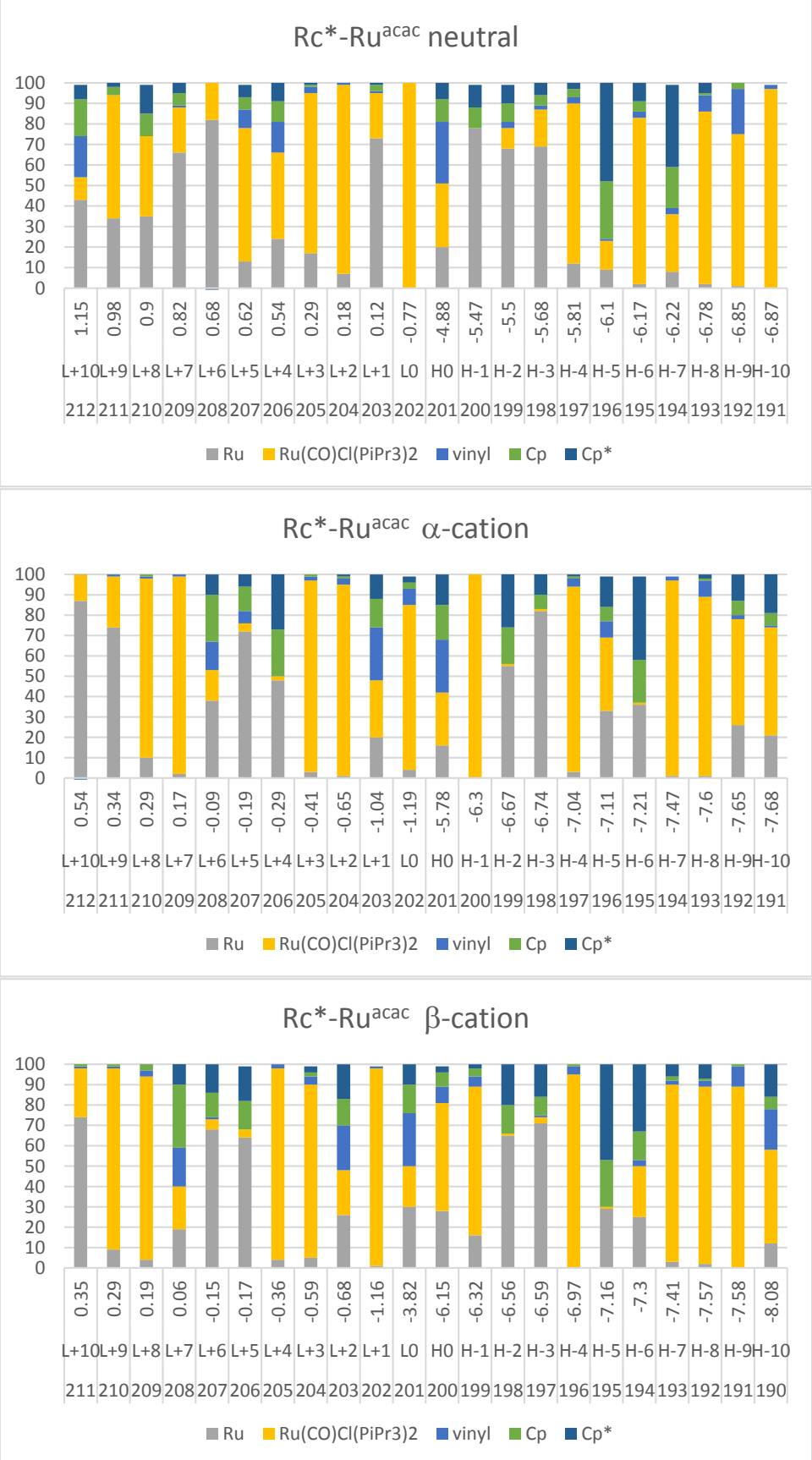

Figure S57: Fragment contributions to the frontier MOs in **Rc*-Ru^{acac}** and **Rc*-Ru$^{acac\ +}$**

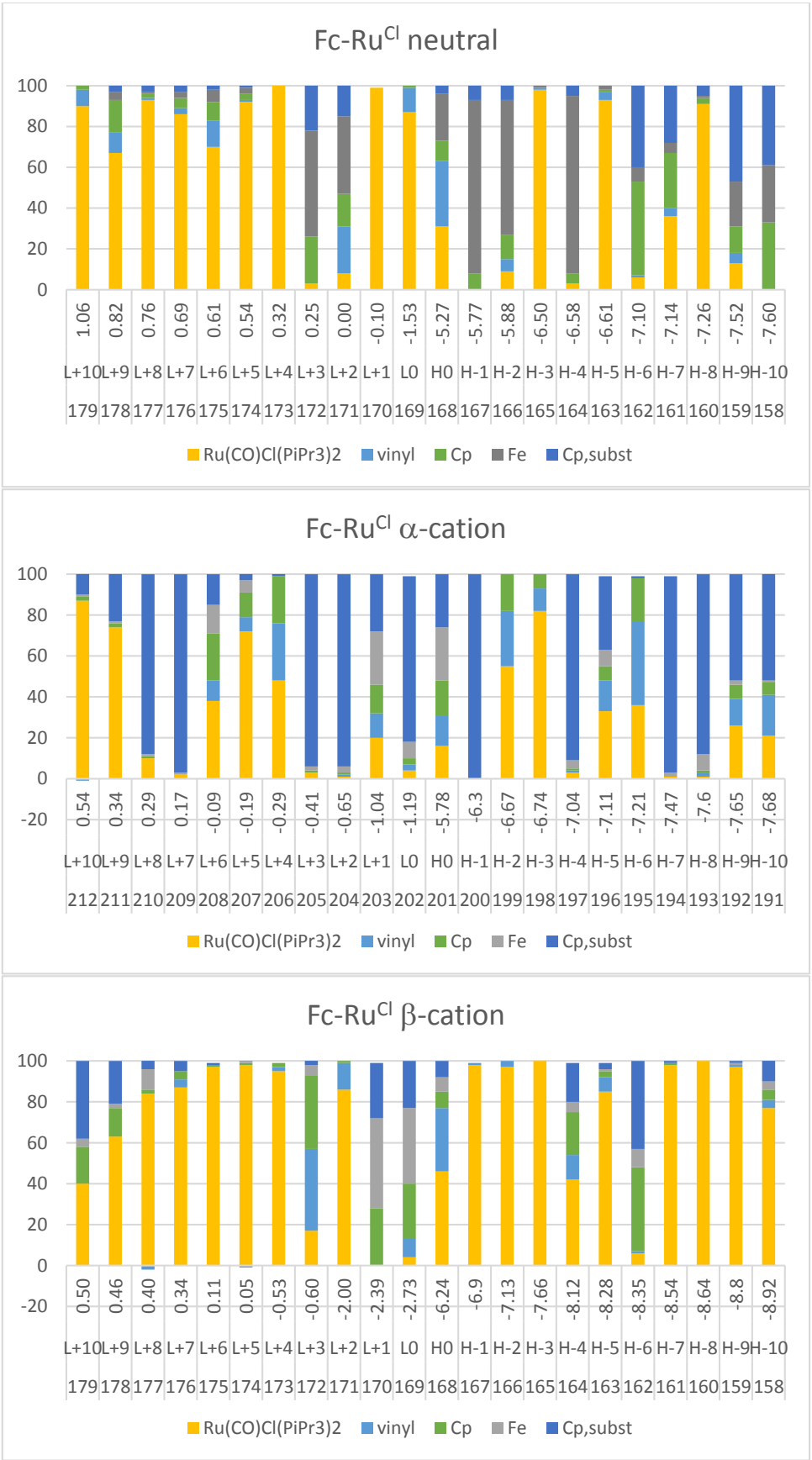

Figure S518: Fragment contributions to the frontier MOs in **Fc-Ru^{Cl}** and **Fc-Ru^{Cl+}**

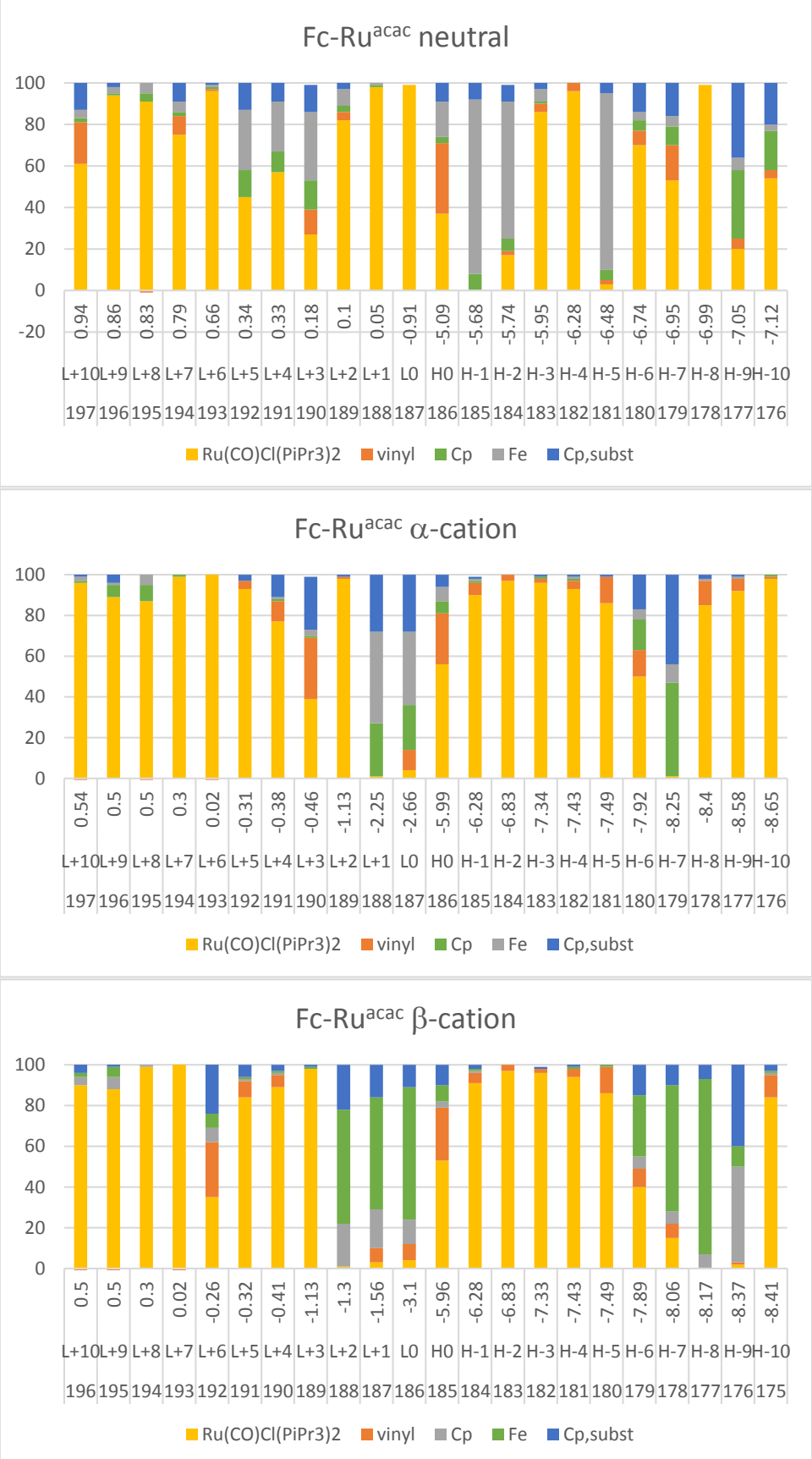

Figure S59: Fragment contributions to the frontier MOs in **Fc-Ru^{acac}** and **Fc-Ru^{acac+}**

13. Brief Discussion of the Relation between the Shape of an IVCT Band and the Electronic Coupling

MV compounds with electronically coupled redox sites typically exhibit an intervalence charge-transfer (IVCT) band at low energy, usually in the near infrared. Analysis of this band often provides information on the strength of the electronic interaction and the degree of ground state delocalization between the redox sites. In particular, it allows to distinguish between MV systems of Class II[11] with inherently different electron densities and structure parameters at the two conjoined redox sites and strongly coupled MV systems of Class III, where both redox sites are electronically and structurally identical. One criterion is the IVCT band width at half height, $\Delta\tilde{\nu}_{1/2}$. According to Mulliken-Hush theory, $\Delta\tilde{\nu}_{1/2}$ of a Class II system is larger or equal to the high-temperature limit as defined in equation 1,[12] while $\Delta\tilde{\nu}_{1/2}$ for a Class III system is appreciably smaller.[13-15] In equation 1, $\tilde{\nu}_{max}$ denotes the energy at the band maximum.

$$\Delta\tilde{\nu}_{1/2,theo} = \sqrt{2310\ \tilde{\nu}_{max}} \qquad \text{(eq. 1)}$$

$$\Gamma = 1 - \frac{\Delta\tilde{\nu}_{1/2,exp}}{\Delta\tilde{\nu}_{1/2,theo}} \qquad \text{(eq. 2)}$$

A more refined version of that relation utilizes the parameter Γ defined in equation 2, which is based on the ratio between the experimental and theoretical band widths. Thus, Γ assumes a value of close to zero for valence-localized MV systems of Class I and very weakly coupled MV systems at the Class I/II borderline, of $0 < \Gamma < 0.5$ for MV systems of Class II, of 0.5 for MV systems at the Class II/III borderline, and of >0.5 for Class III systems.[15] Another criterion that can be used to distinguish between MV systems of Class II or III is the extent of solvatochromism of the IVCT band. In the case of a Class II system, the underlying excitation is accompanied by a shift of charge density from the redox site with the higher electron density to the electron-deficient one. A solvent of higher polarity and higher ε_{DK} will stabilize the more polar state and therefore influence the energy of the IVCT band as opposed to a Class III system, where this transition involves hardly any charge-transfer.

14. Solvatochromism of the IVCT Band

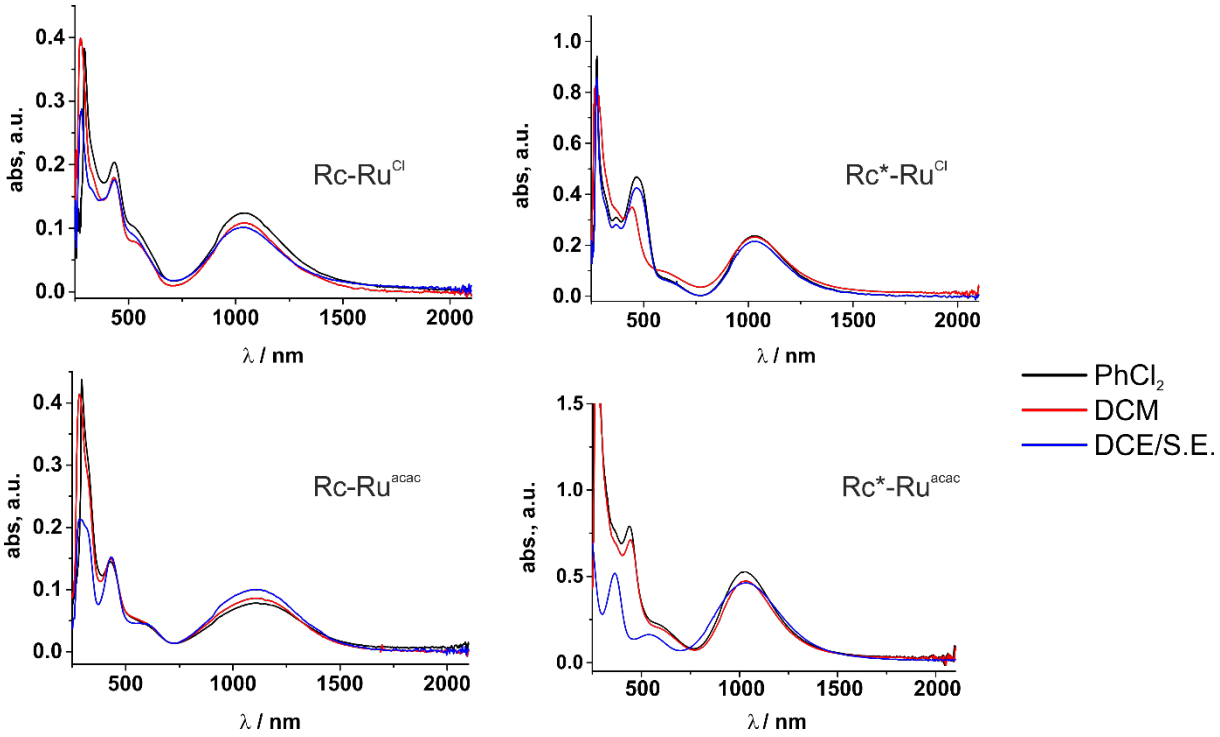

Figure S60: Solvatochromism study of **Rc-Ru^{Cl+}**, **Rc-Ru^{acac+}**, **Rc*-Ru^{Cl+}** and **Rc*-Ru^{acac+}** in *ortho*-dichlorobenzene, dichloromethane and dichloroethane with supporting electrolyte (Bu_4NPF_6).

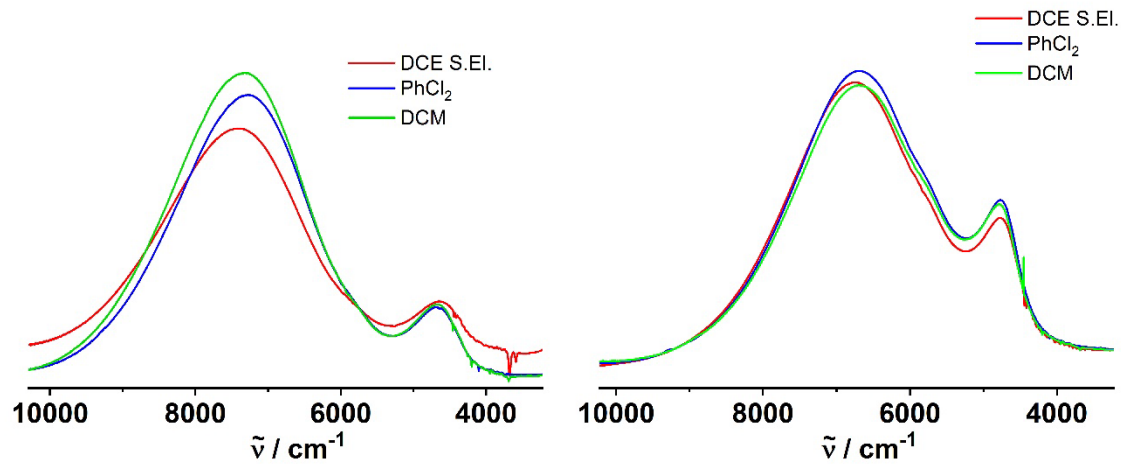

Figure S61: Slight negative solvatochromism found on **Fc-Ru^{Cl}** (left) and **Fc-Ru^{acac}** (right).

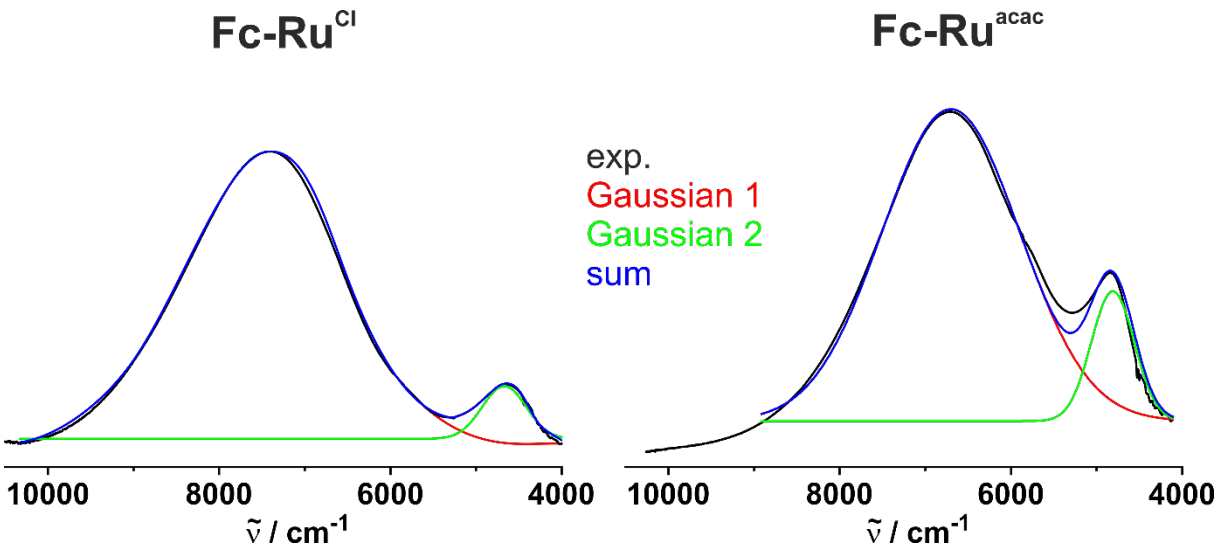

Figure S522: Deconvolution of the NIR bands of the complexes **Fc-Ru^{Cl}** and **Fc-Ru^{acac}** fitted with two Gaussian shaped lines.

15. References

1. Krejcik, M.; Danek, M.; Hartl, F. Simple construction of an infrared optically transparent thin-layer cell: Applications to the redox reactions of ferrocene, $Mn_2(CO)_{10}$ and $Mn(CO)_3$(3,5-di-t-butyl-catecholate)$^-$. *J. Electroanal. Chem.* **1991**, *317*, 179-187.
2. Stoll, S.; Schweiger, A. EasySpin, a comprehensive software package for spectral simulation and analysis in EPR. *J. Magn. Res.* **2006**, *178*, 42-55.
3. Frisch, M. J.; Trucks, G.; Schlegel, H. B.; Scuseria, G. E.; Robb, M. A.; Cheeseman, J. R.; Scalmani, G.; Barone, V.; Mennucci, B.; Petersson, G. A.; Nakatsuji, H.; Caricato, M.; Li, X.; Hratchian, H. P.; Izmaylov, A. F.; Blonio, J.; Zheng, G.; Sonnenberg, J. L.; Hada, M.; Ehara, M.; Toyota, K.; Fukuda, R.; Hasegawa, J.; Ishida, M.; Nakajima, T.; Honda, Y.; Kitao, O.; Nakai, H.; Vreven, T.; Jr., J. A. M.; Peralta, J. E.; Ogliaro, F.; Bearpark, M.; Heyd, J. J.; Brothers, E.; Kudin, K. N.; Staroverov, V. N.; Keith, T.; Kobayashi, R.; Normand, J.; Raghavachari, K.; Rendell, A.; Burant, J. C.; Iyengar, S. S.; Tomasi, J.; Cossi, M.; Rega, N.; Millam, J. M.; Klene, M.; Knox, J. E.; Cross, J. B.; Bakken, V.; Adamo, C.; Jaramillo, J.; Gomperts, R.; Stratmann, R. E.; Yazyev, O.; Austin, A. J.; Cammi, R.; Pomelli, C.; Ochterski, J. W.; Martin, R. L.; Morokuma, K.; Zakrzewski, V. G.; Voth, G. A.; Salvador, P.; Dannenberg, J. J.; Dapprich, S.; Daniels, A. D.; Farkas, Ö.; Foresman, J. B.; Ortiz, J. V.; Cioslowski, J.; Fox, D. J. *Gaussian 09, Revision B.01*, Gaussian Inc., Wallingford, CT, 2010.
4. Andrae, D.; Haeussermann, U.; Dolg, M.; Stoll, H.; Preuss, H. Energy-adjusted ab initio pseudopotentials for the second and third row transition elements. *Theor. Chim. Acta* **1990**, *77*, 123-141.
5. Perdew, J. P.; Burke, K.; Enzerhof, M. Generalized Gradient Approximation Made Simple. *Phys. Rev. Lett.* **1996**, *77*, 3865-3868.
6. Wachters, A. J. H. Gaussian Basis Set for Molecular Wavefunctions Containing Third-Row Atoms. *J. Chem. Phys.* **1970**, *52*, 1033-1036.
7. Cossi, M.; Rega, N.; Scalmani, G.; Barone, V. Energies, structures, and electronic properties of molecules in solution with the C-PCM solvation model. *J. Comput. Chem.* **2003**, *24*, 669-681.
8. Mercier, A.; Yeo, W. C.; Chou, J.; Chaudhuri, P. D.; Bernardinelli, G.; Kündig, E. P. Synthesis of highly enantiomerically enriched planar chiral ruthenium complexes viaPd-catalysed asymmetric hydrogenolysis. *Chem. Commun.* **2009**, 5227-5229.
9. Malachowski, M. R.; Grau, M. F.; Thomas, J. M.; Rheingold, A. L.; Moore, C. E. Heterometallic complexes derived from ruthenocene-functionalized dipyrromethenes. *Inorg. Chim. Acta* **2010**, *364*, 132-137.
10. Sato, M.; Iwai, A.; Watanabe, M. Synthesis and Redox Behavior of Ruthenium(II) 2,3,4,5-Tetramethylruthenocenylacetylide and Related Complexes. Formation of μ-[(Cyclopentadienylidene)-ethylidene]diruthenium Complexes Containing a Strong Metal-Metal Interaction. *Organometallics* **1999**, *18*, 3208-3219.
11. Robin, M. B.; Day, P. Mixed Valence Chemistry - A survey and Classification. *Adv. Inorg. Chem. Radiochem.* **1967**, *10*, 247-422.
12. Hush, N. S. Intervalence Charge Transfer Absorption. Part 2. Theoretical Considerations and Spectroscopic Data. *Prog. Inorg. Chem.* **1967**, *8*, 391-444.
13. Sutin, N. Nuclear, electronic, and frequency factors in electron transfer reactions. *Acc. Chem. Res.* **1982**, *15*, 275-282.
14. Sutin, N. Theory of electron transfer reactions: insights and hindsights. *Prog. Inorg. Chem.* **1983**, *30*, 441-498.
15. Brunschwig, B.; Creutz, C.; Sutin, N. Optical transitions of symmetrical mixed-valence systems in the Class II-III transition regime. *Chem. Soc. Rev.* **2002**, *31*, 168-184.

4. Summary

Mixed-valent compounds, i.e. complexes, where two identical or similar redox-active moieties are present in different oxidation states, are very interesting models to study electron transfer processes. An issue of pivotal importance is, how the unpaired spin and the surplus charge are distributed over the two redox sites in the ground state of such a molecule. In the present thesis, I prepared and investigated series of model complexes that combine a redox-active vinylruthenium moiety and a likewise redox-active ferrocene, ruthenocene or triarylamine entity. In all cases, the intrinsic redox potentials of the two chemically different redox-active constituents are similar and can be selectively and individually tuned by the choice of appropriate coligands or substituents at each of these sites. By employing these model complexes, I was able to explore the borderline regimes between strongly coupled mixed-valent systems of Class II, almost delocalized systems in the Class II/III borderline regime, and intrinsically delocalized mixed-valent systems of Class III or between coupled mixed-valent systems of Class II and equilibrating redox isomers (valence tautomers), which differ with respect to how the charge and spin distribute over the different redox sites.

To this end, we attached a series of β-ketoenolato ligands with different electron-donating capabilities to a five-coordinated ferrocene vinylruthenium complex (Fig. 4.1).

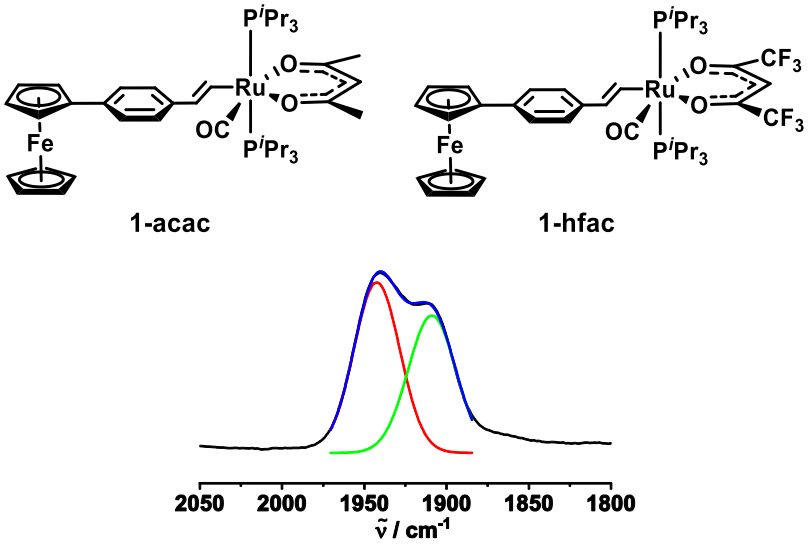

Fig. 4.1: Ferrocenyl vinylruthenium conjugates with various β-ketoenolato ligands.

In doing so, we unearthed examples of valence tautomerism in mixed-valent heterobimetallic complexes. Attachment of the trifluoromethyl-substituted hfac ligand (Fig. 4.1, right) led to charge and spin located at the ferrocenyl site. Introducing the acac ligand (Fig. 4.1, left) produced two coexisting valence tautomers of their associated radical cations, where the spin and charge are either located at the ferrocenium or at the

vinylruthenium site. The phenomenon of valence tautomerism in mixed-valent systems with different redox sites thus relies on the combination of a moderate orbital energy difference and weak electronic communication. This results in an energy barrier for thermal electron transfer of sufficient height to observe both isomers separately. With this system we were able to answer the question, how the solvent polarity, counter ions and temperature affect the valence tautomer equilibrium. By increasing the solvent polarity, the ratio between the two redox isomers was not affected, however the degree of charge localization increased which was observed as an increase of the energy difference between the two carbonyl stretching frequencies (Fig. 6.4).

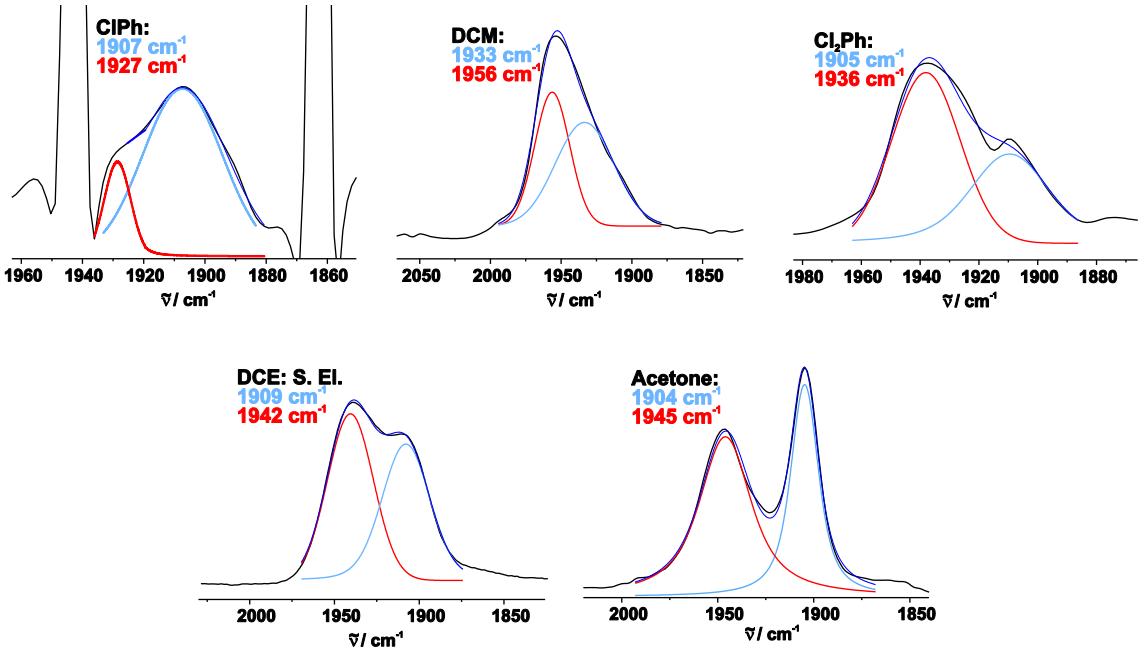

Fig. 4.2: Ru(CO) vibrational spectra of **1-acac** in various solvents.

Counter ions also have a distinct effect on the localization of charge as they differ in their ability to stabilize charges through hydrogen bonding, π-interactions and ion-pairing with the associated radical cation. The temperature has the most prominent influence on the equilibrium. The relative concentrations of both isomers are temperature dependent and at low temperatures, the valence tautomer with an oxidized ferrocenium entity is stabilized, as seen from temperature-dependent EPR and Mößbauer spectra (Fig. 4.3).

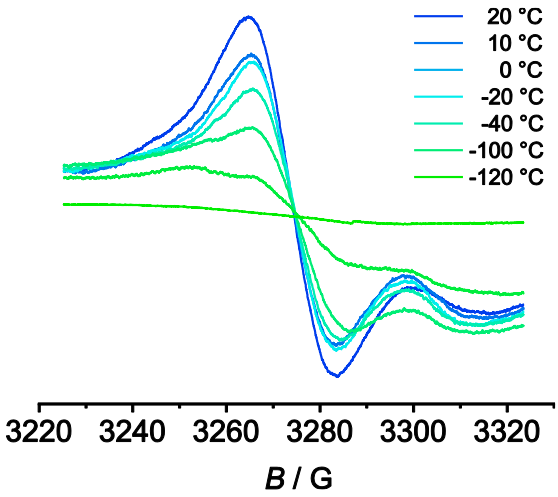

Fig. 4.3: EPR spectrum of **1-acac** at various temperatures, indicating a temperature-dependent valence tautomeric equilibrium.

IR spectroelectrochemistry revealed a two-band pattern of the radical cations in the CO stretching frequency region complying with the coexistence of both isomers (Fig. 4.1, bottom). Further, the electronic band in the near infrared (NIR) region revealed some intervalence charge-transfer character between the two different redox-active moieties with sizable contributions from the nominal bridge.

We next probed how an intrinsically delocalized mixed-valent system with two dislike redox-active subunits responds to perturbations imposed by selectively changing the electron-density and redox potential of one of those sites. This series of compounds was derived from a vinylruthenium triarylamine conjugate with two anisyl rings at the triarylamine subunit (Fig. 4.4). The radical cation of this complex had been previously identified as a fully delocalized mixed-valent system of Class III by virtue of the EPR hyperfine splittings to the ^{31}P nuclei of the phosphine ligands at the vinylruthenium and the ^{14}N nucleus at the triarylamine site as well as by the characteristics of the prominent charge-resonance NIR band. This principal motif was kept but the electron distribution modified by replacing the electron-donating methoxy-substituents by less strongly donating methyl- or electron-withdrawing formyl-, carboxymethyl-, or acetyl-substituents.

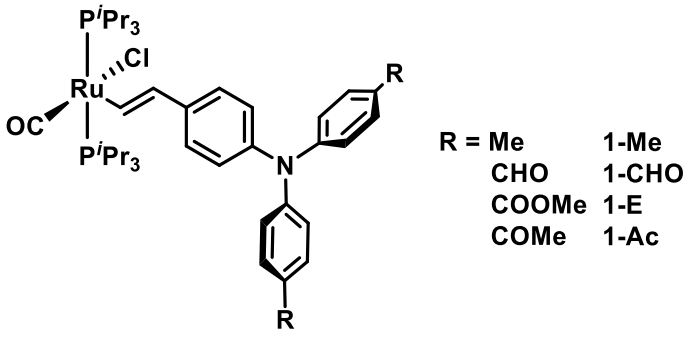

Fig. 4.4: Triarylamine vinylruthenium conjugates with varying electron withdrawing groups at the 4-position of the aryls.

With increasing electron-withdrawing capability, the charge and spin of these systems are increasingly shifted towards the vinylruthenium site. Yet, the electronic coupling remains rather large as the bridge is an integer part of both redox centers. As a consequence, a change of substituents affects both oxidation potentials and an intense electronic NIR absorption is found in the NIR. The features of this NIR band are quite remarkable. The halfwidth at the high-energy side is broader than at the low-energy side, resulting in a skewing of this band (Fig. 4.5).

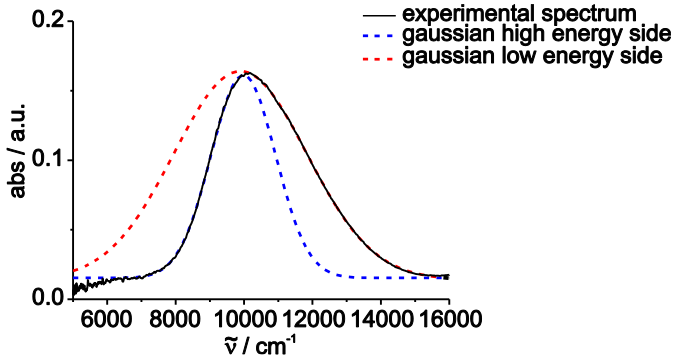

Fig. 4.5: NIR spectrum of the triarylamine vinylruthenium conjugate **1-CHO**$^+$ at room temperature, revealing an asymmetric band shape, fitted by two Gaussians.

This phenomenon is called “low-energy cutoff” and is only rarely observed. The origin of this phenomenon could also be identified by temperature-dependent NIR spectroscopy as caused by a vibronic coupling of the underlying electronic transition to a symmetric vibrational mode of the bridge.

According to the ROBIN and DAY classification system, these complexes can be assigned to the borderline between Class II and Class III. That means that the electronic coupling lies between the partially delocalized (Class II) and completely delocalized limits (Class III). It was therefore possible to access this borderline regime from the limiting case of complete charge delocalization by selectively perturbing one of the conjoined redox sites. I could also demonstrate that mixed-valent systems with non-identical redox sites of this class behave in the very same way as mixed-valent systems with chemically identical ones.

The experimental data were supported by quantum chemical calculations using the density functional theory (DFT) and its time-dependent extension (TD-DFT). This method allows us to first geometrically optimize the molecular structure in a chosen solvent and then to graphically represent the molecular frontier orbitals (MOs), e.g. the highest occupied MO (HOMO) or the spin distribution. Atomic resolution of charge and spin density let us assign their distributions in the complex and TD-DFT helps to identify the nature of the electronic absorptions in the UV/vis/NIR region of the spectrum. Hereby, we were able to assign the NIR band of the radical cations to a π–π^* transition with some

intervalence charge-transfer character. This charge-transfer character was experimentally verified by the small negative solvatochromism, resulting in a blueshift of the IVCT band in more polar solvents (Fig. 4.6).

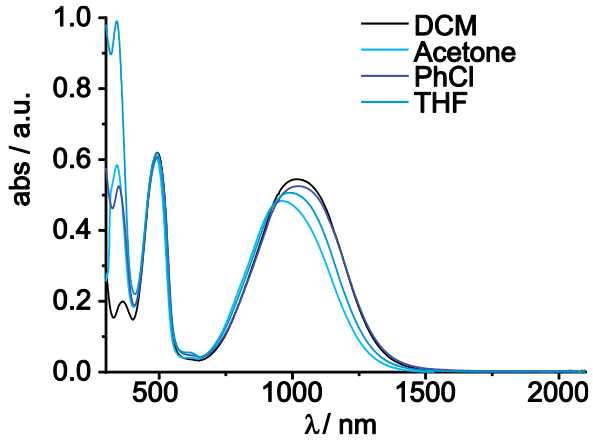

Fig. 4.6: Negative solvatochromism of the NIR band in the mixed-valent triarylamine vinylruthenium conjugate **1-CHO**$^{+}$.

The last project to be discussed in this thesis was the substitution of ferrocene with its heavier homologue ruthenocene in a ruthenocene vinylruthenium complex. Here, the electron density of each individual redox site was influenced by the attachment of an acetylacetonato ligand to the vinylruthenium moiety or by substitution of one cyclopentadienyl (Cp) ligand by a permethylated cyclopentadienyl ligand (Cp*) at the ruthenocenyl site (Fig. 4.7).

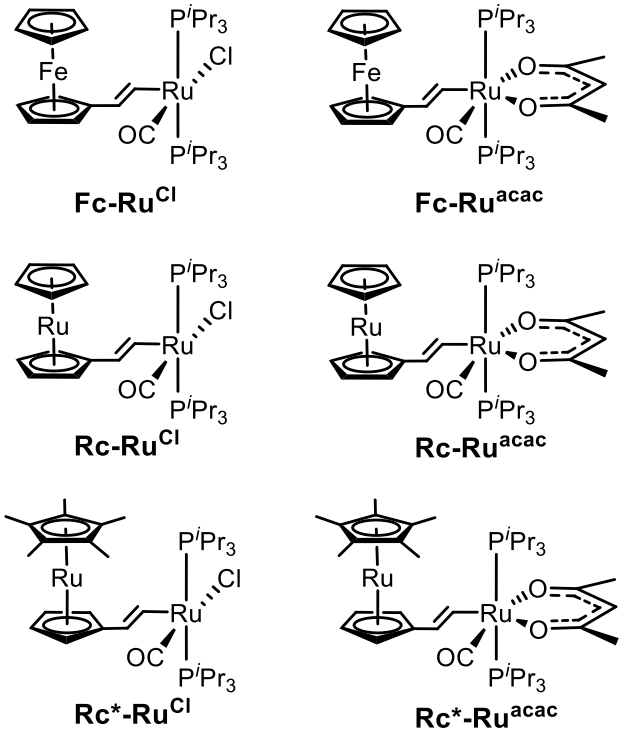

Fig. 4.7: Ferrocene, ruthenocene and pentamethylruthenocene vinylruthenium complexes with a chloro or acetylacetonato ligand.

The radical cations of the corresponding ferrocene vinylruthenium complexes exhibit a Class II behavior, where the charge mainly resides on the ferrocenyl moiety.[169] The ruthenocene homologues behave rather differently. The IR spectroelectrochemistry as well as the quantum chemical calculations rank the radical cations of the ruthenocene vinylruthenium complexes among the delocalized Class III systems. The vibrational shifts of the carbonyl ligand during the first and the second oxidation can be set into relation, leading to a charge density distribution of nearly 50:50 for all ruthenocene derivatives. The derivatives differ only slightly due to their different electron densities.

Table 6: : ν(CO) Values of the metallocene-vinylruthenium complexes in their various oxidation states.

	$\nu(CO)^{exp}$ [cm^{-1}]			$\Delta\nu(CO)$ [cm^{-1}]			$\frac{\Delta\nu(CO)^{+/0}}{\Delta\nu(CO)^{2+/0}}$
	n = 0	n = 1	n = 2	+/0	2+/+	2+/0	
Fc-Ru^{Cl}	1908	1932	2004	24	72	96	0.25
Fc-Ru^{acac}	1893	1921	1966	28	45	73	0.38
Rc-Ru^{Cl}	1908	1952	2004	44	52	96	0.46
Rc-Ru^{acac}	1893	1945	1987	52	42	94	0.55
Rc*-Ru^{Cl}	1908	1940	1999	32	59	91	0.35
Rc*-Ru^{acac}	1893	1932	1981	39	49	88	0.44

The non-solvatochromic behavior of the NIR band indicates no or very little charge transfer. Again, we saw that a smaller difference of the intrinsic redox potential of the two redox-active subunits increases charge delocalization in the mixed-valent state of their conjugates.

EPR spectroscopy on the monooxidized compounds revealed isotropic signals with *g*-values of 2.060 to 2.069 at room temperature. In contrast, the ferrocene-derivatives are only EPR active at very low temperatures and reveal axial signals for the ferrocenium-based spin (Fig. 4.8).

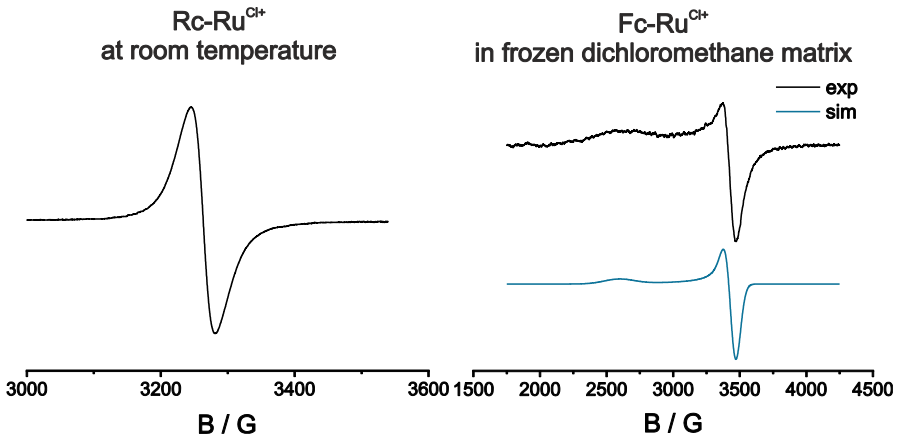

Fig. 4.8: EPR spectra of the mixed-valent ruthenocene and ferrocene vinylruthenium complexes at room temperature and in frozen dichloromethane matrix.

TD-DFT calculated UV/vis/NIR spectra of the neutral and oxidized species fit perfectly to the experimental data and calculated spin density distributions leave no doubt of complete charge and spin delocalization despite the presence of two chemically different redox sites with the same central atom. Also, for complex **Rc-Ru^{acac}** a skewing of the NIR band was observed like in the triarylamine vinylruthenium congeners. Only the ruthenocene vinylruthenium complex with an acetylacetonato ligand revealed a temperature dependent “low-energy cutoff”, again marking the transition between Class III and borderline Class II/III.

In summary, we were able to unearth examples ranging from charge-localized over charge- and spin-delocalized systems to the occurrence of valence tautomerism in asymmetric mixed-valent compounds. The latter was realized by manipulating the intrinsic redox potentials of the two interacting redox-active constituents, i.e. changing the ground state energy difference ΔG, and the energy barrier ΔG^* between the two minima resulting from an electronic coupling of two diabatic potential hypersurfaces (Fig. 4.9).

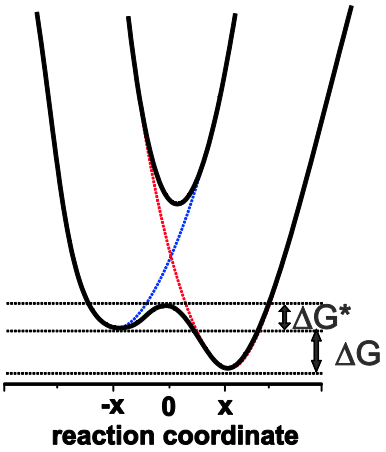

Fig. 4.9: Two diabatic potentials (red and blue lines) and adiabatic potential hypersurfaces for mixed-valent systems with two chemically different redox sites.

5. Outlook

We have shown that slight electronic decoupling and an intrinsic difference in the oxidation potential of the two conjugated redox entities can lead to valence tautomerism. Our system of 6-coordinated ferrocene vinylruthenium complexes could be further enlarged by 1,1'-substitution of the ferrocene or, being inspired by the work of LAPINTE, using a biferrocene. A biferrocene motif could be used in order to generate a possible valence tautomeric couple (Fig. 5.1), which would then lead to up to four coexisting valence tautomers.

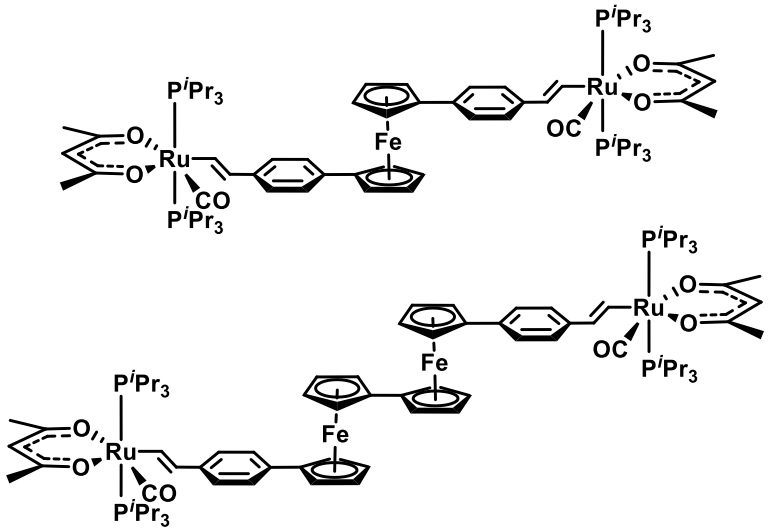

Fig. 5.1: Doubled structure of the valence tautomer system.

In order to enlarge the library of valence tautomeric mixed-valent complexes, we already synthesized a triarylamine vinylruthenium conjugate featuring a biphenyl linkage (Fig. 5.2 R = OMe). IR spectroscopy on the radical cation revealed two coexisting valence tautomers (Fig. 5.2, right).

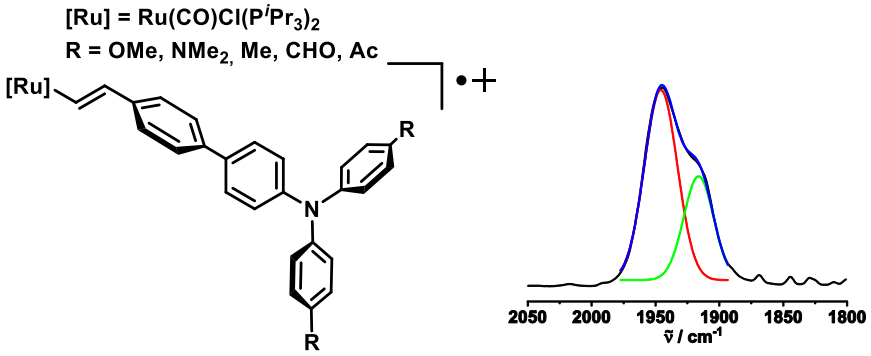

Fig. 5.2: Enlarged π-system on a triarylamine vinylruthenium complex inducing valence tautomerism.

This system could be analyzed in detail in terms of solvent equilibrium dependence, temperature dependence and counter ion effects. Further, one could substitute the

methoxy group by electron withdrawing (e.g. acetyl groups) or more electron donating groups (e.g. dimethylamino groups). Thereby, the valence tautomeric equilibrium could be shifted to one side or the other or even into the weakly coupled limit of Class II with dominant valence localization of just one site.

WALTHER POLIT synthesized a *meta*-substituted triarylamine (Fig. 5.3, left R = OMe) and determined its charge and spin confinement. Due to the decreased electronic coupling compared to its *para*-substituted parent complex, the charge and spin is rather heavily localized on the triarylamine site.[160] This complex could be six-coordinated with a library of β-ketoenolato ligands in order to increase the electron density at the vinylruthenium moiety. Further, the electronic properties of the triarylamine could be modified using electron-donating or -accepting substituents. The resulting complexes are then to be analyzed in order to determine the existence of valence tautomerism or how a change in ground state energies influences the charge and spin (de)localization.

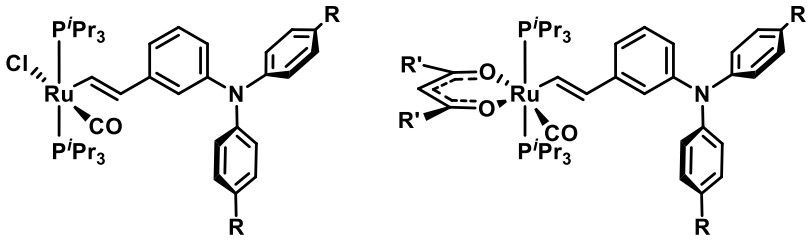

R = OMe, NMe_2, Me, CHO, Ac
R' = Me, CF_3, ^{t}Bu

Fig. 5.3: Asymmetric triarylamine vinylruthenium complexes with *meta*-substitution.

6. Zusammenfassung

Gemischtvalente Verbindungen, also Komplexe mit zwei identischen oder ähnlichen redoxaktiven Gruppen, die in unterschiedlichen Oxidationsstufen vorliegen, sind interessante Modellsysteme für das Studium von Elektronentransferprozessen. Daraus ergibt sich ein äußerst wichtiges Thema, wie sich der resultierende Spin und die Ladung über die zwei Redoxzentren im Grundzustand verteilt. In dieser Arbeit habe ich Modelverbindungen dargestellt und untersucht, welche eine redoxaktive Vinylrutheniumgruppe und eine genauso redoxaktive Ferrocen-, Ruthenocen- oder Triarylamineinheit beinhalten. In allen Fällen sind die intrinsischen Redoxpotentiale der zwei chemisch unterschiedlichen Einheiten ähnlich und können selektiv und individuell, durch die Wahl geeigneter Liganden, verändert werden. Anhand dieser Modelverbindungen war es mir möglich den Grenzfall zu untersuchen, welcher zwischen elektronisch stark gekoppelten Systemen der Klasse II, nahezu delokalisierten Systemen der Übergangsklasse II/III und intrinisch delokalisierten gemischtvalenten Systemen der Klasse III sowie der im Gleichgewicht vorliegenden Redoxisomere (Valenztautomere) entsteht. Diese Valenztautomere unterscheiden sich in der Hinsicht wie sich ihre Ladungs- und Spindichte über die zwei unterschiedlichen Redoxzentren verteilt.

Zu diesem Zweck haben wir eine Serie an β-Ketoenolatoliganden mit unterschiedlich stark elektronendonierendem Charakter an fünffachkoordinierte Ferrocenvinylruthenium Komplexe gebunden (Beispiele in Fig. 4.1).

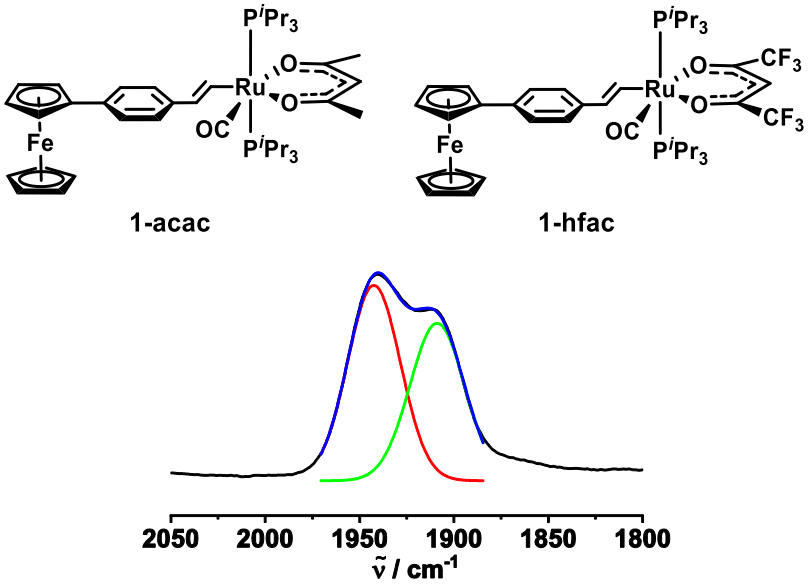

Fig. 6.1: Ferrocenvinylruthenium Konjugate mit unterschiedlichen β-Ketoenolatoliganden.

Hierdurch konnten wir Beispiele von Valenztautomerie in gemischtvalenten, heterobimetallischen Komplexen darstellen. Die Anbindung des trifluormethyl-substituierten hfac Liganden (Fig. 4.1, rechts) am Radikalkation führte zu Ladungs- und Spindichte, welche hauptsächlich an der Ferroceneinheit lokalisiert vorlagen. Der acac Ligand (Fig. 4.1 links) war hingegen dafür verantwortlich, dass sich die Ladung und der Spin in zwei Tautomeren manifestierte, welche sich durch den Ort ihrer Ladungs- und Spindichte unterschieden: Entweder war die Ladung und der Spin des Radikalkations auf der Ferroceneinheit lokalisiert oder am Vinylruthenium Part.

Das Phänomen der Valenztautomerie in gemischtvalenten Systemen mit unterschiedlichen Redoxeinheiten bedingt also eine Kombination aus moderater Orbitalenergiedifferenz mit der Erniedrigung der elektronischen Kopplung. Dies resultiert in einer Aktivierungsbarriere für den thermischen Elektronentransfer, welche genügend groß ist, jedoch bei Raumtemperatur überwunden werden kann.

Mit diesem System konnten wir auch die Frage beantworten, welchen Einfluss Lösungsmittelpolarität, Gegenion und Temperatur auf das Valenztautomerengleichgewicht ausübt. Bei Erhöhung der Lösungsmittelpolarität ist kaum Einfluss auf das Gleichgewicht zu erkennen, jedoch auf die Lokalisierung der Ladung beider Redoxisomere. Dies wurde durch die Vergrößerung der Energiedifferenz beider Carbonylstreckschwingungen beobachtet (Fig. 6.2).

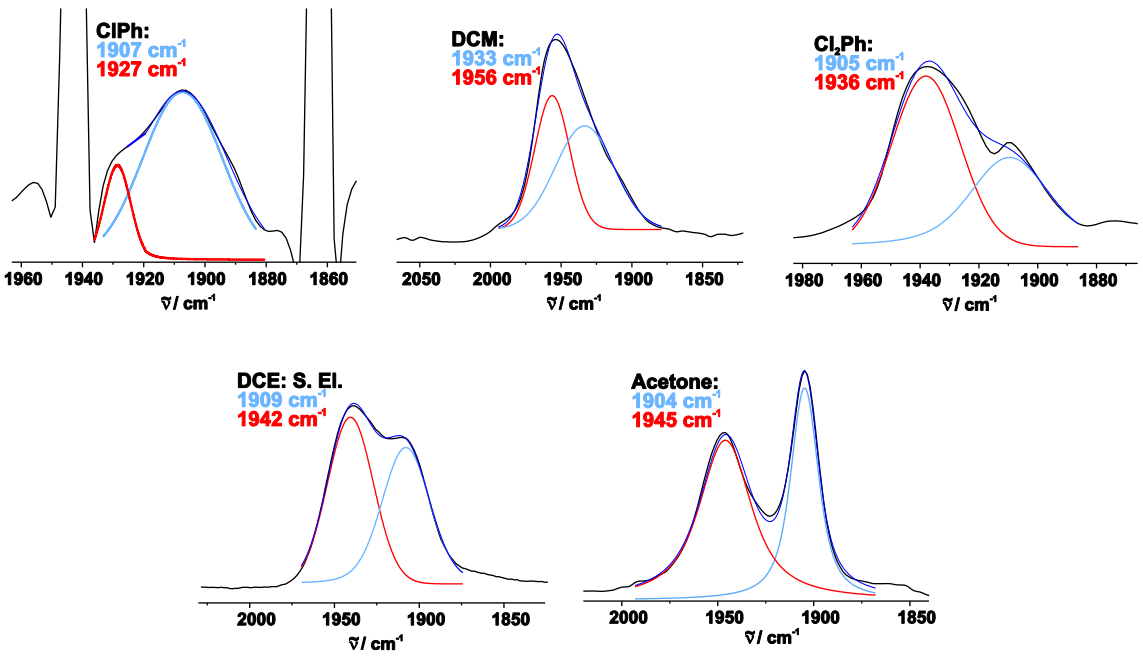

Fig. 6.2: Spektren der Ru(CO) Schwingungen des gemischtvalenten acac-Komplexes der Abbildung 6.1 in unterschiedlichen Lösungsmitteln.

Gegenionen haben einen konkreten Einfluss auf die Lokalisierung der Ladung, da sie sich in ihrer Eigenschaft der Ladungsstabilisierung als auch in deren koordinativen

Fähigkeiten unterscheiden und durch Wasserstoffbrückenbindungen, π-Wechselwirkung und Ionenpaarung sich direkt auf das Radikalraktion auswirken.
Die Temperatur hat jedoch den größten Effekt auf das Valenztautomerengleichgewicht. Die relative Konzentration der beiden Tautomere ließ sich durch eine Änderung der Temperatur beeinflussen, sodass bei tiefen Temperaturen nur noch das ferrociniumbasierte Tautomer vorlag, was durch temperaturabhängige Elektronenspinresonanz (ESR) Spektroskopie und auch Mößbauerspektroskopie nachgewiesen werden konnte (Fig. 6.3).

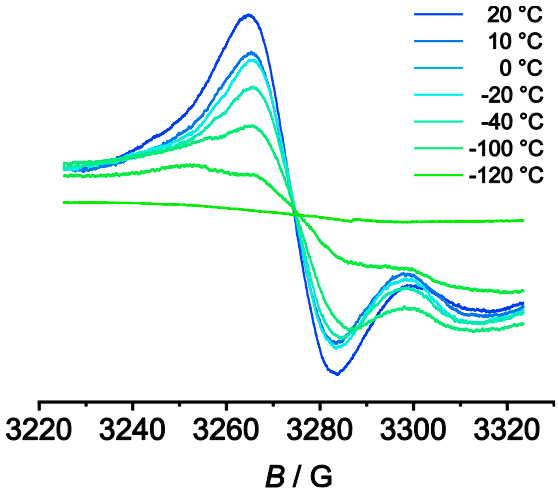

Fig. 6.3: ESR-Spektrum des gemischtvalenten acac-Komplexes in Abbildung 6.1 bei verschiedenen Temperaturen, was auf einen temperaturabhängiges Gleichgewicht der zwei Valenztautomere hindeutet.

IR Spektroskopie zeigte beim acac-Derivat ein Doppelbandenmuster für die Carbonylstreckschwingung, obwohl nur ein einziger Carbonylligand vorlag. Dies bestätigte die Koexistenz zweier Redoxtautomere (Fig. 4.1, unten), welche durch ihre Frequenz zugeordnet werden konnte. Im elektronischen Nahinfrarotspektrum (NIR) wurde eine Bande identifiziert, welche die elektronische Kopplung der zwei Redoxuntereinheiten durch einen Intervalenz-Ladungstransfer repräsentierte, wobei die Brücke einen bedeutenden Beitrag zum Ladungstransfer leistet.
Anschließend betrachteten wir, welchen Einfluss die Änderung der Redoxpotentiale und damit der Elektronendichte auf ein intrisisch delokalisiertes System mit ungleichen Redoxzentren hat. Dafür stellten wir eine Serie an Triarylaminvinylruthenium-Komplexen mit unterschiedlich stark elektronenziehenden Gruppen in der 4-Position der Arylsubstituenten dar (Fig. 4.4).

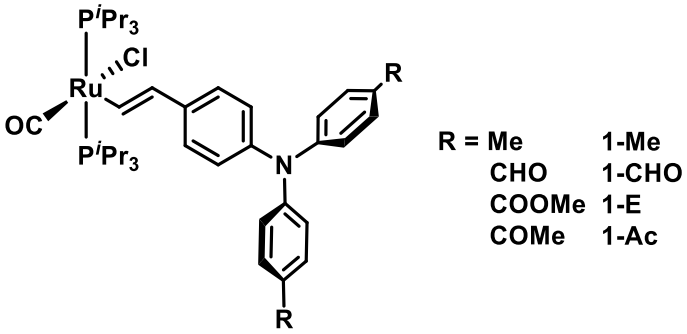

Fig. 6.4: Triarylaminvinylruthenium Konjugate mit unterschiedlichen elektronziehenden Gruppen an der 4-Position der Aryle.

Das Radikalkation dieses Komplexes wurde einst durch ESR-Spektroskopie und der deutlichen NIR Bande als vollständig delokalisiert identifiziert. Das Kernmotiv wurde beibehalten, jedoch ersetzten wir die elektronendonierenden Methoxygruppen durch entweder Methylgruppen, welche einen weniger stark donierenden Charakter haben und durch elektronziehende Formyl-, Carboxymethyl- oder Acetylsubstituenten. Mit steigender elektronenziehendem Charakter wurde die Ladung und der Spin des Radikalkations in Richtung der Vinylrutheniumeinheit verschoben. Die elektronische Kommunikation der zwei Redoxeinheiten blieb dabei aber recht hoch, da die verbindende Brücke selbst einen Teil der beiden Redoxzentren darstellte. Die gute Kopplung wurde auch durch den Einfluss der elektronenziehenden Gruppen auf beide Oxidationspotentiale deutlich, sowie durch die intensiven elektronischen Banden im nahen Infrarot der UV/vis/NIR Spektroelektrochemie. Diese Banden zeichneten sich durch eine weitere Besonderheit aus. Die Halbwertsbreite der hochenergetischen Seite der Bande war deutlich breiter als die der niederenergetischen Seite. Dies resultierte in einer Asymmetrie, welche durch den Begriff „low-energy cutoff“ bekannt ist (Fig. 6.5).

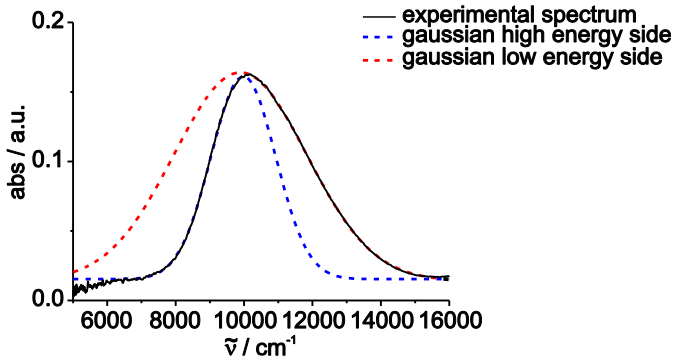

Fig. 6.5: NIR-Spektrum des Triarylaminvinylrutheniumkonjugats **1-CHO**$^+$ bei Raumtemperatur, welches eine asymmetrische Bande aufweist und mit zwei Gausslinien angenähert warden kann.

Das Phänomen des „low-energy cutoffs“ wird nur sehr selten beobachtet. Der Ursprung dieser Asymmetrie konnte durch temperaturabhängige UV/vis/NIR Spektroskopie ermittelt werden. Bei niedriger Temperatur nahm die Stärke der Asymmetrie zu, was auf

eine vibronische Kopplung des elektronischen Übergangs zu einer symmetrischen Schwingungsmode der Brücke schließen ließ.

Das Klassifizierungssystem nach ROBIN und DAY, teilt Komplexe nach ihrer elektronischen Kopplung in drei Klassen ein. Die Triarylaminvinylruthenium Konjugate konnten also dem Grenzbereich zwischen Klasse II (partiell delokalisiert) und Klasse III (komplett delokalisiert) zugeordnet werden.

Es war also möglich das Grenzgebiet von begrenzter bis vollständig delokalisierter Ladung, durch selektives Stören einer der zwei verbundenen Redoxzentren, anzusteuern.

Die experimentellen Befunde wurden zusätzlich durch quantenchemische Rechnungen untermauert, wobei die Dichtefunktionaltheorie (DFT) und deren zeitabhängige Erweiterung (TD-DFT) herangezogen wurden. Diese Methoden ermöglichten es uns die chemischen Strukturen erst geometrisch in einem gewählten Lösungsmittel zu optimieren und dann die molekularen Grenzorbitale (MOs) wie z.B. das höchste besetzte Molekülorbital (HOMO) oder die Spindichteverteilung zu ermitteln. Die atomaufgelösten Werte für Ladung und Spin halfen dabei die Anteile im Komplex zu bestimmen und TD-DFT Rechnungen ermöglichten die Zuordnung der elektronischen Banden im UV/vis/NIR Spektrum. Anhand dieser Methoden konnten wir z.B. die NIR Bande einem π–π^* Übergang zuordnen, welcher einen anteiligen Ladungstransfercharakter aufwies. Der Ladungstransfercharakter wurde anschließend durch eine leichte negative Solvatochromie in Lösungsmitteln steigender Polarität nachgewiesen (Fig. 6.6).

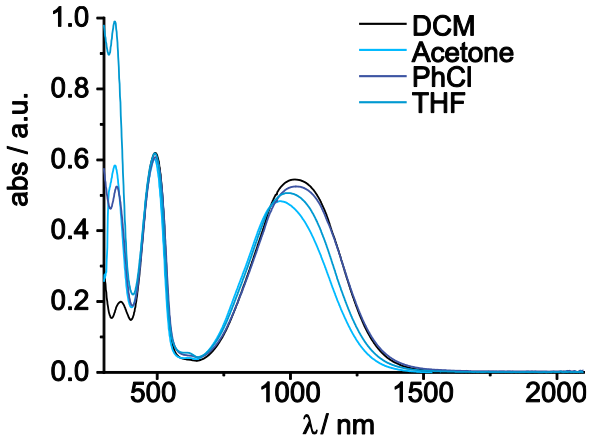

Fig. 6.6: Negative Solvatochromie der NIR Bande im gemischtvalenten Triarylaminvinylruthenium Konjugat **1-CHO**$^+$.

Das letzte Projekt, welches hier in dieser Arbeit diskutiert wurde, beschäftigte sich mit den Auswirkungen des Austauschs von Ferrocen durch sein schwereres Homolog Ruthenocen in Vinylruthenium-Komplexen. Dabei wurde zusätzlich die Elektronendichte der beiden Redoxeinheiten entweder am Metallocen durch 1,2,3,4,5 Pentamethylcyclopentadien (CP*) oder durch Einführung eines acac-Liganden an der Vinylrutheniumeinheit variiert (Fig. 6.7).

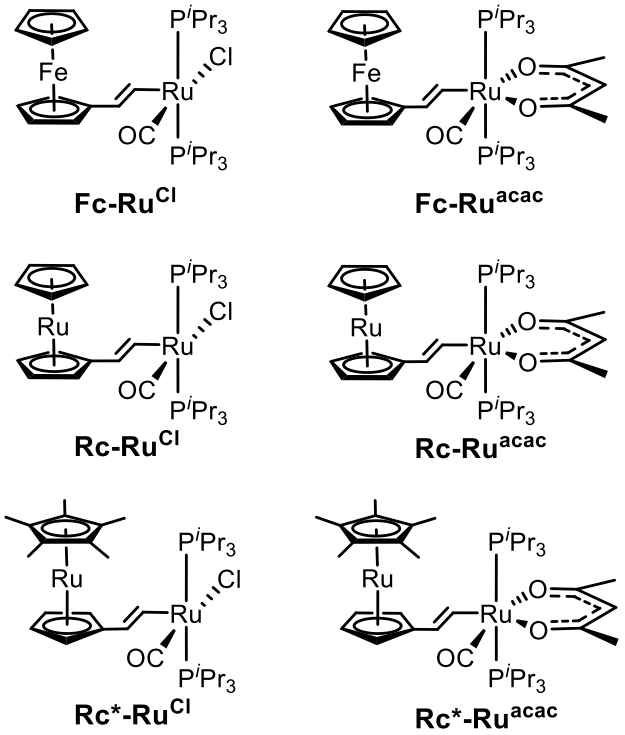

Fig. 6.7: Ferrocen-, ruthenocen- and Pentamethylruthenocenvinylruthenium Komplexe mit chloro- oder acetylacetonato-Ligand.

Die Radikalkationen der korrespondierenden Ferrocenvinylruthenium-Komplexe mit chloro- oder acac-Ligand wurden in der Literatur der Klasse II nach ROBIN und DAY zugeordnet, was partieller Ladungs- und Spindelokalisation entspricht.[169] Bei den ruthenocenbasierten Systemen zeigte sich jedoch ein ganz anderes Bild. Die spektroskopischen Methoden als auch die quantenchemischen Rechnungen zeigten nun ein Klasse III System mit komplett delokalisierter Ladung und Spin an.

Die Energien der CO-Streckschwingungen der neutralen, oxidierten und zweifach oxidierten Spezies können in Relation gesetzt werden, was auf eine nahezu Gleichverteilung der Ladung schließen ließ, welche alle Ruthenocenderivate aufzeigten (Table 7). Die Variation der Liganden und die damit einhergehenden elektronischen Unterschiede der Komplexe hatten nur wenig Einfluss darauf.

Table 7: : Werte der Carbonylstreckschwingungen ν(CO) der Metallocenvinylruthenium-Komplexe in deren verschiedenen Oxidationszuständen.

	$\nu(CO)^{exp}$ [cm^{-1}]			$\Delta\nu(CO)$ [cm^{-1}]			$\frac{\Delta\nu(CO)^{+/0}}{\Delta\nu(CO)^{2+/0}}$
	n = 0	n = 1	n = 2	+/0	2+/+	2+/0	
Fc-Ru^{Cl}	1908	1932	2004	24	72	96	0.25
Fc-Ru^{acac}	1893	1921	1966	28	45	73	0.38
Rc-Ru^{Cl}	1908	1952	2004	44	52	96	0.46
Rc-Ru^{acac}	1893	1945	1987	52	42	94	0.55
Rc*-Ru^{Cl}	1908	1940	1999	32	59	91	0.35
Rc*-Ru^{acac}	1893	1932	1981	39	49	88	0.44

Die nicht solvatochrome NIR Bande ließ auf nur einen sehr kleinen bis nicht vorhandenen Anteil an Ladungstransfer zwischen den beiden Redoxzentren schließen, was ein Indiz für eine Ladungsresonanzbande (CR-Bande) darstellt. Außerdem zeigte die ESR Spektroskopie am gemischtvalenten Radikalkation ein Signal schon bei Raumtemperatur mit *g*-Werten von 2.060 bis 2.069, wobei die ferrocenbasierten Systeme erst bei tiefer Temperatur ESR aktiv wurden und durch axiale Signalsymmetrie deutlich auf einen ferrociniumlastigen Spin hindeuteten (Fig. 6.8).

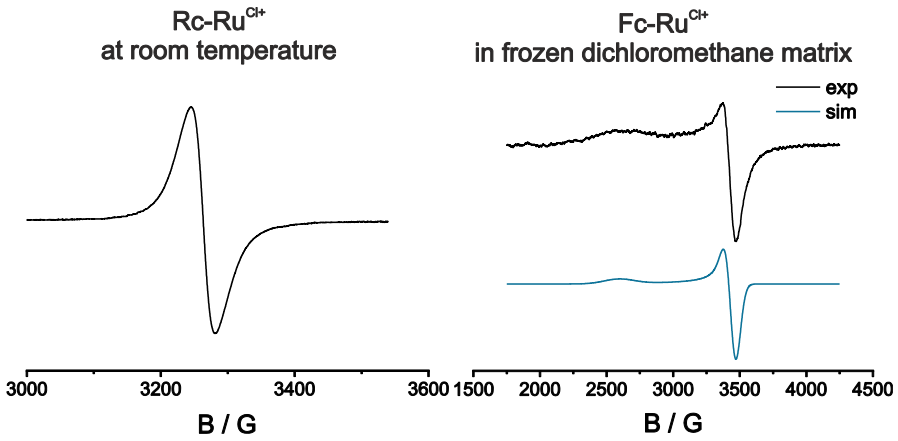

Fig. 6.8: ESR-Spektren der gemischtvalenten Ruthenocen- und Ferrocenvinylruthenium Komplexe bei Raumtemperatur (links) und in gefrorener DCM-Matrix (rechts).

Die elektronischen Banden der UV/vis/NIR Spektroelektrochemie konnten durch TD-DFT Rechnungen zugeordnet werden und die Identität der Nahinfrarotbande als CR-Bande bestätigt werden, was ein weiteres deutliches Indiz für eine Klasse III Verbindung darstellt. Die delokalisierte Spindichteverteilung in den Ruthenocenderivaten wurde auch durch die quantenchemisch berechnete Spindichteverteilung bestätigt und lassen keinen Zweifel an der vollständig delokalisierten Ladung und Spindichte, trotz der chemisch unterschiedlichen Redoxzentren. Weiterhin wurde für den Komplex **Rc-Ru^{acac}** wieder eine asymmetrische NIR-Bande gefunden. Nur dieser Komplex aus der Reihe zeigte einen temperaturabhängigen „low-energy cutoff“, was den Übergang von Klasse III zur Grenzklasse II/III markiert.

Zusammenfassend waren wir in der Lage, asymmetrische, gemischtvalente Komplexe darzustellen, deren elektronischen Eigenschaften Ladungslokalisation, Ladungsdelokalisation oder gar Valenztautomerie induzieren.

Letzteres wurde einerseits durch die Änderung der intrinsischen Redoxpotenziale erreicht und dem damit zusammenhängenden Unterschied der jeweiligen Grundzustandsenergien ΔG. Andererseits wurde durch die elektronische Kopplung der zwei Untereinheiten eine adiabatische Potentialhyperfläche erzeugt, deren Aktivierungsbarriere ΔG^* das gleichzeitige Auftreten zweier Redoxisomere begünstigt (Fig. 6.9).

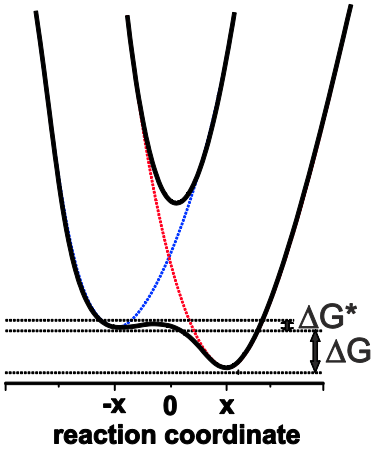

Fig. 6.9: Zwei diabtische Potentiale (rote und blaue Linien) und eine adiabatische Potentialhyperfläche für gemischtvalente Systeme mit unterschiedlichen Redoxzentren.

7. List of References

7.1. Chapter 1 Introduction

1. Seyferth, D. *Organometallics* **2001,** *20*, 1488-1498, doi: 10.1021/om0101947.
2. Zeise, W. C. *Ann. Phys.* **1831,** *97*, 497-541, doi: 10.1002/andp.18310970402.
3. von Frankland, E. *Justus Liebigs Ann. Chem.* **1849,** *71*, 213-216, doi: doi:10.1002/jlac.18490710206.
4. Grignard, V. *CR Hebd. Séances Acad. Sci.* **1900**, 1322–1324.
5. Mond, L.; Langer, C.; Quincke, F. *J. Chem. Soc., Transactions* **1890,** *57*, 749-753, doi: 10.1039/CT8905700749.
6. Kealy, T. J.; Pauson, P. L. *Nature* **1951,** *168*, 1039, doi: 10.1038/1681039b0.
7. Brock, C. P.; Fu, Y. *Acta Crystallogr., Sect. B* **1997,** *53*, 928-938, doi: doi:10.1107/S0108768197005132.
8. Laszlo, P.; Hoffmann, R. *Angew. Chem.* **2000,** *112*, 127-128, doi: 10.1002/(SICI)1521-3757(20000103)112:1<127::AID-ANGE127>3.0.CO;2-2.
9. Connelly, N. G.; Geiger, W. E. *Chem. Rev.* **1996,** *96*, 877-910, doi: 10.1021/cr940053x.
10. Astruc, D. *Organometallic Chemistry and Catalysis*; Springer, 2000.
11. Noviandri, I.; Brown, K. N.; Fleming, D. S.; Gulyas, P. T.; Lay, P. A.; Masters, A. F.; Phillips, L. *J. Phys. Chem. B* **1999,** *103*, 6713-6722, doi: 10.1021/jp991381+.
12. Inkpen, M. S.; Scheerer, S.; Linseis, M.; White, A. J. P.; Winter, R. F.; Albrecht, T.; Long, N. J. *Nature Chemistry* **2016,** *8*, 825, doi: 10.1038/nchem.2553.
13. Astruc, D. *Eur. J. Inorg. Chem.* **2017,** *2017*, 6-29, doi: 10.1002/ejic.201600983.
14. Wilkinson, G. *J. Am. Chem. Soc.* **1952,** *74*, 6146-6147, doi: 10.1021/ja01143a538.
15. Swarts, J. C.; Nafady, A.; Roudebush, J. H.; Trupia, S.; Geiger, W. E. *Inorg. Chem.* **2009,** *48*, 2156-2165, doi: 10.1021/ic802105b.
16. Hill, M. G.; Lamanna, W. M.; Mann, K. R. *Inorg. Chem.* **1991,** *30*, 4687-4690, doi: 10.1021/ic00025a003.
17. Sheats, J. E.; Rausch, M. D. *J. Org. Chem.* **1970,** *35*, 3245-3249, doi: 10.1021/jo00835a014.
18. Yan, Y.; Pageni, P.; Kabir, M. P.; Tang, C. *Synlett* **2016,** *27*, 984-1005, doi: 10.1055/s-0035-1561504.
19. Vanicek, S.; Kopacka, H.; Wurst, K.; Müller, T.; Schottenberger, H.; Bildstein, B. *Organometallics* **2014,** *33*, 1152-1156, doi: 10.1021/om401120h.
20. Vanicek, S.; Kopacka, H.; Wurst, K.; Müller, T.; Hassenrück, C.; Winter, R. F.; Bildstein, B. *Organometallics* **2016,** *35*, 2101-2109, doi: 10.1021/acs.organomet.6b00329.
21. Vanicek, S.; Podewitz, M.; Hassenrück, C.; Pittracher, M.; Kopacka, H.; Wurst, K.; Müller, T.; Liedl, K. R.; Winter, R. F.; Bildstein, B. *Chem. Eur. J.* **2018,** *24*, 3165-3169, doi: 10.1002/chem.201800147.
22. Ware, M. *J. Chem. Educ.* **2008,** *85*, 612, doi: 10.1021/ed085p612.
23. Fleischer, E. B.; Lavallee, D. K. *J. Am. Chem. Soc.* **1972,** *94*, 2599-2601, doi: 10.1021/ja00763a005.
24. Sutton, J. E.; Sutton, P. M.; Taube, H. *Inorg. Chem.* **1979,** *18*, 1017-1021, doi: 10.1021/ic50194a028.
25. Sutton, J. E.; Taube, H. *Inorg. Chem.* **1981,** *20*, 3125-3134, doi: 10.1021/ic50224a001.
26. Tom, G. M.; Creutz, C.; Taube, H. *J. Am. Chem. Soc.* **1974,** *96*, 7827-7829, doi: 10.1021/ja00832a045.

27. Quiroz-Guzman, M.; Brown, S. N. *Acta Crystallogr. Section C* **2010,** *66*, m171-m173, doi: 10.1107/S0108270110019748.
28. Lay, P. A.; Magnuson, R. H.; Taube, H. *Inorg. Chem.* **1988,** *27*, 2364-2371, doi: 10.1021/ic00286a028.
29. Cowan, D. O.; Kaufman, F. *J. Am. Chem. Soc.* **1970,** *92*, 219-220, doi: 10.1021/ja00704a047.
30. Dong, T.-Y.; Chang, C.-K.; Lee, S.-H.; Lai, L.-L.; Chiang, M. Y.-N.; Lin, K.-J. *Organometallics* **1997,** *16*, 5816-5825, doi: 10.1021/om970746e.
31. Robin, M. B.; Day, P. In *Adv. Inorg. Chem. Radiochem.;* Emeléus, H. J.; Sharpe, A. G. Eds.; Academic Press, 1968; pp. 247-422.
32. Marcus, R. A.; Sutin, N. *Biochimica et Biophysica Acta (BBA) - Reviews on Bioenergetics* **1985,** *811*, 265-322, doi: 10.1016/0304-4173(85)90014-X.
33. Sutin, N. *Acc. Chem. Res.* **1982,** *15*, 275-282, doi: 10.1021/ar00081a002.
34. Sutin, N. In *Prog. Inorg. Chem.*; John Wiley & Sons, Inc., 2007; pp. 441-498.
35. Sutin, N. In *Adv. Chem. Phys.*; John Wiley & Sons, Inc., 2007; pp. 7-33.
36. Demadis, K. D.; El-Samanody, E.-S.; Coia, G. M.; Meyer, T. J. *J. Am. Chem. Soc.* **1999,** *121*, 535-544, doi: 10.1021/ja982802o.
37. Demadis, K. D.; Neyhart, G. A.; Kober, E. M.; White, P. S.; Meyer, T. J. *Inorg. Chem.* **1999,** *38*, 5948-5959, doi: 10.1021/ic9907765.
38. Brunschwig, B.; Sutin, N. *J. Am. Chem. Soc.* **1978,** *100*, 7568-7577, doi: 10.1021/ja00492a023.
39. Shin, Y.-g. K.; Brunschwig, B. S.; Creutz, C.; Sutin, N. *J. Phys. Chem.* **1996,** *100*, 8157-8169, doi: 10.1021/jp953395v.
40. Santi, S.; Orian, L.; Durante, C.; Bencze, E. Z.; Bisello, A.; Donoli, A.; Ceccon, A.; Benetollo, F.; Crociani, L. *Chem. Eur. J.* **2007,** *13*, 7933-7947, doi: doi:10.1002/chem.200700052.
41. Lambert, C.; Nöll, G. *J. Am. Chem. Soc.* **1999,** *121*, 8434-8442, doi: 10.1021/ja991264s.
42. Coropceanu, V.; Malagoli, M.; André, J. M.; Brédas, J. L. *J. Am. Chem. Soc.* **2002,** *124*, 10519-10530, doi: 10.1021/ja026437j.
43. Nelsen, S. F.; Ismagilov, R. F.; Trieber, D. A. *Science* **1997,** *278*, 846-849, doi: 10.1126/science.278.5339.846.
44. Atwood, C. G.; Geiger, W. E. *J. Am. Chem. Soc.* **2000,** *122*, 5477-5485, doi: 10.1021/ja994064p.
45. Ito, T.; Imai, N.; Yamaguchi, T.; Hamaguchi, T.; Londergan, C. H.; Kubiak, C. P. *Angew. Chem. Int. Ed.* **2004,** *43*, 1376-1381, doi: 10.1002/anie.200353221.
46. Salsman, J. C.; Kubiak, C. P.; Ito, T. *J. Am. Chem. Soc.* **2005,** *127*, 2382-2383, doi: 10.1021/ja042351+.
47. Curtis, J. C.; Roberts, J. A.; Blackbourn, R. L.; Dong, Y.; Massum, M.; Johnson, C. S.; Hupp, J. T. *Inorg. Chem.* **1991,** *30*, 3856-3860, doi: 10.1021/ic00020a016.
48. Neyhart, G. A.; Hupp, J. T.; Curtis, J. C.; Timpson, C. J.; Meyer, T. J. *J. Am. Chem. Soc.* **1996,** *118*, 3724-3729, doi: 10.1021/ja953566+.
49. Neyhart, G. A.; Timpson, C. J.; Bates, W. D.; Meyer, T. J. *J. Am. Chem. Soc.* **1996,** *118*, 3730-3737, doi: 10.1021/ja9535672.
50. Kondo, M.; Uchikawa, M.; Namiki, K.; Zhang, W.-W.; Kume, S.; Nishibori, E.; Suwa, H.; Aoyagi, S.; Sakata, M.; Murata, M.; Kobayashi, Y.; Nishihara, H. *J. Am. Chem. Soc.* **2009,** *131*, 12112-12124, doi: 10.1021/ja900393e.
51. Rao, K. P.; Kusamoto, T.; Toshimitsu, F.; Inayoshi, K.; Kume, S.; Sakamoto, R.; Nishihara, H. *J. Am. Chem. Soc.* **2010,** *132*, 12472-12479, doi: 10.1021/ja105250f.
52. Sakamoto, R.; Rao, K. P.; Nishihara, H. *Chem. Lett.* **2011,** *40*, 1316-1326, doi: 10.1246/cl.2011.1316.

53. Ratera, I.; Ruiz-Molina, D.; Renz, F.; Ensling, J.; Wurst, K.; Rovira, C.; Gütlich, P.; Veciana, J. *J. Am. Chem. Soc.* **2003,** *125*, 1462-1463, doi: 10.1021/ja0282590.
54. Ratera, I.; Sporer, C.; Ruiz-Molina, D.; Ventosa, N.; Baggerman, J.; Brouwer, A. M.; Rovira, C.; Veciana, J. *J. Am. Chem. Soc.* **2007,** *129*, 6117-6129, doi: 10.1021/ja066351g.
55. Dietrich, J.; Thorenz, U.; Förster, C.; Heinze, K. *Inorg. Chem.* **2013,** *52*, 1248-1264, doi: 10.1021/ic301632y.
56. Fitzgerald, E. C.; Ladjarafi, A.; Brown, N. J.; Collison, D.; Costuas, K.; Edge, R.; Halet, J.-F.; Justaud, F.; Low, P. J.; Meghezzi, H.; Roisnel, T.; Whiteley, M. W.; Lapinte, C. *Organometallics* **2011,** *30*, 4180-4195, doi: 10.1021/om200488b.
57. Lohan, M.; Justaud, F.; Lang, H.; Lapinte, C. *Organometallics* **2012,** *31*, 3565-3574, doi: 10.1021/om300050t.
58. Lohan, M.; Justaud, F.; Roisnel, T.; Ecorchard, P.; Lang, H.; Lapinte, C. *Organometallics* **2010,** *29*, 4804-4817, doi: 10.1021/om100003z.
59. Chen, J.; Wuttke, E.; Polit, W.; Exner, T.; Winter, R. F. *J. Am. Chem. Soc.* **2013,** *135*, 3391-3394, doi: 10.1021/ja400673c.
60. Maurer, J.; Winter, R. F.; Sarkar, B.; Fiedler, J.; Zalis, S. *Chem. Commun.* **2004**, 1900-1901, doi: 10.1039/B405349D.
61. Maurer, J.; Sarkar, B.; Schwederski, B.; Kaim, W.; Winter, R. F.; Záliš, S. *Organometallics* **2006,** *25*, 3701-3712, doi: 10.1021/om0602660.
62. Maurer, J.; Sarkar, B.; Kaim, W.; Winter, R. F.; Záliš, S. *Chemistry – A European Journal* **2007,** *13*, 10257-10272, doi: 10.1002/chem.200700459.
63. Maurer, J.; Linseis, M.; Sarkar, B.; Schwederski, B.; Niemeyer, M.; Kaim, W.; Záliš, S.; Anson, C.; Zabel, M.; Winter, R. F. *J. Am. Chem. Soc.* **2008,** *130*, 259-268, doi: 10.1021/ja075547t.
64. Mücke, P.; Linseis, M.; Záliš, S.; Winter, R. F. *Inorg. Chim. Acta* **2011,** *374*, 36-50, doi: 10.1016/j.ica.2011.03.071.
65. Mücke, P.; Zabel, M.; Edge, R.; Collison, D.; Clément, S.; Záliš, S.; Winter, R. F. *J. Organomet. Chem.* **2011,** *696*, 3186-3197, doi: 10.1016/j.jorganchem.2011.06.028.
66. Linseis, M.; Zalis, S.; Zabel, M.; Winter, R. F. *J. Am. Chem. Soc.* **2012,** *134*, 16671-16692, doi: 10.1021/ja3059606.
67. Esteruelas, M. A.; Werner, H. *J. Organomet. Chem.* **1986,** *303*, 221-231, doi: 10.1016/0022-328X(86)80134-6.
68. Torres, M. R.; Vegas, A.; Santos, A.; Ros, J. *J. Organomet. Chem.* **1986,** *309*, 169-177, doi: 10.1016/S0022-328X(00)99582-2.
69. Werner, H.; Esteruelas, M. A.; Otto, H. *Organometallics* **1986,** *5*, 2295-2299, doi: 10.1021/om00142a019.
70. Werner, H.; Meyer, U.; Peters, K.; Schnering, H. G. v. *Chem. Ber.* **1989,** *122*, 2097-2107, doi: doi:10.1002/cber.19891221109.
71. Marchenko, A. V.; Gerard, H.; Eisenstein, O.; Caulton, K. G. *New J. Chem.* **2001,** *25*, 1244-1255, doi: 10.1039/B103815J.
72. Wuttke, E., University of Konstanz, 2014.
73. Buil, M. L.; Esteruelas, M. A.; Goni, E.; Oliván, M.; Oñate, E. *Organometallics* **2006,** *25*, 3076-3083, doi: 10.1021/om060222r.
74. Wilton-Ely, J. D. E. T.; Honarkhah, S. J.; Wang, M.; Tocher, D. A.; Slawin, A. M. Z. *Dalton Trans.* **2005**, 1930-1939, doi: 10.1039/B501906K.
75. Záliš, S.; Winter, R. F.; Kaim, W. *Coord. Chem. Rev.* **2010,** *254*, 1383-1396, doi: 10.1016/j.ccr.2010.02.020.
76. Jia, G.; Wan Fung, W.; Yeung, R. C. Y.; Xia, H. P. *J. Organomet. Chem.* **1997,** *539*, 53-59, doi: 10.1016/S0022-328X(97)00080-6.
77. Xia, H.; Wen, T. B.; Hu, Q. Y.; Wang, X.; Chen, X.; Shek, L. Y.; Williams, I. D.; Wong, K. S.; Wong, G. K. L.; Jia, G. *Organometallics* **2005,** *24*, 562-569, doi: 10.1021/om0496939.

78. Yuan, P.; Liu, S. H.; Xiong, W.; Yin, J.; Yu, G.-a.; Sung, H. Y.; Williams, I. D.; Jia, G. *Organometallics* **2005,** *24*, 1452-1457, doi: 10.1021/om0490637.
79. Yin, J.; Yu, G.-A.; Guan, J.; Mei, F.; Liu, S. H. *J. Organomet. Chem.* **2005,** *690*, 4265-4271, doi: 10.1016/j.jorganchem.2005.06.031.
80. Montoya, J.; Santos, A.; Echavarren, A. M.; Ros, J. *J. Organomet. Chem.* **1990,** *390*, c57-c60, doi: 10.1016/0022-328X(90)85046-2.
81. Montoya, J.; Santos, A.; López, J.; Echavarren, A. M.; Ros, J.; Romero, A. *J. Organomet. Chem.* **1992,** *426*, 383-398, doi: 10.1016/0022-328X(92)83071-O.
82. Rosario Torres, M.; Santos, A.; Perales, A.; Ros, J. *J. Organomet. Chem.* **1988,** *353*, 221-228, doi: 10.1016/0022-328X(88)83067-5.
83. Seetharaman, S. K.; Chung, M.-C.; Englich, U.; Ruhlandt-Senge, K.; Sponsler, M. B. *Inorg. Chem.* **2007,** *46*, 561-567, doi: 10.1021/ic061389f.
84. Wu, X. H.; Jin, S.; Liang, J. H.; Li, Z. Y.; Yu, G.-a.; Liu, S. H. *Organometallics* **2009,** *28*, 2450-2459, doi: 10.1021/om900018y.
85. Wu, X.-H.; Liang, J. H.; Xia, J.-L.; Jin, S.; Yu, G.-A.; Liu, S. H. *Organometallics* **2010,** *29*, 1150-1156, doi: 10.1021/om901025q.
86. Man, W. Y.; Xia, J.-L.; Brown, N. J.; Farmer, J. D.; Yufit, D. S.; Howard, J. A. K.; Liu, S. H.; Low, P. J. *Organometallics* **2011,** *30*, 1852-1858, doi: 10.1021/om1010534.
87. Ou, Y.-P.; Jiang, C.; Wu, D.; Xia, J.; Yin, J.; Jin, S.; Yu, G.-A.; Liu, S. H. *Organometallics* **2011,** *30*, 5763-5770, doi: 10.1021/om200622q.
88. Wu, X.; Weng, T.; Jin, S.; Liang, J.; Guo, R.; Yu, G.-a.; Liu, S. H. *J. Organomet. Chem.* **2009,** *694*, 1877-1883, doi: 10.1016/j.jorganchem.2009.01.024.
89. Deshpande, S. S.; Gopinathan, S.; Gopinathan, C. *J. Organomet. Chem.* **1991,** *415*, 265-270, doi: 10.1016/0022-328X(91)80124-3.
90. Pevny, F.; Winter, R. F.; Sarkar, B.; Zalis, S. *Dalton Trans.* **2010,** *39*, 8000-8011, doi: 10.1039/C0DT00164C.
91. Jung, S.; Brandt, C. D.; Wolf, J.; Werner, H. *Dalton Trans.* **2004**, 375-383, doi: 10.1039/B314425A.
92. Fox, M. A.; Roberts, R. L.; Khairul, W. M.; Hartl, F.; Low, P. J. *J. Organomet. Chem.* **2007,** *692*, 3277-3290, doi: 10.1016/j.jorganchem.2007.03.042.
93. Armitt, D. J.; Bruce, M. I.; Gaudio, M.; Zaitseva, N. N.; Skelton, B. W.; White, A. H.; Le Guennic, B.; Halet, J.-F.; Fox, M. A.; Roberts, R. L.; Hartl, F.; Low, P. J. *Dalton Trans.* **2008**, 6763-6775, doi: 10.1039/B808798A.
94. Gauthier, N.; Olivier, C.; Rigaut, S.; Touchard, D.; Roisnel, T.; Humphrey, M. G.; Paul, F. *Organometallics* **2008,** *27*, 1063-1072, doi: 10.1021/om700584m.
95. West, P. J.; Schwich, T.; Cifuentes, M. P.; Humphrey, M. G. *J. Organomet. Chem.* **2011,** *696*, 2886-2893, doi: 10.1016/j.jorganchem.2011.02.013.
96. Younus, M.; Long, N. J.; Raithby, P. R.; Lewis, J. *J. Organomet. Chem.* **1998,** *570*, 55-62, doi: 10.1016/S0022-328X(98)00816-X.
97. Kulasekera, E.; Petrie, S.; Stranger, R.; Cifuentes, M. P.; Humphrey, M. G. *J. Organomet. Chem.* **2013,** *748*, 21-28, doi: 10.1016/j.jorganchem.2013.07.010.
98. Gückel, S.; Gluyas, J. B. G.; El-Tarhuni, S.; Sobolev, A. N.; Whiteley, M. W.; Halet, J.-F.; Lapinte, C.; Kaupp, M.; Low, P. J. *Organometallics* **2018,** *37*, 1432-1445, doi: 10.1021/acs.organomet.8b00099.
99. Field, L. D.; George, A. V.; Laschi, F.; Malouf, E. Y.; Zanello, P. *J. Organomet. Chem.* **1992,** *435*, 347-356, doi: 10.1016/0022-328X(92)83404-6.
100. Colbert, M. C. B.; Lewis, J.; Long, N. J.; Raithby, P. R.; Younus, M.; White, A. J. P.; Williams, D. J.; Payne, N. N.; Yellowlees, L.; Beljonne, D.; Chawdhury, N.; Friend, R. H. *Organometallics* **1998,** *17*, 3034-3043, doi: 10.1021/om970130p.
101. Bruce, M. I.; Costuas, K.; Ellis, B. G.; Halet, J.-F.; Low, P. J.; Moubaraki, B.; Murray, K. S.; Ouddaï, N.; Perkins, G. J.; Skelton, B. W.; White, A. H. *Organometallics* **2007,** *26*, 3735-3745, doi: 10.1021/om7002859.

102. Bruce, M. I.; Costuas, K.; Davin, T.; Halet, J.-F.; Kramarczuk, K. A.; Low, P. J.; Nicholson, B. K.; Perkins, G. J.; Roberts, R. L.; Skelton, B. W.; Smith, M. E.; White, A. H. *Dalton Trans.* **2007**, 5387-5399, doi: 10.1039/B712104K.
103. Wuttke, E.; Fink, D.; Anders, P.; Maria Hoyt, A.-L.; Polit, W.; Linseis, M.; Winter, R. F. *J. Organomet. Chem.* **2016,** *821*, 4-18, doi: 10.1016/j.jorganchem.2016.02.031.
104. Richardson, D. E.; Taube, H. *Coord. Chem. Rev.* **1984,** *60*, 107-129, doi: 10.1016/0010-8545(84)85063-8.
105. D'Alessandro, D. M.; Keene, F. R. *Chem. Soc. Rev.* **2006,** *35*, 424-440, doi: 10.1039/B514590M.
106. Winter, R. F. *Organometallics* **2014,** *33*, 4517-4536, doi: 10.1021/om500029x.
107. Santi, S.; Bisello, A.; Cardena, R.; Donoli, A. *Dalton Trans.* **2015,** *44*, 5234-5257, doi: 10.1039/C4DT03581J.
108. Crutchley, R. J. In *Adv. Inorg. Chem.;* Sykes, A. G. Ed.; Academic Press, 1994; pp. 273-325.
109. Evans, C. E. B.; Naklicki, M. L.; Rezvani, A. R.; White, C. A.; Kondratiev, V. V.; Crutchley, R. J. *J. Am. Chem. Soc.* **1998,** *120*, 13096-13103, doi: 10.1021/ja982673b.
110. Lin, Y.-C.; Chen, W.-T.; Tai, J.; Su, D.; Huang, S.-Y.; Lin, I.; Lin, J.-L.; Lee, M. M.; Chiou, M. F.; Liu, Y.-H.; Kwan, K.-S.; Chen, Y.-J.; Chen, H.-Y. *Inorg. Chem.* **2009,** *48*, 1857-1870, doi: 10.1021/ic801271q.
111. Santos, A.; Lopez, J.; Montoya, J.; Noheda, P.; Romero, A.; Echavarren, A. M. *Organometallics* **1994,** *13*, 3605-3615, doi: 10.1021/om00021a037.
112. Maurer, J.; Sarkar, B.; Schwederski, B.; Kaim, W.; Winter, R. F.; Záliš, S. *Organometallics* **2006,** *25*, 3701-3712, doi: 10.1021/om0602660.
113. Sato, M.; Shintate, H.; Kawata, Y.; Sekino, M.; Katada, M.; Kawata, S. *Organometallics* **1994,** *13*, 1956-1962, doi: 10.1021/om00017a061.
114. Sato, M.; Kawata, Y.; Shintate, H.; Habata, Y.; Akabori, S.; Unoura, K. *Organometallics* **1997,** *16*, 1693-1701, doi: 10.1021/om960732t.
115. Kowalski, K.; Linseis, M.; Winter, R. F.; Zabel, M.; Záliš, S.; Kelm, H.; Krüger, H.-J.; Sarkar, B.; Kaim, W. *Organometallics* **2009,** *28*, 4196-4209, doi: 10.1021/om9002945.
116. Pevny, F.; Di Piazza, E.; Norel, L.; Drescher, M.; Winter, R. F.; Rigaut, S. *Organometallics* **2010,** *29*, 5912-5918, doi: 10.1021/om1007133.
117. Mücke, D. P., Universität Konstanz, 2013.
118. Bruning, W. H.; Nelson, R. F.; Marcoux, L. S.; Adams, R. N. *The Journal of Physical Chemistry* **1967,** *71*, 3055-3057, doi: 10.1021/j100868a047.
119. Nelson, R. R.; Adams, R. N. *J. Am. Chem. Soc.* **1968,** *90*, 3925-3930, doi: 10.1021/ja01017a004.
120. Debrodt, H.; Heusler, K. E. In *Zeitschrift für Physikalische Chemie*, 1981; p. 35.
121. Sreenath, K.; Suneesh, C. V.; Ratheesh Kumar, V. K.; Gopidas, K. R. *J. Org. Chem.* **2008,** *73*, 3245-3251, doi: 10.1021/jo800349n.
122. Reynolds, R.; Line, L. L.; Nelson, R. F. *J. Am. Chem. Soc.* **1974,** *96*, 1087-1092, doi: 10.1021/ja00811a024.
123. Walter, R. I. *J. Am. Chem. Soc.* **1966,** *88*, 1923.
124. Reynolds, R.; Line, L. L.; Nelson, R. F. *J. Am. Chem. Soc.* **1974,** *96*, 1087.
125. Steckhan, E. *Angew. Chem., Int. Ed. Engl.* **1986,** *25*, 683.
126. Steckhan, E. *Top. Curr. Chem.* **1987,** *142*, 1.
127. Sherlock, S. J.; Boyd, D. C.; Moasser, B.; Gladfelter, W. L. *Inorg. Chem.* **1991,** *30*, 3626.
128. Connelly, N. G.; Geiger, W. E. *Chem. Rev.* **1996,** *96*, 877.
129. Bender, T. P.; Graham, J. F.; Duff, J. M. *Chem. Mater.* **2001,** *13*, 4105.
130. Amthor, S.; Noller, B.; Lambert, C. *Chem. Phys.* **2005,** *316*, 141.
131. Eberson, L. L., B.; Maartmann-Moe, K.; Sæbø, J.; Fischer,; W., G. *Acta Chem. Scand.* **1987,** *41b*, 367-378, doi: 10.3891/acta.chem.scand.41b-0367.

132. Khanasa, T.; Jantasing, N.; Morada, S.; Leesakul, N.; Tarsang, R.; Namuangruk, S.; Kaewin, T.; Jungsuttiwong, S.; Sudyoadsuk, T.; Promarak, V. *Eur. J. Org. Chem.* **2013,** *2013*, 2608-2620, doi: 10.1002/ejoc.201201479.
133. Wang, Y.-J.; Sheu, H.-S.; Lai, C. K. *Tetrahedron* **2007,** *63*, 1695-1705, doi: 10.1016/j.tet.2006.11.058.
134. He, Z.; Kan, C.-W.; Ho, C.-L.; Wong, W.-Y.; Chui, C.-H.; Tong, K.-L.; So, S.-K.; Lee, T.-H.; Leung, L. M.; Lin, Z. *Dyes and Pigments* **2011,** *88*, 333-343, doi: 10.1016/j.dyepig.2010.08.001.
135. Mallegol, T.; Gmouh, S.; Meziane, M. A. A.; Blanchard-Desce, M.; Mongin, O. *Synthesis* **2005,** *2005*, 1771-1774, doi: 10.1055/s-2005-865336.
136. Dapperheld, S.; Steckhan, E.; Brinkhaus, K.-H. G.; Esch, T. *Chem. Ber.* **1991,** *124*, 2557-2567, doi: 10.1002/cber.19911241127.
137. Walter, R. I. *J. Am. Chem. Soc.* **1966,** *88*, 1923-1930, doi: 10.1021/ja00961a014.
138. Amthor, S.; Noller, B.; Lambert, C. *Chem. Phys.* **2005,** *316*, 141-152, doi: 10.1016/j.chemphys.2005.05.009.
139. Barlow, S.; Risko, C.; Chung, S.-J.; Tucker, N. M.; Coropceanu, V.; Jones, S. C.; Levi, Z.; Brédas, J.-L.; Marder, S. R. *J. Am. Chem. Soc.* **2005,** *127*, 16900-16911, doi: 10.1021/ja054136e.
140. Coropceanu, V.; Gruhn, N. E.; Barlow, S.; Lambert, C.; Durivage, J. C.; Bill, T. G.; Nöll, G.; Marder, S. R.; Brédas, J.-L. *J. Am. Chem. Soc.* **2004,** *126*, 2727-2731, doi: 10.1021/ja039263u.
141. Heckmann, A.; Lambert, C. *J. Am. Chem. Soc.* **2007,** *129*, 5515-5527, doi: 10.1021/ja068235j.
142. Heckmann, A.; Amthor, S.; Lambert, C. *Chem. Commun.* **2006**, 2959-2961, doi: 10.1039/B604603G.
143. Kattnig, D. R.; Mladenova, B.; Grampp, G.; Kaiser, C.; Heckmann, A.; Lambert, C. *J. Phys. Chem. C* **2009,** *113*, 2983-2995, doi: 10.1021/jp8107705.
144. Kaupp, M.; Renz, M.; Parthey, M.; Stolte, M.; Wurthner, F.; Lambert, C. *PCCP* **2011,** *13*, 16973-16986, doi: 10.1039/C1CP21772K.
145. Lambert, C.; Noll, G.; Schelter, J. *Nat Mater* **2002,** *1*, 69-73, doi: 10.1038/nmat706.
146. Lambert, C.; Amthor, S.; Schelter, J. *J. Phys. Chem. A* **2004,** *108*, 6474-6486, doi: 10.1021/jp048449s.
147. Lambert, C.; Risko, C.; Coropceanu, V.; Schelter, J.; Amthor, S.; Gruhn, N. E.; Durivage, J. C.; Brédas, J.-L. *J. Am. Chem. Soc.* **2005,** *127*, 8508-8516, doi: 10.1021/ja0512172.
148. Lancaster, K.; Odom, S. A.; Jones, S. C.; Thayumanavan, S.; Marder, S. R.; Brédas, J.-L.; Coropceanu, V.; Barlow, S. *J. Am. Chem. Soc.* **2009,** *131*, 1717-1723, doi: 10.1021/ja808465c.
149. Risko, C.; Coropceanu, V.; Barlow, S.; Geskin, V.; Schmidt, K.; Gruhn, N. E.; Marder, S. R.; Brédas, J.-L. *J. Phys. Chem. C* **2008,** *112*, 7959-7967, doi: 10.1021/jp711954j.
150. Seibt, J.; Schaumlöffel, A.; Lambert, C.; Engel, V. *J. Phys. Chem. A* **2008,** *112*, 10178-10184, doi: 10.1021/jp804779s.
151. Szeghalmi, A. V.; Erdmann, M.; Engel, V.; Schmitt, M.; Amthor, S.; Kriegisch, V.; Nöll, G.; Stahl, R.; Lambert, C.; Leusser, D.; Stalke, D.; Zabel, M.; Popp, J. *J. Am. Chem. Soc.* **2004,** *126*, 7834-7845, doi: 10.1021/ja0395386.
152. Heckmann, A.; Lambert, C.; Goebel, M.; Wortmann, R. *Angew. Chem. Int. Ed.* **2004,** *43*, 5851-5856, doi: 10.1002/anie.200460495.
153. Kaupp, M.; Renz, M.; Parthey, M.; Stolte, M.; Wuerthner, F.; Lambert, C. *Phys. Chem. Chem. Phys.* **2011,** *13*, 16973.
154. Kanal, F.; Ruetzel, S.; Lu, H.; Moos, M.; Holzapfel, M.; Brixner, T.; Lambert, C. *J. Phys. Chem. C* **2014,** *118*, 23586.
155. Heckmann, A.; Lambert, C. *J. Am. Chem. Soc.* **2007,** *129*, 5515.

156. Tang, J. H.; Wu, S. H.; Shao, J. Y.; Nie, H. J.; Zhong, Y. W. *Organometallics* **2013,** *32*, 4564.
157. Yao, C. J.; Zheng, R. H.; Shi, Q.; Zhong, Y. W.; Yao, J. *Chem. Commun.* **2012,** *48*, 5680.
158. Yao, C.-J.; Zheng, R.-H.; Shi, Q.; Zhong, Y.-W.; Yao, J. *Chem. Commun.* **2012,** *48*, 5680-5682, doi: 10.1039/C2CC32471G.
159. Chen, J.; Winter, R. F. *Chemistry - A European Journal* **2012,** *18*, 10733-10741, doi: 10.1002/chem.201200800.
160. Polit, W.; Mücke, P.; Wuttke, E.; Exner, T.; Winter, R. F. *Organometallics* **2013,** *32*, 5461-5472, doi: 10.1021/om4007455.
161. Walther Polit, T. E., Evelyn Wuttke, Rainer F. Winter. *BioInorg. React. Mech.* **2012,** *8 (3-4)*, 85-105, doi: 10.1515/irm-2012-0005.
162. Guasch, J.; Grisanti, L.; Jung, S.; Morales, D.; D'Avino, G.; Souto, M.; Fontrodona, X.; Painelli, A.; Renz, F.; Ratera, I.; Veciana, J. *Chem. Mater.* **2013,** *25*, 808-814, doi: 10.1021/cm400147p.
163. Elsner, O.; Ruiz-Molina, D.; Vidal-Gancedo, J.; Rovira, C.; Veciana, J. *Chem. Commun.* **1999**, 579-580, doi: 10.1039/A900371A.
164. Elsner, O.; Ruiz-Molina, D.; Ratera, I.; Vidal-Gancedo, J.; Rovira, C.; Veciana, J. *J. Organomet. Chem.* **2001,** *637-639*, 251-257, doi: 10.1016/S0022-328X(01)00912-3.
165. Sporer, C.; Ratera, I.; Ruiz-Molina, D.; Vidal Gancedo, J.; Wurst, K.; Jaitner, P.; Rovira, C.; Veciana, J. *J. Phys. Chem. Solids* **2004,** *65*, 753-758, doi: 10.1016/j.jpcs.2003.11.012.
166. Sporer, C.; Ratera, I.; Ruiz-Molina, D.; Zhao, Y.; Vidal-Gancedo, J.; Wurst, K.; Jaitner, P.; Clays, K.; Persoons, A.; Rovira, C.; Veciana, J. *Angew. Chem. Int. Ed.* **2004,** *43*, 5266-5268, doi: 10.1002/anie.200454150.
167. Souto, M.; Guasch, J.; Lloveras, V.; Mayorga, P.; López Navarrete, J. T.; Casado, J.; Ratera, I.; Rovira, C.; Painelli, A.; Veciana, J. *The Journal of Physical Chemistry Letters* **2013,** *4*, 2721-2726, doi: 10.1021/jz4013855.
168. Souto, M.; Morales, D. C.; Guasch, J.; Ratera, I.; Rovira, C.; Painelli, A.; Veciana, J. *J. Phys. Org. Chem.* **2014,** *27*, 465-469, doi: 10.1002/poc.3296.
169. Kowalski, K.; Linseis, M.; Winter, R. F.; Zabel, M.; Záliš, S.; Kelm, H.; Krüger, H.-J.; Sarkar, B.; Kaim, W. *Organometallics* **2009,** *28*, 4196-4209, doi: 10.1021/om9002945.

Chapter 3.2 Publication 1

1. E. Wuttke, D. Fink, P. Anders, A.-L. M. Hoyt, W. Polit, M. Linseis, R. F. Winter, *J. Organomet. Chem*. **2016**, 821, pp. 4-18.
2. F. Pevny, E. Di Piazza, L. Norel, M. Drescher, R. F. Winter and S. Rigaut, *Organometallics*, **2010**, 29, 5912–5918.
3. a) E. Wuttke, Y.-M. Hervault, W. Polit, M. Linseis, P. Erler, S. Rigaut and R. F. Winter, *Organometallics*, 2014, 33, 4672–4686; b) E. Wuttke, F. Pevny, Y.-M. Hervault, L. Norel, M. Drescher, R. F. Winter and S. Rigaut, *Inorg. Chem.*, **2012**, 51, 1902–1915.
4. W. Polit, T. Exner, E. Wuttke and R. F. Winter, *Bioinorg. React. Mech.*, **2012**, 8, 85–105.
5. W. Polit, P. Mücke, E. Wuttke, T. Exner and R. F. Winter, *Organometallics*, **2013**, 32, 5461–5472.
6. J. Chen and R. F. Winter, *Chem. Eur. J.*, **2012**, 18, 10733–10741.
7. J. Chen, E. Wuttke, W. Polit, T. Exner and R. F. Winter, *J. Am. Chem. Soc*., **2013**, 135, 3391–3394.

8. J. Maurer, M. Linseis, B. Sarkar, B. Schwederski, M. Niemeyer, W. Kaim, S. Záliš, C. Anson, M. Zabel and R. F. Winter, *J. Am. Chem. Soc*., **2008**, 130, 259–268.
9. a) C. G. Atwood and W. E. Geiger, *J. Am. Chem. Soc*., **2000**, 122, 5477–5485; b) M. E. Stoll, S. R. Lovelace, W. E. Geiger, H. Schimanke, I. Hyla-Kryspin and R. Gleiter, *J. Am. Chem. Soc.*, **1999**, 121, 9343–9351.
10. S. Scheerer, N. Rotthowe, O. S. Abdel-Rahman, X. He, S. Rigaut, H. Kvapilová, S. Záliš and R. F. Winter, *Inorg. Chem*., **2015**, 54, 3387–3402.
11. M. Linseis, S. Záliš, M. Zabel and R. F. Winter, *J. Am. Chem. Soc*., **2012**, 134, 16671–16692.
12. a) F. Delgado-Pena, D. R. Talham and D. O. Cowan, *J. Organomet. Chem*., **1983**, 253, C43–C46; b) A.-C. Ribou, J.-P. Launay, M. L. Sachtleben, H. Li and C. W. Spangler, *Inorg. Chem.*, **1996**, 35, 3735–3740; c) F. Ding, H. Wang, Q. Wu, T. Van Voorhis, S. Chen and J. P. Konopelski, *J. Phys. Chem. A*, **2010**, 114,
13. C. Patoux, C. Coudret, J. P. Launay, C. Joachim and A. Gourdon, *Inorg. Chem*., **1997**, 36, 5037.
14. a) G. C. Allen and N. S. Hush, *Prog. Inorg. Chem*., **1967**, 8, 357–389; b) N. S. Hush, *Prog. Inorg. Chem*., **1967**, 8, 391–444; c) C. Creutz and "Mixed Valence Complexes of d, in: ^{5}–d^{6} Metal Centers" in Progress in Inorganic Chemistry, vol. 30 (Ed.: S. J. Lippard), John Wiley and Sons, New York, **1983**, pp. 1–73; d) J. R. Reimers and N. S. Hush, *J. Photochem. Photobiol. A*, **1994**, 82, 31–46; e) B. S. Brunschwig and N. Sutin, *Coord. Chem. Rev.*, **1999**, 187, 233–254.
15. a) R. A. Marcus, Annu. *Rev. Phys. Chem*., **1964**, 15, 155–196; b) P. Chen and T. J. Meyer, *Chem. Rev*., **1998**, 98, 1439–1477; c) Y. J. Chen, C.-H. Kao, S. J. Lin, C.-C. Tai and K. S. Kwan, *Inorg. Chem*., **2000**, 39, 189–194; d) S. Barlow, *Inorg. Chem*., **2001**, 40, 7047–7053; e) I. Ratera, C. Sporer, D. Ruiz-Molina, N. Ventosa, J. Baggerman, A. M. Brouwer, C. Rovira and J. Veciana, *J. Am. Chem. Soc*., **2007**, 129, 6117–6129.
16. F. Salaymeh, S. Berhane, R. Yusof, R. de la Rosa, E. Y. Fung, R. Matamoros, K. W. Lau, Q. Zheng, E. M. Kober and J. C. Curtis, *Inorg. Chem*., **1993**, 32, 3895–3908.
17. a) J. T. Hupp, G. A. Neyhart and T. J. Meyer, *J. Am. Chem. Soc*., **1986**, 108, 5349–5350; b) J. C. Curtis, J. A. Roberts, R. L. Blackbourn, Y. Dong, M. Massum, C. S. Johnson and J. T. Hupp, *Inorg. Chem*., **1991**, 30, 3856–3860; c) G. A. Neyhart, J. T. Hupp, J. C. Curtis, C. J. Timpson and T. J. Meyer, *J. Am. Chem. Soc*., **1996**, 118, 3724–3729.
18. H. Schottenberger, J. Lukassser, E. Reichel, A. G. Müller, G. Steiner, H. Kopacka, K. Wurst, K. H. Ongania and K. Kirchner, *J. Organomet. Chem*., **2001**, 637–639, 558–576.
19. a) M. A. Esteruelas and H. Werner, *J. Organomet. Chem*., 1986, 303, 221–231; b) H. Werner, M. A. Esteruelas and H. Otto, *Organometallics*, **1986**, 5, 2295–2299.
20. a) A. V. Marchenko, H. Gérard, O. Eisenstein and K. G. Caulton, *New J. Chem*., **2001**, 25, 1244–1255; b) A. V. Marchenko, H. Gérard, O. Eisenstein and K. G. Caulton, *New J. Chem*., **2001**, 25, 1382–1388.
21. a) H. Werner, U. Meyer, K. Peters and H. G. von Schnering, *Chem. Ber.*, **1989**, 122, 2089–2107; b) M. A. Esteruelas, A. V. Gómez, F. M. Lahoz, A. M. López, E. Oñate and L. A. Oro, *Organometallics*, 1996, 15, 3423–3435; c) H. Werner, W. Stüer, B. Weberndörfer and J. Wolf, *Eur. J. Inorg. Chem.*, **1999**, 1707–1713; d) M. L. Buil and M. A. Esteruelas, *Organometallics*, **1999**, 18, 1798–1800.
22. F. Pevny, R. F. Winter, B. Sarkar and S. Záliš, *Dalton Trans*., **2010**, 39, 8000–8011.
23. K. Kowalski, M. Linseis, R. F. Winter, M. Zabel, S. Záliš, H. Kelm, H.-J. Krüger, B. Sarkar and W. Kaim, *Organometallics*, **2009**, 28, 4196–4209.

24. O. S. Abdel-Rahman, J. Maurer, S. Záliš and R. F. Winter, *Organometallics*, **2015**, 34, 3611–3628.
25. S.-H. Choi, I. Bytheway, Z. Lin and G. Jia, *Organometallics*, **1998**, 17, 3974–3980.
26. a) W. Y. Man, J.-L. Xia, N. J. Brown, J. D. Farmer, D. S. Yufit, J. A. K. Howard, S. H. Liu and P. J. Low, *Organometallics*, **2011**, 30, 1852–1858; b) J.-L. Xia, W. Y. Man, X. Zhu, C. Zhang, G.-J. Jin, P. A. Schauer, M. A. Fox, J. Yin, G.-A. Yu, P. J. Low and S. H. Liu, Organometallics, **2012**, 31, 5321–5333; c) S. Záliš, R. F. Winter and W. Kaim, *Coord. Chem. Rev*., **2010**, 254, 1383–1396.
27. P. Mücke, M. Linseis, S. Záliš and R. F. Winter, *Inorg. Chim. Acta*, **2011**, 374, 36–50.
28. S. J. Sherlock, D. C. Boyd, B. Moasser and W. L. Gladfelter, *Inorg. Chem*., **1991**, 30, 3626–3632.
29. X. Wu, T. Weng, S. Jin, J. Liang, R. Guo, G.-a. Yu and S. H. Liu, *J. Organomet. Chem*., **2009**, 694, 1877–1883.
30. C. Hansch, A. Leo and R. W. Taft, *Chem. Rev*., **1991**, 91, 165–195.
31. a) G. K. Wertheim and R. H. Herber, *J. Chem. Phys*., **1963**, 38, 2106–2111; b) R. L. Collins, *J. Chem. Phys*., **1965**, 42, 1072–1075; c) N. N. Greenwood and T. C. Gibb, in: *Mössbauer Spectroscopy*, Chapman and Hall, London, 1971.
32. a) H. Schottenberger, M. R. Buchmeiser and R. H. Herber, J. Organomet. Chem., **2000**, 612, 1–8; b) T. Yamamoto, T. Morikita, T. Maruyama, K. Kubota and M. Katada, *Macromolecules*, **1997**, 30, 5390–5396.
33. a) W. H. Morrison and D. N. Hendrickson, Inorg. Chem., **1975**, 14, 2331–2346; b) J. A. Kramer and D. N. Hendrickson, *Inorg. Chem*., **1980**, 19, 3330–3337; c) M. F. Moore, S. R. Wilson, M. J. Cohn, T. Y. Dong, U. T. Mueller-Westerhoff and D. N. Hendrickson, *Inorg. Chem*., **1985**, 24, 4559–4565.
34. M. C. B. Colbert, J. Lewis, N. J. Long, P. R. Raithby, A. J. P. White and D. J. Williams, *J. Chem. Soc., Dalton Trans.*, **1997**, 99–104.
35. M. Sato, H. Shintate, Y. Kawata, M. Sekino, M. Katada and S. Kawata, *Organometallics*, **1994**, 13, 1956–1962.
36. a) I. Ratera, D. Ruiz-Molina, F. Renz, J. Ensling, K. Wurst, C. Rovira, P. Gütlich and J. Veciana, *J. Am. Chem. Soc*., **2003**, 125, 1462–1463; b) J. Guasch, L. Grisanti, S. Jung, D. Morales, G. D'Avino, M. Souto, X. Fontrodona, A. Painelli, F. Renz, I. Ratera and J. Veciana, *Chem. Mater*., **2013**, 25, 808–814.
37. M. Kondo, M. Uchikawa, K. Namiki, W.-W. Zhang, S. Kume, E. Nishibori, H. Suwa, S. Aoyagi, M. Sakata, M. Murata, Y. Kobayashi and H. Nishihara, *J. Am. Chem. Soc*., **2009**, 131, 12112–12124.
38. a) E. Evangelio and D. Ruiz-Molina, *C. R. Chim*., **2008**, 11, 1137–1154; b) G. D'Avino, L. Grisanti, J. Guasch, I. Ratera, J. Veciana and A. Painelli, *J. Am. Chem. Soc*., **2008**, 130, 12064–12072.
39. a) M. Lohan, P. Ecorchard, T. Rüffer, F. Justaud, C. Lapinte and H. Lang, *Organometallics*, **2009**, 28, 1878–1890; b) J. M. Speck, D. Schaarschmidt and H. Lang, *Organometallics*, **2012**, 31, 1975–1982; c) J. M. Speck, R. Claus, A. Hildebrandt, T. Rüffer, E. Erasmus, L. van As, J. C. Swarts and H. Lang, *Organometallics*, **2012**, 31, 6373–6380.
40. P. Mücke, M. Zabel, R. Edge, D. Collison, S. Clément, S. Záliš and R. F. Winter, *J. Organomet. Chem*., **2011**, 696, 3186–3197.
41. E. Bill, Mfit, Max-Planck Institute for Chemical Energy Conversion, Mülheim an der Ruhr, 2008.
42. G. M. Sheldrick, SHELXL-97, University of Göttingen, **1997**.

7.2. Chapter 3.3 Publication 2

1. Bruning, W. H.; Nelson, R. F.; Marcoux, L. S.; Adams, R. N. J. *Phys. Chem*. **1967**, 71, 3055– 3057 doi: 10.1021/j100868a047
2. Nelson, R. R.; Adams, R. N. *J. Am. Chem. Soc*. **1968**, 90, 3925– 3930 doi: 10.1021/ja01017a004
3. Debrodt, H.; Heusler, K. E. *Z. Phys. Chem*. **1981**, 125, 35– 40 doi: 10.1524/zpch.1981.125.1.035
4. Sreenath, K.; Suneesh, C. V.; Ratheesh Kumar, V. K.; Gopidas, K. R. J. Org. Chem. **2008**, 73, 3245– 3251 doi: 10.1021/jo800349n
5. Reynolds, R.; Line, L. L.; Nelson, R. F. *J. Am. Chem. Soc.* **1974**, 96, 1087– 1092 doi: 10.1021/ja00811a024
6. Eberson, L.; Larsson, B.; Maartmann-Moe, K.; Sæbø, J.; Fischer, G. W. *Acta Chem. Scand.* **1987**, 41b, 367– 378 doi: 10.3891/acta.chem.scand.41b-0367
7. Connelly, N. G.; Geiger, W. E. *Chem. Rev.* **1996**, 96, 877– 910 doi: 10.1021/cr940053x
8. Dapperheld, S.; Steckhan, E.; Brinkhaus, K.-H. G.; Esch, T. *Chem. Ber*. **1991**, 124, 2557– 2567 doi: 10.1002/cber.19911241127
9. Walter, R. I. *J. Am. Chem. Soc*. **1966**, 88, 1923– 1930 doi: 10.1021/ja00961a014
10. Steckhan, E. *Angew. Chem., Int. Ed. Engl*. **1986**, 25, 683– 701 doi: 10.1002/anie.198606831
11. Steckhan, E. *Top. Curr. Chem*. **1987**, 142, 1– 69 doi: 10.1007/3-540-17871-6_11
12. Bender, T. P.; Graham, J. F.; Duff, J. M. *Chem. Mater*. **2001**, 13, 4105– 4111 doi: 10.1021/cm010281p
13. Amthor, S.; Noller, B.; Lambert, C. *Chem. Phys*. **2005**, 316, 141– 152 doi: 10.1016/j.chemphys.2005.05.009
14. Talipov, M. R.; Hossain, M. M.; Boddeda, A.; Thakur, K.; Rathore, R. *Org. Biomol. Chem.* **2016**, 14, 2961– 2968 doi: 10.1039/C6OB00140H
15. Hankache, J.; Wenger, O. S. *Chem. Rev*. **2011**, 111, 5138– 5178 doi: 10.1021/cr100441k
16. Heckmann, A.; Lambert, C. *Angew. Chem., Int. Ed.* **2012**, 51, 326– 392 doi: 10.1002/anie.201100944
17. Coropceanu, V.; Gruhn, N. E.; Barlow, S.; Lambert, C.; Durivage, J. C.; Bill, T. G.; Nöll, G.; Marder, S. R.; Brédas, J.-L. *J. Am. Chem. Soc*. **2004**, 126, 2727– 2731 doi: 10.1021/ja039263u
18. Barlow, S.; Risko, C.; Chung, S.-J.; Tucker, N. M.; Coropceanu, V.; Jones, S. C.; Levi, Z.; Brédas, J.-L.; Marder, S. R. *J. Am. Chem. Soc*. **2005**, 127, 16900– 16911 doi: 10.1021/ja054136e
19. Barlow, S.; Risko, C.; Coropceanu, V.; Tucker, N. M.; Jones, S. C.; Levi, Z.; Khrustalev, V. N.; Antipin, M. Y.; Kinnibrugh, T. L.; Timofeeva, T.; Marder, S. R.; Brédas, J.-L. *Chem. Commun*. **2005**, 764– 766 doi: 10.1039/B415018J
20. Zheng, S.; Barlow, S.; Risko, C.; Kinnibrugh, T. L.; Khrustalev, V. N.; Jones, S. C.; Antipin, M. Y.; Tucker, N. M.; Timofeeva, T. V.; Coropceanu, V.; Brédas, J.-L.; Marder, S. R. *J. Am. Chem. Soc*. **2006**, 128, 1812– 1817 doi: 10.1021/ja0541534

21. Odom, S. A.; Lancaster, K.; Beverina, L.; Lefler, K. M.; Thompson, N. J.; Coropceanu, V.; Brédas, J.-L.; Marder, S. R.; Barlow, S. *Chem. Eur. J*. **2007**, 13, 9637– 9646 doi: 10.1002/chem.200700668
22. Risko, C.; Coropceanu, V.; Barlow, S.; Geskin, V.; Schmidt, K.; Gruhn, N. E.; Marder, S. R.; Brédas, J.-L. J. *Phys. Chem. C* **2008**, 112, 7959– 7967 doi: 10.1021/jp711954j
23. Lancaster, K.; Odom, S. A.; Jones, S. C.; Thayumanavan, S.; Marder, S. R.; Brédas, J.-L.; Coropceanu, V.; Barlow, S. *J. Am. Chem. Soc*. **2009**, 131, 1717– 1723 doi: 10.1021/ja808465c
24. Kaafarani, B. R.; Risko, C.; El-Assaad, T. H.; El-Ballouli, A. a. O.; Marder, S. R.; Barlow, S. J*. Phys. Chem. C* **2016**, 120, 3156– 3166 doi: 10.1021/acs.jpcc.5b11061
25. Lambert, C.; Noell, G. *J. Am. Chem. Soc*. **1999**, 121, 8434– 8442 doi: 10.1021/ja991264s
26. Coropceanu, V.; Malagoli, M.; André, J. M.; Brédas, J. L. *J. Am. Chem. Soc*. **2002**, 124, 10519– 10530 doi: 10.1021/ja026437j
27. Lambert, C.; Nöll, G. *J. Chem. Soc*, Perkin Trans. 2 **2002**, 2039– 2043 doi: 10.1039/B207736A
28. Lambert, C.; Nöll, G.; Schelter, J. *Nat. Mater*. **2002**, 1, 69– 73 doi: 10.1038/nmat706
29. Low, P. J.; Paterson, M. A. J.; Puschmann, H.; Goeta, A. E.; Howard, J. A. K.; Lambert, C.; Cherryman, J. C.; Tackley, D. R.; Leeming, S.; Brown, B. Crystal, *Chem. Eur. J.* **2004**, 10, 83– 91 doi: 10.1002/chem.200305200
30. Szeghalmi, A. V.; Erdmann, M.; Engel, V.; Schmitt, M.; Amthor, S.; Kriegisch, V.; Nöll, G.; Stahl, R.; Lambert, C.; Leusser, D.; Stalke, D.; Zabel, M.; Popp, J. *J. Am. Chem. Soc*. **2004**, 126, 7834– 7845 doi: 10.1021/ja0395386
31. Lambert, C.; Amthor, S.; Schelter, J. *J. Phys. Chem. A* **2004**, 108, 6474– 6468 doi: 10.1021/jp048449s
32. Lambert, C.; Risko, C.; Coropceanu, V.; Schelter, J.; Amthor, S.; Gruhn, N. E.; Durivage, J. C.; Brédas, L.-L. *J. Am. Chem. Soc*. **2005**, 127, 8508– 8516 doi: 10.1021/ja0512172
33. Heckmann, A.; Amthor, S.; Lambert, C. *Chem. Commun*. **2006**, 2959– 2961 doi: 10.1039/B604603G
34 Amthor, S.; Lambert, C. *J. Phys. Chem. A* **2006**, 110, 1177– 1189 doi: 10.1021/jp0550309
35. Seibt, J.; Schaumloeffel, A.; Lambert, C.; Engel, V. *J. Phys. Chem. A* **2008**, 112, 10178– 10184 doi: 10.1021/jp804779s
36. Kattnig, D. R.; Mladenova, B.; Grampp, G.; Kaiser, C.; Heckmann, A.; Lambert, C. *J. Phys. Chem. C* **2009**, 113, 2983– 2995 doi: 10.1021/jp8107705
37. Kaupp, M.; Renz, M.; Parthey, M.; Stolte, M.; Wuerthner, F.; Lambert, *C. Phys. Chem. Chem. Phys.* **2011**, 13, 16973– 16986 doi: 10.1039/c1cp21772k
38. Mladenova, B.; Kattnig, D. R.; Kaiser, C.; Schäfer, J.; Lambert, C.; Grampp, G. *J. Phys. Chem. C* **2015**, 119, 8547– 8553 doi: 10.1021/acs.jpcc.5b01386

39. Schäfer, J.; Holzapfel, M.; Mladenova, B.; Kattnig, D.; Krummenacher, I.; Braunschweig, H.; Grampp, G.; Lambert, C. *J. Am. Chem. Soc.* **2017**, 139, 6200– 6209 doi: 10.1021/jacs.7b01650
40. Nie, H.-J.; Yang, W.-W.; Zheng, R.-H.; Shi, Q.; Chen, H.; Yao, J.; Zhong, Y.-W. *Inorg. Chem.* **2015**, 54, 1272– 1282 doi: 10.1021/ic5024967
41. Jahnke, A. C.; Proppe, J.; Spulber, M.; Palivan, C. G.; Herrmann, C.; Wenger, O. S. *J. Phys. Chem. A* **2014**, 118, 11293– 11303 doi: 10.1021/jp5082164
42. Heckmann, A.; Lambert, C. *J. Am. Chem. Soc*. **2007**, 129, 5515– 5527 doi: 10.1021/ja068235j
43. Kanal, F.; Ruetzel, S.; Lu, H.; Moos, M.; Holzapfel, M.; Brixner, T.; Lambert, C. *J. Phys. Chem. C* **2014**, 118, 23586– 23598 doi: 10.1021/jp508032k
44. Yao, C.-J.; Zheng, R.-H.; Shi, Q.; Zhong, Y.-W.; Yao, J. *Chem. Commun*. **2012**, 48, 5680– 5682 doi: 10.1039/c2cc32471g
45. Tang, J.-H.; Wu, S.-H.; Shao, J.-Y.; Nie, H.-J.; Zhong, Y.-W. *Organometallics* **2013**, 32, 4564– 4570 doi: 10.1021/om400519b
46. Chen, J.; Winter, R. F. *Chem. Eur. J.* **2012**, 18, 10733– 10741 doi: 10.1002/chem.201200800
47. Linseis, M.; Záliš, S.; Zabel, M.; Winter, R. F. *J. Am. Chem. Soc.* **2012**, 134, 16671– 16692 doi: 10.1021/ja3059606
48. Oßwald, S.; Breimaier, S.; Linseis, M.; Winter, R. F. *Organometallics* **2017**, 36, 1993– 2003 doi: 10.1021/acs.organomet.7b00194
49. Maurer, J.; Linseis, M.; Sarkar, B.; Schwederski, B.; Niemeyer, M.; Kaim, W.; Záliš, S.; Anson, C.; Zabel, M.; Winter, R. F. *J. Am. Chem. Soc*. **2008**, 130, 259– 268 doi: 10.1021/ja075547t
50. Záliš, S.; Winter, R. F.; Kaim, W. *Coord. Chem. Rev.* **2010**, 254, 1383– 1396 doi: 10.1016/j.ccr.2010.02.020
51. Mücke, P.; Linseis, M.; Záliš, S.; Winter, R. F. *Inorg. Chim. Acta* **2011**, 374, 36– 50 doi: 10.1016/j.ica.2011.03.071
52. Wuttke, E.; Hervault, Y.-M.; Polit, W.; Linseis, M.; Erler, P.; Rigaut, S.; Winter, R. F. *Organometallics* **2014**, 33, 4672– 4686 doi: 10.1021/om400642j
53. Abdel-Rahman, O. S.; Maurer, J.; Záliš, S.; Winter, R. F., *Organometallics* **2015**, 34, 3611– 3628 doi: 10.1021/acs.organomet.5b00401
54. Man, W. Y.; Xia, J.-L.; Brown, N. J.; Farmer, J. D.; Yufit, D. S.; Howard, J. A. K.; Liu, S. H.; Low, P. J. *Organometallics* **2011**, 30, 1852– 1858 doi: 10.1021/om1010534
55. Xia, J.-L.; Man, W. Y.; Zhu, X.; Zhang, C.; Jin, G.-J.; Schauer, P. A.; Fox, M. A.; Yin, J.; Yu, G.-A.; Low, P. J.; Liu, S. H. *Organometallics* **2012**, 31, 5321– 5333 doi: 10.1021/om300338j
56. Sherlock, S. J.; Boyd, D. C.; Moasser, B.; Gladfelter, W. L. *Inorg. Chem*. **1991**, 30, 3626– 3632 doi: 10.1021/ic00019a011
57. Maurer, J.; Winter, R. F.; Sarkar, B.; Fiedler, J.; Záliš, S. *Chem. Commun*. **2004**, 1900– 1901 doi: 10.1039/B405349D
58. Maurer, J.; Sarkar, B.; Schwederski, B.; Kaim, W.; Winter, R. F.; Záliš, S. *Organometallics* **2006**, 25, 3701– 3712 doi: 10.1021/om0602660

59. Linseis, M.; Winter, R. F.; Sarkar, B.; Kaim, W.; Záliš, S. Multistep Electrochromic *Organometallics* **2008**, 27, 3321– 3324 doi: 10.1021/om8003338
60. Mücke, P.; Zabel, M.; Edge, R.; Collison, D.; Clément, S.; Záliš, S.; Winter, R. F. *J. Organomet. Chem.* **2011**, 696, 3186– 3197 doi: 10.1016/j.jorganchem.2011.06.028
61. Scheerer, S.; Rotthowe, N.; Abdel-Rahman, O. S.; He, X.; Rigaut, S.; Kvapilová, H.; Záliš, S.; Winter, R. F. *Inorg. Chem*. **2015**, 54, 3387– 3402 doi: 10.1021/ic503075e
62. Fink, D.; Weibert, B.; Winter, R. F. *Chem. Commun*. **2016**, 52, 6103– 6106 doi: 10.1039/C6CC00936K
63. Pfaff, U.; Hildebrandt, A.; Korb, M.; Oßwald, S.; Linseis, M.; Schreiter, K.; Spange, S.; Winter, R. F.; Lang, H. *Chem. Eur. J*. **2016**, 22, 783– 801 doi: 10.1002/chem.201503687
64. Scheerer, S.; Linseis, M.; Wuttke, E.; Weickert, S.; Drescher, M.; Tröppner, O.; Ivanović-Burmazović, I.; Irmler, A.; Pauly, F.; Winter, R. F. *Chem. Eur. J.* **2016**, 22, 9574– 9590 doi: 10.1002/chem.201601384
65. Wu, X.; Weng, T.; Jin, S.; Liang, J.; Guo, R.; Yu, G.-a.; Liu, S. H. *J. Organomet. Chem*. **2009**, 694, 1877– 1883 doi: 10.1016/j.jorganchem.2009.01.024
66. Wu, X. H.; Jin, S.; Liang, J. H.; Li, Z. Y.; Yu, G.-a.; Liu, S. H. *Organometallics* **2009**, 28, 2450– 2459 doi: 10.1021/om900018y
67. Ou, Y.-P.; Jiang, C.; Wu, D.; Xia, J.; Yin, J.; Jin, S.; Yu, G.-A.; Liu, S. H. *Organometallics* **2011**, 30, 5763– 5770 doi: 10.1021/om200622q
68. Tian, L. Y.; Liu, Y. M.; Tian, G.-X.; Wu, X. H.; Li, Z.; Kou, J.-F.; Ou, Y.-P.; Liu, S. H.; Fu, W.-F. *Dalton Trans*. **2014**, 43, 4093– 4101 doi: 10.1039/c3dt52677a
69. Xia, J.; Ou, Y.-P.; Meng, X.-G.; Yin, J.; Yu, G.-a.; Liu, S. H. Eur. *J. Inorg. Chem*. **2014**, 2014, 247– 255 doi: 10.1002/ejic.201301304
70. Zhang, J.; Ou, Y.; Xu, M.; Sun, C.; Yin, J.; Yu, G.-A.; Liu, S. H. *Synthesis and Eur. J. Inorg. Chem.* 2014, **2014**, 2941– 2951 doi: 10.1002/ejic.201402106
71. Kong, D.-D.; Xue, L.-S.; Jang, R.; Liu, B.; Meng, X.-G.; Jin, S.; Ou, Y.-P.; Hao, X.; Liu, S.-H. *Chem. Eur. J.* **2015**, 21, 9895– 9904 doi: 10.1002/chem.201500509
72. Zhang, J.; Sun, C.-F.; Wu, X.-H.; Zhang, M.-X.; Yin, J.; Yu, G.-A.; Liu, S. H. *Int. J. Electrochem. Sci.* **2016**, 11, 7875– 7889 doi: 10.20964/2016.09.34
73. Polit, W.; Exner, T.; Wuttke, E.; Winter, R. F. *BioInorg. React. Mech*. **2012**, 8, 85– 105 doi: 10.1515/irm-2012-0005
74. Polit, W.; Mücke, P.; Wuttke, E.; Exner, T.; Winter, R. F. *Organometallics* **2013**, 32, 5461– 5472 doi: 10.1021/om4007455
75. Chiu, K. Y.; Su, T.-H.; Huang, C. W.; Liou, G.-S.; Cheng, S.-H. *J. Electroanal. Chem.* **2005**, 578, 283– 287 doi: 10.1016/j.jelechem.2005.01.010
76. Yano, M.; Ishida, Y.; Aoyama, K.; Tatsumi, M.; Sato, K.; Shiomi, D.; Ichimura, A.; Takui, T. *Synth. Met*. **2003**, 137, 1275– 1276 doi: 10.1016/S0379-6779(02)01137-2

77. Wuttke, E.; Fink, D.; Anders, P.; Maria Hoyt, A.-L.; Polit, W.; Linseis, M.; Winter, R. F. *J. Organomet. Chem.* **2016**, 821, 4– 18 doi: 10.1016/j.jorganchem.2016.02.031
78. Pevny, F.; Di Piazza, E.; Norel, L.; Drescher, M.; Winter, R. F.; Rigaut, S. *Organometallics* **2010**, 29, 5912– 5918 doi: 10.1021/om1007133
79. Wuttke, E.; Pevny, F.; Hervault, Y.-M.; Norel, L.; Drescher, M.; Winter, R. F.; Rigaut, S. *Inorg. Chem*. **2012**, 51, 1902– 1915 doi: 10.1021/ic2022177
80. Hupp, J. T.; Neyhart, G. A.; Meyer, T. J. *J. Am. Chem. Soc*. **1986**, 108, 5349– 5350 doi: 10.1021/ja00277a052
81. Ott, I.; Kowalski, K.; Gust, R.; Maurer, J.; Mücke, P.; Winter, R. F. *Bioorg. Med. Chem. Lett.* **2010**, 20, 866– 869 doi: 10.1016/j.bmcl.2009.12.080
82. Planells, M.; Abate, A.; Hollman, D. J.; Stranks, S. D.; Bharti, V.; Gaur, J.; Mohanty, D.; Chand, S.; Snaith, H. J.; Robertson, N. J. *Mater. Chem. A* **2013**, 1, 6949– 6960 doi: 10.1039/c3ta11417a
83. Chowdhury, A.; Mukherjee, P. S. *J. Org. Chem*. **2015**, 80, 4064– 4075 doi: 10.1021/acs.joc.5b00348
84. Kim, C.; Choi, H.; Paek, S.; Kim, J.-J.; Song, K.; Kang, M.-S.; Ko, J. J. *Photochem. Photobiol., A* **2011**, 225, 17– 25 doi: 10.1016/j.jphotochem.2011.09.020
85. Li, Z. a.; Ye, T.; Tang, S.; Wang, C.; Ma, D.; Li, Z. *J. Mater. Chem. C* **2015**, 3, 2016– 2023 doi: 10.1039/C4TC01923G
86. Werner, H.; Esteruelas, M. A.; Otto, H. *Organometallics* **1986**, 5, 2295– 2299 doi: 10.1021/om00142a019
87. Hill, A. F. In *Comprehensive Organometallic Chemistry II*; Shriver, D. E.; Bruce, M. I., Eds.; Pergamon: Oxford, U.K., **1995**; Vol. 7, pp 399– 411.
88. Marchenko, A. V.; Gérard, H.; Eisenstein, O.; Caulton, K. G. *New J. Chem*. **2001**, 25, 1244– 1255 doi: 10.1039/b103815j
89. Marchenko, A. V.; Gérard, H.; Eisenstein, O.; Caulton, K. G. *New J. Chem*. **2001**, 25, 1382– 1388 doi: 10.1039/b103113a
90. Richardson, D. E.; Taube, H. *Coord. Chem. Rev*. **1984**, 60, 107– 129 doi: 10.1016/0010-8545(84)85063-8
91. D'Alessandro, D. M.; Keene, F. R. *Dalton Trans*. **2004**, 3950– 3954 doi: 10.1039/b413980a
92. Winter, R. F. *Organometallics* **2014**, 33, 4517– 4536 doi: 10.1021/om500029x
93. Santi, S.; Bisello, A.; Cardena, R.; Donoli, A. *Dalton Trans*. **2015**, 44, 5234– 5257 doi: 10.1039/C4DT03581J
94. Hassenrück, C.; Mücke, P.; Scheck, J.; Demeshko, S.; Winter, R. F. Eur. *J. Inorg. Chem*. **2017**, 2017, 401– 411 doi: 10.1002/ejic.201600776
95. Krejcik, M.; Danek, M.; Hartl, F. *J. Electroanal. Chem. Interfacial Electrochem.* **1991**, 317, 179– 187 doi: 10.1016/0022-0728(91)85012-E
96. Selby, T. D.; Blackstock, S. C. *J. Am. Chem. Soc.* **1998**, 120, 12155– 12156 doi: 10.1021/ja9821091
97. Ovchinnikov, A. A. *Theor. Chim. Acta* **1978**, 47, 297– 304 doi: 10.1007/BF00549259
98. Barlow, S.; Risko, C.; Odom, S. A.; Zheng, S.; Coropceanu, V.; Beverina, L.; Brédas, J.-L.; Marder, S. R. *J. Am. Chem. Soc*. **2012**, 134, 10146– 10155 doi: 10.1021/ja3023048

99. Nie, H.-J.; Yao, C.-J.; Shao, J.-Y.; Yao, J.; Zhong, Y.-W. *Chem. Eur. J.* **2014**, 20, 17454– 17465 doi: 10.1002/chem.201403847
100. Koide, T.; Furukawa, K.; Shinokubo, H.; Shin, J.-Y.; Kim, K. S.; Kim, D.; Osuka, A. *J. Am. Chem. Soc.* **2010**, 132, 7246– 7247 doi: 10.1021/ja101040s
101. Li, Y.; Heng, W.-K.; Lee, B. S.; Aratani, N.; Zafra, J. L.; Bao, N.; Lee, R.; Sung, Y. M.; Sun, Z.; Huang, K.-W.; Webster, R. D.; López Navarrete, J. T.; Kim, D.; Osuka, A.; Casado, J.; Ding, J.; Wu, J. *J. Am. Chem. Soc*. **2012**, 134, 14913– 14922 doi: 10.1021/ja304618v
102. Abe, M. *Chem. Rev*. **2013**, 113, 7011– 7088 doi: 10.1021/cr400056a
103. Renz, M.; Theilacker, K.; Lambert, C.; Kaupp, M. *J. Am. Chem. Soc.* **2009**, 131, 16292– 16302 doi: 10.1021/ja9070859
104. Parthey, M.; Kaupp, M. *Chem. Soc. Rev*. **2014**, 43, 5067– 5088 doi: 10.1039/C3CS60481K
105. Völker, S. F.; Renz, M.; Kaupp, M.; Lambert, C. *Chem. Eur. J*. **2011**, 17, 14147– 14163 doi: 10.1002/chem.201102227
106. Carlson, R. K.; Odoh, S. O.; Tereniak, S. J.; Lu, C. C.; Gagliardi, L. *J. Chem. Theory Comput.* **2015**, 11, 4093– 4101 doi: 10.1021/acs.jctc.5b00412
107. Nelsen, S. F.; Konradsson, A. E.; Weaver, M. N.; Telo, J. P. *J. Am. Chem. Soc.* **2003**, 125, 12493– 12501 doi: 10.1021/ja036066m
108. Nelsen, S. F. *Chem. Eur. J.* **2000**, 6, 581– 588 doi: 10.1002/(SICI)1521-3765(20000218)6:4<581::AID-CHEM581>3.0.CO;2-E
109. Low, P. J.; Paterson, M. A. J.; Goeta, A. E.; Yufit, D. S.; Howard, J. A. K.; Cherryman, J. C.; Tackley, D. R.; Brown, B. *J. Mater. Chem*. **2004**, 14, 2516– 2523 doi: 10.1039/B404731A
110 Sutin, N. *Prog. Inorg. Chem*. **1983**, 30, 441– 499 doi: 10.1002/9780470166314.ch9
111 Brunschwig, B. S.; Creutz, C.; Sutin, N. *Chem. Soc. Rev*. **2002**, 31, 168 doi: 10.1039/b008034i
112. Coropceanu, V.; Lambert, C.; Nöll, G.; Brédas, J. L. *Chem. Phys. Lett*. **2003**, 373, 153– 160 doi: 10.1016/S0009-2614(03)00553-0
113. Coropceanu, V.; André, J. M.; Malagoli, M.; Brédas, J. L. *Theor. Chem. Acc*. **2003**, 110, 59– 69 doi: 10.1007/s00214-003-0445-3
114. Creutz, C.; Newton, M. D.; Sutin, N. J. *Photochem. Photobiol., A* **1994**, 82, 47 doi: 10.1016/1010-6030(94)02013-2
115. Stoll, S.; Schweiger, A. *J. Magn. Reson*. **2006**, 178, 42– 55 doi: 10.1016/j.jmr.2005.08.013
116. Frisch, M. J.; Trucks, G.; Schlegel, H. B.; Scuseria, G. E.; Robb, M. A.; Cheeseman, J. R.; Scalmani, G.; Barone, V.; Mennucci, B.; Petersson, G. A.; Nakatsuji, H.; Caricato, M.; Li, X.; Hratchian, H. P.; Izmaylov, A. F.; Blonio, J.; Zheng, G.; Sonnenberg, J. L.; Hada, M.; Ehara, M.; Toyota, K.; Fukuda, R.; Hasegawa, J.; Ishida, M.; Nakajima, T.; Honda, Y.; Kitao, O.; Nakai, H.; Vreven, T.; Montgomery, J. A., Jr.; Peralta, J. E.; Ogliaro, F.; Bearpark, M.; Heyd, J. J.; Brothers, E.; Kudin, K. N.; Staroverov, V. N.; Keith, T.; Kobayashi, R.; Normand, J.; Raghavachari, K.; Rendell, A.; Burant, J. C.; Iyengar, S. S.; Tomasi, J.; Cossi, M.; Rega, N.; Millam, J. M.; Klene, M.; Knox, J. E.; Cross, J. B.; Bakken, V.; Adamo, C.; Jaramillo, J.; Gomperts, R.; Stratmann, R. E.; Yazyev, O.; Austin, A. J.; Cammi, R.; Pomelli, C.; Ochterski, J. W.; Martin, R. L.;

Morokuma, K.; Zakrzewski, V. G.; Voth, G. A.; Salvador, P.; Dannenberg, J. J.; Dapprich, S.; Daniels, A. D.; Farkas, Ö.; Foresman, J. B.; Ortiz, J. V.; Cioslowski, J.; Fox, D. J. Gaussian 09, revision B.01; Gaussian Inc.: Wallingford, CT, **2010**.
117. Andrae, D.; Haeussermann, U.; Dolg, M.; Stoll, H.; Preuss, H. *Theor. Chim. Acta* **1990**, 77, 123– 141 doi: 10.1007/BF01114537
118. Perdew, J. P.; Burke, K.; Ernzerhof, M. *Phys. Rev. Lett.* **1996**, 77, 3865– 3868 doi: 10.1103/PhysRevLett.77.3865
119. Cossi, M.; Rega, N.; Scalmani, G.; Barone, V. *J. Comput. Chem.* **2003**, 24, 669– 681 doi: 10.1002/jcc.10189

7.3. Chapter 3.4 Publication 3

1. LeVanda, C.; Bechgaard, K.; Cowan, D. O. *J. Org. Chem.* **1976**, *41*, 2700-2704.
2. Cowan, D. O.; LeVanda, C.; Park, J.; Kauffman, F. *Acc. Chem. Res.* **1973**, *6*, 1-7.
3. Kramer, J. A.; N. Hendrickson, D. *Inorg. Chem.* **1980**, *19*, 3330-3337.
4. Hendrickson, D. N.; Oh, S. M.; Dong, T.-Y.; Kambara, T.; Cohn, M. J.; Moore, M. F. *Comm. Inorg. Chem.* **1985**, *4*, 329-349.
5. Dong, T.-Y.; Kambara, T.; Hendrickson, D. N. *J. Am. Chem. Soc.* **1986**, *108*, 4423-4432.
6. Lowery, M. D.; Hammack, W. S.; Drickamer, H. G.; Hendrickson, D. N. *J. Am. Chem. Soc.* **1987**, *109*, 8019-8024.
7. Lohan, M.; Ecorchard, P.; Rüffer, T.; Justaud, F.; Lapinte, C.; Lang, H. *Organometallics* **2009**, *28*, 1878-1890.
8. Lohan, M.; Justaud, F.; Roisnel, T.; Ecorchard, P.; Lang, H.; Lapinte, C. *Organometallics* **2010**, *29*, 4804-4817.
9. Lohan, M.; Justaud, F.; Lang, H.; Lapinte, C. *Organometallics* **2012**, *31*, 3565-3574.
10. Wilson, L. E.; Hassenrück, C.; Winter, R. F.; White, A. J. P.; Albrecht, T.; Long, N. J. *Eur. J. Inorg. Chem.* **2017**, *2017*, 496-504.
11. Wilson, L. E.; Hassenrück, C.; Winter, R. F.; White, A. J. P.; Albrecht, T.; Long, N. J. *Angew. Chem. Int. Ed.* **2017**, *56*, 6838-6842.
12. Hoffmann, V.; le Pleux, L.; Häussinger, D.; Unke, O. T.; Prescimone, A.; Mayor, M *Organometallics* **2017**, *36*, 858-866.
13. Sato, M.; Hayashi, Y.; Shintate, H.; Katada, M.; Kawata, S. *J. Organomet. Chem.* **1994**, *471*, 179-184.
14. Sato, M.; Hayashi, Y.; Kumakura, S.; Shimizu, N.; Katada, M.; Kawata, S. *Organometallics* **1996**, *15*, 721-728.
15. Sato, M.; Shintate, H.; Kawata, Y.; Sekino, M.; Katada, M.; Kawata, S. *Organometallics* **1994**, *13*, 1956-1962.
16. Colbert, M. C. B.; Lewis, J.; Long, N. J.; Raithby, P. R.; White, A. J. P.; Williams, D. J. *J. Chem. Soc., Dalton Trans.* **1997**, 99-104.
17. Sato, M.; Kawata, Y.; Shintate, H.; Habata, Y.; Akabori, S.; Unoura, K. *Organometallics* **1997**, *16*, 1693-1701.
18. Sato, M.; Iwai, A.; Watanabe, M. *Organometallics* **1999**, *18*, 3208-3219.
19. Kuwana, T.; Bublitz, D. E.; Hoh, G. *J. Am. Chem. Soc.* **1960**, *82*, 5811-5817.
20. Denisovich, L. I.; Zakurin, N. V.; Bezrukova, A. A.; Gubin, S. P. *J. Organomet. Chem* **1974**, *81*, 207-216.
21. Sohn, Y. S.; Schlueter, A. W.; Hendrickson, D. N.; Gray, H. B. *Inorg. Chem.* **1974**, *13*, 301-304.

22. Kukharenko, S. V.; Strelets, V. V.; Kudinov, A. R.; Kreidlin, A. Z.; Peterleitner, M. G.; Denisovich, L. I.; Rybinskaya, M. I. *J. Organomet. Chem.* **1996**, *519*, 1-5.
23. Swarts, J. C.; Nafady, A.; Roudebush, J. H.; Trupia, S.; Geiger, W. E. *Inorg. Chem.* **2009**, *48*, 2156-2165.
24. Polit, W.; Mücke, P.; Wuttke, E.; Exner, T.; Winter, R. F. *Organometallics* **2013**, *32*, 5461-5472.
25. Robin, M. B.; Day, P. *Chem. Radiochem.* **1967**, *10*, 247-422.
26. Kowalski, K.; Linseis, M.; Winter, R. F.; Zabel, M.; Záliš, S.; Kelm, H.; Krüger, H.-J.; Sarkar, B.; Kaim, W. *Organometallics* **2009**, *28*, 4196-4209.
27. Pevny, F.; Di Piazza, E.; Norel, L.; Drescher, M.; Winter, R. F.; Rigaut, S. *Organometallics* **2010**, *29*, 5912-5918.
28. Wuttke, E.; Fink, D.; Anders, P.; Maria Hoyt, A.-L.; Polit, W.; Linseis, M.; Winter, R. F. *J. Organomet. Chem* **2016**, *821*, 4-18.
29. Wuttke, E.; Hervault, Y.-M.; Polit, W.; Linseis, M.; Erler, P.; Rigaut, S.; Winter, R. F. *Organometallics* **2014**, *33*, 4672-4686.
30. Polit, W.; Exner, T.; Wuttke, E.; Winter, R. F. *Bioinorg. React. Mech.* **2012**, *8*, 85-105.
31. Hassenrück, C.; Winter, R. F. *Inorg. Chem.* **2017**, *56*, 13517-13529.
32. Chen, J.; Wuttke, E.; Polit, W.; Exner, T.; Winter, R. F. *J. Am. Chem. Soc.* **2013**, *135*, 3391-3394.
33. Hassenrück, C.; Mücke, P.; Scheck, J.; Demeshko, S.; Winter, R. F. *Eur. J. Inorg. Chem.* **2017**, *2017*, 401-411.
34. Sato, M.; Kawata, Y.; Kudo, A.; Iwai, A.; Saitoh, H.; Ochiai, S. *J. Chem. Soc., Dalton Trans.* **1998**, 2215-2224.
35. Sato, M.; Kubota, Y.; Kawata, Y.; Fujihara, T.; Unoura, K.; Oyama, A. *Chem. Eur. J.* **2006**, *12*, 2282-2292.
36. Bruce, M. I.; Jevric, M.; Perkins, G. J.; Skelton, B. W.; White, A. H. *J. Organomet. Chem.* **2007**, *692*, 1757-1765.
37. Werner, H.; Esteruelas, M. A.; Otto, H. *Organometallics* **1986**, *5*, 2295-2299.
38. Hill, A. F. Comprehensive Organometallic Chemistry II. In Shriver, D. E.; Bruce, M. I., Eds. Pergamon: Oxford, 1995; Vol. 7, pp 399-411.
39. Marchenko, A. V.; Gérard, H.; Eisenstein, O.; Caulton, K. G. *New J. Chem.* **2001**, *25*, 1244-1255.
40. Marchenko, A. V.; Gérard, H.; Eisenstein, O.; Caulton, K. G. *New J. Chem.* **2001**, *25*, 1382-1388.
41. Choi, S.-H.; Bytheway, I.; Lin, Z.; Jia, G. *Organometallics* **1998**, *17*, 3974-3980.
42. Hill, M. G.; Lamanna, W. M.; Mann, K. R. *Inorg. Chem.* **1991**, *30*, 4687-4690.
43. Barrière, F.; Camire, N.; Geiger, W. E.; Mueller-Westerhoff, U. T.; Sanders, R. *J. Am. Chem. Soc.* **2002**, *124*, 7262-7263.
44. Barrière, F.; Geiger, W. E. *J. Am. Chem. Soc.* **2006**, *128*, 3980-3989.
45. Maurer, J.; Linseis, M.; Sarkar, B.; Schwederski, B.; Niemeyer, M.; Kaim, W.; Záliš, S.; Anson, C.; Zabel, M.; Winter, R. F. *J. Am. Chem. Soc.* **2008**, *130*, 259-268.
46. Gassman, P. G.; Sowa, J. R.; Hill, M. G.; Mann, K. R. *Organometallics* **1995**, *14*, 4879-4885.
47. Maurer, J.; Sarkar, B.; Schwederski, B.; Kaim, W.; Winter, R. F.; Záliš, S*Organometallics* **2006**, *25*, 3701-3712.
48. Linseis, M.; Winter, R. F.; Sarkar, B.; Kaim, W.; Záliš, S. *Organometallics* **2008**, *27*, 3321-3324.
49. Wuttke, E.; Pevny, F.; Hervault, Y.-M.; Norel, L.; Drescher, M.; Winter, R. F.; Rigaut, S. *Inorg. Chem.* **2012**, *51*, 1902-1915.
50. Scheerer, S.; Rotthowe, N.; Abdel-Rahman, O. S.; He, X.; Rigaut, S.; Kvapilová, H.; Záliš, S.; Winter, R. F*Inorg. Chem.* **2015**, *54*, 3387-3402.

51. Pfaff, U.; Hildebrandt, A.; Korb, M.; Oßwald, S.; Linseis, M.; Schreiter, K.; Spange, S.; Winter, R. F.; Lang, H *Chem. Eur. J.* **2016**, *22*, 783-801.
52. Abdel-Rahman, O. S.; Jan, M. T.; Oßwald, S.; Winter, R. F. *J. Organomet. Chem.* **2017**, *849-850*, 98-116.
53. Wu, X. H.; Jin, S.; Liang, J. H.; Yong, Z.; Yu, G.-a.; Liu, S. H. *Organometallics* **2009**, *28*, 2450-2459.
54. Ou, Y.-P.; Jiang, C.; Wu, D.; Xia, J.; Yin, J.; Jin, S.; Yu, G.-A.; Liu, S. H. *Organometallics* **2011**, *30*, 5763-5770.
55. Tian, L. Y.; Liu, Y. M.; Tian, G.-X.; Wu, X. H.; Li, Z.; Kou, J.-F.; Ou, Y.-P.; Liu, S. H.; Fu, W.-F. *Dalton Trans.* **2014**, *43*, 4093-4101.
56. Zhang, J.; Ou, Y.; Xu, M.; Sun, C.; Yin, J.; Yu, G.-A.; Liu, S. H. *Eur. J. Inorg. Chem.* **2014**, *2014*, 2941-2951.
57. Kong, D.-D.; Xue, L.-S.; Jang, R.; Liu, B.; Meng, X.-G.; Jin, S.; Ou, Y.-P.; Hao, X.; Liu, S.-H*Chem. Eur. J.* **2015**, *21*, 9895-9904.
58. Zhang, J.; Sun, C.-F.; Wu, X.-H.; Zhang, M.-X.; Yin, J.; Yu, G.-A.; Liu, S. H. *Int J. Electrochem. Sci.* **2016**, *11*, 7875-7889.
59. Fink, D.; Weibert, B.; Winter, R. F. *Chem. Commun.* **2016**, *52*, 6103-6106.
60. Fink, D.; Bodensteiner, M.; Linseis, M.; Winter, R. F. *Chem. Eur. J.* **2018**, *24*, 992-996.
61. Fink, D.; Linseis, M.; Winter, R. F. *Organometallics* **2018**, *37*, 1817-1820.
62. Krejcik, M.; Danek, M.; Hartl, F. *J. Electroanal. Chem.* **1991**, *317*, 179-187.
63. Koelle, U.; Salzer, A. *J. Organomet. Chem.* **1983**, *243*, C27-C30.
64. Prins, R.; Korswagen, A. R. *J. Organomet. Chem.* **1970**, *25*, C74-C76.
65. Duggan, D. E. M.; Hendrickson, D. N. *Inorg. Chem.* **1975**, *14*, 955-970.
66. Miller, J. S.; Glatzhofer, D. T.; O'Hare, D. M.; Reiff, W. M.; Chakraborty, A.; Epstein, A. J. *Inorg. Chem.* **1989**, *28*, 2930-2939.
67. Pevny, F.; Winter, R. F.; Sarkar, B.; Záliš, S. *Dalton Trans.* **2010**, 8000-8011.
68. Mücke, P.; Zabel, M.; Edge, R.; Collison, D.; Clément, S.; Záliš, S.; Winter, R. F. *J. Organomet. Chem.* **2011**, *696*, 3186-3197.
69. Linseis, M.; Záliš, S.; Zabel, M.; Winter, R. F. *J. Am. Chem. Soc.* **2012**, *134*, 16671-16692.
70. Abdel-Rahman, O. S.; Maurer, J.; Záliš, S.; Winter, R. F. *Organometallics* **2015**, *34*, 3611-3628.
71. Coropceanu, V.; Malagoli, M.; André, J. M.; Brédas, J. L. *J. Chem. Phys.* **2001**, *115*, 10409-10416.
72. Barlow, S.; Risko, C.; Odom, S. A.; Zheng, S.; Coropceanu, V.; Beverina, L.; Brédas, J.-L.; Marder, S. R. *J. Am. Chem. Soc.* **2012**, *134*, 10146-10155.
73. Allen, G. C.; Hush, N. S.. *Prog. Inorg. Chem.* **1967**, *8*, 357-389.
74. Hush, N. S. *Prog. Inorg. Chem.* **1967**, *8*, 391-444.
75. Brunschwig, B.; Creutz, C.; Sutin, N. *Chem. Soc. Rev.* **2002**, *31*, 168-184.
76. Lambert, C.; Nöll, G. *J. Am. Chem. Soc.* **1999**, *121*, 8434-8442.
77. Coropceanu, V.; Lambert, C.; Nöll, G.; Brédas, J. L. *Chem. Phys. Lett.* **2003**, *373*, 153-160.
78. Coropceanu, V.; Gruhn, N. E.; Barlow, S.; Lambert, C.; Duvirage, J. C.; Bill, T. G.; Nöll, G.; Marder, S. R.; Brédas, J.-L. *J. Am. Chem. Soc.* **2004**, *126*, 2727-2731.
79. Coropceanu, V.; Malagoli, M.; André, J. M.; Brédas, J. L. *J. Am. Chem. Soc.* **2002**, *124*, 10519-10530.
80. Cheng, T.; Tan, Y. N.; Zhang, Y.; Zhang, Y. Y.; Meng, M.; Lei, H.; Chen, L.; Liu, C. Y. *Chem. Eur. J.* **2015**, *21*, 2353-2357.
81. Bailey, S. E.; Zink, J. I.; Nelsen, S. F. *J. Am. Chem. Soc.* **2003**, *125*, 5939-5947.
82. Richardson, D. E.; Taube, H. *Coord. Chem. Rev.* **1984**, *60*, 107-129.
83. D'Alessandro, D. M.; Keene, F. R. *Chem. Soc. Rev.* **2006**, *35*, 424-440.
84. Winter, R. F. *Organometallics* **2014**, *33*, 4517-4536.
85. Santi, S.; Bisello, A.; Cardena, R.; Donoli, *Dalton Trans.* **2015**, *44*, 5234-5257.

86. Evans, C. E. B.; Naklicki, M. L.; Rezvani, A. R.; White, C. A.; Kondratiev, V. V.; Crutchley, R. J. *J. Am. Chem. Soc.* **1998**, *120*, 13096-13103.
87. Lin, Y.-C.; Chen, W.-T.; Tai, J.; Su, D.; Huang, S.-Y.; Lin, I.; Lin, J.-L.; Lee, M. M.; Chiou, M. F.; Liu, Y.-H.; Kwan, K.-S.; Chen, Y.-J. *Inorg. Chem.* **2009**, *48*, 1857-1870.
88. Crutchley, R. J. *Adv. Inorg. Chem.*, Sykes, A. G., Ed. Academic Press: 1994; Vol. 41, pp 273-325.
89. Ammar, F.; Savéant, J. M. *J. Electroanal. Chem.* **1973**, *47*, 115-125.
90. Salaymeh, F.; Berhane, S.; Yusof, R.; de la Rosa, R.; Fung, E. Y.; Matamoros, R.; Lau, K. W.; Zheng, Q.; Kober, E. M.; Curtis, J. C. *Inorg. Chem.* **1993**, *32*, 3895-3908.
91. De la Rosa, R.; Chang, P. J.; Salaymeh, F.; Curtis, J. C. *Inorg. Chem.* **1985**, *24*, 4229-4231.
92. Bertrand, P. *Chem. Phys. Lett.* **1985**, *113*, 104-107.
93. Tuczek, F.; Solomon, E. I. *Inorg. Chem.* **1993**, *32*, 2850-2862.
94. Brunschwig, B. S.; Sutin, N. *Coord. Chem. Rev.* **1999**, *187*, 233-254.
95. Barlow, S. *Inorg. Chem.* **2001**, *40*, 7047-7053.
96. Santi, S.; Orian, L.; Durante, C.; Bencze, E. Z.; Bisello, A.; Donoli, A.; Ceccon, A.; Benetello, F.; Crociani, L. *Chem. Eur. J.* **2007**, *13*, 7933-7947.
97. Santi, S.; L.Orian; Durante, C.; Bisello, A.; Benetollo, F.; Crociani, L.; Ganis, P.; Ceccon, A. *Chem. Eur. J.* **2007**, *13*, 1955-1968.
98. Chen, P.; Meyer, T. J *Chem. Rev.* **1998**, *98*, 1439-1477.
99. Demadis, K. D.; Hartshorn, C. M.; Meyer, T. J. *Chem. Rev.* **2001**, *101*, 2655-2686.
100. Lear, B. J.; Glover, S. D.; Salsman, C.; Londergan, C. H.; Kubiak, C. P. *J. Am. Chem. Soc.* **2007**, *129*, 12772-12779.
101. Glover, S. D.; Goeltz, J. C.; Lear, B. J.; Kubiak, C. P. *Coord. Chem. Rev.* **2010**, *254*, 331-345.
102. Kubiak, C. P *Inorg. Chem.* **2013**, *52*, 5663-5676.
103. Gassman, P. G.; Winter, C. H *J. Am. Chem. Soc.* **1988**, *110*, 6130-6135.

8. Appendix: Publications as co-author

1. Vanicek, S.; Kopacka, H.; Wurst, K.; Müller, T.; Hassenrück, C.; Winter, R. F.; Bildstein, B. *Organometallics* **2016,** *35*, 2101-2109 doi: 10.1021/acs.organomet.6b00329.

2. Wilson, L. E.; Hassenrück, C.; Winter, R. F.; White, A. J. P.; Albrecht, T.; Long, N. J. *Angew. Chem.* **2017,** *129*, 6942-6946, doi: 10.1002/ange.201702006.

3. Wilson, L. E.; Hassenrück, C.; Winter, R. F.; White, A. J. P.; Albrecht, T.; Long, N. J. *Eur. J. Inorg. Chem.* **2017,** *2017*, 496-504, doi: 10.1002/ange.201702006.

4. Vanicek, S.; Podewitz, M.; Hassenrück, C.; Pittracher, M.; Kopacka, H.; Wurst, K.; Müller, T.; Liedl, K. R.; Winter, R. F.; Bildstein, B. *Chemistry – A European Journal* **2018,** *24*, 3165-3169, doi: 10.1002/ejic.201601036.

5. Weststrate, N.-a.; Bouwer, S.; Hassenrück, C.; van Jaarsveld, N. A.; Liles, D. C.; Winter, R. F.; Lotz, S. *J. Organomet. Chem.* **2018,** *869*, 54-66, doi: 10.1016/j.jorganchem.2018.05.022.

6. Inge Schlapp-Hackl, Christopher Hassenrück, Klaus Wurst, Holger Kopacka, Thomas Müller, Rainer F. Winter*, Benno Bildstein*, *Eur. J. Inorg. Chem*. **2018**, 4434-4441, doi: 10.1002/ejic.201800774

7. Stefan Vanicek, Markus Jochriem, Christopher Hassenrück, Souvik Roy , Holger Kopacka, Klaus Wurst, Thomas Müller, Rainer F. Winter* , Erwin Reisner*, and Benno Bildstein*, *Organometallics*, **2019**, *38*, 6, 1361-1371, doi: 10.1021/acs.organomet.8b00681